

# WOFEX 2017

proceedings of the 15<sup>th</sup> annual workshop

Faculty of Electrical Engineering and Computer Science,  
VŠB – Technical University of Ostrava

ISBN 978-80-248-4056-7



# WOFEX 2017 wofex

<http://wofex.vsb.cz/2017/>

15<sup>th</sup> annual workshop,  
Ostrava, 12<sup>th</sup> September 2017  
Proceedings of papers

*Organized by*

VŠB – Technical University of Ostrava  
Faculty of Electrical Engineering and Computer Science



WOFEX 2017

© Michal Krátký, Jiří Dvorský, Pavel Moravec, editors

ISBN 978-80-248-4056-7

This work is subject to copyright. All rights reserved. Reproduction or publication of this material, even partial, is allowed only with the editors' permission.

Page count: 485  
Impression: 200  
Edition: 1<sup>st</sup>  
First published: 2017

This proceedings was typeset by pdfL<sup>A</sup>T<sub>E</sub>X.

Published by Faculty of Electrical Engineering and Computer Science, VŠB – Technical University of Ostrava

# Preface

The workshop WOFEX 2017 (PhD workshop of Faculty of Electrical Engineering and Computer Science) was held on September 12<sup>th</sup> September 2017 at the VŠB – Technical University of Ostrava. The workshop offers an opportunity for students to meet and share their research experiences, to discover commonalities in research and studentship, and to foster a collaborative environment for joint problem solving. PhD students are encouraged to attend in order to ensure a broad, unconfined discussion. In that view, this workshop is intended for students and researchers of this faculty offering opportunities to meet new colleagues.

This book of proceedings includes 77 papers of faculty PhD students and 3 papers of external authors. The proceedings of WOFEX 2017 are also available at the web site <http://wofex.vsb.cz/2017/>. I would like to thank the authors and the Organizing Committee from Department of Computer Science, namely Jiří Dvorský and Pavel Moravec, for their arduous editing work.

September 2017

Michal Krátký  
Program Committee Chair  
WOFEX 2017



# Organization

## Program Committee

Chair:

Michal Krátký (VŠB – Technical University of Ostrava)

Members:

Pavel Brandštetter (VŠB – Technical University of Ostrava)

Radim Briš (VŠB – Technical University of Ostrava)

Zdeněk Dostál (VŠB – Technical University of Ostrava)

Petr Chlebiš (VŠB – Technical University of Ostrava)

Stanislav Rusek (VŠB – Technical University of Ostrava)

Václav Snášel (VŠB – Technical University of Ostrava)

Vladimír Vašínek (VŠB – Technical University of Ostrava)

## Organizing Committee

Jiří Dvorský (VŠB – Technical University of Ostrava)

Pavel Moravec (VŠB – Technical University of Ostrava)

Hana Dluhošová (VŠB – Technical University of Ostrava)

*Workshop Location:*

Campus of VŠB – Technical University of Ostrava

17. listopadu 15, 708 33 Ostrava–Poruba, Czech Republic

12<sup>th</sup> September 2017

<http://wofex.vsb.cz/2017/>



# Table of Contents

## Study Programme P2649 Electrical Engineering

### Electrical Power Engineering (3907V001)

Calculation Energy Storage in the Off-grid System with Vehicle-to-Grid Technology . . . . .	1
<i>Vojtěch Blažek</i>	
Outdoor Power Stations CCTV Systems that Work Synergistically with the Security Lighting . . . . .	7
<i>Petr Bos and Karel Sokanský</i>	
Measurement of Stray Currents Caused by Electric Traction in the Vicinity of the Hoštejn Municipality . . . . .	13
<i>Jiří Cigánek</i>	
Reliability Evaluation of the Electric Power Distribution Systems . . . . .	19
<i>Dung Vo Tien, Radomír Goňo, Radim Briš, and Zbigniew Leonowicz</i>	
Partial Discharges Detection on Medium Voltage Overhead Power Lines .	25
<i>Jan Fulneček and Stanislav Mišák</i>	
Creating and Measuring Bipolar Ultra-Low Voltage Step-Up Converter ..	31
<i>Petr Hawliczek and Radomír Goňo</i>	
Comparison of Dynamic Model of Asynchronous Machine and Real Asynchronous Machine . . . . .	37
<i>Martin Král and Radomír Goňo</i>	
Analysis of the Failure Rate of MV Circuit Breakers . . . . .	43
<i>David Lazecký</i>	
Analysis of Measured Values and Digital Model Created by Software EMTP-ATP . . . . .	49
<i>Tomáš Mozdřeň</i>	
Research into the Connection of Biogas Station to the 22kV Distribution Grid . . . . .	55
<i>Ladislav Novosád</i>	
Evaluation of Dependency of the Energy Generated by Wind Power Plant on Season . . . . .	61
<i>Michal Petružela</i>	
Light Parameters of Public Lighting in the Sphere of Mesopic Vision . . . .	65
<i>Karel Sokanský, Richard Baleja, and Tomáš Novák</i>	

**Electrical Machines, Apparatus and Drives  
(2642V004)**

Model Reference Adaptive System for Sensorless Control of Induction Motor Drive .....	71
<i>Cuong Dinh Tran, Sang Dang Ho, Thinh Cong Tran, Chau Si Thien Dong, Hau Huu Vo</i>	
Simulation of Vector Control with RF-MRAS Observer .....	77
<i>Petr Chamrád</i>	
Increase the Efficiency of Induction Motors .....	83
<i>Pavel Pečínka and Stanislav Kocman</i>	
Optimization of PID Controller for Brushless DC Motor Drive using PSO algorithm .....	90
<i>Sang Dang Ho, Cuong Dinh Tran, Thinh Cong Tran, Chau Si Thien Dong, Hau Huu Vo</i>	
Rotor Time Constant Estimation Using Genetic Algorithm for Induction Motor Drive .....	96
<i>Thinh Cong Tran, Cuong Dinh Tran, and Sang Dang Ho</i>	

**Electronics (2612V015)**

Topology for Scalable Large-scale Battery Systems .....	102
<i>Matěj Golembiovský</i>	
Design of Platform for Robot Cooperation and Swarm Robotics .....	108
<i>Jakub Kolařík</i>	
Application Software for Electrohydraulic Brakes System of the Electric Vehicle .....	114
<i>Samuel Przeczek</i>	

**Technical Cybernetics (2612V045)**

Preparing a Four Wheel Electric Vehicle for an Autonomous Operation ..	120
<i>Jan Dedek, Jiří Kozíorek, and Jan Žídek</i>	
Calculation of Trajectories for Simple Inverted Pendulum using PyTrajectory .....	126
<i>Tomáš Dočekal</i>	
Multipurpose Sensor for Human Movement Analysis .....	132
<i>Jan Foltyn</i>	
Energy Savings in Buildings with Controlled Environments .....	138
<i>Kateřina Gecová and David Vala</i>	
A Novel Algorithm for Creation of Quaternions from Inertial Data .....	144
<i>Radek Halfar</i>	



Fetal ECG Extraction from Abdominal ECG Using Adaptive and Non-adaptive Algorithms: An Overview . . . . .	150
<i>Radana Kahánková, Jan Žídek, and Radek Martinek</i>	
Using Electrical Energy from Electric Car Battery by Automotive Recharger Standards Connections . . . . .	156
<i>Martin Mikolajek, David Vala, and Bohumil Horák</i>	
Automated Extraction of Blood Stream Volumetric Parameters . . . . .	162
<i>Tomáš Ondraczka</i>	
Energy Harvesting from Human Movement . . . . .	168
<i>Radka Pavelková, David Vala, and Pavel Šuránek</i>	
Mobile Applications Analyzing the Use of Central Operating Rooms . . . . .	173
<i>Tomáš Urbanczyk</i>	

## **Study Programme P1807 Computer Science, Communication Technology and Applied Mathematics**

### **Computer Science (1801V001)**

Effective Big Data Analysis on single-node Apache Spark with Self-Organizing Map Libraries . . . . .	178
<i>David Andrešič and Petr Šaloun</i>	
Context Recognition and Type-checking Tools for the TIL-Script Language	183
<i>Michal Fait</i>	
Detecting Human Action using the Microsoft Kinect ONE Sensor . . . . .	189
<i>Rafał Gasz</i>	
Betweenness Centrality Algorithm and Node Importance Extension . . . . .	195
<i>Jiří Hanzelka</i>	
Catch the Stegogramme – Detection of the Steganography Content with the Application of ANN . . . . .	201
<i>Jakub Hendrych</i>	
Preprocessing Big Data in Field of Marketing Models using Clusters in Cloud . . . . .	207
<i>Tomáš Janečko</i>	
An Overview of Parallel Itemset Mining Algorithms . . . . .	213
<i>Adam Kašpar, Vojtěch Kotík, and Jan Platoš</i>	
Evolutionary Synthesis of Artificial Neural Networks . . . . .	219
<i>Lumír Kojecký</i>	
New Approach To Steganography Detection Via Steganalysis Framework .	225
<i>Radim Kunčický</i>	

Action Recognition Based on the Skeleton and Depth Images . . . . .	231
<i>Radek Šimkanič</i>	
An Approach To Customer Behavior Modelling Using Markov Decision Process . . . . .	237
<i>Markéta Štáková</i>	
Controlling the Dynamic of Evolutionary and Swarm Algorithms via the CML . . . . .	244
<i>Lukáš Tomaszek</i>	
Machine Learning based Forecasting in Active Demand Side Management	250
<i>Tomáš Vantuch</i>	
MinEnt – Grammar-Based Compression . . . . .	256
<i>Michal Vašínek</i>	
Malware Detection based on Multiple PE Headers Identification . . . . .	261
<i>Filip Zatloukal</i>	
A Malware Detection on PE header Information . . . . .	267
<i>Jiří Znoj</i>	
<b>Computational and Applied Mathematics</b>	
<b>(1103V036)</b>	
Univariate Hölder Optimization Algorithm Using Space Filling Curves and its Application to Multidimensional Global Optimization . . . . .	273
<i>Michaela Bailová</i>	
Bayesian and Frequentist Approach to Logistic Regression . . . . .	279
<i>Michal Běloch</i>	
Reduced Basis Solver for Stochastic Galerkin Solution of the Darcy flow with a Random Material on Given Interfaces . . . . .	284
<i>Michal Bérés</i>	
Fourier Representation of Paths in Path Integral Monte Carlo Simulations	290
<i>Rajko Čosić</i>	
Sampling from Posterior Distribution of Material Parameters using an Approximation . . . . .	294
<i>Simona Domesová</i>	
Parallel Space-time Finite Element Methods . . . . .	300
<i>Ladislav Foltyn</i>	
Equality Constrained Minimization Problem Solved by the Modified SMALE Algorithm . . . . .	306
<i>Pavla Jirůtková</i>	
On Modified Handicap Labelings . . . . .	312
<i>Petr Kovář and Matěj Krbeček</i>	

Non-Affine Element Transformations in Linear Elasticity . . . . .	318
<i>Lukáš Malý</i>	
Numerical Computation of Two Electron Integrals . . . . .	324
<i>Martin Mrovec</i>	
Molecular Dynamics . . . . .	330
<i>Stanislav Paláček</i>	
Preliminary Results of a SMALBE+MPGP Algorithms for Training a Linear SVM Classifier . . . . .	336
<i>Marek Pecha and David Horák</i>	
Using Bootstrap Methods with <i>R</i> -Project For Comparison Ways of Treatment of Critical Limb Ischemia . . . . .	342
<i>Lenka Přibyllová</i>	
Extremal Graphs from Geometric Designs . . . . .	349
<i>Tom Raiman</i>	
On Decomposition of Distance Magic Graphs of Odd Order . . . . .	355
<i>Adam Silber and Petr Kovář</i>	
Local Eigenvalue Analysis using Contour Integral Method . . . . .	360
<i>Erika Straková and Dalibor Lukáš</i>	
Using the Random Forests Algorithm for Medical Data Analysis . . . . .	366
<i>Adéla Vrtková</i>	
Mixture Failure Rate: A Study based on Product of Spacings . . . . .	371
<i>Tien T. Thach and Radim Briš</i>	
<b>Communication Technology (2601V018)</b>	
Influence of Load by High Power on the Optical Coupler . . . . .	377
<i>Lukáš Bednárek</i>	
VoIP Honeypot Development used in the CESNET Network . . . . .	383
<i>Ladislav Behán</i>	
Analysis of Bitrate and Chroma Subsampling on Video Quality Assessment	389
<i>Jaroslav Frnda</i>	
Optical Vehicle-to-Vehicle (V2V) Communication: Analyze of Photometric Quantities STOP Škoda Octavia III . . . . .	395
<i>Peter Hajduk and Vladimír Vašínek</i>	
Radiation Influence on the Attenuation of the Cabled and Uncabled Optical Fibers . . . . .	400
<i>Lukáš Hájek and Vladimír Vašínek</i>	

Comparison of Selected Optical Properties of Thin Layers of PDMS with Luminophores . . . . .	406
<i>Jan Jargus</i>	
Fiber-optic Technology in Sensory Applications . . . . .	412
<i>Jan Nedoma</i>	
Measurement of CCT Planar Structures Made of Polydimethylsiloxane Doped with Yellow Luminophore . . . . .	418
<i>Martin Novák</i>	
Docker is a Useful Tool to Design Information Systems . . . . .	424
<i>Lukáš Orčík and Miroslav Vozňák</i>	
Design of an All-Fiber EDFA Laser System for Simulation Power Load of Backbone Network . . . . .	429
<i>Radek Pobořil</i>	
Active Pre-equalizer for Broadband Over Visible Light . . . . .	435
<i>Tomáš Stratil and Vladimír Vašínek</i>	
Measurement Numeric Aperture of The Optical Fiber Exposed to Thermal and Radiation Aging . . . . .	441
<i>Aleš Vanderka</i>	
Measurement of Chromaticity Temperature and Polydimethylsiloxane Attenuation Constants . . . . .	446
<i>Jan Zavadil</i>	
Fiber Optical Sensor of Electric Current with Bragg Grating . . . . .	452
<i>Stanislav Žabka</i>	

## External Authors

Algorithms Comparison for Electrical Insulator Key Features Detection . .	457
<i>Jakub Osuchowski</i>	
UAV as a System which Enables Localization of Pollutants on the Industrial Area . . . . .	463
<i>Ślawomir Szymocha</i>	

## Author Index

# Calculation Energy Storage in the Off-grid System with Vehicle-to-Grid Technology

Vojtěch Blažek

Department of Electrical Power Engineering, FEECS,  
VŠB – Technical University of Ostrava, 17. listopadu 15,  
708 33 Ostrava – Poruba, Czech Republic  
vojtech.blazek@vsb.cz

**Abstract.** The off-grid is a system without connection to the external network. This system is normally powered by batteries. The battery is charged from many sources, for example photovoltaic panels or wind turbines. The trend of the present era is the electric car. This electric car can be connected to the off-grid system and share its battery capacity. This technology is called Vehicle-to-Grid. This technology also allows the electric car to be charged from the off-grid system, when off-grid have surplus of electric energy. On the other hand system allows discharge car when off-grid needs more energy.

**Keywords:** Off-grid, Storage Device, Vehicle-to-Grid, Electric car

## 1 Introduction

Our off-grid is located in the campus of the Technical University of Ostrava. The off-grid is currently powered by batteries Ferak KMP 375. Batteries are charged by two arrays 2 kWp photovoltaic panels. To be able to supply a nominal voltage of 48 V, the batteries are connected in series. The capacity of this connection is 15 kWh. In the future, the battery capacity will be extended by the battery in an electric car. This capacity sharing technology is called a vehicle-to-grid. [1,2,3]

During the day, the battery is charged by the photovoltaic panels. When the battery is fully charged, the inverter stops supplying electricity to the battery to avoid over-charging and thus shortening of battery life. [1,2,3]

In future, off-grid system after charging the batteries Ferak, will supply surplus energy to the electric car. This will improve the efficiency of our off-grid system as photovoltaic panels can deliver electricity for a day. This results in a reduction of local emissions. Furthermore, we are able to accumulate more energy in the off-grid system. [3,4]

In this article, I will deal with the relationship between generated electricity from photovoltaic panels and global irradiation. Based on the statistical apparatus I intend to calculate how much extra energy could be stored in an electric vehicle. Based on this data I calculate the driving distance of the accumulated energy.

## 2 Reference day

Within the measured data, I discovered the day when the panels produced electricity throughout the day without any limitations. This day will be the reference day. On this day I will apply mathematical apparatus, which I will use on data from first week in April 2015, when the battery has been fully charged, and there was a limitation of electricity production. Date of reference day is 10. 4. 2015.

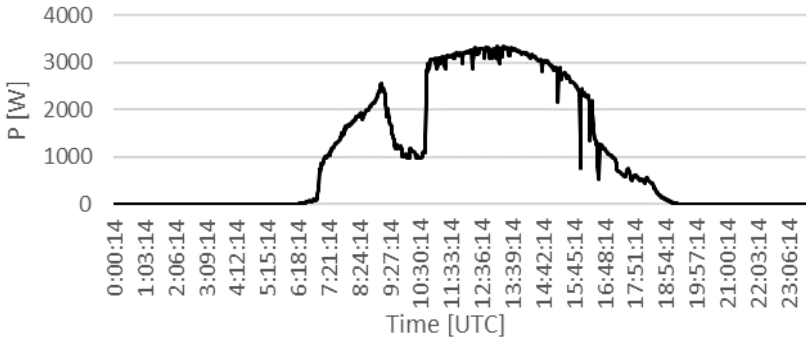


**Fig. 1.** Total electricity production from photovoltaic panels in off-grid system on reference day

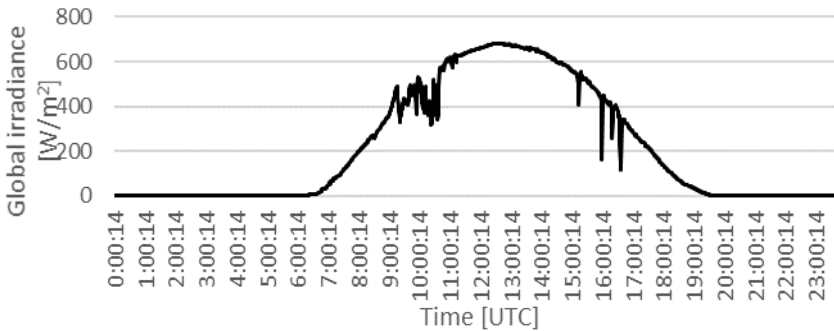


**Fig. 2.** Measured intensity of global irradiance on reference day

## 3 Regression

In software Statsgraphics, I applied a linear regression between the generated electrical energy and the global irradiance from the data measured on the reference days. Subsequently, the equation verified whether the model complies with the regression model formula. [3] The linear regression equation is

$$P = 4,75804 \cdot E_e [\text{W}] \quad (1)$$

$P$  – Calculated Generable Electricity

$E_e$  – Global Irradiation

At the following figures, we can see a comparison of the produced electricity and the theoretically produced electricity.

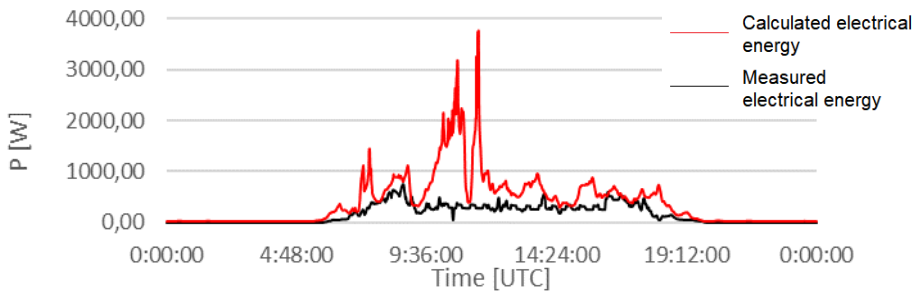


**Fig. 3.** Day 1.4. 2015

The total measured electrical output for that day was 4 031,1 Wh. Total calculated generable electricity for this day is 9 438,3 Wh. The difference between calculated and measured electrical energy is 5 407,2 Wh, see fig. 3.

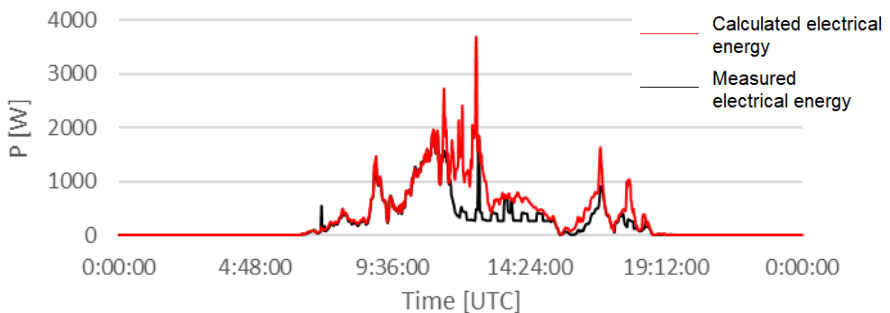


**Fig. 4.** Day 2.4. 2015

The total measured electrical output for that day was 5 529,9 Wh. Total calculated generable electricity for this day is 8 512,54 Wh. The difference between calculated and measured electrical energy is 2 983,45 Wh, see fig. 4.

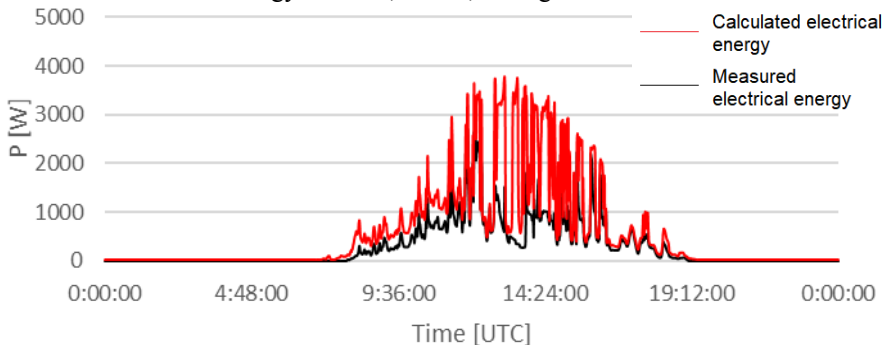


**Fig. 5.** Day 3.4. 2015

The total measured electrical output for that day was 7 141 Wh. Total calculated generable electricity for this day is 13 549 Wh. The difference between calculated and measured electrical energy is 6 407 Wh, see fig. 5.

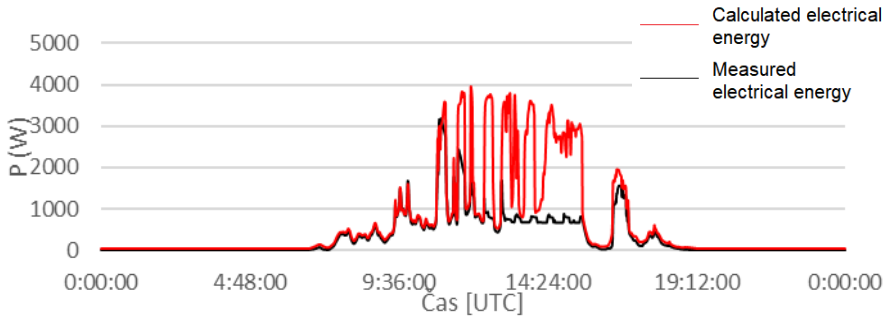


**Fig. 6.** Day 4.4. 2015

The total measured electrical output for that day was 7 559 Wh. Total calculated generable electricity for this day is 14 373 Wh. The difference between calculated and measured electrical energy is 6 814 Wh, see fig. 6.

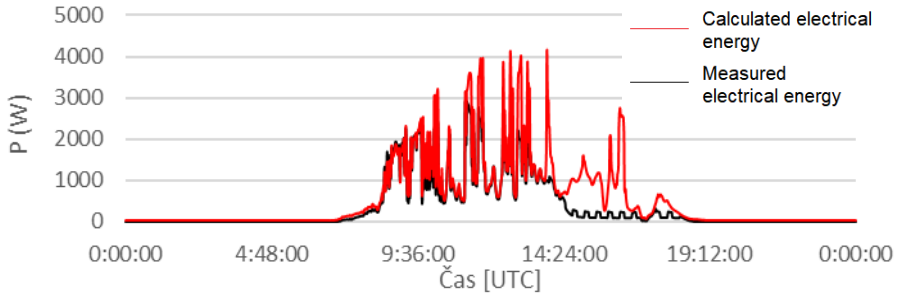


**Fig. 7.** Day 5.4. 2015

The total measured electrical output for that day was 8 728 Wh. Total calculated generable electricity for this day is 12 852 Wh. The difference between calculated and measured electrical energy is 4 124 Wh, see fig. 7.

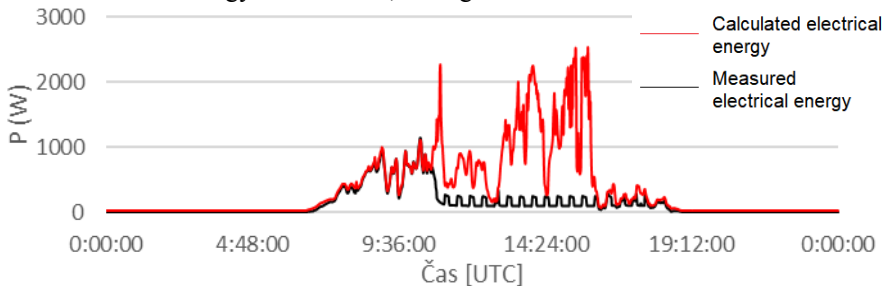


**Fig. 8.** Day 6.4. 2015



The total measured electrical output for that day was 3 186 Wh. Total calculated generable electricity for this day is 8 639 Wh. The difference between calculated and measured electrical energy is 5 453 Wh, see fig. 8.

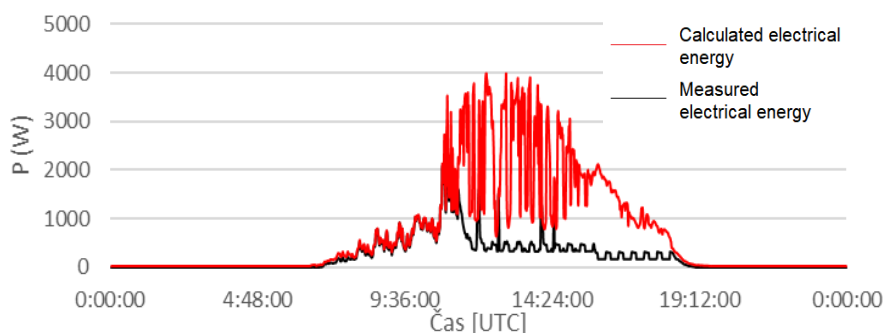


**Fig. 9.** Day 7.4. 2015

The total measured electrical output for that day was 5 969 Wh. Total calculated generable electricity for this day is 16 466 Wh. The difference between calculated and measured electrical energy is 10 775 Wh, see fig. 9.

#### 4 The electric vehicle's driving distance from extra accumulated electricity

**Table 1.** Driving distance gained from extra accumulated electricity

Description	Consumption	Date 1.4.	Date 2.4	Date 3.4.	Date 4.4	Date 5.4.	Date 6.4	Date 7.4
	[kWh/km]	Range [km]	Range [km]	Range [km]	Range [km]	Range [km]	Range [km]	Range [km]
Economic ride without heating and air conditioning	0,15	32, 4	17,9	38,4	40,9	24,7	32,7	64,7
Normal ride with heating, outdoor temperature around 0 °C	0,249	19,5	10,8	23,1	24,6	14,9	19,7	38,9
Normal ride without heating and air conditioning	0,185	26,3	14,5	31,2	33,2	20,1	26,5	52,4

The type of electric car to be connected to the off-grid is a Nissan Leaf with a battery capacity of 30 kWh. In the table, for the sake of clarity, what is the theoretical

range of that extra accumulated energy. I made the calculations based on data from the electric car manufacturer. In addition, Recharge efficiency is 90%. In the first week of April, we could produce extra 41 962 watts of energy for off-grid.

## 5 Conclusion

Part of my thesis is research and development of hybrid off-grid system at VŠB campus. Nowadays, a rebuilding of this system is required in the laboratory due to the inclusion of an electric car. Upon completion of this reconstruction, the testing and debugging of this system will be required. In the end, the upgraded system with a vehicle-to-grid technology should work completely autonomously including charging and discharging of the electric car. In this article, I calculated how much extra energy is possible to accumulate in the electric car connected to our off-grid system.

**Acknowledgements.** This paper is supported by the following projects: LO1404: Sustainable development of ENET Centre; CZ.1.05/2.1.00/19.0389 Development of the ENET centre research infrastructure; SP2017/159 Students Grant Competition and TACR TH01020426, Czech Republic.

## References

- [1] Kubalik, P., Misak, S., Stuchly, J., Vramba, J., & Uher, M. (2014, May). Suitable energy storage in Off-Grid systems. In *Environment and Electrical Engineering (EEEIC), 2014 14th International Conference on* (pp. 345-349). IEEE.
- [2] Lukáš Prokop, Stanislav Mišák, Jindřich Stuchlý. Possibilities of storage capacity sharing using e-vehicles - An introduction. Proceedings Of The 8th International Scientific Symposium On Electrical Power Engineering (Elektroenergetika 2015)
- [3] Corey D. White, K. Max Zhang, Using vehicle-to-grid technology for frequency regulation and peak-load reduction, *Journal of Power Sources*, Volume 196, Issue 8, 2011, Pages 3972-3980, ISSN 0378-7753, <http://dx.doi.org/10.1016/j.jpowsour.2010.11.010>.
- [4] Z. Darabi and M. Ferdowsi, "Aggregated Impact of Plug-in Hybrid Electric Vehicles on Electricity Demand Profile," in *IEEE Transactions on Sustainable Energy*, vol. 2, no. 4, pp. 501-508, Oct. 2011. doi: 10.1109/TSTE.2011.2158123
- [5] Litschmannová, M. Úvod do statistiky; VŠB – TU Ostrava, Fakulta elektrotechniky a informatiky: Ostrava, 2012, 380s. energy storage in Off-Grid systems. In *Environment and Electrical Engineering (EEEIC), 2014 14th International Conference on* (pp. 345-349). IEEE.

## Publications

Petružela, M., Blažek, V.: 3D Simulation of the vertical axis Wind Turbines, In *Proceedings of the 18th International Scientific Conference on Electric Power Engineering (EPE)*. Ostrava: VŠB - Technical University of Ostrava, Faculty of Electrical Engineering and Computer Science, Department of Electrical Power Engineering, 2017. DOI: 10.1109/EPE.2017.7967299

# Outdoor Power Stations CCTV Systems that Work Synergistically with the Security Lighting

Petr Bos and Karel Sokanský

Department of Electrical Power Engineering, FEECS,  
VŠB – Technical University of Ostrava, 17. listopadu 15,  
708 33 Ostrava – Poruba, Czech Republic  
[petr.bos@vsb.cz](mailto:petr.bos@vsb.cz)

**Abstract.** At present time, in the operation of the outdoor electric power stations providers access their unattended operation. Linked to this there is necessary to know what is happening in the station not only during the day, but especially at night. Since the operation of the entire lighting system in normal operation is highly uneconomical and generates light pollution too, the solution is that in permanent night operation is only lighting system providing illumination around the fence for security cameras and for visibility of the borders of power station from outside. Synergistically with this type of lighting should be set up security cameras system providing information about potential disruption perimeter of the power station.

The article deals with the proper selection and mutual synergy of outdoor lighting systems and security cameras system. The issue is not only in the power stations, but generally in using of the cameras systems in industrial applications which are dependent on artificial lighting.

Main chapters of the article will solve following problems. At the beginning it is necessary to describe the need to choose the color of light of artificial lighting system to spectral sensitivity of chips inside the cameras. It will continue with recommending for a design of artificial lighting system with respect to the placement of cameras. It means the design which calculates not only with horizontal illuminance, but cameras (vertical) illuminance too. The camera illuminance is necessary for recording of images the whole distance between the luminaires. The whole policy of illumination for cameras must be re-evaluated compared to standard public lighting systems design. In the last part of this article will be described relations between the horizontal illuminance, the camera illuminance, luminance and illuminance on the camera which are given by manufacturers.

**Keywords:** electric power stations, lighting system, camera system, spectral sensitivity, illuminance.

## 1 Introduction

The article deals with the proper selection and mutual synergy of outdoor lighting systems and security cameras system. The issue is not only in the power stations, but generally in using of the cameras systems in industrial applications which are dependent on artificial lighting. That is why this article describes the basic principles that must be followed when designing lighting systems, which are used not only for ensuring visual tasks of workers and staff, but also for the cameras (security, diagnostic, ..... ) systems.

The right choice of lighting system plays an important role in the operation of the camera and its legibility and quality of images. To these camera systems could transmit relevant visual information in the electric station is necessary correctly settings of illumination.

Camera systems can also be used in other fields of industry for instance for diagnostic purposes (eg. for checking defects). These cameras ensure high performance, which is based not only on high-speed recording and processing the images, but they also offers reliable, repeatable performance in even the most challenging vision applications. Cameras systems for diagnostics work in different ways: high processing power, high definition, vision tools, connectivity to other systems, automatically selected features, set parameters, and operate in real conditions without setting. An important factor of all cameras is their sensitivity, which specifies under what minimal lighting conditions the camera chip can record an image. The higher the value of the camera chip sensitivity is the better it is able to record the image at low intensities of ambient lighting.

The principle of a camera lies in capturing luminance of illuminated objects. The most favorable situation of a camera for good distinctness of record is when luminous flux strikes upon an illuminated object from the direction of the camera. Then, the highest luminance and the best resolution are achieved. Commonly used cameras have according to catalogue data camera sensitivity of colour capturing  $E = 0.4 \text{ lx}$  and of monochrome capturing  $E = 0.05 \text{ lx}$ . During the measurement was verification that this value is on the camera chip.

When designing the lighting system, it is important to use luminaires that are in the direction of the view of camera able to attain required camera illuminance and at the same time horizontal illuminance on working area.

When use luminaires with flat glass and without tilting will be ensure, than the camera will not be any high luminance in the direction of capturing. High values of luminance could cause saturation of the sensor in the camera system. To determine the camera illuminance must be met certain parameters. These parameters are mentioned below in the article.

Between the main parameters belongs the necessity of provide enough lighting and its regularity. It must be ensured vertical illuminance and camera illuminance. Than the camera system must be no saturation in area of the highest luminance and on the contrary it has to satisfactory image resolution in the area of the lowest luminance. When installing and setting the camera, the camera doesn't have to rotate into the direct view of the luminaires.

## 2 Artificial light spectral adaptation to the camera chip spectral sensitivity

Due to the rapid development of LED luminaires for public lighting it is necessary to consider the maximum usable radiated and reflected flux from these lighting systems working with various camera systems. Individual chips used in camera systems with its spectral sensitivity generally are not the same as a sensitivity of human eye. Human eye have maximum sensitivity around wavelength 555 nm. Chips spectral sensitivity is shifted into the infrared and ultraviolet radiation too and their maximum of sensitivity is not so significant. In comparing to high pressure sodium lamps, the LED's have possibilities to change the radiated spectrum (correlated color temperature – CCT) and to maximize receiving of incident radiation on camera chip. For the spectral radiating optimizing it is necessary to selected LED's so as to achieve both light-technical parameters of the human eye on the task area and reflected received radiation flux on the camera chip in its maximum spectral sensitivity. The paper describes how to adapt the correlated color temperature of LED's inside the luminaires and lighting system to the chip used in particular camera. The procedure is described and demonstrated on the LED lighting system mounted as a guarding around the fence in the outdoor power station.

## 3 Requirements for placement of cameras in connection with the artificial lighting system

This section described recommendations for the placement of security cameras working together with artificial lighting system. In terms of camera installation is required, in addition to all the basic principles of the placement of cameras, to carry on them in terms of potential high luminance of lighting system luminaires in the camera angle of view and also in terms of positioning of the luminaires in the selected area. Second condition is very important because of the scanning area will be probably in the same direction as a maximum radiation of luminaire next to camera. Due to the reflective properties of the materials it is assumed that the monitored objects will occur to the maximum reflection in the back direction to the camera and therefore there will cause a maximum camera chip excitation.

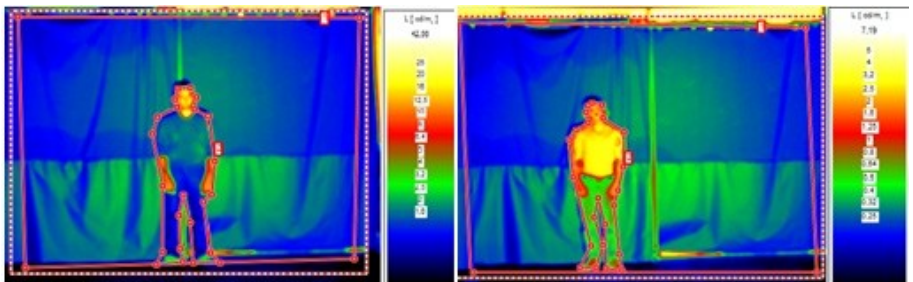
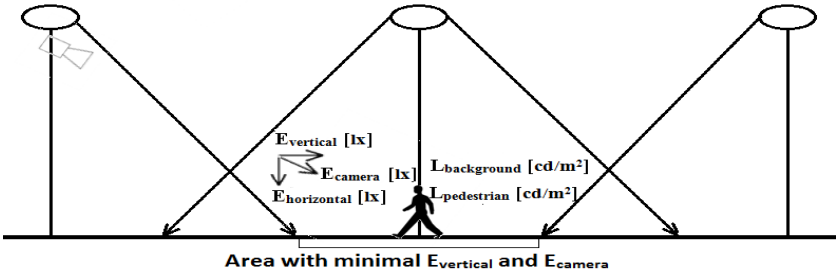


Fig. 1. Example luminance map with dark background and dark and light clothes.

**Table 1.** Evaluation of light parameters - camera switching with dark background

Dark background ( $\rho$ is lower than 0.03)		
	From RGB to BW mode	From BW to RGB mode
$E_v$ camera (lx)	4	2.3
$E_v$ captured surface (lx)	37	200
$L_{av}$ dark pedestrian (cd/m <sup>2</sup> )	0.46	2.55
$L_{av}$ background (cd/m <sup>2</sup> )	0.28	1.56
$L_{av}$ light pedestrian (cd/m <sup>2</sup> )	1.48	7.52
$L_{av}$ background (cd/m <sup>2</sup> )	0.34	1.83

- $E_v$ ...vertical illuminance (lx)
- $L_{av}$ ...average luminance (cd/m<sup>2</sup>)
- $\rho$ ...real situation could only approach these limits of reflection. There are laboratory limits of it.



**Fig. 2.** Standard lighting systems.

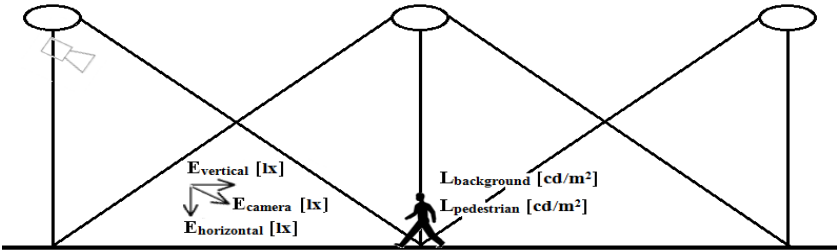


**Fig. 3.** Philosophy of lighting system from the perspective of the camera system.

#### 4 Change of philosophy in security lighting systems designing

The security lighting systems have to meet not only the requirements for visual tasks of humans, but also requirements for security cameras too. From the perspective of the requirements for visual performance must be achieved between the columns for luminaires only a normative horizontal illuminance and of course uniformity in the working area. From the point of view of the cameras it is contrary important provide in the working area camera illuminance.

In standard design of lighting system there are different requirements for point of view, differences over working area and different requirements for the distribution of luminous flux from luminaires. In compliance with the normative regulations cannot be respected desired camera illuminance in the whole evaluated area between two columns for luminaires. The figure 3 gives recommendations how to design a security artificial lighting system so that it respected with both horizontal and camera illuminance in the whole working area. [1] [2] [3]

## 5 Relations between the light requirements of cameras manufacturers and standards for outdoor lighting

In this part of the article is summarization of the requirements for a combination of cameras and outdoor lighting systems. These requirements are supplemented by calculations and measurements of luminance, illuminance, spectral radiations and real outputs of cameras systems from outdoor power station. [4] [5]

### 5.1 Measurement of spectral characteristics of LED light sources

Spectral radiant exitance moves to higher wavelengths with rising correlated colour temperature. Constant  $x$  said on vertical axis of spectral characteristics is relative to radiant output. Calculation was done to find out the maximal adaptation of luminaires to camera. Calculation of constant  $x$ :

$$x \cdot \sum_{400}^{750} A \cdot \Delta B = P \quad (1)$$

$$x = \frac{P}{\sum_{400}^{750} A \cdot \Delta B} \quad (2)$$

- A...relative spectral energy distribution [%]
- B...wavelength [nm]
- P...output [W]

**Table 2.** Transfer function for camera sensor used in power stations and in the diagnostics

Luminaire type	Transfer function of camera sensors
CCT and area	
3000K – power station	88,90%
4000K – power station	85,90%
3000K - diagnostics	79,3%
6000K - diagnostics	68,7%

The transfer functions for the LEDs used in the power stations were comparable. The transfer function for LEDs with correlated colour temperature 3000 K was 88.9 %. For correlated colour temperature 4000 K, the transfer function was 85.9 %.

The transfer functions for LEDs used in diagnostics were different. The decrease was 10.6 %. The value 100 % is relative to values of ideal spectral sensor speed at all wavelengths.

From the above measurements, it is evident that the increasing correlated colour temperature of the LEDs decreases the transfer function. However, it is important that the transfer function is maximal for the correct setting of cameras and lighting systems in power stations.

## 6 Conclusion

Both in electrical stations and diagnostics, it is important to preserve the correct settings between the cameras and the lighting systems. This article proposes recommendations for correct setting of lighting systems and cameras. Designing lighting systems emphasizes the right choice of correlated colour temperature to ensure the best possible transfer function between the lighting system and the camera. Decreasing transfer function reduces the resolution of the camera and may cause a very low visibility of the camera. Other important parameters in the design of lighting systems include horizontal illuminance, vertical illuminance and camera illuminance. From the point of view of the design of lighting systems must be ensured the horizontal illuminance and uniformity. From the point of view of camera settings is important preservation of camera illuminance in the working area.

## 7 Acknowledgment

This article was prepared with the support of the project "Analysis of visibility of transport infrastructure for safety increasing during night, sunrise and sunset" VI2VS/571, by institution of VSB-TU Ostrava.

## 8 References

1. I. Ullman, P. Bos, J. Ullman, "New outdoor lighting-Operation and maintenance," 17th International Scientific Conference on Electric Power Engineering, 2016, art. no. 7521823, ISBN 978-150900907-7.
2. P. Bos, R. Baleja, K. Sokansky, T. Novak, I. Ullman, "Selection of lighting systems for electrical stations CEPS in connection with the introduction of LED," 8th International Scientific Symposium on Electrical Power Engineering, 2015, pp. 220-223.
3. P. Bos, R. Baleja, K. Sokansky, T. Novak, I. Ullman, "Outdoor lighting versus surveillance camera systems in electrical substations CEPS," 16th International Scientific Conference on Electric Power Engineering, 2015, pp. 464-467.
4. I. Ullman, J. Otypka, T. Mlcak, "New development in control system CEPS, a.s. electrical substation outdoor lighting," 15th International Scientific Conference on Electric Power Engineering, 2014, art. no. 6839516, pp. 649-654.
5. I. Ullman, "Implementing new outdoor lighting in electrical stations according to CEPS a. S. Standards," 14th International Scientific Conference on Electric Power Engineering, Kouty Nad Desnou, pp. 63-67.



# Measurement of Stray Currents Caused by Electric Traction in the Vicinity of the Hoštejn Municipality

Jiří Cigánek

Department of Electrical Engineering, FEECS,  
VŠB – Technical University of Ostrava, 17. listopadu 15,  
708 33 Ostrava – Poruba, Czech Republic  
ciganek@vsb.cz

**Abstract.** The article examines current fields in the vicinity of a railway platform of the SUDOP type and in the surroundings of the municipality of Hoštejn. The subject of measurement were stray currents in the vicinity of the municipality of Hoštejn. The measured values were used for reaching a conclusion and for recommending measures aimed at reducing the impacts of stray currents.

**Keywords:** electric railways; platform; current density; rail; gabion

## 1 Introduction

The occurrence of the so-called stray currents represents a major problem in the vicinity of a railway track. Stray current is a current which passes from a rail during the crossing of a railway vehicle into the earth and returns back to the power supply station. These currents disrupt concrete foundations in the vicinity of the railway substructure. Station platforms are some of the places through which these currents pass. This contribution deals with an examination of these fields in the railway platform of the SUDOP type. It compares a fault-free state in which a rail is connected with a gabion through a lightning arrester by means of a conductor and a case in which there occurs a breakdown of the lightning arrester. In this case there therefore occurs a significant voltage surge in the gabion and thus also passage of stray currents.

The term “platform” refers to a part of the railway substructure (a transport area and a pathway) intended for boarding or alighting of passengers and for handling of minor consignments. A gabion or a gabion structure is an element of a cube or cuboid shape made of a hexagonal steel wire mesh, welded steel nets or possibly high-strength polymer geogrids filled with natural aggregate, quarried rock, earth, recycled material, etc.

## 2 Measurement and Its Aim

The aim was measurement of stray currents caused by the influence of electric traction in the municipalities of Hoštejn and Hněvkov. The following activities were carried out in the above-mentioned locations:

- Measurement before the disconnection of the protective bonding of the gabion, the earthing of the lighting and traction supports directly at the train stop in Hoštejn;
- Measurement after the disconnection of the above-mentioned protective bonding;
- Measurement after the depolarization of the underground installations.

## 3 The Description of the Identified Situation

The municipality of Hoštejn is located on the railway line between the Prague Main Station and the Olomouc Main Station, in the section Česká Třebová – Zábřeh na Moravě. The municipality of Hněvkov is situated in the vicinity of the railway line, about 3.5 km from the municipality of Hoštejn. The railway line is electrified by a direct-current traction system of 3kV. From the point of view of conditions for the occurrence of stray currents, the track bed in Hoštejn is suitable. The sleepers are made of concrete B91, the fastening system is W14 Vossloh and the rails are UIC 60. The track bed is made of ballast without visible soil admixtures. The protection against electric shock in non-live conductive parts in the danger area of the electric traction is provided by protective bonding through surge arresters with a repeatable function (UPO 500 and UPO 250). The gabion is connected with the railing at the Hoštejn train stop.

## 4 Used Measurement Methods

The measurements (or the assessment or calculation) were carried out according to:

ČSN 03 8375	Corrosion protection of underground or underwater metallic pipelines
ČSN EN 13508:2001	Measurement procedures in cathodic protection
ČSN EN 12954:2001	Cathodic protection of underground or underwater metallic equipment – General principles and applications for pipelines

The numerical values of the monitored quantities were measured and recorded by the KORODAT data collectors. All measuring devices used for the measurement were checked (calibrated) according to the Metrological Rules of SZDC M15.

## 5 Measurement Conditions

Air temperature of 15°C, moist soil, overcast weather.

## 6 The List of Measurement Points

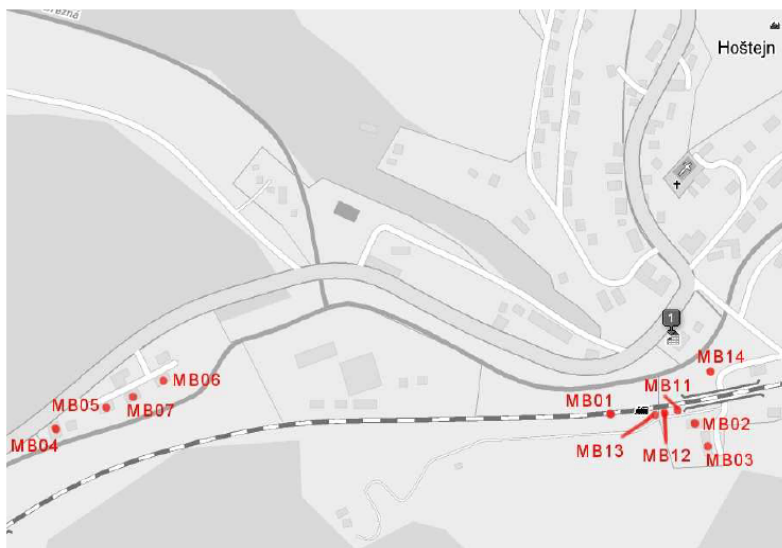


**Fig. 1.** Distribution of the measurement points in the municipality of Hoštejn

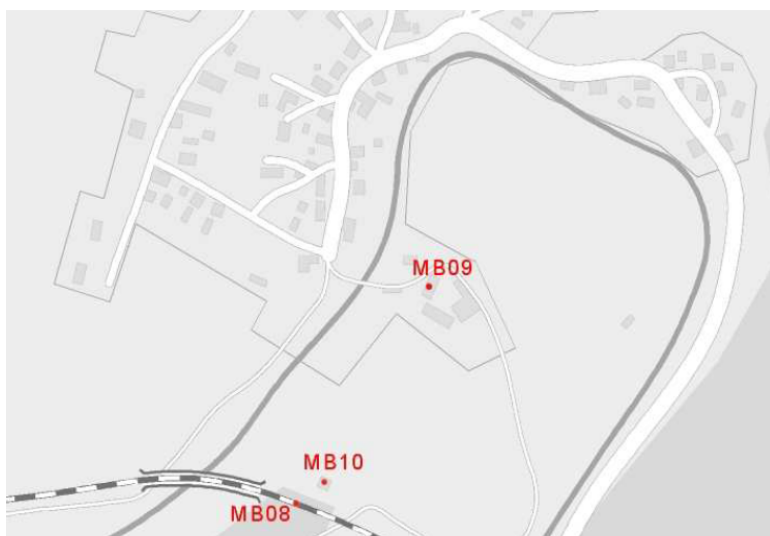


**Fig. 2.** Distribution of the measurement points in the municipality of Hněvkov

7 Graphic Results of the Measurement

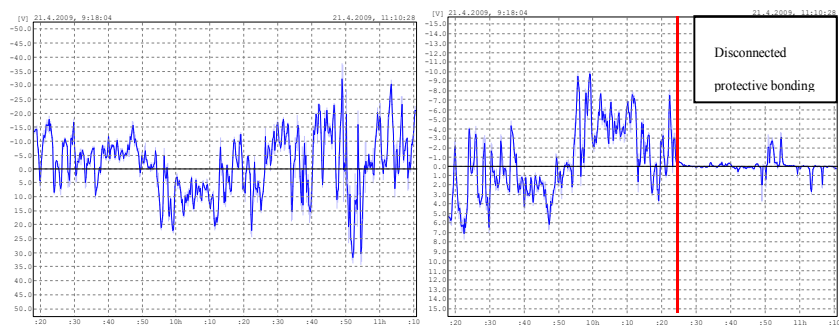


**Fig. 3.** Measurement point 01: Overhead wire track, Measurement point 03: PEN, Hoštejn, Land Registry No. 53

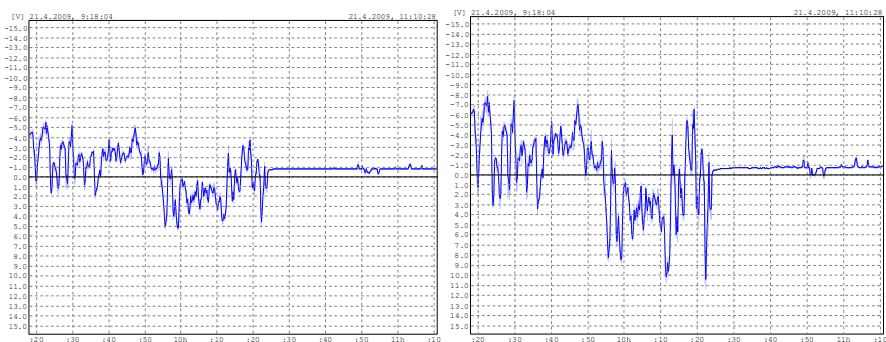


**Fig. 4.** Measurement point 11: Lighting No.1, Measurement point 12: Gabion at platform TP 69

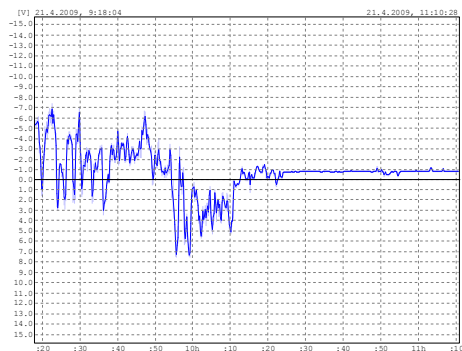


**Fig. 5.** Measurement point 13: Gabion at platform TP 75

## 8 Measurement Results and Assessment

As a result of the measurement, faulty protective bonding (connection of the protective bonding conductor to the earthing strap of the platform and the gabion structure) was found in two cases when the protective bonding was disconnected from the overhead wire track at the platform of the Hoštejn train stop. A current of 5A in both directions was measured in the protective bonding conductors.

No further faults were identified after the disconnection of the faulty protective bonding. The structure of the gabion and the earthing strap of the lighting poles was galvanically isolated from the overhead wire track.

The disconnection of the faulty protective bonding showed immediately on the graphic records of the above-mentioned gabion and the earthing strap and at the same time on the underground installations.

## 9 Proposed Measures and conclusion

Measurements of stray currents should be carried out again after six months. All protective bonding should be gradually disconnected directly from the overhead wire track at the Hoštejn train stop in the direction of Zábřeh na Moravě with the aim of identifying possible conductive connection to the gabions or the earthing strap.

On the basis of the results from the follow-up measurements, I recommend the following:

1. To install a small station of cathodic protection on the possible underground installations;
2. To install a three-conductor or five-conductor wiring with a residual-current device of non-live parts with a sacrificial anode in the houses in the vicinity of the train stop in Hoštejn.

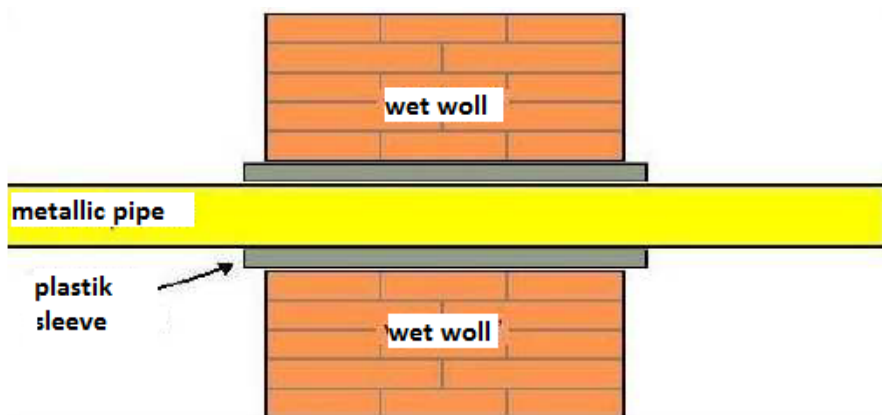


Fig. 6. Insulation of the metallic pipe passing through a wall

## 10 Bibliography

- [1] Paleček, Selected Chapters from Electrical Engineering Problems in Transportation Engineering university textbook, VŠB-TU Ostrava 1996
- [2] L. Ivánek, Models and Transfer Parameters for Propagation of Reverse Currents in Electric Traction post-doctoral thesis, Ostrava 1998
- [3] ČSN EN 50122-2 Railway applications – Fixed installations - Part 2: Protective provisions against the effects of stray currents caused by DC traction systems as amended
- [4] Materials of SŽDC.

# Reliability Evaluation of the Electric Power Distribution Systems

Dung Vo Tien<sup>1</sup>, Radomír Goňo<sup>1</sup>, Radim Briš<sup>2</sup>, and Zbigniew Leonowicz<sup>3</sup>

<sup>1</sup>Department of Electrical Power Engineering, FEECS,  
VŠB – Technical University of Ostrava, 17. listopadu 15,  
708 33 Ostrava – Poruba, Czech Republic  
{dung.vo.tien.st, radomir.gono}@vsb.cz

<sup>2</sup>Department of Applied Mathematics, FEECS,  
VŠB – Technical University of Ostrava, 17. listopadu 15,  
708 33 Ostrava – Poruba, Czech Republic  
radim.bris@vsb.cz

<sup>3</sup>Wroclaw University of Science and Technology  
zbigniew.leonowicz@pwr.edu.pl

**Abstract.** This paper introduced the graph analysis method for calculating the reliability of the electric power distribution system. The reliability indices are evaluated based on splitting the distribution system by sections, establishing matrix structure, relations between sections. The proposed method is programmed using MATLAB and tested in evaluating the reliability of a distribution system.

**Keywords:** Analytical method, connection matrix, distribution system, graph analysis, MATLAB, reliability.

## 1 Introduction

The distribution system is defined as a group of distributed generations or distribution substations, medium voltage transmission line and loads, it carries electricity from the transmission system to individual consumers. Its primary emphasis is to provide electrical energy to its customers as possible with an acceptable degree of quality. It is important to have some reliability calculation of the distribution from the electric power system design and planning process in order to ensure acceptable continuity of supply in the failures and forced outages of plant and the regular scheduled maintenance. Reliability of power supply is one of the features of power quality [3].

There are two main categories of evaluation techniques: analytical and simulation. Analytical techniques use mathematical models and evaluate the measures or indicators by using algebraic solutions. Simulation techniques estimate the measures or indicators by simulating the actual process and random behavior of the system [3]. Methods for calculating the reliability of distribution system have been analyzed and proposed through many publications [1], [2], [3]. However, it is necessary to have a simple and programmable method can be applied to various distribution systems. Techniques to calculate the reliability of the distribution system are different from the transmission system. In this paper, the graph analysis method is introduced to calculate electric power distribution system reliability. The proposed method is programmed using MATLAB and tested in evaluating the reliability of a distribution system.

## 2 Analytical Method

### 2.1 Section

In general, a distribution system includes loads, transmission line, circuit breaker, disconnector and sources. The distribution system is divided into different areas due to the operation of the breakers or the disconnector, each separated area is called a section. The failures of components in one section can influence on the whole system reliability.

### 2.2 Connection Matrix

When one section has a fault, the neighboring section maybe disconnected in short time (the operation time of the device) or long time, it depends on the configure of distribution and the sources or the distributed generation. In order to express the system configuration and the connection states when the failure occurs, this paper presented three kinds of connection matrices.

The first connection matrix  $A_k(i,j)$  expresses whether section  $i$  is connected to resource  $k$  with unlimited capacity, when the failure occurs in section  $j$ . The matrix has only the values of 0 or 1 for its elements according to their connection states.

- $A_k(i,j) = 0$  if the failure occurs in section  $j$ , resource is not supply for section  $i$ .
- $A_k(i,j) = 1$  if the failure occurs in section  $j$ , resource is supply for section  $i$ .

The second connection matrix  $C(i,j)$  is defined in the effect of the connection between sections by the circuit breaker or the disconnector.  $C(i,j) = 1$  if the failure occurs in section  $j$ , section  $i$  is recovered in the limited time (is called  $r_{ij}$ ).  $C(i,j) = 0$  for the other situation. If all the connection between sections use circuit breaker,  $C(i,j)$  becomes a zero matrix.

The third connection matrix  $T(i,j)$  like as matrix  $C(i,j)$ , but it is replaced by operation time or the time for annual maintenance of the connection device to isolate section  $i$  when the failure occurs in section  $j$ .

### 2.3 The Component Reliability Parameters

The component reliability parameters for calculating the reliability of distribution system includes: the failure rate  $\lambda_0$  (/100km.year) and the repair time  $r_L$  (hours/time) of transmission lines; the operate time  $r_D$  (hours) of the disconnector to isolate section when its failure and the time for annual maintenance  $r_{mD}$  (hours); the annual maintenance rate  $\lambda_m$  (/year) of each section and the time  $r_{ms}$  (hours) for annual maintenance. This information is possible to retrieve with accurate databases of distribution companies [4], [5].



## 2.4 The Reliability Calculation of Distribution System

The time of interruption power supply of section i, when the failure occurs in section j is given by

$$T_{Fij} = \{C(i, j).r_{Dij} + [1 - A(i, j)].r_j\}.\lambda_j = \{C(i, j).T_1(i, j) + [1 - A(i, j)].r_j\}.\lambda_j \quad (1)$$

If the distribution systems have more than one source, the equation (1) is written

$$T_{Fij} = \{C(i, j).T_1(i, j) + \prod [1 - A_k(i, j)].r_j\}.\lambda_j \quad (2)$$

Where

- $r_{Dij}$  is the operation time of the disconnector to isolate section j when it failure (hour/time).
- $r_j$  is the time to repair the transmission of section j (hour/time).
- $\lambda_j$  is the failure rate of section j,  $\lambda_j = \lambda_0.L_j$  (times/year),  $L_j$  is length of transmission line of section j.

The time of interruption power supply of section i when annual maintenance in section j is given by

$$T_{Mij} = \{A(i, j).r_{mD} + [1 - A(i, j)].r_{ms}\}.\lambda_m = \{A(i, j).T_2(i, j) + [1 - A(i, j)].r_{ms}\}.\lambda_m \quad (3)$$

If the distribution systems have more than one source, the equation (3) is written

$$T_{Fij} = \{C(i, j).T_2(i, j) + \prod [1 - A_k(i, j)].r_j\}.\lambda_j \quad (4)$$

Assume that have no two or more failures and have no two or more annual maintenance occurs simultaneously, the time of interruption power supply of section i when the failure and annual maintenance in all sections is given by

$$T_i = \sum_{j=1}^n T_{Fij} + \sum_{j=1}^n T_{Mij} \quad (5)$$

Based on equation from (1) to (5), the time of interruption power supply of one section and the distribution can be calculated. A MATLAB function named “**reliability**” is developed for the reliability evaluation of the electric power distribution systems.

The loss energy of section i cause by interruption power supply is given by

$$E_{Li} = \sum_{j=1}^n \frac{1}{T}.\lambda_j.P_i(t).T_i = \sum_{j=1}^n \lambda_j.P_m.T_i \quad (6)$$

Where  $T = 8760$  (hours),  $P_i(t)$  is the loads of section i,  $P_m$  is defined by formula

$$P_m = \frac{\int_0^{8760} P(t)dt}{8760} \quad (7)$$

The energy loss of the distribution system cause by interrupting power supply (or the Energy Not Supplied) can be calculated by

$$E_L = \sum_1^n E_{Li} \quad (8)$$

### 3 Case Study and Results

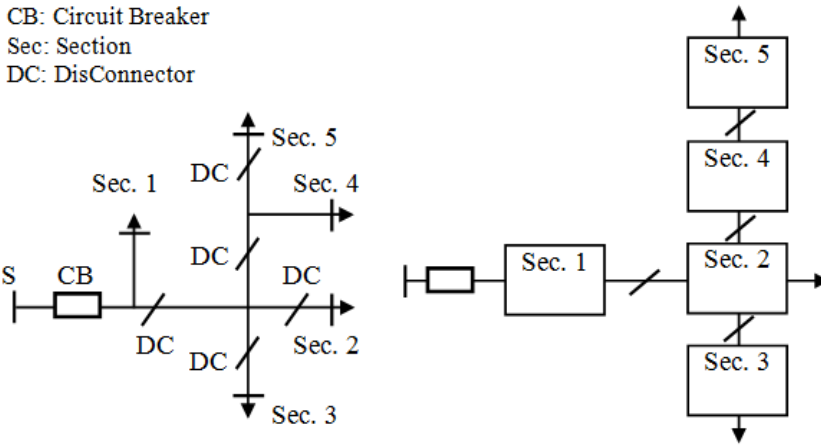


**Fig. 1.** The distribution system with five sections.

The case study taken from one distribution system from Vietnam as in Fig. 1 and it is separated into five sections by one circuit breaker and four disconnectors. The case study can be represented as follows:

- Case I: The original distribution system.
- Case II: All the sections are connected by circuit breaker.
- Case III: Using the reserved source connection at section 3.

**Table 1.** System parameters

Section	1	2	3	4	5
$\lambda_0$ (/yr)	0.094	1.126	0.339	0.061	0.132
$n_i$	34	126	80	15	25
$P_i$ (MW)	0.35	1.942	1.798	0.34	0.50

The information of distribution system:  $\lambda_0 = 4$  (/100km.year),  $r_L = 8$  (hours/time),  $r_D = 2$  (hours),  $r_{mD} = 0.5$  (hours),  $\lambda_m = 2$  (/year),  $r_{mS} = 2$  hours. The detail parameters for each section are given in Tab.1.

Based on defining the connection matrix in section I, the matrixes of these case studies can be constructed in Tab. 2. The distribution system in this paper, the capacity of the substation is assumed to be unlimited. For example, in case I, the fourth column vector  $[1 \ 1 \ 1 \ 0 \ 0]^T$  of matrix A shows that sections 1, 2 and 3 are connected to the substation while sections 4 and 5 are not, when the failure occurs in section 4.

**Table 2.** Connection matrix

Connection matrix	Case I	Case II	Case III	
A	$\begin{bmatrix} 0 & 1 & 1 & 1 & 1 \\ 0 & 0 & 1 & 1 & 1 \\ 0 & 0 & 0 & 1 & 1 \\ 0 & 0 & 1 & 0 & 1 \\ 0 & 0 & 1 & 0 & 0 \end{bmatrix}$	$\begin{bmatrix} 0 & 1 & 1 & 1 & 1 \\ 0 & 0 & 1 & 1 & 1 \\ 0 & 0 & 0 & 1 & 1 \\ 0 & 0 & 1 & 0 & 1 \\ 0 & 0 & 1 & 0 & 0 \end{bmatrix}$	$A_1 = \begin{bmatrix} 0 & 1 & 1 & 1 & 1 \\ 0 & 0 & 1 & 1 & 1 \\ 0 & 0 & 0 & 1 & 1 \\ 0 & 0 & 1 & 0 & 1 \\ 0 & 0 & 1 & 0 & 0 \end{bmatrix}, A_2 = \begin{bmatrix} 0 & 0 & 0 & 1 & 1 \\ 1 & 0 & 0 & 1 & 1 \\ 1 & 1 & 0 & 1 & 1 \\ 1 & 0 & 0 & 0 & 1 \\ 1 & 0 & 0 & 0 & 0 \end{bmatrix}$	
C	$\begin{bmatrix} 0 & 1 & 1 & 1 & 1 \\ 0 & 0 & 1 & 1 & 1 \\ 0 & 0 & 0 & 1 & 1 \\ 0 & 0 & 1 & 0 & 1 \\ 0 & 0 & 1 & 0 & 0 \end{bmatrix}$	$\begin{bmatrix} 0 & 0 & 0 & 0 & 0 \\ 0 & 0 & 0 & 0 & 0 \\ 0 & 0 & 0 & 0 & 0 \\ 0 & 0 & 0 & 0 & 0 \\ 0 & 0 & 0 & 0 & 0 \end{bmatrix}$	$\begin{bmatrix} 0 & 1 & 1 & 1 & 1 \\ 0 & 0 & 1 & 1 & 1 \\ 0 & 0 & 0 & 1 & 1 \\ 0 & 0 & 1 & 0 & 1 \\ 0 & 0 & 1 & 0 & 0 \end{bmatrix}$	

The distribution system in this paper with the capacity of the substation is assumed to be unlimited. For example, in case I, the fourth column vector  $[1 \ 1 \ 1 \ 0 \ 0]^T$  of matrix A shows that sections 1, 2 and 3 are connected to the substation while sections 4 and 5 are not, when the failure occurs in section 4.

**Table 3.** Results calculation

/year	The time of interruption (hours)			Energy Not Supplied (MWh/year)		
Case	I	II	III	I	II	III
Sec. 1	12.068	8.752	12.068	4.224	3.063	4.224
Sec. 2	21.824	20.760	17.072	42.382	40.316	18.233
Sec. 3	26.858	26.472	9.908	48.291	47.597	16.358
Sec. 4	25.190	24.248	20.438	8.565	8.244	16.514
Sec. 5	28.982	28.304	24.23	14.491	14.152	16.961

**Table 4.** Reliability Indices of distribution

Index	SAIFI	SAIDI	ASAI	ENS (MWh/year)
Case I	0.630	22.897	0.997386	117.952
Case II	0.630	21.794	0.997512	113.372
Case III	0.425	16.098	0.998162	72.290

The results calculation of three cases is shown in Tab. 3 and the reliability indices of the distribution system for all cases are shown in Tab. 4. Using circuit breaker can be improve the reliability indices than using disconnector because when failures occur, the circuit breaker can cut- off and isolate the fault section out of distribution but disconnector can't. The distribution system with the reserved source have the best reliability indices in three cases. It is clearly that increase reliability of supply generally requires increased capital investment.

## 4 Conclusion

In this paper, an analytical technique using the graph analysis to evaluate reliability is presented. The accuracy of this method is almost comparable to that of MCS (Monte-Carlo Simulation) [1], [2]. The proposed method is applied to calculate reliability indices of one distribution system in any case. The results have shown that graph analysis method is a simple method to evaluate the reliability of the distribution systems in many cases. It is necessary for planning, operation and economic scheduling of the power system.

**Acknowledgements:** This research was partially supported by the SGS grant from VSB-TU Ostrava (No. SP2017/54) and by the project TUCENET (No. LO1404).

## References

1. In-Su Bae, Jin O Kim, "Reliability Evaluation of Distrinuted Generation Based on Operation Mode", *IEEE Transastions on Power Systems*, vol.22, no2, pp.785-790, 2007.
2. In-Su Bae, Jin O Kim, "Reliability Evaluation of customers in a microgrid", *IEEE Transastions on Power Systems*, vol.23, no3, pp.1416-1422, 2008.
3. Marko Cepin, "Assessment of power system reliability". Springer London (2011), ISBN 978-0-85729-687-0.
4. Radomir Gono, Michal Kratky, Stanislav rusek, "Reliability of Distribution Network Components Based on Failure Databases", AASRI Conference on Power and Energy Systems, 2012, vol. 2, pp.75-80.
5. Radomir Gono, "Reliability and Maintenance of Electrical Power System'', invited lecture, Electric Power Engineering (EPE), 2017 18th International Scientific Conference on, July 2017, DOI: 10.1109/EPE.2017.7967362
6. R.Billinton and R.N.Allan, "Reliability Evaluation of Power Systems", 2ed, New York; Plenum, 1996.
7. Roy Billinton, Ajit Kumar Verma, Rajesh Karki, "Reliable and Sustainable Electric Power and Energy Systems Management", Springer India (2014), ISBN 978-81-322-1797-8.

# Partial Discharges Detection on Medium Voltage Overhead Power Lines

Jan Fulneček and Stanislav Mišák

Department of Electrical Power Engineering, FEECS,  
VŠB – Technical University of Ostrava, 17. listopadu 15,  
708 33 Ostrava – Poruba, Czech Republic  
{jan.fulnecek, stanislav.misak}@vsb.cz

**Abstract.** Problematic insulation fault detection is one of the biggest disadvantages of medium voltage covered conductors. During this type of faults, partial discharges activity is usually presented. Based on this knowledge, on-line partial discharges monitor was designed at VSB – TUO to detect insulation faults on medium voltage overhead power lines. This article describes testing of new antenna sensors for this detector, which should replace single layer inductor sensors in a future.

**Keywords:** Covered Conductors, Partial Discharges Detection, BONI Whip Antenna Sensor, Overhead Power Lines

## 1 Introduction

Medium voltage (MV) overhead power lines are usually equipped with regular bare wire AlFe conductors, without any external insulation. In a forested area, ground and interphase faults often occurs on such power lines because of surrounding vegetation. To eliminate this cause of faults, bare wire conductors should be replaced with covered conductors (CC). CC consists of aluminum core, which is covered by a thin layer of XLPE insulation material.

### 1.1 Medium voltage covered conductors

The biggest disadvantage of CC lies in a problematic detection of insulation faults [1]. If a tree or branch stays in a direct contact with CC, partial discharges (PD) may appear inside the XLPE insulation [2]. These discharges are causing slow degradation of CC, resulting into insulation failure (Fig.1). Partial discharges activity creates typical pattern in a time domain of voltage and current signals [3]. Early detection of PD activity can prevent the damage of CC and energy transmit interruption.



**Fig. 1.** Insulation, damaged by PD activity

## 1.2 Partial discharges detection

For continuous power line monitoring, on-line detection system must be used. Today, on-line PD detectors are used mainly for electric machines [4] and high voltage cable diagnostics [5]. High price of PD detectors prevents the spread of their usage on MV equipment. At VSB TUO, PD detector is being developed. This detector is directly designed to be used on MV overhead power lines with CC. Generally, Rogowski's coil is the most common sensor for PD detection. This coreless current transformer provides good sensitivity and wide range of operating frequencies [6]. But the detection with this sensor is problematic due to low value of current, caused by PD activity [7]. This is why VSB TUO detector uses single layer inductors (SLI) as sensors, which are mounted right on the surface of CC (Fig. 2). SLI creates capacitance coupling to a conductor, so it enables voltage measurements.



**Fig. 2.** SLI mounting

## 2 Partial discharges detector configuration

Diagram of the detector is in Fig. 3. SLI output is connected through the capacitance divider, amplifier and multiplexer to the data acquisition device (DAQ) with 8 bit resolution. There are four DAQ inputs, three of them are used for sensors (one sensor for each phase) and the rest one is backup. Sampling frequency is only 40 MS/s to

achieve the lowest possible price of the whole device. Besides voltage measurements, meteorological conditions (temperature and humidity) are also being measured.

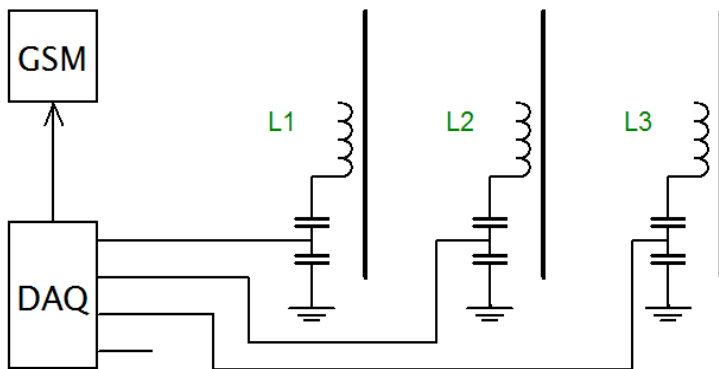


**Fig. 3.** Block diagram of the detector

Collected data are sent through GSM network to a database, which stores and process acquired signals. This database is accessible from internet.

### 2.1 Antenna sensor

Current research focuses on replacement of SLI by whip antenna. Unlike SLI, antenna based sensor for PD activity can be installed near CC without the necessity of power line disconnection. Another advantage is lower price of this sensor, because there is no need for capacitance dividers when the antenna is used. But there also some disadvantages too. The antenna is not able to detect signals with low frequency, so 50 Hz carrier wave is missing in the acquired signal. This makes PD pattern recognition much more complicated.

### 2.2 Antenna data acquisition

At the start of this year, 10 PD detectors with SLI sensors were additionally equipped with the BONI whip antenna [8]. Antennas were mounted on power line's poles, orientated in the same direction as a power line conductors (Fig. 4). The antennas outputs are connected to the backup input of PD detector DAQ, so the original functionality of the detector is preserved.



**Fig. 4.** BONI whip antenna mounted on the pole

### 3 Partial discharges activity detection

On 1st July, first insulation fault was detected by the antenna on detector, situated in Jeseniky Mountains. During the examination of collected data from the PD detector, it became clear that at least first one of these two tree falls probably occurred already on 28th June. On 1st July, PD activity became more significant, so it was automatically detected by the algorithm. Affected power line has high importance, because it is used for Praděd transmitter power supply. Next day, maintain workers found two fallen trees on this power line, situated approximately 300 meters from the PD detector (Fig. 5). Trees were immediately removed from the power line, without any interruption of power supply to the customers.



**Fig. 5.** Source of detected PD activity



## 4 Conclusion

Recent situation confirmed the possibility of PD detection with BONI whip antenna in a range of at least several hundred meters. Future work will focus on collecting and examination of more antenna signals, so it will be possible to improve the algorithm for PD detection. Another task is to estimate the antenna range and also testing of a different antenna designs.

## Acknowledgement

This paper is supported by the following projects: LO1404: Sustainable development of ENET Centre; CZ.1.05/2.1.00/19.0389 Development of the ENET centre research infrastructure; SP2017/159 Students Grant Competition and TACR TH01020426, Czech Republic.

## References

1. J. B. Wareing: Covered Conductor Systems for Distribution, EA Technology continental 2005, available at: <https://stoianconstantin.files.wordpress.com/2011/08/covered-conductor-systems-for-distribution-report-number-5925.pdf>
2. P. Pakonen: Detection of Incipient Tree Faults on high Voltage Covered Conductor Lines, Dissertation thesis at University of Tampere, 2007.
3. N.C. Sahoo, M. M. A. Salama, R. Bartnikas: Trends in partial discharge pattern classification: a survey. In: IEEE Transactions on Dielectrics and Electrical Insulation, Volume 12, Issue 2, April 2005, DOI: 10.1109/TDEI.2005.1430395
4. Partial Discharge Monitoring, Sensor 2017, available at: <http://www.sensor.com/sensormonitoring-solutions/partial-discharge-monitoring>
5. A. A. Khan: General Guidelines for Online Partial Discharge Testing of Power Cables, Available at: <http://electrical-engineering-portal.com/general-guidelines-for-online-partial-discharge-testing-of-power-cables>
6. B. Paophan, A. Kunakorn, P. Yutthagowith: Implementation of a Rogowski's coil for partial discharge detection. In: Electrical Machines and Systems (ICEMS), 2016 19th International Conference, Chiba, Japan 2016, ISBN: 978-4-88686-098-9
7. M. N. K. H. Rohani, C. C. Yii, M. Isa: Effect of unshielded and shielded Rogowski coil sensor performance for partial discharge measurement. In: Research and Development (SCOREd) 2015 IEEE Student Conference, Kuala Lumpur, Malaysia 2015, DOI: 10.1109/SCORED.2015.7449325
8. www.bonito.net, Bonito [Online]. Available: <http://www.bonito.net/boni-whip/en/>

## Publications

S. Misák, T. Jezowicz, J. Fulnecek, T. Vantuch, T. Buriánek, "A novel approach of partial discharges detection in a real environment", in 2016 IEEE 16th International

Conference on Environment and Electrical Engineering (EEEIC). IEEE, 2016, pp. 1-5. DOI: 10.1109/EEEIC.2016.7555556. ISBN 978-1-5090-2320-2.

S. Mišák, J. Fulnecek, T. Vantuch, T. Buriánek and T. Jezowicz, "A complex classification approach of partial discharges from covered conductors in real environment," in IEEE Transactions on Dielectrics and Electrical Insulation, vol. 24, no. 2, pp. 1097-1104, April 2017. DOI: 10.1109/TDEI.2017.006135

S. Mišák, J. Fulnecek, T. Vantuch, T. Buriánek and T. Jezowicz, "Usage of antenna for detection of tree falls on overhead lines with covered conductors," in Advances in Electrical and Electronic Engineering, vol. 15, no. 1, pp. 21-27, 2017. DOI: 10.15598/aeec.v15i1.1894

# Creating and Measuring Bipolar Ultra-Low Voltage Step-Up Converter

Petr Hawliczek and Radomír Goňo

Department of Electrical Power Engineering, FEECS,  
VŠB – Technical University of Ostrava, 17. listopadu 15,  
708 33 Ostrava – Poruba, Czech Republic  
{petr.hawliczek.st, radomir.gono}@vsb.cz

**Abstract.** The paper contemplated the possibility of using the power thermobattery with special bipolar converter that operate from voltages in the tens of millivolts. One converter has been developed and characteristics have been measured and documented. The only thermobattery with such a converter is able to supply low-power devices from the temperature difference of one tenth of a degree Celsius.

**Keywords:** Peltier thermobattery; TEG; ultra-low voltage step-up converter

## 1 Introduction

The quality and efficiency of thermal energy conversion into electric power using Peltier thermobattery has been rising constantly. The use of Peltier thermobatteries in numerous fields of application is still growing. This paper deals with use of Peltier thermobatteries under conditions with a very small difference of temperature, when the current and voltage generated are very low. Utilization of the low current and voltage by various devices requires development of a converter capable to work with such a low voltage. There has been one converter developed to work with the input voltage of around 20 mV already. For some application is 20 mV still too high that's why I focus to decreasing input voltage of converter. When connected, such boosting converter working from the level represented tens of millivolts can supply power to low-consumption equipment using its thermobattery from the temperature difference as low as 0.1 K only. Lower temperature differences can be accommodated by connecting multiple thermobatteries in series. Such small temperature differences are relatively easy to achieve in practice in order to create a source of power with almost unlimited service life to power measurement or communication equipment using solely the low temperature difference.

## 2 Supplying and creating converter

Converter which I created with such low voltage input doesn't exist yet.

The selected power source comprised the thermobattery of classic shape TEG 450-200-45 made by the German company THERMALFORCE.DE. This company is the supplier of high efficiency TEG type thermobatteries with a very wide range of products. They supply various types and shapes of thermobatteries, together with thermobatteries already integrated in various devices [1, 2].

The reason for selecting the thermobattery TEG 450-200-45 was its top voltage generated at the particular temperature level, when compared to other thermobatteries. The thermobattery is sized 57x54x3.4 mm. With the temperature difference of  $\Delta T = 100$  K, the open circuit voltage generated is 23.70 V, 1.09 A in short circuit run with the optimal load of 6.5 W. The internal resistance of this thermobattery is  $14.80 \Omega$ , it generates 0.220 V for the temperature difference of  $\Delta T = 1$  K. The thermal conductance of this thermobattery is 1.40 W/K with the maximum permissible temperature of 200 °C [3].

The Bipolar Ultra-low Voltage Step-Up Converter was built using integrated circuit LTC3109. This is special step-up converter chip capable of raising the voltage from the mere 20 mV fed to the input.

## 3 Converter with LTC3109 Works in Both Polarities

### 3.1 Default connection of the LTC3109 circuit

The Fig. 1 shows the basic wiring diagram for the LTC3109 circuit designed for building of a bipolar step-up converter. Similar integrated circuit is LTC3108 which can work unilar low input voltage [4]. The LTC3109 is able to operate with the bipolar input voltage between 30 mV and 500 mV [5]. Its practical applications concern utilisation of minimum direct voltages to power microchips, communication devices and similar devices [6].

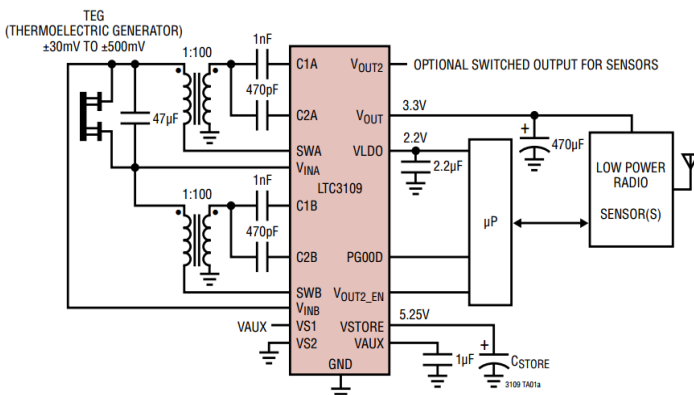


**Fig. 1.** Basic wiring diagram for the LTC3109 circuit [5]

LTC3109 is very similar to the LTC3108. Those are basically two chips LTC3108 within a single case. That enables the converter operate with both polarities. If the converter is connected to a thermobattery with potential chaotic variation of lateral temperatures, the polarity of output voltage will also change. This converter will be working with both polarities, positive as well as negative direction [7].

The converter works with J-FET transistors they are conductive when voltage on gate is 0 V. The converter formed by two LTC3108 circuits must be therefore connected in series. This series connection one converter operates, while the other one just passing electric current through only. Due to losses on the idle converter, the converter with LTC3109 starts working from 30 mV. Hence the higher activation voltage is due to the ability for operation in both polarities.

The basic wiring diagram in Fig. 1 shows that the circuit is basically formed by 2 converters LTC3108. However, the connection actually does differ. The earth must be connected via the internal circuit wiring; otherwise the output voltage would be offset against the input voltage in case of negative supply voltage. There is no galvanic link between the input and output of the converter, yet the negative output pin of GND connects with the negative voltage input pin according to the direction of the supply voltage.

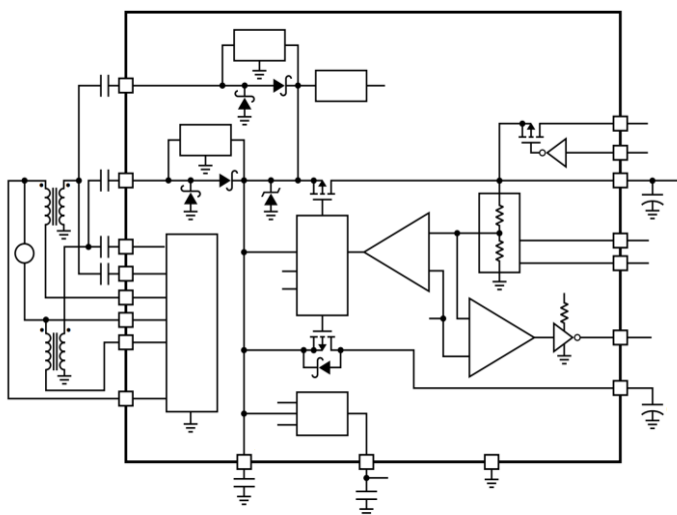
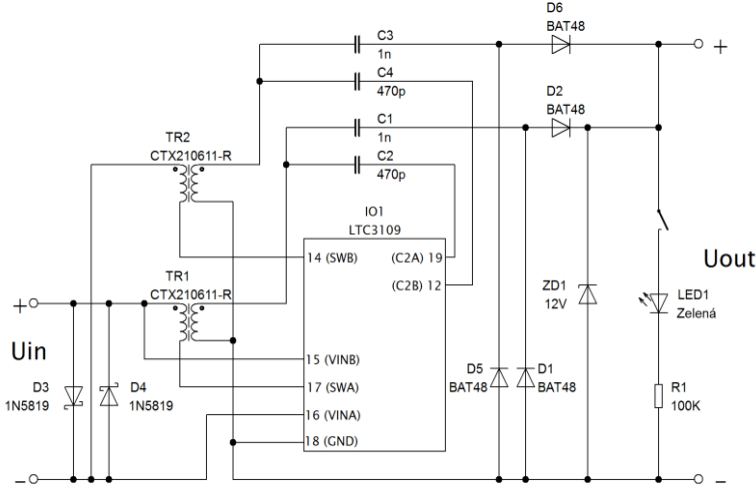


Fig. 2. Internal wiring of LTC3109 circuit [4]

### 3.2 Modified wiring of the LTC3109 circuit

The wiring diagram is modified at the output again, with two pulse pumps formed by four Schottky diodes BAT48 D1 and D2. The two pulse pumps are connected in order to prevent retroactive impact on the circuit via the second transformer, which is not in operation. Schottky diodes D3 and D4 protect the circuit against over-voltage and inversion voltage at the input. ZD1 helps avoid over-voltage at the output and stabilises the output voltage at 12 V. The light emitting diode LED1 with R1 in the

circuit serves for indication of the output voltage when the switch is set to “ON” position. The transformers TR1 and TR2 have been selected for this circuit COILTRONICS - CTX210611-R with the turn ratio of 1:125. The full wiring diagram is shown in Fig. 3.



**Fig. 3.** Wiring diagram for the converter measured with LTC3109

The measured converter with LTC3109 was measured with respect to dependency between the input voltage and the output current with the output voltage limited to 4 V. For the measurement results, see the Fig. 4 and the Table 1.

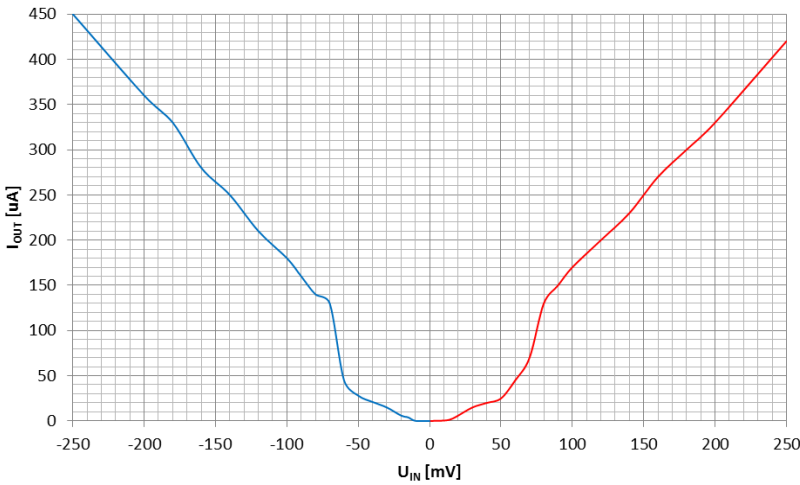


**Fig. 4.** Graph of input voltage on the output current with the output voltage limited to 4V.

The graph shown in Fig. 4 is very similar to the one contained in the datasheet of LTC3109 [7]. However, the current supplied from the converter is lower, which will be probably due to the higher turn ratio in the transformer. The graph in datasheet has been created with respect to the turn ratio of 1:100 and the turn ratio of the connection measured is 1:125. But the greater turn ratio enables the converter operate from lower voltage levels and stable operation level is from the input voltage of 10 mV.

**Table 1.** Dependency of the input voltage on the output current with the converter output voltage limited to 4V

$U_{IN}$ [mV]	$I_{IN}$ [mA]	$I_{OUT}$ (4V) [μA]
0	0	0
10	2	0,5
15	3	2
20	5	6
30	8	15
40	12	20
50	13	25
60	15	45
70	25	70
80	30	130
90	36	150
100	40	170
120	50	200
140	60	230
160	70	270
180	80	300
200	90	330
250	120	420

$U_{IN}$ [mV]	$I_{IN}$ [mA]	$I_{OUT}$ (4V) [μA]
0	0	0
-10	-2	0,2
-15	-3	4
-20	-5	6
-30	-8	15
-40	-12	21
-50	-13	28
-60	-15	45
-70	-30	130
-80	-35	140
-90	-40	160
-100	-45	180
-120	-50	210
-140	-60	250
-160	-75	280
-180	-85	330
-200	-100	360
-250	-140	450

- $U_{IN}$  - Converter input voltage
- $I_{IN}$  - Converter input current
- $I_{OUT}$  (4V) - Converter output current

## 4 Conclusion

Bipolar Ultra-Low Voltage Step-Up converter has been working since voltage level of approximately 30 mV. In the converter there was used integrated circuit LTC3109 featuring the special transistors J-FET actuated basically from the voltage level of 10 mV and started about voltage level of under 30 mV. Converter with thermobattery can works from very low difference of temperatures on the thermobattery as 0.1 K. This effect can be used for creating power source with almost unlimited lifetime and capable of powering measurement or communication devices, for example, using just this low difference in temperature. Future scope is to develop converters differing by their switching transistors. There will be no more used integrated circuits as LTC3109, but different type transistors in order to create a bipolar converter using even lower operating voltage.

## Acknowledgment

This research was partially supported by the SGS grant from VSB – Technical University of Ostrava (No. SP2017/54) and by the project TUCENET (No. LO1404).

## References

1. Thermogeneratoren / Seebeckelemente [online, cit. 2016-01-10]. <http://thermalforce.de/de/product/thermogenerator/index.php?uid=e00f7b7cfb2e445b2e399b9c55c3d6b0&ref=>
2. Generatormodule + Accessories [online, cit. 2016-01-10]. <http://thermalforce.de/de/product/module/index.php?uid=e00f7b7cfb2e445b2e399b9c55c3d6b0&ref=>
3. TEG 450-200-45 [online, cit. 2016-01-10]. [http://thermoelectrics.de/de/product/thermogenerator/TG450-200-45S\\_.pdf](http://thermoelectrics.de/de/product/thermogenerator/TG450-200-45S_.pdf)
4. LTC3108 [online, cit. 2016-01-10]. [www.linear.com/docs/28823](http://www.linear.com/docs/28823)
5. LTC3109 [online, cit. 2016-01-10]. [www.linear.com/docs/29537](http://www.linear.com/docs/29537)
6. P. Mullen, J. Siviter, A. Montecucco, A.R. Knox, A Thermoelectric Energy Harvester with a Cold Start of 0.6 °C, 12th European Conference on Thermoelectrics, Volume 2, Issue 2, 2015, Pages 823–832
7. J.A. Paradiso, T. Starner, Energy Scavenging for Mobile and Wireless Electronics, Pervasive Computing (January – March 2005), Pages 18-27



# Comparison of Dynamic Model of Asynchronous Machine and Real Asynchronous Machine

Martin Král and Radomír Goňo

Department of Electrical Power Engineering, FEECS,  
VŠB – Technical University of Ostrava, 17. listopadu 15,  
708 33 Ostrava – Poruba, Czech Republic  
{martin.kral.st3, radomir.gono}@vsb.cz

**Abstract.** This paper deals the mathematical description of an asynchronous machine. Differential equations are then used to create a dynamic model of asynchronous machine. For the possibility of evaluation the quality of the created model are created at the conclusion the basic characteristics of representing the asynchronous machine. Graphs show almost identical measured and the simulated values. The model is created with a lot of simplification, therefore the simulation model will be not behave identically in all cases, as the real asynchronous motor.

**Keywords:** three phase induction machine, dynamic model of asynchronous machine

## 1 Introduction

The most of industrial motors if one horsepower or larger are three-phase induction machines. Induction machines require no electrical connection to the rotor windings. Instead, the rotor windings are short-circuited. Magnetic flux following across the air gap links these closed rotor circuits. As the rotor moves relative to the air gap flux, Faraday's-law voltages are induced in the shorted rotor windings, causing current to flow in them [1].

Asynchronous motors, especially with a squirrel-cage motor, are for many years the most famous electric motors on our planet. It happened because of their structural simplicity, low cost, high reliability and efficiency.

Mathematical model of the asynchronous motor is difficult and some researchers have developed the model by transferring into d and q axis. However, more accurate model can be derived by using  $\alpha$ ,  $\beta$ ,  $\gamma$  axis. Therefore, this paper is aimed to obtain dynamic model of the motor which has been transferred into three axes [2], [3], [4].

This research was partially supported by the SGS grant from VSB - Technical University of Ostrava (No. SP2017/54) and by the project TUCENET (No. LO1404).

## 2 Mathematical model of asynchronous machine

Due to the design we consider asynchronous machine (ASM) for the nonlinear system with a number of parameters. We tried to find a system of differential equations that would sufficiently and accurately describe the properties of the machine. When we design a mathematical model, we use a series of assumptions that simplify the Assembly model. In particular, the following assumptions:

- Stator and rotor winding is three-phase, coils of phases are spread out symmetricaly along the air gaps,
- three-phase stator and rotor winding is connected into the star,
- magnetic induction along the air gap is ideal sine,
- magnetic circuit has a linear characteristic,
- resistances are constant,
- losses in magnetic circuits are zero [5].

*The equations of stator voltage:*

$$u_{abcs} = r_s \cdot i_{abcs} + \frac{d\psi_{abcs}}{dt} \quad (1)$$

*The equations of rotor voltage:*

$$u'_{abcr} = r'_r \cdot i'_{abcr} + \frac{d\psi'_{abcr}}{dt} \quad (2)$$

*The equation of torsional-mechanical:*

$$\frac{d\omega_r}{dt} = \frac{p}{2 \cdot J} \cdot T_e - \frac{B_m}{J} \cdot \omega_r - \frac{p}{2 \cdot J} \cdot T_L, \quad \frac{d\theta_r}{dt} = \omega_r \quad (3)$$

## 3 Determining circuit model parameters

The equivalent circuit of an induction motor is a very useful tool for determining the motor's response to changes in load. However, if a model is to be used for a real machine, it is necessary to determine what the elements values are that go into the model.

*The No-Load Test:*

The no-load test of an induction motor measures the rotational losses of the motor and provides information about its magnetization current.

*The DC Test for Stator Resistance:*

Basically, a dc voltage is applied to the stator windings of an induction motor. Because the current is dc, there is no induced voltage in the rotor circuit and no resulting rotor current flow. Also, the reactance of the motor is zero at direct current. Therefore, the only quantity limiting current flow in the motor is the stator resistance, and that resistance can be determined.

### *The Locked-Rotor Test:*

This test corresponds to the short-circuit test on a transformer. In this test, the rotor is locked or blocked so that it cannot move, a voltage is applied to the motor, and the resulting voltage, current and power are measured.

### *Results of Determining Parameters:*

I've done tests of the motor as described above. From the measured voltages, currents, and power I calculated the performance parameters for the model of asynchronous machine.

### *Parameters for model:*

$R_s = 3.2\Omega$  (resistance of stator circuit),  $R_r = 2.27\Omega$  (resistance of rotor circuit),  $L_{ms} = 0.133H$  (mutual inductance),  $L_{ls} = 0.0095H$  (stator inductance),  $L'_{lr} = 0.0095H$  (rotor inductance).

## 4 Measurement of the parameters of asynchronous motor

The measurement was carried on the three-phase asynchronous motor, which was measured at the rated voltage and rated frequency. During the measurement was motor in the state of no-load, gradually was increased the load until the motor has reached the rated current and rated torque.

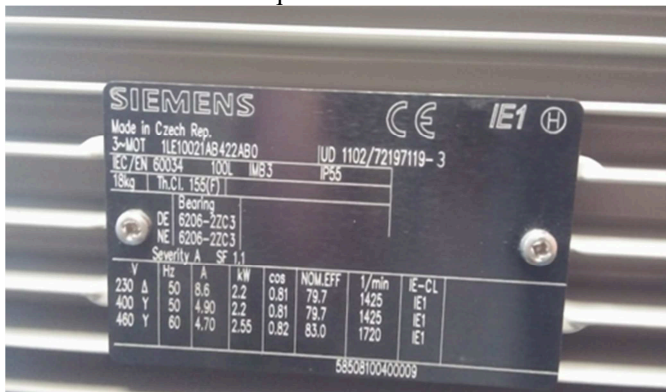


**Fig. 1.** The values of asynchronous motor.

Motor was connecting to grid in star (Y) connection with rated voltage 400 V and frequency 50 Hz.

## 5 Simulation of three phase asynchronous machine in MATLAB Simulink

To create a dynamic model, we took advantage of the differential equation, which is described above. As has been written, these differential equations describe the three

phase asynchronous machine, if the rotor voltages are  $u'_{abcr} = 0$ , this is a machine with a squirrel-cage.

When using the dynamic model of asynchronous machine, model can be used in two modes, the motor and the generator. Simulation mode can be changed by using value of TL (torque of load), if is  $TL > 0$  asynchronous machine is in the motor mode, if is  $TL < 0$  asynchronous machine is in the generator mode.

*The parameters of the machines in the simulation:*

Stator phase voltages:  $u_{abcs} = 231V$ , rotor voltages:  $u'_{abcr} = 0V$  (squirrel-cage),  $p = 4$  (poles),  $R_s = 3.2\Omega$  (resistance of stator circuit),  $R_r = 2.27\Omega$  (resistance of rotor circuit),  $L_{ms} = 0.133H$  (mutual inductance),  $L_{ls} = 0.0095H$  (stator inductance),  $L'_{lr} = 0.0095H$  (rotor inductance),  $B_m = 0.003T$  (magnetic induction),  $J = 0.013kg \cdot m^2$  (moment of inertia),  $f = 50Hz$  (frequency),  $T_L = 15N \cdot m$  (torque of load).

*The simulation results:*

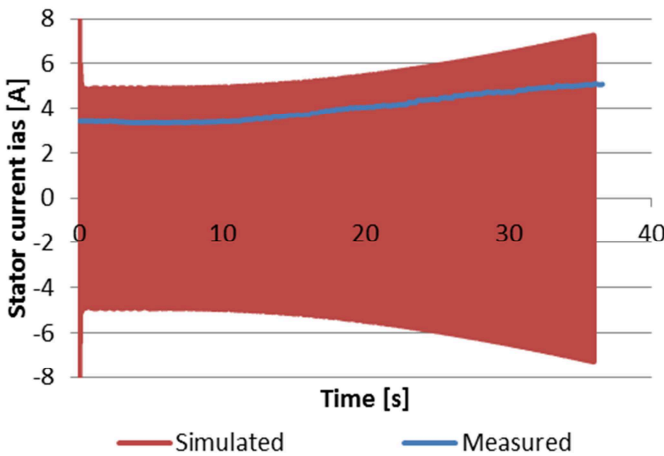


**Fig. 2.** Stator current

In the **Fig. 2** above you can see amplitude of the stator current. The value is different, because the measured value is effective. Simulated current is maximum peak value.

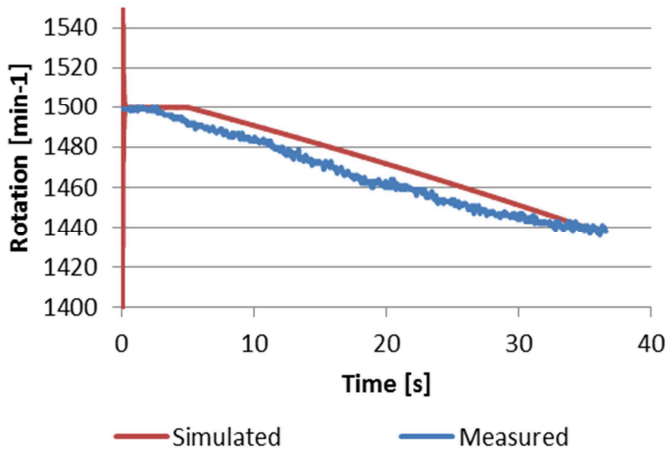


**Fig. 3.** Rotation

In the **Fig. 3** above you can see the inaccuracy, between the measured and simulated value. This difference is caused by the change of torque load. The value of torque load wasn't linear during measurement during simulation was torque load changed with linear change.

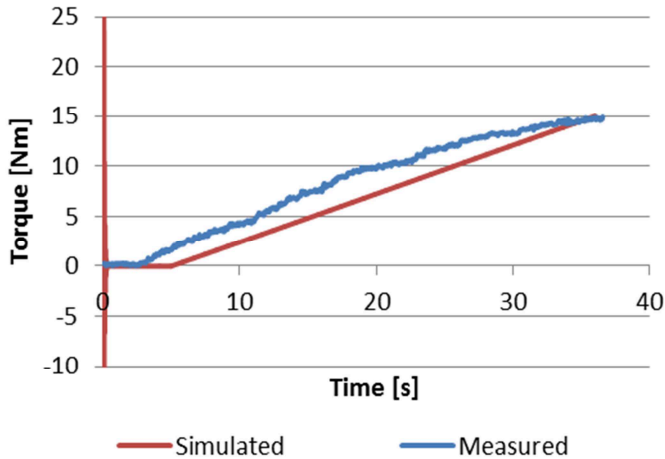


**Fig. 4.** Torque

In the chart for torque (**Fig. 4**) is seen the same displacement, which was mentioned in the **Fig. 3** with the rotation chart.

## 6 Conclusion

At the beginning, the basic differential equations describe the asynchronous machine. From these equations, there are compiled differential equations, which are useful for the description of dynamic model of asynchronous machine.

In the practical part, there was created a dynamic model of asynchronous machine in MATLAB Simulink, which uses the previously described differential equations, which simulate the operation of the asynchronous machine. For simulating there were chosen the parameters of the real machine with a squirrel-cage, these parameters are also listed in this work.

According to the charts, it is clear that the model is close to the real asynchronous motor.

### Acknowledgment.

This research was partially supported by the SGS grant from VSB - Technical University of Ostrava (No. SP2017/54) and by the project TUCENET (No. LO1404).

### References.

1. George McPherso, Robert D. Laramore, An Introduction to Electrical Machines and Transformers, John Wiley & Sons, 1990. 563 p. ISBN 0471635294.
2. Y. Kazakov, I. Palilov, Advanced Model of Squirrel Cage Induction Machine for Broken Rotor Bars Fault Using Multi Indicators, AEEE, December 2016.
3. I. Ouachtouk, S. El Hani, S. Guedira, K. Dahi, L. Sadiki, Research Related Electromechanical Processes in an Asynchronous Traction Motor – Asynchronous Generator with Common Shaft Based on Field Model, AEEE, December 2015.
4. Stephen J. Chapman, Electric Machinery Fundamentals, Fourth Edition McGraw-Hill Higher Education, 2005. 737 p. ISBN 0072465239.
5. Josef Belousek, Trakční pohony s asynchronním motorem Doctoral thesis (VUT Brno), 2013. 136 p.

### Publication of results in this year.

18th International Scientific Conference EPE 2017

### Prices received in this year.

Cena Nadace ČEZ – 1th in the field of electrical machines, devices, systems and drives

# Analysis of the Failure Rate of MV Circuit Breakers

David Lazecký

Department of Electrical Power Engineering, FEECS,  
VŠB – Technical University of Ostrava, 17. listopadu 15,  
708 33 Ostrava – Poruba, Czech Republic  
david.lazecky.st@vsb.cz

**Abstract.** The paper describes results of analysis and evaluation of database of failures and database of circuit breakers. The databases are sources of real values for failure rate estimation and regression analysis for specific region in the Czech Republic with very developed heavy industry. Possible consequences for original assets are presented as well as the comparison of theoretical values and discussion about possible mistakes and outcomes.

**Keywords:** Circuit Breaker, Failure Rate, Analysis, Prediction

## 1 Introduction

The reliability engineering itself is heavily connected with mass production of sophisticated products in factories that began in the last century. Same parts and products became wisely designed and widely available so it is possible to see the reliability evaluation as a part of process of production optimisation but the process was not standardised. After the World War II there was a problem with reliability of military products and equipment that led to the standardisation of the process of reliability evaluation. During the 1960s the first failure databases started to collect the data of failures. The rise of personal computing made the processes of exploration and evaluation easily available for everyone who has access to such a database. [1]

Well maintained and updated databases of failures and outages in electrical energy generation and distribution systems are highly valued in tasks of reliability estimation and malfunction prediction as well as maintenance optimisation. In the case of proper application of exploration methods and calculation process it is also possible to evaluate currently operational assets, eliminate those with higher failure rate and predict the failure rate in future. Of course, the process cannot be stopped. The whole process has to evolve according to new trends globally. The new technology or knowledge in one step of the evaluation process causes changes in the whole system where everything has to be adjusted to the change. [1, 2]

The evaluation of the database of failures is set according to the current standards and trends used by Czech electricity transmission and distribution companies but also implements the evaluation from abroad.

## 2 Databases

Data for the evaluation come from the database of failures that contains all regions in the Czech Republic. Every possible monitored error, failure, etc., which are recorded according to the law and also the internal regulation, is recorded in the database. Due to the calculation process only circuit breakers from relatively small region and last 5 years period have been selected for the evaluation. The limitation is because the corresponding database of all operational circuit breakers covered only this region.

### 2.1 Database of failures

The database of failures contains over 1000 failures in 5 years (2012 – 2016). 51 of these failures match the corresponding database of circuit breakers (CBs). There are also some other restrictions applied. Only failures from categories “operational” and “uncertain” are accepted to the evaluation because those should concern CBs. That means exclusion of causes like “caused by animals” etc.

The following graph shows failure rates by years.

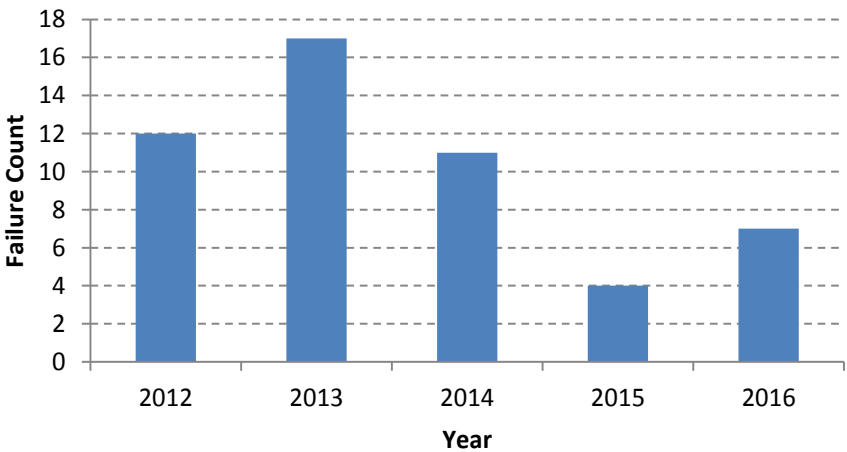


**Fig. 1.** Failure count by single years

By looking at fig. 1 it is possible to see that failures occurred mostly random according to the year. The following table 1 specifies that only 5 CBs suffered more than one failure in evaluated five year interval.

**Table 1.** Failure count of the specific CB

Failure count of the specific CB	Count	[%]
1x	41	89.13%
2x	5	10.87%



## 2.2 Database of MV and HV Circuit Breakers

The database contains over 1000 pieces of CB in a specific region. Due to high level of industrial substations in the region and very specific historical development there are CBs that are currently not used for unspecified period of time but they are still in place and only consumption side is disconnected. According to this situation the limit of age was set as high as the oldest operational CBs in general purpose distribution station – production year 1977.

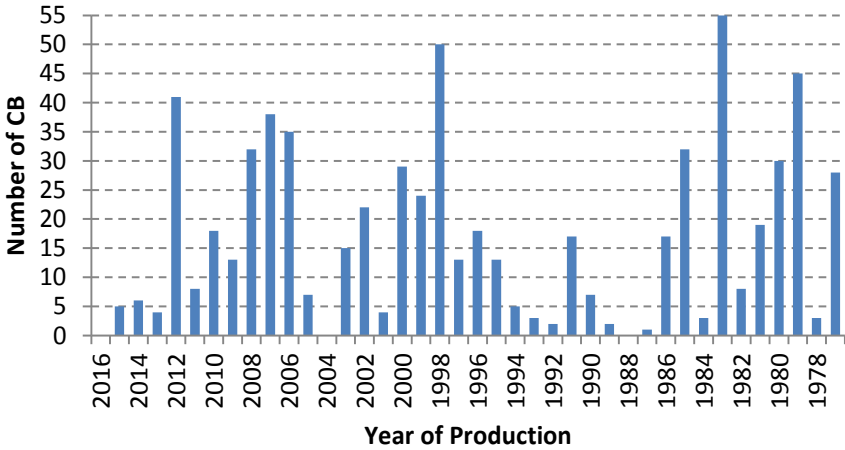


Fig. 2. All CB in region by year of production

## 3 Failure rate

After the exploratory analysis of selected data from the source databases the process continues by sorting and computing the number of CBs and failures for each year of the time interval.

Failure rates are calculated according to the following formula (1) for the 5 year interval of recorded data. The interval of 5 years is generally recommended as the lowest possible for such evaluation because the length of the evaluation interval positive-ly influences the accuracy of results.

$$\lambda = \frac{N}{Z \cdot P} \quad (1)$$

Where  $N$  is the number of failures in the evaluated period,  $Z$  is (average) number of all devices in the evaluated period and  $P$  is time period of evaluation. The  $\lambda$  is the failure rate for each year of the CB age (1/year). [3, 4]

## 4 Regression

The complete regression analysis for failure rate data is performed according to the standard statistical processes. First model applied in Statgraphics software is linear. Second regression model is 2<sup>nd</sup> order polynomial which describes the failure rate quite well. Both models are showed in the following graph for the comparison purposes.

Linear model is used quite frequently but in this case is not appropriate. The P-value of the model is 0.0012 and the R-squared value is 24.92% but the intercept parameter is not significant for the model. The equation is showed below.

$$\lambda = -0.00498517 + 0.000927747 \cdot age \quad (2)$$

2<sup>nd</sup> order polynomial model fits the dataset with the P-value 0.0001 and the R-squared value is 43.37% due to the high differences between values after age of 32 years. Three influential points are deleted from the dataset – last three values of the failure rate. The equation is showed below.

$$\lambda = 0.0067453 - 0.00123298 \cdot age + 0.0000664047 \cdot age^2 \quad (3)$$

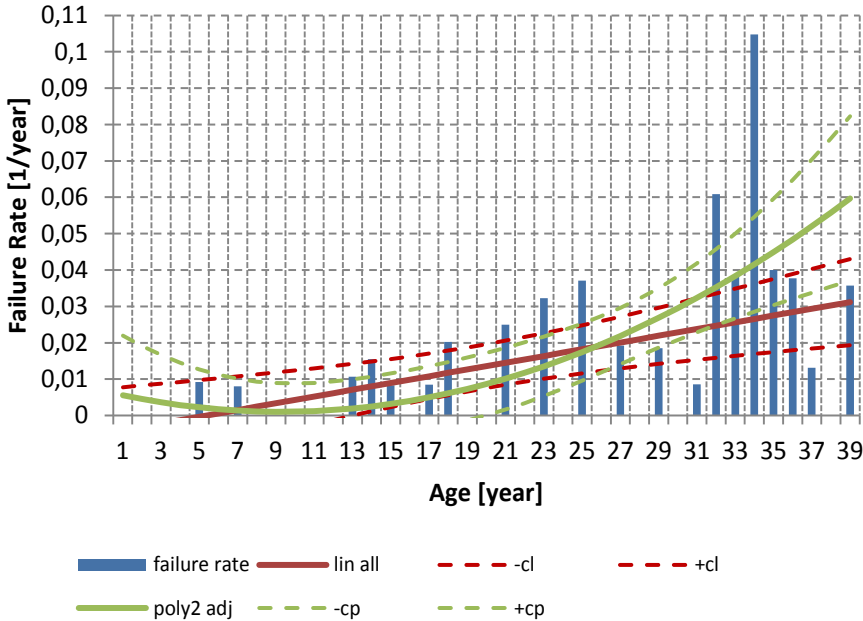


Fig. 3. Plot of fitted models with confidence limits

The limits for the evaluation of the CBs are shown in the table below. The values are recalculated into the unit used in the majority in the Czech Republic – failure rate per year. Two sources are used although the difference is relatively insignificant.

**Table 2.** Failure rate limits

Description	Failure rate (per year)		
	Low	Typical	High
Circuit Breakers [1]	0.001	0.01	0.030
Circuit Breakers [3]	0.015		

## 5 Conclusion

I have performed evaluation and the statistical analysis of the failure rate of HV and MV CBs in very specific region for the time interval five years. The process is described in according sections. The result is the equation of the 2<sup>nd</sup> order polynomial regression that describes 43.37% of data.

The combination of both regression models might fit the dataset better until the age of 26 years. Due to the specific data set it is not possible to perfectly verify the “bath-tub curve” which should be the proper outcome. From the age of 31 – 33 years the dataset and the models are quite uncertain but this age might be the limit for the generally used CBs. Current model should be matched with other regions for verification of the prediction because there is high probability of changes in the future that may result in normalization of the assets according to the other regions.

The regression model might be specified by using longer time interval of the failures data (for example 10 years). The other possibility is bigger region for evaluation. Combination of both alternatives might result in the most specific regression model that could describe the reality very well.

**Acknowledgements.** This research was partially supported by the SGS grant from VSB-TU Ostrava (No. SP2017/54) and by the project TUCENET (No. LO1404).

## References

1. David J. Smith, *Reliability, Maintainability and Risk: Practical Methods for Engineers*; 7<sup>th</sup> edition. Amsterdam: Elsevier, 2007. ISBN: 978-0-7506-6694-7
2. Ali A. Chowdhury, Don O. Koval, *Power distribution system reliability: practical methods and applications*; Hoboken: Wiley, 2009. ISBN: 978-0470-29228-0
3. J. Piskac, & J. Marko, *Regulations for electric power system no. 2 – failure statistics at electricity distribution* (Prague, CZ: CEZ, 1974)
4. Distribution companies of the Czech Republic, *Distribution network grid code, appendix no. 2 - methodology of reliability determination of electric power supply and distribution network equipments* (Prague, CZ: ERU, 2005)
5. R. Briš, *Statistika I.*; VŠB – TU Ostrava, Fakulta elektrotechniky a informatiky: Ostrava, 2004.
6. M. Litshmannová, *Úvod do statistiky*; VŠB – TU Ostrava, Fakulta elektrotechniky a informatiky: Ostrava, 2012, 380s.

## Publications

D. Lazecký, V. Král, S. Rusek, R. Goňo, Software Solution Design for Application of Reliability Centered Maintenance in Preventive Maintenance Plan. In *Proceedings of the 18<sup>th</sup> International Scientific Conference on Electric Power Engineering (EPE)*. Ostrava: VŠB - Technical University of Ostrava, Faculty of Electrical Engineering and Computer Science, Department of Electrical Power Engineering, 2017. DOI: 10.1109/EPE.2017.7967354.

# Analysis of Measured Values and Digital Model Created by Software EMTP-ATP

Tomáš Mozdřeň

Department of Electrical Power Engineering, FEECS,  
VŠB – Technical University of Ostrava, 17. listopadu 15,  
708 33 Ostrava – Poruba, Czech Republic  
tomas.mozdren.st1@vsb.cz

**Abstract.** This paper deals with the analysis of measured values at the Technology Center in Ostrava - Vítkovice, on the power converter, which are then compared between the created digital model. This model was created using the EMTP - ATP software. The current simulation configuration is based on a block diagram of all unconventional power sources.

**Keywords:** Analysis; digital model; technological center; software; AC bus; power converter

## 1 Introduction

Power engineering represents one of the key domains in economy of each country. Every government aims to ensure safe and stable power supply and this also has the top priority among objectives of countries in the European Union. Hence the mankind keep seeking ways to reduce their dependency on exhaustible fossil fuels. The exhaustible resources are paralleled by their alternate comprising renewable energy resources (RES). That was the reason for establishment of the Technological Centre in Ostrava (TCO), adapted to the needs of unused buildings within the industrial zone of Vitkovice municipality. TCO represents one of the detached departments of the VSB-TU Ostrava subsidised within the ENET project.

The objectives of research include utilisation and practical verification of accumulation of electric power supplied from either the distribution grid or power generating units installed within the TCO. This summary is the initial step within the energy system prior to creation of any dynamic model of the TCO to enable examination of energy balances, analysis of transients and short-circuit effects that may occur on sources themselves and the distribution system.

## 2 Connections and Technologies at TCO

The simplified electric diagram of the technological centre in Ostrava is illustrated by the Fig. 1. Individual energy sources have been divided a drawn into technological blocks for legibility purposes, these blocks are formed per basic functioning principles of the

sources or with respect to the assumed relevance to other technologies within the TCO. The primary supply of power to TCO and the power outlet from the centre are ensured in terms of connection to the local distribution system. The backbone source of electric output from TCO is the co-generation unit with an asynchronous generator with the power output of 100 kW cooperating with a gas piston combustion engine. This unit is supplied with gas fuel from the processing thermal cracker with typical continuous supply of 250-450 kg of the fuel material per hour (depending on its composition). The topology of electric power distribution system of TCO comprises the main AC bus with the option to connect onto the backup AC bus. The whole distribution system at the centre has been designed and built as fully subsistent with potential opportunity to switch into island operation mode with 3x230/400V and with the optional power supply to the adjacent industrial buildings. Installation of various accumulation systems forms a vital part of the whole TCO. This accumulation is ensured with various types of batteries that are always linked to the main direct-current bus DC 400V. The bus enables distribution of electric power into the individual parts and components of the system using inverters. The linkage between direct-current buses and buses featuring standard network parameters is ensure by means of solid-state power inverters accompanied by the coupling transformers and impedance coils TR1+TL1 and TR2+TL2 enable two-way transmission of power between buses.

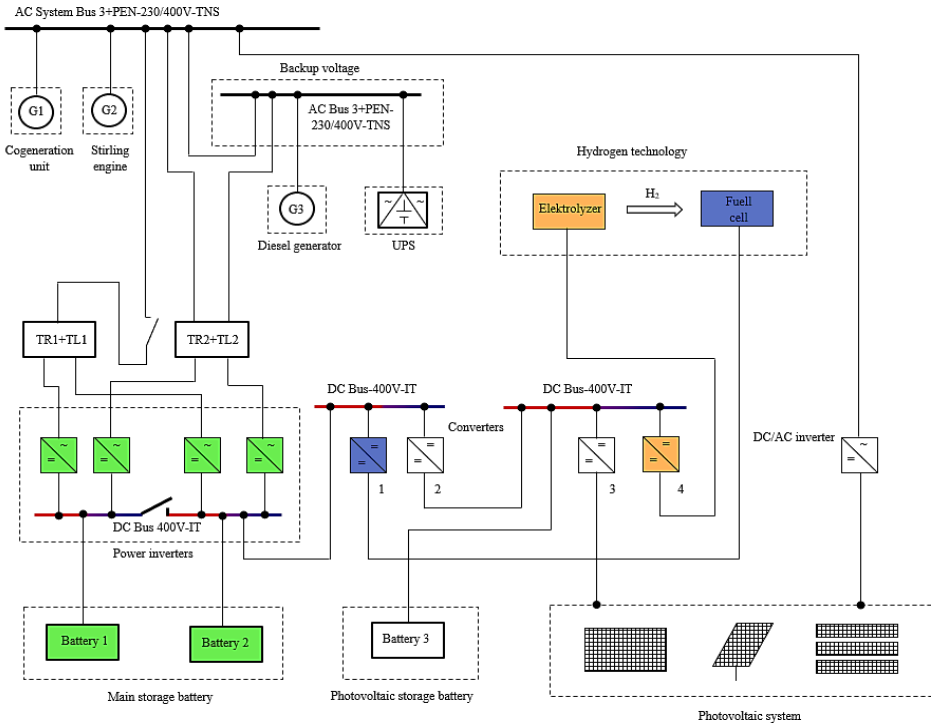


**Fig. 1** Connection of real AC sources within TCO into individual blocks [1]

### 3 Simulation and real data on power converter

The simulation that was created in the EMTP-ATP program shows the power transfer during charging to the batteries via the power converter (the inverter operates in the recti-

fier mode) and the comparison of the actual measured values on the inverter are described in this chapter. Table 1 shows the required values in the EMTP - ATP simulation software.

**Table 1** Information about sources for simulation

Information about source and LC filters					
3 phase source		LC filter AC side		LC filter DC side	
$U_m$	153.4 V	L1	19 mH	L2	19 mH
		C1	750 uF	C2	500 uF

Overall scheme sources which has been modified shown in Fig. 2.

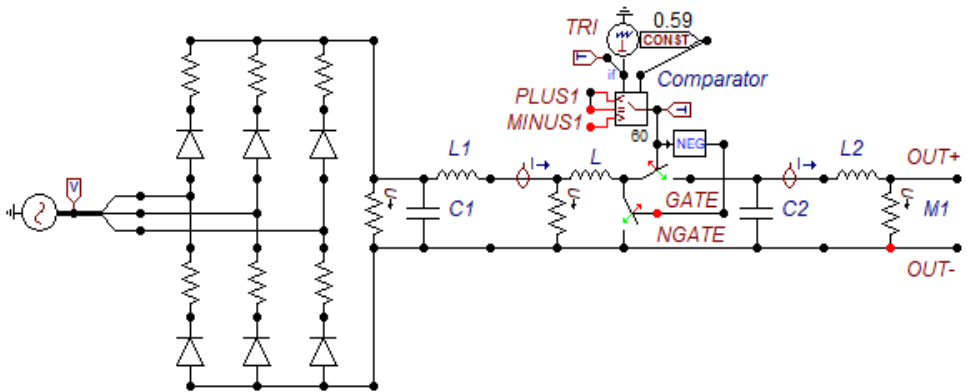


**Fig. 2** Adapted schema for transfer energy charging battery from network [2], [3], [4]

The digital model was developed from the desired state of measurement where the charged batteries from the AC network. For this reason, it is fully modeled in the computer model 6-pulse rectifier, which is directed through the diodes and LC filter feeding is its progress cut off to controlled boost DC/DC converters entered only the smooth progress of the DC voltage supply. LC filter at the output of the rectifier has been set to the value of  $L1 = 19 \text{ mH}$  and  $C1 = 750 \text{ }\mu\text{F}$ . Since you need to smooth out and the progress of the voltage and current at the output of the DC/DC converters, so here he was elected to the LC filter, its value is set to the value of  $L2 = 19 \text{ mH}$  and  $C2 = 500 \text{ }\mu\text{F}$ . Resistor M1 can be regulated output current  $I$

Maximum voltage source for the simulation was determined from the measured values of the voltage transformation, where Fourier transform is shown on Fig. 4 with effective value 108.4 V

$$U_m = U \cdot \sqrt{2} = 108,4 \cdot \sqrt{2} = 153,4V \quad (1)$$

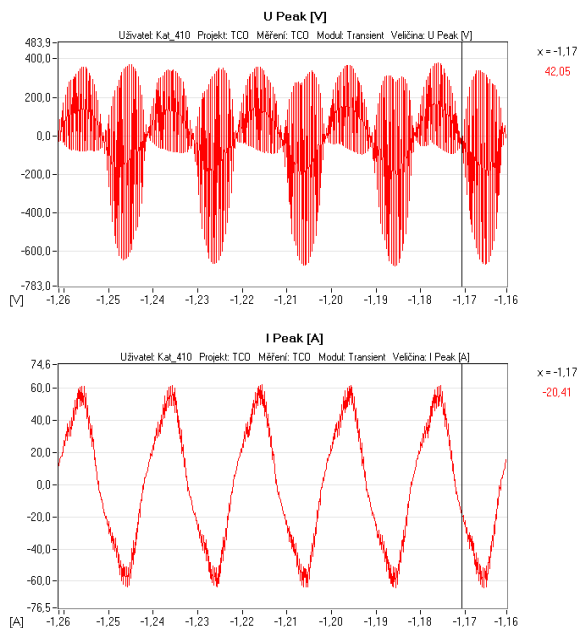


Fig. 3 Real course of voltage and current with using BK-ELCOM

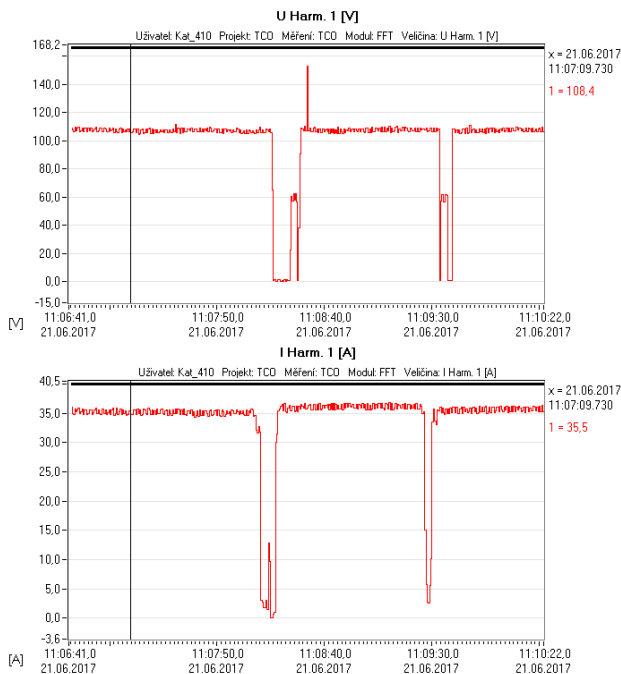
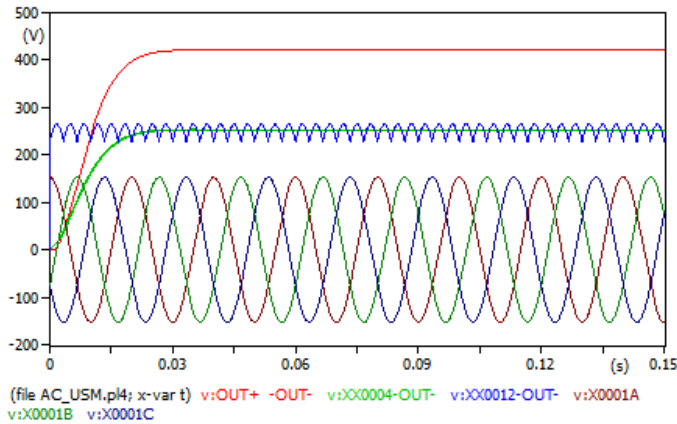


Fig. 4 Real course of voltage and current of Fourier transform with using BK-ELCOM





**Fig. 5** Simulation course of input three-phase voltage and output voltage after rectification and output voltage on DC/DC inverter

The course of the simulation shown in Fig. 5 can be read simulated values of the input three-phase voltage, output values of DC voltage without LC filter (blue waveform). The rectified DC voltage with the LC filter can be seen on green waveform. The red waveform shows the increased required voltage at the output side of the DC / DC converter. On Fig. 5. voltage and current drops can also be read, indicating when the individual probes were dropped to the next measured phase of the inverter.

In Table 2 the input values that entered the inverter on the AC side were measured using the BK-ELCOM analyzer and the output values on the inverter were measured using a digital clamp meter and a digital voltmeter of both Fluke type.

**Table 2** Information about measuring values

Measuring values from BK			
Input AC side		Output DC side	
<b>U</b>	108.4 V	<b>U</b>	455.4 V
<b>I</b>	35.5 A	<b>I</b>	21.5A

The value of the output voltage and current from the DC / DC converter is shown in Fig. 6. From the graph it is clear that the desired voltage values (red waveform) and current (green waveform) approximate to actual measured values, for this reason can be said to create a desired computer model is accurate.

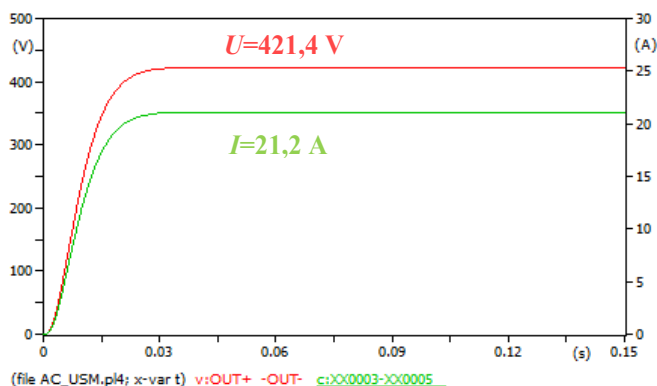


**Fig. 6** Simulation course of voltage and current on output side of DC/DC inverter

## 4 Conclusion

This paper describes the simulation that was created using the EMTP-ATP software and the digital model is then compared to the actual measured values on the inverter using the BK-ELCOM analyzer. The computer model can be configured to simulate the values of the quantities so that they can be read by the actual measured values to determine the correctness of the model and its error. In this case, the model with good accuracy and simulated values is approaching the real measured values.

## Acknowledgements

This research was partially supported by the SGS grant from VSB - Technical University of Ostrava (No. SP2017/54) and by the project TUCENET (No. LO1404).

## References

- [1] T. Mozdren, S. Rusek, R. Gono, and V. Mach, "Use of the EMTP-ATP Software to Develop a Dynamic Model of the Technological Centre," AEEE 2016, vol. 14. no 5, p. 467-474, DOI: 10.15598/aeee.v14i5.1719
- [2] V. Mach, "Wind Power Plant," 2016, [cit. 2016-20-1]. Available at WWW: [http://homen.vsb.cz/~mah30/laborator/PDF/4vetrnael\\_g2.pdf](http://homen.vsb.cz/~mah30/laborator/PDF/4vetrnael_g2.pdf)
- [3] J. Han, M. Bjekic, and Z. Jarda, "Modelling and Analysis of a Low-Voltage DC Distribution System," Open Access Resources. 2015. No 4, p.713-735, DOI:10.3390/resources4030713, ISSN 2079 - 9276
- [4] D. Medved, M. Kolcun, Z. Conka, P. Hocko and M. Novak, "Simulation of faults in the power system and their elimination in the EMTP-ATP," proceedings of the 7th International Scientific Symposium on Electrical Power Engineering, Kosice 2013, pp. 484-487, ISBN 978-80-553-1441-9

# Research into the Connection of Biogas Station to the 22kV Distribution Grid

Ladislav Novosád

Department of Electrical Power Engineering, FEECS,  
VŠB – Technical University of Ostrava, 17. listopadu 15,  
708 33 Ostrava – Poruba, Czech Republic  
ladislav.novosad.st@vsb.cz

**Abstract.** This article is focused on the sum of the results from research on the operation of biogas stations or the possibilities of their involvement in the distribution grid. Some features of biogas stations used as electricity sources are expected to contribute to the stability and optimization of the distribution network operation. The basic prerequisite for successful solution of this problem is the design of a functional model of the electric part of the biogas station. The following text describes the process of designing such a model, along with the prerequisites for further development of this simulator and the possibilities of its use.

**Keywords:** virtual biogas station model, measurement database, biogas station, renewable source, co-generation, co-generation unit, model, simulation

## 1 Introduction

The present article deals with the operation of biogas stations (BGS). As already mentioned, the aim of this article is to outline the possibility of creating a virtual model of the electric part of biogas station; then to verify the functionality of the model and use it to simulate the time dependence of the output power supplied to DG. The output of this model will subsequently be a course of supplied power to DG. Thus created course can be combined with other distribution system models, RES, simulating the operation of a comprehensive distribution grid part. Furthermore, the model will be used for automatic evaluation of measured data from individual biogas stations.

For the above reasons, the article deals with the electrical part of BGS only. BGS power heat balance will not be considered in the model and we will not simulate the actual process of fermentation, or the operation of a non-electric BGS part.

This research was supported by the SGS grant from VSB - Technical University of Ostrava (No. SP2017/54).

## 2 Model functional units

Designed virtual model consists of two main functional units, each of which has a separate output. The graphic part of BGS program was prepared using the Microsoft Visual Basic for Applications in MS Excel.

Model functional units:

- MEASURED DATA ANALYSER – evaluation of the measured data obtained by long-term measurements on BGS
- BGS ELECTRIC OUTPUT SIMULATOR

## 3 Measured data analyser

The aim of this part of the model is the automatic evaluation of a comprehensive set of measured data. A use of database of data obtained through long-term measurements from several BGSs. These measurements were processed in the context of long-term research into renewable sources at the Technical University – FEI. Biogas stations which were used for all three measurements were farm-type without connection to natural gas network and external container for storing biogas. The measurements were always carried out in the BGS main switchboard on the electric power output to the DG. The BGSs were connected to the DG via a 0.4/22kV transformer station. [1,2,3,4,5]

Data obtained through the aforementioned measurements must first be treated to the desired form (style). It is necessary to keep the exact form of the input data (sequence of quantities, spacing) for a proper function. At present, the model is able to retrieve data from three BGSs at the same time and analyse them. Measured data will be loaded into a simulator from a text file.

Individual displayed quantities can be selected both in groups and individually in the analyser program main menu. Then there is the option to choose a number of evaluated or compared BGSs (currently 3 data files maximum).

The outcome of the model evaluation will be both graphical information – diagrams and courses of selected quantities – and statistical information – the number of outages, decreases, total operating time, etc. which can be exported in the form of tables in a text file, as well as the juxtaposition of individual measurements at various BGSs. Examples of evaluation model outputs can be seen in the following examples (Figure 1).

The BGS simulator – measured data analyser is important also because of the functionality of other simulation blocks. Due to the fact that there is not the necessary database of BGS operation data, or the operation of co-generation units in biogas stations, several long-term measurements at BGS were carried out.

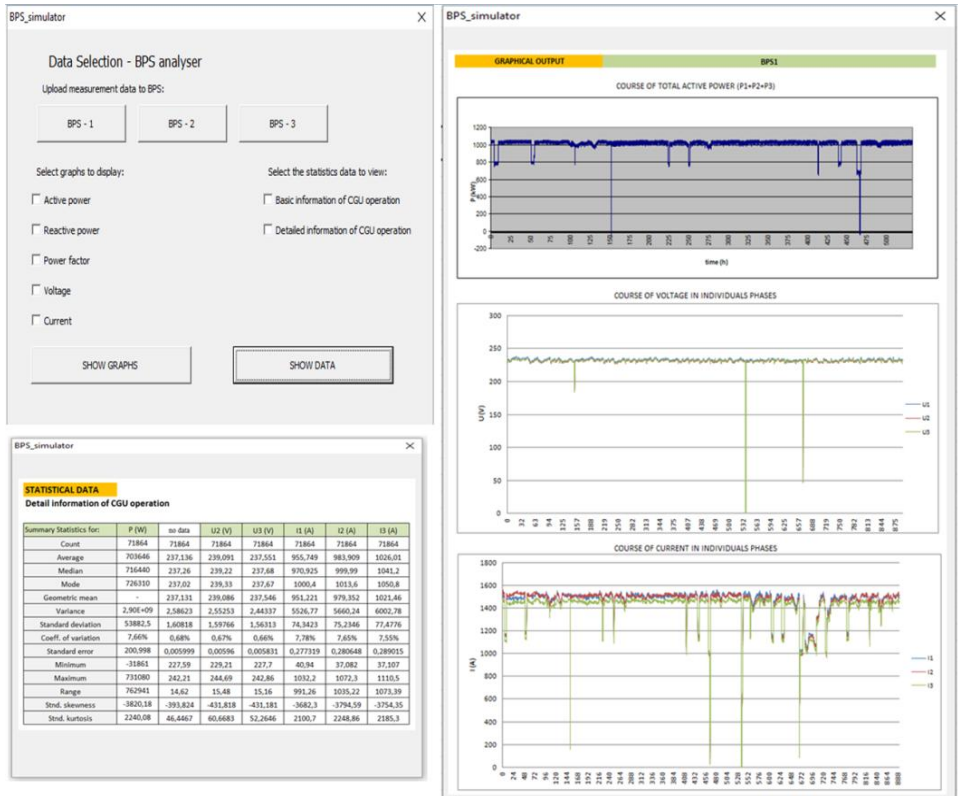


**Fig. 1.** Example of graphical representation of measurement data in Excel and the main control panels of the program

These data will provide the basic statistics about the BGS operation. The number of outages or their frequency together with information about their time course will be primarily analysed. Subsequently, these data will be used for the purposes of electric output of BGS simulation. [7]

## 4 BGS electric output simulator

However, the main purpose of the model will be, as already mentioned, to create a simulation of electric power supply course from the BGS.

The model itself is composed of the following basic parts (Figure 2).

### 4.1 Setting the basic BGS parameters

This block is used to set the basic parameters of the model biogas station. In terms of electrical quantities, these parameters include the size (installed electrical power) and

the number of co-generation units (CGU) located in the BGS, as well as their type, the consumption of biogas and other operational information (see Figure 3).

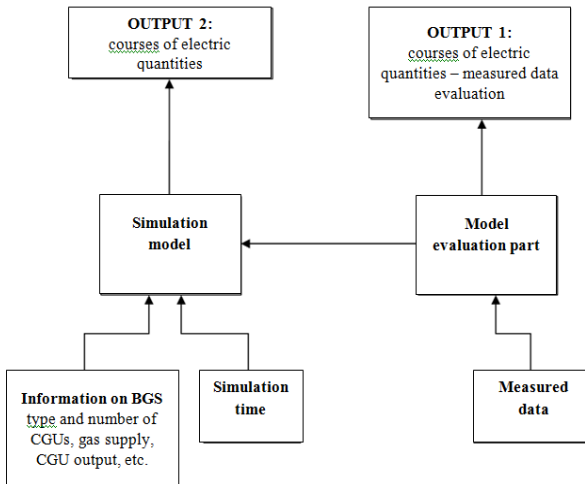


**Fig. 2.** Block display of the main structural elements of the model

In the current state of development of the simulator, the following can be set:

- number of CGUs (1–5 pcs)
- CGU powers (from about 100kW to 1000kW) – each CGU may have different powers
- gas tank size – or a time reserve of biogas for CGU operation

#### 4.2 Measured data analyser – simulation data, measured data

This section was described in the article above, including the importance of measured data for the simulation of the output power from the BGS.

#### 4.3 Calculation – a simulation of the model

This is basically the most important part of the model. The simulation part of the model is designed for the actual calculation/generation of the electric power supply from the BGS simulated course. Basic input information which consist of data on reliability and outages is loaded to the simulation model from the measured data analyser output.

Given that the basic data on the reliability of the CGU operation are not available currently, the evaluation results of the three BGSs will be used for calculations. The calculation is made up of various mathematical operations based on probability and random generation of power outages.

**BPS Simulator**

Basic simulation settings

**Select the number of CGUs**  
The first version of the simulator allows you to select up to 5 CGUs

Select the unit type from the CGU database or setting up a new CGU.

☐ 1. Cogeneration units        or   

☐ 2. Cogeneration units        or   

☐ 3. Cogeneration units        or   

☐ 4. Cogeneration units        or   

☐ 5. Cogeneration units        or   

**Setting simulation time**  
Simulation time can be set within a maximum range of 30 days

Select a time:

   Select a time unit    ☐ Minutes (min)    ☐ Hours (h)    ☐ Days (d)

**Select data to display:**    **Select graph to display:**

☐ Active power    ☐ Basic information of CGU operation    ☐ Show generated data - table

**Fig. 3.** Main parameter settings panel for simulation

The result is then a set of data that can be characterized and displayed as virtual supplied power from BGS. These data can be stored separately in the form of text or graphical outputs.

The generated supplied power courses can be considered as a theoretical course of power supply from CGU and can be used for other simulations, e.g. in combination with electric power renewable sources. [5,8,9]

## 5 Conclusion

The article deals with a biogas station model. The model allows the creation of a theoretical simulated course of power supply from BGS to 22kV distribution grid. The created course can then be used in combination with other simulator outputs and prediction models of individual RES in DG. Cooperation of such models can then result in optimizing the operation of DG using the power available from the BGS. Above all, cooperation with PVP is assumed, thus providing additional options of stabilizing grids at 22kV level, possibly with a connection of BGS to DG in terms of possible support services.

A basic fact identified by both the long-term measurements and the output of the simulator is that BGSs with conventional combustion CGUs are reliable and stable sources of power supply. However, the above simulation process of the so-called

general course of power supply from CGU is affected by several basic BGS disadvantages. These disadvantages include the dependence of supplied power on the CGU operation or on a sufficient amount of biogas. Due to the CGU high operational reliability (outages caused by CGU failure are very rare), the lack of biogas is one of the main reasons for DG power supply failures. This factor may be difficult to evaluate since it is a different factor among all the available measured BGSs as it depends on many factors. The most common causes of CGU failures include improper operation of BGS or CGU, particularly in terms of dosing biomass, and the very type of biomass as well as climatic conditions.

### **The present results were included in the following publications:**

1. Ladislav Novosád, Zdenek Hradílek; Návrh virtuálního modelu elektrického výstupu bioplynové stanice. Mezinárodní vědecká konference Electric Power Engineering EPE (2017).
2. Novosád, Hradílek: Description of Measurements on Biogas Stations, WOFEX 2016, pp. 49-54. VŠB-Technical University of Ostrava, FEECS, 2016, ISBN 978-80-248-3961-5
3. Novosád, Hradílek: Návrh virtuálního modelu bioplynové stanice, ELNET 2016, pp. 20–28, ISBN 978–80–248–4008–6. VŠB – Technical University of Ostrava, FEECS, 2016.
4. Novosád, Hradílek: Model elektrického výstupu z bioplynové stanice, ELEKTROENERGETIKA 2017 September 12-14, 2017, Stará Lesná, Slovakia

## **References**

1. L. Novosád, Data measured in TOZOS Tošanovice BGS, 09-10/2015,
2. M. Spacek, Data measured in Hodoňovice BGS, 08-09/2014
3. J. Jansa, Data measured in Loděnice BGS, 06-08/2013,
4. TOZOS Tošanovice BGS operation book and operation rules, 2013
5. L. Novosád, Z. Hradílek, “Power Analysis of Co-Generation Units at Biogas Station”, Proceedings of the 16th International Scientific Conference on Electric Power Engineering (EPE) 2015 Dlouhé Stráně, 2015, ISBN 978-1-4673-6788-2
6. L. Novosád, Z. Hradílek, “Analysis of Energy Balances Three Biogas Stations in Czech Republic”, Proceedings of the 16th IEEE International Conference on Environment and Electrical Engineering, 2016
7. M. Dummer, M. Litschmannova, “Statistika I.”. Statistika I. VSB – Technical university of Ostrava, 1997, 80-7078-496-2
8. Z. Hradílek, “Elektroenergetika průmyslových a distribučních zařízení,” 1.vyd. VŠB – TU Ostrava. 2008. ISBN 978-80-7225-291-6.,p.315, 2008.
9. K.M.A. Islam, T. M. Khan, M. M. Rahman, M. S. Munna, “2015 3rd International Conference on Green Energy and Technology (ICGET)”,2015,



# Evaluation of Dependency of the Energy Generated by Wind Power Plant on Season

Michal Petružela

Department of Electrical Power Engineering, FEECS,  
VŠB – Technical University of Ostrava, 17. listopadu 15,  
708 33 Ostrava – Poruba, Czech Republic  
michal.petruzela@vsb.cz

**Abstract.** Electric energy generated from wind power is one of most widespread renewable energy resource that can be used to power island system. Although it is widespread, the location must meet certain conditions to be suitable for efficient operation of wind power plant. Also this conditions are not same over whole year. For example during winter the air is colder, and thus denser, therefore the more is power in wind. This is the reason I decided to take measured data of wind power plant to analyse how the amount of generated energy differentiates over year.

**Keywords:** Wind power plant, Renewable energy

## 1 Introduction

Due to continuously growing emphasis on renewable energy sources, there is also increased focus on research on this sources, among which belongs wind power. Wind power is attractive due its low maintenance cost. Currently most widespread type of wind turbine is one with horizontal axis of rotation, the output power from this type varies in wide range from 1 kW to units of MW [1, 2]. On the other hand wind power plants are unstable energy sources and its power output varies less or more during the year with regards to its location [3].

Wind power plant is located at VŠB campus, rated power of its 20 poles permanent-magnet synchronous generator is 10 kW, the type of wind turbine is horizontal axis. Wind power plant operates up to wind speed of 10 m/s, after reaching this limit control unit starts to regulate turbine by changing its yaw and if necessary braking by connecting resistors.

In this article I will search for relationship between energy generated by wind power plant and the season of year and by using statistical apparatus from [4, 5] determine if there is possible relation between this two. This relation should tell us how much energy is approximately generated every month and accordingly to it we can plan maintenance so the least possible amount of energy is not generated.

## 2 Measured data

Dataset is from March till January, values are logged every minute. So every day consists of 1440 one minute averages, and we have 11 months of data which is huge amount. For further analysis I took this data and calculated amount of energy generated per day and summed up energy per day into monthly values. Result of this is shown at following fig. 1.

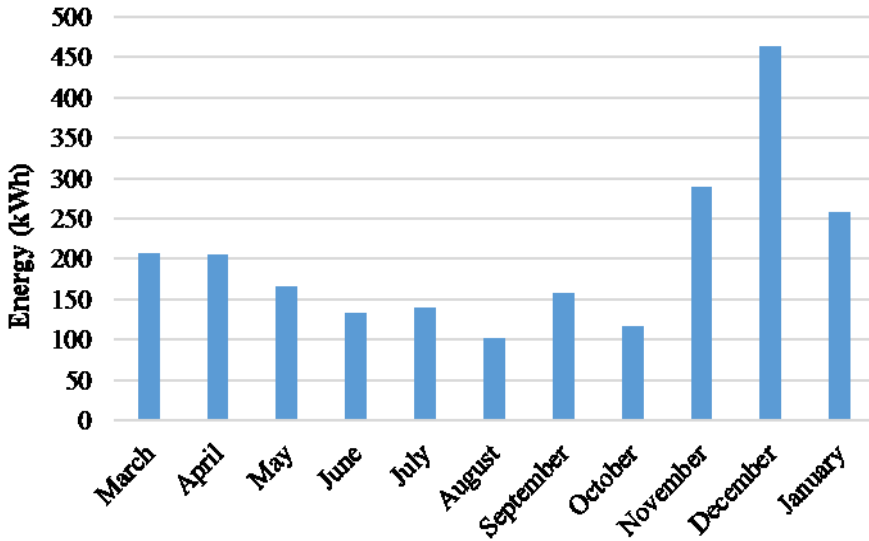


Fig. 1. Generated energy per month

By looking at fig. 1 we see the greater amount of energy is generated in the winter than in the summer, this is according to expectations mentioned above. Most energy, 460 kWh, is generated in December, that is almost 4.6 times more than in the August. The amount of energy generated in August what was only 102 kWh.

## 3 Regression

In software Statgraphics I applied different simple regression models, some of them had high coefficient of determination. For example fourth order polynomial model had coefficient of determination over 95%, but year is periodical so decided to apply nonlinear regression with sine function. Another reason to apply sine function was the monthly energy values loosely reminded this function. Equation of fitted model shown at fig. 2 is:

$$E = 106.896 * \sin(2 * 3.14 * 5.16467 * M + 41.0449) + 204.607 \quad (1)$$

where  $E$  is energy in kWh and  $M$  is Month of the Year.

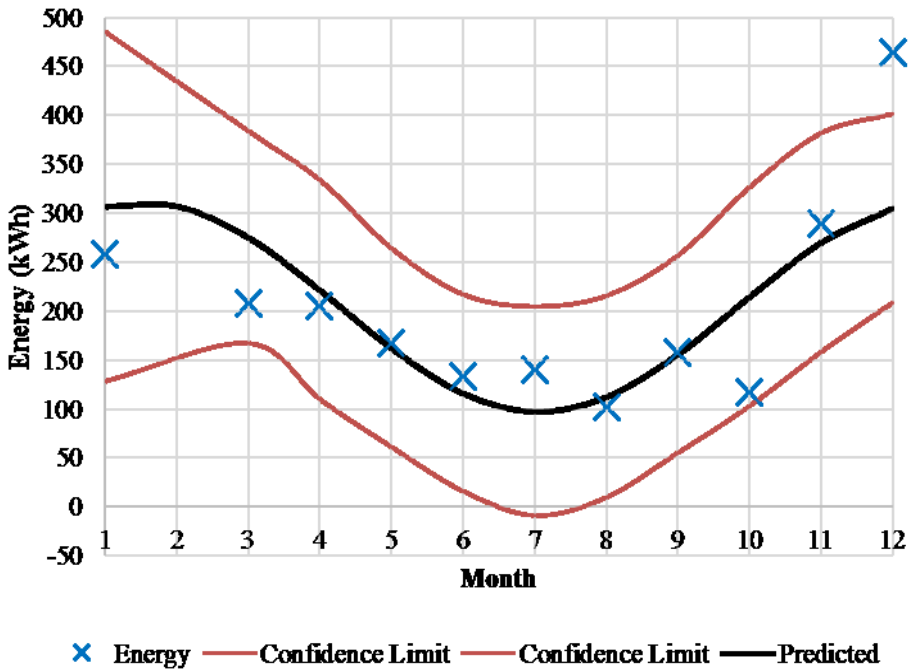


Fig. 2. Plot of fitted model of nonlinear regression

Coefficient of determination is 58.8% it means that the model explains this amount of the variability in the generated energy. This indicates some relationship between variables, in our case energy and month of the year. At fig. 2 blue crosses are measured values of energy and black trace is predicted amount of energy by the equation 1, red traces are limits for confidence level 95%. Even if energy amount in December is beyond confidence limit, relative error of predicted value is “only” 34%, but largest relative error of predicted value is 84% in October.

## 4 Conclusion

I have performed analysis of measured data of generated energy of wind power plant. Firstly I summed up one minute energy values into month values and showed them at fig. 1. Then I attempted to find relationship between generated energy and month of the year by using statistical apparatus. For reason of periodicity of year I applied nonlinear regression using sine function with outcome of coefficient of determination equal to 58.8%. This number is too large to reject hypothesis of relationship between energy and month of the year but isn't large enough to accurately pre-

dict amounts of generated energy. For further assessment is necessary to have data of more than one year. With this data I could decide if accept or reject formula for calculation of the generated energy.

**Acknowledgements.** This paper is supported by the following projects: LO1404: Sustainable development of ENET Centre; CZ.1.05/2.1.00/19.0389 Development of the ENET centre research infrastructure; SP2017/159 Students Grant Competition and TACR TH01020426, Czech Republic.

## References

1. Patel, M.R.: Wind and solar power systems, CRC Press, ISBN 0-8493-1605-7, New York, (1999)
2. Manwell, J., McGowan, J., Rogers, A.: Wind energy explained: theory, design and application, John Wiley & Sons, ISBN 978-0-470-1500-1, New York, (2009)
3. Mišák, S., Prokop, L., Dvorský, J.: Optimizing the mathematical model for prediction of energy production in wind power plants. *Przegląd elektrotechniczny*. r. 87, nr. 2, 74-78 (2011). ISSN 0033-2097.
4. Briš, R., Litschmannová, M.: Statistika I. pro kombinované a distanční studium, Ostrava (2004)
5. Litschmannová, M.: Úvod do statistiky, VŠB – TU Ostrava, Fakulta elektrotechniky a informatiky: Ostrava, (2011)

## Publications

Petružela, M., Blažek, V.: 3D Simulation of the vertical axis Wind Turbines. In *Proceedings of the 18<sup>th</sup> International Scientific Conference on Electric Power Engineering (EPE)*. Ostrava: VŠB - Technical University of Ostrava, Faculty of Electrical Engineering and Computer Science, Department of Electrical Power Engineering, (2017). DOI: 10.1109/EPE.2017.7967299

# Light Parameters of Public Lighting in the Sphere of Mesopic Vision

Karel Sokanský, Richard Baleja, and Tomáš Novák

Department of Electrical Power Engineering, FEECS,  
VŠB – Technical University of Ostrava, 17. listopadu 15,  
708 33 Ostrava – Poruba, Czech Republic  
richard.baleja@vsb.cz

**Abstract.** This paper deals with the problematic of public lighting on roads. The lighting on the roads is a specific case of lighting systems, where an observer is located in an area with relatively low adaptation luminance. That means, that the human eye don't assess the lighting parameters of road lighting according to photopic curve of human eye sensitivity as it does during the daylight, but it uses for this assessment a mesopic sensitivity curve of the human eye. The maximum sensitivity of the sensitivity curve depends on the size of the adaptation luminance, in which the observer is located. For comparing the differences between the values of photopic and mesopic light parameters were realized several measurements of roads lighting. For measurements were selected roads with different light levels and adaptation luminance background as well as different light sources which have different correlated color temperature.

**Keywords:** mesopic vision, photopic vision, luminous flux, correlated colour temperature, spectrophotometr, luminance camera.

## 1 Introduction

A design of public road networks is relatively complicated process by which is essential to respect several regulations and norms. Respective norms need to be abode, naturally, when designing the lighting systems of road networks. But it is convenient many times to respect also other scientific studies and papers which are concerned with issues of public lighting. It is necessary that a designed lighting system would provide requested figures of the norms for the fixed road network category. It is also essential to choose an appropriate type of lighting source. In particular, these are various types of vapor lamps and LED lighting sources. Such lighting sources are naturally indifferent to each other by different technical parameters. For the purposes of this article, it is sufficient if we pay our attention to one spectrum of the lighting sources and correlated colour temperature. Lighting systems are in most cases realised by means of high-pressure sodium vapor lamps and mercury vapor lamps. This way of use of lighting systems is nowadays considered as very uneconomical and vapor lamps are increasingly replaced by LED lamps. [2] [6]

## 2 Sensitivity of the human eye

The human eye is not equally sensitive to the radiance of different wavelengths. The highest possible sensitivity of the human eye under sufficient lighting conditions is determined by the sensitivity of retinal cones during photopic vision. The sensitivity of the human eye also depends on an environment in which is an observer located. There is a difference between an observer who is situated in an environment where is enough of light and an observer who is in dark environment. There are three type of vision of the human eyesight that we distinguish: photopic vision, scotopic vision, and mesopic vision.

The sensitivity of high luminance (photopic – day vision) is regulated in accordance to the photopic curve of the human eye sensitivity. The most of the devices which measure photometric quantities are calibrated in accordance with this curve. Photopic light parameters are for instance light flow of the source or a lighting fixture. A problem appears when an observer moves from a light environment to a dark environment. The curve of human eye sensitivity starts to move from the area of photopic sensitivity (day vision) across the mezopic area to the area of scotopic sensitivity (night vision) which is characteristic of very low brightness (less than 0,005 cd/m<sup>2</sup>). The scotopic curve of the sensitivity of the human eyesight is practically not usable for appraisal of light parameters because the issue is that there are areas with very low luminance in which is practically zero visibility.

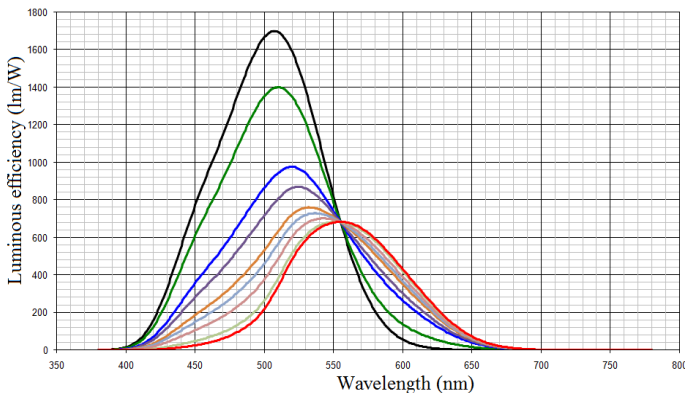


**Fig. 1.** Course of photopic, scotopic and mesopic sensitivities of the human eye [6]

The visualisation of the sensitivity curves is depicted in picture number 1. There is also the curve for photopic vision (red curve) and the curve for scotopic vision (black curve). The curves which are placed between these two curves are the mesopic curves of sensitivity. For every value of luminance, there is one curve of the mesopic sensitivity present. Figures in charts for the photopic and the scotopic curves of sensitivity are accessible from the literature available. It is a little bit more complicated to obtain the mesopic curve of sensitivity for the stated luminance. The mesopic curves of sensitivity were calculated according to CIE. [4] [6]

### 3 Measurement of public lighting parameters

For measuring, it was essential to find areas with the level of photopic lighting approximately equal and where the lighting was realized by means of various lighting sources. Therefore the selection of the suitable locations was demanding. After a careful appraisal, a part of road networks on the Technologická Street in Ostrava was selected for the consideration. The lighting is realized by means of high-pressure sodium vapor lamps with 70 W output and the correlated colour temperature of 2000K. This road network continues to the K Myslivně Street where the lighting system is realized by means of LED lamps with 62 W output and the correlated colour temperature of 4000K. The part of road network at the department store AVION in Ostrava, where the lighting system is realized by means of LED lamps with 75 W output and the correlated colour temperature of 5000K, was also measured in order to compare the exact same LED sources which have the different correlated colour temperature.

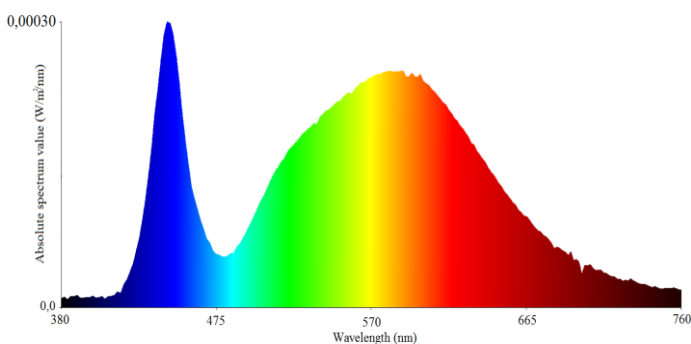


Fig. 2. Absolute spectrum curve of the LED source (4000K) [6]

It is always necessary to choose correctly the colour of a lighting source (correlated colour temperature) when reconstructing old lighting systems or designing a new one. The spectrum of lighting source relates closely to the correlated colour temperature. Development of the spectrum of lighting source determines which wavelengths are for the fixed lighting source dominant and which are not dominant.

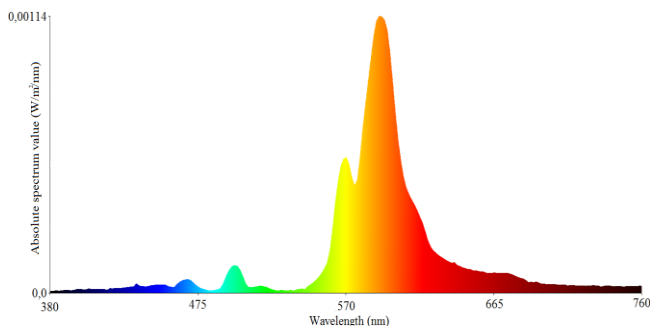


Fig. 3. Absolute spectrum curve of high-pressure sodium lamp (2000K) [6]

For measurement, it was not necessary to measure the illumination of road networks in accordance with ČSN EN 13201-4 road networks lighting – Part 4 Methods of measurement because our task was not discovering if the certain road network is correctly illuminated, but what is the average illuminance of the road. Lighting parameters was measured by means of the spectrophotometer SPIC-200 by the Everfine company. It is possible to measure illuminance level with this device, radiated spectrum and a plenty of other lighting quantities at the same time. This device uses for measurement two sensors. One sensor measures illumination in lux and the other sensor measures radiated spectrum which is noted in the form of a char. [4] [1] [6]

#### 4 Measurement of luminance on the chosen parts of roads

It was essential to carry out luminance analysis of the surroundings in which is located the road network that was being examined. This analysis was carried out in order to assign the corresponding mesopic curve of sensitivity. The luminance analysis was performed in both directions because it was a bidirectional road network with two different directions of coming drivers. Luminance analyser was placed in the height of 1,5 m above the roadway in the corresponding traffic lane in the distance of 60 meters from the beginning of the field on the road network being measured. Six luminance analyses of the surroundings were produced in total. Background luminance and surface luminance of a road network were evaluated at every luminance map. An example of luminance analysis, concretely for the system with LED lamps with the correlated colour temperature of 4000K, is depicted in pictures 4 and 5.



**Fig. 4.** A luminance analysis of the road with LED luminaires (direction 1) [6]



**Fig. 5.** A luminance analysis of the road with LED luminaires (direction 2) [6]



Three types of luminance were always calculated and recorded during the luminance analysis: maximal, minimal and average. The area of the measured part of the road network are visibly depicted in pictures 4 and 5. Width and lengths of the area of the road network is equal to the distance between two light points. Luminance analysis of the background (surroundings) which replaces adaptation luminance was evaluated for the whole area that was scanned by the luminance analyser. The measured and calculated figures of individual directions are situated in the tables number I and II. The same procedure of the analysis of the luminance parameters was used also with other two types of road networks. [3] [5] [6]

**Table 1.** Luminance values for direction 1

Luminance [cd/m <sup>2</sup> ]	Min	Max	Average
Background	0,068	21,051	0,422
Road	0,264	1,799	0,565

**Table 2.** Luminance values for direction 2

Luminance [cd/m <sup>2</sup> ]	Min	Max	Average
Background	0,031	19,842	0,225
Road	0,192	1,243	0,571

## 5 Lighting evaluation of road networks in mesopic area

The results from the measurement of the illuminance on the road networks are depicted in table 3. The values of illumination were calculated from the measured values of spectrums of the lighting source. There are the values of illumination evaluated via the photopic curve of sensitivity (day vision), scotopic curve of sensitivity (night vision) and curves of the mesopic vision.

**Table 3.** The calculated values of illumination for different types of lighting situation

Lighting source	Average illuminance in the sphere of:			
	Photopic vision [lx]	Scotopic vision [lx]	Mesopic Vision direction (1) [lx]	Mesopic Vision direction (2) [lx]
LED 4000K	11,64	16,15	12,47	12,75
LED 5000K	16,16	28,22	19,93	18,62
High pressure sodium vapor lamp 2000K	17,38	6,60	15,75	15,83

## 6 Conclusion

The paper points out to a possibility to verify figures of lighting on road networks in the mesopic area. It is essential to take into consideration also the other important facts which are related to the issue of the mesopic vision when designing lighting systems of public road networks. It can be noted on the grounds of the comparison of the measured and calculated figures depicted in table 3 that the type of lighting source influences perception of lighting in the individual areas of vision. The high-pressure sodium vapor lamps have very low S/P ratio in comparison with LED lamps (both colours). This is caused by the characteristics of the radiated spectrum (figure 3) which dominantly radiates outside the area of the spectral sensitivity of the scotopic vision. This is the reason why the resulting scotopic illumination is significantly lower than the photopic illumination. The figures of LED in the mesopic areas of vision are bigger than in the photopic areas of the lighting. The situation is contrary in the case of high-pressure sodium vapor lamps. The mesopic vision is applied above all in the sphere of LED sources. It applies that the higher the correlated colour temperature or the lower the adaptation luminance of the background, the higher increase of illumination in the mesopic area.

## 7 References

1. J. L. Barbur, A. Stockman, "Photopic, mesopic and scotopic Vision and Changes in Visual Performace" Available from: [http://www.academia.edu/4491812/Photopic\\_Mesopic\\_and\\_Scotopic\\_Vision\\_and\\_Changes\\_in\\_Visual\\_Performance](http://www.academia.edu/4491812/Photopic_Mesopic_and_Scotopic_Vision_and_Changes_in_Visual_Performance)
2. H. Hertenstein, M. Bach, N.J. Gross, F. Beisse, "Marked dissociation of photopic and mesopic contrast sensitivity even in normal observers," Graefe's Archive for Clinical and Experimental Ophthalmology, 2016, vol. 254, pp. 373–384. ISSN 0721832X.
3. J. Škoda, P. Baxant, M. Krbal, S. Sumec, and T. Pavelka, "Photometry of LED sources," Przeglad Elektrotechniczny, 2013, vol. 89, no. 6, pp. 341–344. ISSN 00332097.
4. J. Novotný, "Mobile Illuminance Measurement of Road Lighting," Proceedings of the 21th International Conference LIGHT SVĚTLO 2015, pp. 129–131, ISBN 978-80-214-5244-2.
5. J. Habel, P. Žák, "Význam mezopického vidění pro prax," Available from: <http://www.odbornecasopisy.cz/svetlo/casopis/tema/vyznam-mezopickeho-videni-pro-praxi--16105>
6. R. Baleja, K. Sokansky, T. Novak, T. Hanusek, P. Bos. "Measurement and evaluation of the road lighting in mesopic and photopic vision" IEEE Lighting Conference of the Visegrad Countries, Lumen V4. ISBN: 978-150903305-8.

# Model Reference Adaptive System for Sensorless Control of Induction Motor Drive

Cuong Dinh Tran, Sang Dang Ho, Thinh Cong Tran,  
Chau Si Thien Dong, Hau Huu Vo

Faculty of Electrical and Electronics Engineering, Ton Duc Thang University,  
19 Nguyen Huu Tho Str., Tan Phong Ward, District 7, Ho Chi Minh City, Vietnam  
{trandinhcuong, hodangsang, trancongthinh, dongsiethienchau,  
vohuuuau}@tdt.edu.vn

**Abstract.** The paper describes a machine model method for estimating speed rotor of induction motor called Model Reference Adaptive System (MRAS). The MRAS is chosen for its simple construction and good tracking capability. The paper contains the mathematical description of the MRAS and the Field Oriented Field Control (FOC). The simulation results for sensorless speed control of induction motor are shown to present features of MRAS speed estimators.

**Keywords:** MRAS, induction motor, vector control, FOC, speed control, sensorless control.

## 1 Introduction

Induction motors (IM) are used widely in practice because they are robust, reliable, simple construction and inexpensive in comparison to others. We can see their applications from industrial systems to home applications. Operating an electromechanical system of IM in which it is necessary to control various parameters, such as voltages, currents and speed. The most way of doing this is by using the technical called Vector control (or Field Oriented Control). Stator voltages and currents are easily measured at the motor terminals. The rotor speed can be obtained by the use a mechanical speed sensor at the motor shaft or a speed estimator. Because the use and the maintenance of the speed sensor in a good condition requires high costs, so many ongoing researches have concentrated on eliminating the speed sensor without deteriorating the dynamic performance of the drive control system.

There are two approaches to speed estimation for sensorless control of induction motor: model based approach and non model based approach. The non model approach based technique tracks a machine anisotropy for example: using high – frequency signal injection, utilizing rotor bar slot harmonics and carrier frequency signal injection, artificial neural networks, fuzzy neural networks..., whereas the methods with model are based on some mathematical model of the induction motor.

The objective of this paper is to present the rotor speed estimation by using method with machine model. One of the most popular machine model methods for estimating speed rotor is based on the Model Reference Adaptive System (MRAS) proposed by W. Yanonan in 1987 [2].

The MRAS approach has two models. The first model called Reference Model estimates rotor flux by using voltages and current signals of IM. The secondary model called Adaptive Model estimates rotor flux by using current signal and output of Adaptation Mechanism (estimated electrical rotor speed). The outputs (estimated rotor flux) are compared to find the difference. The difference is used to drive a suitable adaptive mechanism for estimating rotor speed. This estimating signal is used to control speed of IM over wide range by Field Oriented Control technique (FOC).

## 2 The Field Oriented Control Technique

The induction motor to be controlled is in a closed loop with the FOC block (see Fig. 1) which generates switching commands for inverter to achieve the desired speed of rotor.

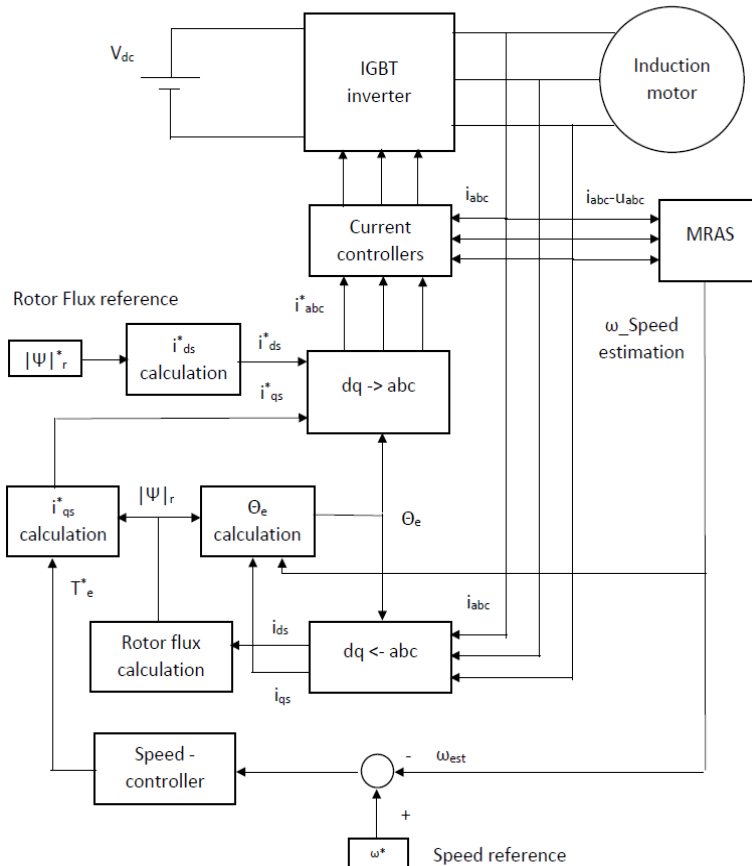


**Fig. 1.** Block diagram of vector control technical without sensor

FOC (or vector-control) algorithm is summarized below [3]:

- Measure the stator phase currents  $i_a$ ,  $i_b$  and  $i_c$ .
- Transform the set of these three-phase currents onto a two-axis system. This conversion provides the variables  $i_\alpha$  and  $i_\beta$  from the measured  $i_a$ ,  $i_b$  and  $i_c$  values where  $i_\alpha$  and  $i_\beta$  are time-varying quadrature current values.
- Calculate the rotor flux and its orientation.
- Rotate the two-axis coordinate system such that it is in alignment with the rotor flux.
- Using the transformation angle calculated at the last iteration of the control loop.
- This conversion provides the  $i_d$  and  $i_q$  variables from  $i_\alpha$  and  $i_\beta$ . This step is more commonly known as the Park Transformation.
- Flux error signal is generate using reference flux and estimated flux value.
- A PI controller is then used to calculate  $i_d^*$  using this error signal.
- $i_d^*$  and  $i_q^*$  are converted to a set of three phase currents to produce  $i_a^*$ ,  $i_b^*$ ,  $i_c^*$ .
- $i_a^*$ ,  $i_b^*$ ,  $i_c^*$  and  $i_a$ ,  $i_b$ ,  $i_c$  are compared using hysteresis comparator to generate inverter gate signals.

### 3 Model Reference Adaptive System

In a MRAS (see Fig. 2), some state variables,  $x_d$ ,  $x_q$  (e.g. rotor flux-linkage components:  $\Psi_{rd}$ ,  $\Psi_{rq}$ ) of the induction machine (which are obtained by using measured stator voltages and currents) are estimated in a reference model and are then compared with state variables  $\hat{x}_d$ ,  $\hat{x}_q$ , estimated by using an adaptive model.

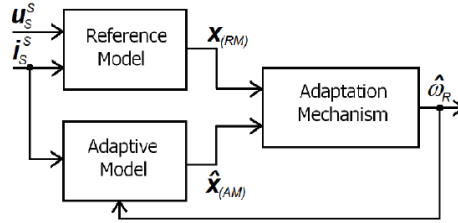


**Fig. 2.** Structure of the model reference adaptive system

The difference between these state variables is then used in an adaptation mechanism, which outputs the estimated value of the rotor speed  $\hat{\omega}_r$  and adjusts the adaptive model until satisfactory performance is obtained.

MRAS algorithm is summarized below [4]:

- Transform the set of three phase voltages and currents into two phase stationary reference frame ( $\alpha$ ,  $\beta$ ):  $u_s^s$ ,  $i_s^s$
- Stator voltages and stator currents are used to estimated rotor flux linkage in Reference model with following equation :

$$\Psi_{r(RM)}^s = \frac{L_r}{L_m} \left( \int (\bar{u}_s^s - R_s \bar{i}_s^s) dt - \left[ \frac{L_s L_r - L_m^2}{L_r} \right] \bar{i}_s^s \right) \quad (1)$$

- Stator currents and the rotor angular speed are used to estimated rotor flux linkage in Adaptive model with following equation :

$$\hat{\psi}_{r(AM)}^s = \int [(j\hat{\omega}_r - \frac{1}{T_r})\hat{\psi}_r^s + \frac{L_m}{T_r}\bar{i}_s^s] dt \quad (2)$$

- Compare two rotor flux signals to find the difference. This difference is evaluated by the adaptation mechanism. The adaptation mechanism use classical PI\_controller to produce the estimated value of the rotor speed.

$$\phi(e) = \hat{\psi}_{r(AM)}^s \times \bar{\psi}_{r(RM)}^s \quad (3)$$

$$\phi(e) = \hat{\psi}_{r\alpha(AM)}^s \bar{\psi}_{r\beta(RM)}^s - \hat{\psi}_{r\beta(AM)}^s \bar{\psi}_{r\alpha(RM)}^s$$

$$\hat{\omega}_r = K_1 \phi(e) + K_2 \int \phi(e) dt \quad (4)$$

Where  $K_1 > 0, K_2 > 0$ .

## 4 Simulation results

Model Reference Adaptive Technique for speed sensorless rotor flux oriented induction motor drives is simulated by MATLAB-SIMULINK (Fig. 3).

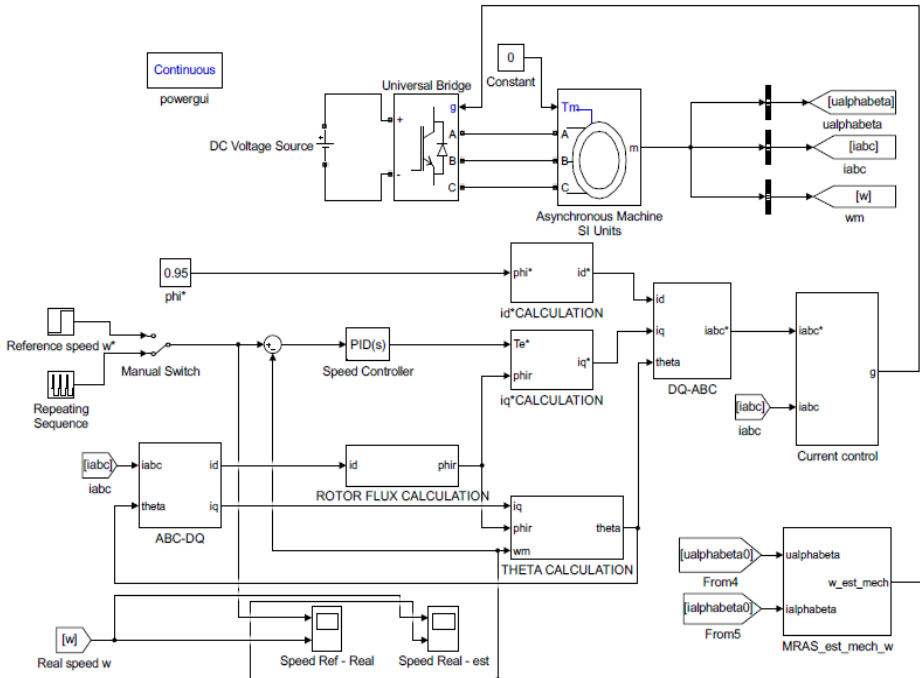


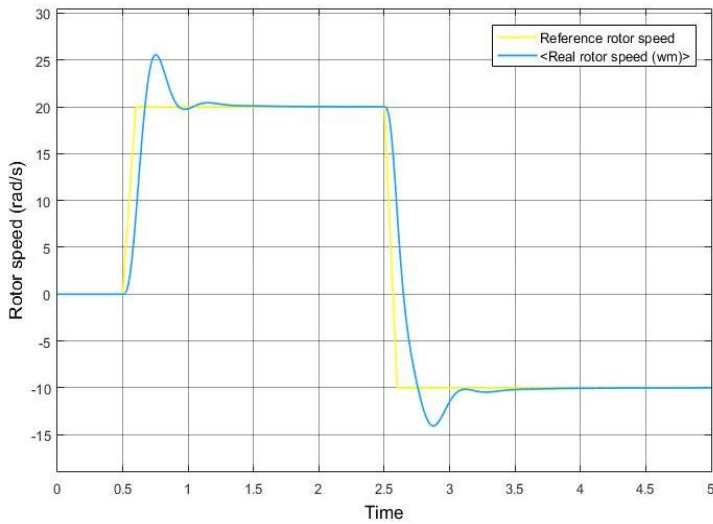
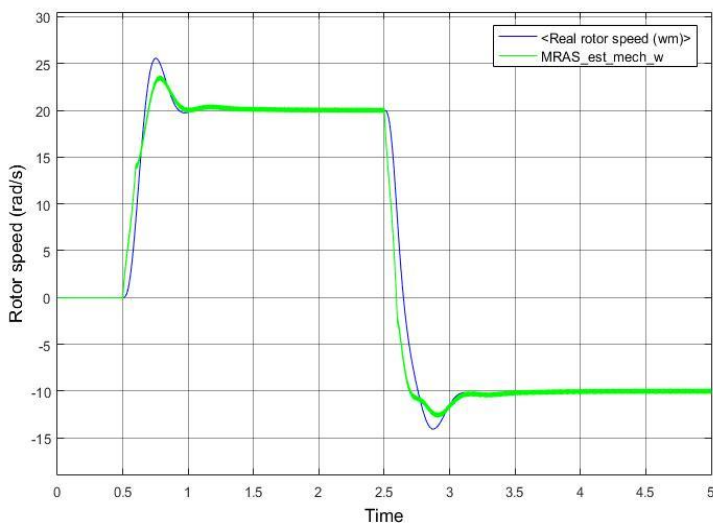
Fig. 3. Matlab Simulink model for speed sensorless using MRAS

The simulation studies are carried out on a 1.5 HP induction motor with parameters given in Tab. 1 [1].

**Tab. 1.** Parameters of the induction motor - 1.5 HP, 415 V, 1430 rpm

Parameter	Value
Pole pairs	2
$L_s, L_r, L_m$	0.5192 H, 0.5192 H, 0.4893 H
$R_s, R_r$	6.03 $\Omega$ , 6.085 $\Omega$
Moment of inertia	0.01178 $\text{kgm}^2$

In the following simulation, the MRAS is used for estimated the speed rotor at low range speed with no-load condition.

**Fig. 4.** Reference rotor speed and actual rotor speed of the induction motor**Fig. 5.** Reference rotor speed and estimated rotor speed of the induction motor

## 5 Conclusion

The paper presents Model Reference Adaptive technique for estimating the rotor angular speed. The MRAS results depend on the precision of the parameters and the speed control range. For this reason, it is necessary to incorporate other observer methods in MRAS for improved results.

## Acknowledgement

In the paper, there are the results of the project reg. no. SP2017/104 funded by the Student Grant Competition of VSB-Technical University of Ostrava. This research was supervised by Prof. Ing. Pavel Brandstetter, CSc.

## References

1. Mini Sreejeth and Avinash Mehra, Estimation of Stator Resistance in Sensorless Induction Motor using MRAS, ICPEICES-2016
2. Mugdha Bhandari, Shivaji Gavade, Shwetha S H, Model Reference Adaptive Technique for Sensorless Speed Control of Induction Motor using Matlab\Simulink, IJETCSE, April 2015.
3. Hafeezul Haq, Mehedi Hasan Imran, H.Ibrahim Okumus, Mohammad Habibullah, Speed Control of Induction Motor using FOC Method, IJERA, March 2015, pp.154-158
4. P. Brandstetter, Sensorless Controlled of Induction Motor using Modified MRAS, IREE, May – June 2012.



# Simulation of Vector Control with RF-MRAS Observer

Petr Chamrád

Department of Electronics, FEECS,  
VŠB – Technical University of Ostrava, 17. listopadu 15,  
708 33 Ostrava – Poruba, Czech Republic  
`petr.chamrad@vsb.cz`

**Abstract.** This article is focused on sensorless vector control simulation of induction motor. In the introduction of this article is described problematics of drives without position sensor using of method RF-MRAS. Interpretation is focused on mathematical model of RF-MRAS observer and implementation algorithm into existing vector control structure. In the next section are shown principles of estimation of rotor angle speed and motor shaft position. The results of simulations are presented in conclusion of this paper.

**Keywords:** Induction motor, Simulink, Vector control, Sensorless vector control, RF-MRAS, Estimation of rotor angle speed, estimation of position space vector of rotor flux

## 1 Introduce

Electrical drives are part of every industry. They can be found in the hard industry (metallurgy, mining, constructing, etc.) where they form driving units for lots of working mechanisms. In present, in the structures of drives are used alternating motors (mostly induction motors).

Modern control methods of alternating machines include vector control. Its realization consists in separating the stator current into two orthogonal components of current, namely torque component of current and flux component of current. Independent regulation of both components of the current will produce the same AC drive behavior as with DC motors. The torque component of current allows to control the torque of engine and the flux component of current affects magnetization of machine.

The disadvantage of vector control is the need to measure the position of motor shaft by position sensor which is connected to the rotor. These devices are quite sensitive to shock and vibrations. Due to this fact, the robustness of entire drive decreases and the probability of system failure increases. Therefore, the development of drives is currently focused on the possibilities of so-called sensorless control. This is a relatively new way of control drives which is still evolving. The following paper will explain the method of RF-MRAS sensorless control.

## 2 Vector control of induction motor

The vector control of induction motor consists in separating of stator current vector  $\mathbf{i}_1^S$  into two orthogonal components of currents that affect the torque of the machine and its magnetization. For easy realization of the vector control structure, the stator current is oriented into coordinate system (OSS) with orientation to the coupled magnetic flux of the rotor  $\Psi_2^O$  resulting from the passage of the flux component of current to the main (magnetizing) inductance. A graphical representation of the decomposition of the vectors is shown in fig. 1.

The vector control is based on the mathematical model of induction motor for stator and rotor voltage (1). Following derivation and correlation of equations (1) we obtain the formula for stator current  $\mathbf{i}_1^S$  (2). After conversion equations (1) and (2) into OSS we obtain a set of equations describing the induction motor behavior (relations (3) and (4)). This equations can be further described in component from (6) and (7) the current component  $i_{1x}$  (6) and the current component  $i_{1y}$  (7), we can get an idea of the induction motor behavior in the vector control.

$$\mathbf{u}_1^S = R_S \mathbf{i}_1^S + L_S \frac{d\mathbf{i}_1^S}{dt} + L_m \frac{d\left(\mathbf{i}_2^R e^{j\varepsilon}\right)}{dt}, \quad \mathbf{u}_2^R = R_R \mathbf{i}_2^R + L_R \frac{d\mathbf{i}_2^R}{dt} + L_m \frac{d\left(\mathbf{i}_1^S e^{-j\varepsilon}\right)}{dt} \quad (1)$$

$$\mathbf{i}_1^S = T_R \frac{d\mathbf{i}_m^S}{dt} + (1 - j\omega_e T_R) \mathbf{i}_m^S \quad (2)$$

$$\mathbf{u}_1^O = R_S \mathbf{i}_1^O + \sigma L_S \frac{d\mathbf{i}_1^O}{dt} + j\omega_{im} \sigma L_S \mathbf{i}_1^O + (1 - \sigma) L_S \frac{d\mathbf{i}_1^O}{dt} + j\omega_{im} (1 - \sigma) L_S \mathbf{i}_m^O \quad (3)$$

$$\mathbf{i}_1^O = T_R \frac{d\mathbf{i}_m^O}{dt} + j\omega_{im} T_R \mathbf{i}_m^O + (1 - j\omega_e T_R) \mathbf{i}_m^O \quad (4)$$

$$\mathbf{i}_1^O = i_{1x} + j i_{1y}, \mathbf{u}_1^O = u_{1x} + j u_{1y}, \mathbf{i}_m^O = i_{mx} + j i_{my} \quad (5)$$

$$\sigma T_S \frac{di_{1x}}{dt} + i_{1x} = \frac{u_{1x}}{R_S} + \omega_{im} \sigma T_S i_{1y} - (1 - \sigma) T_S \frac{di_m}{dt} \quad (6)$$

$$\sigma T_S \frac{di_{1y}}{dt} + i_{1y} = \frac{u_{1y}}{R_S} - \omega_{im} \sigma T_S i_{1x} - (1 - \sigma) T_S \omega_{im} i_m \quad (7)$$

$$\omega_2 = \omega_1 - \omega_m = \frac{1}{i_m T_R} i_{1y} \quad (8)$$





$$\omega_{mest} = \Phi(e) K_R \left( 1 + \frac{t}{\tau_R} \right) \quad (14)$$

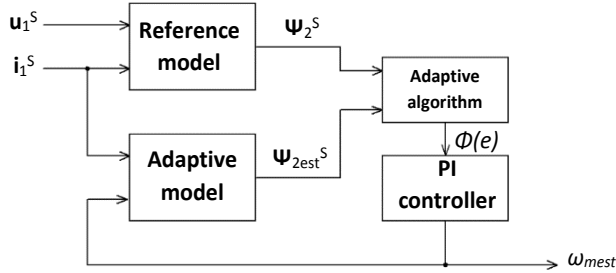


Fig. 3. Structure of observer RF – MRAS

## 4 Results of RF-MRAS simulation

Analysis of the RF-MRAS control method was performed in the Matlab-Simulink PC program. On the basis of the theoretical analysis (above) a simulation of the sensorless vector control RF-MRAS method with induction motor type P112M04 (MEZ Frenštát) was created. Simulation of vector control took place when the motor started and the reversed from 0rpm to 100rpm and -100rpm, and after a while breaking at -10rpm with reversion to -10rpm and eventually stopping the motor. The results are shown in fig. 4 and fig. 5.

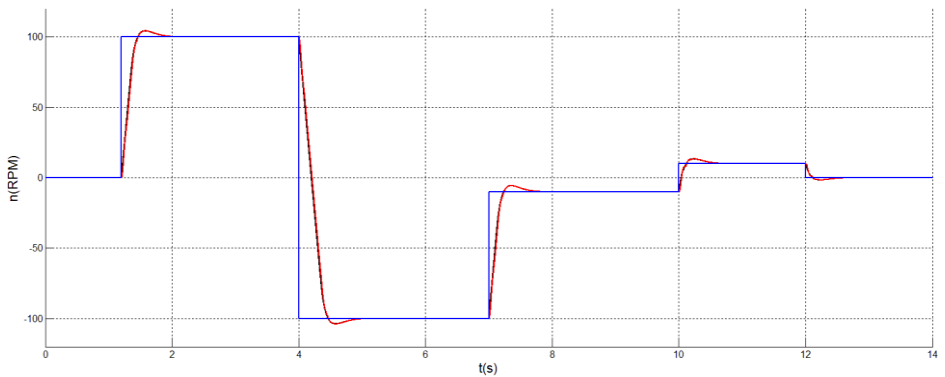


Fig. 4. Trace of requested value (blue), real value (red) and estimated value (black) of speed induction motor in sensorless vector control

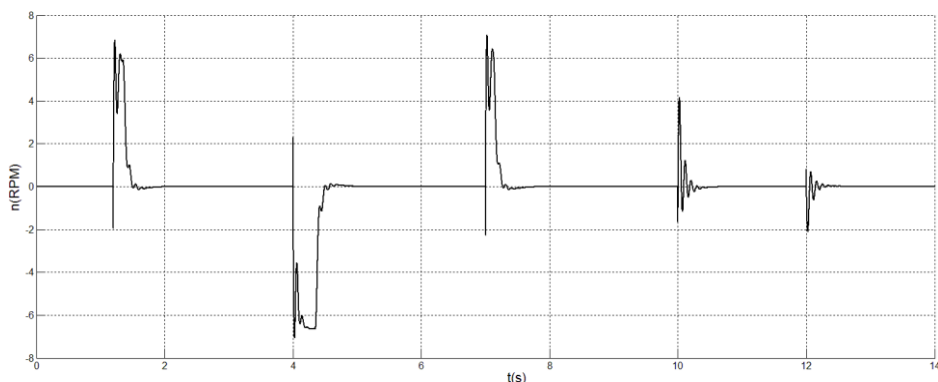


Fig. 5. Trace of calculation difference between real and estimated speed of induction motor in sensorless vector control

## 5 Conclusion

It is worth noting that the above mentioned sensorless control method, intended to estimate the orientation variables, is not in any way capable of fully replacing the position and engine speed sensors of the motor shaft. The signals emanating from the observers are loaded with an error that is strongly dependent on the control mode, the operating range (speed range), and the machine parameters. Defined nominal motor parameters may change over time over the short term (eg. due to engine warming) or long term (eg. by changing parameters due to engine aging). Last but not least, the rated parameters of the machine also affect the frequency converter. The listed of the phenomena influences the precision of the estimation of the orientation quantities and also adversely affect the dynamics of the drive with the vector control. On the other hand, these algorithms are sufficiently accurate and can serve as a tool for a representing the position sensor in the event of the malfunction and allow the machine to run in emergency mode, for example.

## 6 References

1. Brandstetter, P.: *Electric Controlled Drives III*, VSB – Technical University of Ostrava, Ostrava 2012
2. *Field Orientated Control of 3-Phase AC-Motors*, Retrieved from Texas Instruments: <http://www.ti.com/lit/an/bpra073/bpra073.pdf>

# Increase the Efficiency of Induction Motors

Pavel Pečínka and Stanislav Kocman

Department of Electrical Engineering, FEECS,  
VŠB – Technical University of Ostrava, 17. listopadu 15,  
708 33 Ostrava – Poruba, Czech Republic  
{pavel.pecinka.st, stanislav.kocman}@vsb.cz

**Abstract.** This paper presents possibilities to increase the efficiency of three-phase squirrel cage induction motors. The necessary legislative requirements are stated in the first part of the paper, which are basically the main reason for efficiency increasing. After that a theoretical basis and explanation of the design for efficiency increasing follow. The final part presents the results of measurements on the concrete samples of induction motors of different efficiency classes, their comparison, evaluation and comparison with the limits prescribed by the relevant standards.

## 1 Introduction

In general, the electric motors are the most important industrial devices in the field of drive technology. According to available information, they constitute about 65% of the total electricity consumption [1]. The most common type of these motors is three-phase induction motor with a squirrel cage. The physical principle and the process of functioning of the induction motor are generally known. Because in the past two decades society's interest in solutions in the field of energy savings has increased, so the legislature started devoting more to this problem. Specifically, for reducing the amount of electricity consumption, the European Union issued the EuP Directive and EU Directive 2009/125/EC. These directives have been incorporated into the legislation of all EU member states [2]. In the Czech Republic the standard IEC 60034-30-1 is also directive with the effective date of January 1, 2015.

## 2 Legislative requirements

All manufacturers are trying to produce induction motors with the highest possible efficiency. This is mainly due to the customer's requirements and legislative requirements. To unify the measurements of efficiency within the European Union, the measurement should be done according to the standard EN 60034-2-1 [10]. Based on the measurement results it is possible to classify each measured machine according to its rated power, the rated frequency and the number of poles to the efficiency classes from IE1 to IE4 [4]. Time schedule for each class began dating on June 16, 2011. From this date must be induction motors supplied for the European market at least in the efficiency class IE2 (High).

Since this date motors with the efficiency class IE1 (Standard) are not allowed to be supplied to the markets in the European Union. The next change occurred on Janu-

ary 1, 2015. From this date induction motors with the rated output of 7.5 - 375 kW must comply with the efficiency class IE3 (Premium) or IE2 on condition that the motor is fed by frequency converter. The last change was made on January 1, 2017. Since that date the induction motors with the rated output of 0.75 - 375 kW must comply with the efficiency class IE3 or in the case of motors fed by frequency converter with the efficiency class IE2. In Fig. 1 a graphical representation of the efficiency classes [3]. The dependence of the efficiency classes on the power is shown in Fig. 2 [3].

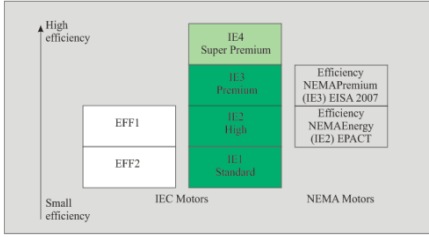


**Fig. 1** Efficiency classes [2]

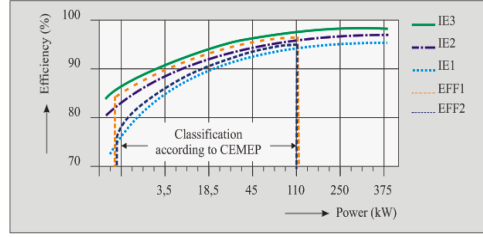


**Fig. 2** Dependence of the efficiency classes on the output power [2]

### 3. Distribution of losses in induction motor

First, for a description of the exact design solutions it is necessary to realize that the efficiency is determined how the induction motor converts input electrical energy into useful work. Therefore it can be concluded that the efficiency is the ratio of the mechanical shaft power  $P$  to the power  $P_1$  supplied to the induction motor. So, the efficiency can be defined by the equation:

$$\eta = \frac{P}{P_1} = \frac{P_1 - \Delta P}{P_1} \cdot 100 \text{ (%)}$$
 (1)

where  $\Delta P$  are the losses in the induction motor. In the induction motor various types of losses arise.

Losses involved in the induction motor can be divided into five basic categories. The first category is the iron losses. Their exact expression is problematic, because of the magnetic characteristics are not linear. The iron losses can be further divided into hysteresis losses and eddy current losses. For the magnitude of the hysteresis losses this equation is defined [11], [12]:

$$\Delta P_h = k_h \cdot B^n \cdot \frac{f}{50} \cdot m \text{ (W)}$$
 (2)

where  $k_h$  is a hysteresis material constant at 50 Hz,  $B$  is the magnetic flux density,  $f$  is the frequency,  $m$  is the mass and  $n$  is a coefficient characterizing the material



type (the values of  $n$  range from 1,6 to 2,0) [2], [5]. The magnitude of the eddy current losses is formulated as:

$$\Delta P_e = k_e \cdot B^2 \cdot \left( \frac{f}{50} \right)^2 \cdot m \text{ (W)}, \quad (3)$$

where  $k_e$  is a material constant for a given material at a frequency of 50 Hz. A next group of losses are losses in the stator winding. These are essentially Joule losses generated by passing a current through a conductor. The following group is the losses in the rotor winding analogous to the losses in the stator winding. The following formulas can be defined in [5], [11] as follow:

$$\Delta P_{\text{Cuslot}} = J^2 \cdot S \cdot \rho \cdot l_{\text{cond}} \text{ (W)}, \quad (4)$$

where  $J$  is the current density in the slot,  $S$  is the cross-section area of the slot,  $\rho$  is the resistivity of the material winding and  $l_{\text{cond}}$  is the length of the winding,

$$\Delta P_{\text{Cu}} = \sum_i \Delta P_{\text{Cuslot } i} \text{ (W)}, \quad (5)$$

where  $i$  is the number of the slots.

The fourth group is the additional losses. Their exact identification is not easy; because this group includes losses arising due to the eddy currents in the windings, on the surface, in the teeth of the stator and rotor, due to a pulsation of the magnetic flux, nonlinearities, inequality of the air gap and leakage flux of spatial harmonics [11]. The methods determining these losses are given in the standard [10]. Another group of losses is not of the electrical character, but a mechanical one. These losses primarily include losses arising from friction in bearings and ventilation losses. Their approximate determination is possible by the equation [7]:

$$\Delta P_m = \Delta P_0 - \Delta P_{\text{Cu0}} - \Delta P_{\text{Fe}} \text{ (W)}, \quad (6)$$

where  $P_0$  are no-load losses,  $\Delta P_{\text{Cu0}}$  the Joule losses under no-load and  $\Delta P_{\text{Fe}}$  described in (7) are the iron losses and their size is the sum of the losses described by (2) and (3):

$$\Delta P_{\text{Fe}} = \Delta P_h + \Delta P_e \text{ (W)}. \quad (7)$$

#### 4. Design possibilities for efficiency increasing

The methods increasing the efficiency of induction motors can be deduced from the previous chapter. The principle is that we try to reduce each of these types of losses using other constructions or designing of the induction motor. If we focus on the

iron losses, so for their decreasing we have two basic options. The first one is a change of the length of the stator packet. When packet stretching, the value of the magnetic flux density will be lower at the same value of the magnetic flux, therefore the magnetic circuit will be less saturated causing a reduction of the losses in the iron. Another, very often used method of reducing the iron losses is using better materials for the construction of the magnetic circuit. Material with lower loss number will have lower losses at the same value of magnetic flux density and the same volume of material. If we focus on losses in the stator and rotor windings it is possible to conclude that for the reduction of losses it is necessary to reduce the resistance of the wire itself, as can be seen in (4). In the stator winding increasing the number of wires or using a lower layer of insulation, but with respect to the slot filling and the required thermal insulation class. As regards the rotor winding the cross-section of the rotor slots and the short circuit rings can be increased. It is also possible to use a material other than aluminum. To reduce the additional losses magnetic wedges can be used. Next, an optimal air gap should be taken into account and also the optimal ratio of the stator and rotor slots as given in [12], which is defined by the formula:

$$Q_2 = Q_1 \pm 4 \cdot p \quad (-), \quad (8)$$

where  $Q_2$  is the number of the rotor slots,  $Q_1$  is the number of the stator slots,  $p$  is the number of the pole pairs.

An elimination of the mechanical losses is only possible to a certain extent, because the bearings are necessary for proper function of the induction motor needing a proper care to ensure their quality. The fan is also necessary for the proper induction motor function; therefore its proper design is essential.

It is necessary to combine all of these ways of reducing losses not only for efficiency increasing, but also for other parameters such as relative breakdown torque, relative starting current, power factor and next ones, which must be also guaranteed by the manufacturers. Another integral and often the most important part of the combining design modifications is the price of the final product. Therefore it is necessary to consider whether the change in design brings the desired output for the demanded price.

## 5. Experimental measurements

The number of publications is devoted to the evaluation of motor efficiency, some results of experimental measurements can be found e.g. in [13-18].

To compare the efficiency of tested induction motors in various efficiency classes, experimental measurement have been realized for three induction motors of the same series, but with another efficiency class (IE1, IE2, IE3). The measured circuit is in Fig. 3.

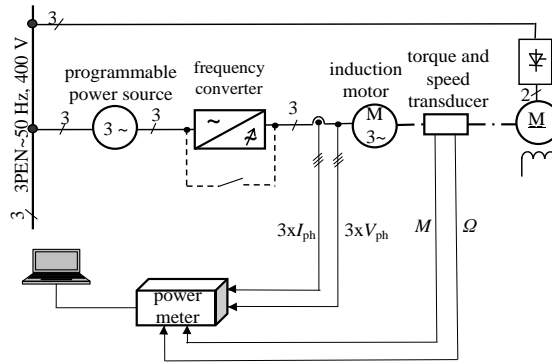


**Fig 3.** Block diagram of tested electrical drives

The electric drives have been fed by a programmable power source Pacific 3120ASX enabling to set required values of voltage characteristics, i.e. the nominal frequency of 50 Hz and phase voltage of 230 V, and the balanced harmonic supply voltage. The source allows a connection of external feedback to compensate the voltage drop on the cable from the source to the drive. The induction motors have been supplied by the source either directly or with inserted frequency inverter as can be seen in Fig. 3. In both cases only efficiency of the motors has been measured.

The following Table I presents the nominal parameters of the individual tested induction motors.

TABLE I. PARAMETERS OF TESTED MOTORS

Parameter	Value	Value	Value
Nominal power	4 kW	4 kW	4 kW
Nominal voltage	400 V	400 V	400 V
Nominal current	8,4 A	8,2 A	7,9 A
Nominal frequency	50 Hz	50 Hz	50 Hz
Nominal power factor	0,83	0,81	0,82
Nominal speed	1440 min <sup>-1</sup>	1440 min <sup>-1</sup>	1460 min <sup>-1</sup>
Nominal torque	27 N·m	27 N·m	26 N·m
Nominal efficiency	83,1 %	86,6 %	88,6 %
Efficiency class	IE1	IE2	IE3

These tested induction motors have been loaded from 30 to 100 % of the nominal load. The measurements have been carried out for the connection of the motors directly to the power source and for the connection via the frequency converter. Comparison of motor efficiencies in the drive fed directly by the source (i.e. uncontrolled drive) and fed via the frequency converter (i.e. controlled drive) is shown for the frequency of 50 Hz.

In Table II, a comparison of the efficiency of induction motors in the controlled and uncontrolled drives under the nominal load at the frequency of 50 Hz is shown.

TABLE II. COMPARISON OF EFFICIENCY OF INDUCTION MOTORS IN CONTROLLED (VSD) AND UNCONTROLLED (DOL) DRIVES UNDER THE NOMINAL LOAD AT THE FREQUENCY OF 50 HZ

Efficiency	motor IE1	motor IE2	motor IE3
nominal (catalogue)	83,1 %	86,6 %	88,6 %
DOL	83,4 %	85,7 %	88,5 %
VSD	82,5 %	85,1 %	88,7 %

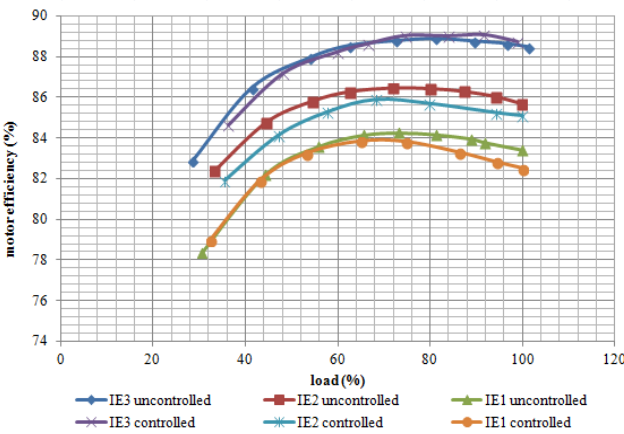


Fig 4. Comparison of efficiency of motors in controlled and uncontrolled drives at the frequency of 50 Hz

# Conclusion

The efficiency of all three measured induction motors with direct on line connection to the source, i.e. with standard efficiency IE1, increased efficiency IE2 and high efficiency IE3, recorded during the measurements under the nominal load are in conformity with a prescribed limit of motor efficiency declared by standards [8], [9] with a sufficient reserve. The measured values of efficiency of the motor with the efficiency class IE1 are about few decimals higher than the manufacturer's guaranteed values at 100%, 75% and 50% of the nominal load. On the contrary, they are lower for the motor IE2, but for the motor IE3 they are almost identical. As regards the nominal load the difference can be seen in Tab. II.

In case the motors have been fed by the frequency converter, the efficiencies of motors of classes IE1 and IE2 are lower in comparison to the values of the uncontrolled motors, especially at high rates of the load, as can be seen in Fig. 4. As can be detected from the measurements, the operation of these motors in variable speed drives with a frequency converter in comparison to its operation directly from the source causes efficiency decreasing up to c. one percent, which is within the limit

stated by the relevant standards. For the motor IE3 its efficiency in both cases is very similar. As regards the nominal load the difference can be seen again in Tab. II.

So it can be stated that the frequency converter with a PWM control has not a significant influence on the efficiency of induction motors.

The deviation in the efficiency between the IE3 motor on the one hand and the IE1 and IE2 motors on the other hand will be caused with the most probability by design differences in the construction of the motor. The main differences will lie in the used material of the sheets and in the perfect value of magnetic circuit saturation – then by the optimal design in term of the efficiency.

The legislation prescribes the use of motors of the efficiency class IE3 either for the direct on line connections or for the connections in combination with a frequency converter. It also allows using motors of the efficiency class IE2 fed by the frequency converter.

## References:

- [1] N. Pavelková, "Účinnosti elektrických motorů a snižování spotřeby elektrické energie," ELEKTRO 2008, pp 1-2.
- [2] R. Boháč, "Analýza možností zvýšení účinnosti asynchronních elektromotorů," Ostrava 2014, pp. 5-7.
- [3] G. Holub, "Nové třídy účinnosti asynchronních elektromotorů," ELEKTRO 2011, pp. 1
- [4] IEC 60034-30 standard on efficiency classes for low voltage AC motors, IEC 2014.
- [5] M. Jarmara, Č.. Ondrůšek, "Výpočet ztrát univerzálního motoru metodou konečných prvků," Elektrověst 2004, pp 6
- [6] J. Janeček, "Řízení různých typů motorů jedním měničem frekvence s optimalizovanou spotřebou energie," AUTOMA 2011 pp. 17-19
- [7] K. Chmelík, Asynchronní a synchronní elektrické stroje. VŠB-TUO Ostrava 2002.
- [8] ČSN EN 60034-30. Točivé elektrické stroje-Část 30: Třídy účinnosti jednotáčkových trojfázových asynchronních motorů nakrátko (IE kód), ÚNMZ, 2009.
- [9] ČSN EN 60034-1. Točivé elektrické stroje-Část 1: Jmenovité údaje a vlastnosti, ČNI, 2005.
- [10] ČSN EN 60034-2-1. Točivé elektrické stroje-Část 2-1: Standardní metody určování ztrát a účinnosti ze zkoušek (s výjimkou strojů pro trakční vozidla), ČNI, 2008.
- [11] G. N. Petrov, Elektrické stroje 2. Academia ČSAV, Praha 1982.
- [12] L. Cigánek, Stavba elektrických strojů. SNTL, Praha 1958.
- [13] A. Boglietti, R. Bojoi, A. Cavagnino, A. A. Tenconi, "Efficiency Analysis of PWM Inverter Fed Three-Phase and Dual Three-Phase High Frequency Induction Machines for Low-Medium, Power Applications," IEEE Trans. on Industrial Electronics, 2008, No. 5, pp. 2015-2022.
- [14] A. Decner, "The efficiency of electric drives supplied from frequency converters (PWM)," in Energy Efficiency in Motor Driven Systems, Springer, 2003, pp. 78-85.
- [15] S. Kocman, P. Orsák, "Srovnání účinnosti elektrických pohonů s asynchronními motory," Electric Power Engineering, 2011, pp. 187-190.
- [16] P. Orsák, S. Kocman, L. Paulínský, "Efficiency determination of inverter-fed induction motor for low power applications," in Przegląd Elektrotechniczny, 2012, pp. 305-307.
- [17] W. Deprez, O. Göll, R. Belmans, "Vagaries of efficiency measurement methods for induction motors," Proc. of Energy Efficiency in Motor Driven Systems (EEMODS) conference. Heidelberg, Germany. 2005, vol. 1, p. 158 - 168.
- [18] P. Van Roy, R. Belmans, "Assessment of efficiency of low voltage, three phase motors," in Energy Efficiency in Motor Driven Systems, Springer, 2003, pp. 95-100.

# Optimization of PID Controller for Brushless DC Motor Drive using PSO algorithm

Sang Dang Ho, Cuong Dinh Tran, Thinh Cong Tran,  
Chau Si Thien Dong, Hau Huu Vo

Faculty of Electrical and Electronics Engineering, Ton Duc Thang University,  
Nguyen Huu Tho Street, Tan Phong Ward, District 7, Ho Chi Minh City, Vietnam  
{hodangsang, trandinhcuong, trancongthinh, dongsithienchau,  
vohuuhaui}@tdt.edu.vn

**Abstract.** This paper presents a method to determine the optimal Proportional-Integral-Derivative (PID) controller parameters, for speed control of Brushless DC (BLDC) Motor by using a Particle Swarm Optimization (PSO) algorithm. It is difficult to tune the parameters and get satisfied control characteristic by using the conventional PID controller. The proposed approach has superior features, including easy implementation, stable convergence characteristic and good computational efficiency. The BLDCM is modeled in Simulink and the PSO algorithm is implemented in MATLAB.

**Keywords:** BLDC motor, PSO, PID, speed control, Optimization, Particle Swarm Optimization

## 1 Introduction

Several years ago, many types of motors were developed to minimize the problems that are faced by brushes DC motors. Among those types of motors, the use of brushless DC motor has recently received much attention. This is because the BLDC motor offers many advantages including higher efficiency, low maintenance, and more compact construction. Hence, the BLDC motors are widely used for variable speed drive systems of the industrial application and electric vehicles [1].

Normally, PID controller is an optimum choice for controlling the speed of the BLDC motor. The conventional PID controller algorithm is simple, stable, easy adjustment and high reliability. The famous method to find PID parameters is Ziegler-Nichols rule, but sometimes are not the best. So, it can be realized by using genetic optimization technique based on three different cost functions to find the best PID control parameters. The main obstacles facing PID control technique is sudden change in set point and parameter variation, it makes the PID control gives poor response.

In this paper, a method to determine PID controller parameters using the PSO algorithm is proposed. This paper has been organized as follows: in section 2, the BLDC motor is described and the current controller model of it is shown. In the section 3, the conventional PID is reviewed and in section 4, the PSO algorithm is reviewed also. Section 5, describes how PSO is used to design the PID controller optimally for BLDC motor. The results obtained by the proposed method via Matlab/Simulink are presented in section 6. The paper is concluded in section 7.

## 2 Brushless DC Motor

Permanent magnet DC motors use mechanical commutator and brushes to achieve the commutation. The stator of BLDC motor is the coil, and the rotor is the permanent magnet. The stator develops the magnetic field to rotate the rotor. Hall effect sensor detects the rotor position as the commutating signals. Therefore, BLDC motors use permanent magnets instead of coil in the armature and so do not need brushes. The speed of the BLDC motor is controlled by means of a three-phase and half-bridge pulse width modulation (PWM) inverter. BLDC motor not only has the advantages of DC motor such as better velocity capability and no mechanical commutator but also has the advantages of AC motor such as simple structure, higher reliability and free maintenance. In addition, brushless DC motor has the following advantages: smaller volume, high torque, and simple system structure. So it is widely applied in areas which needs high performance drive [1].

It is desirable to provide current limitation and fast torque dynamic control for many electric drive applications. A simple method that can offer these requirements is the use of torque hysteresis controller (THC) technique. Fig.1 shows the structure of torque hysteresis controller for BLDC motor [1].

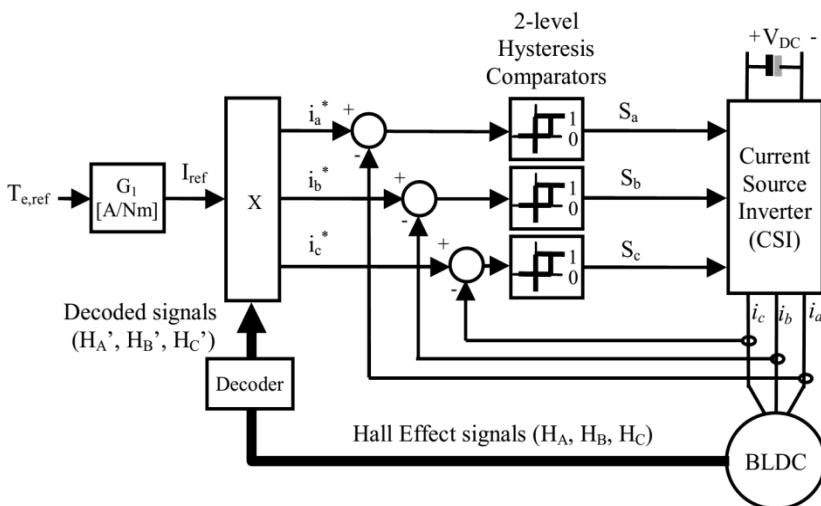


**Fig. 1.** Structure of Torque Hysteresis Controller (THC) drive for BLDC Motor

As shown by Fig.1, the motor currents need to be controlled satisfying to their references ( $i_a^*$ ,  $i_b^*$ , and  $i_c^*$ ). The generations of reference currents are based on the torque demand ( $I_{ref} = T_{e,ref} \cdot G_1$ ) and decoded signals ( $H_A'$ ,  $H_B'$  and  $H_C'$ ) which are derived from the Hall Effect signals ( $H_A$ ,  $H_B$  and  $H_C$ ).

Each phase current is controlled by using a 2-level hysteresis comparator, which is responsible to produce appropriate switching status to be fed into the inverter, either to increase or decrease the phase current such that its error (or current ripple) is restricted within the hysteresis band (HB). In such a way, the reference current for each phase will have the same pattern waveform with the respective decoded signals.

### 3 Overview Of Particle Swarm Optimization

Particle swarm optimization (PSO) is a population based stochastic optimization technique developed by Dr. Eberhart and Dr. Kennedy in 1995 [2]. The technique is derived from research on swarm such as fish schooling and bird flocking. According to the research results for a flock of birds, birds find food by flocking. The observation leads the assumption that every information is shared inside flocking. Moreover, according to observation of behavior of human groups, behavior of each individual is also based on behavior patterns authorized by the groups such as customs and other behavior patterns according to the experiences by each individual. The assumption is a basic concept of PSO [2]. In the PSO algorithm a flock of particles are put into the d-dimensional search space with randomly chosen velocities and positions knowing their best values so far ( $P_{best}$ ) and the position in the d-dimensional space. For example, the  $i$ -th particle is represented as  $X_i = (X_{i,1}, X_{i,2}, \dots, X_{i,d})$  in the d-dimensional space. The best previous position of the  $i$  th particle is recorded and represented as  $Pbest_i = (Pbest_{i,1}, Pbest_{i,2}, \dots, Pbest_{i,d})$

The index of best particle among all of the particles in the group is  $Gbest_d$ . The velocity for particle  $i$  is represented as  $V_i = (V_{i,1}, V_{i,2}, \dots, V_{i,d})$ . The modified velocity and position of each particle can be calculated using the current velocity and the distance from  $Pbest_{i,d}$  to  $Gbest_d$  as shown in the following formulas [2]:

$$V_i^{(t+1)} = V_i^{(t)} + C_1 Rand_1 (Pbest_i - X_i^{(t)}) + C_2 Rand_2 (Gbest_i - X_i^{(t)}) \quad (1)$$

$$X_i^{(t+1)} = X_i^{(t)} + V_i^{(t+1)} \quad (2)$$

where  $V_i^{(t)}$ -current velocity of agent  $i$  at iteration  $t$ ;  $V_i^{(t+1)}$ - new velocity of agent  $i$  at iteration  $t+1$ ;  $C_1$ - adjustable cognitive acceleration constants (self confidence);  $C_2$  - adjustable social acceleration constant (swarm confidence);  $Rand_{1,2}$  - random number between 0 and 1;  $X_i^t$  - current position of agent  $i$  at iteration  $t$ ;  $Pbest_i$  - personal best of agent  $i$ ;  $Gbest$  - global best of the population;  $X_i^{(t+1)}$ - denotes the position of agent  $i$  at the next iteration  $t+1$

### 4 Proposed PSO-PID Controller

The PID algorithm is described by [4]:

$$u(t) = K_p e(t) + K_i \int_0^t e(t) dt + K_d \frac{de(t)}{dt} \quad (3)$$

Where  $u$  is the control signal,  $e$  is the control error,  $K_p$ ,  $K_i$  and  $K_d$  are the proportional of the error, the integral of the error and the derivative of the error. The controller is able to calculate the control signal based on different weights, which can drive the controlled object. For a PID-controlled system, there are often four indices to depict the system performance: ISE, IAE, ITAE and ITSE. They are defined as follows [4]:

$$ISE = \int_0^\infty e^2(t) dt \quad (4) \quad IAE = \int_0^\infty |e(t)| dt \quad (5)$$



$$ITAE = \int_0^{\infty} t|e(t)|dt \quad (6)$$

$$ITSE = \int_0^{\infty} t.e^2(t)dt \quad (7)$$

In this paper, a proposed PSO-PID controller using the PSO algorithm was developed to improve the step transient response of BLDC system. The PSO algorithm was mainly utilized to determine three optimal controller parameters  $K_p$ ,  $K_i$  and  $K_d$  such that the controlled system could obtain a good step response output. The  $ITAE$  is used to describe the performance for different parameters in this case.

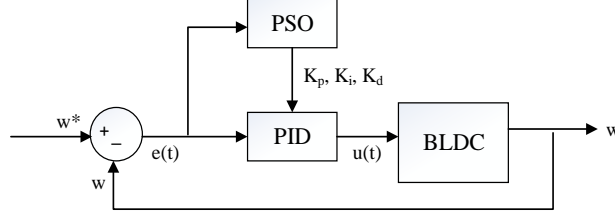


**Fig. 2.** The BLDC control system based on PSO-PID controller

As Fig.2, the system input is referent rotor speed ( $w^*$ ), the output of PID is  $u(t)$ , which used to control the torque of BLDC motor, and the rotor speed  $w$  is system output.

The process to find optimized parameters of PID controller is shown in Fig.3

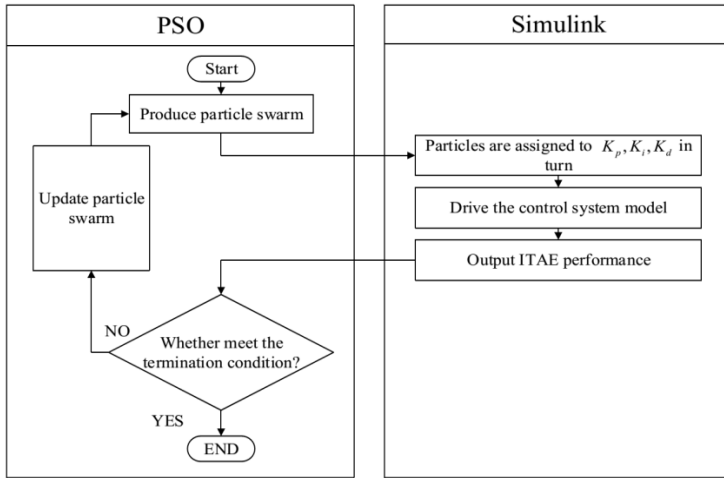


**Fig. 3.** The process of optimization.

## 5 Matlab / Simulink and Result

The Matlab/Simulink models are described as Fig.4 and the parameters of BLDC motor are given by Table-1.

The PSO-PID controller parameters are: Population size=20; Iteration=30;  $w = 0.8$ ;  $C_1=C_2=2$ ;  $K_{pmin}=1$ ;  $K_{pmax}=10000$ ;  $K_{imin}=0$ ;  $K_{imax}=500$ ;  $K_{dmin}=0$ ;  $K_{dmax}=20$ .

The performance result of PSO-PID controller after 30 iterations is shown in Fig.5 as well as fitness value.

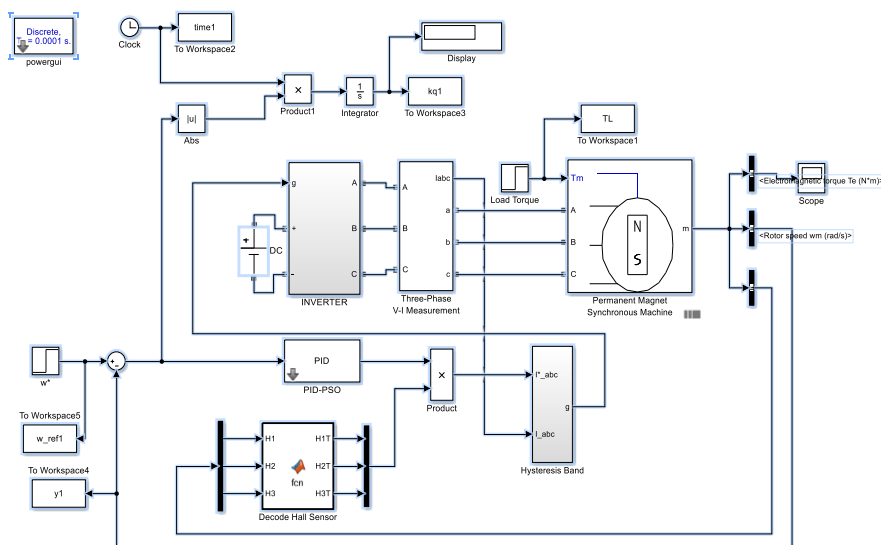


**Fig. 4.** Matlab/Simulink model of PSO-PID controller of BLDC motor

TABLE-1: PARAMETERS OF BLDC MOTOR

Parameter	Value
Number of Pole	4
Stator phase resistance	0.2 $\Omega$
Stator phase inductance	0.0085 H
Flux linkage established by magnets	0.175 Wb
Moment of inertia	0.089 kgm <sup>2</sup>

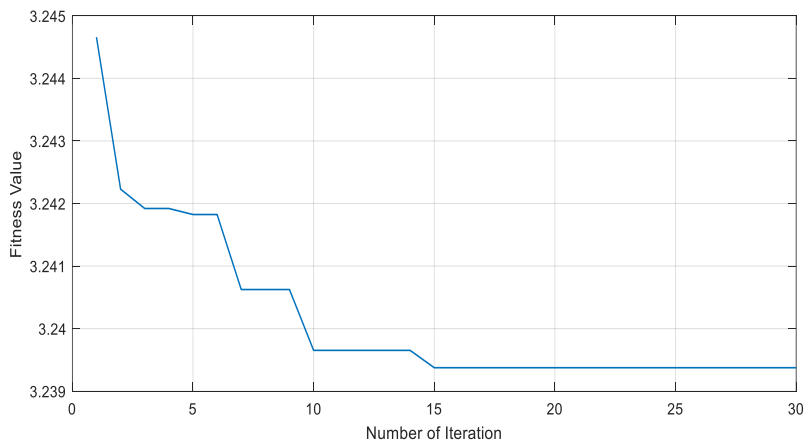


**Fig. 5.** The best fitness value

The following results according to the Fig.5 are:

$$K_p = 7698; K_i = 85.52; K_d = 16.4; ITAE = 3.329$$

The speed response of BLDC motor by using optimized parameters above is shown in Fig.6.

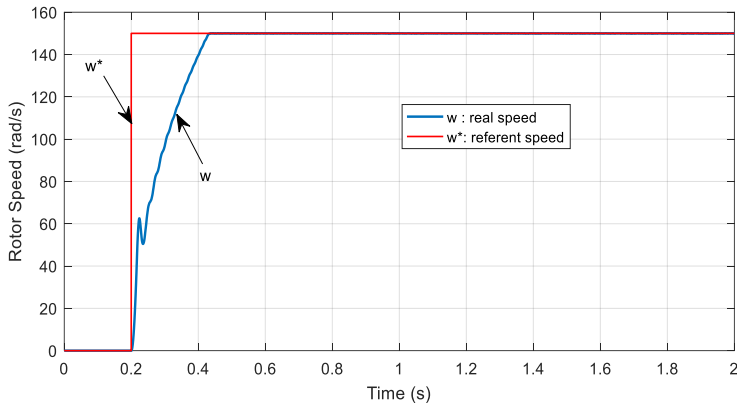


**Fig. 6.** The speed response curve with the best parameters of  $K_p$ ,  $K_i$  and  $K_d$

## 6 Conclusions

In this paper a new design method to determine PID controller parameters using the PSO method is presented. Obtained through simulation of BLDC motor, the results show that the proposed controller can perform an efficient search for the optimal PID controller, this method can also improve the dynamic performance of the system in a better responding.

## Acknowledgement

In the paper, there are the results of the project reg. no. SP2017/104 funded by the Student Grant Competition of VSB-Technical University of Ostrava. This research was supervised by Prof. Ing. Pavel Brandstetter, CSc.

## References

1. Bahari N., Jidin A., Abdullah A. R. and Othman M. N., "Modeling and Simulation of Torque Hysteresis Controller for Brushless DC Motor Drives", IEEE Symposium on Industrial Electronics and Applications ISIEA, 2012.
2. J. Kennedy and R. Eberhart, "Particle swarm optimization", in Proc. IEEE Int. Conf. Neural Networks, vol. IV, Perth, Australia, 1995, pp. 1942–1948.
3. Gaing Z.L., "A Particle Swarm Optimization approach for Optimum Design of PID controller in AVR System", IEEE Transactions On Energy Conversion, Vol. 19, No.2, pp. 284-291, 2004.
4. K. Ang, G. Chong, and Y. Li, PID control system analysis, design, and technology, IEEE Trans.Control System Technology, vol. 13, pp. 559-576, July 2005.

# Rotor Time Constant Estimation Using Genetic Algorithm for Induction Motor Drive

Thinh Cong Tran, Cuong Dinh Tran, and Sang Dang Ho

Faculty of Electrical and Electronics Engineering, Ton Duc Thang University,  
19 Nguyen Huu Tho street, Dist. 7, Ho Chi Minh City, Vietnam  
{trancongthinh, trandinhcuong, hodangsang}@tdt.edu.vn

**Abstract.** The paper presents the determination of the time constant of the IFOC field oriented control modeling for induction motor by genetic algorithm. The first part of paper is the mathematical modeling. The second is genetic algorithm for estimating the rotor time constant. The identification method is showed as an optimization problem where the fitness function is the total square error between the motor and the commanded stator currents. The third part is the simulation in Matlab-Simulink environment, the results indicate that it is possible to accurately determine the time constant Rotor on IFOC model with proposed algorithm.

**Keywords:** A.C. drive, induction motor, IFOC control, rotor time constant, genetic algorithm, optimization.

## 1 Introduction

We know that between the motor parameters and the parameters set up in the controller are not the same 100%. In this article shows how to define it. There are two different models are possible using: model of the Field Oriented Controllers, the first is Indirect Field Oriented Controller (IFOC) in which only the rotor flux position is obtained from the sensor and the others is the Direct Field Oriented Controller (DFOC) in which the rotor flux position are estimated [2]-[8].

The IFOC controlled induction motor drives are widely used in high performance motion control. Because of torque/flux decoupling, the vector control achieves a good dynamic response and an accurate motion control as the control of separately excited DC motors. However, in real-time implementation, precise decoupling which requires accurate motor parameters cannot be completely achieved due to significant plant uncertainties. These uncertainties include external disturbances, unpredictable parameter variations, and un-modeled plant nonlinear dynamics. Consequently this deteriorates the dynamic performance of the drive significantly. Generally speaking, the performance of this control system depends on the accuracy of the mathematical model of induction motor [3]-[8].

We will use a genetic algorithm to determine the rotor time constant accurately provide reliable parameters for the control system thus allowing the motor operates with high efficiency.

Genetic algorithms are search algorithms based on the mechanics of natural selection and natural genetics [4]-[5]-[7]. One of the most important advantages of genetic algorithm over traditional optimization procedures is able to find the global minimum, instead of a local minimum. Another advantage is that genetic algorithms use information of fitness function, no derivatives or other auxiliary knowledge which is not always easily obtainable. Genetic algorithms require the natural parameter set of the optimization problem to be coded as a finite length string over some finite alphabet. A simple genetic algorithm that gives good results in many practical problems is composed of the following genetic operators: Reproduction, Crossover and Mutation.

## 2 Mathematical model of the vector controlled induction motor

The equations of the Induction Motor (IM) model in  $x$ - $y$  coordinates are expressed as follows [10]:

$$v_{sx} = (R_s + pL_s)i_{sx} - L_s\omega_e i_{sy} + pL_m i_{rx} - L_m\omega_e i_{ry} \quad (1)$$

$$v_{sy} = L_s\omega_e i_{sx} + (R_s + pL_s)i_{sy} + L_m\omega_e i_{rx} + pL_m i_{ry} \quad (2)$$

$$0 = pL_m i_{sx} - L_m\omega_{sl} i_{sy} + (R_r + pL_r)i_{rx} - L_r\omega_{sl} i_{ry} \quad (3)$$

$$0 = L_m\omega_{sl} i_{sx} + pL_m i_{sy} + (R_r + pL_r)i_{ry} + L_r\omega_{sl} i_{rx} \quad (4)$$

The electromagnetic torque in terms of  $x$ - and  $y$ - axes components is given by:

$$T_e = \frac{3}{2} P_p L_m (i_{sy} i_{rx} - i_{sx} i_{ry}) \quad (5)$$

If the vector control is established such that  $y$ -axis rotor flux is set zero, and  $x$ -axis rotor flux is maintained constant then we have equations:

$$\psi_{rx} = L_m i_{sx} \quad (6)$$

The slip frequency is calculated from the stator reference current  $i_{sy}^*$  and the motor parameters:

$$\omega_{sl} = \omega_e - \omega_r = \frac{1}{T_r} \frac{i_{sy}^*}{i_{sx}} \quad (7)$$

Where  $T_r = L_r / R_r$  is the rotor time constant.

$$T_e = \frac{3}{2} p_p \frac{L_m}{L_r} \psi_{rx} i_{sy} \quad (8)$$

Hence, only  $y$ - axis stator current controls the electromagnetic torque.

For the coordinate transformation, the rotor flux position  $\theta_e$  is necessary. It is calculated from the rotor speed  $\omega_r$  and slip frequency  $\omega_{sl}$  as follows [6]:

$$\theta_e = \int (\omega_r + \omega_{sl}) dt \quad (9)$$

Fig. 1 shows the speed control structure of the induction motor drive.

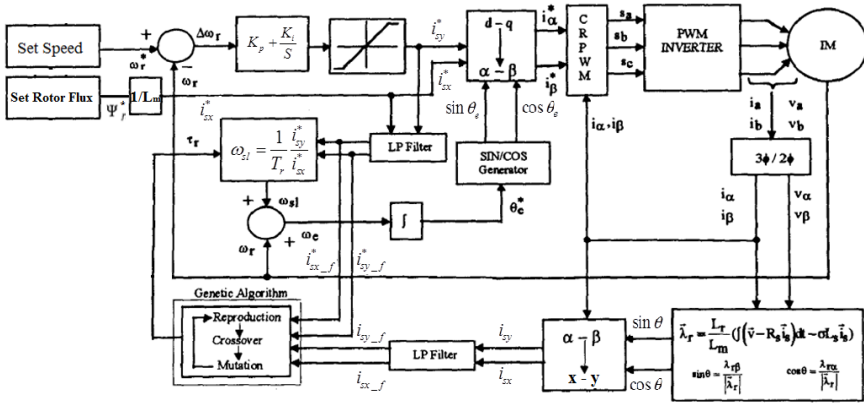


Fig. 1. The IFOC principle models of IM speed controller

### 3 Mathematical model for the rotor time constant estimation

With IFOC modeling of induction motor in steady state the following hypotheses can be made [4]:

$$\hat{i}_{sx} = i_{sx}^*; \hat{i}_{sy} = i_{sy}^* \quad (10)$$

In detuning conditions the relations between the motor and the commanded stator currents can be expressed as [4]-[9]:

$$\hat{i}_{sx} = i_{sx}^* \frac{\sqrt{1 + \left(\frac{i_{sy}^*}{i_{sx}^*}\right)^2}}{\sqrt{1 + \left(\frac{T_r}{T_r^*} \frac{i_{sy}^*}{i_{sx}^*}\right)^2}}; \hat{i}_{sy} = i_{sy}^* \frac{\sqrt{1 + \left(\frac{i_{sy}^*}{i_{sx}^*}\right)^2}}{\sqrt{1 + \left(\frac{T_r}{T_r^*} \frac{i_{sy}^*}{i_{sx}^*}\right)^2}} \quad (11)$$

Where  $T_r$ , and  $T_r^*$ , are respectively the motor and the controller rotor time constant. The identification procedure for rotor time constant can be written as an optimization problem.

From expression (10), (11) the error functions between the commanded and the motor currents in a synchronous reference frame can be expressed as follows:

$$\varepsilon_1\left(\frac{T_r}{T_r^*}\right) = \hat{i}_{sx} - i_{sx}^*; \varepsilon_2\left(\frac{T_r}{T_r^*}\right) = \hat{i}_{sy} - i_{sy}^* \quad (12)$$

and the total square error or (fitness function) by

$$\varepsilon = \varepsilon_1^2 + \varepsilon_2^2 \quad (13)$$

To compensate for the error  $\theta_s$ , the parameter  $T_r$  will be defined such that  $\varepsilon$  reaches the smallest value (min).

#### 4 Rotor time constant estimation using genetic algorithm

The genetic algorithms are finding important applications in optimization of technical systems. As an intelligent control technology the genetic algorithms can give robust adaptive response of an electrical drive with nonlinearity, parameter variation and load disturbance effect [1]-[4]-[5]. The block scheme of the GA to determine rotor time constant is shown in the Fig 2.

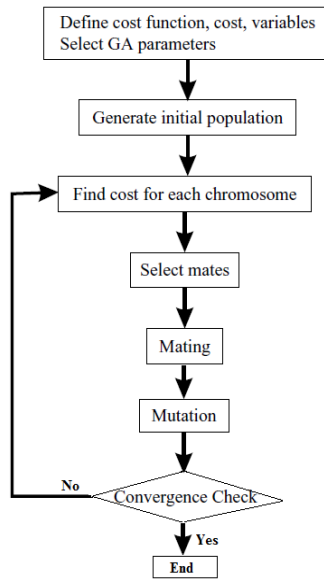


**Fig. 2.** The flowchart for Genetic Algorithms

We used binary genetic algorithm. The parameter is coded as a 12 bit unsigned binary number, as showed in Table 1. The optimization parameters for the execution of the genetic algorithm are shown in Table 2.

The precision of this mapped coding for  $T_r \in [0.05, 2.0]$  is  $\xi = \frac{2-0.05}{2^{12}-1} = 0.000476$

**Table 1:** Parameter coding

$T_r$	Binary
0.05	000000000000
0.050476	000000000001
.....	.....
$0.05 + 1.948744 = 1.998744$	111111111110
2.0	111111111111

**Table 2:** Optimization parameters

Parameter	value
Probability of mutation	0.05
Probability of crossover	0.5
Population size	8
Generation	5-10

## 5      Simulation results

The induction motor drive was simulated using MATLAB-SIMULINK. The basic parameters of the induction motor is  $P = 1\text{HP}$ ,  $U_{dc} = 270\text{V}$ ,  $P_p = 2$ ,  $R_s = 0.87\Omega$ ,  $R_r = 0.228\Omega$ ,  $L_m = 0.0347\text{H}$ ,  $L_{ls} = 0.0008\text{H}$ ,  $L_{lr} = 0.0008\text{H}$ ,  $L_s = L_r = 0.0355\text{H}$ ,  $T_r = L_r/R_r = 0.1557\text{s}$ ,  $J = 1.662 \text{ kg.m}^2$ ,  $F = 0.12 \text{ kg.m}^2$ . The value  $T_r = 0.1557\text{s}$  is exactly parameter of the induction motor. The results were obtained from the GA algorithm which is combined with the model.

Table 3: Implementation of the GA model with the generation is 10

The order of generation	$T_r$ of the first run	$T_r$ of the second run	$T_r$ of the third run	$T_r$ of the manufacturer
1	0.2190	0.6207	0.2090	
2	0.2190	0.6145	0.2090	
3	0.2176	0.1476	0.2090	
4	0.1680	0.1476	0.1171	
5	0.1680	0.1476	0.1171	
6	0.1680	0.1476	0.1171	
7	0.1528	0.1485	0.1481	
8	0.1528	0.1485	0.1481	
9	0.1547	0.1485	0.1481	
10	0.1547	0.1485	0.1481	0.1557

From the table above, we see the values of  $T_r$  always converge to the true value of  $T_r$  is 0.1557 s, this confirmed the correctness of the model and algorithm. The response of torque producing current component  $i_{sy}$  is shown in Fig. 3.

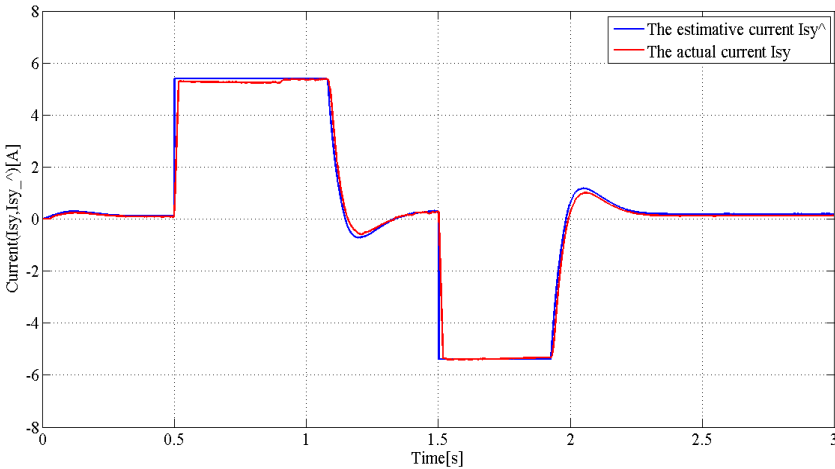


Fig. 3. The time response of torque producing current component  $i_{sy}$ ,  $i_{sy}^{\wedge}$

The current trajectory ( $i_{sy}^{\wedge}$ ) is calculated according to the real current ( $i_{sy}$ ) with the correct rotor time constant of the induction motor.



## 6 Conclusion

In the IFOC control of induction motor drive, if the parameter deviations ( $T_r$ ) is large, leads to the controlled performance of the motor decrease (this shown through the response of torque and speed [3]-[8]). This paper dealt with mathematical basis and how to estimate the rotor time constant by binary genetic algorithms with cost function as equation (11) and (13) to accurately get rotor time constant.

## Acknowledgement

In the paper, there are the results of the project reg. no. SP2017/104 funded by the Student Grant Competition of VSB-Technical University of Ostrava. This research was supervised by Prof. Ing. Pavel Brandstetter, CSc.

## References

1. P. Brandstetter, *Sensorless Control of Induction Motor Using Modified MRAS*. International Review of Electrical Engineering - IREE, Vol. 7, N. 3, pp. 4404-4411, 2012.
2. R. De Doncker, F. Profumo and M. Pastorelli, *Self Tuning of Induction Motor Servo Drives using the Universal Field Oriented Controller*, IEEE-Transactions on Power Electronics, vol. 9, n. 4, pp. 357-366, July 1994.
3. P. Brandstetter, M. Dobrovsky, M. Kuchar, *Implementation of Genetic Algorithm in Control Structure of Induction Motor A.C. Drive*. Advances in Electrical and Computer Engineering, Volume 14, Number 4, 2014.
4. Lino Rosell Valdenebro, Edson Bim, *A Genetic Algorithms Approach for Adaptive Field Oriented Control of Induction Motor Drives*. UNICAMP - FEEC -DSCE, Caixa Postal 6101, 13081-970 Campinas, SP -Brasil.
5. P. Vas, *Artificial-intelligence-based electrical machines and drives*. Oxford science publication, 1999.
6. Manoj Datta, Md. Abdur Rafiq, and B. C. Ghosh, *Genetic Algorithm Based Fast Speed Response Induction Motor Drive without Speed Encoder*. POWERENG 2007, Setubal, Portugal, April 12-14, 2007.
7. KRMV. Chandrakala, S. Balamurugan, K. Sankaranarayanan, *Genetic algorithm tuned optimal variable structure system controller for enhanced load frequency control*. International Review of Electrical Engineering - IREE, vol. 7, no. 2, pp. 4105-4112, 2012.
8. P. Girovsky, J. Timko, J. Zilkova, *Shaft sensor-less FOC control of an induction motor using neural estimators*. Acta Polytechnica Hungarica, vol. 9, no. 4, pp. 31-45, 2012.
9. D. Fodor, G. Griva, F. Profumo *Compensation of Parameters Variations in Induction Motor Drives using a Neural Network*. University of Bucharest, Romania, and Politecnico di Torino, Italy.
10. A. Saghafinia, HW. Ping, MA. Rahman, *High performance induction motor drive using hybrid fuzzy-PI and PI controllers*. A review. International Review of Electrical Engineering - IREE, vol. 5, no. 5, pp. 2000-2012, 2010.

# Topology for Scalable Large-scale Battery Systems

Matěj Golembiovský

Department of Cybernetics and Biomedical Engineering, FEECS,  
VŠB – Technical University of Ostrava, 17. listopadu 15,  
708 33 Ostrava – Poruba, Czech Republic  
`matej.golembiovsky@vsb.cz`

**Abstract.** This thesis compares various topologies of sequencing of accumulator cells and accumulator batteries. This comparison takes into account factors of security, installation difficulty, complexity and cost of the electronics, and efficiency of the final product.

## 1 Introduction

Due to the fast-growing field of renewable energetics, in which the production of electric energy is largely dependent on the climate conditions, the need to store large amounts of electric energy also grows rapidly. For these particular reasons a number of new technologies are being developed, apart from already established technologies such as pumped-storage hydroelectricity. This ranges from water fission and subsequent storage of the hydrogen which is later on transformed back into electric energy using fuel cells, to transformation into heat and subsequent tying in a chemical reaction, all the way up to the storage in accumulator batteries. Because of the difficulties in transformation of energy in form of heat into electricity and also largely ineffective process of storing hydrogen and its transformation into electric energy, accumulator batteries are becoming a topic of interest.

Modern accumulator cells are however very sensitive to violations of operation parameters that could lead to accumulator's premature degradation. It is for these reasons that the cells in accumulator batteries are combined with sophisticated electronics which is tasked with keeping the operation parameters within allowed boundaries. These electronics are called Battery management system (BMS). The aim of this article is to evaluate various topologies of sequencing of accumulator cells and BMS, especially with focus on efficiency and cost of the final solution.

## 2 Scaling

In order to accommodate the broadest range of applications, it is necessary to design a modular battery system. Such system should meet the following criteria:

- main components identical to any large system

- standardization of main components (failure of one developer will not jeopardize the production),
- easy installation by the staff with minimal training requirements,
- low production cost
- expandability

This leads to following parameters of basic battery module:

- can be moved by one person – up to 25 kg, capacity 4-5 kWh,
- uses cells 18650 – manufactured by the largest number of developers
- works with safe small voltage of up to 60 DC - 48 V system in use of Li-ion cell 14 serially connected cells(nom voltage 50.4 V, max voltage 58.8 V,
- hot-swap (when using at least 2 modules in the system).

If we wish to accommodate a broad range of applications, from portable systems all the way up to systems which are capable of providing electrical energy for entire villages or even cities, it is necessary to develop a number of base units which will be able to connect the respective battery modules and mediate the stored energy.

### 3 Topology of battery modules

The base for topology of battery modules is the demand for a system voltage of 48V. This will be achieved by connecting 14 accumulator cells serially. To achieve the needed capacity it is necessary to add more cells connected in parallel way. This serial-parallel connection can be done in two ways, as demonstrated in figure 1.

When choosing the suitable connection of the cells it is important to realize that to each cell a BMS, or a balance module which guards the cells parameters, respectively, needs to be connected. In the case of 1a connection, it would also be suitable to use modules for distribution of load into individual branches. The subsequent connection with BMS in mind can then look as follows 2. The advantage of the solution 2a is accurate information about all cells in the system, this feature comes, however, at the cost of disproportionate price and size of BMS, as each individual cells requires its own balance module.

In contrast, solution 2b is not significantly demanding in cost of BMS. Its disadvantage is potential hazard in case of failure of one of the cells. In that case the other parallel connected cells are capable of providing considerable energy and power which could lead to an explosion of the damaged cell. Eliminating this problem is very simple, the connection needs to be altered in accordance with 3. This solution is also relatively cheap. After altering the connection, the faulty cell is automatically disconnected with increased current supplied by the other cells in parallel connection, as this current causes melting of the safety. The subsequent drop in capacity caused by failure of one of the cells is generally insignificant, and the BMS ensures that the rest of cells are still run in optimal conditions.

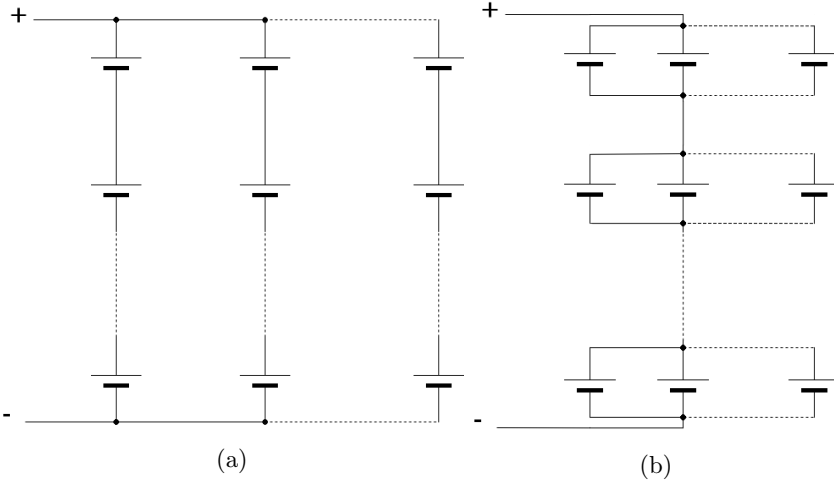


Fig. 1: Serial-parallel connection of cells

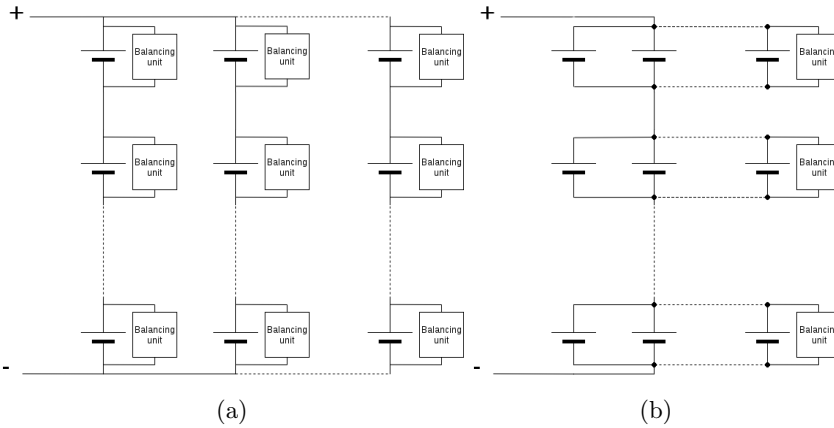


Fig. 2: Serial-parallel connection of cells with BMS

## 4 Topology of modules connection

The aim of development of scaling system for large scale battery systems is to cover a number of applications, from the smallest portable applications to applications capable of powering buildings, villages and cities. Each of these applications, however, has its specific demands when it comes to voltage and power supplied. Last but not least, the distance for which the energy is transferred from the accumulator also differs.

In order to cover the largest possible number of applications, it is sufficient to divide the units which connect battery modules into 3 different topologies.

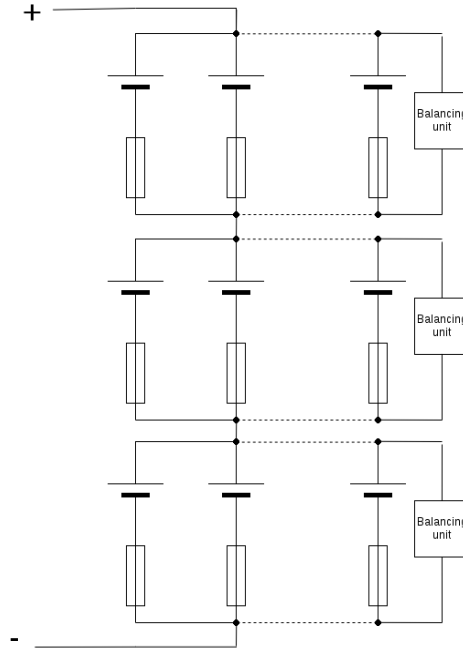


Fig. 3: Safe solution with fuses

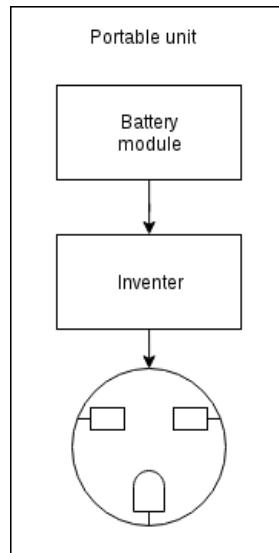


Fig. 4: Portable unit

- Portable unit – Contains one battery module and an inverter see scheme 4. This unit presupposes usage in areas without available electric energy and so does not include accumulator charger.

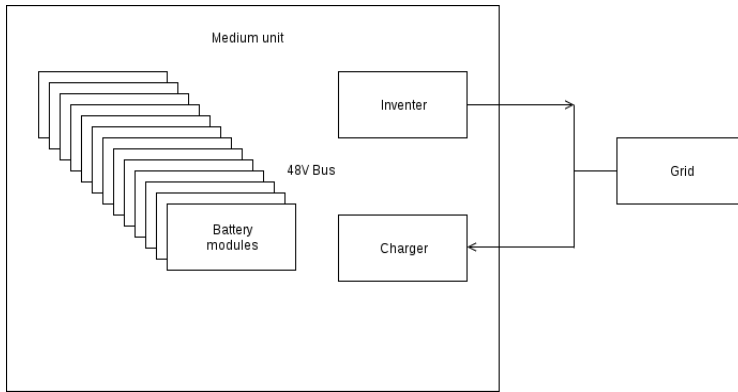


Fig. 5: Medium unit

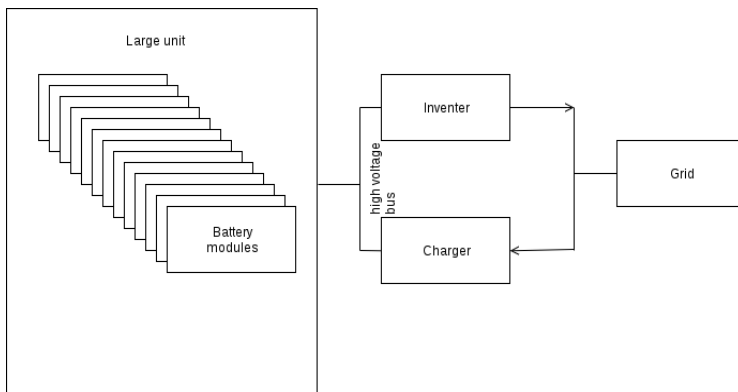


Fig. 6: Large unit

- Medium unit – This unit is capable of taking several battery modules which can be added or disconnected while running, supposing that disconnecting a module would not cause a drop in power which could not be supplied below the currently used power. This makes maintenance and service of battery modules easier. Apart from battery modules, this unit also contains an inverter and accumulator charger. It is therefore possible to store energy in accumulators or supply it into the grid as necessary. The only drawback of this solution is system voltage of 48 V and therefore larger losses during high power levels.
- Large unit – allows for serial connection of battery modules see 6. These units can be connected both serially or parallel, which allows for almost unlimited scaling. These units, however, do not contain neither a charger nor an inverter, as they are expected to be integrated in large substations with their own charging and energy drawn from accumulators.

## 5 Conclusion

The possibilities of sequencing of accumulator cells and batteries and their combinations with BMS, as well as subsequent connection of thusly created battery modules into larger units, which could power portable applications, buildings, villages or even entire cities, have been discribed in this article. The information presented is a result of a study of this topic,

A prototype of a battery module that will subsequently be put into test and on which the outlined possibilities of implemetion of large scale battery systems will be verified, is currently being developed.

# Design of Platform for Robot Cooperation and Swarm Robotics

Jakub Kolařík

Department of Cybernetics and Biomedical Engineering, FEECS,  
VŠB – Technical University of Ostrava, 17. listopadu 15,  
708 33 Ostrava – Poruba, Czech Republic  
jakub.kolarik@vsb.cz

**Abstract.** This article deals with design, construction and testing on the robot with a specific role in group of the robots. For example purpose was used an applications of FLC (Fuzzy Logic Controller) to effectively describe and capture the desired system behavior. The robotics platform also includes a full range of various sensors that collect data and in later use will be able to navigate the whole group in open area. Communication among team is realized via Bluetooth and Wi-Fi technologies. This robot contains a series of sensors as ultrasound, gyroscopic sensors, LIDAR (Light Detection And Ranging), and camera.

**Keywords:** mobile robot; communication; sensors; fuzzy; swarm

## 1 Introduction

Collective of robots, which are usually described in robotics like a swarm, can be used for wide range of purposes. Inspiration and given name of these robots came from animals like ants, bees or termites. These animals can work like complex and precise system despite their size and small nervous system. Individuals have only limited options and can precept only fraction of their surroundings, but in sheer number they can use different mechanics and perceive whole information and act like one organism. Their biggest advantage is usage of simple, substitutable individuals in contrary to a single sophisticated unit. Swarm collective in robotics usually consists of identical individuals, but sometimes there is requirement which must be utilized by unit with special equipment. We can achieve hive-like relationship in robotics, too, if we diverse special hardware equipment between specialized groups of robots. In contrary to swarm ideology, we must give these individuals or small units some sort of intelligence and autonomy. Due to that, other members can have just basic sensor equipment for navigation but use shared complex information about surrounding and carry out different tasks. For purpose of creating more natural intelligence we can use and benefit from choice of linguistic description of control system. This way, we can describe a reaction of unit on events alike organism in a real-life.



## 2 Objectives of the project

Problematic of the main project deals with design and construction of multiple robotic platforms what will be used to form robot collective. They will be used for experiments, testing new approach and education purposes. This specific project deals with controlling of first prototype afore-mentioned mobile platform with use of sensors like on autonomous cars. For this project were given these goals.

1. Autonomous movement in surrounding. First iteration, in which robot is moving on its own in an open area with primary use of data from ultrasonic sensors.
2. Advance data processing. Second iteration, in which robot is using data from camera and LIDAR to move, find obstacles and defined objects.
3. Interpretation of data from sensors: third iteration, in which robot use all data acquired from sensors to describe his surroundings and upload information to shared map.
4. Movement adaption according to map: in the last iteration, the data acquired by all robots will be used to accomplish a given goal.

## 3 Description of the hardware structure

The basis of the robotic platform is RC car model LRP S8 Rebel in scale 1:8. From this model, the chassis and the motors were taken (Fig. 1). The forward and reverse movement is provided by the BLDC motor with hall sensors with power 2.3 kW when the 14 V is used and by the electronic speed controller (ESC) with active cooler. The steering is handled by the hobby servo. The chassis design is based on Ackerman steering geometry with four wheel drive. The source of energy is two cells Li-pol battery with capacity 8000 mAh and nominal voltage 7.4 V.

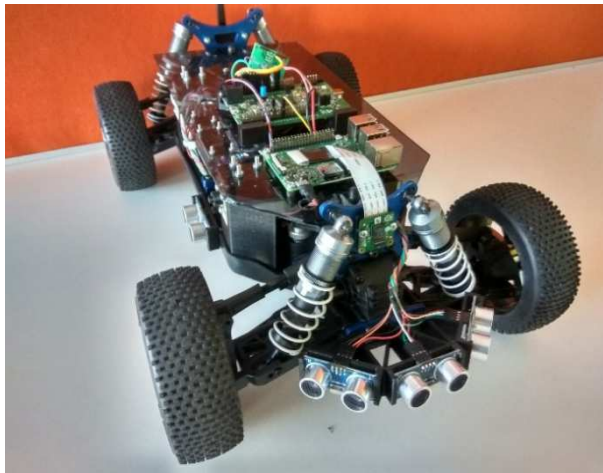


**Fig. 1.** Prototype of designed platform

The main sensor for obstacle detection is a small LIDAR RPLIDAR A2. It is intended specially for use on mobile robots. The measured area has radius of 6 m. In the task of detecting the obstacles, the LIDAR is supplemented with eight ultrasonic distance sensors, which are situated equally around the robot. The next sensor, which is used on the robot, is 10-DOF sensor (degrees of freedom). It includes three axis accelerometer, three axis gyroscope, three axis magnetometer, and barometer. For the purpose of the global navigation in the outdoor areas, the GPS module is used. The local navigation makes use of the quadrature encoder located on the shaft of the driving motor. It is essential to take care of battery to avoid the possible damage, so the voltages of both cells are measured independently and also the actual current drawn from the battery.

The 32bit microcontroller STM32F4 with core ARM Cortex M4 was chosen for the control task on the middle level. It provides enough performance to ensure the required performance and it is equipped with many other resources, too (memory, peripherals, and pins number). This chip enables very fast processing of all acquired information and their distribution to the superior system, which is formed by small computer Raspberry Pi 3. This version includes the WiFi and Bluetooth module, which could be used for communication purposes with the next robots or other systems. The external camera module is connected to the Raspberry Pi. It has the resolution 8 MP and is capable to record the video in several modes, for example with 1080p resolution and 30 fps.

## 4 Design of controlling system

This experiment is focused on designing autonomous controlling system. This system was used to test platform performance. Desired form of robot cooperation can be seen as a distributed system. Each mobile robot unites data from its sensors and carries them to higher layers.

We can utilize FLC system in this application due to use of Raspberry Pi 3 with corresponding computing power. For this purpose a library in programming language Python with visualization was created. Library is based on Mamdani model of FLC controller [2]. This model consists of fuzzyfication of inputs, processing rules and defuzzification by COG method. Model Takagi-Sugeno has smaller computational demands, but was excluded from this part on behalf of different characteristic of output function. This model will be used later.

Library was created to be less computationally intensive. It uses basic instruction without complex multi-iteration loops, integrations, etc. One of the most demanding processes is defuzzification. To decrease the computational demands, membership functions can be defined just by triangle or trapezoid. With these limitations we can define ‘area’ and ‘centre of gravity’ of this function with basic mathematic operations. When membership function is created, all parameters are computed and saved like constants. In every other iteration these constants are just multiplied by input variables.

Library is written in object-style code. In the first iteration of experiments, fuzzyfication of only ultrasonic sensors was used. Data measured by the ultrasonic sensors were primarily used to control angle of Ackermann steering gear. Secondary, there were used to control the speed of robot including its reverse.

Each signal from ultrasonic sensors corresponds to different membership function. Range of input variables correspond to effective range of ultrasonic sensor from 2 to 400 cm and consist of three membership functions. FLC controller in its current state has eight input variables and two outputs. For demonstration purpose, graphs showing membership functions of input variable and 3D maps of rules from Matlab were used. With all ultrasonic sensor used, we can safely move in every direction without risk of collision.

#### 4.1 Intersection of controlling systems

Because we anticipate later changes, we prepared movement system based on model Takagi-Sugeno. The system will connect the commands from superior system with outputs given by fuzzy controller. In case of emergency, system will continuously transfer movement control from superior system to fuzzy controller and thus prevent hazards of collision.

Similar system will be able to link the data from robot sensors with information from map to determine optimal route to chosen destination. This system will be based on one of many swarm movement models [3].

This system is needed due to later stages of development, in which this platform will contain basic algorithm to navigate through area. Searching algorithm will be based on GOAP (Goal Oriented Action Planning), which is a method of programming artificial-intelligence in games. This method is simplified version of automated planner STRIPS (Stanford Research Institute Problem Solver) developed by Richard Fikes and Nils Nilsson in 1971 at SRI International [1].

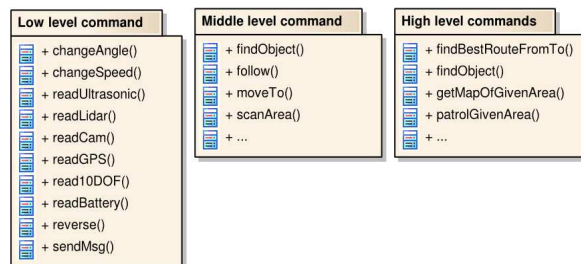


**Fig. 2.** Example action routines

Controlling system enables the use of action routines (Fig. 2), which will describe all actions that robot can perform and can help him to accomplish his goal. Action routines will be divided into multiple levels according their complexity. Action routines from higher level will usually consist of one or multiple commands from lower levels. These action routines will contain preconditions and they will be rated by their difficulty and possible gain to enable alternative approach of solving problems.

**4.2      Inter robot communication and data acquisition**

Another step to form swarm collective is a creation of communication network. This network will serve to transfer data between robots, uploading them to map and it gives us the possibility of direct control and debugging. There is separated article dealing with problematic of data acquisition and low-level controlling of hardware platform. All data from the sensors are processed by STM and transferred by serial communication to Raspberry Pi. These data are transferred to Raspberry Pi. After that, data are broadcasted by build-in Wi-Fi module (Fig. 3).

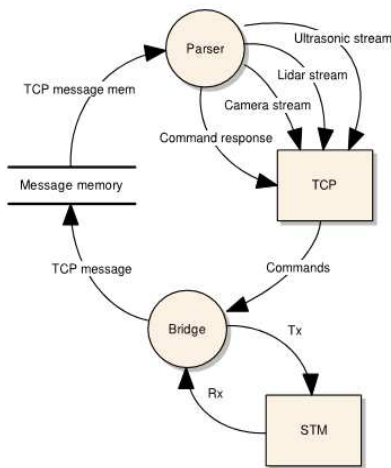


**Fig. 3.** Graphical interpretation of controlling system

Because of high quantity of outgoing information, we need to separate each data stream (Fig. 4). To do that, we used multiple ports for this issue. With this system every other robot can listen do data stream of other robots and make active use of their information. This method will be subjected to experiments to find optimal usage of this information to our application.

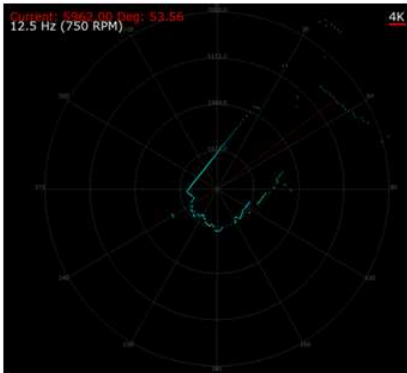


**Fig. 4.** Visualization of LIDAR data stream

## 5 Conclusion

The article has dealt with the design and realization of the controlling system for robotic platform used for robot cooperation and swarm robotics. Because of size of designed unit, they will operate in smaller number than typical application. This paper focused on description of basic components of controlling system at Raspberry Pi with basic introduction of fuzzy logic and its key components. All parts of controlling system are briefly described, including the Fuzzy library and different parts of decision mechanism. Control system is based on fuzzy logic approach. Multiple fuzzy models were used to create motion control system for this mobile platform. This system is used to prevent collisions with obstacles even when superior system is controlling movement of the platform.

This project is in early stage of development and therefore experiments were made only at one unite. Main goal of this phase was creation of platform, testing of motion control, measuring data from all sensors and their interpretation. In future research, advance algorithm for movement control will be applied.

## 6 References

1. Fikes, Richard E., and Nils J. Nilsson. "STRIPS: A new approach to the application of theorem proving to problem solving." *Artificial intelligence* 2.3-4 (1971): 189-208.
2. Marino, Alessandro, et al. "Fuzzy behavioral control for multi-robot border patrol." *Control and Automation, 2009. MED'09. 17th Mediterranean Conference on. IEEE, 2009.*
3. Tsankova, Diana, et al. "Immune network control for stigmergy based foraging behaviour of autonomous mobile robots." *International Journal of Adaptive Control and Signal Processing* 21.2-3 (2007): 265-286.

# Application Software for Electrohydraulic Brakes System of the Electric Vehicle

Samuel Przeczek

Department of Electronics, FEECS,  
VŠB – Technical University of Ostrava, 17. listopadu 15,  
708 33 Ostrava – Poruba, Czech Republic  
`samuel.przeczek.st@vsb.cz`

**Abstract.** This article describes the assembly functional concept and the development of application software electrohydraulic brake system of the electric vehicle DemoCar. The introductory part analyzes ABS assistance system with regard to the use of this module for installations in a vehicle DemoCar. Also included is a description of the mutual cooperation between electronic systems of the vehicle. Theoretical part is deals with the conceptual solutions of the electrohydraulic brake system, selection of brake system components, their analysis and design of the control unit, called BCU.

**Keywords:** CAN-bus; electric vehicle; microcontroller; control unit; ABS; brake system; ABS/ASR/ESP module; assistance system; C/C++; MQX; TWR-PXS20; application software

## 1 Introduction

In the automotive industry plays an important part two concepts: safety and reliability. For braking systems are particularly important. In case of failure the car has become dangerous for the persons inside the vehicle but also for other road users. Therefore, it is important to diagnose faults.

The braking system ensures slowdown and blocks spontaneous movement of the vehicle. Brake systems work on the principle of increasing the frictional resistance. During braking is kinetic energy of vehicle converted to heat and escapes into the surroundings.

## 2 Braking System

Composition of the hydraulic brake system includes the following components: a main brake cylinder, a vacuum booster, a buffer tank for brake fluid and connecting piping. According to the Law it is necessary that the hydraulic part was divided into two circuits.

Through brake pedal are circuits collectively controlled. In case of failure on one of the circuits will not cause a complete failure of braking system but remain braked at least some of the wheels.

### 3 Assistance Systems

These systems can be divided into two categories: active and passive. Active elements are trying to avoid the accident and passive minimize the consequences of an accident. Both categories increase the safety of drivers and crew. Among active include the following:

ABS - this is the anti-lock braking system of wheel which is active in critical driving situations. In this case the system provides steerability and substantially reduces the risk of skidding. On a dry road vehicle without ABS has a shorter braking distance but on wet this situation is reversed. The essence of ABS is the constant rotation of the wheels when braking. This ensures adhesion between the wheel and the road. Locked wheels do not transmit side forces and the vehicle is unable to turn.

ESP - reduces the risk of collision, sideslip or leave the roadway and overturning vehicles in critical situations. This system cooperates with activated ABS and ASR. Based on the values of the sensor compares the required track of the vehicle with real. If the values differ and are evaluated as critical, the system intervenes through targeted brake intervention in engine management and transmission. This creates the opposite torque than the vehicle has in skid.

### 4 ABS System

Behind the development of the ABS stands Bosch. The first performance was in 1978, but the beginnings of reflection on the implementation of system to cars is close to the beginnings of the 20th century. The company in 1936 filed a patent on "Device for preventing heavy braking wheels of a motor vehicle." Only with the advent of electronic control of this system can be developed and implemented, which was fast enough and rugged for use in motor vehicles. Leadership in the use of this system in the vehicle was holding the Mercedes - Benz S-Class, which offered it like special equipment. System for the whole period of its development has been continuously improved in its present form. The latest generation entered series production in 2010 under the name ABS 9th have also been adding new features such as ASR, ESP and more. Figure 2 shows the evolution of ABS and ESP from 1978 until the present generation.

#### 4.1 Control Unit

The control unit is designed for direct montage on hydraulic modulator. This leads to savings in cabling which would be needed for its connection with the solenoid valves in the hydraulic modulator. The control unit monitors the braking using Hall sensors and speed of wheels affects braking interventions with pumps and solenoid valves.

## 4.2 Hydraulic Unit

The task of the hydraulic modulator is change brake pressure which causes a change of brake force. In the modulator pressure is contained pump which serves for decreasing or increasing the brake pressure. There is also a damping chamber which serves to dampen pressure fluctuations in the brake circuit. To modulate braking effect occurs through the inlet and outlet valves for hydraulic circuits each wheel.

The modulator consists of the following components: 1 - motor 2 - pump (2pc), 3 - hydraulic valve block, 4 - damping chambers (2pc), 5 - pressure sensor, 6 - control unit (ECU), 7 - coil valve (12pc), 8 - solenoid valve (12pc).

By contrast, overflow and the intake valves for actively increasing the pressure on the brakes of the individual wheels. Forms one whole together with the control unit. In the hydraulic brake circuit is disposed between the master cylinder and the brake cylinders al. This modulator is an actuator that receives and executes commands from the controller.

Communication with the surroundings takes place via the CAN bus. This bus is also used for serial diagnostics. Unit also receives analog signals from the wheel speed sensor and the brake pedal sensor. About the status of ABS system, the driver is informed via the ABS, EBD lamps which are located on the dashboard. Power unit is divided into three branches: the power supply of the electric motor and control unit, power supply solenoid valves and power supply which is activated through the switch box after ignition.

## 5 Electronic System of Vehicle DemoCar

The project DemoCar serves to demonstrate the work of students involved in automotive electronics. Further, as means for development of new methods assistance systems of the chassis and the development of modern communication means. It is a quad with an independent electric drive of each wheel. The vehicle is remote controlled 16-channel radio. Operated are the control drive systems, power steering, brakes, lights, power and central control system. Selected data telemetry is possible to visually monitor to display the radio.

## 6 Theoretical Design

In the draft of the brake system was used hydraulic unit of assistance system ABS / ASR / ESP. This module is controlled from the control unit. The control unit receives and processes commands from radios which are entered by the user. Further communicates with the other control unit. It also designed an emergency brake which is ensures emergency stop vehicle.



## 7 Application Software

Development of application software was carried out in CodeWarrior 10.4 It uses a real-time operating system MQX 4.0 which is characterized by simplicity and rapid deployment of developed applications. The structure of the application software is written in C programming language.

The entire run application software can be divided into six interdependent tasks. This is one primary (main task), which creates and runs the other.

Listing each tile:

- CAN\_0\_Rx\_task (CANcontrol)
- CAN\_0\_Tx\_task (CANcontrol)
- CAN\_1\_Rx\_task (CANabs)
- CAN\_1\_Tx\_task (CANabs)
- CHECK\_ABS.

After power supply ON occurs in the Main Task as first initialized CAN modules. In functions CAN\_Init\_0 and CAN\_Init\_1 are sets the required parameters buses, create a communication mailboxes, install the operating function interrupt to receive data from the CAN buses. In the last step activates the bus. Then comes the activation of tasks which are serving for receiving and sending data via the CAN bus. Each CAN module has its task to send and to receive data. Within these tasks are also dealing with functions for braking. The last task is activated CHECK\_ABS which is responsible for checking the status of ABS / ASR / ESP module. All these procedures are performed only once, at startup.

Now will be described function of task CAN\_0\_Rx\_task. It is the task for receive on the bus CANcontrol. Task runs in a cyclic running, in which they take data. For receiving data, the library functions for MQX that the received data stored in the variable and generates an event. To prevent overwriting data, the event data locks. Then checks the ID data if it is ID with the required data. If yes, there is a further data processing. The variable is then released and is waiting for new data. Specifically, this task can receive data transmitted from the transmitter via the central control unit, steering control unit and drive control unit. Data received from the transmitter are follows: a request to start the handbrake, the requirement to run forward or backward. The requirement to forward or reverse is evaluated braking algorithm as a condition for determining whether to apply the brakes. Data from the steering control unit only carry information about whether the module is fine or at her encountered an error. In case of failure of this module to perform an emergency stop. From the drive control unit are also receives information about its status and motor speeds. Again, when an error DCU performed an emergency stop. Speed data engines used as criteria for evaluating the intensity of braking.

Task CAN\_1\_Rx\_task receives on bus CANabs data from the ABS / ASR / ESP module. These are evaluated whether the module is communicating properly or there is a problem. This evaluation takes place in the task CHECK\_ABS. As this evaluation is described below.

The sending task CAN\_0\_Tx\_task bus CANcontrol sends a defined identifier information if the ABS / ASR / ESP module working correctly or is it a problem. This information is used by the drive control unit. This message is sent every second. This reporting format is standardized and it also use drive control unit and steering control unit.

Now will be described function task CHECK\_ABS. Task uses data that are received on a bus CANabs that sends ABS / ASR / ESP module. On this bus is the chosen one identifier on which the does not change message in any activity of module. Within the selected identifier is checked value of zero byte. After checking the value of the variable in which this value is stored reseted and control is run again. In possibly not imposing new value, which corresponds to the state in which the ABS / ASR / ESP module in fine, the bus CANcontrol sent to DCU information about this extraordinary situation. The drive control unit turn off the engines and brake control unit activates the emergency brake.

Sending data to the ABS / ASR / ESP module runs in task CAN\_1\_Tx\_task. In this task is carries braking algorithm. First is defined forms of required messages for starting the pump and opening and closing of solenoid valves. First, the function is called to pressurize the emergency brake. This function is called only if the first run. Re-calling is possible if emergency braking be held and the pressure in accumulator will not be sufficient to re emergency stop. Then, it is checked whether the condition for starting the parking brake. Starting the parking brake depends on two criteria. The vehicle must have a zero velocity, and the user must enter this requirement corresponding lever on the transmitter. Followed by the main braking loop. Carrying out this loop is again conditioned by two conditions. State of steering control unit and drive control unit must be fine. Otherwise, the mode is launched an emergency brake and vehicle is stopped. The braking algorithm is divided into five parts. These parts represent the intensity of braking. Conditions for achieving certain intensities indicate two parameters: vehicle speed and the lever position indicating the direction of movement of the vehicle on the transmitter. Layout braking effect is divided into 5 levels.

This intensity distribution braking is done because it provides smooth braking torque and reduce wear on brake discs and brake pads. For example, at low speed is not necessary to perform intensive braking but only lightly braking and at a speed approaching the maximum intensity braking high in the case of full setting lever backwards when it is assumed that the user needs necessarily stop, but at the same speed and small deflection lever backward, intensity is small and there is only a slowing down.

These intensities are realized by sequentially arranged data messages that are sent to ABS / ASR / ESP module. Because this procedure is exercised in diagnostic mode module, it is necessary before any braking sequence of messages to activate the diagnostic mode. This mode is active only for 5 seconds. If the unit is not in this diagnostic mode, the messages that are sent to it are not executed. Between each message occurs

security delays for sending the following. Removing these delays or reductions lead to unpredictable behavior ABS / ASR / ESP module. The module receives messages but is not able in such a short period of time to execute and perform them in random order.

After sending the message to activate the diagnostic mode, followed by the message to activate the pump, opening the intake valves (HSV) and closing the overflow valve (TCV). This operation takes in all of the braking intensity the same period. This is 80 ms. Followed by the message only to close the overflow valve. The pump is off and intake valves are open. The intensity of the braking torque is modulated using delay between commands. Delay times are given in Table 1.

**Table 1.** Delays

Intesity 1	Intesity 2	Intesity 3	Intesity 4	Intesity 5
5315 ms	5290 ms	5265 ms	5240 ms	5212 ms

Application software solves the following situations:

- 5 levels of intensity braking,
- Parking brake,
- Receiving from transmitter,
- Receiving of the state DCU and SCU
- Receiving a motor speed of DCU,
- Check the condition of the ABS unit
- Sending other units BCU status information,
- Pressuring of emergency brake.

## 8 References

1. BOSCH, R.: Bezpečnostní a komfortní systémy. Robert Bosch GmbH, 56 s., 1998. ISBN 80-902585-9-X.
2. DULANSKÝ, D.: Sestavení funkční koncepce a vývoj aplikačního software elektronického systému servořízení elektromobilu Democar. Ostrava, 2016, Diplomová práce. Vysoká škola báňská – Technická univerzita Ostrava. Vedoucí práce Ing. Petr Šimoník, Ph.D.
3. WOLF, O.: Sestavení funkční koncepce a vývoj aplikačního software elektronického systému pohonu 4x4 elektromobilu Democar. Ostrava, 2016, Diplomová práce. Vysoká škola báňská – Technická univerzita Ostrava. Vedoucí práce Ing. Petr Šimoník, Ph.D.

## 9 Acknowledgement

In the paper, there are the results of the project reg. no. SP2017/130 funded by the Student Grant Competition of VSB-Technical University of Ostrava. This research was supervised by Ing. Petr Simonik, Ph.D.

# Preparing a Four Wheel Electric Vehicle for an Autonomous Operation

Jan Dedek, Jiří Koziorek, and Jan Žídek

Department of Cybernetics and Biomedical Engineering, FEECS,  
VŠB – Technical University of Ostrava, 17. listopadu 15,  
708 33 Ostrava – Poruba, Czech Republic  
[jan.dedek@vsb.cz](mailto:jan.dedek@vsb.cz)

**Abstract.** This thesis deals with making four wheel small size electrical vehicle autonomous. Especially about stage called the 0 iteration, which focus on preparing platform to autonomous operation.

**Keywords:** Electromobility; Autonommous operation; Lidar; Camera; USS

## 1 Introduction

During last years electro mobility and autonomous driving systems became highly progressive. Companies like Tesla Motors or Google Inc. have been starting development autonomous cars. Their goal is to provide comfort and safe traveling without the need to have a driver. This idea will have a huge impact on the safety of long distance traveling and of course on the price of city transport. Autonomous systems have worked well on close systems like metros (underground trains) for decades. The only limitation which prevents using this old technology in daily city traffic is the lack of data about possible obstacles around vehicle. These obstacles can be people, animals and other vehicles. Limitations were not only sensors but mainly data processing in hard real time. In the last decade image processing and LIDAR data processing in real time have become possible thanks to huge progress in computing performance. This paper deals with one year work on Selvo DH-C2 small electrical vehicle, which was predetermined to be used in golf playground or in farmland. This vehicle had steering wheel, accelerator, mechanical brake, two seats and lots of cargo space. During work in this academic year it has lost majority of its parts to prepare this vehicle for autonomous operation.

## 2 Iteration 0 preparing the platform

In this section the work during the last six months which prepared platform for autonomous driving is shown. Project is divided to stages or better said iterations. Each iteration has its goal and after the end of the iteration guarantees fully functional vehicle. Goal of iteration zero is to prepare platform for true science work, make the vehicle steerable by electrical controls, set up sensors and computing systems. Because of lack of skilled workforce and long waiting time all of mechanical and electrical engineering work has to be done by postgraduates.

## 2.1 RFID access

Firstly the issues of lost keys had to be solved. Keys and its placement is shown in picture 1a. RFID reader and usage of university cards has been chosen as conceivable solution. PCB (printed circuit board) with STM microcontroller, signal buzzer and Bluetooth connection were developed and built into vehicle using 3D printed parts as shown in picture 1b. Because of the need for general access, a general card was added. Adding and removing another authorized card is possible only with this card. In future, Bluetooth connection will be used to maintain authorization.

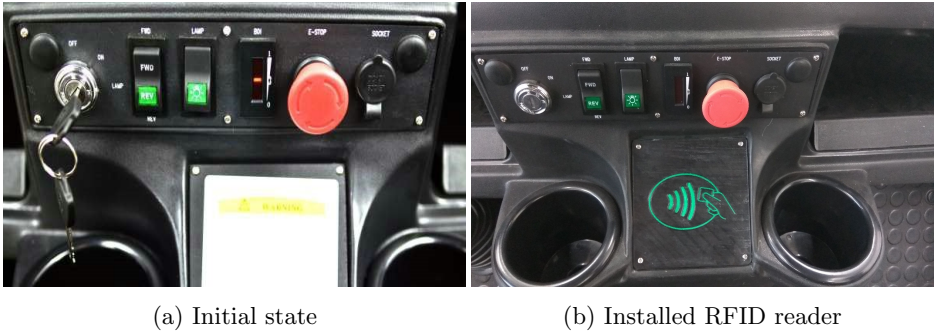


Fig. 1: Replacing of vehicle access system

## 2.2 LIDAR

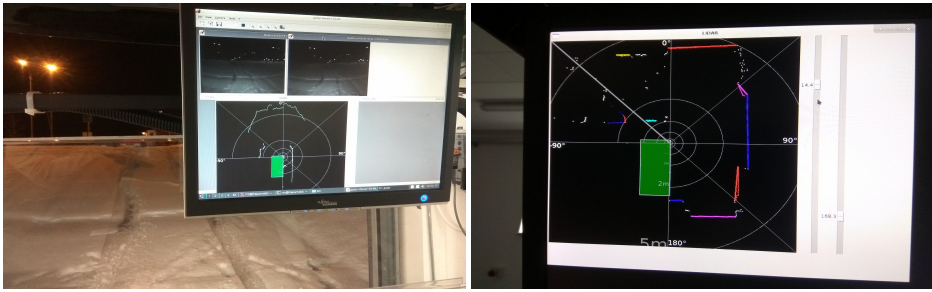
The next step in the plan was to mount LIDAR (light detection and ranging) sensor on platform to start the recognition of the world around the platform. With some experience with low cost LIDAR it has been decided to use some professional solution with supreme parameters. First LIDAR was bought from Sick Company. With operating angle of 270 degrees and effective scanning range of up to 50 meters it fulfilled expectation. To use the entirety of the scanning angle, Lidar was placed into front right corner of the vehicle (as shown on picture 2 ) to help driver to park and globally cover driver's blind points.

The biggest problem remains to be mounting LIDAR parallel to the ground in both axes. In first testing ride our LIDAR seemed to be mounted well but its little tilt caused that in range of 30 meters it detected ground instead of possible obstacles. For primary testing it is a decent result, but nowadays the whole holding mechanism of LIDAR is being developed from the scratch. Meanwhile an application for the visualization was finished so that it could be used for on board data representation. The first version of this application is shown on picture 3a the latest on picture 3b.

In future additional LIDARs are planned, one in the front left corner and one with smaller angle to the middle of the back of the vehicle. This topology has



Fig. 2: Placement of LIDAR on the vehicle



(a) First trial

(b) Last version

Fig. 3: Data output representation from LIDAR sensor

been chosen due to maximal coverage of the weak points, and also considering common movement pattern of the vehicle.

### 2.3 Computing resources

As mentioned before, an additional computing system is required to acquire, interpret and visualize data. Because of high data density, enormous volume and relatively high speed data transmission, high performance computer is needed. Also because of automotive environment, and confined space inside platform, small, resistant and well cooled system is required. Well-equipped ZOTAC ZBOX MI551 was chosen and filled with high tech computing parts. For example 16GB 1866MHz DDR3 RAM memory, or 512GB NVMe SSD disk. Computer and other devices are shown in picture 4a. Both of its 1Gb Ethernet slots were connected to 1Gb switch, connectivity was gain from USB3.0 to RJ45 Gb Ethernet connector also connected to switch. All this connectivity has been needed to use cameras, LIDAR, and other Ethernet using devices. Also Wi-Fi connection was established to provide actual telemetry data. Strong gain antennas are shown in picture 4b. Each of these devices have been powered from several power sources mounted also on board and partially switched from switch panel board shown in picture 4c.

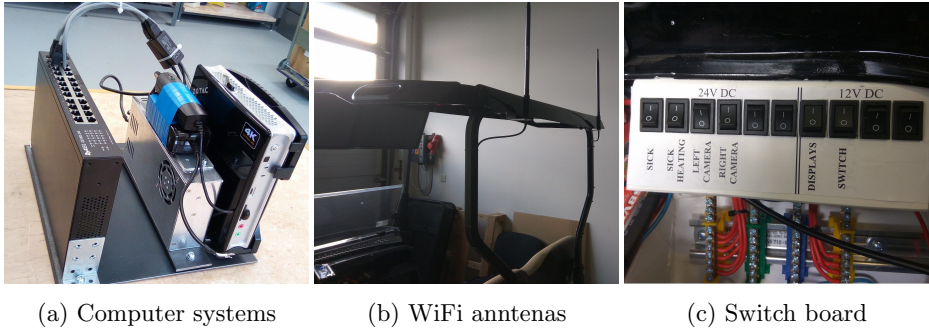


Fig. 4: Part of computing and powering systems

## 2.4 Cameras and displays

Main source of information is always image processing. For example, new Tesla cars depend only on image processing from multiple cameras around the entire vehicle. In this project camera is not only one kind of sensors but most of information for driving control will rely on image processing. First step in camera choosing was defining crucial parametres such as resolution, view angle, FPS (frames per second) rate, and because of automotive environment also International Protection Marking (IP code). External company recommended several configurations. A best resolution and small view angle configuration has been chosen. Basler camera, resolution 1920x1200px; Kowa objective with view angle of 83 degrees. All has been mounted onto IP53 case. Both of the cameras were connected to ethernet switch with 1Gb net lines and cameras were connected to local power lines. Placement of cameras will change a bit due to the processing algorithm needs. But centrally they are heading front and little down with concentric viewpoint for future stereovision needs. Layout of cameras is shown in picture 5a.

Displays were chosen to fit in to vehicle regarding both the possibility to drive normally or only with driver relying on preceeded data. Both of the displays were adjusted to be powered up with internal vehicle power source. Placement and new layout of HMI (human-machine interface) is shown in picture 5b.

## 2.5 Electromechanical remote control

Finally, when all sensors, data processor, tuned HMI, bundled wires, and tested several emergency states, the work can proceed to goal of Iteration 0: Manual driving only by using sensor data representation from displays. Nevertheless, work proceeded to Iteration 1, specifically replacement of original manual actuators such as steering wheel and pedals, to pure electrically actuated system.

The only electric input of vehicle has been the speed regulation. Work started with consideration and lot of calculation about torque and speeds. The decisions have been as follows: Instead of steering wheel the stepper motor with belt



(a) Placement of cameras



(b) Placement of displays

transmission is sufficient. Instead of brake pedal stepper motor linear gear is the best known solution for now. Last change was direct PWM (pulse width modulation) inverter control instead of accelerator pedal.

Unfortunately, because of incompetent employees of faculty, all that mechanical work had to be invented, developed, created and mounted by postgraduates. This slowed down scientific work and forced postgraduates to learn about mechanical issues, test prototype solution, find contract to fabricate parts and weld it together. Project team learned a lot, but for the price of a few months of their time.

Linear gear was bought and assembled together. The main problem was to fix it into a specific place in the platform and replace the the brake pedal with lever. This issue has been solved by bending plate, see picture 6a. Mechanical parts which hold high moment the lever were milled in CPIT by postgraduates of Faculty of Mechanical Engineering on high tech machine. Results are shown in picture 6b. Whole breaking mechanism is shown in picture 6c. Steering wheel was cut and cogwheel was fixed on the steering axis. Because of high torques, massive stepper motor housing was needed. First prototype was printed on 3D printer. Final parts were cut in water jet laboratory under supervision of professor Libor Hlavac and welded together by Jakub Kaminsky. Process of water cutting is in picture 6d, welding is in picture 6e and final placement is in picture 6f. PWM speed control was provided by RTOino, which is a clone of Arduino.

As interface for both stepper motors drivers recommended by manufacturer were chosen. As supervisor a PC can be used, but a decision was made to use STM development board because of its real-time approach to all possible situations. This STM board has ethernet connection, so in the future, it will send prefabricated data from image processing, and said ARM microcontroller will be executing these orders. As main the advantage of this approach is real-time response, security and mainly safety. This is due to the fact that a PC, even with RTOS (real time operation system), has significantly bigger chance to fail than microcontroller in embedded system. Considering consequence of potential fail in platform which can ride more than 30kmph and its weight is more than a ton, the circumspect approach is needed.



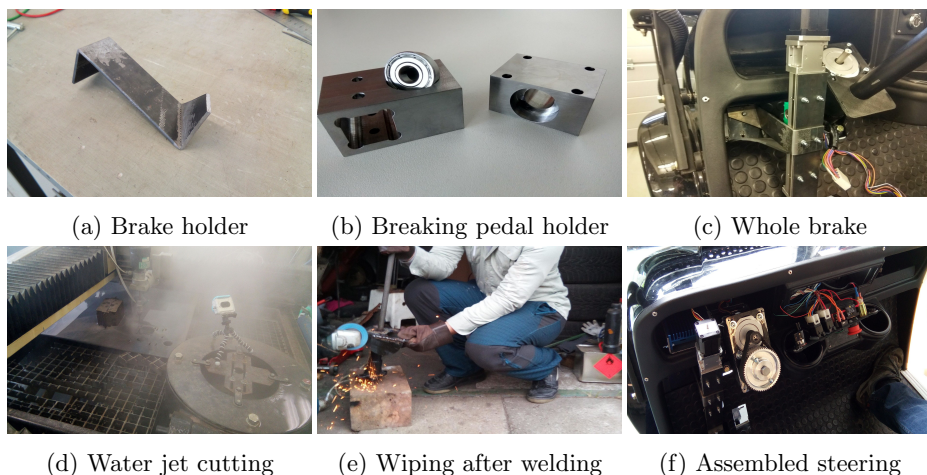


Fig. 6: Electromechanical parts for autonomous driving

### 3 Conclusion

As shown in picture 7 our team developed a remote control vehicle prepared for autonomous driving. At this point platform can be driven only by cellphone via Bluetooth connection. This approach is not the best because of connection instability, thus we are making wired connection for remote control. The work was started in the beginning of this academic year but technically we started working in 2/2017. At this point some background processes such as manufacturing professional PCB (printed circuit board), or making vehicle more representative are underway. In the next academic year we will continue working on this platform.



Fig. 7: Remote controlling of vehicle via cellphone by the operator

# Calculation of Trajectories for Simple Inverted Pendulum using PyTrajectory

Tomáš Dočekal

Department of Cybernetics and Biomedical Engineering, FEECS,  
VŠB – Technical University of Ostrava, 17. listopadu 15,  
708 33 Ostrava – Poruba, Czech Republic  
tomas.docekal@vsb.cz

**Abstract.** The article deals with control design for nonlinear underactuated system. The simple inverted pendulum was chosen as a case study for this process. The first part is focused on modeling of the inverted pendulum using state-space description with regard to usability in the real laboratory plant. The main part is concerned to solving optimal control problem. PyTrajectory library is presented as one of the tools usable for these purposes. It is based on boundary value problem method and the result is state trajectories and feed-forward control for transition between states.

**Keywords:** simple inverted pendulum; underactuated system; PyTrajectory

## 1 Introduction

Every day we are in contact with a number of systems, many of which are controlled by electronic device. Most of these (or probably all) are nonlinear. In some cases it is possible to not take into account the deviations from linear models, however a large number of systems do not allow that. In such cases, it is necessary to use more complex control methods. One of the groups that belong to nonlinear are underactuated systems. That means they are equipped with lower number of actuators than degrees of freedom. It is possible to find them not only in industry, e.g. robotic arms, but also in daily life, e.g. cars, boats or planes. One subgroup of the underactuated systems is balancing systems involving Segway, quadcopters and many other systems.

When people study, it is advisable to try new knowledge on practical example. Control of the simple inverted pendulum on the cart has been chosen as the first case study from underactuated systems for more reasons. First of all, it is a challenging and interesting task, also attractive for students and researchers. It is a very good example of feedback control system, combining classical algorithms (PID) and more advanced algorithms based on so called modern control theory [1, 2].

This paper shows clearly the concept of the mathematical model and control algorithm through inputs from two encoder signals (pendulum angle and cart position) and a PWM signal representing manipulated value brought to power electronic unit and DC motor.

## 2 Modeling and control of inverted pendulum on the cart

There are more approaches and equations describing a simple pendulum model. Physical laboratory plant can be adopted for identification in the form expressed by Fig. 1.

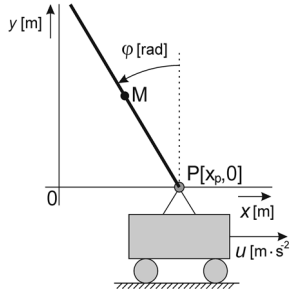


**Fig. 1.** Inverted pendulum scheme for analytical identification

It is possible to derive Eq. (1) for a pendulum movement

$$l \cdot \varphi'' - g \cdot \sin \varphi + b \cdot \varphi' - u \cdot \cos \varphi = 0 \quad (1)$$

where

$l$	(m)	pendulum length to the mass center  MP
$\varphi$	(rad)	pendulum angle
$g$	(m · s <sup>-2</sup> )	gravity acceleration
$b$	(m · s <sup>-1</sup> )	damping coefficient
$u$	(m · s <sup>-2</sup> )	cart acceleration

In order to get the full state-space description of the system, Eq. (1) can be extended by two state variables representing position and speed of the cart, supposing  $u$  as controlled input. The entire state-space description of inverted pendulum can be described by Eq. (2) - Eq. (5)

$$x'_1 = x_2 \quad (2)$$

$$x'_2 = \frac{g}{l} \cdot \sin \varphi + \frac{u}{l} \cdot \cos \varphi - b \cdot \varphi' \quad (3)$$

$$x'_3 = x_4 \quad (4)$$

$$x'_4 = u \quad (5)$$

where

$x_1$	(rad)	pendulum angle
$x_2$	(rad · s <sup>-1</sup> )	pendulum angular speed
$x_3$	(m)	cart position
$x_4$	(m · s <sup>-1</sup> )	cart speed

## 2.1 Closed loop speed control

This full state-space description contains variable  $u$ , which is acceleration of the cart. When using the real laboratory plant the output of control system is integrated to obtain speed setpoint value  $v$  as can be seen in Fig. 2.

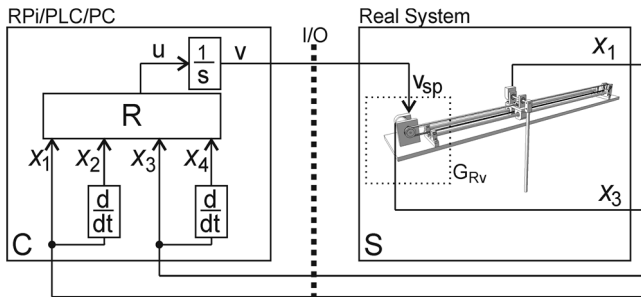


Fig. 2. Control of the real system of inverted pendulum on the cart

If the real speed of the cart (DC motor is connected with it) is the same as the setpoint value, the real acceleration will be also the same as value  $u$  calculated by control system. To achieve this goal it is necessary to design the speed control loop (shown in Fig. 3). This closed loop includes the dynamic of the DC motor and PID controller designed using modulus optimum method [3]. In the first phase of work, this part (DC motor and electronic unit for a speed control) was approximated by a fast 1<sup>st</sup> order system. It is possible to include this part into the state-space description of model for later trajectory calculating, the Eq. (3) and (5) will be changed and the variable  $u$  will represent the cart speed instead of acceleration, however these changes are not necessary if the  $\tau$  is small enough.

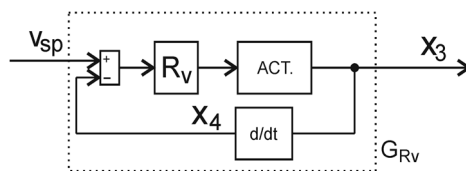


Fig. 3. Diagram of speed control loop

All three mentioned variants can be used for inverted pendulum simulations:

- without closed loop speed control (ideally transfer function is equal to one),
- with 1<sup>st</sup> order system simulating dynamics of speed loop,
- with complete closed loop system containing PID controller and DC motor transfer function.

The last option is closest to real laboratory plant because it captures not only the dynamics but also other features of controller, e.g. saturation of manipulated value.

## 2.2 Control system structure

On the side of control system it is required to track calculated states trajectories over time. Structure of control system is shown in Fig. 4, where the reference state trajectories are  $x^*(t)$ . The values of state variables may be also constant over time and then we are talking about setpoint tracking. Looking at the simple inverted pendulum, the trajectory tracking is swing up from lower stable position to unstable inverted position or in opposite direction swing down. Balancing in the inverted position is then setpoint tracking.

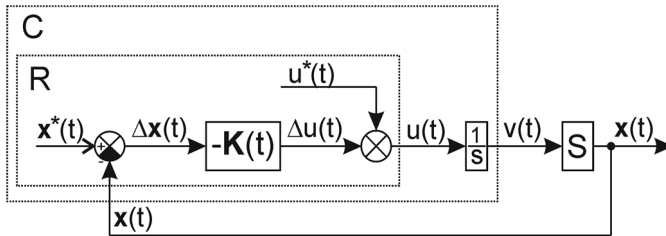


Fig. 4. General diagram of the control system structure

The value  $u(t)$  on the output of control system consists of two parts. The first one is calculated trajectory of this variable  $u^*(t)$  for open loop control. The second is based on deviation of real states of the system  $x(t)$  from reference state trajectories  $x^*(t)$ . The following part of the article is about calculation of states and open loop control variable trajectories. The method of controller  $K(t)$  computation is not the topic of this paper.

## 3 Trajectory calculation using PyTrajectory library

This library is made in Python. It is intended to be used for trajectory generation for nonlinear systems. That means determination of transition between two states with possible constraints for states. In general terms we are talking about solving optimal control problem. This is defined by cost function consisting of two parts, Mayer term penalizing starting and end points, and Lagrange term penalizing transition. The boundary value problem uses cost function with Mayer term only. The result is feed-forward control for entered nonlinear system. Solving a boundary value problem via a collocation method is the base of the library. PyTrajectory was developed at Dresden University of Technology [4].

The Python version 2.7 is needed for working with this library. There are also some dependencies on other libraries, which is necessary to install before PyTrajectory (shown in Table 1).

**Table 1.** PyTrajectory dependencies

NumPy	package for scientific computing with Python, working with N-dimensional array
SymPy	Python library for symbolic mathematics
SciPy	package for scientific computing with Python, numerical routines for numerical integration and optimization
Matplotlib	optional package for visualization
IPython	optional package for debugging

The easiest way how to install these packages is to use the pip module, which is a part of Python. If there is some problems (especially on the Windows operating systems), it is useful to download precompiled binaries from [5].

The first step when using this library is to enter the dynamic of the nonlinear system into the new python script which includes appropriate libraries.

```
def f(x,u):
    x1, x2, x3, x4 = x    # system variables
    u1, = u               # input variable
    l = 0.15              # length of the pendulum
    g = 9.81              # gravitational acceleration
    b=0.0225              # dumping coefficient
    ff = [ x2,
           g/l*sin(x1)-b/l*x2+1/l*u1*cos(x1),
           x4,
           u1]
    return ff
```

The next step is to specify boundary conditions, which mean start and end times, and states and variable  $u$  values in these times. It is possible to add some constraints of state variables too. After these settings the problem can be solved.

```
a = 0.0
xa = [pi, 0.0, 0.0, 0.0]
b = 2.0
xb = [0.0, 0.0, 0.0, 0.0]
ua = [0.0]
ub = [0.0]
con = { 2 : [-0.4, 0.35], 3 : [-0.8, 0.5]}
S = ControlSystem(f, a, b, xa, xb, ua, ub, constraints=con, kx=5, use_chains=False)
S.solve()
```

The result is trajectories between specified states for states and feed-forward control  $u$ , see Fig. 5.

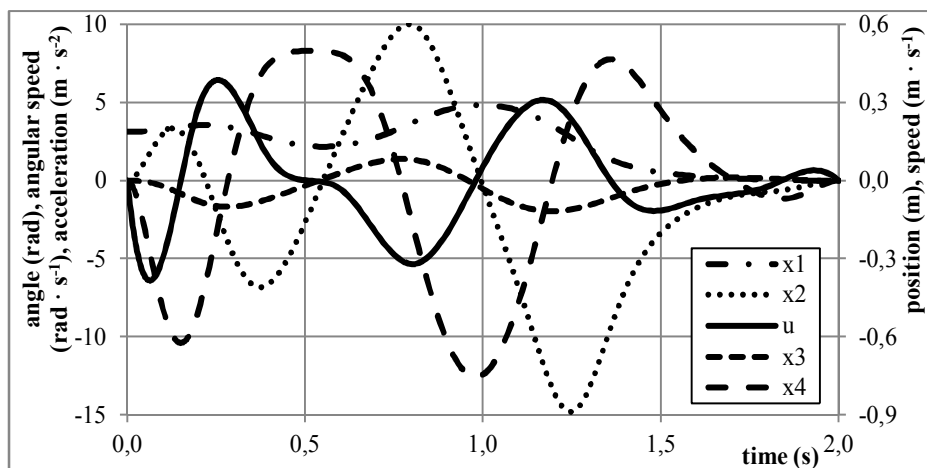


Fig. 5. Swing up states trajectories and feed-forward control

## 4 Conclusion

The first part of this paper is focused on state-space description of chosen case study simple inverted pendulum. The used description allows the application of the calculated control to the real laboratory plan using the closed loop speed control.

The next part was about PyTrajectory library. After installation, PyTrajectory is useful instrument to calculate trajectories and feed-forward control for nonlinear systems. It was used to obtain these for swing up of simple inverted pendulum.

Calculated trajectories was used for design controller  $K(t)$ . The result was tested in MIL simulation (Model In the Loop) realized in SIMULINK and SIL/PIL simulations (Software In the Loop, Processor In the Loop) [6] which are real-time simulations. They were designed using REX control system and running on Raspberry Pi platform. It was then possible to transfer these simulations into control system for real laboratory plant.

## References

1. Kirk, Donald E. *Optimal control theory: an introduction*. Courier Corporation, 2012.
2. Tripathi, Saurabh Mani. *Modern control systems: an introduction*. Jones & Bartlett Publishers, 2008.
3. Docekal, Tomas, and Stepan Ozana. "Advanced PID tuning based on the modulus optimum method for real systems." *AIP Conference Proceedings*. Vol. 1836. No. 1. AIP Publishing, 2017.
4. PyTrajectory's documentation, <https://pytrajectory.readthedocs.io/en/master/>
5. Unofficial Windows Binaries for Python. <http://www.lfd.uci.edu/~gohlke/pythonlibs/>
6. Ozana, Stepan, and Tomas Docekal. "The concept of virtual laboratory and PIL modeling with REX control system." *Process Control (PC), 2017 21st International Conference on*. IEEE, 2017.

# Multipurpose Sensor for Human Movement Analysis

Jan Foltyn

Department of Cybernetics and Biomedical Engineering, FEECS,  
VŠB – Technical University of Ostrava, 17. listopadu 15,  
708 33 Ostrava – Poruba, Czech Republic  
[jan.foltyn@vsb.cz](mailto:jan.foltyn@vsb.cz)

**Abstract.** Inertial sensors are nowadays commonly used in many applications including medical devices, consumer electronics, automotive etc. Thanks to this wide range of use, a development of micro electro mechanical sensors has significantly grown in past ten years. There are some devices on the market, designed for measurement of human body motion. Some of them can be used for research, allowing user to change settings of sensors or data transmission using their software development kits. But the aim of this project was to develop the data measurement unit and control every acquisition process inside, with possibility to extend the device in the future. Also, segments of this complex device can be used in other custom applications. Therefore, a multipurpose device for analysis of human body movement was developed.

**Keywords:** Inertial Measurement Unit, Bluetooth Low Energy, accelerometer, magnetometer, gyroscope, angular velocity sensor, barometer, Bluegiga, low power, STM32

## 1 Introduction

The use of inertial sensors in many applications grown significantly with the evolution of micro electro-mechanical sensors (MEMS). Evolution of wireless technologies in industrial, scientific and medical bands helped to a development of wireless battery powered inertial sensors. In medical systems, these sensors can be used for human (muscle) activity observation, or fall detection [1]. In digital imaging and image acquisition, inertial sensors are used in optical stabilizers. In automotive industry, they are useful to estimate the location with no presence of GPS signals. In mobile devices MEMS sensors allows control via gestures and checking the device orientation. They are also used to record body movement to create 3D models on PC, so inertial sensors are widely used. There are some companies, producing inertial sensors for medical application like Inertia, Cometa, STT, X-IO or XSENS. Comparing their products, it was found, that bit resolutions and ranges of researched devices are mostly the same, as they match the requirements of inertial measurement units (IMU) for medical applications. But their wireless technology, sampling rates and therefore a power consumption differs [2-6].



Some of the solutions available on market provides software development kits, so the user can program his own algorithms on a PC. But access to the embedded code is always forbidden as it is company know how, so when the control of data acquisition and data processing is required in the embedded system, there is no other choice but develop custom hardware and embedded software.

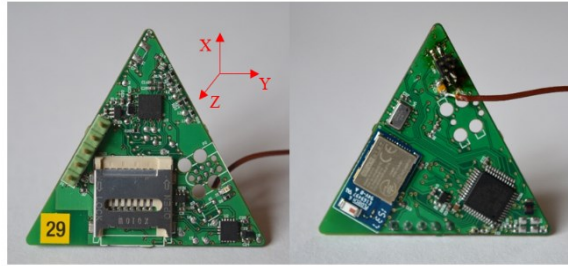


**Fig. 1.** Assembled prototype of inertial measurement unit

## 2 Device overview

This new measurement unit consists of one ultra-low power accelerometer ADXL362, barometric sensor MS5611 and ST-Microelectronics inertial sensor LSM9DS0 containing accelerometer, magnetometer and gyroscope. An input for temperature sensor is also implemented for possible extension in the future. Whole unit is controlled with STM32L0 family low power microcontroller unit (MCU) and the data output can be transmitted to a remote PC or mobile device via Bluetooth Low Energy, using Bluegiga BLE113 module. SD card slot for long term measurement is also implemented on board.

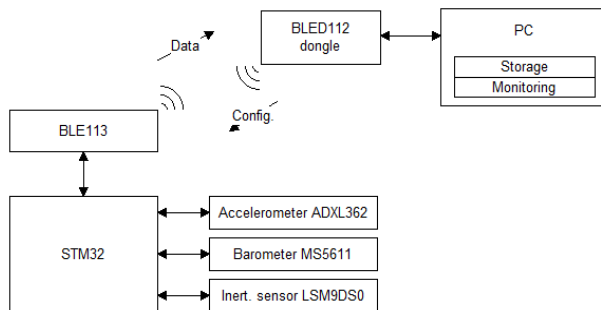


**Fig. 2.** Schematic of whole measurement system

Communication between sensors and microcontroller is established via SPI bus and BLE113 uses communication via 2 wire UART. The sensors are configured with a setting, selected by user in PC software. The configuration is sent to microcontroller via

Bluetooth LE. Temporarily unused sensors are turned off to save energy. Activ'Platform is small device using CR2032 lithium battery as a power supply. That's why the hardware for this device was developed with respect to low power consumption. Measured data are collected from chosen sensors and stored in packets, which are continuously transmitted via Bluetooth. To skip the hardware requirements of PC, a Bluegiga BLED112 dongle was used as Bluetooth master. The dongle is connected to computers USB port and communicates through the virtual COM port. PC application for Windows is controlling the dongle communication, storage of data to user folder and shows measured values on real-time monitor.

3 Wireless communication

Bluetooth Low Energy (BLE) is a wireless technology using Industrial Scientific and Medical frequency band (ISM). Generally, Bluetooth Smart is a technology, containing Bluetooth Classic and Low Energy (LE) and it depends on the end product, if both technologies are applied. Bluegiga BLE113 is a single mode device and contains just a LE part. BLE is achieving low power consumption at the expense of data throughput. Even if this technology is not primarily developed to achieve high speed of transmission, transmitting data with sampling frequency of several hundred hertz to make a real-time monitor, gives a good feature to this technology, even at the expense of the low power feature. The maximal speed that can be achieved using BLE113 module is approximately 60kbps, with maximal connection period 7.5ms [7, 8].

Bluetooth LE is using general attribute protocol (GATT) as a buffer of data to be sent via BLE. In our application, it should contain service and characteristics for each sensor. Unfortunately, to write 9 characteristics into a GATT database via UART API commands takes too much time and it's impossible to achieve high data rate that way. Therefore, a custom communication protocol was made, using just 3 GATT characteristics, allowing us to achieve highest possible throughput with BLE113 module. Three commands with total 56 bytes of data are sent to the module in every connection interval, when the protocol is sending the maximum payload.

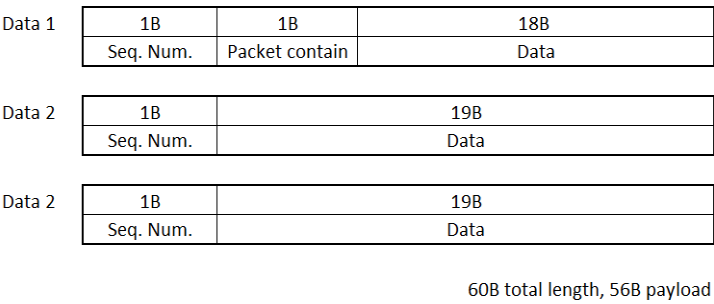


Fig. 3. Communication protocol

Communication protocol uses three characteristics with 20 octets. Packet contain byte describes the data in payload. Each bit represents one sensor from which we are receiving the data. The sequence numbers are used to sort data after receiving and to check if no error occurred.

## 4 Embedded software

First version of embedded software was developed to test the BLE performance, because distributor's documentation about performance of BLE113 module wasn't too satisfying. After testing the communication on experimental data, it was found that the maximum BLE data rate of BLE113 module, with no error, is 60kbps. That is not high, compared to other (not low power) technologies, but enough, to make a monitor of human body inertial data with relatively cheap BLE single mode device.

After testing the performance, a custom driver for each sensor was developed. C drivers includes configuration functions and functions for reading data from the sensor. Drivers were developed with respect to low power operation, but also possibility of high data rates. Each sensor is configured from the data, received from pc and after works independently on the STM32 MCU. Sensors are collecting data in their internal FIFO memories, and after they reach the set point, they generates the interrupt and transmit their FIFOs into MCU. MCU firmware sorts the data and stores them in circular buffers. The data are read from the circular buffers in each connection interval. Amount of read data is dependent on sensor's sampling frequency. There are some limitations set in configuration PC software, so the amount of data cannot exceed the highest possible data rate.

## 5 PC software

For a wireless configuration, data monitoring and storage, the C# software was developed, using Microsoft Visual Studio 2013. This application works with BLED112 dongle (BLE113 module USB equivalent) connected to USB port on PC.

Application is switching between two forms (between two windows). One controls Bluetooth connection, configuration of hardware platform and data saving settings. Second form serves as a monitor to show measured data.

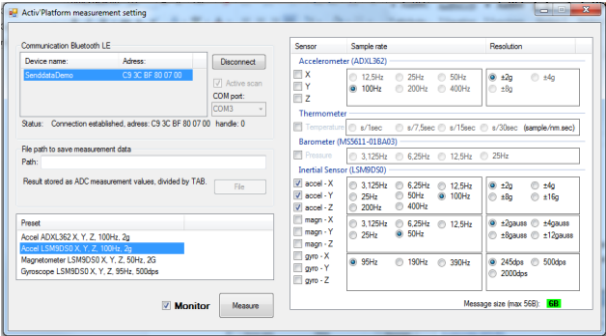


Fig. 4. Application GUI (connection and configuration of measurement unit)

First GUI, shown after start of the application, allows the user to connect desired BLE device and then set the measurement unit configuration or to choose one of the presets. After confirmation of settings, first GUI is hidden and Second GUI with real time monitor is started. Data are stored in .csv file or .txt file, split by tab character. This format is very suitable for Excel or Matlab import. Software contains also setting for offset calibration, which is stored in .xml file. The .xml file contains setting for single hardware platform. For multiple hardware platforms, user can create more setting files. Log file location can be changed in the setting GUI. If the file location setting is omitted, log file is created in the application's data directory.

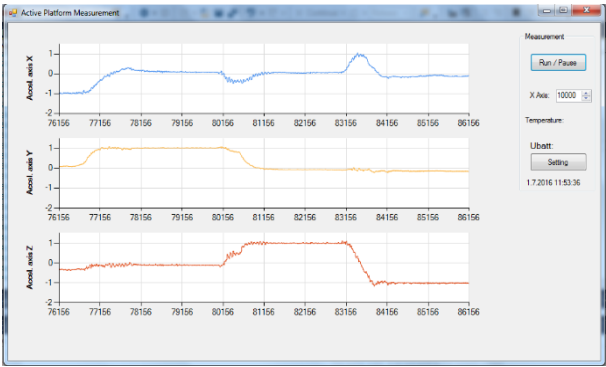


Fig. 5. Monitor with the acceleration data

## 6 Conclusion

Result of this project is a recently build hardware platform that can collect data from three hardware sensors and communicate with remote device via Bluetooth Low Energy. Measured physical variables are acceleration, angular velocity, magnetic induction, ambient temperature and atmospheric pressure. Maximal throughput of BLE module mentioned in this article was tested with experimental data. BLE throughput and

power can be reduced to achieve the best possible power consumption for its application. Device drivers were developed with respect to low power or high throughput, so the user has an opinion, which one to choose.

A significant part of the work was devoted to PC software, used to control and collect the data from wireless platform. Software stores the data to custom folder and displays the charts in real time. Therefore, it can be used in a future to monitor any biosignal and communicate via Bluetooth Low Energy. All the source code was developed using .NET4.5 framework, so the software can run on any computer with Win7 or higher.

A wide range of settings, applied in sensor drivers and PC software, can also offer a best possible compromise for the device application in the future, so parts of this complex device can be used in other custom inertial sensors. And finally, this device give us an availability to implement new algorithms right on the hardware platform and not just to use it as a conventional data streaming IMU.

## References

1. J. D. Bronzino, *The Biomedical Engineering Handbook*, Boca Raton: CRC/Taylor, 2006.
2. „X-IO Technologies, X-BIMU,“ [Online]. Available: <http://www.x-io.co.uk/products/x-bimu/>.
3. „X-IO Technologies, X-IMU,“ [Online]. Available: <http://www.x-io.co.uk/products/x-imu/>.
4. „stt systems,“ [Online]. Available: <http://www.stt-systems.com/products/inertial-motion-cap-ture/stt-ibs/>.
5. „Inertia Technology,“ [Online]. Available: <http://inertia-technology.com/promove-mini>.
6. „Cometa, WaveTrack,“ [Online]. Available: <http://www.cometasystems.com/products/wavetrack-inertial-system>.
7. H. Robin, *Bluetooth low energy, The Developer's Handbook*, Upper Saddle River, NJ: Prentice Hall, 2012.
8. J. Rowberg, „[HOW-TO]: Maximize throughput with BLE modules,“ 2012. [Online]. Available: <https://bluegiga.zendesk.com/entries/22400867--HOW-TO-Maximize-throughput-with-the-BLE112-BLED112>.

# Energy Savings in Buildings with Controlled Environments

Kateřina Gecová and David Vala

Department of Cybernetics and Biomedical Engineering, FEECS,  
VŠB – Technical University of Ostrava, 17. listopadu 15,  
708 33 Ostrava – Poruba, Czech Republic  
[katerina.gecova.st@vsb.cz](mailto:katerina.gecova.st@vsb.cz)

**Abstract.** The paper deals with the process of managing the internal environment of buildings and about ways of energy savings. The requirements for building parameters relate mainly to the quality of sealing of window and door openings. Although this method ensures less energy loss, it also restricts ventilation, which causes the burden of the human thermoregulatory system, fatigue and also reduced concentration ability. The stay of the persons in the room is characterized by increasing temperature and humidity of the air and also by the increasing concentration of carbon dioxide. Therefore, it is necessary to monitor and regulate these parameters in the internal environment to minimize heat loss while ensuring the most suitable conditions for the human organism. The realized sensor is integrated into the building, allowing for the measurement of parameters and their subsequent control according to the required values.

**Keywords:** building control, measurement, internal environment, energy saving, carbon dioxide.

## 1 Introduction

This work focuses on monitoring and environmental parameters management in modern buildings for reducing energy costs and providing the optimal temperature suitable for the human organism. In order to reduce the energy performance of buildings, doors and windows with better tightness are used there. However, the measure limits the ventilation of the indoor environment, which can lead to the formation of molds and hence the accumulation of dangerous substances in the atmosphere of the building. Insufficient ventilation also causes progressive deterioration of the quality of indoor air in the form of increasing temperature and humidity and also increasing concentration of carbon dioxide which produces a human during breathing. For this reason, insufficient ventilation has a negative impact not only on the building itself but also on human health.

For the air quality monitoring can be used a wide range of commercially accessible products, which also serves to obtain air quality data with individual air control systems in the building. One of the bus systems, which is now widely used, is the KNX bus.

This paper goes from the author's diploma work, the aim of which was the design of the sensor unit and the subsequent testing of the prototype. Individual sensors give

information about quality of the indoor environment. This system enables individual parameters to be controlled by the KNX bus to achieve optimal values.

The sensor unit has been designed to be able to provide a sufficiently accurate measurement. Commercially available devices meet these requirements, but their modular capability is relatively limited. The designed unit has a larger number of required sensors in one module, which is advantageous not only in financial terms but also simplifies the installation and management.

## **2 Impact of inner building environment on human**

Basic parameters that are most frequently measured and assessed in the inner premises were selected for this work. These are the following parameters: air temperature, relative humidity and pressure, carbon dioxide and carbon monoxide concentration, as well as dustiness.

The thermal comfort is important for thermal loading evaluation. Being in the state of thermal comfort, body temperature is in such balance with the ambient temperature that the thermoregulatory human system is not loaded. The most important is the endeavor to maintain a constant temperature of the body core on the value of 37 °C.

The value of air humidity in the inner premises is influenced by atmosphere outdoor humidity, the quantity of people, as well as different technological and other sources. Relative humidity in the room should get about 30 - 65 %, since the ideal values for a human body are the values in the range of 40 - 45 %.

Bioclimatology deals with the influence of weather on the human organism. Although the human is in some measure fit to the weather changes, more significant effects can cause, for example, headache, arthrodynia or myalgia for sensitive persons. At low air pressure, blood pressure rises, which could be dangerous for persons with blood circulation diseases.

Carbon dioxide is a usual part of air (fresh outdoor air contains about 400 ppm). CO<sub>2</sub> rises as a result of organic substances oxidation. CO<sub>2</sub> usually gets into the inner building environment as a product of human, animals and herbs breathing. It increases its concentration in case of insufficient ventilation. At concentrations above 1000 ppm, the ability to concentrate may decrease, over 2000 ppm may cause headaches, when the 5000 ppm is exceeded, the heart rate is accelerated and the 45000 ppm may cause unconsciousness or even death. The exhaled air is above 50000 ppm. A human is able to produce 13 to 77 liters of CO<sub>2</sub> per hour depending on exercised activity.

Carbon monoxide is colorless gas, tasteless and odorless, is not irritable and is lighter than air. The natural concentration in air moves between 50–230 µg/m<sup>3</sup>.

Dust particles are marked as PM (particulate matter); they are divided onto two fractions, PM<sub>2,5</sub> and PM<sub>10</sub>. From the point of view of their composition and size, this fraction threatens the human health more than PM<sub>10</sub>, the particles of which reach the size from 2.5 µm up to 10 µm. The most common problems and diseases caused by dust are respiratory problems, decreased lung function and lung cancer cardiovascular diseases.

### 3 Automation of buildings

KNX/EIB bus is the worldwide standardized communication system, which serves in the buildings as a network information connection of devices, such as sensors, actuators, metering devices, etc. Buses, which ensure a mutual interconnection of particular elements, as well as a digital transition of data, can be realized in a form of a Twisted Pair (TP), or with help of a power cable, an optic cable or via the remote radio connection.

Manufacturers focusing on KNX/EIB products offer a series of productions from sensors, through actuators up to the sources. The total quantity of KNX compatible devices of different brands reaches the number of several thousands. These are mainly power supplies, amplifiers, sensors, actuators and so on.

### 4 Development/design of sensors unit

To meter the required parameters of the inner environment, the following sensors were selected.

For temperature and relative humidity metering, there was selected a sensor SHT21 produced by Sensirion Company based on the capacitive principle of humidity measurement. BMP280 produced by Bosch Company is a sensor for measurement of absolute barometric pressure and its function is based on the piezo-resistive effect. A sensor Telaire T6713 was selected for measurement of CO<sub>2</sub> concentration in the atmosphere; its metering range is from 0 to 5000 ppm. The sensor works on the principle of the non-dispersion infrared spectrometry (NDIR). The sensor for carbon monoxide measurement TGS5042 has the metering range from 0 to 10000 ppm. The principle of its function is an electrochemical element that works as a battery. The optical dust sensor GP2Y1010AU0F produced by Sharp Company works on the basis of an infrared LED diode and a photo-transistor.

For the realization of all necessary settings and possibility of reading of the measured values, it was necessary to choose a certain communication medium. A microcontroller serves for these purposes, by means of which it is possible to set parameters of separate sensors according to the particular requirements of the module, as well as performance of collection of the measured data in the required format. Though, for now, in this state, there is no possibility to send data between sensors and the KNX bus itself. The mediator of this communication is the KNX chip NCN5120, which processes sending and receiving data by the bus. By this, the bus non-regulated voltage becomes the stabilized voltage, which afterwards serves both for the proper power supply and for power supply of extern devices, for example, a microprocessor.

The resulting module with sensor unit, microcontroller and KNX chip is shown in the figure below.



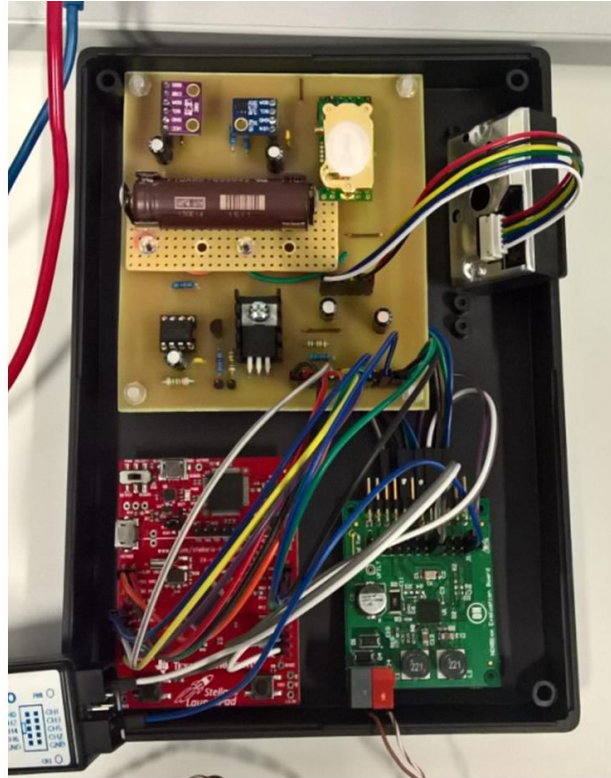


**Fig. 1:** Connected sensor unit

After user initiation of the module by means of its connection to the power supply, the initialization of the entire process will go on. The used peripherals are adjusted in this phase in the program, i.e. a permission of connection to particular pins of the microcontroller. At the same time, a record to the registers goes on for the digital sensors, which ensure the required setting of communication and data collection. Afterwards, the measurement of separate parameters is performed, the values of which are stored by means of a serial line into a corresponding file, and - most of all - are sent via NCN5120 chip on KNX bus. These results can be used for assessment of the inner building environment or for alarms.

## 5 Experimental metering

For demonstration of the changes of separate parameters of the environment depending on the conditions of the given room, several short-term and long-term measurements were performed. The mentioned activities were carried-out in one of the classrooms of VŠB-TU during learning.

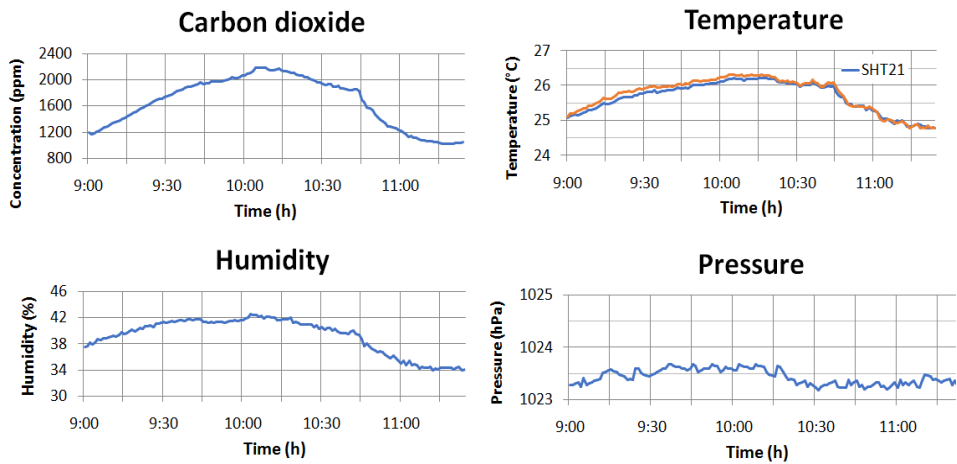


**Fig. 2:** Measurement of classroom environment parameters.

During the measurements, the concentration of carbon dioxide, the temperature and the humidity of the air increased due to the presence of persons in the room. By steady ventilation, the values were reduced accordingly.

To verify the accuracy of the solution, a hierarchy of physical and group addresses for individual sensors was created in ETS5. Furthermore, a gradual measurement of all the parameters that were entered into the ETS5 table in the appropriate order was commenced, as can be seen in the figure below. The first column represents the source address, the second individual address, and in the third one the names of the individual parameters, i.e. CO<sub>2</sub>, T1 and T2 temperatures, pressure, humidity, CO and dust.

Zdrojová adresa	Cílová adresa	Název cíle zdroje	Typ	DPT	Info
5.1.64	31/1/1	CO2	GroupValueWrite	9.008 parts/million (ppm)	3C 1E   1349,12 ppm
5.1.64	31/1/2	T1	GroupValueWrite	14.068 temperature (°C)	41 B9 33 33   23,15 °C
5.1.64	31/1/3	T2	GroupValueWrite	14.068 temperature (°C)	41 B7 D7 0A   22,98 °C
5.1.64	31/1/4	Tlak	GroupValueWrite	14.058 pressure (Pa)	44 80 10 F5   1024,53 Pa
5.1.64	31/1/5	Vlhkost	GroupValueWrite	5.004 percentage (0..255%)	\$22   34 %
5.1.64	31/1/6	CO	GroupValueWrite	9.008 parts/million (ppm)	01 40   3,2 ppm
5.1.64	31/1/7	Prach	GroupValueWrite	14.017 density (kg/m³)	36 6A E1 8A   3,5E-06 kg/m³
5.1.64	31/1/1	CO2	GroupValueWrite	9.008 parts/million (ppm)	3C 1D   1347,84 ppm
5.1.64	31/1/2	T1	GroupValueWrite	14.068 temperature (°C)	41 B9 47 AE   23,16 °C
5.1.64	31/1/3	T2	GroupValueWrite	14.068 temperature (°C)	41 B7 D7 0A   22,98 °C
5.1.64	31/1/4	Tlak	GroupValueWrite	14.058 pressure (Pa)	44 80 10 A3   1024,52 Pa
5.1.64	31/1/5	Vlhkost	GroupValueWrite	5.004 percentage (0..255%)	\$22   34 %
5.1.64	31/1/6	CO	GroupValueWrite	9.008 parts/million (ppm)	01 40   3,2 ppm
5.1.64	31/1/7	Prach	GroupValueWrite	14.017 density (kg/m³)	36 64 2B 8E   3,4E-06 kg/m³

**Fig. 3:** The result of the measurement in the ETS5

## 6 Conclusion

The realized module of the environment sensors was proposed as a universal unit for measurement of the monitored parameters in the inner building premises. Beside of that, the device also offers an additional connection of other sensors by means of both via remaining analogue inputs or via the I<sup>2</sup>C microcontroller interface. However, the scalability of the device can be also used in the opposite direction. These are the cases where it is not necessary to monitor the state of the environment here in detail. So, several from the already connected sensors were not be used. By this reason, the module is configured so that any from the sensors can be omitted and the device can be fitted for any individual requirements of the user.

Other differences from the commercial device are undoubtedly variability and setting of the limit values of the sensors. The sensors of the usual devices are usually set to certain boundary values of the given measured parameter, which remain practically constant. It can be, for example, a value of 1500 ppm for the carbon dioxide concentration, whereas an alarm is sent in case of this limit exceeding. The realized device is however able to change these values dynamically, evaluate data even during the course of the measurement and fit itself on the basis of these statistics to the given environment.

## 7 Acknowledgement

This paper has been elaborated in the framework of the project „Control of technological systems with renewable and alternate energy sources 2017“ SP2017/150 and „A practical training program for staff developing a low-carbon economy in the border region“ reg. no. CZ.11.3.1190.0/0.0/15\_005/0000048, supported by European Union in framework program INTERREG V-A Czech republic-Poland.

## 8 References

- Technika a způsoby měření parametrů vnitřního prostředí. In: TZB-info. Praha: Top-info, 2012. [vetrani.tzb-info.cz/vnitri-prostredi/9217-technika-a-zpusoby-mereni-parametru-vnitriho-prostredi](http://vetrani.tzb-info.cz/vnitri-prostredi/9217-technika-a-zpusoby-mereni-parametru-vnitriho-prostredi)
- Vliv změny klimatu na zdraví lidí, zvířat a rostlin. In: PUBLIC HEALTH [online]. Brusel 2009 Komise Evropských společenství [ec.europa.eu/health/ph\\_threats/climate/docs/com\\_2009-147\\_cs.pdf](http://ec.europa.eu/health/ph_threats/climate/docs/com_2009-147_cs.pdf)
- KNX/EIB – Celosvětově normalizovaný systém inteligentní instalace (2). VF SERVIS [online]. Teplice: 2011 - VFSERVIS, 2011 [cit. 2017-04-26]. [www.vfservis.cz/files/001947\\_eti\\_29.pdf](http://www.vfservis.cz/files/001947_eti_29.pdf)
- MERZ, Hermann, Thomas HANSEMANN a Christof HÜBNER. Automatizované systémy budov: sdělovací systémy KNX/EIB, LON a BACnet. Praha: Grada, 2008. Stavitel. ISBN 978-80-247-2367-9.

# A Novel Algorithm for Creation of Quaternions from Inertial Data

Radek Halfar

Department of Cybernetics and Biomedical Engineering, FEECS,  
VŠB – Technical University of Ostrava, 17. listopadu 15,  
708 33 Ostrava – Poruba, Czech Republic  
radek.halfar@vsb.cz

**Abstract.** The article describes a new method for creation of quaternions that can be used for motion processing from data recorded using inertial sensors that is placed on the body of patient. Description of motion in quaternions is advantageous in terms of numerical difficulty and motion description without singularity.

**Keywords:** Quaternions, Kalman Filter, Data fusion

## 1 Introduction

Classification of types of movements performed by the person is an important biomechanical analysis, such as physical activity in terms of type and quality of the motion for diagnostic purposes and for rehabilitation, guidance systems and fitness applications. Now the development of fitness applications, led to rapid developments in the field of sensors and algorithms [1]. To measure activity are used either alone accelerometer [2] or gyro sensors or inertial units [3], which are a combination of accelerometers, gyroscopes and magnetometers. These inertial sensors provide in most cases, information on the exercise movement, particularly its rotation expressed in quaternions [4].

For analysis of the kinds of physical activity of people are mainly used the signals provided by the accelerometers and the different approaches for analysing measured data [5-8].

## 2 Material and Methods

### 2.1 Quaternions

The term quaternion math is marked non-commutative extension of complex numbers in three-dimensional space. They were first described by Irish mathematician, physicist and astronomer Sir William Rowan Hamilton (1805-1865), who found a formula for multiplication of four basic units quaternion for which there is a relationship

$$i^2 = j^2 = k^2 = i \cdot j \cdot k = -1$$

Each rotation can be described as

$$(\varphi, \hat{u})$$

where  $\varphi$  is an angle of rotation and  $\hat{u}$  is the axis of rotation.

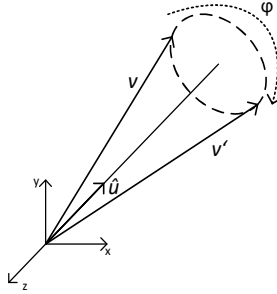


**Fig. 1.** Angle and axis of rotation

The rotation of the vector  $v = [v_x, v_y, v_z]$  around the axis of rotation  $u = [u_x, u_y, u_z]$  ( $u$  is an unit vector) by an angle  $\varphi$  is possible to do very gracefully using quaternion  $q$ .

If  $q$  is an unit quaternion ( $\|q\| = 1$ ), where:

$$q = \cos\left(\frac{\varphi}{2}\right) + i\left(u_x \sin\left(\frac{\varphi}{2}\right)\right) + j\left(u_y \sin\left(\frac{\varphi}{2}\right)\right) + k\left(u_z \sin\left(\frac{\varphi}{2}\right)\right)$$

Vector  $u$  is represented by pure quaternion  $p = [0, u] = [0 + iux + juy + kuz]$ .

The result – vector  $v'$  is afterward represented as pure quaternion calculated by the equation:

$$v' = qp\bar{q}$$

## 2.2 Creation of quaternion

Exist several ways of transforming inertial data to quaternion space. First of all is using kinetic equations. Kinetic equations show a very close relation between the time derivation of the orientation representing the quaternion and the angular velocity of the coordinate system B (body) to the coordinate system E (earth), measured by the gyroscope attached to the body.

Let  $q$  be quaternion, where  $q = [s, (x, y, z)]$  and  $\omega = (\omega_x, \omega_y, \omega_z)$  is vector of angular velocity, then quaternion derivation with respect to time is defined as:

$$\frac{dq(t)}{dt} = \frac{1}{2} \omega(t)q(t)$$

Using rules for quaternion multiplication we get following terms.

$$\frac{ds(t)}{dt} = -\frac{1}{2}(\omega_x(t)x(t) + \omega_y(t)y(t) + \omega_z(t)z(t))$$

$$\frac{dx(t)}{dt} = \frac{1}{2}(\omega_x(t)s(t) + \omega_y(t)z(t) - \omega_z(t)y(t))$$

$$\frac{dy(t)}{dt} = \frac{1}{2}(\omega_y(t)s(t) + \omega_z(t)x(t) - \omega_x(t)z(t))$$

$$\frac{dz(t)}{dt} = \frac{1}{2}(\omega_z(t)s(t) + \omega_x(t)y(t) - \omega_y(t)x(t))$$

Another way to create quaternion is to use data fusion (fusion of more data source which represent same information in order to achieve maximum accuracy). One of types of these algorithms are following:

- The complementary filter is very simple and numerically unpretentious.

- The Kalman filter is a mathematical apparatus for time domain filtering. The advantage of this filter is the ability to remove the noise from the signal without any knowledge of the interference.
- Madgwick's filter formulates the problem of data fusion of attitude calculate form gyroscope and from accelerometer and magnetometer as a minimization problem that solves using gradient techniques.

### 3 Main results

For creation of quaternions from inertial data was proposed a novel algorithm that combines a Kalman filter with approach proposed by Madgwick. The idea of the algorithm is that the data from Madgwick's algorithm is inserted as a measurement input into a nonlinear Kalman fitter, which then makes an estimate of the measured magnitude and thus improves the accuracy of the algorithm.

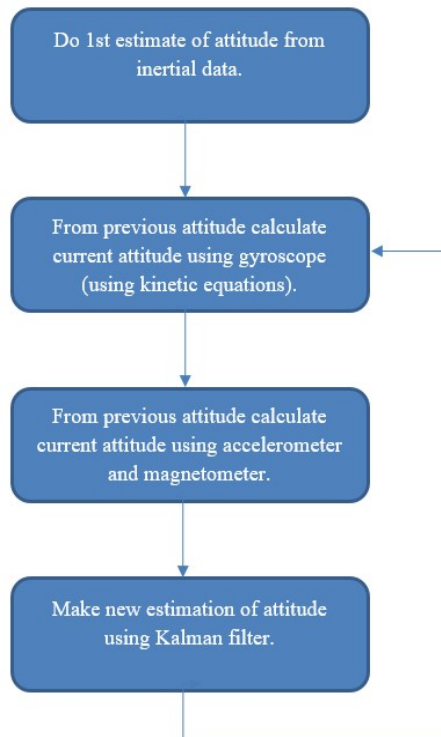


**Fig. 2.** Flow chart of proposed algorithm.

In the Fig. 3 and 4 can be seen, that proposed algorithm can due to data fusion remove noise, which is typical for inertial sensors (for gyro it is drift (see Fig. 4) and for accelerometer and magnetometer is white noise and distortion from linear acceleration and magnetic distortion (see Fig. 3)).

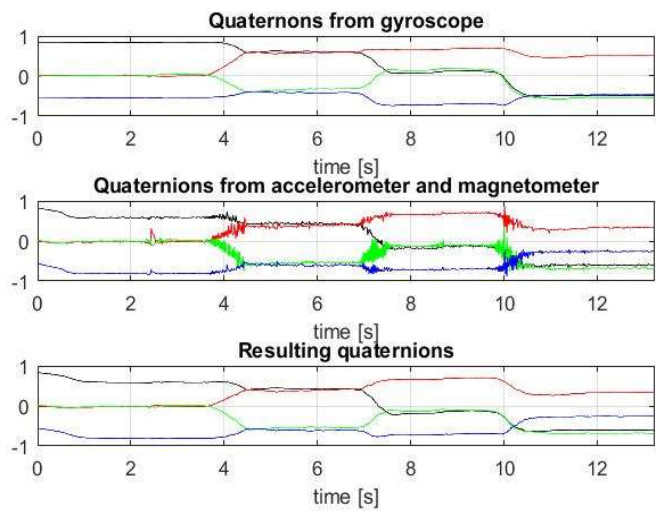


**Fig. 3.** Resulting quaternions ( $\phi$  (black),  $u_x$  (red),  $u_y$ (green)  $u_z$ (blue)) calculated from gyroscope, accelerometer and magnetometer, estimated from Kalman filter.

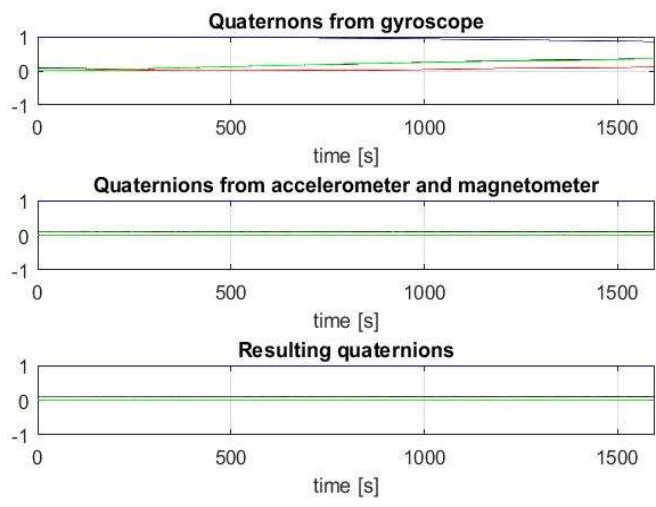


**Fig. 4.** Resulting quaternions ( $\phi$  (black),  $u_x$  (red),  $u_y$ (green)  $u_z$ (blue)) calculated from gyroscope, accelerometer and magnetometer, estimated from Kalman filter.



## 4 Conclusions

From the figures can be seen, that resulting algorithm reduce noise from inertial sensors and therefore can be used for biomechanical analysis do human motion.

## References

1. C.-C. Yang and Y.-L. Hsu, "A review of accelerometry-based wearable motion detectors for physical activity monitoring," *Sensors*, vol. 10, pp. 7772-7788, 2010.
2. W. Zijlstra and A. L. Hof. (2003) Assesment of spatio-temporal gait parameters from trunk accelerations during human walking. *Gait Posture*. 1-10.
3. C. Kirtley, *Clinical Gait Analysis: Theory and Practice*: Elsevier Health Sciences, 2006.
4. A. M. Sabatini, "Kalman-filter-based orientation determination using inertial/magnetic sensors: Observability analysis and performance evaluation," *Sensors*, vol. 11, pp. 9182-9206, 2011.
5. D. M. Karantonis, M. R. Narayanan, M. Mathie, N. H. Lovell, and B. G. Celler, "Implementation of a real-time human movement classifier using a triaxial accelerometer for ambulatory monitoring," *IEEE Transactions on Information Technology in Biomedicine*, vol. 10, pp. 156-167, 2006.
6. B. Najafi, K. Aminian, A. Paraschiv-Ionescu, F. Loew, C. J. Bula, and P. Robert, "Ambulatory system for human motion analysis using a kinematic sensor: monitoring of daily physical activity in the elderly," *IEEE Transactions on Biomedical Engineering*, vol. 50, pp. 711-723, 2003.
7. M. J. Mathie, A. C. Coster, N. H. Lovell, and B. G. Celler, "Accelerometry: providing an integrated, practical method for long-term, ambulatory monitoring of human movement," *Physiological measurement*, vol. 25, p. R1, 2004.
8. C. N. Scanaill, S. Carew, P. Barralon, N. Noury, D. Lyons, and G. M. Lyons, "A Review of Approaches to Mobility Telemonitoring of the Elderly in Their Living Environment," *Annals of Biomedical Engineering*, vol. 34, pp. 547-563, 2006.

# Fetal ECG Extraction from Abdominal ECG Using Adaptive and Non-adaptive Algorithms: An Overview

Radana Kahánková, Jan Židek, and Radek Martinek

Department of Cybernetics and Biomedical Engineering, FEECS,  
VŠB – Technical University of Ostrava, 17. listopadu 15,  
708 33 Ostrava – Poruba, Czech Republic  
radana.kahankova@vsb.cz

**Abstract.** The fetal ECG as a carrier of a huge amount of valuable information that, if extracted properly, could be helpful in increasing the quality of fetal monitoring. This paper aims to summarize the results of the scientific work of the student under the supervision of associate professors Jan Zidek and Radek Martinek. It was focused mainly on the fECG extraction from an abdominal ECG signal by means of the adaptive and non-adaptive algorithms.

## 1 Introduction

In today's clinical practice, ultrasound technology is widely used for fetal heart rate (fHR) monitoring since it is both simple to use and cheap. The conventional method, cardiotocography (CTG), measures both fetal heart rate (fHR) and uterine contractions. Since it is based on the principle of ultrasound, it carries potential problems of reliability, accuracy, can be influenced by fetal or maternal movement, and also insertion of the maternal heart rate (mHR) are recognized. Moreover, this method only produces an averaged fHR and cannot offer the monitoring of beat-to-beat variability. In addition, the effect of ultrasound on the fetus is not completely clear hence it is not recommended for long-term monitoring.

This paper focuses mainly on the processing of the signals associated with electrical activity of the fetal heart, which is described by the Fetal Electrocardiogram (fECG) and thus carries important information about physical state of the unborn child. Fetal ECG monitoring seems to be the most promising method to detect the fetal hypoxia at present. Although it was proposed several decades ago, it has not been fully utilized yet due to its limited ability to extract the fetal signal reliably.

The electrical potentials can be recorded by means of invasive or non-invasive methods. First mentioned is performed by using an Invasive Scalp Electrode (ISE). This method is considered to be accurate because the signal is recorded directly from the fetal scalp. Therefore it is often used in addition to conventional CTG to ensure highest possible accuracy. However its drawback is that it can be used only during the labor and its invasive nature endangers both mother and the fetus.

Noninvasive method of fECG measuring is performed using electrodes placed on the maternal abdomen. In contrast with CTG, the signals are measured with no need of exposing the fetus by any energy, thus it is much more suitable for a long-term ambulatory monitoring. Moreover, since it is non-invasive, it can be used not only during the labor but before it, too. Nevertheless, the desired signal (fECG) is weak compared to

the undesired signals produced by fetal and maternal body. Most of these signals (muscle and respiration activity, fetal movement, uterine activity, etc.) do not overlap in frequency domain significantly, therefore can be eliminated by using conventional filtering techniques [1 – 7].

However, the challenging task is the elimination of the maternal heart signal represented by Maternal Electrocardiogram (mECG). It overlaps with the fECG signal in time and in frequency domain as well and its amplitude is many times higher. In this work, author introduces some of the methods and the testing of some adaptive and non-adaptive systems for fECG extraction from composite abdominal signal.

The main task when using adaptive algorithms is setting their parameters properly. Currently, the parameters setting is simple, intuitive, and mostly based on the previous experience or the current output signal quality assessment. Authors therefore provide an example of a method for the optimization of filter parameters (filter length, forgetting factor, and Soft-constrained initialization factor) using a grid search.

## 2 Methods for fECG elicitation

There are many methods that have been used for extraction of the fECG in the past as illustrated in Fig. 1. They can be divided to two main groups – adaptive and non-adaptive. In the literature focused on fECG extraction, variety of the methods and their performance was tested with different degree of success. Based on the findings, author decided to test the most used algorithms herself.

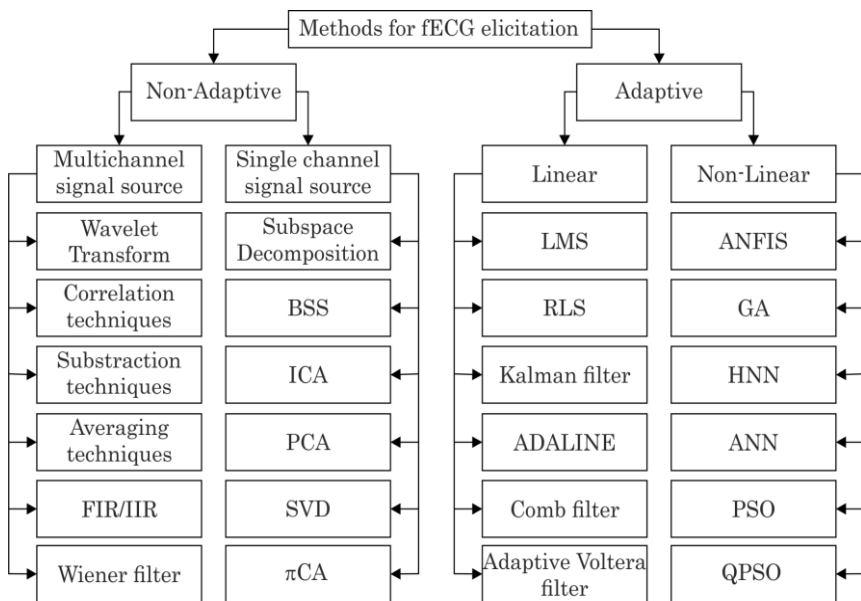


**Fig. 1.** Methods for fECG elicitation

Adaptive methods can be divided into two groups – linear and non-linear. Firstly, the adaptive algorithms were tested. In [1] – [7] authors designed and tested linear adaptive system using Recursive Least Squares (RLS) and Least Mean Squares (LMS) algorithms, namely standard RLS algorithm and its modified version – Fast Transversal filter (FTF), standard LMS algorithm and its modified versions – Normalized LMS (NLMS), Block LMS (BLMS) and Delay LMS (DLMS).

Non-linear adaptive techniques include artificial intelligence-based techniques such as Fuzzy inference systems. Authors tested the performance of Artificial Neuro-Fuzzy system (ANFIS) for fECG extraction, in [2] and [3]. The result showed that the non-linear systems improve the fECG extraction.

Beside adaptive methods, authors tested also non-adaptive ones, namely Independent component analysis (ICA) and Principal Component Analysis (PCA). These results are soon to be published in Advances in Electrical and Electronic Engineering (AEEE) journal.

### 3 Methodology

In this section, the methodology for most of the experiments provided by author will be described. Fig. 2 illustrates a theoretical multichannel adaptive noise cancellation system for fECG extraction. There are two kinds of the input signals recorded by multiple leads – primary and reference. Primary inputs consist of maternal and fetal components and are recorded by abdominal leads ( $AB_1$ - $AB_n$ ). Reference signals are considered to consist only of maternal component and are recorded by thoracic leads ( $TH_1$ - $TH_n$ ).

Adaptive algorithms (AA) produce approximated mECG signals considered as noise, and are subtracted from the primary input (aECG) signals so that the error signal  $e_1(k)$ - $e_n(k)$  that is back propagated to the training algorithm is the desired fECG signal (fECG<sub>1</sub>-fECG<sub>n</sub>) with some noise. Coefficients of the Finite Impulse Response (FIR) Filters are periodically updated by the training AA based on the back-propagated error signal [34].

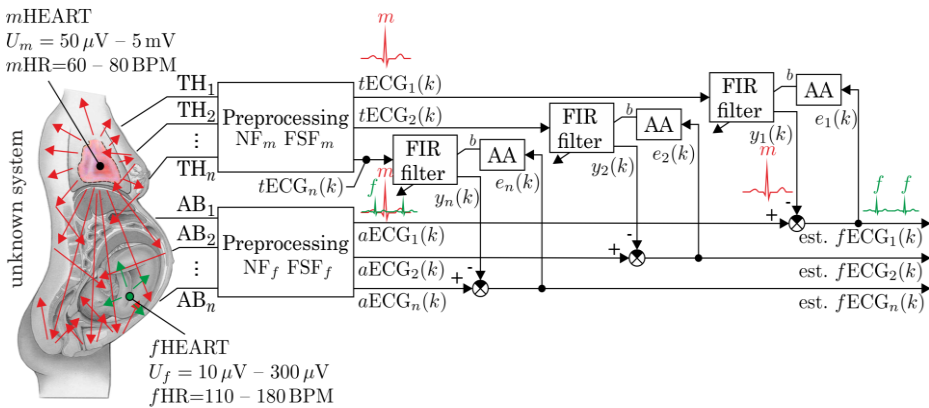


Fig. 2. Theoretical multichannel adaptive system for fECG extraction

## 4 Results and publications

In [1] and [2], the extraction of fECG from the composite ECG signal obtained from the abdominal lead was discussed. The main point of this paper was to introduce some of the most used Least Mean Squares (LMS) based Finite Impulse Response (FIR) Adaptive Filters and to determine which of them are the most effective under varying circumstances. Experimental results suggested the ideal combination of the chosen settings for these functions. Results of fECG extraction were assessed by Percentage Root-Mean-Square Difference (PRD), input and output Signal to Noise Ratios (SNRs), and Root Mean Square Error (RMSE). Based on simulation conclusions, optimal convergence constant value and filter order were empirically determined. Setting the optimal value of the convergence constant and filter order of adaptive algorithm can be considered a contribution to original results. These results can be used on real records fECG, where it is difficult to determine because of the missing reference. Based on [1] and [2], the chapter of the book was created (see [3]), where authors summarized the influence of the human body and concluded that the non-linear systems improve the fECG extraction. Figure 3 shows the results from [1]. The quality is evaluated by the parameter PRD, which should approach the zero value for reaching ideal extraction. The Standard LMS shows the best results in the case of LMS based methods, while the Standard RLS algorithm outperforms the RLS based methods. In addition, both of them are very stable and have relatively low computational time. By using the evaluation approach, the ideal filter length  $M$  setting may be suggested (ranging from 35 to 40 for the filters in fig. 3).

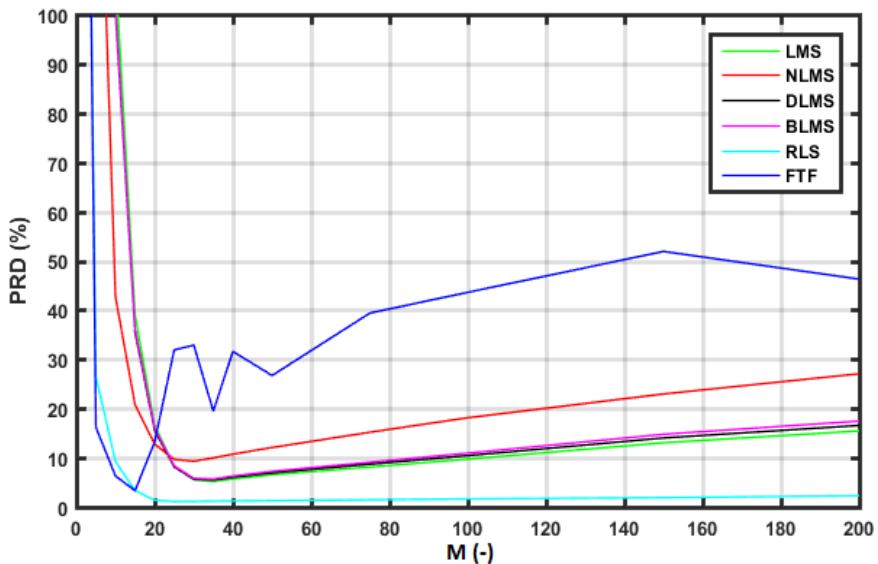
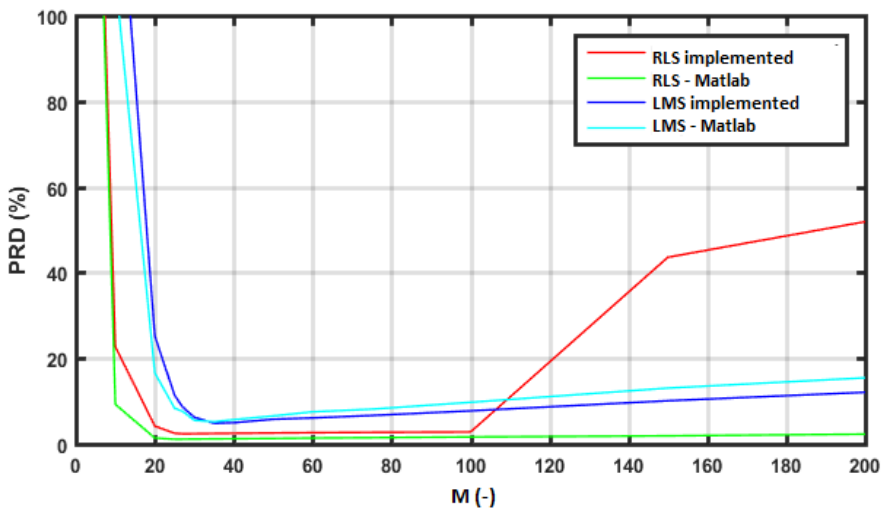


Fig. 3. Filtration quality of the tested LMS and RLS-based algorithms

In [4], authors introduced the most suitable representatives (according to the previous experiments published in [1] and [2]) from the Least Mean Squares (LMS) and Recursive Least Square (RLS) based Finite Impulse Response (FIR) Adaptive Filters. However, in this paper more suitable synthetic data were used. Moreover, authors designed and implemented the algorithms to achieve better results than when using the algorithms included in MATLAB® library (see comparison of the results in Fig. 3). Experimental results suggested the ideal combination of the chosen filters' settings (Step size, filter length, forgetting factor etc.). Results of fECG extraction were evaluated by the same objective parameters. This paper discusses the RLS-based filters as more accurate and therefore more suitable to use for this task.

Fig. 4 shows the influence of the filter length value on the filtration efficiency. Considering the ideal filtration with the value of PRD=0%, the implemented RLS algorithm shows the same results in the stable area ( $M \in (20, 100)$ ), while the implemented LMS algorithm slightly outperforms the MATLAB® LMS algorithm.



**Fig. 4.** Performance comparison of the filters included in the MATLAB® library and implemented by the authors.

In [5], the authors presented LMS-based algorithms for the optimization of the training symbols for the Minimum Mean Square Error (MSE) equalizer.

In ICCS conference in Sinai, Romania, the author presented her article Fetal ECG Extraction from Abdominal ECG Using RLS based Adaptive Algorithms. The paper was awarded as a Best PhD student paper of the conference and will be soon published.

## 5 Conclusion and future work

The author suggests further research in this field. There is a need to test other algorithms and more suitable synthetic data should be used. On the other hand, there is also need for the tests with real data. The problem is the lack of suitable real data available

for the public use. There is an existing cooperation between the authors and university hospital on creating a database of the real data that can be used for experiments.

When recording the data, a lot of factors decreasing the signal quality must be considered. Authors tested the influence of the electrode placement on the signal quality in [6]. Additionally, author tested the influence of the gestation age in article Influence of gestation age on the performance of adaptive systems for fetal ECG extraction, soon to be published in AEEE journal.

Author is currently focused on testing the proposed methods also in the field of fetal phonography (see [7]). The aim of the future work is developing a technique able to monitor vital functions of the child for early diagnose of fetal hypoxia leading to decrease of the unnecessary C-sections.

## 6 References

1. MARTINEK, Radek; KAHANKOVA, Radana; SKUTOVA, Hana; ZIDEK, Jan; KOZIOREK, Jiri. *Adaptive Signal Processing Techniques for Extracting Abdominal Fetal Electrocardiogram*. 10th International Symposium on Communication Systems, Networks and Digital Signal Processing, CSNDSP16, 20-22 July 2016, Prague, Czech Republic. (WoS, SCOPUS)
2. MARTINEK, Radek; SKUTOVA, Hana; KAHANKOVA, Radana; KOUDELKA, Petr; BILIK, Petr; KOZIOREK, Jiri. *Fetal ECG Extraction Based on Adaptive Neuro-Fuzzy Interference System*. 10th International Symposium on Communication Systems, Networks and Digital Signal Processing, CSNDSP16, 20-22 July 2016, Prague, Czech Republic. (WoS, SCOPUS)
3. MARTINEK, Radek; KAHANKOVA, Radana; SKUTOVA, Hana; KONECNY, Jaromir; BILIK, Petr; ZIDEK, Jan; NAZERAN, Homer. *Nonlinear Adaptive Signal Processing Improves the Diagnostic Quality of Transabdominal Fetal Electrocardiography*. Chapter in a book: *Advanced Biosignal Processing and Diagnostic Methods*, Austria, InTech, pp. 55-84, ISBN 978-953-51-2520-4, print ISBN 978-953-51-2519-8, DOI: 10.5772/64068.
4. KAHANKOVA, Radana; MARTINEK, Radek; BILIK, Petr. *Non-Invasive Fetal ECG Extraction from Maternal Abdominal ECG Using LMS and RLS Adaptive Algorithms*. Third International Afro-European Conference for Industrial Advancement November 21-23, 2016, Marrakesh, Morocco.
5. MARTINEK, Radek; RAZERA, George; KAHANKOVA, Radana; ZIDEK, Jan. *Optimization of the Training Symbols for Minimum Mean Square Error Equalizer*. Third International Afro-European Conference for Industrial Advancement November 21-23, 2016, Marrakesh, Morocco.
6. MARTINEK, Radek; KAHANKOVA, Radana; NAZERAN, Homer; KONECNY, Jaromir; JEZEWSKI, Janusz; JANKU, Petr; BILIK, Petr; ZIDEK, Jan; NEDOMA. *Non-Invasive Fetal Monitoring: A Maternal Surface ECG Electrode Placement-Based Novel Approach for Optimization of Adaptive Filter Control Parameters Using the LMS and RLS Algorithms*. *Sensors*, 2017, 17.5: 1154, DOI:10.3390/s17051154. (WoS, IF= 2,033, SCOPUS)
7. MARTINEK, Radek; NEDOMA, Jan; FAJKUS, Marcel; KAHANKOVA, Radana; KONECNY, Jaromir; JANKU, Petr; NAZERAN, Homer. *A Phonocardiographic-Based Fiber-Optic Sensor and Adaptive Filtering System for Noninvasive Continuous Fetal Heart Rate Monitoring*. *Sensors*, 2017, 17.4: 890, DOI:10.3390/s17040890. (WoS, IF= 2,033, SCOPUS)

# Using Electrical Energy from Electric Car Battery by Automotive Recharger Standards Connections

Martin Mikolajek, David Vala, and Bohumil Horák

Department of Cybernetics and Biomedical Engineering, FEECS,  
VŠB – Technical University of Ostrava, 17. listopadu 15,  
708 33 Ostrava – Poruba, Czech Republic  
`martin.mikolajek@vsb.cz`

**Abstract.** This paper contains information about using electric connection between electric car battery and other electric devices by standard charger socket. Article talks about types of battery charger sockets and includes information about practical test by CHAdeMO connector. The aims of this problematics is talking about own electric connection and mention physical and software layers for giving information about battery status. Own electronic systems of electric car monitors status of batteries therefore the connection by the automotive socket to battery is allowed if the car main unit communicate by connected station by definite correct communication. The last chapter of this topic talks about practical communication test for electrical connection by automotive electric socket.

**Keywords:** electric car, charger connection, CAN bus, PLC

## 1 Introduction

In recent years, the number of electric vehicles has increased for normal using in traffic. It should be noted that the electric car contains a huge battery and can be used for other uses. Not only like energy for moving the car. This situation occurs when the electric car is located on the spot without electricity. For example, using in some campsites or cooperation with electric batteries with electricity in family houses. [2] [3]

But there is a question. How we can connect to a battery? We are talking about a certified vehicle that contains a battery somewhere in the car. Normally is impossible to connect to battery directly. For the following reasons: The battery provides high voltages that can be dangerous to humans. Thinking about solution with direct connection to the battery will be possible only in cases person who have electricity knowledges and certification for work with high voltage. Second reason: The status of battery with must be monitored. Monitoring of battery ensures controller in electric car. In the case of a low voltage battery or cell, the next discharge will be stopped. If the battery has a problem, the battery is disconnected from the charging socket. Therefore, the best way to connect to a battery is to connect by using a normal car charger socket. But normally charging socket is without voltage. Because contactor of battery is disconnected. The electric contactor will be connected after the control units receive communication signal from the charger over charging socket. If we need connect to battery by standard charging socket. Connected device powered by car battery must be contain same communication like charging station. During the connection, it is important to send messages between the vehicle and the connected device or charging station. The aim of this



paper is to analyze the functioning of the communication and charging sequences and practical testing of how the battery contactor can be activated in an electric vehicle.

## 2 Type of socket high speed charging connection

These days, each electric vehicle has a type of charging standard. Can be used CHAdeMO, CCS or Tesla Supercharger for Tesla electric cars. Combo CCS socket allows DC and AC charging.



**Fig. 1.** CHAdeMO and CCS sockets chargers standards [4]

Each standard includes contact for own charging and controls and communications contacts. The research of this paper cover only CHAdeMO standard. This type of socket is more sophisticated because it contains controls contacts and CAN bus communication contacts. [4] [5]

## 3 Information about CHAdeMO connection

Charger socket CHAdeMO contains this contacts:

- Charge sequence signal 1 - start signal
- Charge sequence signal 2 - start signal
- Connector proximity detection - information about connected cable
- Vehicle charge permission - feedback from car
- Communication signal CAN H a CAN L

Detailed information can be obtained from the documentation „IEEE Standard Technical Specifications of a DC Quick Charger for Use with Electric Vehicles“. This documentation also contains information about starting connections sequences. In general, the initial sequence works as follows: After cable connect the cable signal is detected on proximity detection wire. Next steps are about activating Charge sequence signal 1, 2. After that electric car send information about battery status by CAN bus. Station connected by CHAdeMO standard receives message and confirms information and send message request for switching on contactor by specific CAN message. [1]

## 4 CAN analysis protocol communication for CHAdeMO socket

The communication protocol contains some basic information. Communication is provided by own messages. Connection protocol specified message from connected station and from electric car. Each message has a specific CAN address and contains some important information for the charging process. Each message with its own address contains information in 8 bytes. Message from car to battery charger station contain ID: 100,101,102 and from station to car ID 108,109. Own messages includes these informations.

Electric car to battery charger:

ID 100 - maximum voltage of battery  
 ID 101 - maximum time of charge, estimation time of charge, capacity of battery  
 ID 102 - number of chademo protocol, voltage, actual current, error messages, status messages, delivered energy

Battery charger to electric car:

ID 108 - socket identifikator, maximal provide voltage, maximal provide current, threshold voltage  
 ID 109 - number of chademo protocol, actual provided voltage, actual current, status and error messages, remaining charging time [1]

## 5 Analysis of communication protocol during charging electric car

The first step was the practical verification of the CAN communication protocol during charging an electric car. This test required an electric car with CHAdeMO and some methods for CAN bus listening. Electric car Nissan leaf was like choice for test. For CAN bus listening was used special CHAdeMO cable. CAN bus was listening by PC via USB - CAN adapter using. The CAN bus analysis window is shown in the next figure. Very important setting during the test was "Listening Mode" select. Because for this option communication adapter unaffected CAN communication between charger station and electric car. In the cases inactive "listening mode" receiving communication messages during charging are confirmed by USB- CAN interface. This using can of CAN adapter be dangerous for recharging process in case when the message not receive by car or recharge station, but confirm be only by USB-CAN adapter. [6]

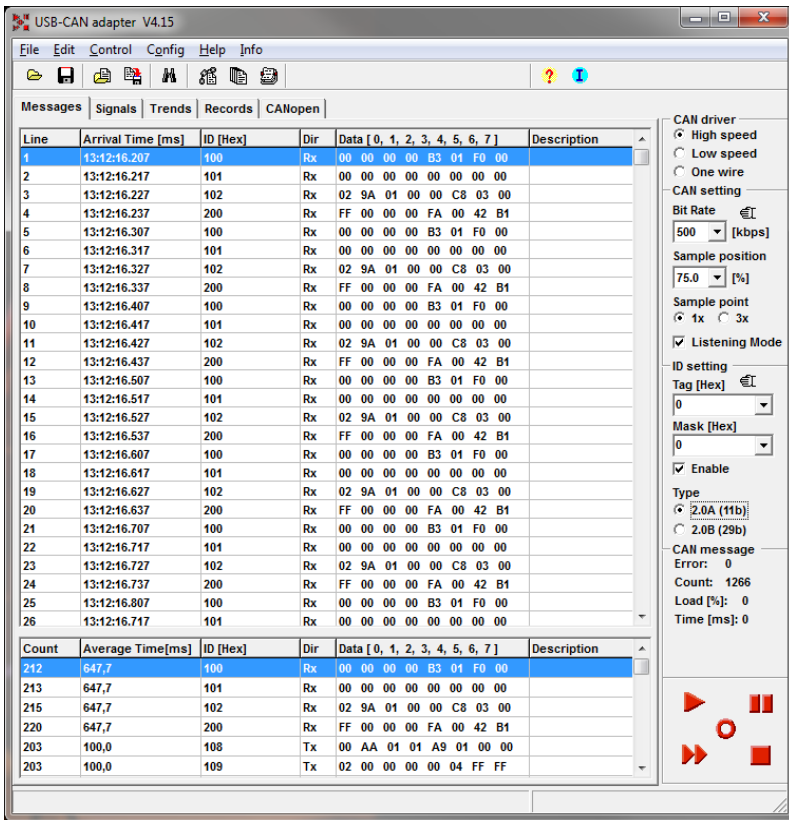
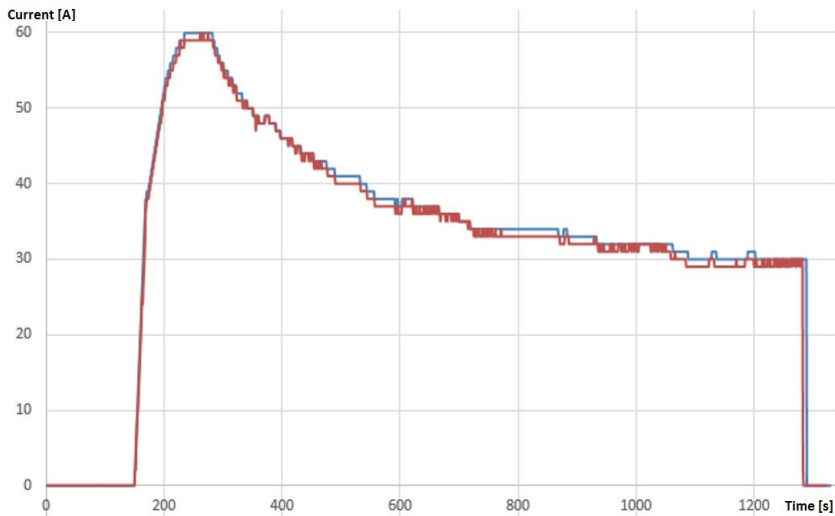


Fig. 2. Software USB - CAN adapter V4.15

Messages have been recorded to "csv" file. After that was started analysis for saved raw data. Each message was recognized by CHAdemo protocol. [1] After raw data decoding was possible gets information about the status of charging, voltage, current etc. For example was detected this: The charger station tests isolation status by gradual increasing voltage to 500 V. If this test access the charger station can starts with re-charging. Decoded data was verification by comparing current information messages from charger station and electric car. This information was includes in message with ID 102 and 109. Both current values was similar during the charging. The current flow during charging is shown on the next figure.



**Fig. 3.** Charge current graph by the communications CAN messages from charger station (red line) message ID 109 and electric car (blue line) message ID 102

## 6     Proposal prototype of discharging device by CHAdeMO standard

This part of paper in fact is talking about realization battery discharger station by own solution. This device must contains CHAdeMO socket with central unit for communication defined CAN bus protocol. The proposed device contains program logic controller with CAN interface. The PLC system send and receive information by CAN protocol. The proposed device also includes electrical parts for switching on and off the control signals in CHAdeMO socket like example charge sequence signal 1,2 and proximity detection.

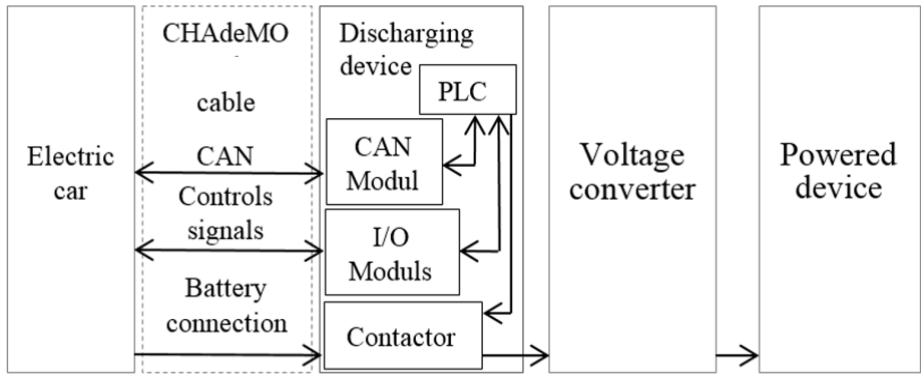


**Fig. 4.** Block schematic for prototype of discharging device by CHAdeMO standard

## 7 Conclusion

Practical tests with the CHAdeMO standard were aimed at comparing the communication message from the CAN bus during charging. For all test was used real certificated car Nissan Leaf. First test included raw data decoding and compare by the standard protocol. Discharging station was realize by PLC Teco, CAN communication module and input output modules. Station also contains contactors and relays and CHAdeMO recharging cable.

Program of PLC included communication messages witch specific ID by the standard protocol. During the test discharging device was possible set contactor in electric car. Important thing is compliance starting controls sequences by the CHAdeMO standard. After that was possible measure battery voltage on CHAdeMO socket. For keeping set electric contactor is important permanent communication by CAN bus. Communications messages from car must be confirmed by PLC with CAN communication modules. In this paper topic included provides basic information how we can connect to electric car battery by CHAdeMO standard. It is a plan for continue with this research. Especially research will be focused on discharging battery from electric car and measurements and reading battery status by CAN bus.

## References

1. 2030.1.1-2015 - IEEE Standard Technical Specifications of a DC Quick Charger for Use with Electric Vehicles
2. Friedrischkova, K., Vala, D. Energy-independent concept of a house using an electric vehicle traction (2016) IFAC-PapersOnLine, 49 (25), pp. 535-540.
3. Friedrischková, K., Vala, D., Horak, B. The use an Electric vehicle as a power source (2015) ICINCO 2015 - 12th International Conference on Informatics in Control, Automation and Robotics, Proceedings, 1, pp. 164-170.
4. CHAdeMO uznán jako evropský dobíjecí standard | Hybrid.cz. Hybrid.cz | Elektromobily, elektrokola, elektroskutry, auta na plyn CNG, LPG, testy [online]. [cit. 20.07.2017]. From: <http://www.hybrid.cz/chademo-uznan-jako-evropsky-dobijeci-standard>
5. What Are The Power Limits of Available DC Quick Charging Standards?. Inside EVs | Electric Vehicle News, Reviews, and Reports [online]. Copyright © 2017 [cit. 20.07.2017]. From: <http://insideevs.com/what-are-the-power-limits-of-available-dc-quick-charging-standards/>
6. USB-CAN adapter – TRIPLE drivers V4.2 (high/ low/ one wire) | IMFsoft, s.r.o.. IMFsoft, s.r.o. [online]. Copyright © 2006 [cit. 20.07.2017]. From: <https://imfsoft.com/en/category-can-bus/usb-can-adapter-triple-drivers-v4-2-high-low-one-wire>

# Automated Extraction of Blood Stream Volumetric Parameters

Tomáš Ondraczka

Department of Cybernetics and Biomedical Engineering, FEECS,  
VŠB – Technical University of Ostrava, 17. listopadu 15,  
708 33 Ostrava – Poruba, Czech Republic  
tomas.ondraczka@vsb.cz

**Abstract.** The paper deals with the design of the fully automated system which is intended for volumetric measurement in digital records acquired by digital subtraction angiography. The system is proposed, acquisition of two images, performs blood vessels segmentation with a target of volumetric parameters modelling and measurement. Individual blood vessels represent the area of interest, therefore, the software separates them from image background with using mathematical morphological operations and image thresholding. An output of blood vessel is consequently attenuated with a target of volume extraction. After volume calculation and extraction, the pixel to millimetres calibration is performed. The individual SW outputs can be utilised for blood vessels diagnostic information improvement and objectification of volumetric measurement from raw data.

**Keywords:** Image segmentation, image preprocessing, filtration, angiography, blood vessels, volume extraction

## 1 Introduction

The system realisation for implementation of new SW possibilities for diagnostic medical instruments is substantially important. It gives an improvement of current clinical possibilities which fundamentally simplify diagnosis. In the case of the digital subtraction angiography, the volume and flow measurement in the blood stream is significant improvement and necessity for modern diagnostic. Nowadays, implemented algorithms for this purpose are not sufficient, and they are not reliable from the view of the physician's requirements and needs. This application has ambitions to significantly simplify diagnosis in the context of an assessment of unblocking arteries, for example after stenting or for blood clot elimination.

One of the essential steps is blood vessels segmentation so that we obtain model reflecting geometrical and spatial blood vessels features. Before applying segmentation, the image preprocessing is necessary. Consequently, brightness pixel intensities are normalised. This paper deals with performing the image thresholding by the adaptive thresholding. This step presents the main contribution in the whole segmentation

context. The segmentation output is consequently modified by the morphological operations, so that was ensured imaging of the blood vessels system without adjacent structures which should be suppressed in the model.

The segmentation outputs are intended for consequent utilisation of blood flowing measurement. A user can manually specify a blood vessel part where volumetric parameter will be calculated.

## 2 Segmentation procedure

Preprocessed image is thresholded. In the principle, the thresholding algorithm goes through image matrix and compares pixel value with predetermined threshold value. The threshold is set by the adaptive method. The software adjusts a threshold on the base of the histogram. The adaptive algorithm utilises setting of variable thresholding values for variable image data. We use the adaptive thresholding on the base of the variable thresholding [1,2,8]. Image data are divided into different parts by the segmentation window [1,3,4,5]. The resulting image is segmented by more thresholding than only one. The thresholding procedure is described in the Fig. 3.



**Fig. 1.** Native CTA image (left) and thresholded image (right).

## 3 Morphological segmentation

The morphological erosion followed by dilation is used for elimination of smaller objects detected by the thresholding method. For this task, the methods of the mathematical morphology appear as good compromise. These methods work with images in the binary form, thus image input and output have binary form [1,3,6,7].

### 3.1 Morphological opening

The morphological opening is defined by the erosion followed the dilatation where these methods use the same structural element (mask shape is same). The opening is described by the equation (3) [1,9,10] where  $B$  denotes the input binary matrix,  $M$  is the dilatation mask (structural element),  $\ominus$  is erosion,  $\oplus$  is dilatation. The output of the morphological method is shown in the Fig. 4

$$B \circ M = (B \ominus M) \oplus M \quad (1)$$



**Fig. 2.** Native CTA image (left) and morphological segmentation (right).

## 4 Volumetric measurement

Measurement of volume in an image is performed in several steps. Firstly, structural thinning is performed, consequently volume calculation is performed, and finally, data are calibrated on the basis of the reference value to millilitres.

### 4.1 Thinning

The principle of the thinning method is repeating using erosion. It is permanent object decreasing in a condition that object structure is perceived. Thus, repeated erosion must be modified, so that we avoid object splitting [2,4,6].

In a middle pixel, line pixel creating the image, number of iterations is saved. In the practice, this method measures the distance from the pixel to pixel between object edge and middle pixel. Thus, in this case, blood vessel diameter is measured. This value is consequently utilised in the next step of volume calculation [2,4,6]. The thinning procedure is depicted in the Fig. 5.



**Fig. 3.** A binary model of a blood vessel (left) and thinning procedure (right).

### 4.2 Volume calculation

A volume is calculated from values saved in the image after performing thinning procedure. These values are scanned pixel after pixel from the input image, the volume of the truncated cone is calculated from them by the equation (4) where  $V$  is volume,  $h$  is height  $r_1$ ,  $r_2$  are diameters. The values are consequently saved into the first pixel, where



diameter value is rewritten to the volume. The second pixel is not changed so that the calculation would not be distorted.

$$V = \frac{\pi h}{3}(r_1^2 + r_1 r_2 + r_2^2) \quad (2)$$

The method works with the assumption that a blood vessel in a human body has a cylindrical shape, and in order to avoid distortion by various blood vessel deformation, the height of the truncated cone is given as one pixel. The reason why this method does not work with cylinder volume calculation is that the adjacent vessel diameters are not identical. The final volume of the whole blood stream is calculated by summing values in the input image.

### 4.3 Calibration

Value calibration on millimetres is performed by a reference value (etalon). This etalon is represented by circular shape in the image. Optionally, it is added a circular object with diameter 23 millimetres. The object is found by modified Hough transformation (Fig. 6.).



**Fig. 4.** Native CTA image with reference circular object (left) and segmentation result of the Hough transformation (right).

## 5 Area of interest

The area is specified by the user in the input image with applied contrast agent which is the output of digital subtraction angiography examination. A user marks the area of interest manually. In this area, the volume is calculated in pixels. A respective area is imagined which is marked by red, and blood vessels are automatically marked blue. The result is noted into the table (Fig. 7.).

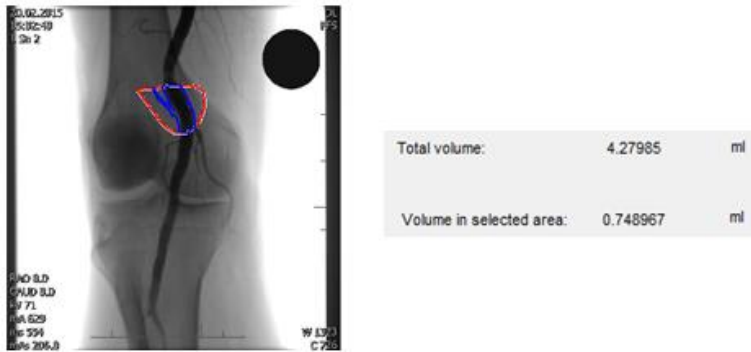


**Fig. 5.** The region of interest (RoI) specified by the user (left) and table of volumetric measurements (right).

## 6 Conclusion

An important clinical aspect of blood vessels examination is modelling and consequent extraction of volumetric blood parameters. We propose the SW method performing modelling blood vessels elements. This model is consequently utilised for extraction of the blood volume. We counted with the fact that the image data do not have to be acquired in the subtracted format, but we can just process native data and data with contrast agent. The segmentation process is relatively reliable, but in the cases of the tiny vessels having same intensities as image background, the segmentation method is not effective. The final output of the model is the volume extraction from the area of interest specified by the user. In the future time, we are going to focus on contrast agent flow in the blood vessels. This modification of our application is significantly important for selection of spots where the plaque is present on the blood vessels walls. By this procedure, it will be possible to measure volume before and after stent applying, thus we will be allowed for performing of stent effect objectification.

## 7 Reference

1. ONDRACZKA, T., Z. MACHACEK, J. KUBICEK, I. BRYJOVA, M. CERNY, J. KOZIOREK a V. PROCHAZKA. Automated image detection of the main bloodstream stem from CT angiography image. In: IFAC-PapersOnLine. 2016, 49(25), s. 109-114. DOI: 10.1016/j.ifacol.2016.12.019. ISSN 24058963.
2. Klepaczko, A., Szczypiński, P., Deistung, A., Reichenbach, J.R., Materka, A. *Simulation of MR angiography imaging for validation of cerebral arteries segmentation algorithms* (2016) Computer Methods and Programs in Biomedicine, 137, pp. 293-309.
3. Lesage, D., Angelini, E.D., Funka-Lea, G., Bloch, I. *Adaptive particle filtering for coronary artery segmentation from 3D CT angiograms* (2016) Computer Vision and Image Understanding, 151, pp. 29-46.
4. Samet, R., Yildirim, Z. *A new methodology for blood vessel segmentation on lung CT images* (2016) Proceedings - NICOGRAPH International 2016, NicoInt 2016, art. no. 7564036, pp. 1-7.

5. Moazzam Jawaid, M., Liatsis, P., Narejo, S. *Automated Extraction of the Coronary Tree by Integrating Localized Aorta-Based Intensity Distribution Statistics in Active Contour Segmentation* (2015) Proceedings - 2015 International Conference on Developments in eSystems Engineering, DeSE 2015, art. no. 7563618, pp. 83-87.
6. Tziomalos, K., Athyros, V.G., Karagiannis, A. *Vascular calcification, cardiovascular risk and microRNAs* (2016) Current Vascular Pharmacology, 14 (2), pp. 208-210.
7. Davis, B., Marin, D., Hurwitz, L.M., Ronald, J., Ellis, M.J., Ravindra, K.V., Collins, B.H., Kim, C.Y. *Application of a novel CT-based iliac artery calcification scoring system for predicting renal transplant outcomes* (2016) American Journal of Roentgenology, 206 (2), pp. 436-441.
8. Slaby,R.; Hercik R.; Machacek Z. *Compression methods for image processing implementation into the low capacity device*, In Technical Gazette, Volume 20, No.6, 2013, p. 1087-1090, ISSN 1330-3651.
9. B. Babusiak, M. Gala, “*Detection of Abnormalities in ECG*“. In Information Technologies in Biomedicine (ITIB 2012). Springer-Verlag Berlin Heidelberg, 2012. ISBN 978-3-642-31195-6, ISSN 0302-9743, p. 161-171.
10. Haska, J. , Pies, M., Machacek, Z. *Image signal processing, analysis and detection for robotic system*. International Conference on Control, Automation and Systems. 2014, Pages 1060-1063. ISSN: 15987833 ISBN: 978-899321506-9.

# Energy Harvesting from Human Movement

Radka Pavelková, David Vala, and Pavel Šuránek

Department of Cybernetics and Biomedical Engineering, FEECS,  
VŠB – Technical University of Ostrava, 17. listopadu 15,  
708 33 Ostrava – Poruba, Czech Republic  
[radka.pavelkova.st@vsb.cz](mailto:radka.pavelkova.st@vsb.cz)

**Abstract.** The article informs about the possibility of generating electrical energy from the human movement. Our body can power eg. mobile sensors for applications where the connection to the external sources is impossible. The observed energy comes from human walking when the bearer carries heavy objects on his back. A system includes the useful load, springs and other mainly electrical elements, which helps to get heavy load of backpack to resonance and thus an optimal yield of power generation. Energy is transformed and then stored in batteries of super capacitors and prepare for powering small electronic or mobile sensors. The work starts after motion analysis of human movement with the Motion Capture technology. It helps us to prepare electromechanical design of the generator and then experimentally verified efficiency. The experimental results were compared with simulations prepared in MATLAB and with results of other studies with the same topic.

**Keywords:** Key words: energy harvesting, measurement, backpack, motion capture, simulation, kinematics

## 1 Introduction

Most of the electrical equipment is powered by the energy from the fossil fuels or natural gas and coal, which transform the thermal power to electric energy. Nowadays requirements grow and it is necessary to use more ecological energy production of power and protect nonrenewable resources for the next generation. Also, is important to be independent from providers of these raw materials. This is the main reason to invent the devices with low energy consumption, which can be powered by renewable resources. Grow development of these devices, the technologies for getting small amount of the electric energy become more popular. These systems are profitably used in mainly in autonomic systems, where is the need to ensure a continual power supply source with help of batteries.

Among the traditional energy sources for autonomic systems are batteries, combustion micromotors, fuel microelements or radioactive sources. These sources also have disadvantages. To ensure their long-term operation, it is necessary to store and add fuel or replace batteries.

Energy can be "extracted" from a human body with the use of two methods: on the basis of movement and heat. This work summarizes in short the content of the diploma work focused to the human walking and the use of this periodic movement for electric energy generation.

Within this work, the human's respectively mass point's kinematics was studied, analyzed and was found as sufficient for electric energy generating with a possibility of powering certain mobile sensors with a low electric input. The „Motion Capture“ technology from XSens Company was used. The device works on the principle of sensors placed onto particular moving segments of the body, which read their position in time and calculate their speed and acceleration. This analysis contributes to the creation of the mathematic model in the MATLAB Simulink software that calculates with all variables incoming into the system. The generator was inserted into a touristic backpack. This generator copies body movements at walking, and the body transfers its kinetic / potential energy to it. The built-in part of the generator contains a series of mechanical components, which must be "adjusted" depending on the movement and load character. Consequently, the following parameters are monitored: needed spring forces, friction in the linear guidance of displacement of movement absorption, for example, by means of a proper rotary electric energy generator.

## 2 Analysis of human movements

As mentioned earlier in the first part, in the beginning we had to determine, how much kinematic energy will be transferred by the human body for the electric energy generation. At particular steps, the center of gravity of the human body copies the path with a typical shape of the circular contour sector. So, the center of gravity makes a movement in the vertical direction up and down, which corresponds with walking. Provided the mass of the backpack must execute a corresponding movement, the body has to hand-over the energy  $E$  to the load to cover the path  $\Delta y$ . The energy transfer from the body to the load can be calculated as an increment of the potential energy of the load in the change of the height  $\Delta y$ . The energy corresponding, for example, with the use of a load of 20kg, which was tested in the most of previous experiments with this matter, the walking speed of 1.7m/s at the acceleration of 5m/s and the angle of deflection from the balanced position at the step of 30°, the approximate vertical deflection of 5cm, is approximately 11J. To confirm these presumptions, the results of the measurement taken over from the Motion Capture software were used.

This knowledge served for dimensioning and selection of a suitable linear guidance and other components and parameters of the electronics of the system. Upon selection of the linear guidance and bearings, there were considered the weight of the load in the backpack, the distance between the linear guidance and the body, as well as the acceleration of the body system as a whole.

### 3 Simulation in MATLAB Simulink

During designing of the backpack system, the big role plays the force of the springs, absorption, friction, which rise as a result of the friction of the linear guidance and power take-off from the rotary generator. Also the weight of the backpack itself, respectively the load. It is necessary to consider these variables to reach the maximum electric power at the given frequency of the load movement along the linear guidance.

We could consider the general formula for calculation of the resonance frequency in case that no absorption of the system would occur. It occurs during this experiment, and that is by two ways. Firstly, due to the above mentioned friction of the bearings of the linear guidance, and secondly by taking-off of energy by the rotary generator. That is why there was made a mathematic mode, which also includes the following absorption coefficient  $b$ .

This mathematic model is described by the differential formula:

$$x'' = y'' - (b/m)x' + (b/m)y' - (k/m)x + (k/m)y$$

Where:

$m$  – load mass,

$x(t)$  – time flow of the load position,

$y(t)$  – time flow of the backpack mechanical structure position,

$b$  – absorption coefficient,

$k$  – springs force.

This differential formula was consequently re-written into the MATLAB Simulink environment and serves for setting of the backpack parameters, which will cause the resonance movement and calculation with the maximization of the generated power.

### 4 Backpack structure

The backpack itself is a mechanic system - the moving mass suspended on the spring system. The linear movement is converted via the transmission by a toothed belt to the rotary movement. The electromagnetic rotary generator generates electric energy during its movement. The proposal of the mechanics must be sophisticated to ensure achievement of the maximum effectiveness with a variable weight of the load in the backpack, and at the same time with the lightest structure to avoid loading of the carrier.

The key element of the system is the electronic circuits transforming the output from the generator to the useful voltage level. The circuits include a DC/DC converter with a non-inverted output with a possibility of the input current regulation. There is a profitably used feature that the input voltage can be higher and lower than the output one (it is influenced by the walking speed). The electric energy from the converter is accumulated by an ultra-capacitor. This energy is later used, for example, for the recharging of a battery or other electronic systems.

The electronic system maintains the voltage in the ultra-capacitor under the upper limit and consumes this excess energy, which cannot be more stored. Thanks to it, the circuit works in the automatic mode.



Fig. 4: The overall view to the electro-mechanic structure of the Energy backpack

## 5 Development and realization

For better imagination, an electro-mechanic system was modeled in 3D in the Autodesk Inventor software and afterwards experimentally assembled from the accessible material.

The aim was that the weight of the structure does not exceed 3 kg. This was achieved by choosing a suitable material and the cross-sections in the structure, thanks to which the weight of the system was significantly reduced. The mechanical components of the backpack are made of wood and aluminum.

## 6 System energy gain metering

The verification of the features and the energy gain of the system was carried out by several methods. The device was modeled by means of the Motion Capture technology, consequently there was created a model in Matlab Simulink serving for the spring systems adjustment. The assembled real model was observed with simulated results.

During its movement, the backpack copies the movements of the human body. The measurement be going on the electrohydraulic excitation system with the resonance frequency of 3Hz at the test load with the weight  $m=12\text{kg}$ , when the maximum energy gain of the system was achieved.)

This frequency couldn't be achieved by human walking, and it is clear that it will be necessary to correct the settings of springing and absorption of the system so that it corresponds with the ergonomic parameters of human walking.

## 7 Conclusion

The work proposed to create an experimental prototype of the backpack with the Energy Harvesting system, which should generate electric energy at walking that can be

used for powering mobile sensors. To enable designing of this device, I needed theoretical knowledge of the human movement kinematics, the Energy Harvesting technology, as well as possibilities of electric energy conversion.

Before work initiation, we explored already existing devices that use the movement of the human body to generate energy. As a suitable movement, human walking was selected, which is an enough big source for powering small electronics and mobile sensors.

With this knowledge, the human walking kinematics was analyzed by means of a mathematic simulation in the Simulink software and with help of the Motion Capture technology for observation of the human walking parameters by means of sensors, which monitor particular segments of the body. For this work, the shoulder movement data were used, which correspond with the movement of the human mass point and which are also copied by the backpack structure. The backpack uses the human kinetic energy, and thanks to it shifts the weight along the linear guidance with the amplitude of 6 - 7 cm and the acceleration of 10 - 12 m·s<sup>-2</sup> at the optimal laboratory conditions, and 4 cm and the acceleration up to 10 m·s<sup>-2</sup> during a real test at walking.

The backpack power is variable, as well as the human walking. That's why this experiment was measured on the hydraulic testing device, which is able to provide frequency and amplitude stability. An average power of the backpack 2,76 W was measured. The power of the backpack is limited by its structure, which has the bearing capacity up to 20 kg. During power metering, the backpack prototype of the backpack was created in the Inventor software, which preserves the weight less than 3 kg, but at the same time will have far higher bearing capacity about 40 kg. An adequate power increasing is expected.

## 8 Acknowledgement

This paper has been elaborated in the framework of the project „Control of technological systems with renewable and alternate energy sources 2017“ SP2017/150 and „A practical training program for staff developing a low-carbon economy in the border region“ reg. no. CZ.11.3.1190.0/0.0/15\_005/0000048, supported by European Union in framework program INTERREG V-A Czech republic-Poland.

## 9 References

1. Zboril, J. (2014) Alternativní zdroj napájení pro mobilní snímač polohy [online]. Ostrava, VSB-TUO Dostupné z: [https://dspace.vsb.cz/bitstream/handle/10084/104550/ZBO0011\\_FMMI\\_B3922\\_3902R040\\_2014.pdf?sequence=1](https://dspace.vsb.cz/bitstream/handle/10084/104550/ZBO0011_FMMI_B3922_3902R040_2014.pdf?sequence=1)
2. Mastny, P. and coll. (2011) Obnovitelné zdroje elektrické energie. ČVUT Praha, ISBN 978-80-01-04937-2
3. Kaminsky, J., Vrtek, M. (1998) Obnovitelné zdroje energie VŠB-TUO, ISBN 80-7078-445-8



# Mobile Applications Analyzing the Use of Central Operating Rooms

Tomáš Urbanczyk

Department of Cybernetics and Biomedical Engineering, FEECS,  
VŠB – Technical University of Ostrava, 17. listopadu 15,  
708 33 Ostrava – Poruba, Czech Republic  
tomas.urbanczyk@vsb.cz

**Abstract.** This paper focuses on the occupancy of the central operating rooms at the Faculty Hospital in Brno. The timeline of the operating room is formed and the individual delays between the defined phases are verified statistically. The timeline phase relative to one patient follows from the requirements of the sponsor and is listed in the article.

Recording is done using a mobile device with a mobile application for android platform. The application is simple, easy to read, and takes into account Cognition of work in the final record.

**Keywords:** Central operating rooms, Analysis, Time, Android

## 1 Introduction

Recently, large hospitals have moved to central operating theaters for operational efficiency. These are several operating theaters concentrated in the same premises, designed for most medical disciplines ranging from python to gynecology. Such a concept reduces the economic difficulty and logistics of the hospital's operational tract. Nonetheless, unwanted time delays occur in the operational plans. [1]

The hospital attempted to address this problem by various operational protocols, but the result was not satisfactory due to the introduction of a human factor error. The article is based on working with real-time locating systems (RTLS) [4]. The output of this system is the current location information about the entity. This system uses wireless technology (most often RFID) for data transfer. [3]

## 2 Problem definition

As mentioned, the central operating theaters are economically advantageous, but non-compliance with operational plans due to time gaps leads to economic losses. Hospitals therefore appeal to the management and smooth use of all operating theaters without unnecessary time delays.

The use of full deployment of the RTLS system is not possible here because the operating theaters are located in an open space, and the system implementation would be complicated and costly in this case. [4]

### 3 Implementation of new solution

Our solution is not concerned with the overall management and planning of the operational plan, but it looks for the potential risks of delay. An initial analysis was performed, which included the following requirements:

- The system must not burden personnel
- It must be simple to operate
- Capable of measuring seven defined time slots
- Justify unexpected events.

A mobile application mapping patient movement was created in the premises of the central operating theaters. Each hall will receive a mobile device with a mobile application that measures single phase time [5].

#### 3.1 Analysis and definition of concepts

Phase is an operation sale that is time-measurable. Seven phases emerged from the request.

1. **Arrival to the Hall** - This phase ends when the patient is transferred to the operating bed.
2. **Beginning of Anesthesia Preparation** - The patient takes an anaesthesiologist.
3. **End preparation of anesthesia** - The doctor has completed anesthesia.
4. **Start of operation** - Operator is present and operation commenced.
5. **End of operation** - The operator has completed the operation.
6. **End of anesthesia** - The doctor wakes the patient.
7. **Departure from the room** - The patient leaves the operating room

Timing of these phases is statistically evaluated. Application testing is performed on four operating theaters. Extreme latencies are searched for in individual phases and focal points are focussed. For extreme reasons, already known recurring events have been identified. The following were recorded:

- *Technical issue* - At any stage, a technical problem may arise that may cause delays in the operation plan.
- *Patient arrived late* - The patient did not arrive at the central operating theater according to the operational plan.
- *Hall cleaning* - Delay due to non-sterile environment
- *No material*
- *Opt-out* - Phase change, a push in a mobile application, is always done by a human, so it is also necessary to treat the application against human errors.

- *Operator is missing*
- *Other* - An event that is not predefined.

Not all events are available in all phases because their probability of occurrence is near zero. The event type identifies the cause of the delay and allows the user to write a note to each of them. [1]

## 4 Creating an application

The app was created in android studio 2.3.3 for platform android with API 19. Low api ensures seamless running of app I on mobile devices with older android versions. Application is simple and low on performance.

After installation, the user will dial the current operating room marked with a number. Then it enters an application where one button creates a new patient and measures the individual phases. [6]

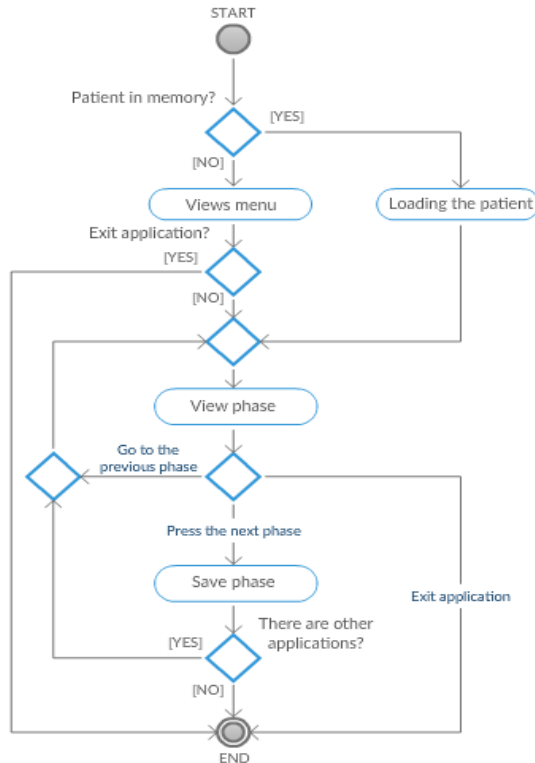


**Fig. 1.** Mobile application activity diagram from the user perspective. The diagram shows that each phase is stored in a file. The patient has a unique id and application is treated against the wearer.

#### 4.1 Graphic design

Application graphics are created in Photoshop. The application is dominated by a round button large enough for easy operation. A roll-down bar is created in the alliance that contains the icons of the individual events that may occur. The events are then plotted on the desktop with the ability to write a note that is created using a dialog window.

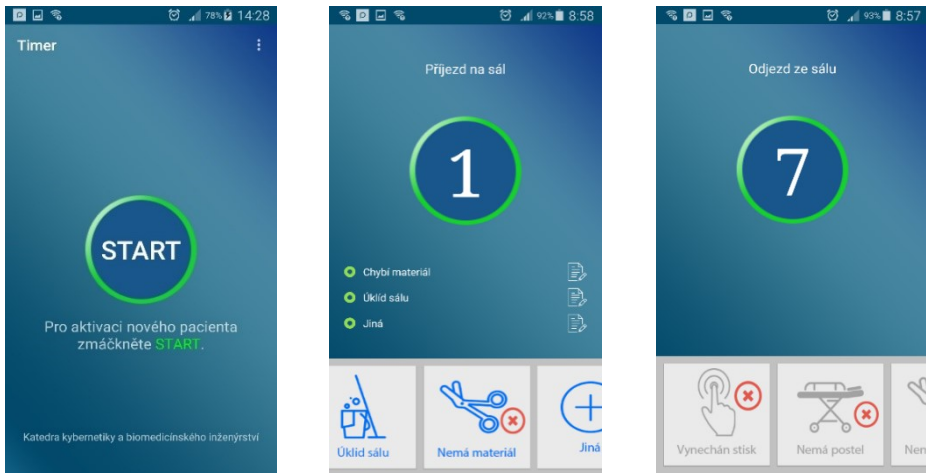


**Fig. 2.** The first image on the left is the menus. The start button creates a new patient. The middle image shows the first phase of the selected events. The selected events will appear in the ListViews options for making a note of a note. The user moves to stage seven until the patient clicks on the button and returns to the menu. Dial window.

### 5 Export data

Data is stored in internal memory in a CSF file called logFILE. Figure 1 shows that each phase is stored separately. Files are also stored in the file. Write the file as follows:

- Press:

ID\_S;TYPE;ID\_Z;ID\_F;TIME

(Hall number; press or event; unique procedure number; phase; time)

- Event:

ID\_S;TYPE;ID\_Z;ID\_F;ID\_U;TIME;DESC

(Hall number; press or event; unique number of step; phase; event; time; note). [3]

## 6 Conclusion

In this work was developed a tool for measuring the time of individual phases in the central operating theaters. Mobile applications do not address managing an operation plan, but its time analysis, and it evaluates critical locations where a time lag can occur between operations I during the operation.

At this time, applications are tested and filled with data that should point out the need to change the information system and manage the operating time to avoid overdue delays, thus also to the hospital's financial losses.

When detecting delays in some of the phases, it will then focus on addressing it with RFID authentication and more accurate interfacial recognition.

## 7 References

1. KIM J. VICENTE. Cognitive work analysis toward safe, productive, and healthy computerbased work. Mahwah, N.J: Lawrence Erlbaum Associates, 1999. ISBN 1410603032.
2. Sommerov'a, M. (2011). Základy rfid technologií. Mezinárodní
3. Tomala, K., Plucar, J., Dubec, P., Rapant, L., and Voznak, M. (2013). The data extraction using distributed crawler inside multi-agent system. *Advances in Electrical and Electronic Engineering*, 11(6), 455.
4. Mann, G. (2017). Improving Efficiencies with Real Time Locating Systems in Emergency Departments. *Prehospital and Disaster Medicine*, 32(S1), S37-S38. doi:10.1017/S1049023X17001157
5. HARDERS, Maureen, et al. Improving operating room efficiency through process redesign. *Surgery*, 2006, 140.4: 509-516.
6. PRGOMET, Mirela; GEORGIU, Andrew; WESTBROOK, Johanna I. The impact of mobile handheld technology on hospital physicians' work practices and patient care: a systematic review. *Journal of the American Medical Informatics Association*, 2009, 16.6: 792-801.

# Effective Big Data Analysis on single-node Apache Spark with Self-Organizing Map Libraries

David Andrešič and Petr Šaloun

Department of Computer Science, FEECS,  
VŠB – Technical University of Ostrava, 17. listopadu 15,  
708 33 Ostrava – Poruba, Czech Republic  
{david.andresic.st, petr.saloun}@vsb.cz

**Abstract.** Apache Spark is commonly used platform for big data analysis on large computer cluster. It uses primarily the main memory. We attempted to add a self-organising map library to such one analytical stack. The result is fast and effective even on a single standard computer.

This approach is beneficial for researchers with limited resources. Our idea was experimentally tested and is described here. We chose the Brexit phenomena as our case study for looking for correlations between Twitter *#brexit* hashtag sentiment analysis and stock exchange behaviour.

**Keywords:** Apache Spark, Big Data, Machine Learning, Self-Organizing Maps

## 1 Introduction

The correlation of tweets and stock exchange using statistical approaches is a common subject of research and publication. Our approach for Twitter social network and stock exchange behaviour included public data aggregation and cluster analysis using machine learning techniques (self-organising maps – SOM). For this, we used Apache Spark<sup>1</sup>, a big data processing platform for large computer clusters. We deployed it on a single standard computer for big data pre-processing. Since Spark attempts to handle the data using mainly the RAM, we faced limited resources. Similarly were dealing with different efficiency of SOM libraries in data clustering.

## 2 Methodology and Data Sets

The whole process looked like this:

- Sentiment analysis in order to find out how positive or negative each tweet was.

---

<sup>1</sup> Apache Spark homepage: <http://spark.apache.org/>

- Data joining and aggregating that involved calculations of correlation coefficients and data transformations to a form required by SOM with usage of Apache Spark.
- Cluster analysis using SOM in order to find clusters of most-correlating corporations.

## 2.1 Twitter Sentiment Analysis

We had tweets for *#brexit* for period from 29.4.2016 to 2.7.2016. The sentiment analysis shown that before the referendum (23.6.2016), tweets were meant to be more an EU criticism, while after the referendum, they commented more Brexit itself. The total count of analysed tweets was 21137 (10799 before referendum and 10338 after it).

## 2.2 Stock Exchange Data and Corporation Data

We chose Yahoo Finance<sup>2</sup> as a source of trustworthy data. It provides historical data from many stock exchanges, including London Stock Exchange (1292 corporations). Yahoo Finance allows to download following information: date, opening and closing stock value, daily minimum and maximum and volume of stocks of the day. We added some extra data from Google Finance as well (address, sector and industry, country).

## 3 Data Transformation and Aggregation

At first, we used data described in section 2.1 with missing values interpolated. SOM required on each line (representing a single corporation) information about the mean of stock close value and mean of stock volume, their correlation coefficient with sentiment, city, country, sector and industry.

Calculations were divided into three intervals before and after referendum and the whole interval (as described in 2.1). By joining both stock exchange data sets we retrieved information about 962 corporations. Then, the correlation coefficients for stock exchange markers and sentiment analysis in the given day for the given interval were calculated. All using Apache Spark in single-node cluster mode (Intel Core i3 CPU with 2 cores / 4 threads and 8GB RAM). These specifications corresponds with the current commodity hardware for which the Spark is designed (scale out).

We attempted to perform all the data joins and calculations at the same time in RAM. Unfortunately, each selection query took several minutes and calculations were not finished ever after several days. A classic SQL approach with creating an index on stock exchange markers is not possible in a simple way in Apache Spark SQL, it requires a conversion to the low-level RDD and back to the Spark SQL data frame. We therefore modified our code so the calculations would

<sup>2</sup> Yahoo Finance: <https://finance.yahoo.com/>

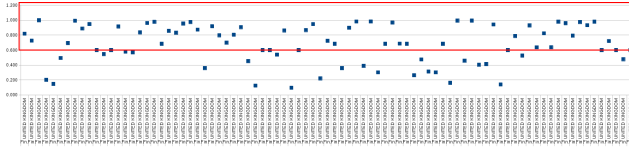


**Fig. 1.** Scatter plot of cluster #3. We can see that most of the points (each represents a corporation in United Kingdom and post-referendum correlation coefficient for close mean) are above the correlation coefficient of 0.6.

be performed iteratively over smaller parts of the data. With this approach, we were able to avoid memory-consuming selection queries in a large data frame and calculations were finished in just about two hours. Using this approach, a single set of calculations works just with the data of a single corporation, which means that this approach can be parallelized and therefore even more faster. The resulting table then contained means of stock values and their volumes of the day for all intervals, all normalized to a range from 0 to 1. Categorical (nominal) attributes were "binarised" (e.g. "London" value in "town" attribute were transformed to a new attribute called "is\_town\_London" with value 0 or 1).

## 4 Cluster Analysis

We chose SOM[3] over the other considered k-means-based algorithms, mainly because of the fact that k-means algorithms are more prone to local minimums[2]. One of the favourite implementations of SOM is Weka<sup>3</sup>. Nevertheless, even after several hours of running with just 100 samples from the data set and grid of size  $5 \times 5$ , calculations were still not finished. We therefore gave a try to an implementation in a *java-ml* library. We ended up with a rectangular grid of size  $5 \times 5$ , 1000 iterations, learning coefficient 0.5 and initial radius 8, that generated 24 most conclusive clusters within several minutes.

Since *java-ml* does not allow a direct access to the neurons in the grid, we were not able to create a typical U-matrix for evaluation. Instead, we used a simple scatter plots. The resulting clusters shown correlation of financial sector in London with the sentiment (Fig. 1, 2 and 3). This is not surprising, since London is considered to be as a financial centre of the United Kingdom with younger and more educated population, active on social networks[4]. We could also see a correlation of financial sector from the whole Great Britain after the referendum (Fig. 1). This could mean, that the financial sector reflected the sentiment on Twitter. On the other hand, technological sector seemed to not correlate at all (just corporations residing directly in Great Britain seemed to correlate a little bit more), as depicted on Fig. 4.

<sup>3</sup> Weka homepage: <http://www.cs.waikato.ac.nz/ml/weka/>





**Fig. 2.** Scatter plot of cluster #8. We can see that most of the points (for almost all correlation coefficients of United Kingdom financial corporations) are above the correlation coefficient of 0.6.

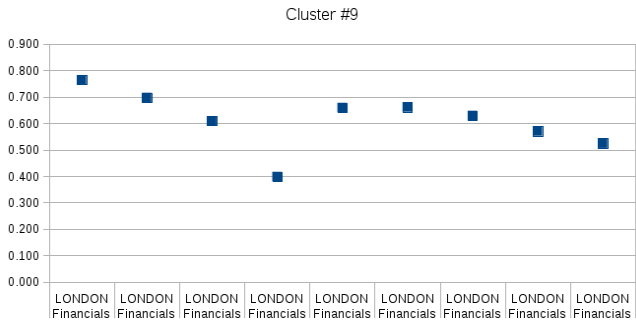


**Fig. 3.** Scatter plot of cluster #9. We can see that most of the points (each represents a corporation in United Kingdom and pre-referendum correlation coefficient for close mean) are above the correlation coefficient of 0.6.

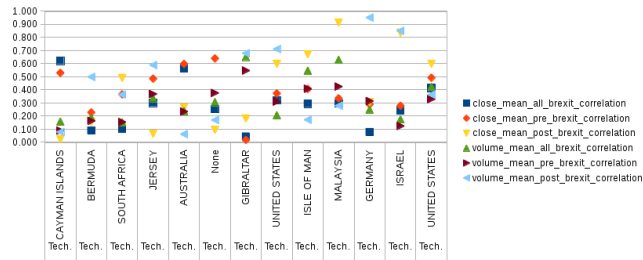


**Fig. 4.** Scatter plot of cluster #11. We can see that most of the points (for almost all correlation coefficients of non-UK technological corporations) are under the correlation coefficient of 0.5.

## 5 Conclusion

Our Brexit case study with London Stock Exchange as an example shown that financial sector of Great Britain strongly correlated with sentiment on Twitter.

This is especially obvious in case of corporations residing in London. On the other hand, technological sector had almost no remarkable correlation. As described in [4] and [5], data from Twitter and other social networks in general usually miss information about demography, age or education of users. For our future work, we shall therefore consider obtaining these data. It is also necessary to have in mind that social network users are just a small, very specific fraction of population [5].

When the Apache Spark is deployed in a single-node cluster mode, limited resources (especially RAM) can cause a slow selection from large data frames. By rewriting the code of joining data frames, we were able to avoid memory-exhausting operations, which allowed to reduce computational time from several days to just two hours. This approach is also parallelizable.

The usage of SOM allowed us to analyse Brexit phenomena with stable and conclusive results in all iterations. The efficiency of SOM libraries turned out to be very different (*java-ml* was much faster than more convenient Weka, which can be interesting for other researchers).

This work was in full version published on an international conference.

## Acknowledgment

The following grants are acknowledged for the financial support provided for this research: Grant Agency of the Czech Republic - GACR P103/15/06700S, Grant of SGS No. SGS 2017/134, VSB-Technical University of Ostrava. The Ministry of Education, Youth and Sports from the National Programme of Sustainability (NPU II) project IT4Innovations excellence in science - LQ1602.

## References

1. A. J. Awan, M. Brorsson, V. Vlassov and E. Ayguade, "Performance Characterization of In-Memory Data Analytics on a Modern Cloud Server," *Big Data and Cloud Computing (BDCloud)*, 2015 IEEE Fifth International Conference on, pp. 1-8, 2015.
2. F. Bao, V. Lobo and M. Painho, "Self-organizing Maps as Substitutes for K-Means Clustering," *Computational Science – ICCS 2005: 5th International Conference, Atlanta, GA, USA, May 22-25, 2005, Proceedings, Part III*, pp. 476-483, 2005.
3. T. Kohonen, "Essentials of the self-organizing map," *Neural Networks*, vol. 37, pp. 52-65, January 2013. [Online]. Available: <http://aisii.azc.uam.mx/mcbc/Cursos/IntCompt/Lectura 8. SOM.pdf>. [Accessed March 10, 2017].
4. L. Vasiliu, R. McDermott, M. Zarrouk, M. Hrlimann, B. Davis, T. Daudert, M. B. Khaled, D. Byrne, S. Fernandez, A. Freitas, F. Caroli, S. Handschuh and Angelo Cavallini, "In or Out? Real-Time Monitoring of BREXIT sentiment on Twitter," *CEUR Workshop Proceedings*, 2016.
5. M. Hürliemann, B. Davis, K. Cortis, A. Freitas, S. Handschuh and S. Fernandez, "A Twitter Sentiment Gold Standard for the Brexit Referendum," *Proceedings of the 12th International Conference on Semantic Systems*, pp. 193-196, 2016.

# Context Recognition and Type-checking Tools for the TIL-Script Language

Michal Fait

Department of Computer Science, FEECS,  
VŠB – Technical University of Ostrava, 17. listopadu 15,  
708 33 Ostrava – Poruba, Czech Republic  
`michal.fait@vsb.cz`

**Abstract.** In this paper, I sum up my work in the last academic year. I was working especially on the problem of context recognition in *Transparent Intensional Logic (TIL)*. Firstly, I describe changes in the *TIL-Script* language that were made during the last year. Then I describe developing, testing and extending my tool for TIL-Script processing. I was also testing another tool, namely the *TIL-Script editor*. In the last section, I present the issues I am currently working on and outline future research.

**Keywords:** TIL-Script, context recognition, type checking

## 1 Introduction

Automatic theorem provers for higher-order logic (known as HOL)<sup>1</sup> are getting an increasingly large interest in logic, mathematics and computer science. These tools are used in automatic theorem proof-checking and as interactive proof assistants. Underlying logic of these tools is usually a version of the simply typed lambda calculus. This makes it possible to operate in an extensional level where the value of a denoted function is an object of predication, and in an intensional level, where the whole function is an object of predication.

Currently there is another application gaining interest, namely natural language processing. There are great amounts of text data that need to be analyzed and formalized, and we also need to build up question-answer systems which will make it possible to infer implicit (or computable) knowledge from these large explicit knowledge bases.

However, since natural language is so rich that it includes hyperintensional contexts where the meaning of another expression is an object of predication, the simply typed intensional lambda calculi are not powerful enough to be successfully applied in this area. To this end we use Transparent Intensional Logic (TIL). From the formal point of view, TIL is a hyperintensional, partial, typed lambda calculus with procedural semantics. Hence in TIL we have the tools to distinguish and operate in not only an extensional or intensional level, but also in a hyperintensional level. This is so because we

---

<sup>1</sup> See [2].

explicate meanings hyperintensionally, i.e. as abstract procedures encoded by expressions. These procedures are rigorously defined as TIL constructions.

Currently the group of researchers of our department (of which I am a member) develops the computational variant of TIL, the TIL-script functional language. Our goal is the development of a question-answer system operating on a natural language. During the development process, this language has been adjusted and improved. Up to now we have developed the tools for validating TIL-Script constructions including their syntactic analysis and type checking. We have also implemented the algorithm for context recognition; this algorithm recognizes the three variants of a context in which a construction can occur, namely extensional, intensional and hyperintensional. This is crucial for a valid application of extensional logical rules in all kinds of context, and thus also for the development of TIL inference machine.

The goal of this paper is to describe what has been done in this area in the last year. This concerns in particular a new version of the TIL-Script grammar, the development and testing the tools for type checking and context recognition.

## 2 Development of the TIL-Script language

First, we made some improvements of the TIL-Script language so that the TIL-Script version 5 and 5.1 were defined. These changes concern in particular the TIL-Script grammar, and they are recorded in a corresponding changelog.

### 2.1 TIL-Script version 5

This version brought some mostly cosmetic improvements, so that the grammar became easier to read and understand. Some non-terminal symbols were re-written and simplified. Also the rules for numbers were changed to avoid conflicts in non-terminal symbols.

### 2.2 TIL-Script version 5.1

Version 5.1 was developed after testing TIL-Script editors and type control. This version comes with two main improvements. First, we added ten new keywords representing built-in TIL-Script functions that we need to manipulate constructions in proofs and when deriving consequences. Here is the list of new keywords.

- **No**: the polymorphic function that associates a given set  $S$  with the set of all sets disjunctive with  $S$ . Thus, **No** applied on a set  $S_1$  and then  $S_2$  returns the truth-value **True** if  $S_1$  and  $S_2$  have an empty intersection.
- **Sing**: the polymorphic partial function that returns as its value the only element of a singleton (i.e. a one element set), otherwise (i.e. if a given set is empty or has more than one element) the function **Sing** is undefined

- **Sub**: this function operates on procedures, i.e. TIL constructions of type `*` like this. `[Sub A B C]` substitutes the construction provided by `A` for all the occurrences of the construction provided by `B` into the construction provided by `C`. As a result, the Composition `[Sub A B C]` provides an adjusted construction.
- **Tr**: given an object of any type, the polymorphic function `Tr` returns its Trivialization
- **TrueC**: given a construction `C` that is typed to construct a truth-value, `[TrueC@wt 'C]`  $\nu$ -constructs the truth-value `True`, if `C`  $\nu$ -constructs the truth-value `True` in a given world `w` and time `t` of evaluation, otherwise `False`.
- **FalseC**: given a construction `C` that is typed to construct a truth-value, `[FalseC@wt 'C]`  $\nu$ -constructs the truth-value `True`, if `C`  $\nu$ -constructs the truth-value `False` in a given world `w` and time `t` of evaluation, otherwise `False`.
- **ImproperC**: given a construction `C` that is typed to construct a truth-value, `[ImproperC@wt 'C]`  $\nu$ -constructs the truth-value `True`, if `C` is  $\nu$ -improper in a given world `w` and time `t` of evaluation, otherwise `False`.
- **TrueP**: given a construction `C` that is typed to  $\nu$ -construct a proposition `P`, `[TrueP@wt C]`  $\nu$ -constructs the truth-value `True`, if the proposition `P` takes the truth-value `True` in a given world `w` and time `t` of evaluation, otherwise `False`.
- **FalseP**: given a construction `C` that is typed to  $\nu$ -construct a proposition `P`, `[FalseP@wt C]`  $\nu$ -constructs the truth-value `True`, if the proposition `P` takes the truth-value `False` in a given world `w` and time `t` of evaluation, otherwise `False`.
- **UndefP**: given a construction `C` that is typed to  $\nu$ -construct a proposition `P`, `[UndefP@wt C]`  $\nu$ -constructs the truth-value `True`, if the proposition `P` is undefined in a given world `w` and time `t` of evaluation, otherwise `False`.
- **ToInt** – conversion of Real number to Int

The new keywords together with the types of functions they represent are summarized in **Table 1**.

Keyword	Type
No	<code>((Bool (Bool Any)) (Bool Any))</code>
Sing	<code>(Any (Bool Any))</code>
Sub	<code>(* * * *)</code>
Tr	<code>(* Any)</code>
TrueC	<code>((((Bool *) Time) World)</code>
FalseC	<code>((((Bool *) Time) World)</code>
ImproperC	<code>((((Bool *) Time) World)</code>
TrueP	<code>((((Bool ((Bool Time) World)) Time) World)</code>
FalseP	<code>((((Bool ((Bool Time) World)) Time) World)</code>
UndefP	<code>((((Bool ((Bool Time) World)) Time) World)</code>
ToInt	<code>(Int Real)</code>

**Table 1.** New keywords in the TIL-Script version 5.1

The second improvement consists in providing the possibility to write polymorphic type “Any” with optional numbering (`Any`, `Any1`, `Any2` etc.). This feature enables us

to determine whether a function with two or more arguments of polymorphic type `Any` requires all the arguments to be of the same type or not. For example, the polymorphic function `"="` is of type `(Bool Any Any)`, because the two compared objects must be of the same type. On the other hand, consider, for instance, the function `Compare-Cardinality` that associates any two sets with `True` if the sets have the same cardinality, otherwise `False`. Thus, the function `Compare-Cardinality` is of a polymorphic type `(Bool (Bool Any1) (Bool Any2))`.

### 3 Development of the TIL-Script processing tool

In this year, I worked on my tool for processing the TIL-Script language, in particular the type-checking algorithm and the algorithm for recognizing the context in which a sub-construction  $C$  occurs within a super-construction  $D$ . This system is a C# console application using a module written in the logic programming language Prolog. Parsing of the input TIL-Script file is written in C# and other features like type control and context recognition are written in Prolog. The results are exported into an XML file; this functionality is also written in Prolog. The system has been developed as a part of my Master thesis and in this year it has been extended and improved. Now I am going to describe those improvements and special functionalities.

I made some minor changes in the structure of the additional output into console window to make the results more explicit and easier to read. Furthermore, another new feature is the detection of an undefined object followed by a warning, and the detection of a free variable that is not defined globally. In such a case, the type of an object is not defined, and the type-checking fails. Another issue that I dealt with has been the removal of Trivialization when the Trivialized construction occurs within the scope of Double Execution. In other words, this law has been implemented:  $\wedge^2[...'C...'] = [...C...]$ . This functionality had been malfunctioning in the former version.

There are other two greater extensions that I am going to describe in the following subsections.

#### 3.1 Comparing two context recognition algorithms

After testing my tool, the TIL-Script editor and the context recognition algorithm based on rigorous definitions from [1, pp. 370-397], I decided to implement an alternative context recognition algorithm based on the description of the main ideas of context recognition provided by my supervisor. The goal of this double checking was to discover whether the rigorous definitions correspond to those simple ideas (see section 4.1). Yet, soon I found out that a manual comparing the results of the two context recognition algorithms running on a large input file would be a too tedious process. Hence, in order to make this process reasonably tractable, I extended my tool with the functionality that compares the results of the two context recognition algorithms. This sub-procedure calls the two implemented algorithms and computes the context by applying both the algorithms. If there are any differences between the results, the module prints them in the following format.

```
Difference: #16#1 - [\x [\y ['Div y x]]]  
in #16 - [[\x [\y ['Div y x]]] ['Cot '5]]  
1st algorithm: Intensional  
2nd algorithm: Extensional
```

### 3.2 Handling polymorphic types.

The module dealing with polymorphic types Any has been implemented in the testing phase of type control (see section 4.2). The former version accepted polymorphic type Any when processing the input TIL-Script file, but the type-checking module failed and indicated a construction dealing with Any as type-theoretically incoherent. Hence, there was a need to improve the type-checking module. The new, improved version, correctly accepts the Composition dealing with any type in case the parameters are defined as having the polymorphic type “Any”. Another improvement consists in accepting and dealing with the indexed polymorphic types Any1, Any2, etc., see the description above (Section 2.2).

## 4 Testing the tools for context recognition and type control

Another task was testing the TIL-Script editor developed in the Java extension of Eclipse IDE by David Ježek and Jan Kožusznik. I performed the tests together with testing my C# Prolog program, and compared the results. The subject of testing were the two main functionalities, namely the context-recognition and type-checking procedures.

### 4.1 Testing the context recognition module

For testing the context-recognition procedure, a large file containing the TIL-Script constructions were created. This file contains many test cases with some problematic and more complex ones. The results of the both context-recognition tools were compared and the wrong cases were indicated and corrected both in my tool and in the TIL-Script editor. Additionally, I analyzed some complicated constructions and checked in detail, step by step, whether my tool complies with the formal definitions that can be found in [1], Chapter 11. I also implemented and tested the alternative context-recognition description, compared the results, and thus proved the adequateness of the rigorous definitions.

### 4.2 Testing the type-checking module

To this end I used the sample large file created for context recognition. Basically, the type-checking procedure was implemented correctly in both tools. Yet, there were problems that cropped out and had to be solved out, namely handling indexed polymorphic types, fixing the determined set of keywords (changes mentioned above in Section

2.2) and dealing with integer and real numbers (Int – Real transfer became implicit, the opposite operation must be explicitly specified with a new function ToInt).

## 5 Conclusion and future research

In this paper, I introduced the new version 5.1 of the TIL-Script language, together with development improvements of the tools for context recognition and type checking in TIL-Script. The main results are these two correctly working tools. Thus, we are in a position to extend these tools so that they can become the basis of the TIL-Script inference machine.

Now I deal with the substitution of  $\nu$ -congruent, equivalent, and procedurally isomorphic constructions depending on the context in which a construction occurs. The substitution tool will be implemented in Prolog as an extension of the current tool. Having recognized whether the constructions are  $\nu$ -congruent, equivalent, or procedurally isomorphic, the program will generate a new adjusted construction, i.e. the result of a correct substitution of identicals.

## 6 Publications

- Duží, M., Fait, M., Menšík, M.: Context Recognition for a Hyperintensional Inference Machine. To appear in the AIP proceeding of ICNAAM 2016, International Conference of Numerical Analysis and Applied Mathematics.
- Duží, M., Fait M.: The Algorithm of Context Recognition in TIL. In RASLAN 2016, The Tenth Workshop on Recent Advances in Slavonic Natural Language Processing, A.Horák, P.Rychlý, A.Rambousek (Eds.), pp. 51-62, <https://nlp.fi.muni.cz/raslan/raslan16.pdf>

## Acknowledgements

These research activities have been pursued within and supported by the grant project No. GA15-13277S, ‘Hyperintensional logic for natural language analysis’, and also by the internal grant agency of VSB-TU Ostrava, project No. SP2017/133, ‘Knowledge modeling and its applications in software engineering III’.

## References

1. Duží, M., Materna P. (2012): *TIL jako procedurální logika*. Aleph Bratislava.
2. Gordon, M.J.C., Melham, T.F. (1993): *Introduction to HOL*. Cambridge University Press.



# Detecting Human Action using the Microsoft Kinect ONE Sensor

Rafał Gasz

Department of Computer Science, FEECS,  
VŠB – Technical University of Ostrava, 17. listopadu 15,  
708 33 Ostrava – Poruba, Czech Republic

`rafal.gasz.st@vsb.cz`

Faculty of Electrical Engineering, Automatic Control and Computer Science, Opole  
University of Technology, ul. Prószkowska 76, 45-758 Opole, Poland  
`r.gasz@po.opole.pl`

**Abstract.** This article covers the possible applications of automatic human detection mechanisms using digital data and analysis of activities performed by these people. The possible uses of Kinect sensor were also described, especially the Skeleton model library, which can be successfully used to evaluate the type of action performed. The most commonly used methods for detecting action and potential further development are described synthetically.

## 1 Introduction

The ability to automatically recognize and define the actions performed by a human is a fairly new topic in literature, but it is attracting more and more attention. Systems that provide such possibilities would be very useful in many areas of life: in cars as systems supporting drivers' decisions, systems analysing potential pedestrian behaviour or driver-assistance systems, in urban monitoring analysis for detecting potentially dangerous tasks, as medical aid for analysing activity during rehabilitation or for elderly people to help them maintain active lifestyle.

Various types of sensors can be used for these tasks, the easiest to use will be the RGBD sensors, especially those used in games, because they are relatively cheap and provide a lot of information about the external environment. RGBD sensors market availability has fostered the development of promising ways to create reliable and cost-effective solutions [1]. Using depth sensors such as Microsoft Kinect or other similar devices is possible thanks to action recognition systems using depth maps which are a very good source of information because they do not affect changes in environment conditions, can provide body shape and simplify the problem of human detection and segregation [2]. In addition, the availability of a skeletal model retrieved from depth maps allows for a compact representation of the human body which has many applications [3].

## 2 Microsoft Kinect sensor

The Microsoft Kinect sensor is a device that allows the user to interact with a computer system without using a controller, but via an interface that utilizes the gestures made using limbs and the whole body, and with the use of voice commands. This device has two cameras, an infrared projector, four-microphone array, accelerometer and a motorized tilt. The first camera is a standard RGB video camera with a resolution of 640x480, used for video processing (including facial recognition) and colour and texture mapping to virtual objects. The second camera is part of the sensor subsystem which returns depth data. This subsystem operates on the principle of measuring distance with structural light. The infrared projector displays cloud of points in front of the camera, the locations of which are recorded by the infrared camera. The depth data obtained from camera has a resolution of 300x200 and then it is interpolated to a 640x480 video camera resolution. Distance sensor has a range of 0.4-6.5m [4].

Distance data in all points gives the programmer ability to detect, for example, a human silhouette and gestures. The use of structural light method allows the sensor to operate flawlessly only in closed areas – the reading is sensitive to sunlight. Kinect is also used in image processing and robotics, especially mobile. It is a cheap replacement for expensive laser sensors for in-door use. Developed libraries allow the sensor to be used through a PC with various operating systems. This software allows obtaining so-called point clouds from depth measurements and video camera. These data may be further used in different applications, including 3D object detection, 2D, 2.5D and 3D map creation or localization and navigation of mobile robots, so-called. SLAM algorithms.

## 3 Kinect sensor skeletal model

The NUI Skeleton API provides information about the position of two players, standing in front of the Kinect sensor (Beta Kinect SDK version – gives the ability to analyse 6 players). Data collected by the sensor provide information about the position of 20 body parts, allowing determining their coordinates relative to sensor. These points form the player's skeleton. With these points, the programmer is able to recognize the current position and pose of a person relative to sensor. It is also possible to determine the coordinates of individual body parts and appropriately respond to changes in their positions. Skeletal points to which there is software access are shown in Figure 1.

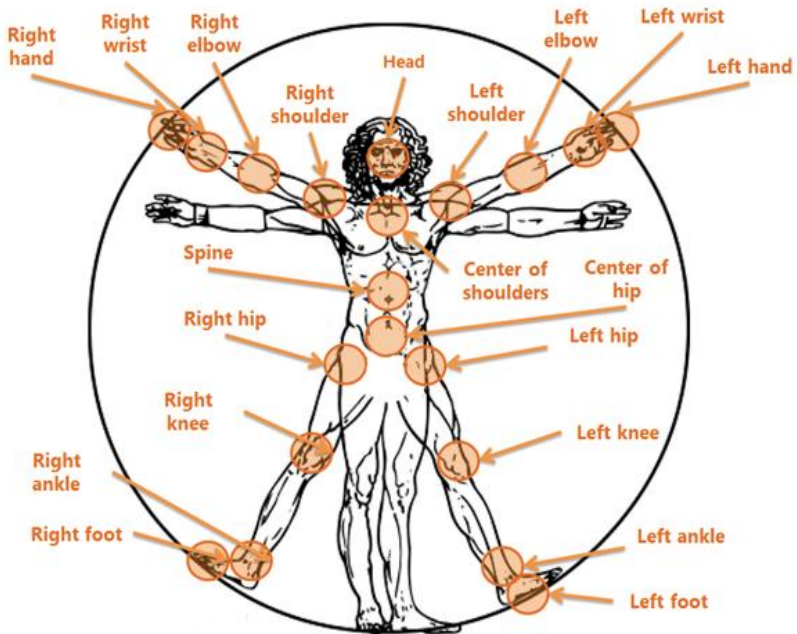


**Fig. 1.** Characteristics point of the skeleton model [5]

Skeletal tracking works in two modes: active and passive. The active mode in Kinect SDK Beta version can be used for up to two people located within the sensor range (Figure 2), while passive mode is used for the remaining four people. The difference between these two modes is that silhouettes tracked in passive mode provide only data about their location, while silhouettes tracked in active mode give us access to data about the individual points and their locations.

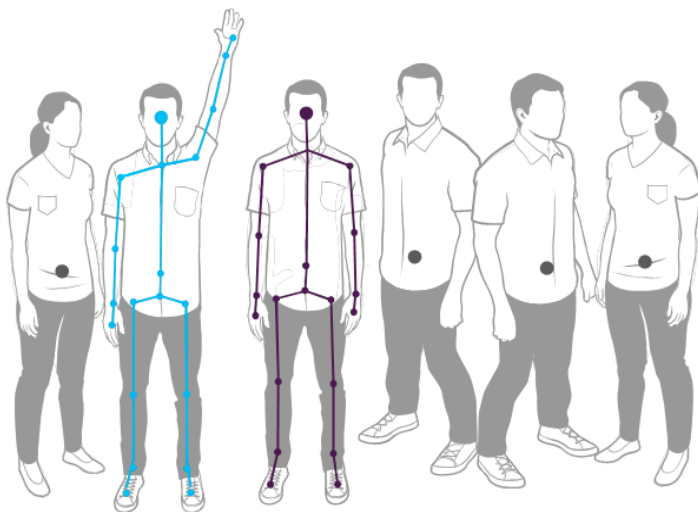


**Fig. 2.** Skeletal tracking [5]

After initializing the modes in which Skeletal tracking operates, data is sent in frames, containing a table with coordinates of every point. Programmer is able to determine the mode in which the captured silhouette is located. To do this, it is necessary to use the libraries included in Kinect SDK. The implementation of one of the libraries responsible for this has been defined as a state machine that allows assigning a given state to a particular skeleton: `SkeletonTrackingState.Tracked`, `SkeletonTrackingState.NotTracked`, `SkeletonTrackingState.PositionOnly`.

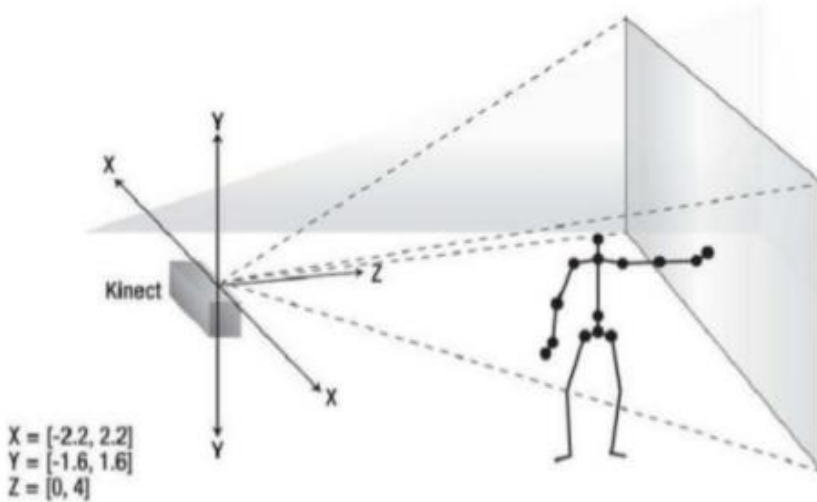


**Fig. 3.** Determining points in space [5]

Every point has a position relative to the sensor (Figure 3), defined by a vector – `Vector4(x, y, z, w)`, where the first three attributes define its coordinates, and the fourth attribute allows data filtering. Every captured silhouette has a unique `TrackingID` attribute that allows distinguishing it from the next captured frames. In addition, NUI Skeleton API provides algorithms that assist in filtering and smoothing the movement of program objects, which are modelled after the respective points. It is manifested in a loss of vibration effect caused by sensor sensitivity which is the result of sensor data being averaged after passing appropriately configured smoothing attributes.

## 4 Action recognition

Recognition of actions and movements of people consists of many elements, such as: walking, running, sitting, jumping, swinging, etc. The method of recognizing individual actions is a difficult task, as there might be many variations of human body movement [6]. Furthermore, each person has a different body shape, size, and gesture movement, which may result in various interpretations of these actions [2].

Skeletal joints extracted from depth frames can also be combined with RGB data. Spatio-temporal Interest Points (STIP) are typically used in action recognition where

data are represented by RGB frames. This approach can be also extended to depth and skeleton data [7]. Obtained results are very good, but the noise of depth and background estimation may have an impact on percentage point detection, so the depth of the STIP function has to be maintained using skeleton position or RGB videos. Instead of using spatio-temporal features, another approach for human activity recognition relies on graph-based methods for sequential modelling of RGB data. This concept can be extended to depth information, and the proposed approach is based on a coupled hidden conditional random fields model, where master objects sequences are extracted from RGB and depth data. The main advantage of this approach is the capability to preserve the dynamics of individual sequences, even if the complementary data from RGB and depth are shared.

In order to detect an action, a partial approach can be used as well – the human body is divided into five different parts, and human actions are represented with the use of motion parameters of the individual body parts, and their motion is considered horizontally and vertically, including rotations in plane. Then, classification is carried out by comparing PCA coefficients.

Performing the analysis of human body movements using the methods described yields good results.

## 5 Conclusions

The article discusses possible applications of the Skeleton model with the Microsoft Kinect sensor in recognition of actions performed by people. These applications are currently widely discussed, as the automation of this process in the field of medicine and broadly defined security (monitoring) and many other fields finds more and more practical use, and existing algorithms and sensors do not quite meet the expectations.

The algorithms known from RGB image analysis described by the author can be successfully used in analysing skeletal model obtained using the Kinect sensor. The use of this device offers great development potential, as it is relatively cheap set of high quality sensors. Further work will focus on developing a fully autonomous model capable of conducting a simple analysis of various types of activities.

## References

1. Aggarwal J. K., Xia L.: Human activity recognition from 3D data: a review, *Pattern Recognition Letters*, 2014, doi: 10.1016/j.patrec.2014.04.011
2. Gasparini S., Cippitelli E., Gambi E., Spinsante S., Flórez-Revuelta F.: Performance analysis of self-organising neural networks tracking algorithms for intake monitoring using Kinect, *Proceedings of the 1st IET International Conference on Technologies for Active and Assisted Living*, 2015
3. Shotton J., Fitzgibbon A., Cook M.: Real-time human pose recognition in parts from single depth images, *Proceedings of the IEEE Conference on Computer Vision and Pattern Recognition (CVPR '11)*, June 2011, Providence, Rd, USA, IEEE, pp. 1297–1304
4. Kinect documentation: <https://developer.microsoft.com/en-us/windows/kinect/develop>

5. Kinect SDK documentation: <https://msdn.microsoft.com/pl-pl/library/kinect-sdk--wprow-adzenie.aspx>
6. Rahmani H., Mahmood A., Huynh D. Q., Mian A.: HOPC: histogram of oriented principal components of 3D pointclouds for action recognition, In: Fleet D., Pajdla T., Schiele B., Tuytelaars T., editors, Computer Vision—ECCV 2014, Vol. 8690, Springer, 2014, pp. 742–757
7. Zhu Y., Chen W., Guo G.: Evaluating spatiotemporal interest point features for depth-based action recognition, Image and Vision Computing, 2014, doi: 10.1016/j.imavis.2014.04.005
8. Liu A.A., Nie W., Su Y., Ma L., Hao T., Yang Z.: Coupled hidden conditional random fields for RGB-D human action recognition, Signal Processing, 2015, doi: 10.1016/j.sigpro.2014.08.038

# Betweenness Centrality Algorithm and Node Importance Extension

Jiří Hanzelka

Department of Computer Science, FEECS,  
VŠB – Technical University of Ostrava, 17. listopadu 15,  
708 33 Ostrava – Poruba, Czech Republic  
IT4Innovation, VŠB – Technical University of Ostrava, 17. listopadu 15,  
708 33 Ostrava – Poruba, Czech Republic  
`jiri.hanzelka@vsb.cz`

**Abstract.** The purpose of this paper is to show progress on developed parallel Betweenness centrality algorithm that was extended about node importance, so one node can influence Betweenness centrality more then the others. Implementation is based on Message Passing Interface at High Performance Computing environment. Experiments prove almost same speed compared to algorithm without modification.

**Keywords:** Betweenness centrality, MPI, HPC, node importance

## 1 Introduction

The important area of computations are big graph problems which are mostly used in order to model large real life networks, i.e. traffic networks, social networks but also in areas like the modeling of connections in the human brain [3]. For example, one of the used algorithms in area of traffic networks is betweenness centrality described in this paper. The general assumption of betweenness centrality in traffic routing is that the most frequently used roads can be considered as bottlenecks [2]. The main goal of betweenness centrality is to identify such bottlenecks in a traffic network represented by oriented weighted graph. This way, betweenness centrality can help to optimize routing since it allows us to monitor how bottlenecks change during the day. Since betweenness centrality is based on the shortest path search, it can also be used to monitor and examine bottlenecks behavior based on wide number of factors. Besides the distance, graph weights could reflect actual weather conditions, speed, time of the day, etc. Betweenness centrality algorithm is described in Section 2.

Betweenness centrality from Ulrik Brandes does not take into calculation importance of node in the graph. For traffic routing it was interesting to modify this, so it could give us better understanding when something happens in the graph. For example when some new shop opens, we would like to see how bottlenecks in traffic network will change. So for this node we would increase node importance for shortest paths directing to this node. There is also opposite situation, when people are leaving some area, after end of some action (concert,

cinema, ...). In this situation we would increase importance of node for shortest paths directing from this node. It can also give us better result when we specify node importance for each node in the graph for example depending on population counts in areas of graph. Detailed information about this modification is in Section 3.

## 2 Betweenness

Betweenness centrality is widely used graph metric used mainly in order to find the most significant nodes within the graph. Betweenness centrality quantifies the number of times a node is a bridge along the shortest paths between two other nodes.

The mathematical representation (defined by Freeman in 1977) can be written as

$$C_B(v) = \sum_{s \neq v \neq t \in V} \frac{\sigma_{st}(v)}{\sigma_{st}},$$

where  $V$  is a set of nodes,  $\sigma_{st}$  denotes number of shortest paths from  $s \in V$  to  $t \in V$  (where  $\sigma_{st} = 1$  for  $s = t$ ) and  $\sigma_{st}(v)$  denotes the number of shortest paths from  $s$  to  $t$  that  $v \in V$  lies on.

For the purpose of testing algorithm the input graph for betweenness centrality is generated from the Czech Republic traffic network map that was obtained from OpenStreetMap project [5]. The traffic network graph is stored in a simple csv file with one edge in each row.

Originally we used our implementation of betweenness centrality algorithm from Ulrik Brandes for directed graph with edge lengths that can be used for traffic networks. Pseudo code is taken from publication [6] and is shown in Algorithm 1. Our betweenness centrality is implemented in C++ that was parallelized by OpenMP and MPI [4].

## 3 Modification

Each node in modified version of betweenness centrality contains two real numbers  $alpha \in \mathbb{R}_{\geq 1}$  and  $beta \in \mathbb{R}_{\geq 1}$

- $alpha$ (source node importance) - increases betweenness on shortest paths directing from this node
- $beta$ (destination node importance) - increases betweenness on shortest paths directing to this node

This betweenness gain on shortest paths is proportional to these values. For example if  $alpha$  is 2 for node  $A$ , then betweenness centrality gain on nodes that are on the shortest paths from node  $A$  to all other nodes is two times bigger. If these values are 1, then algorithm works as original code from Ulrik Brandes. Illustration of change in  $alpha$  value can be seen in Fig. 1 where betweenness



---

**Algorithm 1:** Original betweenness centrality for directed graph with edge lengths

---

**input** : directed graph  $G = (V, E)$  with edge lengths  $\lambda : E \rightarrow \mathbb{R} > 0$   
**data** : priority queue  $Q$  with keys  $dist[\cdot]$   
           stack  $S$  (both initially empty) and for all  $v \in V$   
            $dist[v]$ : distance from source  
            $Pred[v]$ : list of predecessors on shortest paths from source  
            $\sigma[v]$ : number of shortest paths from source to  $v \in V$   
            $\delta[v]$ : dependency of source on  $v \in V$   
**output**: betweenness  $c_B[v]$  for all  $v \in V$  initialized to 0

```

1  foreach  $s \in V$  do
2      foreach  $w \in V$  do  $Pred[w] \leftarrow$  empty list ;
3      foreach  $t \in V$  do  $dist[t] \leftarrow \infty$ ;  $\sigma[t] \leftarrow 0$  ;
4       $dist[s] \leftarrow 0$ ;  $\sigma[s] \leftarrow 1$  enqueue  $s \rightarrow Q$ 
5      while  $Q$  not empty do
6          extract  $v \leftarrow Q$  with minimum  $dist[v]$ ; push  $v \rightarrow S$ 
7          foreach vertex  $w$  such that  $(v, w) \in E$  do
8              if  $dist[w] = dist[v] + \lambda(v, w)$  then
9                   $dist[w] \leftarrow dist[v] + \lambda(v, w)$ 
10                 insert/update  $w \rightarrow Q$  with new key
11                  $\sigma[w] \leftarrow 0$ 
12                  $Pred[w]$  gets empty list
13             end
14             if  $dist[w] = dist[v] + \lambda(v, w)$  then
15                  $\sigma[w] \leftarrow \sigma[w] + \sigma[v]$ 
16                 append  $v \rightarrow Pred[w]$ 
17             end
18         end
19     foreach  $v \in V$  do  $delta[v] \leftarrow 0$  ;
20     while  $S$  not empty do
21         pop  $w \leftarrow S$ 
22         foreach  $v \in Pred[w]$  do  $\delta[v] \leftarrow \delta[v] + \frac{\sigma[v]}{\sigma[w]} \cdot (1 + \delta[w])$  ;
23         if  $w \neq s$  then  $c_B[w] \leftarrow c_B[w] + \delta[w]$  ;
24 end

```

---

centrality is calculated just from node  $A$  to all other nodes and red edge means, that this edge is on the shortest path to all other nodes.

Change in  $\beta$  value can be seen in Fig. 2, where betweenness centrality is also calculated just from node  $A$  to all other nodes, but there is visible change when  $\beta$  value is changed from 1 to 2 for node  $D$ . Pseudo code of this modification can be seen in Algorithm 2.

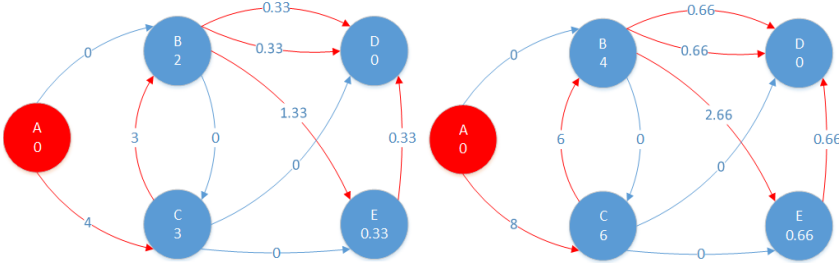


Fig. 1: Comparison of betweenness gain for node A, when  $\alpha_A = 1$  on the left and  $\alpha_A = 2$  on the right

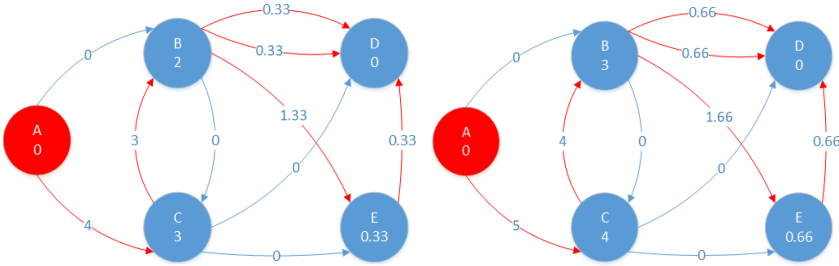


Fig. 2: Comparison of betweenness gain for node A, when  $\beta_D = 1$  on the left and  $\beta_D = 2$  on the right

## 4 Experiments

This experiment was focused on measuring the difference in speeds of the original and modified betweenness centrality algorithm parallelized using MPI on a graph generated from the actual Czech Republic traffic network described earlier as an input. The performance was tested on SALOMON cluster operated by IT4Innovations National Supercomputing Center. Original implementation took in average 4804 seconds generated graph when serial version was used. Modified

---

**Algorithm 2:** Modification of original betweenness centrality for directed graph with edge lengths

---

**input** : directed graph  $G = (V, E)$  with edge lengths  $\lambda : E \rightarrow \mathbb{R} > 0$   
            $\alpha[v]$ : source node importance  
            $\beta[v]$ : destination node importance

**data** : priority queue  $Q$  with keys  $dist[\cdot]$   
           stack  $S$  (both initially empty) and for all  $v \in V$   
            $dist[v]$ : distance from source  
            $Pred[v]$ : list of predecessors on shortest paths from source  
            $\sigma[v]$ : number of shortest paths from source to  $v \in V$   
            $\delta[v]$ : dependency of source on  $v \in V$

**output:** betweenness  $c_B[v]$  for all  $v \in V$  initialized to 0

```

1  foreach  $s \in V$  do
2    foreach  $w \in V$  do  $Pred[w] \leftarrow$  empty list ;
3    foreach  $t \in V$  do  $dist[t] \leftarrow \infty$ ;  $\sigma[t] \leftarrow 0$  ;
4     $dist[s] \leftarrow 0$ ;  $\sigma[s] \leftarrow 1$  enqueue  $s \rightarrow Q$ 
5    while  $Q$  not empty do
6      extract  $v \leftarrow Q$  with minimum  $dist[v]$ ; push  $v \rightarrow S$ 
7      foreach vertex  $w$  such that  $(v, w) \in E$  do
8        if  $dist[w] = dist[v] + \lambda(v, w)$  then
9           $dist[w] \leftarrow dist[v] + \lambda(v, w)$ 
10         insert/update  $w \rightarrow Q$  with new key
11          $\sigma[w] \leftarrow 0$ 
12          $Pred[w]$  gets empty list
13       end
14       if  $dist[w] = dist[v] + \lambda(v, w)$  then
15          $\sigma[w] \leftarrow \sigma[w] + \sigma[v]$ 
16         append  $v \rightarrow Pred[w]$ 
17       end
18     end
19   foreach  $v \in V$  do  $\delta[v] \leftarrow 0$  ;
20   while  $S$  not empty do
21     pop  $w \leftarrow S$ 
22     foreach  $v \in Pred[w]$  do
23        $\delta[v] \leftarrow \delta[v] + \frac{\sigma[v]}{\sigma[w]} \cdot (\alpha[s] + \beta[w] - 1 + \delta[w])$ 
24     end
25     if  $w \neq s$  then  $c_B[w] \leftarrow c_B[w] + \delta[w]$  ;
26 end

```

---

version took 4847 seconds for same graph. Difference in speed of modified version compared to original one is lesser than 1 percent.

## 5 Conclusion

In this paper, we described modification of betweenness centrality from Ulrik Brandes, so it can take into calculation node importance in the graph. Purpose of this modification was that betweenness centrality can give us better understanding when something happens in the graph. For example in traffic routing when some new shop opens, we would like to see how bottlenecks in traffic network will change. So one node can influence betweenness centrality more than others.

Modification was tested and compared with our earlier implementation of original version of algorithm. It was tested on real data set using the graph generated from the Czech Republic traffic network. It is obvious from results in Section 4 that overhead of this modification is under 1 percent. Paper about this modification is in preparation and will be sent to conference ICDMAI 2018, that will be held in India. More tests about original implementation of betweenness centrality algorithm can be found in publication [1].

## References

1. J. Hanzelka, R. Skopal, K. Slaninová, J. Martinovič, J. Dvorský, Graph problems performance comparison using Intel Xeon and Intel Xeon-Phi, ACSS, 2016 (accepted and revised)
2. K. Fujisawa, H.P. Matsuo, Graph analysis & HPC Techniques for Realizing Urban OS, ISC15, 2015
3. L. Lovász, Large Networks And Graph Limits, Colloquium Publications Volume 60, 2012
4. Message Passing Interface Forum, MPI: A Message-Passing Interface Standard : Version 2.2, <http://www.mpi-forum.org/docs/mpi-2.2/mpi22-report.pdf>, cited Feb 28th 2015
5. OpenStreetMap [online], <http://www.openstreetmap.org>, cited Jun 1st 2016
6. U. Brandes, A Faster Algorithm For Betweenness Centrality, Journal of Mathematical Sociology, 2001

# Catch the Stegogramme – Detection of the Steganography Content with the Application of ANN

Jakub Hendrych

Department of Computer Science, FEECS,  
VŠB – Technical University of Ostrava, 17. listopadu 15,  
708 33 Ostrava – Poruba, Czech Republic  
[jakub.hendrych@vsb.cz](mailto:jakub.hendrych@vsb.cz)

**Abstract.** Steganography can be used for illegal activities. It is very important to be prepared. To detect steganography images we have counter-technique known as steganalysis. There are different types of steganalysis, depending on if the original artifact (cover) is known or not. In terms of practical use, most important are methods of “blind steganalysis”, that can be applied to image files and because we do not have the original cover for comparison. This article deals with the application of neural networks on the issues of steganalysis. In our work is important to understand the behavior of the targeted steganography algorithm. Then we can use it as weaknesses to increase the detection capability. In our case we are focus on steganography algorithm OutGuess2.0. We analyze the ability of the detector, which utilizes calibration process and blockiness calculation to detect the presence of steganography message in suspected image. We apply the artificial neural network on this methodology. Resulting detection success rate is discussed in this paper.

**Keywords:** Steganography, steganalysis, neural network, ANN, JPEG

## 1 Introduction

The development of information technologies has brought new opportunities to apply the methods of steganography. It is the art of hiding information into a cover – in computer science the covers are especially images or videos files [1]. The observer is unaware that the picture or video (stegogramme) contains some secret message [2]. Especially the use of steganography on the corporate sector is very dangerous and can lead to leaking of company secrets. Consider a situation where an offender A sent a harmless email with JPEG image to a company network. Accomplish B embeds some company secret to this JPEG image by using steganography system and sends it back to A. Then is easy for A use a steganography decoder to decode the JPEG image and obtain a company secrets. There are many others similar scenarios – consider using of social networks, internet forums, etc. In this case, as the cover was used one

of the most commonly image formats – JPEG – again, for the observer (company security layer) it is just harmless and unsuspecting image.

The opposite of steganography is steganalysis, which serve us to detect a steganogrammes. There are different types of steganalysis, depending on the fact, if the cover is known or not during the analysis. If so, it is “targeted steganalysis”. Otherwise it is called “blind steganalysis”. In terms of practical use, important are especially the analysis techniques of “blind steganalysis”, that can be applied to image and video files.

## 2 Description of related works

If we want to detect steganogrammes, first we must determine with which steganography system (algorithm) was information inserted. There are several types of methodologies, how to enter information into the cover [3]. The simplest method is a modification of the least significant bit (LSB) of image pixel [4, 5]. Modification of the bit may be performed sequentially or randomly. However, these methods of inserting information directly into spatial regions of the image are easily detectable [6]. Therefore, new methods were developed [7]. The information was embedded into the transform domain. The JPEG technology uses the compression that converts image into DCT domain. This DCT domain presents the data as the high and low frequencies. High frequencies are related to the areas of an image with high details, but low frequencies are associated with low details. To reduce the size of JPEG image, some of high details are removed – the human eye is unable to distinguish these areas. So there is no obstacle to modifying these values (DCT coefficients) to hide the secret information. Exactly this methodology is used by the steganography tool OutGuess2.0 [8] on which we are focusing in this paper. It is an open source algorithm and therefore will be most likely used for embedding the secret information into the picture cover. OutGuess2.0 is also implemented with own GUI, which does not need great knowledge of steganography of the end user and increasing the likelihood of use in the corporate sector.

Many of the state of art methods [8 - 10] were tested on the low resolution gray-scale images. This is the feature that does not reflect the realistic scenarios. Some researches were already done. Proposing methods [9, 10] were tested on one low resolution images and detection capability was from 66% - 94% according to the selected steganography algorithm and secret message length. Also the authors [11] propose new methodology based on the universality to detect several steganography algorithms but for the cost of detection success rate. For our detector the emphasis is placed on the high detection success rate, colorful JPEG support, the secret message length invariance and the detection of DCT steganography algorithm OutGuess2.0. Also the high detection success rate (such as [12]) improved by the application of ANN will be discussed in this paper.

### 3 Proposed method

The authors [8, 13] presents a new methods of steganalysis, specifically “blind steganalysis”. Thus, there is not a cover image, that we can compare with the suspected image and detect differences. This disadvantage authors remove by using a method called calibration. The input of this method is a suspected image and the output is a calibrated image. Calibrated image is not a 100% copy of the cover image, but it is very similar. The algorithm of creating the calibrated image is consisted from the several steps, such as cropping and application of different quality factors during the compression.

From the following figures (Fig. 1) we can see how the calibration process works for stegogramme (with 1000B embedded message) and for clear image. Of course comparison of each pixel between the suspect image and the calibrated image cannot be same, but we can clearly see the difference between the stegogramme and clear image.

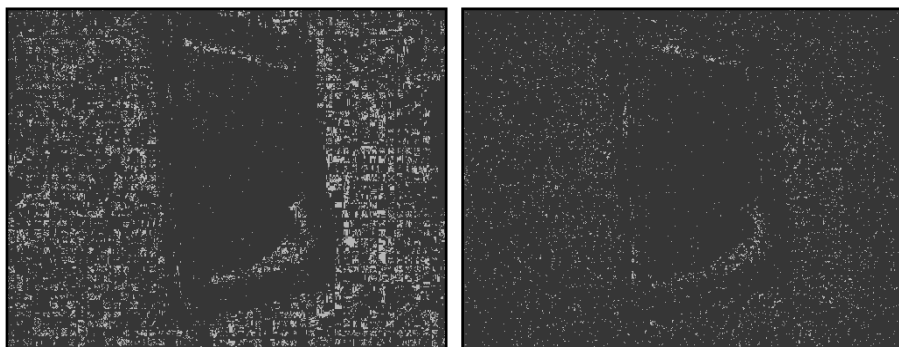


**Fig. 1.** Difference between stegogramme (left) and clear image (right)

We improve the calibration process for colorful JPEG images and from observing and from behavior of steganography algorithm OutGuess2.0 we can see the high frequency domains (high details) are used for embedding the secret message (Fig. 2).

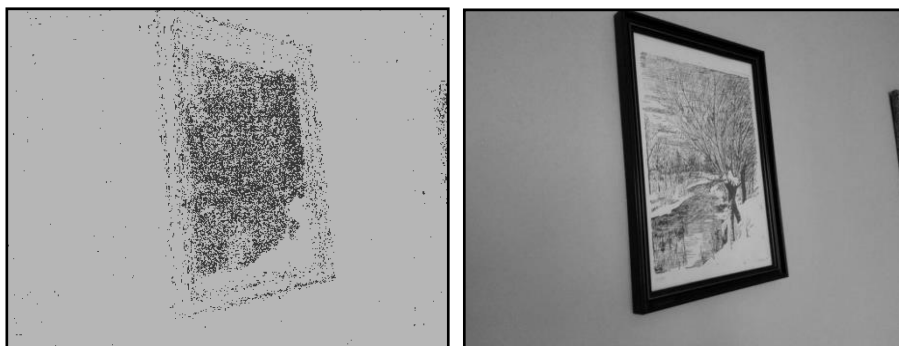


**Fig. 2.** Embedding to the high frequency domain (left) of the stegogramme (right)

If we know, that the OutGuess2.0 is focused on modification of the high frequency domains, we can use this fact for improvement of detection capability. For the blockiness calculation we exclude the low frequency domains of the suspected image, because this areas can distorts the result. This improvement has positive effect on behavior of the detector itself.

We also need to find a metric that would detect the presence of hidden message in the image. This metric must respond to the variable lengths of the messages. The authors [14] present blockiness values. It is a statistical property that is different for the calibrated and the suspected image, so we can determine whether the image is stegogramme. A blockiness value is defined as the sum of spatial discontinuities along the boundary of all 8x8 blocks of JPEG image. In other words, stegogrammes will contain different coefficients along the borders of 8x8 blocks than the clear image.

By combining these two methodologies we can now detect a stegogrammes. Blockiness calculation is applied on suspected and calibrated image. Consequently, we can easily compare both blockiness values  $B_S$  and  $B_C$  to determine whether the suspect image is a stegogramme or not. If the value  $B_S > B_C$  it is a stegogramme. Conversely, if the value  $B_S < B_C$  it is a clear image without the embedded message. Now we will apply the neural network.

Our ANN is consisted from three neurons – two inputs and one output neuron. To the input we sent blockiness values of the suspected and calibrated images. The output then generates a value of 1 or 0. Value 1 indicates stegogramme and value 0 indicates a clear image without any secret message.

## 4 Experiments and discussion

For development and testing purposes, we create a database of color JPEG images (~27 000 images) taken with two devices - Huawei P7 and LG-D605 cameras. The database is consisted from two parts – the test and the train section. Each section contains clear images and stegogrammes created by steganography algorithm OutGuess2.0. Individual's images are available in five different resolutions – 800 x 449, 1024 x 575, 1440 x 809, 2560 x 1438 and 4200 x 2358. For every resolution we prepared 320 images with message length of 10B, 320 images with message length of 50B, same amount of the images for message lengths 200B, 500B, 800B and 1000B.

The following chart (Fig. 3) shows the success rates of the steganography detector with use of the ANN. From the result it is clear that the detector achieves good results. Also, we can confidently say that the detector responds better to the images that have a higher resolution (approximately more than 3 MPx). During the subsequent testing, we also discovered that the success rate of detection is also dependent on the actual length of embedded message, especially in smaller resolution. For this purpose we prepared specific testing sets.



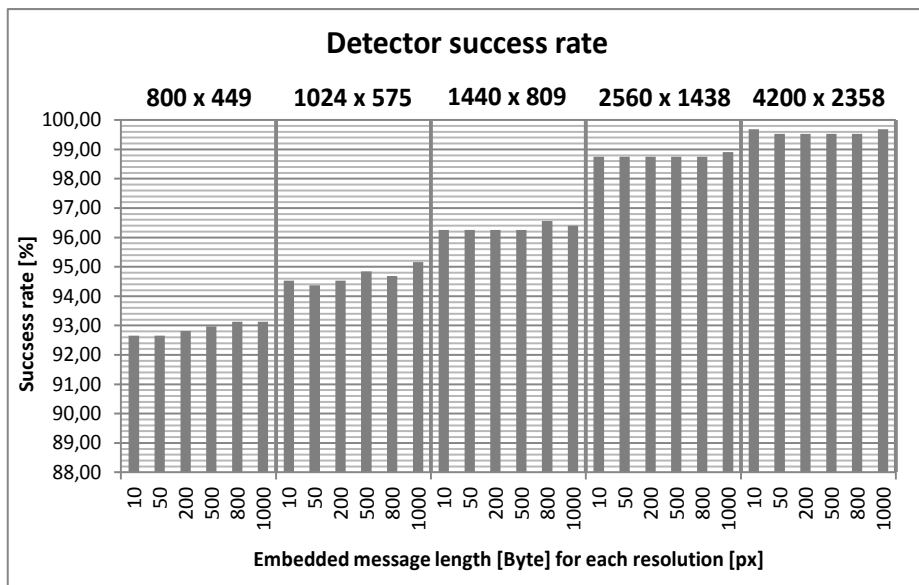


Fig. 3. Chart of success rate of the detection capability with the application of ANN

## 5 Conclusion

In this paper, we discussed detection of the steganography content and detection capability of such detector. Paradoxically, we assumed that embedded messages will be better detectable on the smaller images than the larger ones, since the modification should be easier to detect – the opposite was true, it is done by blockiness calculation, because it is statistical properties and for high resolution we have more data to calculate with smaller distortion. As the addition to this detection process we propose the upgrade that using the weaknesses of behavior of the targeted steganography algorithm OutGuess2.0. This improvement affects the behavior of the detector – the detector is now stricter in classification. If we compare our research to the state of the art methods [8 - 11] we are now able to test even high resolution colorful JPEG images with very satisfying success rate (93% - 99%) for different secret message payload (10B – 1KB).

In the future work, we want to add detection capability for the next DCT steganography systems such as F5 [15] algorithm. Some testing was already done and results are very promising. We also want to implement internet services that include detection of others algorithms such as StegHide or JSteg. These algorithms does not use DCT domain for embedding the message.

The very idea of steganography does not mean necessarily an equivalent to some illegal activity. Can be also used, like digital watermarking, to protect our own data. As well as additional data layer (alternative to metadata) without changing of visual content itself. However, there is always a chance that the steganography will be misusage and that is why we must be prepared.

## Publications

- HENDRYCH, Jakub; LIČEV, Lačezar; KUNČICKÝ, Radim. Detector of the Steganography Images with the Application of Artificial Neural Network. International Multidisciplinary Scientific GeoConference Surveying Geology and Mining Management, SGEM 2017. ISSN: 1314-2704.
- HENDRYCH, Jakub; KUNČICKÝ, Radim; LIČEV, Lačezar. New Approach to Steganography Detection via Steganalysis Framework. 2<sup>nd</sup> International Scientific Conference “Intelligent information technologies for industry”. IITI 2017.

## References

1. DOËRR, Gwenaël; DUGELAY, J.-L. Security pitfalls of frame-by-frame approaches to video watermarking. *IEEE Transactions on Signal Processing*, 2004, 52.10: 2955-2964.
2. MARVEL, Lisa M.; BONCELET, Charles G.; RETTER, Charles T. Spread spectrum image steganography. *IEEE Transactions on image processing*, 1999, 8.8: 1075-1083.
3. BHATTACHARYYA, Souvik. A survey of steganography and steganalysis technique in image, text, audio and video as cover carrier. *Journal of global research in computer science*, 2011, 2.4.
4. CHAN, Chi-Kwong; CHENG, Lee-Ming. Hiding data in images by simple LSB substitution. *Pattern recognition*, 2004, 37.3: 469-474.
5. WANG, Ran-Zan; LIN, Chi-Fang; LIN, Ja-Chen. Image hiding by optimal LSB substitution and genetic algorithm. *Pattern recognition*, 2001, 34.3: 671-683.
6. FRIDRICH, Jessica; GOLJAN, Miroslav. Reliable detection of LSB steganography in color and grayscale images. U.S. Patent No RE40,477, 2008.
7. WALIA, Ekta; JAIN, Payal; NAVDEEP, Navdeep. An analysis of LSB & DCT based steganography. *Global Journal of Computer Science and Technology*, 2010, 10.1.
8. FRIDRICH, Jessica; GOLJAN, Miroslav; HOGEA, Dorin. Attacking the outguess. In: *Proceedings of the ACM Workshop on Multimedia and Security*. Juan-les-Pins, France, 2002.
9. CHEN, CL Philip, et al. A pattern recognition system for JPEG steganography detection. *Optics Communications*, 2012, 285.21: 4252-4261.
10. LIU, Qingzhong, et al. An improved approach to steganalysis of JPEG images. *Information Sciences*, 2010, 180.9: 1643-1655.
11. GUL, Gokhan; KURUGOLLU, Fatih. A new methodology in steganalysis: breaking highly undetectable steganography (HUGO). In: *International Workshop on Information Hiding*. Springer Berlin Heidelberg, 2011. p. 71-84.
12. ANDRIOTIS, Panagiotis; OIKONOMOU, George; TRYFONAS, Theo. JPEG steganography detection with Benford's Law. *Digital Investigation*, 2013, 9.3: 246-257.
13. FRIDRICH, Jessica. Feature-based steganalysis for JPEG images and its implications for future design of steganographic schemes. In: *International Workshop on Information Hiding*. Springer Berlin Heidelberg, 2004. p. 67-81.
14. FU, Dongdong, et al. JPEG Steganalysis Using Empirical Transition Matrix in Block DCT Domain. In: *MMSP*. 2006. p. 310-313.
15. WESTFELD, Andreas. F5—A Steganographic Algorithm. In: *Information Hiding: 4th International Workshop, IH 2001, Pittsburgh, PA, USA, April 25-27, 2001*. Proceedings. Springer Science & Business Media, 2001. p. 289.

# Preprocessing Big Data in Field of Marketing Models using Clusters in Cloud

Tomáš Janečko

Department of Computer Science, FEECS,  
VŠB – Technical University of Ostrava, 17. listopadu 15,  
708 33 Ostrava – Poruba, Czech Republic  
tomas.janecko@vsb.cz

**Abstract.** This paper presents an application of Apache Spark cluster for preprocessing of selected marketing data. Based on available realistic data, Hadoop cluster is reused. Customer behavior is represented by a set of states of the model with assigned rewards corresponding to the expected return value. Outputs then represents analysis of the links between the structured data.

**Keywords:** Apache Hadoop, big data, preprocessing, cloud computing, statistics, telemetry

## 1 Introduction

Since financial institutions such as the one in our article collect extreme amounts of data every day, there is need to sort these bulks of information and extract valuable contexts. These emerging links help marketers to understand sequences of past actions, to learn from them and to extrapolate for future marketing actions. Thus we may include hereby presented methods as a part of strategic marketing planning. Although the area of marketing big data analysis and processing is dynamically developing, it still cannot be considered as prevalent in the daily marketing practice.

## 2 Experiment Design

### 2.1 Solution Files

In our solution we have received several types of documents. The files had to be processed, categorized and passed through their semantic value.

- Files - all received files
- Non dictionary files - files that are not a dictionary and contain "live" data
- Relevant files - files that are not empty and can be used in further analyzes
- Processed files - Files that have been subjected to advanced analysis using Apache Spark

In the next figure 1, it is possible to see the distribution of the total number of files per type. From the collected data shows that 57% of the files contain "live" data collection obtained during use of the system and 86% of the files contain values that can be reused. Of these, 24% of the structured files required the necessary pre-processing in the cloud computing infrastructure.

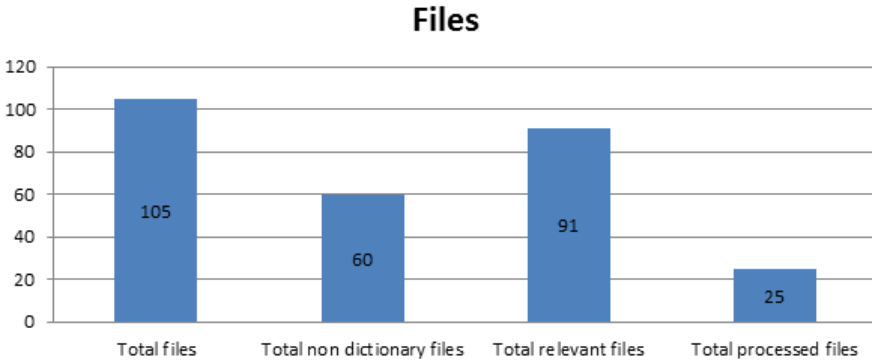


**Fig. 1.** Total count of file types

## 2.2 File Clustering

To obtain more detailed statistics, the source files are grouped according to their meaning and content value. The distribution was made to the following groups:

- appl - application
- bplan - business plan
- clv - customer lifetime value
- contr - contract
- crb2 - credit bureau
- crm - campaign
- dict - dictionary
- chan - channel
- churn2 - churn
- score - scoring
- seg - segment
- visualization - grouped visualizations

After the individual groups were identified, algorithms were designed to reduce the complexity of the data model by correctly selecting the attributes:

- selection of suitable attributes

- selection of appropriate records
- discretion of data

The results of these operations are presented in figure 2. It shows the initial amount of attributes contained in the system and their target number after the preprocessing phase.

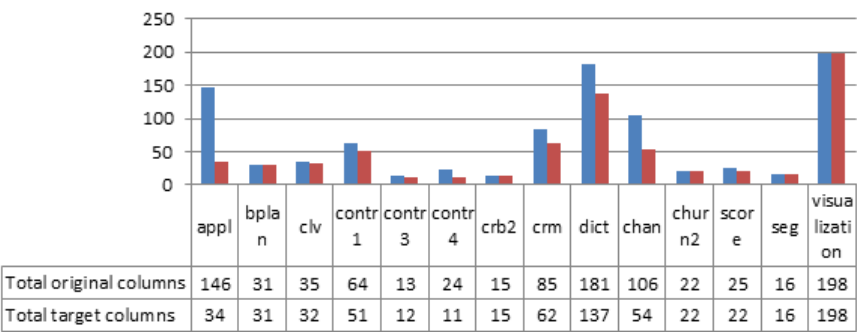


Fig. 2. Attributes per document group

By examining, we came to the conclusion that the largest drop in attributes was in the application section that contained "live" data. These data primarily had a value about users and related to their unambiguous identification. Issues in this area are mainly data confidentiality, personal data protection and processing by third parties.

If we look at the results of this phase from the overall ratio, also here is the data cleansing a major factor. The ratio of the filtered attributes is described in table 1.

- Filtered attributes - the ratio of all removed attributes across the system
- Filtered processing attributes - the ratio of all dropped attributes in files that have been preprocessed in Apache Spark

Table 1. Attributes filter ratio

Attributes	Filter ratio
Filtered attributes	28,21%
Filtered processing attributes	35,59%

The same steps that were applied to the attributes (vertical axis) were also performed within individual records (horizontal axis). This has resulted in the

reduction of entities that would ultimately distort the calculated models. The ratio of filtered entities is described in table 2.

- Filtered rows - the ratio of all deleted records across the system
- Filtered processing rows - the ratio of all deleted records in files that have been pre-processed in Apache Spark

**Table 2.** Rows filter ratio

Rows	Filter ratio
Filtered rows	15,90%
Filtered processing rows	20,90%

The resulting view of the entire dataset is presented in table 3.

- Total original cells - total number of cells in the system
- Total cells - total number of cells in the system after the pre-processing phase
- Cell loss ratio - ratio of all filtered cells

**Table 3.** Total cells ratio

Cells	Cells ratio
Total original cells	3303352118
Total cells	2092834204
Cells loss ratio	36,65%

In summary, we have reached the data structure, which is reduced by about 1.2 billion cells, while a significant part is still formed by the dictionaries.

**2.3 Performance**

During all operations, the duration of individual operations and system performance was recorded. The technical specification of the infrastructure that was used is as follows:

- Apache Spark - version 2.1.0 (Linux)
- Master - 2 nodes
- Slave - 4 nodes

Master nodes are machines that are memory optimized due to the high demands on the synchronization of the entire process. In the detailed description of each machine, the configurations were as follows:

- Master node - 4 cores, 28 GB RAM, 200 GB SSD
- Slave node - 8 cores, 28 GB RAM, 400 GB SSD

The overall robustness of the architecture is presented in table 4.

**Table 4.** Infrastructure resources overview

Total cores	Total memory (GB)	Total storage (TB)
40	168	2

The results of the measurements and the average values obtained are presented in table 5. The table aggregates metrics related to attributes, records and also a conversion of performance to 1 million records. The measurements obtained are output from the Apache Spark platform.

**Table 5.** Performance metrics

Average processing time per column/file (s)	Average processing time per column/mil. rows (s)	Average rows processing time (s)
0,84	0,21	0,02

### 3 Results

Over a group of obtained data was necessary to analyze the links between the structured files and to perform operations that work with the raw data structure on the basis of the discovered relations. These steps were necessary to uncover the nature and patterns in the data.

Upon closer measurement, it was found that the dataset contains a total of approximately 3.3 billion atomic cells representing a specific value of the attribute in the system. From the above findings, it has become clear that the *Big Data Ecosystem* will need to be used for further data processing. For our solution was selected technologies *Apache Spark*.

## 4 Conclusion

From the above findings, we came to the conclusion that the main problem in the data was their confidentiality. This whole area is therefore based on a cloud data protection solution. One possible solution to this problem is to use homomorphic encryption. A fully homomorphic scheme can be used in many applications, and one of these can be, for example, the implementation of secure cloud computing [4].

This problem was partially resolved by Craig Gentry in his dissertation, describing the use of a fully homomorphic encryption scheme (FHE). Thanks to Gentry's technology, the analysis of encrypted information can produce as detailed results as if the original data were fully readable to all [5].

The results from these experiments were published in MENDEL - Soft Computing Journal, Volume 23, No. 1, June 2017, ISSN: 1803-3814.

**Acknowledgement:** The following grants are acknowledged for the financial support provided for this research: Grant Agency of the Czech Republic - GACR P103/15/06700S, Grant of SGS No. SGS 2017/134, VSB-Technical University of Ostrava. The Ministry of Education, Youth and Sports from the National Programme of Sustainability (NPU II) project IT4Innovations excellence in science - LQ1602. Research presented in this article was conducted in collaboration with PricewaterhouseCoopers Česká republika, s.r.o.

## References

1. Wessling, H.: Aktivní vztah k zákazníkům pomocí CRM: strategie, praktické příklady a scénáře. Praha: Grada, 2003. Manažer. ISBN 8024705699.
2. Zaharia, M.: Apache Software Foundation, UC Berkeley AMPLab, Databricks. <http://spark.apache.org/docs/latest/> (2017). [Online; accessed 3-May-2017]
3. Laskowski, J.: Mastering Apache Spark 2. <https://www.gitbook.com/book/jaceklaskowski/mastering-apache-spark/details> (2017). [Online; accessed 20-June-2017]
4. Pejlová, A.: Homomorphic encryption schemes. Charles University, Faculty of Mathematics and Physics (2013)
5. Gentry, C.: A Fully Homomorphic Encryption Scheme. Symposium on the Theory of Computing (STOC), 2009, pp. 169-178
6. Microsoft Corporation: Azure Windows VM. <https://docs.microsoft.com/en-us/azure/virtual-machines/windows/sizes-general> (2017). [Online; accessed 20-June-2017]
7. Stehlé, D., Steinfeld, R. : Advances in Cryptology - ASIACRYPT 2010: 16th International Conference on the Theory and Application of Cryptology and Information Security, Singapore, December 5-9, 2010. Proceedings. ISBN: 978-3-642-17373-8



# An Overview of Parallel Itemset Mining Algorithms

Adam Kašpar, Vojtěch Kotík, and Jan Platoš

Department of Computer Science, FEECS,  
VŠB – Technical University of Ostrava, 17. listopadu 15,  
708 33 Ostrava – Poruba, Czech Republic  
{adam.kaspar, vojtech.kotik, jan.platos}@vsb.cz

**Abstract.** This paper is an overview of itemset mining algorithms and the published parallel approaches. First chapter of this paper will discuss about the main motivation, why to use itemset mining algorithms and what are the main pros of their parallelization as well. At the second chapter, I will discuss more deeply about itemset mining algorithms and also about the differences between them. Third part will discuss about parallelization of Apriori based Eclat algorithm together with achieved results. At the conclusion I will discuss about my current results and about my future research.

**Keywords:** data mining, apriori, big data, algorithm, computations, parallelization

## 1 Introduction

Big data is a term that describes the large volume of data both structured and unstructured that inundates a business on a day-to-day basis. But its not the amount of data thats important. Its what organizations do with the data that matters. Big data can be analyzed for insights that lead to better decisions and strategic business moves.

Currently, we have a large amount of computational algorithms. Most of them is based on Apriori algorithm. Data mining algorithms are divided into two based branches - string mining and itemset mining.

String mining typically works with closed alphabet for elements that occurs in a sequence. String sequence could have various length. A typical use case of string mining could be found in conjunction with DNA research. String mining is here used for examination of known patterns of DNA sequences[1].

Itemset mining is useful for problems, related to sequence mining. A typical use of itemset mining is in marketing applications for discovering regularities between items on shopping lists.

Among commonly used algorithms for string mining belongs PrefixSpan, FreeSpan and for itemset data mining belongs FP-Growth, FP-Tree, Eclat, Max-Miner. Some of them I will describe at this paper.

## 2 Association rule mining

Association rule learning is a rule-based machine learning method for discovering interesting relations between variables in large databases. It is intended to identify strong rules discovered in databases using some measures of interestingness[2]. Example of these strong rules are association rules for discovering regularities between products that appears on receipt. For example, let's have rule  $\{\text{apple, orange}\} \Rightarrow \{\text{strawberry}\}$ . This rule indicates, that if customer buys apple and orange together in one purchase, than the most likely the customer will have also strawberry in his shopping cart.

### 2.1 Apriori algorithm

Apriori is a base algorithm, belonging into frequent item set algorithms. The main idea is based on searching of larger and larger sets of items as those item sets occurs sufficiently often in the database[3].

Algorithm was designed by Agrawal and Srikant in 1994. Apriori works over databases, with transactions. These transactions could be for example collections of shopping cart items, bought by customers.

**Basic functionality.** Apriori works with "bottom up" approach, it means, that at each step of algorithm are frequent subsets extended about new item. This step is called as candidate generation. After the candidate generation, resulted groups of candidates are tested against the data in the database. The algorithm ends, when no extension of frequent subsets is found. Entire scheme of apriori algorithm is visible on the figure 1.

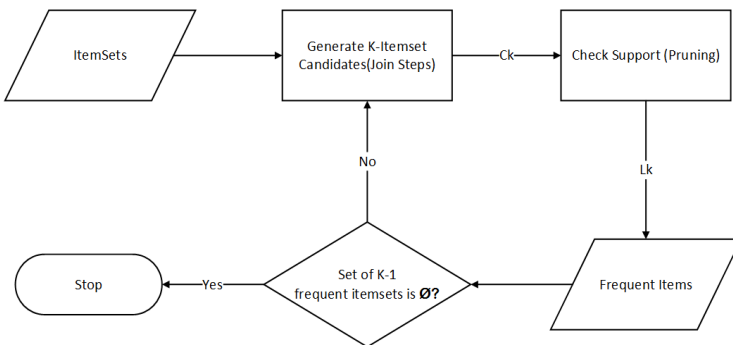


**Fig. 1.** Apriori algorithm scheme.

## 2.2 Eclat

Eclat (Equivalence Class Transformation) algorithm belongs among frequent itemset mining algorithms. This algorithm was first introduced by Mohammed J. Zaki, Srinivasan Parthasarathy, Wei Li and Mitsunori Ogihara in 1997 [3].

**Basic functionality.** The basic idea is based on depth-first search mining using set intersection. Algorithm is suitable for sequential and also parallel execution. At the beginning, algorithm expects vertical database as his input. After that, Eclat works with tid-set of each item and verifies, that each itemset-tidset pair  $\langle X, t(x) \rangle$  with all the others pairs  $\langle Y, t(Y) \rangle$  to generate new candidates  $N_{xy}$ . If the candidate  $N_{xy}$  is frequent, then this candidate is added to the set  $P_x$ . Then, recursively, it finds all the frequent itemsets in the  $X$  branch[4], see pseudo-implementation on listing below.

---

**Algorithm 1:** Eclat(Transactions:  $T$ , Minimum support:  $minsup$ )

---

```

1 begin
2   Initialize set  $\mathcal{ET}$  to single tuple  $(Null, T)$  ;
3   while any node in  $\mathcal{ET}$  has not been examined do
4     Select an unexamined tuple  $(P, T(P))$  from  $\mathcal{ET}$  for examination;
5     Generate candidates extensions  $C(P)$  of each tuple  $(P, T(P))$ ;
6     Determine frequent extension  $F(P) \subseteq C(P)$  by support counting of
       individual items in smaller projected database  $T(P)$ ;
7     Remove infrequent items in  $T(P)$ ;
8     foreach each frequent item extension  $i \in F(P)$  do
9       Generate  $T(P \cup \{i\})$  from  $T(P)$ ;
10      Add  $(P \cup \{i\}, T(P \cup \{i\}))$  into  $\mathcal{ET}$ ;
11    end
12  end
13  return set of tuples  $\mathcal{ET}$ 
14 end

```

---

Main advantage of Eclat is, that this algorithm have very fast support counting. On the other hand, among main disadvantage of this approach is that intermediate tid-lists may become too large for memory[8].

## 2.3 FP-Growth

The Frequent Pattern Growth (FP-Growth) algorithm was firstly proposed by J.Han in 2000[5]. In his work, Han proved, that FP-Growth is more efficient, than other frequent pattern methods, like for example well-known Apriori[6] algorithm or Eclat[3].

FP-Growth algorithm is one of the possible ways, how to find frequent itemsets. Concretely, it uses a divide-and-conquer strategy. As a base algorithm is

used special data structure, named as frequent-pattern tree (FP-tree). Algorithm works as follows: first of all, it creates FP-Tree. This tree structure represents frequent items. After this step, the FP-Tree is divided into a set of conditional databases. Each database is then mined separately.

Main advantage of this algorithm against Apriori is, that FP-Growth reduces the search costs looking for short patterns recursively and then concatenating them in the long frequent patterns, offering good selectivity.

From performance reasons, for large databases, it isn't possible to hold entire FP-Tree in the main memory. Solution is to divide database into set of smaller databases and then construct an FP-Tree from each smaller database[7].

**FP-Tree structure.** Structure of FP-Tree consists of following elements. Tree contains root node, which is labeled as null element. This element references child elements, named as item-prefix subtrees[5].

Each node in item-prefix subtree consists of these fields:

- Item ID
- Count: the number of transactions represented by the portion of the path reaching the node.
- Node-link: links to the next node in the FP-tree carrying the same item-name, or null if there is none.

After the FP-Tree is constructed, then FP-Growth algorithm is called. See figure 2, where entire FP-Tree structure is sufficiently explained.

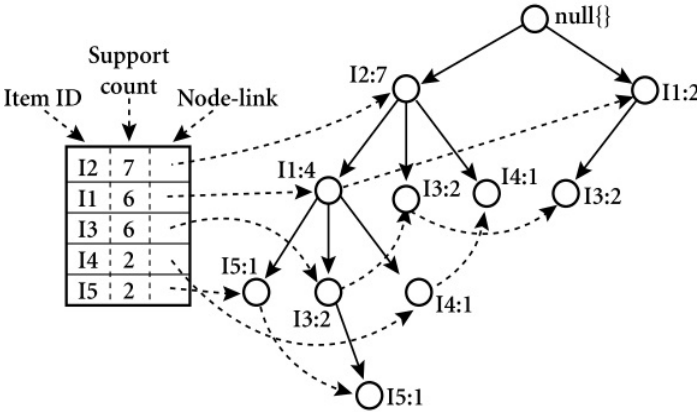


**Fig. 2.** FP-Tree structure[7].

### 3 Parallel implementation of Apriori algorithm

This section contains a description of our preliminary results in Apriori algorithms that was parallelized using OpenMP technology. Our implementation is adaptation

of the Eclat approach with vertical organization of transactions. As was mentioned earlier, the Eclat algorithm works in iterations, and three phases are processed in each iteration.

1. Candidate generation phase where a list of candidates of length  $k$  is generated from the frequent itemsets of length  $k - 1$ .
2. Computation of the support phase where a support is computed for each generated candidate.
3. Pruning phase where the candidates with support lower than a min-support are removed.

The experiments shows that he bottle-neck of the algorithm is the second phase, where the support is computed. We used parallelization of this phase using the OpenMP.

### 3.1 Results

In our experiments we used a Windows based system with 2x Intel Xeon E5-2680 v2 @ 2.8GHz 10 core, 768 GB RAM. The dataset used in our experiments is Supermarket dataset from the Weka software. We tested our algorithm on two version of a dataset. One has 925,400 transactions, and the second has 4,627,000 transactions and 216 features. The results are depicted in Figure 3.

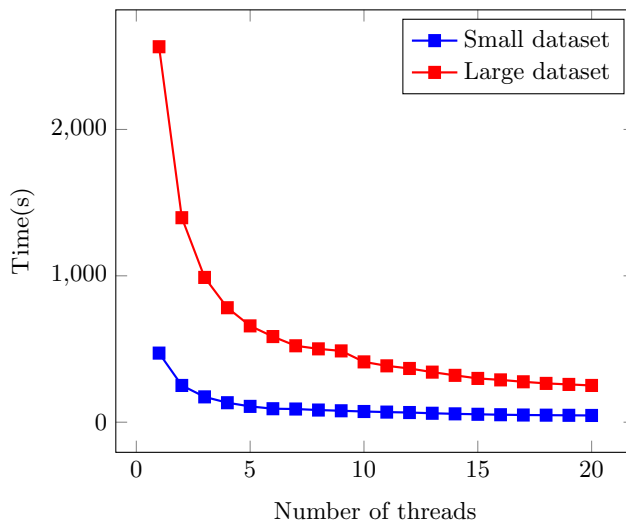


**Fig. 3.** Processing time of parallel version of Eclat algorithm on small (S) and large (L) dataset with different number of threads used.

As may be seen, the second phase is really the most important, because when the number of threads is increased by factor two, the time decreases with the

same factor. This preliminary results shows that the parallelization is possible, but it is limited by the amount of memory. The tested dataset is small even in its full variant. We set the minimum support to 0.1 and the maximum speed-up of 90.3%.

## 4 Conclusion and future work

The itemset mining and associative rule mining algorithm is very useful tool in data analysis. More exactly, this tools may discover the hidden relations between set of items, such as shopping carts, medical results, web logs, etc.

In these day, where such data volume is growing and becomes millions and billions transactions with thousands features it is necessary to design efficient parallel version of the algorithm.

In this paper, we presented a review of published parallel version of classical algorithm as well as preliminary results of our applications. The algorithm are efficiently parallelize but the algorithm have to be modified to maintain reasonable memory requirements. This will be the future work in this task.

## Acknowledgment

This work was supported by the project SP2017/100 “Parallel processing of Big Data IV”, of the Student Grant System, VŠB-Technical University of Ostrava.

## References

1. Mohamed Abouelhoda, Moustafa Ghanem: String Mining in Bioinformatics. Springer Berlin Heidelberg, Berlin (2010)
2. Gregory Piatetsky-Shapiro, William J. Frawley: Discovery, Analysis and Presentation of Strong Rules. AAAI/MIT Press, Cambridge, MA (1991)
3. M. Zaki, S. Parthasarathy, M. Ogihara, and W. Li: New Algorithms for Fast Discovery of Association Rules. AAAI Press, Menlo Park, CA, USA (1997)
4. Mohammed Javeed Zaki, Srinivasan Parthasarathy, Mitsunori Ogihara, and Wei Li: New Algorithms for Fast Discovery of Association Rules. University of Rochester, Rochester NY (1997)
5. J. Han, H. Pei, and Y. Yin: Mining Frequent Patterns without Candidate Generation. ACM Press, New York, NY, USA (2000)
6. Rakesh Agrawal, Ramakrishnan Srikant: Fast Algorithms for Mining Association Rules. IBM Almaden Research Center, San Jose, CA (1991)
7. Jiawei Han and Micheline Kamber: Data Mining: Concepts and Techniques. Morgan Kaufmann (2006)
8. Jiawei Han, Vipin Kumar: CIS527: Data Warehousing, Filtering, and Mining Lecture. CIS, Temple University (2004)

# Evolutionary Synthesis of Artificial Neural Networks

Lumír Kojecký

Department of Computer Science, FEECS,  
VŠB – Technical University of Ostrava, 17. listopadu 15,  
708 33 Ostrava – Poruba, Czech Republic  
lumir.kojecky@vsb.cz

**Abstract.** This article describes part of our research focused on mutual comparison of dynamics of swarm and neural based algorithms – synthesis of artificial neural networks, whose dynamics is then analyzed. We focused on synthesis by means of Analytic Programming, creating networks of tree structure, and then on pure evolutionary synthesis, creating networks with an arbitrary graph structures.

**Keywords:** Artificial Neural network, Evolutionary algorithm, SOMA, PSO, Open MPI

## 1 Introduction

Our current research is focused on swarm and neural based algorithms that represent a class of search methods that can be used for solving optimization problems and challenges of learning. These are two different kinds of algorithms, distinct in its nature, however, they have common attributes of its dynamics – both are based on parallelism, both process and store information, exhibit universal behavior like chaos, intermittence, etc.

The main aim of this paper is to show our approaches how to synthesize a neural network structure, and how to train the network for the further analysis of its behavior. For our experiments, specific hardware and algorithms have been used. All relevant information about algorithms is mentioned and referred here. In fact, we have merged artificial neural networks, evolutionary and swarm algorithms with parallel programming and hardware.

## 2 Used Methods and Algorithms

### 2.1 Self-Organizing Migrating Algorithm

Self-Organizing Migrating Algorithm (SOMA) is a swarm-based optimization algorithm [3] imitating cooperative behavior of individuals searching the best food source. Each individual is represented as a point in  $N$ -dimensional hyperspace and process of searching are in essence vector operations between these points. Quality of the food source, individual's fitness, is determined by so-called fitness

(cost) function  $f_{cost}$ . Purpose of SOMA (and also another optimization algorithms) is in fact searching the global minimum of  $f_{cost}$  on the desired interval.

SOMA is initialized by randomly generated population of individuals, where each individual is evaluated by  $f_{cost}$ . At the start of each migration loop is chosen an individual with the best fitness – the leader. All other individuals then move through the space towards the leader, searching their best position with the best fitness on the way. Exploration of the hyperspace in allowed dimensions is controlled by so-called binary perturbation vector (PRT), which is created before each individual's step towards the leader. As a result, individuals do not move directly towards the leader and probability of finding the global minimum increases.

## 2.2 Particle Swarm Optimization

Particle Swarm Optimization (PSO) is also swarm-based optimization algorithm [1], inspired by social behavior of animals/insects. The principle of PSO is based, like in SOMA, also on following individuals (particles) with better fitness. Purpose, individual definition, or  $f_{cost}$  definition is the same like in SOMA.

PSO is also initialized by randomly generated population of particles with a randomly initialized velocity vector, where each individual is also evaluated by  $f_{cost}$ . Each particle stores its position  $pBest$  with its so far best fitness value in its local memory. A particle position  $gBest$  with the population best fitness value is stored in a common population memory. In each migration loop, each particle velocity vector is recalculated, and all particles are moved to their new positions according to the vector. The vector recalculation is based on the current particle position,  $pBest$  position, and also  $gBest$  position.

## 2.3 Parallel SOMA

As will be described in Sec. 3, synthesis of an ANN includes an evolutionary design of the ANN structure and also, in each  $f_{cost}$ , another evolutionary estimation of synapse weights. This process (called metaevolution [4]) is very computationally intensive and takes a huge amount of time – more than 30 hours on a single computer with a relatively small network.

Therefore, to reduce the computational time, the evolutionary algorithms were implemented also in Open MPI, one of the most widespread programming architecture. Since the evaluation time of each individual is generally different (each ANN can consist of different number of synapses), we implemented [2] a master-slave load balancing algorithm where the master rank distributes the work to slave ranks to evaluate each individual.

## 3 Experiment Design

We focused on two approaches to synthesize an artificial neural network. The first approach is by means of Analytic Programming, which synthesizes ANN as a



mathematical expression. The second approach synthesizes ANN with arbitrary (i.e. complex network) structure by evolutionary graph synthesis.

In our previous research we investigated several evolutionary algorithms and their impact on symbolic regression. Based on the results, SOMA will be used to synthesize the network structure, and PSO will be used to estimate values of the used constants (i.e. weights).

Cost function definition is the same for both approaches. At the input there is an ANN and training set with a sample (i.e. XOR) problem. The function returns the total error of the network.

### 3.1 Synthesis by Means of Analytic Programming

Analytic Programming (AP) [6] is one of methods of symbolic regression, where a simple elements (like mathematical operators or variables) are composed into a more complex units like mathematical function. This process can be used for example to synthesize the most suitable mathematical formula to approximate an input data, to synthesize a logical circuit whose output function corresponds to the truth table, or to synthesize an ANN that properly responds to inputs from a training set.

The main principle of AP is the composition of simple elements into a more complex units. The simple elements are placed in so-called General Functional Set (GFS), which consists these three elements for our purposes:

1.  $+$  – a simple addition function with two arguments
2.  $AN$  – an artificial neuron – parameterized hyperbolic tangent function
3.  $K \cdot x$  – a weighted input for the AN

At the AP input there is a set of integers-pointers to the GFS. At the output there is a synthesized ANN that consists of the indexed elements – arguments of the elements are substituted in a FIFO order as next indexed elements. The process is visualized in Fig. 1. To find the most suitable ANN structure it is necessary to find the best input number set that can be represented as an individual in arbitrary evolutionary algorithm (i.e. SOMA or PSO).

After ANN structure synthesis there are several parameters-constants (i.e. parameter of  $AN$  or weight of an input), whose values are not known at this time. It is therefore necessary to estimate values of these constants by means of a secondary evolutionary algorithm.

Current ANN synthesis approach by means of AP is designed to synthesize ANN with only one or two inputs [5], placed as inputs  $x$  and  $y$  into the GFS. Our goal is, however, to synthesize an ANN with arbitrary number of inputs. Therefore, we placed only one general input  $x$  into the GFS. At the time of ANN composition, the variable is indexed, and the particular input value is used. The indexation is based on round-robin technique – for example for two network inputs, the input sequence will be  $x_0, x_1, x_0, x_1, \dots$ .

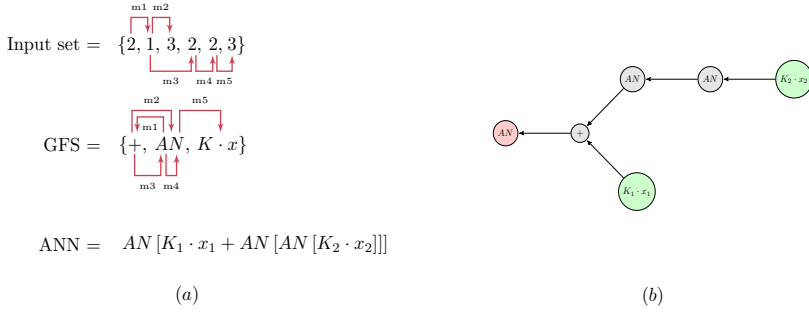


**Fig. 1.** Illustration of the expression synthesis process (a) and its output visualization (b) as a graph. The green nodes represent the network input, while the red node represents the network output

### 3.2 Synthesis by Means of Evolutionary Algorithm

In the process of synthesis of an ANN structure by means of EA, individuals are generated in range  $[0, 1]$  like  $[0.91 \ 0.75 \ 0.32 \ 0.64]$ . This vector of dimension  $n^2$  is then converted into the  $n \times n$  matrix  $\begin{bmatrix} 1 & 1 \\ 0 & 1 \end{bmatrix}$ , where each item is rounded. This matrix represents an adjacency matrix of the result graph – neural network.

In the network,  $x$  nodes having at least one output connection are marked as inputs,  $y$  nodes having at least one input connection, are marked as outputs. Then, non-input nodes with no input connection and non-output nodes with no output connections are removed. In the adjacency matrix, edges are considered as weighted ( $w_i$ ). Like all parameters in AP, all weights  $w_i$  are estimated by means of a secondary evolutionary algorithm to get the lowest network error for the training set. A sample weighted adjacency matrix and its corresponding graph is visualized in Fig. 2.

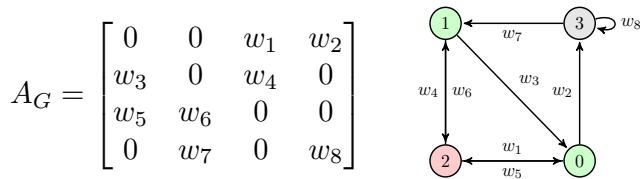


**Fig. 2.** A weighted adjacency matrix and its network. The green nodes (0 and 1) represent the network input, while the red nodes (2) represent the network output

## 4 Results

Simulations were performed on Anselm, x86-64 based cluster hosted at national supercomputing center IT4Innovations. The simulations were done for both synthesis by means of AP and EA. Each simulation provided an ANN that successfully responded to provided training set (mainly XOR problem). An example of the output ANN is visualized in Fig. 3 for AP synthesis, and Fig. 4 for EA synthesis.

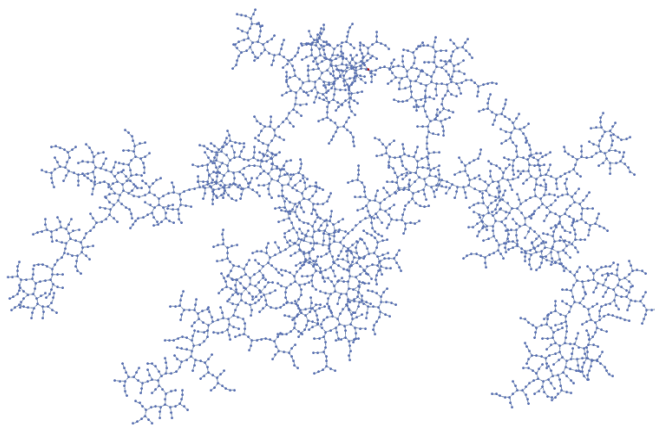


**Fig. 3.** A sample generated network containing 500 nodes to solve the XOR problem

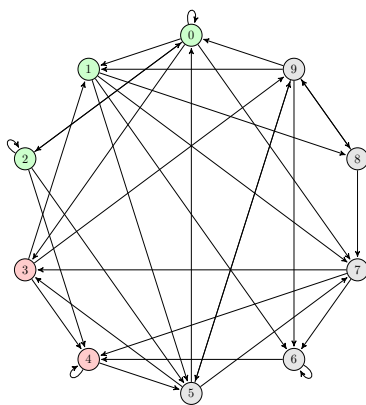


**Fig. 4.** A sample network structure to solve the XOR problem. The green nodes represent the network input, while the red nodes represent the network output

## 5 Conclusion

In this paper we synthesized several neural networks that successfully responded to provided training set for both proposed approaches. One (AP) provided results in form of tree structure, the other synthesized neural networks in form of an arbitrary graph (i.e. complex network), whose dynamics was analyzed in one of our publications.

The process of synthesis by means of AP took several minutes on Anselm for hundreds of elements ( $n$ ) – addition function or artificial neuron – each element has up to two connections with evolutionary estimated parameters. In synthesis by means of EA there are  $\mathcal{O}(n^2)$  estimated parameters and the process takes huge amount of time – parallel processing is necessary.

As was mentioned above, we are trying to find similarities in dynamics behavior between ANN and EAs, and in the future we want to open following questions: What range equivalence between parallel algorithms like ANN and swarm systems exists? Is there only dynamical equivalence or also topological one? What impact have different dynamical regimes on the system information capacity processing?

The full version of this paper, including analysis of cellular automata, complex networks, or deterministic chaos was sent as a chapter to the High-Performance Simulation Based Optimization book.

## Acknowledgment

The following grants are acknowledged for the financial support provided for this research: Grant Agency of the Czech Republic – GACR P103/15/06700S, Grant of SGS No. SGS 2017/134, VSB-Technical University of Ostrava. The Ministry of Education, Youth and Sports from the National Programme of Sustainability (NPU II) project "IT4Innovations excellence in science - LQ1602".

## References

1. Kennedy, J., Kennedy, J.F., Eberhart, R.C.: Swarm intelligence. Morgan Kaufmann (2001)
2. Kojecký, L., Zelinka, I., Šaloun, P.: Evolutionary synthesis of automatic classification on astroinformatic big data. *International Journal of Parallel, Emergent and Distributed Systems* pp. 1–19 (2016)
3. Onwubolu, G.C., Babu, B.: New optimization techniques in engineering, vol. 141. Springer Science & Business Media (2004)
4. Oplatková, Z.: Metaevolution-synthesis of evolutionary algorithms by means of symbolic regression. Tomas Bata University in Zlín (2008)
5. Vařacha, P.: Neural network synthesis (2011)
6. Zelinka, I.: Analytic programming by means of soma algorithm. In: *Proceedings of the 8th International Conference on Soft Computing, Mendel*. vol. 2, pp. 93–101 (2002)

# New Approach To Steganography Detection Via Steganalysis Framework

Radim Kunčický

Department of Computer Science, FEECS,  
VŠB – Technical University of Ostrava, 17. listopadu 15,  
708 33 Ostrava – Poruba, Czech Republic  
radim.kuncicky@vsb.cz

**Abstract.** The aim is to propose basic steganalytical tool that can use multiple methods of analysis. We describe two detection methods that were implemented. These methods include improved detection capability than conventional steganalytical tools thanks to use of artificial neural network and several other innovative improvements. In our work is important to understand the behavior of the targeted steganography algorithm. Then we can use its weaknesses to increase the detection capability. We analyze prepared stegogrammes by application of several conventional algorithms such as image difference.

Two of our plug-ins are focused on steganography algorithms Steghide, OutGuess2.0 and F5. These algorithms are open source and easy accessible, so the risk of their abuse is high. We use several approaches, such as calibration process and blockiness calculation to detect the presence of steganography message in suspected image. Calibration process is designed for creation of calibration image, that represents the original cover work and for comparison to suspected image. Blockiness calculation serves us as a statistical metric that react to the presence of secret message. Next we deploy the artificial neural network to improve detection capability.

Second plug-in utilizes a detection method that is based on analysis of inner structures of JPEG format. This detection method uses overall quality calculation based on quantization tables and Huffman coding table. These informations are processed by neural network that is able to decide whatever the suspicious file contains embedded data and which steganography algorithm was used to create this file.

**Keywords:** Steganography, Steganalysis, JPEG, ANN, Stegogramme, Out-Guess, F5, Steghide

## 1 Introduction

The rise of computers opened new possibilities for criminals and created new security discipline - cybercrime. The new computer world created new possibilities for usage of cryptography. Nowadays almost all data transfers are protected with cryptographic methods. But we can still detect that the data are transferred and cryptanalysts can attempt to break used cipher. Along with cryptography exists very close, but not so known discipline – the steganography.

Main aim of steganography is to hide a data in some kind of cover. Incidental observer is unaware that the picture or video [1] (stegogramme) contains some secret message [2].

## 2 Description of related works

Threat by steganography is very high. Many of the steganography algorithms were developed [3]. From the simplest one as a modification of the least significant bit (LSB) of image pixel [4, 5] to more advanced algorithms that using transform domain for embedding a secret message [6]. The example of such algorithms: Steghide, F5 and OutGuess2.0 [7] on which we are focusing in this paper. These algorithms are also implemented with own GUI, which does not need great knowledge of steganography for the end user. This fact also increases the likelihood of using in a corporate sector.

Many of the state of art methods [7 - 9] were tested on the low resolution grayscale images. This is the feature that does not reflect the realistic scenarios. Proposing methods [8, 9] were tested on one low resolution images and detection capability was from 66% - 94% according to the selected steganography algorithm and secret message length. Also the authors [10] propose new methodology based on the universality to detect several steganography algorithms but for the cost of detection success rate.

A lot of detection methods were introduced in past, but nowadays there are still no complex frameworks aimed to detect such a steganography images. This is essence of our work. We suggest a development of plug-in based framework that allows a complex analysis of JPEG format. For our framework the emphasis is placed on the high detection success rate, colorful JPEG support, the secret message length invariance and the detection of DCT steganography algorithms Steghide, F5 and OutGuess2.0. Also the high detection success rate (such as [11]) improved by the application of ANN will be discussed in this paper. We will describe first two detection methods that we implemented and improved.

## 3 Proposed methods

### 3.1 Detection method based on Huffman table coding analysis

This detection method was introduced in [12]. During a research we found some innovative ways how to improve this detection algorithm. Our implementation allows not just steganography file detection but gives a possibility to detect exact steganography algorithm that was used to create the file. The method involves artificial neural network that is used to analyze Huffman coding table which is a part of JPEG format.

Huffman coding is used to code values of discrete cosine transformation with variable length codes which are assigned according to statistical probabilities. Frequently used values are coded with short codes and vice versa. JPEG format contains up to 4

Huffman coding tables that defines mapping between codes and values. Direct current part (DC) and alternate current part (AC) of discrete cosine transformation coefficients are coded separately for luminance component (Class 0) and red and blue component (Class 1). Values in each table generally show count of each code lengths that appears in image file. We interpret these tables as histograms of codes lengths. During steganography data injection some changes in Huffman coding occurs. These changes contain some hidden pattern that can be found in every steganography file and is unique to each steganography tool. Example of Huffman tables before and after manipulation can be found in Figure 2.

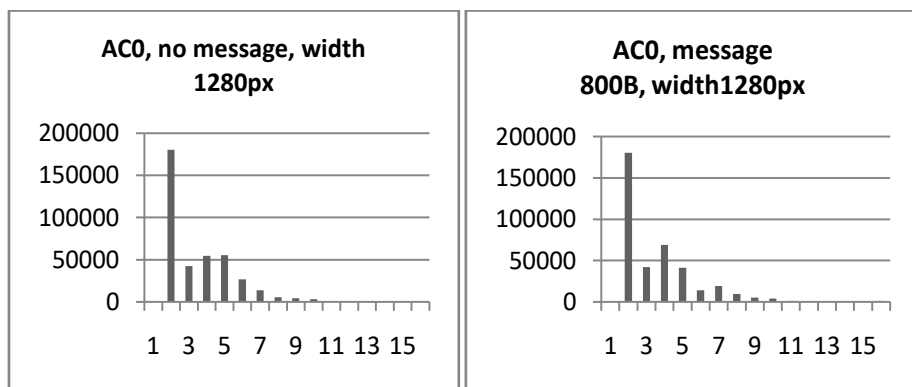


**Fig.1.** Huffman coding table for clear image (left) and the same image with steganography embedded data (right)

Other points of interest are image resolution, which gives an idea about total number of codes and quality of each image component (chrominance and luminance) that gives an idea about compression ratio.

### 3.2 Detection method based on calibration process and blockiness calculation

The JPEG technology uses the compression that converts image into finite frequency domain. This domain presents the data as the amplitudes of high and low frequencies. High frequencies are related to the areas of an image with high details, and low frequencies are associated with low details. To reduce the size of JPEG image, some of high details are removed – the human eye is unable to distinguish these areas. There is no obstacle to modifying these values (DCT coefficients) to hide the secret information. Exactly this methodology is use by the steganography tools OutGuess2.0 and F5.

The authors in [7, 12] present a new method for the blind steganalysis. This method uses no cover image, that we can compare with the suspected image and detect differences. This disadvantage is overcome by using a method called calibration process. Output of this method is calibrated image that is alternative to the original cover JPEG. More about this process is described in [13].

We improved the calibration process for colorful JPEG images. From the observing and from the behavior of steganography algorithm OutGuess2.0, we know that the

OutGuess2.0 is focused on modification of the high frequency domains. We can use this fact to improve the detection capability. For the blockiness calculation we can exclude the low frequencies of the suspected image, because this areas can distorts the result. This improvement has positive effect on behavior of the detector itself. The method is now stricter in classification between stegogramme and clear image.

Blockiness calculation is the metric that react to the presence of hidden message. This calculation is described in [13, 14]. It is a statistical property that is different for the calibrated and the suspected image, so we can determine whether the image is stegogramme. A blockiness value is defined as the sum of spatial discontinuities along the boundary of all 8x8 macroblocks of a JPEG image.

By combining these two methodologies we can now detect a stegogrammes. Blockiness calculation is applied on suspected and calibrated image. Consequently, we can easily compare both blockiness values  $B_S$  and  $B_C$  to determine whether the suspect image is a stegogramme or not. If the value  $B_S > B_C$  it is a stegogramme. Conversely, if the value  $B_S < B_C$  it is a clear image without the embedded message.

### 3.3 Application of the Artificial Neural Network

For both detection methods (section 3.1 and 3.2) we consequently apply the artificial neural network. Neural networks are inspired by biological neural networks. Due to this fact, we are able to simulate a simple function of the human mind. Similar to the case of the human model, the artificial neural network (ANN) needs to gain experiences by learning. According to these experiences it will then decide. In our neural networks we used the Perceptron model. It is one of the most used models, whose potential is defined as the weighted sum of the incoming signals. If the threshold is exceeded, it leads to excitation of the neuron, otherwise it leads to inhibition. In order to properly recognize the input values of the ANN, every neurons weight must be correctly set. This is done by learning from training set.

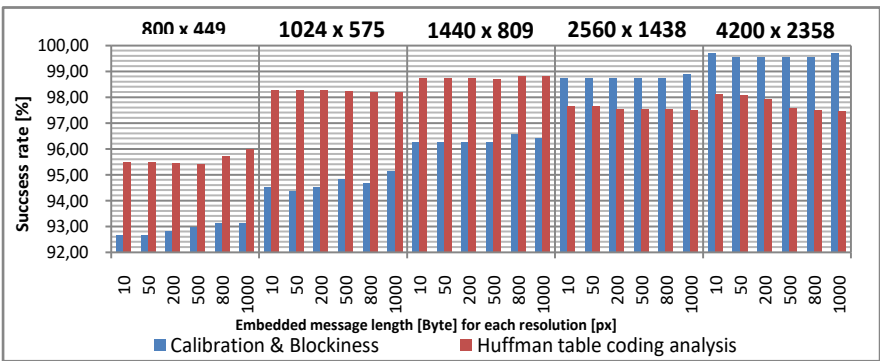


**Fig.2.** Detection capability of the method using calibration process, blockiness calculation and Huffman table coding analysis method with the application of ANN



For detection method based on Huffman table coding analysis (section 3.1) we used following ANN. Neural network itself uses feed forward perceptron topology with hidden layer. Plug-in that is part of framework utilizes ANN with 68 input neurons, 2 hidden layer of 128 neurons and two output neurons – each for one steganography algorithm with range 0 – 1, where 1 signs for highest probability for given algorithm. The input vector is made of 64 Huffman tables coefficients, two quality values and two values for the resolution of image.

For detection method based on calibration process and blockiness calculation (section 3.2) is the ANN consisted from three neurons – two inputs and one output neuron. To the input we sent blockiness values of the suspected and calibrated images. The output then generates a value of 1 or 0. Value 1 indicates stegogramme and value 0 indicates a clear image without any secret message.

## 4 Experiments and discussion

Data are processed with artificial neural networks that are able to detect hidden changes introduced above. For testing purposes we had to create testing database. Our database consists from more than 49 000 images from two cameras – Huawei P7 and LG-D605. Images are available in five different resolutions – 800 x 449, 1024 x 575, 1440 x 809, 2560 x 1438, 4200 x 2358 and variable six lengths of hidden messages 10, 50, 200, 600, 800 and 1000 bytes of English written text. This database was divided into two parts, training set and testing set.

Detection method using Huffman table coding analysis with ANN is very modern approach. It excels in speed of calculation – ANN simulation is very fast, but ANN requires training that can take inconsiderable time. Learning of above mentioned topology using gradient descent with momentum and adaptive learning rate backpropagation take more than 4 hours and not always end with success. Our ANN is actually able to detect two algorithms – Steghide and OutGuess2.0 with tested success rate of 96%.

Detection method using calibration process and blockiness calculation with ANN excels in detection capability and in speed of learning of the neural network. Calculation speed depends on image resolution. It is done by blockiness calculation. This method is able to detect hidden message embedded by two algorithms – OutGuess2.0 and F5 with tested success rate from 93% to 99%. The following Figure 3 shows the chart of success and error rates of the detection method. We can confidently say that the method responds better to the images that have a higher resolution (approximately more than 3 Mpx).

## 5 Conclusion

These two methods are a good basis for a blind analysis of suspicious file. Although these methods do not reach one hundred percent success rate, with increasing number of analysis steps we can identify the most suspicious files. Steganography is most dangerous in commercial sector, but a real amount of steganography material data

transfers will be really small. This raises the biggest problem – false positivity. But we can assume that illegal activity will not be a one-off. For example, repeated warnings in communication of one employee can be a good indicator of risk.

If we compare our research to the state of the art methods [7 - 10] we are now able to test even high resolution colorful JPEG images with very satisfying success rate (93% - 99%) for different secret message payload (10B – 1KB). Thanks to plug-in base system our framework can be easily extended and use to analyze other steganography algorithms or add another analysis methods. As another improvement we suggest implementation of JPEG data reader that can be used to obtain all data and structures from the format and also the image data itself. Data obtained in this way can help to extend implemented methods and can be used to depth analysis.

## References

1. DOËRR, Gwenaël; DUGELAY, J.-L. Security pitfalls of frame-by-frame approaches to video watermarking. *IEEE Transactions on Signal Processing*, 2004, 52.10: 2955-2964.
2. MARVEL, Lisa M.; BONCELET, Charles G.; RETTER, Charles T. Spread spectrum image steganography. *IEEE Transactions on image processing*, 1999, 8.8: 1075-1083.
3. BHATTACHARYYA, Souvik. A survey of steganography and steganalysis technique in image, text, audio and video as cover carrier. *Journal of global research in computer science*, 2011, 2.4.
4. CHAN, Chi-Kwong; CHENG, Lee-Ming. Hiding data in images by simple LSB substitution. *Pattern recognition*, 2004, 37.3: 469-474.
5. WANG, Ran-Zan; LIN, Chi-Fang; LIN, Ja-Chen. Image hiding by optimal LSB substitution and genetic algorithm. *Pattern recognition*, 2001, 34.3: 671-683.
6. WALIA, Ekta; JAIN, Payal; NAVDEEP, Navdeep. An analysis of LSB & DCT based steganography. *Global Journal of Computer Science and Technology*, 2010, 10.1.
7. FRIDRICH, Jessica; GOLJAN, Miroslav; HOGEEA, Dorin. Attacking the outguess. In: *Proceedings of the ACM Workshop on Multimedia and Security*. Juan-les-Pins, France, 2002.
8. CHEN, CL Philip, et al. A pattern recognition system for JPEG steganography detection. *Optics Communications*, 2012, 285.21: 4252-4261.
9. LIU, Qingzhong, et al. An improved approach to steganalysis of JPEG images. *Information Sciences*, 2010, 180.9: 1643-1655.
10. GUL, Gokhan; KURUGOLLU, Fatih. A new methodology in steganalysis: breaking highly undetectable steganography (HUGO). In: *International Workshop on Information Hiding*. Springer Berlin Heidelberg, 2011. p. 71-84.
11. ANDRIOTIS, Panagiotis; OIKONOMOU, George; TRYFONAS, Theo. JPEG steganography detection with Benford's Law. *Digital Investigation*, 2013, 9.3: 246-257.
12. FRIDRICH, Jessica. Feature-based steganalysis for JPEG images and its implications for future design of steganographic schemes. In: *International Workshop on Information Hiding*. Springer Berlin Heidelberg, 2004. p. 67-81.
13. LICEV, Lacey; HENDRYCH, Jakub; KUNCICKY, Radim. Neural Stegoclassifier. In: *IT Convergence and Security (ICITCS)*, 2016 6th International Conference on. IEEE, 2016. p. 1-3.
14. FU, Dongdong, et al. JPEG Steganalysis Using Empirical Transition Matrix in Block DCT Domain. In: *MMSP*. 2006. p. 310-313.

# Action Recognition Based on the Skeleton and Depth Images

Radek Simkanič

Department of Computer Science, FEECS,  
VŠB – Technical University of Ostrava, 17. listopadu 15,  
708 33 Ostrava – Poruba, Czech Republic  
`radek.simkanic.st@vsb.cz`

**Abstract.** In this paper, a new method called Matrix Descriptor of Changes (MDC) is introduced, which is used for the recognition of various classes of human activities. The proposed method is designed to create the matrix of a constant size for all actions, which can be regarded as a main contribution of the new method. The method is tested on three types of input features: (i) HoG, (ii) 3D positions of the joints of skeleton, and (iii) invariant angular feature of the skeleton. The recognition results are evaluated by the SVM classifier on two datasets.

**Keywords:** human action recognition, skeleton joints, depth map, 3D action feature representation

## 1 Introduction

Computer vision and image analysis is an interdisciplinary field focusing on processing and obtaining useful information from the image. One of the important and interesting topics is a human action recognition. This research has a great potential in many applications such as medical applications, public surveillance or even entertainment. This field is enriched with the available depth cameras with a good quality and real-time capturing.

The rest of the paper is organised as follows. In Section 2, the related works are briefly presented and classified into several types. In Section 3, the details of the new MDC method are stated. The experimental results are reported in Section 4. The conclusion can be found in Section 5.

## 2 Related works

By taking into consideration the type of input data, the activity recognition methods can be classified into the following five categories. (i) RGB, grayscale, IR, and similar images; (ii) depth maps; (iii) captured poses of skeleton (skeleton, exoskeleton, MoCap); (iv) other data; (v) combination of the above. In this section, only the works from the categories "depth maps", "captured poses of skeleton", and combination of the both are mentioned.

The approaches based on the depth maps reach good results and simplify the implementation better than RGB approaches. The Depth Motion Maps (DMM) introduced in [1] can be regarded as a frequently used method. This method has an easy implementation in which the sum of the differences between the consecutive depth maps are computed. The Space-Time Occupancy Pattern (STOP), which is introduced in [8], is a method based on the space-time probabilistic occupancy grid. The representation based on cloud points was applied to the 4D subvolumes sampled by a weighted sampling scheme in a random occupancy pattern (ROP) in [10]. One of the possible approaches to capturing the skeleton poses is presented in [2]. A combination of input data types is preferred in [11], where the data from the joints of skeleton and depth maps are simultaneously used. The authors observed that their method was resistant to noises and errors in skeleton joint positions that can be caused by severe occlusion. One of the interesting approaches based on capturing the poses of skeleton and using the Self-Similarity Matrix (SSM) is presented in [5]. SSM can be applied to more types of data.

### 3 Proposed method

This section gives a detailed description of the new method for the recognition of human actions. The analysis is based on the skeleton or depth maps. The method is partially inspired by the Self-Similarity Matrix (SSM), which is commonly used for action recognition [5], visualising of musical structure and rhythm [4], video analysing[3], etc. It describes the input features over time. The disadvantages of SSM include different sizes of the matrix for different actions since every action of the subject may have a different time duration. This problem with the size was an inspiration for me to develop a new method. The proposed method is designed to create the matrix of a constant size for all actions. The method is based on measuring the time-integrating distance between all the pairs of particular entries of the feature vector (the details are presented in the next section). The new method is tested on the three types of input features: (i) HoG [9] created from the depth maps in which the background was removed, and that were centered according to the location of the person, and that were cut out to the size of  $192 \times 240$ ; (ii) 3D positions of the joints of skeleton, and (iii) invariant angular features of skeleton. The invariant angular features of skeleton were published in [7]. The angles are measured (in radians) between the bones that meet at one joint. This description of skeleton pose is invariant to rotation and skeletal size.

#### 3.1 Matrix Descriptor of Changes

In this section, a new method called Matrix Descriptor of Changes (MDC) is introduced, which is used for the recognition of various classes of human activities. This method generates a symmetric matrix containing the space-time information within the specified time interval.

Let  $a_{i,t}$  be the value of the  $i$ -th feature obtained at a time  $t$ . For all  $N$  features obtained at  $t$ , the feature vector  $a_t = (a_{0,t}, a_{1,t}, \dots, a_{N-1,t})$  is introduced. The feature vectors obtained for all values of  $t \in \tau \equiv \{T_s, \dots, T_e\}$  create a sequence of feature vectors. We note that in the case of the angle descriptors, the angles are directly used as the values of the entries  $a_{i,t}$ . In the case of joint coordinates, three entries of the feature vector are used for the coordinates of each joint (i.e. the particular coordinates are placed into the vector). In the case of HoG, the whole feature vector is determined by HoG directly.

We define the distance between two feature vectors by the formula

$$d_{\tau,i,j} = \sum_{t \in \tau} \|a_{i,t} - a_{j,t}\|_2 \cdot g_{\tau}(t), \quad (1)$$

where  $g_{\tau}(\cdot)$  is a function introducing the weights of the differences from the particular times. We use the Gaussian function for this purpose (it is normalised such that it gives the unit value after the integration).

For the sequence of feature vectors, a distance  $N \times N$  matrix

$$MDC_{\tau} = \begin{bmatrix} 0 & d_{\tau,0,1} & \dots & d_{\tau,0,N-1} \\ d_{\tau,1,0} & 0 & \dots & d_{\tau,1,N-1} \\ \vdots & \vdots & \ddots & \vdots \\ d_{\tau,N-1,0} & d_{\tau,N-1,1} & \dots & 0 \end{bmatrix} \quad (2)$$

is computed that is used for the final recognition, which can be done by an arbitrary classifier. In our case, we use SVM.

### 3.2 MDC Pyramid

In the previous subsection, the MDC matrix has been introduced. Naturally, if the time interval  $\tau$  is too long, it may happen that the details that are important for recognition may be lost. A natural solution is to divide the original interval into several new subintervals, to create the MDC matrices for all the subintervals, and to use all the matrices for the final recognition. We use the hierarchical binary subdivision of the intervals. The first level of pyramid uses the whole time interval. In each next level, the intervals are divided into halves (Fig. 1).

The matrices are generated in a similar way as was described in the previous subsection. Only the function  $g_{\tau}(\cdot)$  is shrunk appropriately such that it has small values at the beginning and at the end of each interval that is being considered.

The matrices for all the time intervals are used for recognition. For example, seven matrices are generated and used in the pyramid that is depicted in Fig. 1. Generally, the number of pyramid levels should be chosen with respect to how the actions that are to be recognised are complicated. One and three levels are used in the experiments.

### 3.3 Action recognition

Either the single MDC matrix within the whole time interval or all MDC matrices generated from all MDC pyramid layers are used for classification. The

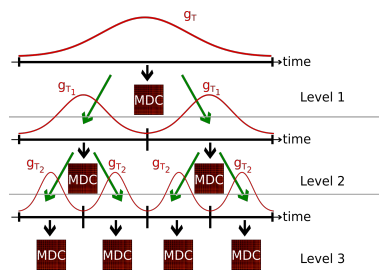


**Fig. 1.** The partitioning of the original action interval, and generating the MDC matrices from the interval itself and all its subintervals. The green arrows show how the intervals are split. The black arrows indicate generating the MDC matrices.

classification is performed in experiments by the SVM classifier with intersection kernel.

## 4 Experiments

In this section, the experimental results are shown by applying the new method to two datasets: (i) MSR Action3D Dataset [6], and (ii) UTKinect-Action3D dataset [12]. Both datasets contain the depth maps with the resolution of  $310 \times 240$  points and the skeletons of actions. The new method is compared with one of the state-of-the-art methods, namely with the method called Depth Motion Maps [1]. Both the methods use the same depth data described in Section 3. In the case of the new method, the calculation of HoG uses only four orientation bins for time savings. The MSR-Action3D Dataset contains 20 action types,

Methods	MSR Action3D				UTKinect-Action3D			
	1:2 samples		50:50 subjects		50:50 samples		50:50 subjects	
	F1	ACC	F1	ACC	F1	ACC	F1	ACC
DMM + SVM	0.957	0.996	0.729	0.973	0.727	0.945	0.697	0.939
MDC <sub>angles</sub>	0.739	0.973	0.374	0.937	0.788	0.958	0.768	0.954
MDC <sub>angles</sub> 1-3	0.79	0.979	0.484	0.948	0.929	0.986	0.909	0.982
MDC <sub>positions</sub>	0.854	0.985	0.667	0.967	0.727	0.945	0.556	0.911
MDC <sub>positions</sub> 1-3	0.898	0.989	0.722	0.972	0.848	0.97	0.737	0.947
MDC <sub>both</sub>	0.868	0.987	0.689	0.969	0.758	0.952	0.606	0.921
MDC <sub>both</sub> 1-3	0.914	0.99	0.736	0.974	0.889	0.978	0.828	0.966
MDC <sub>HoG</sub>	0.925	0.992	0.615	0.962	0.788	0.958	0.606	0.921
MDC <sub>HoG</sub> 1-3	0.889	0.989	0.667	0.967	0.869	0.974	0.788	0.958

**Table 1.** The results of the methods

each action is performed by 10 human subjects who repeat the same action 2 or

3 times. The UTKinect-Action3D dataset contains 10 action types, each action is performed by 10 human subjects again, every action is repeated two times.

The performances of the new and the reference methods are shown in Table 1 which is divided into two parts corresponding to the datasets. The table distinguishes between three types of different tests: (i) The term "1:2 samples" means that one of the three samples is used for training and the remaining two samples are used for testing the detection quality, (ii) "50:50 samples" means that a half of the samples is used for training and the rest is used for testing, (iii) "50:50 subjects" means that a half of the subjects is used for training and the remainings are used for testing. The quality of detection is measured by the F1 score and accuracy (ACC).

As has already been mentioned in Section 3, the new method is tested on the three types of features. Both a single MDC (Section 3.1) as well as the MDC pyramid (Section 3.2) have been used.  $MDC_{\text{angles}}$ ,  $MDC_{\text{positions}}$ , and  $MDC_{\text{HoG}}$  refer to the case in which invariant angular features, 3D positions of the joints, and HoG, respectively, are used.  $MDC_{\text{both}}$  joins two matrices, namely  $MDC_{\text{angles}}$  and  $MDC_{\text{positions}}$  that are then used for classification together.  $MDC_{\text{angles}1-3}$ ,  $MDC_{\text{positions}1-3}$ ,  $MDC_{\text{HoG}1-3}$ , and  $MDC_{\text{both}1-3}$  are similar to the first situation in essence. The change now is that the three-level MDC pyramid is used.

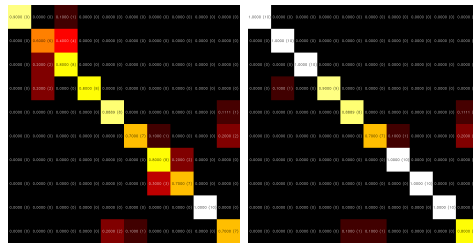


**Fig. 2.** Confusion matrices (from left) of  $MDC_{\text{angles}}$  and  $MDC_{\text{angles}1-3}$ . All are of type "50:50 samples" from UTKinect-Action3D dataset.

In most cases, the MDC pyramid provides better results than single MDC, especially in UTKinect-Action3D dataset. This is clearly visible in the confusion matrices (Fig. 2). The confusion matrix summarises the results of testing the algorithm. Each column of the matrix represents the instances in a predicted class while each row represents the instances in an actual class. The results in the confusion matrices (Fig. 2) are created from the results of  $MDC_{\text{angles}}$  (95.8 %) and  $MDC_{\text{angles}1-3}$  (98.6 %) from the UTKinect-Action3D dataset. It follows that the new method is at least comparable (or even better) with the state-of-the-art method DMM.

## 5 Conclusion

This article has presented a new method for the description of space-time data. The tests in the area of human action recognition have been carried out. The experiments have shown that the new method can be successfully used in this area, and that it is fully comparable with the state-of-the-art method DMM. We believe that the new method has a potential for further development.

## References

1. Chen, C., Liu, K., Kehtarnavaz, N.: Real-time human action recognition based on depth motion maps. *Journal of Real-Time Image Processing* vol. 12(issue 1), 155–163 (2016)
2. Cippitelli, E., Gasparrini, S., Gambi, E., Spinsante, S.: A human activity recognition system using skeleton data from rgbd sensors. *Computational Intelligence and Neuroscience* vol. 2016, 1–14 (2016)
3. Cooper, M., Foote, J.: Scene boundary detection via video self-similarity analysis. In: *Proceedings 2001 International Conference on Image Processing (Cat. No.01CH37205)*. pp. 378–381. IEEE (2001)
4. Foote, J.: Visualizing music and audio using self-similarity. In: *Proceedings of the seventh ACM international conference on Multimedia (Part 1) - MULTIMEDIA '99*. pp. 77–80. ACM Press, New York, New York, USA (1999)
5. Junejo, I.N., Dexter, E., Laptev, I., Perez, P.: View-independent action recognition from temporal self-similarities. *IEEE Transactions on Pattern Analysis and Machine Intelligence* vol. 33(issue 1), 172–185 (2011)
6. Li, W., Zhang, Z., Liu, Z.: Action recognition based on a bag of 3d points. In: *2010 IEEE Computer Society Conference on Computer Vision and Pattern Recognition - Workshops*. pp. 9–14. IEEE (2010)
7. Ohn-Bar, E., Trivedi, M.M.: Joint angles similarities and hog2 for action recognition. In: *2013 IEEE Conference on Computer Vision and Pattern Recognition Workshops*. pp. 465–470. IEEE (2013)
8. Vieira, A.W., Nascimento, E.R., Oliveira, G.L., Liu, Z., Campos, M.F.: On the improvement of human action recognition from depth map sequences using spacetime occupancy patterns. *Pattern Recognition Letters* vol. 36, 221–227 (2014)
9. Walk, S., Majer, N., Schindler, K., Schiele, B.: New features and insights for pedestrian detection. In: *2010 IEEE Computer Society Conference on Computer Vision and Pattern Recognition*. pp. 1030–1037. IEEE (2010)
10. Wang, J., Liu, Z., Choroski, J., Chen, Z., Wu, Y.: Robust 3d action recognition with random occupancy patterns. In: *Computer Vision - ECCV 2012*, pp. 872–885. Springer, Berlin (2012)
11. Wang, J., Liu, Z., Wu, Y., Yuan, J.: Mining actionlet ensemble for action recognition with depth cameras. In: *2012 IEEE Conference on Computer Vision and Pattern Recognition*. pp. 1290–1297. IEEE (2012)
12. Xia, L., Chen, C.C., Aggarwal, J.K.: View invariant human action recognition using histograms of 3d joints. In: *2012 IEEE Computer Society Conference on Computer Vision and Pattern Recognition Workshops*. pp. 20–27. IEEE (2012)



# An Approach To Customer Behavior Modelling Using Markov Decision Process

Markéta Štáková

Department of Computer Science, FEECS,  
VŠB – Technical University of Ostrava, 17. listopadu 15,  
708 33 Ostrava – Poruba, Czech Republic  
`marketa.stakova.st@vsb.cz`

**Abstract.** This paper presents an application of Markov Decision Process method for modeling of selected marketing processes. Based on available realistic data, MDP model is constructed. Customer behavior is represented by a set of states of the model with assigned rewards corresponding to the expected return value. Outcoming arcs then represent actions available to the customer in the current state. Favorable outcome rate of available actions is then analyzed, with emphasis on the suitability of the model for future predictions of customer behavior.

**Keywords:** marketing, model, Markov process, probability, evolutionary algorithms

## 1 Introduction

Since financial institutions such as the one in our article collect extreme amounts of data every day, there is need to sort these bulks of information and extract valuable contexts. These emerging links help marketeers to understand sequences of past actions, to learn from them and to extrapolate for future marketing actions. Thus we may include at this moment presented methods as a part of strategic marketing planning. Although the area of marketing big data analysis and processing is dynamically developing, it still cannot be considered as prevalent in the daily marketing practice.

Careful observation of customer's actions in the course of time gives us an overview of his needs and habits. This basic awareness gives us good starting position for developing meaningful CRM (customer relationship management) through means of premeditated and valid marketing communication. As Wessling [1] states, CRM is mainly shaped by human potential, market processes, technologies, and data. It revolves in cycles consisting of:

1. understanding customer's values
2. making contact
3. developing the company-customer relation
4. consolidation
5. decline
6. termination

In the majority of stages mentioned above, it is necessary to distribute clients among segments by grouping them according to their behavior for the analysis to yield applicable results. Since this strategy is done on historical data, it results in predictions. Traditionally, the businesses would perform SWOT (strengths, weaknesses, opportunities, threats) analysis on manually assembled historical data. However, even though our approach is more demanding, it can bring much deeper and comprehensive insight hence more reliable and clear view.

Predictions can be then used for marketing planning. The aim is to please business's needs by satisfying the client. The knowledge of the market is dependent on sufficient amount of reliable data. Thus we suggest paying attention to their correct collection. Marketing action should be shaped by several prerequisites to reach strategically valid goal for the enterprise. The communication shall respect the profile of the targeted person. This way, he will obtain an offer for a product he is the most likely interested in. Moreover, we can set the timing of the offer and frequency it might repeat with. In case of having quality input data, we are also able to assess which channel to use to approach him.

Some methods such as Markov Chains (MC) thus bring an opportunity to make the communication more cost effective and efficient in order not to overload the client with irrelevant information. This might potentially result in higher awareness and responsiveness to the offer from the part of the customer. In [2], resource allocation is optimized by use of MC model. [3] shows the application of MC to show switches between economic expansions and recessions, lately improved in [4]. Customer relationship can be represented by MC as well [5]. However, MC approach may not yield desirable outputs, e.g., the efficiency of product offers and campaigns. This led to the development of an extension to MC called Markov Decision Processes (MDP). Since then, MDP was used for optimization of marketing planning and budgeting [6, 7, 8, 9].

In this paper, MDP based approach to modeling of customer behavior based on data obtained by several financial institutions is presented. Customer behavior is represented by MDP model with states determined by a configuration of three selected attributes of the customer. These attributes were considered to influence the most the choice of action by the customer. The aim of the research was then to evaluate each state correspondingly to the initial evaluation and possible outcome of actions taken in that state. From the results, the most profitable (i.e., rewarding) sequence of actions may be identified, providing the institution with insight which policies should be adjusted to increase the return value of the customer.

## 2 Motivation

The main motivation arose from the co-author's marketing communications background and the previous efforts to go beyond classical methods of learning from collected data. Observation of the dynamic business environment imposes new challenges on data processing and their interpretation for immediate use. It has been noted that data is received from multiplying channels and the demand of linking them in joint

interpretation will automatically follow. Thus in this paper, we work with Markov Decision Processes to see new possibilities in client's behavior prediction.

### 3 Experiment design

#### 3.1 Data Preprocessing

Due to the complexity and a large volume of obtained real data, it was necessary to carry out the preprocessing phase. During this phase, data was cleaned and normalized, reducing the complexity of the data set. Main operations of the preprocessing phase were as follows:

- selection of the most influential attributes
- selection of appropriate records
- handling incomplete data columns

For the preprocessing, Apache Spark Framework was chosen as a suitable tool. Apache Spark [10] is fast and general-purpose cluster computing system. Originally, obtained data contained 3.3 billion atomic cells in total, each representing a specific value. After all, operations were performed, size of the data set was reduced to 2.1 billion cells, resulting in 36.65% reduction mainly due to the sparsity of some data columns.

#### 3.2 Markov Decision Process

Markov Decision Process (MDP) is a discrete time stochastic control process [11, 12]. In situations, where the outcome can be considered partly random and partly under control of some decision maker, MDP can provide a mathematical framework for modeling of related decision making. At each time step  $t$ , the process is in some state  $s$ . Then, the decision chooses one action an available at state  $s$ . At the next time step  $t + 1$ , the process randomly moves into new state  $s'$ . Then, decision maker receives reward  $R_a(s, s')$  corresponding with  $s'$ . State transition function  $P_a(s, s')$  represents the probability of the process moving into state  $s'$  by decision maker choosing action  $a$ . In this way, the next state  $s'$  depends only on the current state  $s$  and action  $a$  (thus making it independent of all previous states and chosen actions), therefore satisfying the Markov property.

#### 3.3 State Vector

As previously mentioned, states in the MDP model were determined by a configuration of the state vector. Elements of this vector consisted of three attributes from provided data which were considered the most influential on the behavior of the customer:

- Monthly change in Balance
- Offer success ratio

- Monthly change in Debt to income (DTI) ratio

The monthly difference was chosen as the most apparent indication of a change in customer behavior. Values of elements were then divided into three categories for each element, following comparison to a set of thresholds (categories for each element are shown in Tab. 1).

Table 1 State vector element categories

Attribute	Categories
Balance	Decreasing, Stable, Increasing
Offers	Poor, Average, Good
DTI	Decreasing, Stable, Increasing

Each possible combination of shown categories then resulted in a state. In our research, 27 possible states of the customer were identified.

### 3.4 MDP Model

Based on the available data, all states were considered to be adjacent to every other state. Actions were represented by a change of category for one or more elements of the state vector (e.g., balance change from stable to decreasing over a month). Directed arcs represent possible movement from the state into another states of the model. While this could, in theory, make the model difficult to be graphically represented and managed, in reality, many of these arcs would correspond to zero probability of movement between states. This is due to the use of input data in the form of monthly differences, which prevent rapid changes in the behavior of the customer. Therefore, reasonably lucid MDP model could be obtained (see Fig.1).

The model was constructed using modified adjacency matrix, which contained outgoing probability of state moving into another state as well as probability of remaining in the state. The thickness of arcs in Fig. 1 corresponds to these probabilities. Also, probabilities of a state being the output of an arc were computed and also visualized in Fig. 1 (light coloration represents states that are rarely an output state, while darker colors represent frequent output states). It could be seen, that both thickness of arcs and coloration point to state 11 as the one which most of the customers reached and remained in (i.e., making state 11 absorbing state in this model). This can be explained by state 11 representing customer with no significant monthly changes in both balance and DTI and with poor offer success rates. Simply put, we can consider such customer to have either stable or seldom used the account.

Another important observation in Fig. 1 is inactivity of two-thirds of the states present in the model. This is mainly due to limited data on offer campaigns and their success rates. It should be also noted, that this is the main reason for the prevalence of states representing customers with poor or no response to offers made by the institution.

Next step of our research was to compute reward function values for each of the active states in MDP model. For this, value iteration method was chosen as the suitable tool. However, some of the states can be considered undesirable for the institution, such as states corresponding to the customer with decreasing balance and increasing DTI. Similarly, beneficial states were identified as well. Then, initial rewards were assigned

to these states ranging from -10 and -5 for undesirable ones to 5 and 10 for desirable ones. Remaining states were assigned the value of 0. Resulting MDP model is shown in Fig. 2, where green states represent desirable states, and red states represent undesirable ones, with the exact set of reward values, also presented in Tab. 2 and Tab. 3.

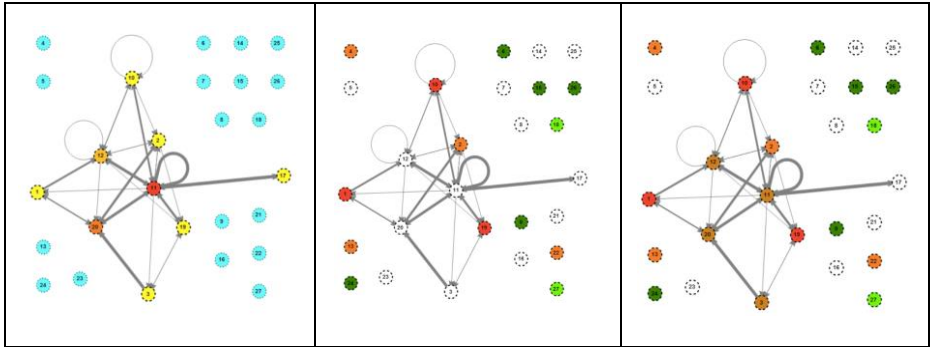


Figure 1 MDP Model

Figure 2 MDP model with initial reward values

Figure 3 MDP model with updated reward values

Table 2 Reward values before value iteration

State	1	2	3	4	5	6	7	8	9	10	11	12	13	14
Value	-10	-5	0	-5	0	5	0	0	5	-10	0	0	-5	0

Table 3 Reward values before value iteration

State	15	16	17	18	19	20	21	22	23	24	25	26	27	15
Value	5	0	0	10	-10	0	0	-5	0	5	0	5	10	5

The first observation is the lack of positively rewarded states amongst the active ones. Therefore, it could be expected that there will be no positively rewarded state following value iteration.

## 4 Results

As MDP outputs show, convergence was reached after 120 iterations resulting in MDP model shown in Fig. 3. Computed reward values are shown in Tab. 4 and Tab. 5 and are represented in Fig. 3 by varying degrees of red coloration of active states.

Table 4 Reward values followig value iteration

State	1	2	3	4	5	6	7	8	9	10	11	12	13	14
Value	-12.9	-8.6	-3.5	-5	0	5	0	0	5	-13.8	-2.7	-3.4	-5	0

Table 5 Reward values following value iteration

State	15	16	17	18	19	20	21	22	23	24	25	26	27
Value	5	0	-2.4	10	-12.6	-3.3	0	-5	0	5	0	5	10

As it was predicted, only initially negatively rewarded states influenced reward values of active states (i.e., all formerly "neutral" states were influenced by states 1, 2, 10 and 19). Normally, this step in MPD model evaluation would be followed by identification of optimal policy for the institution to maximize the return value of the customer. However, as it was previously mentioned, no positively rewarded active state is present in the MDP model. Therefore, in our research, the optimal policy would be for the customer to reach state 11 and remain in that state to minimize total loss (contrary to the intended maximization of customer return value). Again, as state 11 represents customer with no significant monthly changes in both balance and DTI and with poor offer success rate, it could not be considered an optimal policy from the view of the institution.

## 5 Conclusion

In this paper, MDP is used for modeling of the selected marketing process to maximize return value of the customer. MDP model using states in the form of configuration of state vector was constructed, using modified adjacency matrix derived from provided realistic data. Then, reward values were computed for each state following value iteration method application.

The original aim of presented work was to identify the best course of actions forming optimal policy for the institution to increase the return value of its customers in its future campaigns. However, due to sparse nature of available realistic data combined with the choice of the state vector, two-thirds of states in MDP model were inactive, since no customer reached them. As all of the states which are considered to be desirable from the view of the institution were part of that group, the active states either remained neutral or were assigned negative reward following value iteration method. Therefore, instead of maximizing potential reward, the model could only be used to minimize potential loss. This policy was then represented by customer reaching and remaining in absorbing state of the MDP model.

As the performed research did not avail desirable outcome, further adjustments to MDP model construction and data gathering were discussed and are currently being applied. In future works, more attributes influencing the customer behavior will be introduced into MDP model creation by use of segmentation instead of states represented by state vector configuration. This should allow the model to be less dependent on the nature of single variable while allowing some degree of control over the number of states in MDP model. Better data mining and data processing methods will be applied as well. Also, evolutionary algorithms will be used for achieving better fitness of the MDP model to given data for more accurate prediction of the customer behavior.

For future research, we propose the use of evolutionary algorithms (EA) in two major ways: firstly to use "classical" EA to estimate parameters of the MDP model to fit the behavior of the model more closely to real data. The second approach consists of using the symbolic regression (SR) like genetic programming [13], grammatical evolution [14] or analytic programming [15]. In this part, SR will be used to synthesize MDP models including its parameters according to used datasets.

## 6 Acknowledgements

The following grants are acknowledged for the financial support provided for this research: Grant Agency of the Czech Republic - GACR P103/15/06700S, Grant of SGS No. SGS 2017/134, VSB-Technical University of Ostrava. The Ministry of Education, Youth and Sports from the National Programme of Sustainability (NPU II) project "IT4Innovations excellence in science - LQ1602". Special thanks belong to PricewaterhouseCoopers company for support and experimental data sets that were used in our experiments.

## References

1. Wessling, H.: Aktivní vztah k zákazníkům pomocí CRM: strategie, praktické příklady a scénáře. Praha: Grada, 2003. Manažer. ISBN 8024705699.
2. DeMaagd, N.: The Application of Stochastic Processes in the Sciences: Using Markov Chains to Estimate Optimal Resource Allocation, Population Distribution, and Gene Inheritance. Honors Projects. Paper 290 (2014).
3. Hamilton, J.D.: A New Approach to the Economic Analysis of Nonstationary Time Series and the Business Cycle. *Econometrica* 57(2), 357{384 (1989).
4. Calvet, L.E.: How to Forecast Long-Run Volatility: Regime Switching and the Estimation of Multifractal Processes. *Journal of Financial Econometrics* 2 (1), 49{83 (2004).
5. Pfeifer, P.E., Carraway, R.: Modeling Customer Relationships as Markov Chains. *Journal of Interactive Marketing* 14(2), 43{55 (2000).
6. Labbi, A., Berrospi, C.: Optimizing marketing planning and budgeting using Markov decision processes: an airline case study. *IBM Journal of Research and Development - Business optimization* 51(3), 421{431 (2007).
7. Bauerle, N., Rieder, U.: MDP algorithms for portfolio optimization problems in pure jump markets. *Finance and Stochastics* 13(4), 591{611 (2009).
8. Perez, I., Hodge, D., Le, H.: Markov decision process algorithms for wealth allocation problems with defaultable bonds. *Advances in Applied Probability* 48(2), 392{405 (2016).
9. Rösch, A., Schmidbauer, H.: Action Selection in Customer Value Optimization: An Approach Based on Covariate-Dependent Markov Decision Processes. *Proceedings of the 2009 International Conference on Data Mining DMIN 09, Las Vegas*. ISBN: 1-60132-099-X.
10. Zaharia, M.: Apache Software Foundation, UC Berkeley AMPLab, Databricks. <http://spark.apache.org/docs/latest/> (2017). [Online; accessed 3-May-2017]
11. Bellman, R.E.: A Markovian Decision Process. *Journal of Mathematics and Mechanics* 6(5), 679{684 (1957).
12. Howard, R.A.: *Dynamic programming and Markov processes*. Cambridge, Massachusetts, 1960. The M.I.T. Press.
13. Koza, J. R.: *Genetic programming: on the programming of computers by means of natural selection*. Vol. 1. MIT press, 1992.
14. O'Neil, M., Ryan, C.: Grammatical evolution. In *Grammatical Evolution*, pp. 33-47. Springer US, 2003. Harvard
15. Zelinka, I., Davendra, D., Senkerik, R., Jasek, R., Oplatkova, Z.: Analytical Programming - a Novel Approach for Evolutionary Synthesis of Symbolic Structures, *Evolutionary Algorithms*, Prof. Eisuke Kita (Ed.), InTech, 2011. DOI: 10.5772/16166.

# Controlling the Dynamic of Evolutionary and Swarm Algorithms via the CML

Lukáš Tomaszek

Department of Computer Science, FEECS,  
VŠB – Technical University of Ostrava, 17. listopadu 15,  
708 33 Ostrava – Poruba, Czech Republic  
`lukas.tomaszek@vsb.cz`

**Abstract.** In this article, we want to briefly summarize the results of research about swarm and evolutionary algorithms, networks and coupled map lattices. We describe the main ideas of the research with regards on the author's publications.

**Keywords:** swarm algorithms, evolutionary algorithms, complex networks, coupled map lattices

## 1 Introduction

In this article, we summarize our research results of several different areas: swarm and evolutionary algorithms, networks and coupled map lattices (CML). In our research, we are attempting to convert run of swarm [2,5,19] or evolutionary algorithms [3,12] into networks and subsequently into CMLs. We can analyze given networks by a well-developed theory about complex networks [1,8] and make algorithm better and faster. Also, a CML can be analyzed, or we can attempt to control it [4,10]. Whole process we can see in Figure 1.

In the next parts, we describe how we can convert the algorithm into a network, how we can convert a network into a CML and we show how we can control the run of an algorithm.

## 2 Network models

Models can be divided into two groups. The first group is based on interactions between individuals (particles) in the algorithm. For example the interactions between leader and jumping individuals in the self-organizing migrating algorithm or crossing between individuals in the population in the differential evolution. The second model is based on time series. We can look at each algorithm as a time series of evaluations of a cost function, and from such series, we can create a graph.



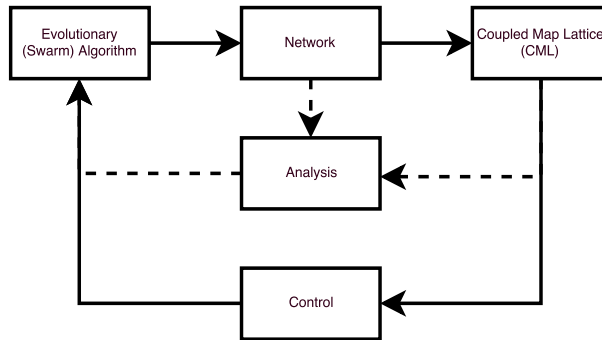


**Fig. 1.** Motivation

## 2.1 Interaction models

As it has been mentioned, the interaction model is based on interactions between individuals (particles, fireflies) in the algorithm. The vertex in the network represents individual (particles), and the edge represents the interactions in the algorithm. Also, if we take in mind the weighted networks, the weight may represent the strength of the interactions. As the best option for later CML control shows the model based on ant behavior in nature. This model has been presented in [22]. Also we presented different kind of models (probabilistic, added) which uses the interactions as the main part of the network. All interactions models for self-organizing migrating algorithm has been described in [17]. Also for other algorithms we can create networks, as it has been described in [9,11].

## 2.2 Time evolution models

The second mentioned models base on time series. We can look at all algorithms as a series of evaluation of cost function, and from such series, we can create a network. For example, we can use native visibility graph [7]. In [15] we demonstrate such model on the self-organizing migrating algorithm.

## 3 Networks

Given networks can be analyzed [1,8] and may give us some feedback about the algorithm. For example, we can calculate global properties like diameter, average path length or clustering coefficient to determine which network, and consequently which run of an algorithm, is better. Or we can count metrics like degree centrality, closeness centrality or eigenvector centrality to differentiate between good and bad individuals. With the feedback, we can make algorithm better and faster. Some basic analysis and improvements you can find in [6,13,16,18,21]. Also, in Figure 2 you can see an example of network for the self-organizing migrating algorithm.

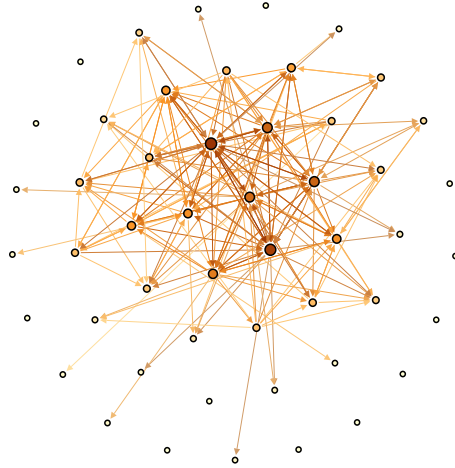


**Fig. 2.** Example of the network for the self-organizing migrating algorithm.

## 4 CMLs from networks

Networks cannot be only analyzed, but also they can be converted into a CML. In each row of a CML, you can find time evolution of a given property of one vertex. So if the network has  $n$  vertices and  $m$  time windows, the CML will have  $n$  rows and  $m$  columns. In the evolutionary and the swarm algorithms, time windows are represented by generations (migration loops), and vertices represented the individuals (particles). So in our case,  $n$  is equal to the population size and the  $m$  is equal to the number of generations or migration loops. Conversion of the self-organizing migrating algorithm into a CML has been described in [14].

## 5 CML control

Last part of our research contains the controlling of the CML and subsequently algorithms. The control means that, in given time, we attempt to find such inputs (pings) that lead the CML into the required state. CML can be controlled statically or dynamically. In statical control, we return the CML into the original state, when selecting wrong pings and we try different ones. By original state, we mean the last state of the CML, where we did not use the pings. In dynamical control (also called real-time control) we do not return the CML into the original state. We continue from the new state of the CML with new pings.

As a simplest control mechanism we can select another evolutionary or swarm algorithm. So, during the control, we will run two algorithms. Master and slave. Slave algorithm will focus on the finding optimal solution on a cost function and the master will control the slave algorithm. Controlling has been well described in [20].

Till now, the controlling phase of swarm or evolutionary algorithm was not presented, but results of such controlled run of the self-organizing migrating algorithm you can see in Figure 3. Also, you can see in Figure 4 the run of the uncontrolled algorithm, to be able to see the difference.

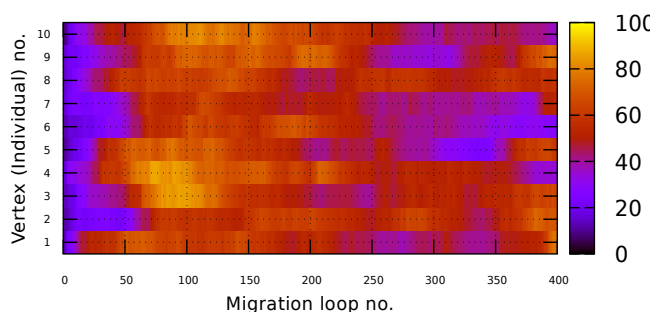


**Fig. 3.** Classical run of the self-organizing migrating algorithm on CEC 2015 benchmark function no. 1

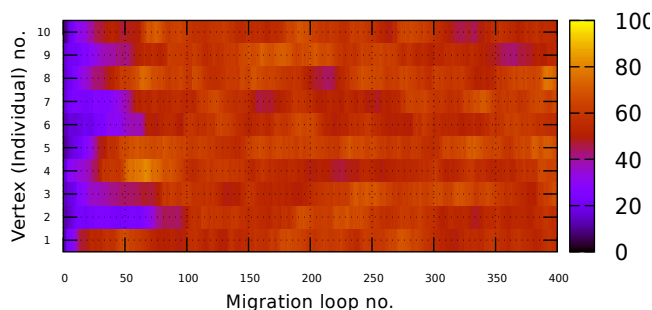


**Fig. 4.** Controlled run of the self-organizing migrating algorithm on CEC 2015 benchmark function no. 1

## 6 Conclusion and publications of the author

In this article, we sum the progress of our research. In this part, we want to briefly revise the process with regard to the publications of the author of the paper.

We briefly described how we can convert the run of evolutionary or swarm algorithm into a network [15,17,22], then we described, what we can do with the given networks [13,16,18,21] and how such networks can be converted into a CML [14]. At the end, we demonstrate, that the CML and consequently the algorithm may be controlled. This paper is just a review of our previous work and did not describe all ideas deeply, so for more information please look at the referred articles.

## Acknowledgment

The following grants are acknowledged for the financial support provided for this research: Grant Agency of the Czech Republic - GACR P103/15/06700S and by Grant of SGS No. SP2017/134, VSB Technical University of Ostrava.

## References

1. Stefano Boccaletti, Vito Latora, Yamir Moreno, Martin Chavez, and D-U Hwang. Complex networks: Structure and dynamics. *Physics reports*, 424(4):175–308, 2006.
2. Donald Davendra, Ivan Zelinka, et al. Self-organizing migrating algorithm. *New Optimization Techniques in Engineering*, 2016.
3. Kalyanmoy Deb, Amrit Pratap, Sameer Agarwal, and TAMT Meyarivan. A fast and elitist multiobjective genetic algorithm: Nsga-ii. *IEEE transactions on evolutionary computation*, 6(2):182–197, 2002.
4. Kuniyiko Kaneko. *Coupled Map Lattice*, pages 237–247. Springer US, Boston, MA, 1991.
5. James Kennedy. Particle swarm optimization. In *Encyclopedia of machine learning*, pages 760–766. Springer, 2011.
6. Pavel Krömer, Miloš Kudělka, Roman Senkerik, and Michal Pluhacek. Differential evolution with preferential interaction network. In *Evolutionary Computation (CEC), 2017 IEEE Congress on*, pages 1916–1923. IEEE, 2017.
7. Lucas Lacasa, Bartolo Luque, Fernando Ballesteros, Jordi Luque, and Juan Carlos Nuno. From time series to complex networks: The visibility graph. *Proceedings of the National Academy of Sciences*, 105(13):4972–4975, 2008.
8. Mark Newman. *Networks: an introduction*. Oxford university press, 2010.
9. Michal Pluháček, Roman Šenkeřík, Jakub Janošík, Adam Viktorin, and Ivan Zelinka. Study on swarm dynamics converted into complex network. In *Proceedings-30th European Conference on Modelling and Simulation, ECMS 2016*. European Council for Modelling and Simulation (ECMS), 2016.
10. Eckehard Schöll and Heinz Georg Schuster. *Handbook of chaos control*. John Wiley & Sons, 2008.

11. Roman Senkerik, Adam Viktorin, Michal Pluhacek, Jakub Janostik, and Zuzana Kominkova Oplatkova. Study on the time development of complex network for metaheuristic. In *Artificial Intelligence Perspectives in Intelligent Systems*, pages 525–533. Springer, 2016.
12. Rainer Storn and Kenneth Price. Differential evolution—a simple and efficient heuristic for global optimization over continuous spaces. *Journal of global optimization*, 11(4):341–359, 1997.
13. Lukas Tomaszek and Ivan Zelinka. On performance improvement of the soma swarm based algorithm and its complex network duality. In *Evolutionary Computation (CEC), 2016 IEEE Congress on*, pages 4494–4500. IEEE, 2016.
14. Lukas Tomaszek and Ivan Zelinka. Evolutionary dynamics control via its cml conversion. Accepted in print, 2017.
15. Lukas Tomaszek and Ivan Zelinka. Soma network model based on native visibility graph. Accepted in print, 2017.
16. Lukas Tomaszek and Ivan Zelinka. *Analysis of SOMA Algorithm Using Complex Network*. in print.
17. Lukas Tomaszek and Ivan Zelinka. *Conversion of SOMA Algorithm into Complex Networks*. in print.
18. Lukas Tomaszek and Ivan Zelinka. *Improvement of SOMA Algorithm Using Complex Networks*. in print.
19. Xin-She Yang. Firefly algorithms for multimodal optimization. In *International symposium on stochastic algorithms*, pages 169–178. Springer, 2009.
20. Ivan Zelinka. Real-time deterministic chaos control by means of selected evolutionary techniques. *Engineering Applications of Artificial Intelligence*, 22(2):283–297, 2009.
21. Ivan Zelinka and Lukas Tomaszek. Competition on learning-based real-parameter single objective optimization by soma swarm based algorithm with somaremove strategy. In *CEC*, 2016.
22. Ivan Zelinka, Lukas Tomaszek, and Lumir Kojecky. On evolutionary dynamics modeled by ant algorithm. In *Intelligent Networking and Collaborative Systems (INCoS), 2016 International Conference on*, pages 193–198. IEEE, 2016.

# Machine Learning based Forecasting in Active Demand Side Management

Tomáš Vantuch

ENET Center VŠB, VŠB – Technical University of Ostrava, 17. listopadu 15,  
708 33 Ostrava – Poruba, Czech Republic  
Department of Computer Science, FEECS,  
VŠB – Technical University of Ostrava, 17. listopadu 15,  
708 33 Ostrava – Poruba, Czech Republic  
`tomas.vantuch@vsb.cz`

**Abstract.** Electricity is currently the most important energy vector in the domestic sector and industry. Unlike fuels, electricity is hard (and expensive) to store, what has always originated in the need of precise coupling between generation and demand. In addition, the design of intelligent energy flow control strategies requires sustainable qualitative aspects of the energy as well. For these reasons, the electric load forecasting as well as power quality forecasting are vital, but depending on who is doing this prediction, the time scale might be completely different. It differs among energy suppliers covering the grids of larger areas where reactions of the system are in bigger scale and forecasting horizon is longer, and self-sustainable operating systems that handles energy supply of a single unit (one or at most several dwellings) where system needs to operate in shorter, almost on-line, responsive time supported by short-term forecasting.

**Keywords:** Partial Discharges, Complex Networks, Random Forest, Feature Extraction, Covered Conductors

## 1 Introduction

This paper should serve as a short review of our experiments and papers in the field of machine learning applications in energetics during the current year. The mentioned contributions are related to the project of Active Demand Side Management (ADSM) [14].

Electric load forecasting as a supportive tool in controlling mechanisms is vital and has been described in many research projects. As one of its applications, the Active Demand Side Management (ADSM) proposed by Misak et al. [14] counts with this ability to support the maximal efficiency of energy use gathered from renewable energy sources. The ADSM deals with energy management on levels of the single household or several residences at most.

The topic of electric load forecasting in the field of data science is well established, which is proved by several successful competitions [9, 10, 7] and high quality review studies [21, 2, 13, 19]. The majority of forecasts are based on previous electric load patterns and current weather since they are considered as

some of the most relevant variables affecting the buildings' heat losses and therefore the conditioning demand that accounts for around 40% of the total energy demand (depending on the climate).

Apart from the development of energy storage systems and sophisticated control algorithms for electric power flow management, some of the decisive factors in this respect are the quality of electric power and the adherence of PQ parameters to required limit ranges. The short-circuit power in the Off-Grid system is usually several times lower when compared to the short-circuit power in the conventional On-Grid systems, and the value changes during various operating modes of power converter [1, 3, 8]. One of the possibilities to keep PQ parameters in the required limits is to optimize the converter working point by Maximum Power Point Tracker (MPPT) regulator or time shifting of the selected appliances to the time with a higher short-circuit power [16, 11, 6]. Based on the above, it is vital to detect online or forecast the occurrences of possible PQ disturbances, to suppress or avoid them in the first place.

## 2 Experimental Applications

Two main issues were examined in this field currently as it was mentioned before. It was the electric load forecasting and the power quality forecasting. The following subsection describes different approaches or algorithm applications in this area.

### 2.1 Short-term electric load forecasting by fuzzy linear regression

The short-term electric load forecasting was ensured in our last study [25]. The proposed algorithm based on ensemble of multi objective optimized fuzzy linear regression was according to our available literature applied for the first time. The model is based on simplicity brought by Tanaka's fuzzy linear regression model and optimization by MOO approach which was already proposed in previous studies [17, 18]. Our contribution multiplies this concept and turns it into boosted fuzzy regression where the final decision comes from the second layer of fuzzy regression calculated from fuzzy inputs of previous models. This increases the robustness of the entire model which implies higher forecasting performance with lower over-fitting.

The testing was performed on dataset acquired in our laboratory at the Centre Enet, simulating the household conditions during one month period. The basic common appliances simulates the electric load that was randomly shuffled based on the weather conditions, battery power and user's behavior.

The statistical autocorrelation helped in design of feature extraction approach, where variables with high relevancy (last  $n$ -observations, inner-outer temperature, application of Analog Ensemble Algorithm [4]) were extracted. The final performance close to 8% (CV-RMSD) for 10 minutes ahead forecasting proves the quality of the entire model.

## 2.2 Machine learning algorithms comparison on short and long-term electric load forecasting

The motivation of this paper was to design and evaluate an electric load forecasting model making use the historical data of the forecast variable and the outside temperature only [22]. The adjusted time scales were a short-term one hour and a long-term one week ahead forecasting. These scales differed in extracted features as well as in algorithms' adjustment. The energy load forecasting served for calculation of an expected energy consumption for a given week. The summation of residuals divided by the total energy consumption in the observed week (cumulative error per week - CEPW), the coefficient of variation of Root-mean-square error (CV-RMSD) and Mean absolute percentage error (MAPE) were the tree criteria applied for the evaluations of forecasting models. The models applied in the paper were the artificial neural network, support vector regression, random forest regression, extreme gradient boosting and flexible neural tree.

The entire experiment was ensured in the international cooperation with University at Murcia in Spain and also the dataset was supported by their from complex IoT platform which gathered data of electric load in their department buildings.

The best models were able of prediction with error close to 18% CV-RMSD and 8% MAPE for next hour forecasting and 27% CV-RMSD or 11% MAPE for one week ahead forecasting. As we can see, the application of different time horizons implies a selection of different input variables which affects their relevancy and overall performance of the model. The uncertainty and noisiness inside of the data had negative impact on the total performance and this fact is necessary of consideration in our future studies.

## 2.3 Power quality forecasting by support vector regression and particle swarm optimization

The regression based forecasting of the power quality was performed by model based on support vector regression which hyper-parameters were optimized by particle swarm optimization [15]. Since it was one of the first proposals of PQ management based on forecasting instead of online detection and reactions [12, 20], its innovative aspect was obvious.

Relevancy of the input variables was estimated making use the Kraskov algorithm for mutual information estimation and for each PQ parameter (frequency, THDu, THDc, Plt and Pst) the separate SVR and input variables were optimized. The results were very promising. More than 65% of PQ disturbances were avoided in advance and the rest still can be suppressed by online reactions which are able to extend this model in the future work.

## 2.4 Multi objective optimization in power quality forecasting

Our previously proposed models for power quality (PQ) forecasting solved this issue in separate way. Each PQ parameter was predicted by separate computational model [24, 15]. The PQ parameters are context-dependent variables



therefore it is reasonable to propose a united computational model that will be able to forecast disturbances on all involved qualitative parameters combined. This different point of view brought the necessity of new evaluative criteria. In [23], we proposed a set of generic criteria based on classification performance measures. They calculates the Power Quality Predictive Performance accuracy, precision and recall from general set of disturbances ( $D$ ) which can be weighted according to defined priors. These criteria served as objective functions and are defined as follows.

$$\begin{aligned} D &= \{D_{FREQ}, D_{THDC}, D_{THDV}, D_{PLT}, D_{PST}\} \\ D_i &= \{D_i^{tp}, D_i^{tn}, D_i^{fp}, D_i^{fn}\} \\ W &= \{w_1, w_2, \dots w_n\} \end{aligned} \quad (1)$$

$$PQPP_{acc} = \frac{\sum_{i=1}^N (D_i^{tp} + D_i^{tn})w_i}{\sum_{i=1}^N D_i w_i} \quad (2)$$

$$PQPP_{prec} = \frac{\sum_{i=1}^N D_i^{tp} w_i}{\sum_{i=1}^N (D_i^{tp} + D_i^{fp})w_i} \quad (3)$$

$$PQPP_{rec} = \frac{\sum_{i=1}^N D_i^{tp} w_i}{\sum_{i=1}^N (D_i^{tp} + D_i^{fn})w_i} \quad (4)$$

Based on those three criteria, the multi objective optimization of the classification algorithm was ensured.

The performance achieved in our tests varied among 70-99% in four different time scales (1, 5, 10 and 15 minutes ahead). These results were very satisfactory and considered as huge improvement.

### 3 Discussion and conclusions

The task of energy flow control in the Smart-Grid platform is definitely a complex issue and previously proposed models are only partial solutions. Since their results were very promising, the best models will be deployed in our experimental platform for further testing of the entire ADSM platform. The increase of forecasting performance has still high priority. The demand side management relies on optimization of the user's consumption based on generated power, future electric load and the PQ parameters' responses, therefore the error generated

in forecasting modules significantly implies the overall effectiveness of the entire demand side management.

The application of Analog Ensemble Algorithm for electric load forecasting brought several highly relevant features. The further experiments revealed that the making use of the lagged values of electric load is still required in order to improve the forecasting accuracy. Very similar scenario has been observed in almost all available studies [5]. This will be considered in our future work during deeper examination and searching for other relevant features in both problems.

Nowadays applications of unconventional computation models based on swarm intelligence, evolutionary optimization and fuzzy logic are gaining interest of the researchers. Our proposed model involving concept of boosted fuzzy regression brings opportunities of further extensions and testing, type-2 fuzzy logic extension is definitely one of them.

## References

1. Affi, S., Darwish, M.: Impact of hybrid renewable energy systems on short circuit levels in distribution networks. In: Power Engineering Conference (UPEC), 2014 49th International Universities. pp. 1–5. IEEE (2014)
2. Ahmad, A., Hassan, M., Abdullah, M., Rahman, H., Hussin, F., Abdullah, H., Saidur, R.: A review on applications of ann and svm for building electrical energy consumption forecasting. *Renewable and Sustainable Energy Reviews* 33, 102–109 (2014)
3. Das, J.: Power system analysis: short-circuit load flow and harmonics. CRC press (2016)
4. Delle Monache, L., Eckel, F.A., Rife, D.L., Nagarajan, B., Searight, K.: Probabilistic weather prediction with an analog ensemble. *Monthly Weather Review* 141(10), 3498–3516 (2013)
5. Din, G.M.U., Marnierides, A.K.: Short term power load forecasting using deep neural networks. In: Computing, Networking and Communications (ICNC), 2017 International Conference on. pp. 594–598. IEEE (2017)
6. Erdinc, O., Paterakis, N.G., Catalão, J.P.: Overview of insular power systems under increasing penetration of renewable energy sources: Opportunities and challenges. *Renewable and Sustainable Energy Reviews* 52, 333–346 (2015)
7. Haberl, J.S., Thamilsaran, S.: Great energy predictor shootout ii: Measuring retrofit savings—overview and discussion of results. Tech. rep., American Society of Heating, Refrigerating and Air-Conditioning Engineers, Inc., Atlanta, GA (United States) (1996)
8. Hojabri, M., Toudeshki, A., et al.: Power quality consideration for off-grid renewable energy systems. *Energy and Power Engineering* 5(05), 377 (2013)
9. Hong, T., Pinson, P., Fan, S.: Global energy forecasting competition 2012 (2014)
10. Hong, T., Pinson, P., Fan, S., Zareipour, H., Troccoli, A., Hyndman, R.J.: Probabilistic energy forecasting: Global energy forecasting competition 2014 and beyond (2016)
11. Lawey, A.Q., El-Gorashi, T.E., Elmirghani, J.M.: Renewable energy in distributed energy efficient content delivery clouds. In: 2015 IEEE International Conference on Communications (ICC). pp. 128–134. IEEE (2015)

12. Mahela, O.P., Shaik, A.G., Gupta, N.: A critical review of detection and classification of power quality events. *Renewable and Sustainable Energy Reviews* 41, 495–505 (2015)
13. Metaxiotis, K., Kagiannas, A., Askounis, D., Psarras, J.: Artificial intelligence in short term electric load forecasting: a state-of-the-art survey for the researcher. *Energy conversion and Management* 44(9), 1525–1534 (2003)
14. Mišák, S., Stuchlý, J., Platoš, J., Krömer, P.: A heuristic approach to active demand side management in off-grid systems operated in a smart-grid environment. *Energy and buildings* 96, 272–284 (2015)
15. Misak, S., Stuchly, J., Vantuch, T., Burianek, T., Seidl, D., Prokop, L.: A holistic approach to power quality parameter optimization in ac coupling off-grid systems. *Electric Power Systems Research* 147, 165–173 (2017)
16. Morsi, W.G., El-Hawary, M.: Power quality evaluation in smart grids considering modern distortion in electric power systems. *Electric Power Systems Research* 81(5), 1117–1123 (2011)
17. Nasrabadi, M.M., Nasrabadi, E., Nasrabady, A.R.: Fuzzy linear regression analysis: a multi-objective programming approach. *Applied mathematics and computation* 163(1), 245–251 (2005)
18. Özelkan, E.C., Duckstein, L.: Multi-objective fuzzy regression: a general framework. *Computers & Operations Research* 27(7), 635–652 (2000)
19. Raza, M.Q., Khosravi, A.: A review on artificial intelligence based load demand forecasting techniques for smart grid and buildings. *Renewable and Sustainable Energy Reviews* 50, 1352–1372 (2015)
20. Saini, M.K., Kapoor, R.: Classification of power quality events—a review. *International Journal of Electrical Power & Energy Systems* 43(1), 11–19 (2012)
21. Suganthi, L., Samuel, A.A.: Energy models for demand forecasting—a review. *Renewable and sustainable energy reviews* 16(2), 1223–1240 (2012)
22. Vantuch, T., Gonzalez-Vida, A., P. Ramallo-González, A., F. Skarmeta, A., Misak, S.: Multi term electric load forecasting ((in press))
23. Vantuch, T., Misak, S., Jezowicz, T., Burianek, T., Snasel, V.: The power quality forecasting model for off-grid system supported by multi-objective optimization. *IEEE Transactions on Industrial Electronics* (2017)
24. Vantuch, T., Mišák, S., Stuchlý, J.: Power quality prediction designed as binary classification in ac coupling off-grid system. In: *Environment and Electrical Engineering (EEEIC), 2016 IEEE 16th International Conference on*. pp. 1–6. IEEE (2016)
25. Vantuch, T., Prilepok, M.: An ensemble of multi-objective optimized fuzzy regression models for short-term electric load forecasting ((in press))

# MinEnt – Grammar-Based Compression

Michal Vašínek

Department of Computer Science, FEECS,  
VŠB – Technical University of Ostrava, 17. listopadu 15,  
708 33 Ostrava – Poruba, Czech Republic  
`michal.vasinek@vsb.cz`

**Abstract.** This paper summarizes development of the MinEnt data compression algorithm. The algorithm belongs to the family of grammar based compression algorithms. The resulted code is constructed by successive replacement of patterns in an input text for a new, yet unused symbol. The main focus of my work is to state precisely conditions under whose any replacement of one pattern for the other pattern will lead to the drop of the zero order entropy and its associated entropic size of an input text. In the paper the equation that governs any replacements will be presented and its implications on the resulted size of the compressed file will be discussed.

**Keywords:** data compression, grammars, Re-Pair, MinEnt, entropy

## 1 Introduction

We begin by brief introduction to the problem of the measuring the information content of some data. Let  $m$  be a message consisting of symbols from alphabet  $\Sigma$  and let  $|m|$  denotes the length of the message measured as the number of symbols. Each symbol  $c \in \Sigma$  occurs in  $m$  with frequency  $f(c)$  and corresponding probability  $p(c)$ . Using the Shannon's equation[1] we can compute the entropy  $H$  of the distribution of symbols in  $m$ :

$$H(X) = - \sum_{x \in \Sigma} p(x) \log p(x) \quad (1)$$

where  $X$  is a random variable representing symbols from  $\Sigma$ . The quantity  $H(X)$  computed by (1) is often called zero-order entropy and its unit are bits. In this paper, whenever we will use the term entropy we always refer to the zero-order entropy. The entropy gives us a theoretical bottom limit of the average number of bits per one symbol that any compression algorithm can achieve when it possess only with the knowledge of the distribution of symbols, i.e. we don't know any conditional relations between symbols or group of symbols. Given that our input message  $m$  has the length  $|m|$  we can compute the bottom limit of bits we need to compress  $m$ :

$$|m|^H = |m|H(X) \quad (2)$$

we call the quantity  $|m|^H$  an entropic size of the message<sup>1</sup>. Throughout the paper we will use following additional notation: if we use subscript in the message notation  $m_0$  resp.  $m_1$ , then it represents two states of the message, before resp. after some function was applied on the message.

There are two well known statistical compression algorithms that are able to achieve bits per byte ratio (bpB)<sup>2</sup> very close to the entropy or at least within precisely defined boundary. These algorithms are Arithmetic[4] and Huffman[3] coding. This is a vital assumption because it allows researchers to develop other algorithms that modify the inner structure of the input message and then the outcome of such processing is compressed by one of these statistical algorithms. The grammar-based compression algorithms are class of algorithms that modify the inner structure of input data.

## 2 Grammar-Based Compression

The class of algorithms dealing with exchanges of different n,m-grams are called grammar-based algorithms. Their purpose is to provide a set of production rules inferring the content of the message. Using the Chomsky hierarchy, we identify two classes of formal grammars used in data compression: context-free grammars (CFG) and context-sensitive grammars (CSG). The problem of the search for the most compact context-free grammar representation of a message is NP-hard, unless  $P = NP$  [5]. Instead of searching for the optimal solution, researchers aim their focus on a development of heuristic and greedy algorithms.

### 2.1 Re-Pair

Re-Pair is the algorithm proposed by Larsson and Moffat in [2]. It repeatedly performs following steps:

1. Find the most frequent digram  $\alpha\beta$  in  $m$ .
2. Replace all occurrences of  $\alpha\beta$  by some new symbol  $\gamma$ .
3. Repeat Step 1 and 2 until every digram appears only once.

Each replacement  $\alpha\beta \rightarrow \gamma$  is stored in a dictionary and together with a final message forms an outcome of the algorithm. The Re-Pair algorithm is easy to implement using linked lists and priority queue. It is algorithm with  $O(n)$  time complexity and it can compress an input message into at most  $2H_k + o(n \log |\Sigma|)$  bits, where  $H_k$  is the k-order entropy. It is also very fast in decompression.

---

<sup>1</sup> In data compression we usually identify symbols as byte values and hence each symbol occupies exactly 8 bits.

<sup>2</sup> bpB = the size of the compressed message measured in bits / the number of bytes in the input message.

### 3 MinEnt

The MinEnt[6] algorithm is closely related to the Re-Pair but it differs in the Step 1. Instead of the selection of the most frequent digram it selects digram that minimizes  $|m_1|^H$ , where  $|m_1|^H$  is an entropic size of the outcome of replacement  $\alpha\beta \rightarrow \gamma$ :

1. Select digram  $\alpha\beta$  in message  $m_0$  so that the change of entropic size of the message  $\Delta|m|^H = |m_0|^H - |m_1|^H$  is maximal.
2. Replace all occurrences of  $\alpha\beta$  by some new symbol  $\gamma$ .
3. Repeat Step 1 and 2 until every digram appears only once.

The Step 1 of the MinEnt algorithm can be formally described as:

$$\arg \min_{\alpha, \beta \in \Sigma_0} |m_1 = \text{MinEnt}(m_0, \alpha\beta \rightarrow \gamma)|^H \quad (3)$$

To demonstrate the difference between Re-Pair and MinEnt, consider the following example:

#### Example 1

$$m_0 = aababcdcdb$$

The entropic size of  $m_0$  is  $|m_0|^H = 19.71$  bits. There are two non-overlapping digrams that occur twice:  $ab$  and  $cd$ .

$$(m_0, ab \rightarrow e) = aeecdcdcb$$

$$(m_0, cd \rightarrow e) = aababeeb$$

Based on the Re-Pair algorithm, we do not know which digram should be preferred, because both have the same frequency. In the MinEnt case, we can compute  $|m_1|^H$  for both cases, yielding  $|m_1|_{ab}^H = 18$  bits and  $|m_1|_{cd}^H = 12.49$  bits, and so, the replacement  $cd \rightarrow e$  will be the preferred one.

#### 3.1 Calculation of $\Delta|m|^H$

At first glance, it seems that we need to perform each possible replacement, compute their entropic size change, revert it back and eventually select the replacement that minimizes  $|m_1|^H$ . This would be highly inefficient solution. Instead we found that the value of  $|\Delta m|^H$  can be computed for any digram only with the knowledge of frequencies of symbols and digrams. Suppose the replacement  $\alpha\beta \rightarrow \gamma$  then the equation for computation of  $|\Delta m|^H$  is:

$$\begin{aligned} \Delta|m|^H &= |m_0| \log c_1 - \log c_1 \sum_{x \in \{\alpha, \beta\}} f_0(x) \\ &+ \sum_{x \in \{\alpha, \beta\}} f_0(x) \log c_2(x) + \Delta f_0(x) \log p_0(x) + \Delta f_0(x) \log c_2(x) \quad (4) \\ &- \Delta f(\gamma) [\log \Delta f(\gamma) - \log (|m_0| + \Delta m)] \end{aligned}$$

where quantities used in the equation are:

- $\Delta m = f_0(\alpha\beta) \dots$  the change of the message length measured in the number of symbols.
- The compression factor  $c_1$ :

$$c_1 = \frac{|m_0|}{|m_0| + \Delta m} \quad (5)$$

- The compression factor  $c_2(x)$  of particular symbol  $x$  :

$$c_2(x) = \frac{f_0(x) + \Delta f(x)}{f_0(x)} c_1 = F(x) c_1 \quad (6)$$

Generally it holds that:  $\Delta m = \Delta f(\alpha) = \Delta f(\beta) = \Delta f(\gamma) = f(\alpha, \beta)$ , but in a special case if  $\alpha = \beta$ , then  $\Delta f(\alpha)/2 = \Delta f(\gamma)$ . See [6] for derivation and more details.

## 4 Results and Discussion

We first present comparison of the Re-Pair and MinEnt algorithms with a standard ZIP algorithm over selected files<sup>3</sup> and then we will discuss achieved results. In Table 1 we present resulting filesize of the three text files compressed by different algorithms.

**Table 1.** The comparison of the resulting size of the compressed files measured in bytes for Re-Pair, MinEnt and ZIP algorithms.

Filename	$m_0$	Re-Pair	MinEnt	ZIP
book1	768,771	249,957	249,822	319,275
book2	610,856	170,079	166,533	210,115
bible.txt	4,047,392	872,215	847,187	1,228,642

The main reason why MinEnt overcomes Re-Pair is that it selects different replacements than Re-Pair. It prefers digrams that are constituted from symbols of lower frequencies. If we return back to the Example 1, we saw that the Re-Pair algorithm have no clue to make a decision between the two different replacements having the same digram frequency, on the other hand MinEnt will always prefer digrams constituted of symbols with lower frequency.

The usual path of the MinEnt algorithm is that it first selects digrams of lower frequency meanwhile digrams with higher frequency are selected in later iterations of the algorithm. Due to the need of precomputation of  $|\Delta m|^H$  values,

<sup>3</sup> Calgary and Canterbury corporas, available online at: <http://www.corpus.canterbury.ac.nz/>.

MinEnt algorithm is slightly slower in compression phase, but it is still  $O(n)$  algorithm. There is no difference in decompression times between the two.

The both algorithms evolves into the approximately same size measured in the number of symbols, but the construction of the MinEnt achieves lower values of the zero order entropy and hence it achieves better compression.

From the comparison of both algorithms with ZIP algorithm we see that this type of grammar-based compressors is able to achieve significantly better compression results.

## 5 Conclusion

It was shown, that the proposed MinEnt algorithm is able to achieve slightly better compression ratio than the state of the art grammar-based compressor Re-Pair. Generally the class of grammar-based compression algorithms achieves very competitive compression ratio in comparison with standard compression utilities like ZIP.

The main benefit of the development of the underlying theory is that it provides a deep insight into understanding of changes of entropy conveyed by each symbol and as a result it was showed that it is worth to replace symbols with lower frequency first as these symbols carry more bits.

### Publications

The MinEnt algorithm was published in Entropy journal in the section Information Theory.

### Acknowledgement

This work was supported by the project SP2017/100 Parallel processing of Big Data IV, of the Student Grant System, VSB - Technical University of Ostrava.

## References

1. Shannon, C.E.: A mathematical theory of communication. Bell system technical journal, Vol. 27 (1948)
2. Larsson, N. J. and Moffat, A.: Off-line dictionary-based compression. Data Compression Conference(DCC), pp. 1722-1732 (2000)
3. Huffman, David A.: A Method for the Construction of Minimum-Redundancy Codes. Proceedings of the I.R.E., pp. 1098-1102 (1952)
4. Rissanen, J.; Langdon G.: Arithmetic coding. IBM Journal of Research and Development, 23(2), pp. 149-162 (1979)
5. Charikar, M., Lehman, E., Liu, D., Panigrahy, R., Prabhakaran, M., Sahai, A., Shalat, A.: The smallest grammar problem. IEEE Transactions on Information Theory, 51(7), pp. 2554-2576 (2005)
6. Vasinek, M., Platos, J.: Prediction and Evaluation of Zero Order Entropy Changes in Grammar-Based Codes. Entropy, 19(5), 223 (2017)



# Malware Detection based on Multiple PE Headers Identification

Filip Zatloukal

Department of Computer Science, FEECS,  
VŠB – Technical University of Ostrava, 17. listopadu 15,  
708 33 Ostrava – Poruba, Czech Republic  
vsb@zatloukal.net

**Abstract.** Malware detection and analysis are very important topics. A lot of detecting methods already exists, but none of the method is able to detect all kind of malware, especially all new kinds of threads. Our research focus on multiple methods, currently on malware detection by metadata. There exists group of malware named parasitic viruses - they infects other files and connect its code into the host file. This paper describes results of method detecting parasitic viruses by multiple PE headers identification.

**Keywords:** malware detection, file virus, parasitic virus, multiple PE headers.

## 1 Introduction

The subject of our research is a malware detection and testing of related detection methods. The aim is to use an unconventional approach to malware detection, to improve the existing methods or to create a new method. The currently examined topic is a malware detection by using metadata. Malware detection by metadata testing is a topic that isn't published often and this is the reason why we chose it for our research. This paper describes a detection method based on the idea of malware detection by multiple PE headers occurrence.

## 2 The overview of malware detection methods

### 2.1 Signature based detection

It's the most commonly used detection method [1]. The method uses known patterns to detect malware. These patterns are loaded from an internal database. The method is able to detect malware fast, but it can't detect new kinds of threats if they are not stored in the internal database. This is the reason, why antivirus programs must upgrade their internal databases. Methods also can't effectively deal with malware obfuscation [2].

**2.2 Behavior based detection**

This method uses its own internal sandbox where the malware runs. The antivirus then analyses the actions performed by malware. This method is able to recognize both existing and new kinds of threads. A disadvantage of this method is a longer detection time needed to perform actions in the sandbox. Also, not all malware functions are performed because of application code conditional branching or not all requirements are met for malicious code activation.

**2.3 Hybrid analysis**

Hybrid analysis is the combination of static and dynamic analysis. In a first place, static analysis is applied and then software is running in controlled environment [3].

**2.4 Statistical based detection and Different approach**

Statistical based method finds different attributes of software and then analyses these properties by statistic methods. An example of this method are Hidden Markov Models (HMMs) [4].

Ashu Sharma et al. also adds two more techniques: Machine Learning and Malware Normalization [5].

**3 The overview of malware infection methods**

One example of the malware category are parasitic viruses which used some of the following methods to copy its own code to legitimate files. Some methods can damage target file, some not - it's possible to divide the methods to two groups: destructive and non-destructive methods.

**3.1 Prepending Viruses**

In the process of the infection, the virus puts its own code in front of the code of original file. If such file is executed, OS runs malicious code instead of the legitimate code first, but the original code is executed also to hide malicious behavior, so the user could not identify it.

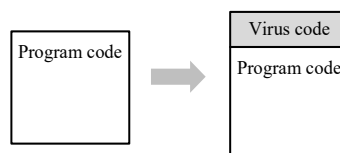


**Fig. 1.** The example of an infection by a prepending virus.

### 3.2 Appending Viruses

The virus appends its code at the end of the infecting file. Because the malicious code is at the end of the file, the malware must also change the original code to assure malware activation when the file is executed.

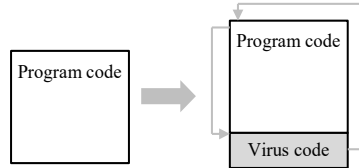


Fig. 2. The example of an infection by an appending virus.

### 3.3 Inserting

The malicious code is placed at the address to which the entry point value points and the rest of the code is moved under the malicious code. The entry point is a value referring to the start of the executable code itself. Another way to put the code in non-destructively is to spread the code to the unused places in the file. That code doesn't have to be continuous but at the end of each section, a jump instruction must be inserted.

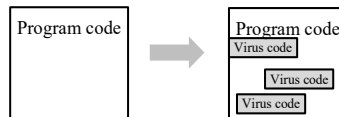


Fig. 3. The example of an infection by an inserting virus.

### 3.4 Overwriting Viruses

A malware infecting the file in a way that the original file is overwritten by the virus's own copy. Unlike others, this method is destructive. The virus can overwrite the file from the beginning but it can also choose another start location (Random Overwriting Viruses). If the executable file is overwritten from the beginning, the PE header is also overwritten and the original program will not be able to run without a header reconstruction (instead, the malware will run). If a random section of the original file is overwritten, it's possible that the program will work but it will also crash probably.

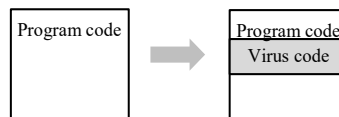


Fig. 4. The example of an infection by an overwriting virus.

## 4 PE format

Portable Executable (PE) is a format defining a form and a section layout of the executable files. PE is a data structure in the binary form that is used by Windows system for exe files, dll libraries and other executable formats. PE keeps the file description information which is used by Windows OS loader and also keeps the program code itself. PE format and blocks are described below [6]:

### 4.1 PE format blocks

**DOS MZ header.** Defined as “IMAGE\_DOS\_HEADER” structure. The first 64 bytes of the file is a header guarantee of DOS compatibility and it's included even in current applications. The first value of the header is named as “e\_magic” (so-called magic number) and it's used to identify the DOS mode. The value must be always equal to 0x54AD (“MZ” in ASCII). The header also contains the “e\_lfanew” value which is a relative offset to the PE header.

**DOS stub.** A section for the DOS code itself. Nowadays, it is compiled to only show the message: “This program cannot be run in DOS mode.”.

**PE header.** A structure also defined as “IMAGE\_NT\_HEADERS” containing the signature, “IMAGE\_FILE\_HEADER” structure and “IMAGE\_OPTIONAL\_HEADER” structure. It's the main header for the Windows executables and it consists of a variety of fields placed in “signature”, “COFF header” and “PE Optional Header” structures. The description of the fields itself exceeds the scope of this paper but in the research, the “signature” value, “machine” value, “magic” value and “AddressOfEntryPoint” value are the important ones:

PE “signature” value has the similar meaning as “e\_magic” value from the DOS MZ header. The value is equal to 0x50450000 (“PE\0\0” in ASCII) and it's used to the identification of PE header. The machine value holding the type of CPU the code is compiled for (the value is used for compatibility check). “Magic” field is a 2-byte value placed at the beginning of the optional header and representing the architecture type (0x010B for PE32, 0x020B for PE64, 0x0107 ROM). “AddressOfEntryPoint” is an address of the application entry point (address where the applications code begins).

**Section table.** Defined in “IMAGE\_SECTION\_HEADER” structure. Each section has its own section header and these headers are used to describe each of the following sections. The headers contain section name, relative address, section size and other values. The number of sections and their names can be different because the compiler controls these sections and names.

**Sections.** The sections contain of data created by compiler, code itself and metadata corresponding with the code. Sections names are controlled by a compiler, but the most

commonly used names are [7]: .text, rdata, .data, .idata, .edata, .pdata, rsrc and reloc. As the sections can be interesting for a malware analysis, deep description is above the paper scope, because they are not directly used in following experiment.

## 5 Experiment

Goal of our research is to scan a representative number of samples and to determine how often is malware bound to host file by one of the described method. It will be also tested if it's possible to find malware by detecting multiple PE headers. Necessary condition is that malware connects itself to the code without destroying the header of the previous file. The experiment focuses on connecting the malicious code only on executable files.

### 5.1 Dataset

Our dataset is composed of 9101 Windows programs in PE file format. 5099 of them are malicious software and 4002 user friendly (clean) executable files or DLLs. Most of the friendly applications are stored as compressed packages or installers. It was needed to install (or unpack) all of these applications first, because a scan of these packages/installers will return the results for the packed format instead of the unpacked application itself. Malware applications are already in the required format.

### 5.2 Multiple PE header detection

For our research, a new application was developed. Application allows us to perform required actions effectively. When scanning for multiple PE headers, our software search in the binary mode for signatures and magic values of PE headers and DOS headers. If any of the value is presented, the software performs a check whether the found value isn't just a binary sequence of data but if it really belongs to the PE header.

## 6 Results

After testing all samples, it was discovered that 504 of total 5099 malware samples have multiple PE headers. It's interesting that also 231 of legitimate software from the total of 4002 includes multiple PE headers. After a closer look on the tested malware, most of them are really connected at some host file and act as parasitic viruses. A closer look at the legitimate software shows that most of the hits (56.278 %) are caused by an application named "uninstall000.exe". This file is a legitimate application created by „Inno Setup" software and is used as an application uninstaller. Other hits are caused by packages including another software inside but also by a small amount of legitimate applications.

## 7 Discussion and Future work

It is provable that there is a significant number of viruses connecting itself to another files, including its headers. It's possible to detect the multiple header but this doesn't automatically mean that this file is a malware. But there is also space for improving of the scanning method. It will be possible to exclude legitimate files including multiple PE headers (as "uninstall000.exe") in future work. Malware writers also implement mechanisms to avoid multiple infections of the same file. Following research will include a deeper look at these mechanisms to use them for malware detection. Malware detection by multiple PE headers will be also combined with other detection methods.

## 8 Acknowledgment

The following grants are acknowledged for the financial support provided for this research: Grant of SGS No. SGS 2016/175, VSB-Technical University of Ostrava and The Technology Agency of the Czech Republic TACR TF01000091.

## 9 References

1. AYCOCK, John Daniel. *Computer viruses and malware*. New York: Springer, 2006. ISBN 0387341889.
2. BORELLO, Jean-Marie; MÉ, Ludovic. Code obfuscation techniques for metamorphic viruses. *Journal in Computer Virology*, 2008, 4.3: 211-220.
3. UPPAL, Dolly; MEHRA, Vishakha; VERMA, Vinod. Basic survey on malware analysis, tools and techniques. *International Journal on Computational Sciences and Applications (IJCSA)*, 2014, 4.1: 103-12.
4. Wong, W., & Stamp, M. (2006). Hunting for metamorphic engines. *Journal in Computer Virology*, 2(3), 211-229.
5. Sharma, A., & Sahay, S. K. (2014). Evolution and detection of polymorphic and metamorphic malwares: A survey. *arXiv preprint arXiv:1406.7061*.
6. PE Format. (n.d.). Retrieved July 25, 2017, from [https://msdn.microsoft.com/en-us/library/windows/desktop/ms680547\(v=vs.85\).aspx](https://msdn.microsoft.com/en-us/library/windows/desktop/ms680547(v=vs.85).aspx)
7. SIKORSKI, Michael a Andrew HONIG. *Practical malware analysis: the hands-on guide to dissecting malicious software*. San Francisco: No Starch Press, 2012. ISBN 978-1-59327-290-6.

# A Malware Detection on PE header Information

Jiří Znoj

Department of Computer Science, FEECS,  
VŠB – Technical University of Ostrava, 17. listopadu 15,  
708 33 Ostrava – Poruba, Czech Republic  
jiri.znoj@vsb.cz

**Abstract.** Detection of unknown malware is very important for prevention of a zero-day attack. Such a detection could be done in many ways. This work is focused on detection by classification techniques of data from 32-bit and 64-bit PE headers. Library for getting information from PE headers and data set source are presented together with already existing algorithms for classification with information about the use in the past for detection of data from PE headers.

**Keywords:** PE file, PE header, Classification, Malware detection

## 1 Introduction

Company McAfee quarterly publishes reports with malware statistics. According to a report from June 2017, in the first quarter of the 2017, there were more than 30 million new malware samples detected by McAfee alone. At the beginning of the 2017, over 600 million samples of malware had been detected by McAfee Labs since their inception. [1] According to monthly reports of Symantec Company, 66.3 million new malware variants were detected in June 2017 [2]. In 22nd Symantec's report from April 2017, we can find that 357 million new malware variants were discovered (by Symantec) [3].

Last year (2016) research about malware detection began and based on that using data from headers PE (Portable Executable) files were chosen. More about PE format could be read in article Peering Inside the PE: A Tour of the Win32 Portable Executable File Format [4].

Yujie Fan et al. in their works wrote that actions of portable executables can be well represented by Application Programming Interface (API) – one of the most effective features using methods based on heuristic [17].

Some of related works are mentioned in section 2, followed by section 3 with already achieved progress and explored classification techniques. Section 4 describes future work and conclusion and this work ends with Acknowledgements in section 5.

## 2 Related Work

More than fifteen years ago (2001), D. Schultz et al. proposed an idea of using PE files for malware detection. They used algorithm RIPPER (Repeated Incremental Pruning to Produce Error Reduction) on DLLs extracted from Import Table and that same algorithm on data composed from function calls called by the DLLs (extracted from Import Table). When function calls were used, judging by Overall Accuracy and False Positive Rate, algorithm had a better result. D. Schultz et al. used Naïve Bayes algorithm and a Multi-Classfier system in their work as well [11].

Five years later (2006) J. Zico Kolter et al. tried to improve D. Shultz et al.'s work by using executables data represented as n-grams. Algorithms Naive Bayes, Instance-based Learner, Decision Trees, Support Vector Machines, and Boosted Classifiers for machine learning were used [12].

Three years later (2009), Shafiq et al. came up with a framework called PE-Miner for malware detection. This framework was compared with woks mentioned above in this section, with better results. After pre-processing, algorithms used for classification were Decision Tree, Instance-based learning, Repeated Incremental Pruning to Produce Error Reduction, Naïve Bayes and Support Vector Machines (using Sequential Minimal Optimization). This work had significant improvements compared to the both above-mentioned works [13].

After another four years (2013), Usukhbayar Baldangombo et al. created software named PE-Miner for reading PE file headers and extracting used DLLs and called functions from those DLLs. Data extracted in this way are stored in database and used by algorithms Decision Tree, Naïve Bayes and Support Vector Machines. Only DLLs used by PE files, only called API functions by PE files or DLLs together with API calls were used by the mentioned algorithms [14].

One year later (2014), Jinrong Bai et al. used information obtained from PE headers Decision Tree with boosting as an algorithm for classification, with bagging and without these features the algorithm Random Forest was used in this work too [15].

Last year (2016) Bojan Kolosnjaji et al. used framework Tensorlow and framework Theano for creation and training of neural networks. Convolutional neural network was used for counting API calls getting from PE headers. This was combined with Long short-term memory for recording API in Cuckoo sandbox to observe and learn behavioural modelling [16].

## 3 Working on Antivirus program to prevent Zero-day attack

### 3.1 C++ library for reading PE files for future use

Several existing libraries for reading PE files were explored, but none of those worked as needed. We created a library for reading headers based on Yoda's Protector [5]. We provided there many fixes, extended functionality for 64-bit files and changed outputs



to desirable forms (see Fig. 1). The goal was to have C++ library without GUI (Graphical user interface), returning libraries and functions used by given PE files without redundant unwanted data.

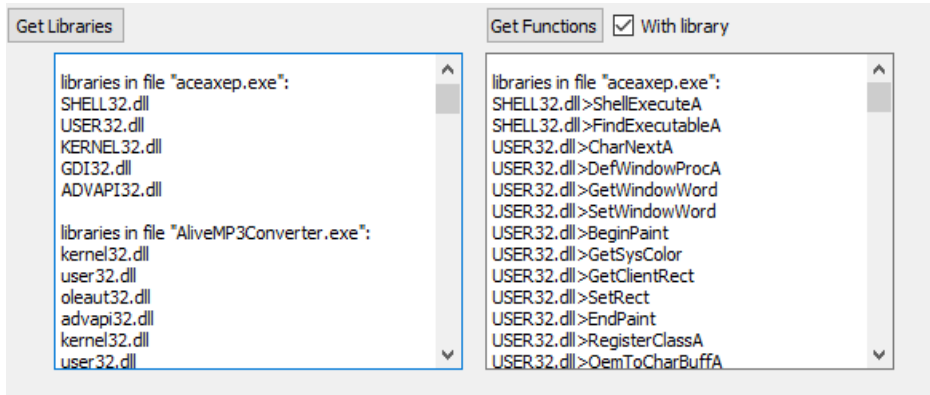


Fig. 1. C++ library for reading PE files for future use

### 3.2 Collecting malware and goodware samples

For detecting malware, we need, of course, collection of many malware and goodware (not malware) samples. Getting malware samples was not a complex task (contrary to getting goodware) owing to Microsoft Malware Classification Challenge (BIG 2015) with 17.77GB test archive and 17.52 GB train archive [6], VX Heaven with more than 270 000 samples (62 Gb) [7] or another malware collections.

For getting goodware samples, we created a script to download programs from sites studna [8], sourceforge [9], filehippo [10] extendable to more than these. You can see the output from this script in Fig. 2. As another source, I used my private collection of executable files.

```
http://www.scam-sensor.com/files/ScamSensorForOutlookInstaller.exe
http://www.screensavershot.com/step35.exe
http://www.smitka.org/download/microrun.zip
http://downloads.solarwinds.com/solarwinds/Release/SU/SU-FTP-Server-Windows-v15.0.0.zip
http://www.revolutionarystuff.com/swapper/SwapperSetup.exe
http://www.willingssoftware.com/download/willingwebcam553.exe
step35.exe - download finished.
http://www.labf.com/download/aceaxep.exe
http://www.av54you.com/downloads/AVSDVDPlayer.exe
http://ibrowser.fcodersoft.com/ftp/ibrowser.zip
willingwebcam553.exe - download finished.
http://www.brooksnet.com/software/intelliscribe/intelliscribe.exe
ipscan-win32-3.3.1.exe - download finished.
http://www.stereo.cz/download.asp?co=sd402.exe
http://www.decompiler-swf.com/download/flash_decompiler.exe
SwapperSetup.exe - download finished.
```

Fig. 2. Collecting malware and goodware samples

### 3.3 Learning method(s) and classification technique

The following structure of methods used for classification is based on book Data Mining: Practical Machine Learning Tools and Techniques [20].

#### Inferring rudimentary rules – 1R

Number of rules that test on one particular attribute.

#### Statistical modeling – algorithm Naïve Bayes

This technique, unlike 1R, uses all attributes. It is supposed, that all attributes are independent and one attribute is equally important to another one.

Used by D. Schultz et al. for malware detection [11].

#### Divide-and-conquer – Decision trees construction

ID3 algorithm developed by J. R. Quinlan is one way to construct a decision tree [18]. This algorithm was improved by Quinlan and it is known as C4.5 [19].

Used by J. Zico Kolter et al. for malware detection [12].

#### Covering algorithms: Constructing rules

Alternative approach to the decision trees. In each stage a rule, that “covers” some of the instances, is identified. This covering approach leads to a set of rules rather than to a decision tree [20].

Algorithm RIPPER was used by D. Schultz et al., while data set was divided as training set (2/3) and validation set (1/3) [11].

#### Mining association rules

The goal is to find classification rules from every combination of attributes with every combination of values [20].

#### Linear models

When the linear regression approach is used, the class is defined by linear combination of the attributes and weights calculated from the training dataset. Some other approaches are logistic regression using the perceptron, logic regression using Winnow and others [20].

Support vector machines use linear models to implement nonlinear class boundaries. This algorithm was used by Usukhbayar Baldangombo et al. for malware detection [14].

#### Instance-based learning

There is a training set with known classes. Unknown samples are classified by counting distance from training instances and putting to class of nearest training instance.

For distance counting, Euclidean distance could be used. As a well-known algorithm, we can mention k-nearest-neighbors [20].

Shafiq et al. used Instance-based learning in his work for malware detection [13].

### **Clustering**

Instances are divided into natural groups – clusters. K-means is a technique used for clustering. “k” classes are created and instances are classified by counting distance. This is the same way as mentioned in the previous technique. After the classification, the clusters are recalculated.

### **Transformations**

Several transformations techniques were used to prepare a dataset for better results and performance. Attribute selection, boosting, bagging, pruning, anomalies detection, randomization and more.

## **4 Conclusion and Future work**

The goal is to have a program for detection of zero-day attacks. This work is focused on current state of other works in this field and initial state of a new antivirus program.

As a contribution in a new nascent antivirus program, a library was presented for reading PE headers and getting useful data from it, dataset and research for already existing algorithms, and an algorithm used for malware detection on PE headers data.

In the near future, we would like to implement algorithms already used in the past for malware detection from data of PE headers and compare results with new, unused algorithms and algorithms with various transformations for classification.

## **5 Acknowledgements**

The following grants are acknowledged for the financial support provided for this research: Grant Agency of the Czech Republic - GACR P103/15/06700S, Grant of SGS No. SGS 2017/134, VSB-Technical University of Ostrava. The Ministry of Education, Youth and Sports from the National Programme of Sustainability (NPU II) project “IT4Innovations excellence in science - LQ1602”.

## **References**

1. McAfee Labs Threats Report. McAfee, LLC, Santa Clara, CA (2017).
2. Internet Security Threat Report 2015 | Symantec, [https://www.symantec.com/security\\_response/publications/monthlythreatreport.jsp#Malware](https://www.symantec.com/security_response/publications/monthlythreatreport.jsp#Malware), last accessed 2017/07/14.
3. Internet Security Threat Report. Symantec Corporation, Mountain View, CA (2017).
4. Peering Inside the PE: A Tour of the Win32 Portable Executable File Format, <https://msdn.microsoft.com/en-us/library/ms809762.aspx>, last accessed 2017/07/18.

5. Yoda's Protector, <http://yodap.sourceforge.net/index.html>, last accessed 2017/07/18.
6. Microsoft Malware Classification Challenge (BIG 2015) | Kaggle, <https://www.kaggle.com/c/malware-classification/data>, last accessed 2017/07/18.
7. Welcome to VX Heaven!, <http://vxheaven.org/>, last accessed 2017/07/18.
8. Studna.cz - Studna Plná Software, <http://www.studna.cz/>, last accessed 2017/07/18.
9. SourceForge - Download, Develop and Publish Free Open Source Software, <https://sourceforge.net/>, last accessed 2017/07/18.
10. FileHippo.com - Download Free Software, <http://filehippo.com/>, last accessed 2017/07/18.
11. Schultz M., Eskin E., Zadok E., Stolfo S.: Data Mining Methods for Detection of New Malicious Executables. In: SP '01 Proceedings of the 2001 IEEE Symposium on Security and Privacy, pp. 38-49. <https://doi.org/10.1109/SECPRI.2001.924286>, Oakland, California (2001).
12. Kolter J., Maloof M.: Learning to Detect and Classify Malicious Executables in the Wild. *Journal* 7, 2721-2744 (2006).
13. Shafiq M., Tabish S., Mirza F., Farooq M.: PE-Miner: Mining Structural Information to Detect Malicious Executables in Realtime. In: Kirda E., Jha S., Balzarotti D. (eds.) Recent Advances in Intrusion Detection. RAID 2009, LNCS, vol. 5758, pp. 121-141. Springer, Heidelberg (2009).
14. Ian H. Witten, Eibe Frank and Mark A. Hall: Data Mining: Practical Machine Learning Tools and Techniques. 2nd edn. Morgan Kaufmann Publishers Inc., San Francisco (2005).
15. Bai J, Wang J, Zou G.: A Malware Detection Scheme Based on Mining Format Information. *The Scientific World Journal*. 2014(260905), (2014).
16. Kolosnjaji B., Zarras A., Webster G., Eckert C.: Deep Learning for Classification of Malware System Call Sequences. In: Kang B., Bai Q. (eds.) *Advances in Artificial Intelligence*. AI 2016, LNCS, vol. 9992, pp. 137-149. Springer, Cham (2016).
17. Yujie Fan, Yanfang Ye, Lifei Chen: Malicious sequential pattern mining for automatic malware detection. In: *Expert Systems with Applications*. *Journal* 52, 16-25 (2016).
18. Quinlan, J.: Induction of Decision Trees. In: *Machine Learning* 1, pp. 81-106. Kluwer Academic Publishers, Boston (1986)
19. Quinlan, J.: C4.5: programs for machine learning. Morgan Kaufmann Publishers, San Francisco (1993)
20. Witten I, Frank E.: Data Mining: Practical Machine Learning Tools and Techniques, Second Edition (Morgan Kaufmann Series in Data Management Systems). 2nd edn. Morgan Kaufmann Publishers, San Francisco (2005)

# Univariate Hölder Optimization Algorithm Using Space Filling Curves and its Application to Multidimensional Global Optimization

Michaela Bailová

Department of Applied Mathematics, FEECS,  
VŠB – Technical University of Ostrava, 17. listopadu 15,  
708 33 Ostrava – Poruba, Czech Republic  
`michaela.bailova@vsb.cz`

**Abstract.** The concept of the space filling curves opens a way to reducing a multivariate optimization problem into its one-dimensional equivalent. In this paper, we introduce an algorithm for minimizing one-dimensional Hölder continuous functions. We show that the algorithm computes an approximation of an optimal value with the guaranteed precision. Subsequently, the modification of the algorithm is proposed. Both versions of the algorithm are compared and tested on some types of two-dimensional functions.

**Keywords:** Global optimization, dimension reduction, space filling curves, Lipschitz continuity, Hölder continuity

## 1 Introduction

the paper deals with the problem of searching a global minimum

$$F(y^*) = \min_{y \in D} F(y) \quad (1)$$

and a global minimizer  $y^* \in D$ , where  $D$  is an  $N$ -dimensional hypercube defined as follows

$$D = \{y \in \mathbb{R}^N, -\frac{1}{2} \leq y_j \leq \frac{1}{2}, 1 \leq j \leq N\}. \quad (2)$$

We assume that the objective function  $F$  satisfies the Lipschitz condition with a constant  $L$ ,  $0 < L < \infty$ . the main idea of the paper is to use a continuous correspondence  $y$  that turns the problem (1) into the following one

$$F(y^*) = F(y(x^*)) = \min_{x \in [0,1]} F(y(x)), \quad (3)$$

where  $x^* \in [0, 1]$ . In [1], a complete analysis is done to show that a univariate algorithm using the Hölder continuity of the objective function can be used to find an approximation of the global minimum of  $F$  over  $D$ . In this paper, we describe the algorithm and analyze its maximal error. Subsequently, its modified version is presented. The performance of the algorithms is illustrated by numerical experiments.

## 2 Space filling curves

Some important ideas in this section are inspired by [2] and [4].

**Definition 1.** *A space filling curve is a single-valued continuous correspondence  $y$  mapping the unit interval  $[0, 1]$  onto the hypercube  $D$  from (2).*

If  $y$  is a space filling curve, then

$$F(y^*) = \min_{x \in [0,1]} F(y(x)). \quad (4)$$

For the analysis of the algorithm, a Hilbert-type curve is chosen. The concept of a space filling curve has rather a theoretical purpose. For the practical computation, we use "iterates" of the Hilbert curve mapping the unit interval only into  $D$ . The construction of the " $M$ -th iteration"  $y_M$  is described for example in [2], [4]. The curves  $y_M$  for  $M = 0, 1, 2$  and  $N = 2$  are illustrated by Fig. 1. In [1], it was shown that  $F \circ y_M$  is Hölder continuous.

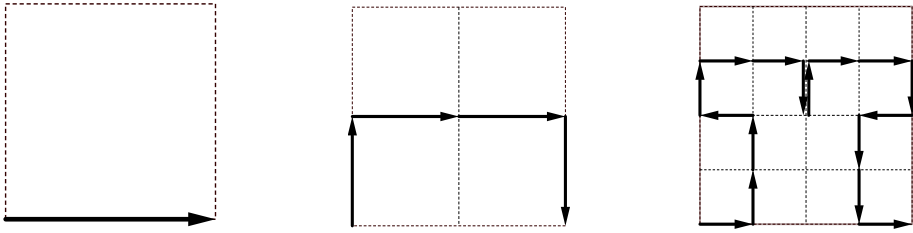


**Fig. 1.** Iterations of the Hilbert curve in two dimensions

**Theorem 1.** *The function  $F \circ y_M$ ,  $M \in \mathbb{N}$ , fulfills the Hölder condition with the constants  $2L\sqrt{N+3}$  and  $\frac{1}{N}$  on interval  $[0, 1]$ , i.e. for all  $x', x'' \in [0, 1]$*

$$|F(y_M(x')) - F(y_M(x''))| \leq 2L\sqrt{N+3}(|x' - x''|)^{\frac{1}{N}}. \quad (5)$$

*Proof.* the proof can be found in [1].

This property is very important and necessary if we intend to use an algorithm presented in the following section.

## 3 Optimization Algorithm

The algorithm is inspired by [2], [3] and is designed for the univariate optimization of the Hölder continuous functions. Let us consider  $g : [a, b] \rightarrow \mathbb{R}$  satisfying the Hölder condition with the constants  $H, \alpha, a, b \in \mathbb{R}, a < b$ . Let  $x_0, x_1, \dots, x_n$  be the trial points from the previous iterations. These points divide  $[a, b]$  into  $n$

subintervals. Let  $I_i$  be an interval with the end points  $x_j, x_k$  that are consecutive,  $j, k \in \{0, \dots, n\}$ ,  $x_j < x_k$ . The lower bounding function on the interval  $I_i$  can be constructed as follows:

$$l_i^n(x) := \max\{l_i^L(x), l_i^R(x)\}, \quad (6)$$

where

$$l_i^L(x) = g(x_j) - H(x - x_j)^\alpha, \quad l_i^R(x) = g(x_k) - H(x_k - x)^\alpha. \quad (7)$$

In Fig.2, we can see the functions  $l_i^L$  and  $l_i^R$ . 2. It can be shown that the function

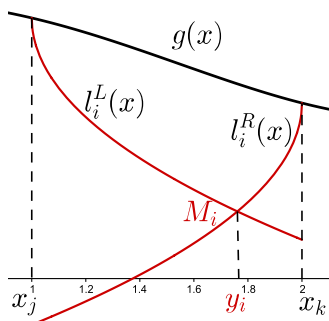


**Fig. 2.** The functions  $l_i^L$  and  $l_i^R$

$$L^n(x) := l_i^n(x), \quad x \in I_i, i \in \{0, \dots, n-1\} \quad (8)$$

is a lower bounding of  $g$  over the interval  $[a, b]$ .

The algorithm computes a value  $y_i \in I_i$  as an  $x$  coordinate of the intersection of  $l_i^L$  and  $l_i^R$ . Then, the characteristic  $M_i$  is computed as follows

$$M_i = l_i^L(y_i) = l_i^R(y_i). \quad (9)$$

Moreover,  $M_i \leq \inf\{g(x), x \in I_i\}$ . In Fig. 2, we can see a graphical interpretation of  $y_i$  and  $M_i$ .

In every iteration, the algorithm chooses an interval  $I_t$  with the lowest value of  $M_t$  and  $x_{n+1} := y_t$  becomes the next trial point. This point divides  $I_t$  into two subintervals. For both of them, new characteristics are computed. If

$$\text{diam}(I_t) \geq \delta, \quad (10)$$

the algorithm computes the approximation of the global minimum

$$g^* = \min \{g(x_i), 0 \leq i \leq n+1\} \quad (11)$$

and the minimizer

$$\bar{x} = \arg \min \{g(x_i), 0 \leq i \leq n+1\}. \quad (12)$$

Otherwise, the next iteration is done the same way. the iterations of the algorithm are completely described in [1].

Let us return to the problem (1). the optimization algorithm introduced in this section can also be used to compute the optimal value of  $F$  along the curve  $y_M$ . As it was mentioned, the function  $F \circ y_M$  is Hölder continuous on  $[0, 1]$  with the constants  $\alpha = \frac{1}{N}$  and  $H = 2L\sqrt{N} + 3$ . In what follows, we assume that  $N = 2$ . We get

$$\sup_{y \in D} \text{dist}(y_M([0, 1]), y) = \frac{1}{2^M}. \quad (13)$$

Now, let us deal with the precision of the algorithm. If  $\varepsilon > 0$  is a desired precision, i.e. if we want to find  $\bar{y} \in D$  such that

$$F(\bar{y}) - \min_{y \in D} F(y) \leq \varepsilon, \quad (14)$$

then we can set the input parameters  $M$  and  $\delta$  so that

$$M \geq \log_2 \frac{2L}{\varepsilon}, \quad \delta \leq 2 \left( \frac{\varepsilon}{2H} \right)^2. \quad (15)$$

the proof can be found in [1]. the statement also gives us some information about the maximal error for the chosen parameters  $M$  and  $\delta$ .

### 3.1 the Optimization Algorithm using an estimation of $H$

The algorithm described above is rather theoretical, because we suppose that the Hölder constant is known a priori. In general, the Lipschitz constant of  $F$  is not known. It is more convenient to use an approximated value of  $H$  computed in each iteration of the algorithm. In [3], two possible ways how to compute the Hölder constant are introduced. This simplification can significantly decrease the number of iterations, but it is necessary to compute the values  $y_i$  and  $M_i$  for every interval. Moreover, the algorithm is rather heuristical and there is no way how to guarantee the error.

## 4 Numerical experiments

In this section, we compare the algorithm with an a priori known  $H$  (referred to as Alg.1) and its modification using an estimation of  $H$  described in 3.1 (referred to as Alg.2). In both algorithms, we use the same stopping criterion (10). For our experiments, two types of functions were chosen. Let us start with the function

$$F(x, y) = \frac{1}{4}((x - 0.4)^2 + \frac{1}{4}(y - 0.6)^2 + 1).$$



It is not difficult to find out that  $F(y^*) = \frac{1}{4}$  and  $y^* = [0.4, 0.6]$ . Let  $\varepsilon = 10^{-2}$  be the desired precision. From (15), we get the input parameters  $\delta = 10^{-5}$  and  $M = 6$ . In Fig.3, we can see the result. The approximations of the optimal values gained by both algorithms are  $F_{\text{Alg.1}}^* = 0.250009765835627$ ,  $F_{\text{Alg.2}}^* = 0.250009765835627$ .

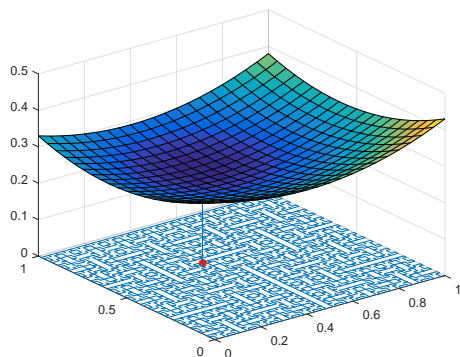


**Fig. 3.** the function  $F$  together with the Hilbert curve and the result of both algorithms.

Now, let us take a smooth function  $G$  with a peak in  $y = [0.4, 0.6]$  and let us set  $\varepsilon = 0.5$ . According to (15), the input parameters can be chosen as follows:  $M = 11$  and  $\delta = 4.33 \cdot 10^{-8}$ . In Fig.4, 5 we can see the result.

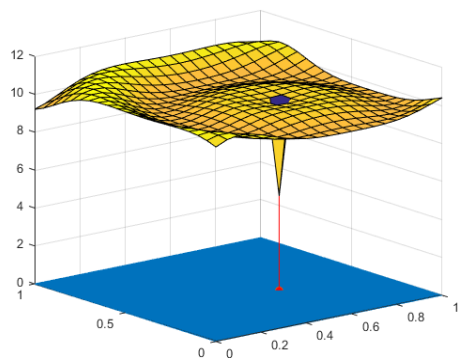


**Fig. 4.** the function  $G$  together with the Hilbert curve and the result of Alg.1.

For the theoretical algorithm, this choice of the input parameters guarantees us a maximal error lower than  $\varepsilon$ . Contrariwise, the error of the other algorithm is significantly bigger, due to its heuristical behavior. the numerical experiment

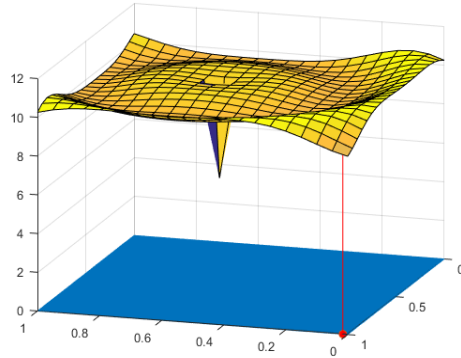


**Fig. 5.** the function  $G$  together with the Hilbert curve and the result of Alg.2.

showed us, that, for some types of functions, there is no way how to guarantee the error.

## 5 Conclusion

In this paper a univariate minimization algorithm using space filling curves was described and analyzed. Subsequently, its modification was proposed. As it was show before, the function  $F \circ y_M$  is Hölder continuous. Thus an algorithm introduced in this paper could be used to find an approximation of the global minimum of  $F$ . It was shown that the algorithm computed the approximation of the optimal value of  $F$  with the guaranteed precision. The algorithm and the analysis will be extended for higher dimensions and used for some practical optimization problems.

## References

1. BAILOVA, M., J. BOUCHALA and P. VODSTRCIL. Global Optimization Using Space Filling Curves. *Advances in Electrical and Electronic Engineering*. 2017, vol. 15, iss. 2, pp. 251–257. ISSN 1336-1376, DOI: 10.15598/aeec.v15i2.2303.
2. SERGEYEV, Ya. D, R. G. STRONGIN and D. LERA. *Introduction to Global Optimization Exploiting Space-Filling Curves*. New York: Springer, 2013. ISBN 978-1-4614-8041-9.
3. LERA, D. and Ya. D. SERGEYEV. Lipschitz and Hölder Global Optimization Using Space-Filling Curves. *Applied Numerical Mathematics*. 2010, vol. 60, iss. 1-2, pp. 115–129. ISSN 0168-9274.
4. SAGAN, H. *Space-Filling Curves*. New York: Springer, 1994. ISBN 978-0-387-94265-0.
5. KUFNER, A., O. JOHN and S. FUCIK. *Function spaces*. Leyden: Noordhoff International Publishing, 1977. ISBN 90-286-0015-9.

# Bayesian and Frequentist Approach to Logistic Regression

Michal Běloch

Department of Applied Mathematics, FEECS,  
VŠB – Technical University of Ostrava, 17. listopadu 15,  
708 33 Ostrava – Poruba, Czech Republic  
michal.beloch@vsb.cz

**Abstract.** When faced with the task of modelling the binary variable, the very first choice is to use the logistic regression. The coefficients of the logistic model are usually obtained by the maximum likelihood estimation. Another approach might be to consider these coefficients as random variables and place the probability distributions on them therefore taking Bayesian route. Both methods are sound and should lead to the similar results, so the natural question is if one method is better than the other. First, both methods are described and then they are applied to real data from the Open University. Finally, the recommendation is given which model suits the data better.

**Keywords:** logistic regression, bayesian approach

## 1 Logistic regression

The logistic regression [1,2] is used whenever we want to model the binary outcome variable  $y$ . It can also be seen as the subset of the generalized linear model.

Let us have  $p$  independent variables  $x = (x_1, x_2, \dots, x_p)$ . Let us denote the conditional probability that event occurred as  $P(Y = 1 | x) = \pi(x)$ . The logit of the regression model is in the form  $g(x) = \beta_0 + \beta_1 x_1 + \beta_2 x_2 + \dots + \beta_p x_p$  and the appropriate regression model is  $\pi(x) = \frac{e^{g(x)}}{1 + e^{g(x)}}$ . Now consider we have the sample of independent observations  $(x_i, y_i)$ ,  $i = 1, 2, \dots, n$ . The unknown values of the regres-

sion model are the parameters  $\beta = (\beta_0, \beta_1, \beta_2, \dots, \beta_p)$ . The estimates of the parameters are usually obtained from the minimalization of the likelihood function. This approach leads to the system of  $p + 1$  equations which is solved with appropriate numerical method.

### 1.1 Bayesian approach to logistic regression

The Bayesian approach [3] treats unknown parameters as random variables instead of constants. It then proceeds in typical Bayesian manner, that is define the prior distribution, find the likelihood function and then combine both information in the posterior distribution.

First, the parameters  $\beta = (\beta_0, \beta_1, \beta_2, \dots, \beta_p)$  must be assigned the probability distribution. It is possible to either use any distribution that best describes our initial knowledge about the parameters or non-informative prior when our understanding of the parameters is limited or lacking. The non-informative prior is usually of the form  $\beta_j \sim N(\mu_j, \sigma_j)$ ,  $j = 0, 1, 2, \dots, p$ . The prevalent choice for expected value is zero and the standard deviation is chosen to be big enough.

Second, concerning the likelihood function, the conditional probability that event occurred is  $P(Y = 1 | x) = \pi(x)$ . The complement, that is the conditional probability did not occur is therefore  $P(Y = 0 | x) = 1 - \pi(x)$ . The addition to the likelihood function for the couple  $(x_i, y_i)$  is  $[\pi(x_i)]^{y_i} [1 - \pi(x_i)]^{1-y_i}$ . Since we consider the observations to be independent, resulting likelihood function is 
$$l(\beta) = \prod_{i=1}^n [\pi(x_i)]^{y_i} [1 - \pi(x_i)]^{1-y_i}.$$

The posterior is obtained via the well-known proportion posterior  $\propto$  prior  $\times$  likelihood. Since this is usually complicated procedure, MCMC simulation is used to estimate the model.

## 2 Application on Open University data

### 2.1 Data description

The data set contains information about the students from the Open University, Walton Hall in Milton Keynes. We want to model whether student will pass the final exam. The students are described by a set of demographic data and performance in graded activities. All the students were attending the same course in the same year.

The number of observations is 616 students. This number is then divide into training group and testing group. The training group contains 500 students and the testing group consists of 116 students.

The observed variables are:

- Final result – Dependant variable we want to model. It has two values, pass or fail.
- Gender – The sex student identifies with. It has two values, male or female.
- Age band – Age group the student falls into. There are two age groups in the data, less than 35 and between 35 and 55.
- Disability – Whether student has some condition (mental or physical) complicating the study. It has two values, yes or no.
- Result of tasks 1 to 6 – The student takes six graded tasks during the semester. These six variables contain his or her results. The values are from range 0 to 100.

## 2.2 Model generation

We want to create the model to assess the probability of successfully passing the final examination based on the described independent variables. Since the dependant

variable is binary, we will use the logistic model of the form  $\pi(x) = \frac{e^{g(x)}}{1 + e^{g(x)}}$ , where

$g(x) = \beta_0 + \beta_1 \cdot \text{Gender} + \beta_2 \cdot \text{Age} + \beta_3 \cdot \text{Disability} + \beta_4 \cdot \text{Task1} + \beta_5 \text{Task2} + \beta_6 \text{Task3} + \beta_7 \text{Task4} + \beta_8 \text{Task5} + \beta_9 \text{Task6}$ . We will consider three models.

The first model is standard logistic regression (S). The second and the third model incorporate the Bayesian approach (B1 and B2). They differ in number of iterations (2,500 and 25,000 respectively) of MCMC. The R software [4] was used to generate the models and the MCMC package [5] was used for the Bayesian approach.

**Table 1.** Parameters of the models

Coefficient	Standard	Bayes 2500	Bayes 25000
Intercept	-6.423837	-6.466367	-6.737139
Gender (Male)	-0.242255	-0.206393	-0.167392
Age (35-55)	0.702672	0.739801	0.743377
Disability (Yes)	-0.646325	-0.519700	-0.665369
Task1	0.039926	0.030126	0.036283
Task2	-0.007205	-0.005483	-0.006806
Task3	0.039926	0.040678	0.041796
Task4	0.009967	0.012493	0.010082
Task5	0.026713	0.027045	0.026677
Task6	0.021184	0.022233	0.022853
Run Time	0.024 s	0.524 s	4.249 s

As can be seen in the table (Table 1.), the values of the coefficients  $\beta$  differ ever so slightly. The significant difference can be seen in the run time that measured how long it takes to compute the coefficients. It shows that simple logistic regression is 22 times faster than Bayesian regression when we use 2,500 iterations and even 177 times faster when we use 25,000 iterations. The important question is how well are the slight changes in parameters reflected in the model. The answer lies in the following table (Table 2.) of linear analysis [6]. This method shows how well model predicts on appropriate groups of success. The first column shows the levels of success. The columns In group denote how many students are classified by appropriate model into the given success level. The columns Occurrence show how many successful states occurred for the given level. The columns Predicted show how many successful states should be for the given level. Finally, the columns Ratio is Occurrence divided by Predicted.

**Table 2.** Linear analysis for the three models

	In group			Occurrence			Predicted			Ratio		
	S	B1	B2	S	B1	B2	S	B1	B2	S	B1	B2
<10	1	1	1	0	0	0	0	0	0	1.00	1.00	1.00
10 – 19	0	0	0	0	0	0	0	0	0	1.00	1.00	1.00
20 – 29	0	1	0	0	0	0	0	0	0	1.00	1.00	1.00
30 – 39	1	0	1	0	0	0	0	0	0	1.00	1.00	1.00
40 – 49	1	1	1	1	1	1	0	0	0	N	N	N
50 – 59	3	2	3	3	2	3	2	1	2	1.50	2.00	1.50
60 – 69	2	3	2	1	2	1	1	2	1	1.00	1.00	1.00
70 – 79	10	9	8	7	6	5	7	7	6	1.00	0.86	0.83
80 – 89	15	13	14	13	11	12	13	11	12	1.00	1.00	1.00
90 – 100	83	86	86	82	85	85	82	81	81	1.05	1.05	1.05
0 – 100	116	116	116	107	107	107	101	102	102	1.06	1.05	1.05

The linear analysis performed on the test dataset shows that the difference in terms of prediction capabilities of the three models is negligible. On every percentage level the models are more or less equivalent as can be seen by comparing the values in the column Ratio.

### 2.3 Conclusion

At first glance it might seem that using the Bayesian approach is just not worth it given higher complexity of the computation which was also proven by the increase in computation time. Therefore, the conclusion is clear, use the standard logistic regression. However we must not forget the important upside of the Bayesian approach and that is the flexibility it offers us. It is possible that using better prior distribution instead

of non-informative could improve the results. It is definitely something to be tested further.

## Acknowledgement

This work was supported by The Ministry of Education, Youth and Sports from the National Programme of Sustainability (NPU II) project “IT4Innovations excellence in science - LQ1602“.

## References

1. Hosmer, D.W., Lemeshow, S. Applied logistic regression, Wiley 2000, ISBN 0-471-35632-8.
2. Briš R., Litschmannová M., STATISTIKA II., E-learningový prvek pro podporu výuky odborných a technických předmětů, v rámci projektu CZ.O4.01.3/3.2.15.2/0326, VŠB TU Ostrava, 2007, ISBN 978-80-248-1482-7.
3. Hilbe, Joseph M. *Practical guide to logistic regression*. ISBN 9781498709576.
4. R Core Team (2014). R: A language and environment for statistical computing. R Foundation for Statistical Computing, Vienna, Austria. URL <http://www.R-project.org/>.
5. Andrew D. Martin, Kevin M. Quinn, Jong Hee Park (2011). MCMCpack: Markov Chain Monte Carlo in R. Journal of Statistical Software. 42(9): 1-21. URL <http://www.jstatsoft.org/v42/i09/>.
6. Hosmer, D.W., and Lemeshow, S. A goodness-of-fit test for the multiple logistic regression model. Communications in Statistics, 1980, A10, 1043-1069.

# Reduced Basis Solver for Stochastic Galerkin Solution of the Darcy flow with a Random Material on Given Interfaces

Michal Béréš

Department of Applied Mathematics, FEECS,  
VŠB – Technical University of Ostrava, 17. listopadu 15,  
708 33 Ostrava – Poruba, Czech Republic  
`michal.beres@vsb.cz`

**Abstract.** This article presents a study of the reduced basis solver for the stochastic Galerkin method (SGM) applied to the Darcy flow problem with a random material on given interfaces. The solution of SGM resulting system of equations is usually a very challenging task. The standard approach to the solution is a use of some iterative method. Standard iterative methods meet two main difficulties when solving SGM system. First, we need new types of preconditioners, which considers the specific structure of the system, and second, the size of the problem can grow so fast that even the solution cannot be stored in the memory. The alternative approach to these difficulties is a reduced basis (RB) solver, which looks for the low-rank representation of the solution.

**Keywords:** Darcy flow, polynomial chaos, Stochastic Galerkin method, reduced basis method

## 1 Introduction and problem setting

This paper is a continuation of the research presented in [1], where we solved the Darcy flow with material given by a random field and used iterative solvers.

Here, we consider Darcy flow on the square  $\mathcal{D} = \langle 0, 1200 \rangle \times \langle 0, 1200 \rangle$ . We assume zero Dirichlet condition on the whole boundary and point loads around the middle of the domain, equivalent to wells with inflow and outflow. We work with the following problem formulation

$$\begin{cases} -\operatorname{div}(k(x; \mathbf{Z}) \cdot \nabla u(x; \mathbf{Z})) = f(x) & \forall x \in \mathcal{D}, \forall \mathbf{Z} \\ u(x; \mathbf{Z}) = 0 & \forall x \in \Gamma_D, \forall \mathbf{Z}, \end{cases} \quad (1)$$

where  $\mathbf{Z} = (Z_1, \dots, Z_M)$  is a vector of independent normal random variables  $Z_i \sim N(\mu = 0; \sigma = 1)$  and  $k(x; \mathbf{Z})$  denotes the random material. The problem and its geometry is taken from [5]. We assume the domain divided into eight sub-domains, see Fig. 1a. The random material is considered as a function of  $M = 7$  random parameters and the domain  $\mathcal{D}$  and has the form

$$k(x; \mathbf{Z}) = k_0(x) + \sum_{i=1}^M k_i(x) \cdot g_i(\mathbf{Z}),$$



where  $k_0(x)$  consists of the mean material field (sum of the constant part of the material in  $\Omega_0$  and mean values of material in other sub-domains),  $k_i(x)$  is characteristic function of  $\Omega_i$  multiplied by scale factor  $\sigma_i$ , and  $g_i(\mathbf{Z}) = \exp(Z_i)$ .

For better illustration of the problem we provide the mean value of the solution, see Fig. 1b.

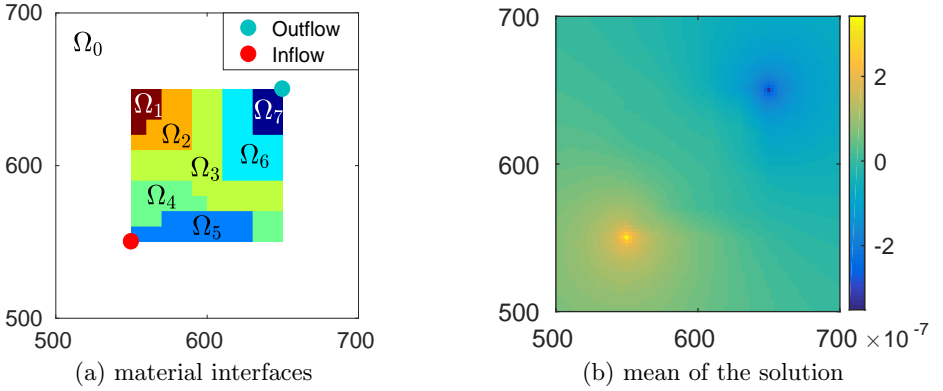


Fig. 1: Problem illustration and mean value of the solution (cutout of the domain)

## 2 The stochastic Galerkin Method

The SGM works similarly to the standard Galerkin method, for a detailed description of SGM see [3]. First, we need the weak formulation

$$\begin{cases} \text{Find } u(x; \mathbf{Z}) \in V, \forall v(x; \mathbf{Z}) \in V : \\ \int_{\mathbb{R}^N} \int_{\mathcal{D}} k(x; \mathbf{Z}) \cdot \nabla_x u(x; \mathbf{Z}) \cdot \nabla_x v(x; \mathbf{Z}) \, dx \, dF\mathbf{Z} = \int_{\mathbb{R}^N} \int_{\mathcal{D}} f(x) \cdot v(x; \mathbf{Z}) \, dx \, dF\mathbf{Z}, \end{cases}$$

where  $V := L^2_{dF\mathbf{Z}}(\mathbb{R}^N, H^1_0(\mathcal{D})) = H^1_0(\mathcal{D}) \otimes L^2_{dF\mathbf{Z}}(\mathbb{R}^N)$ . The tensor structure of the test space allows us to use a tensor product of discretized bases of the spaces  $H^1_0(\mathcal{D})$  and  $L^2_{dF\mathbf{Z}}(\mathbb{R}^N)$  as a discretization of  $V$ .

### 2.1 Assembling the system of equations

We use the finite elements basis  $V_D^h$  (linear elements) as a discretization of  $H^1_0(\mathcal{D})$  and the Hermite polynomials basis (or polynomial chaos (PC) basis)  $V_P^h$  as a discretization of  $L^2_{dF\mathbf{Z}}(\mathbb{R}^N)$ . We denote the discretized test function space as

$$V^h := V_D^h \otimes V_P^h = \langle \varphi_1(x), \dots, \varphi_{N_D}(x) \rangle \otimes \langle \psi_1(\mathbf{Z}), \dots, \psi_{N_P}(\mathbf{Z}) \rangle \subset V.$$

The solution takes the form

$$u^h(x; \mathbf{Z}) = \sum_{i=1}^{N_D} \sum_{j=1}^{N_P} (\bar{u})_{ij} \cdot \varphi_i(x) \cdot \psi_j(\mathbf{Z}). \quad (2)$$

Using the discretization  $V^h$ , we obtain the system of linear equations

$$\mathbb{A} \cdot \bar{u} = \bar{b}, \quad (3)$$

where the individual entries of  $\mathbb{A}$  and  $\bar{b}$  are defined as

$$(\mathbb{A})_{ij,kl} = \int_{\mathbb{R}^N} \int_{\mathcal{D}} k(x; \mathbf{Z}) \cdot \nabla \varphi_i(x) \psi_j(\mathbf{Z}) \cdot \nabla \varphi_k(x) \psi_l(\mathbf{Z}) dx dF\mathbf{Z}, \quad (4)$$

$$(\bar{b})_{ij} = \int_{\mathbb{R}^N} \int_{\mathcal{D}} f(x) \cdot \varphi_i(x) \psi_j(\mathbf{Z}) dx dF\mathbf{Z}. \quad (5)$$

Using the tensor structure of the material function and the test functions, we can rewrite the calculation of  $\mathbb{A}$  and  $\bar{b}$  ( $g_0(\mathbf{Z}) \equiv 1$ ) into

$$\mathbb{A} = \sum_{m=0}^M G_m \otimes K_m,$$

where

$$(K_m)_{i,k} = \int_{\mathcal{D}} k_m(x) \cdot \nabla \varphi_i(x) \cdot \nabla \varphi_k(x) dx,$$

$$(G_m)_{j,l} = \int_{\mathbb{R}^N} g_m(\mathbf{Z}) \cdot \psi_j(\mathbf{Z}) \cdot \psi_l(\mathbf{Z}) dF\mathbf{Z},$$

and

$$\bar{b} = g \otimes f,$$

where

$$(f)_i = \int_{\mathcal{D}} f(x) \cdot \varphi_i(x) dx, \quad (g)_j = \int_{\mathbb{R}^N} \psi_j(\mathbf{Z}) dF\mathbf{Z}.$$

### 3 Reduced basis solver

This section deals mainly with a practical implementation details of the RB, for theoretical background see [4]. An advantage of the tensor structure of the matrix  $\mathbb{A}$ , which we use for the RB solver, is that we can view the system (3) as matrix equations

$$\sum_{m=0}^M K_m \mathbf{x} G_m^T = f g^T. \quad (6)$$

First, we show how to find an approximate solution of the SGM matrix equations with a given RB and then we show the construction of the RB for our model problem. In our text we consider a RB of the matrices  $K_m$ , because in usual applications,  $N_D$  is significantly larger than  $N_P$ . The RB of size  $k$  denotes a set of  $k$  orthonormal vectors  $V_k = [v_1, \dots, v_k] \in \mathbb{R}^{N_D \times k}$ . Then the

matrix  $\mathbf{x}_k = V_k \mathbf{y}_k$  is an low rank approximation of the solution  $\mathbf{x}$ , where  $\mathbf{y}_k$  is a reduced solution matrix. The matrix  $\mathbf{y}_k$  can be obtained from (6) using the Galerkin condition on the residual of  $\mathbf{x}_k$

$$R_k := \sum_{m=0}^M K_m (V_k \mathbf{y}_k) G_m^T - f g^T$$

$$V_k^T R_k = 0 \Rightarrow \sum_{m=0}^M V_k^T K_m V_k \mathbf{y}_k G_m^T = V_k^T f g^T.$$

Note that  $\mathbf{y}_k$  is the solution of similar matrix equations as the original matrix equations

$$\sum_{m=0}^M \bar{K}_m \mathbf{y}_k G_m^T = \bar{f} g^T; \bar{K}_m = V_k^T K_m V_k, \bar{f} = V_k^T f,$$

but with greatly reduced dimension.

Next we discuss the construction of the RB. In this paper, we consider construction using the reduced rational Krylov approximation, see [4]. To construct such approximation, the matrices in the matrix equations formulations need to be symmetric and positive definite (SPD). Note that our formulation of the problem lead to SPD matrix  $K_0$  and symmetric positive semi-definite matrices  $K_m$ . Therefore, we need to reformulate the matrix equations to assure the matrices to be SPD. First, we assume the Cholesky decomposition of  $K_0 = LL^T$  and following reformulation (recall that  $G_0$  is identity matrix)

$$\sum_{m=0}^M K_m L^{-T} L^T \mathbf{x} G_m^T = f g^T \Rightarrow \hat{\mathbf{x}} + \sum_{m=1}^M \hat{K}_m \hat{\mathbf{x}} G_m^T = \hat{f} g^T,$$

where  $\hat{\mathbf{x}} = L^T \mathbf{x}$ ,  $\hat{K}_m = L^{-1} K_m L^{-T}$  and  $\hat{f} = L^{-1} f$ . Next we can shift the spectrum of matrices  $\hat{K}_m$  (positive semi-definite)

$$\hat{\mathbf{x}} \left( I - \sum_{m=1}^M \alpha_m G_m^T \right) + \sum_{m=1}^M \left( \hat{K}_m + \alpha I \right) \hat{\mathbf{x}} G_m^T = \hat{f} g^T,$$

which will result into following matrix equations

$$\hat{\mathbf{x}} B_0 + \sum_{m=1}^M A_m \hat{\mathbf{x}} B_m = \hat{f} g^T, \text{ where } B_0 = I - \sum_{m=1}^M \alpha_m G_m^T, A_m = \left( \hat{K}_m + \alpha I \right).$$

The choice of  $\alpha_m$  is arbitrary (numerical results show that the RB is insensitive to the choice of  $\alpha_m$ , we choose  $\alpha_m = 1$ ), because the matrices  $\hat{K}_m$  are positive semi-definite. Now we can proceed to the RB construction. As mentioned before, we use a sequence of the nested rational Krylov approximation spaces.

To construct the RB, we start with the vector  $v_0 = \hat{f} / \|\hat{f}\|$ . In the first iteration  $i = 0$  we expand the approximation space by

$$W_i = \left[ (A_1 + s_i I)^{-1} v_i, \dots, (A_M + s_i I)^{-1} v_i \right],$$

where  $s_i$  are parameters of the algorithm (we choose  $s_i = 1$ ). We obtain Krylov approximation space  $V = [v_0, v_1, \dots, v_{l_1}]$  by ortho-normalizing  $[v_0, W_0]$  and keeping only most important  $l_1$  vectors (e.g. using singular value decomposition). In the next iterations we repeat the process of expanding the subspace by  $W_i$ .

## 4 Numerical results

For numerical testing, we choose several levels of finite elements (FE) grids (grid level  $n \rightarrow$  discretization  $n \cdot 120 \times n \cdot 120$ ) and polynomial chaos (PC) sizes (maximal polynomial degree  $n \rightarrow \binom{n+7}{n}$  polynomials). We measure the approximation error as relative residual  $\|R_k\| / \|\bar{b}\|$ .

In the first test, we explore the RB approximation error in comparison to the increasing number of finite elements, see Fig. 2. We can observe that between first few coarse levels, the size of the RB needed to achieve the same precision increases greatly, but than stabilizes. This is in agreement with the theoretical results in [4]. The observed behavior is caused by the large approximation error of coarser grids. Once the FE grid is sufficient, the RB size does not grow any larger.

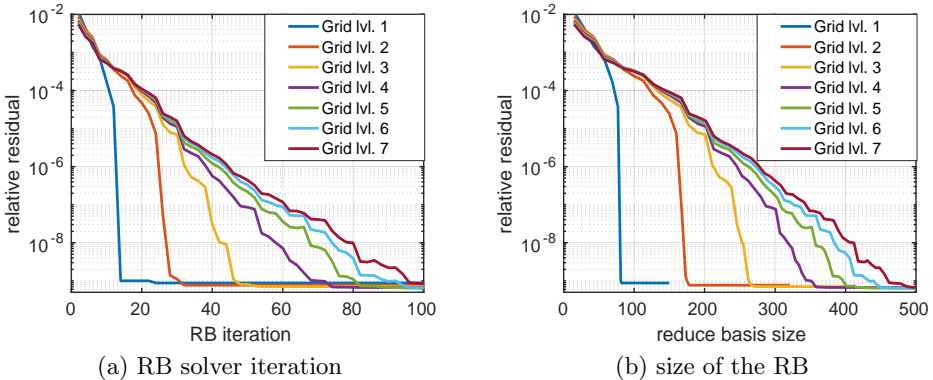


Fig. 2: Convergence relative residual of the RB solver (PC up to degree 5)

In the second test, we investigate the behavior of the RB approximation error in relation to the growing size of the PC, see 3. The results show that we can easily reuse computed RB for larger PC basis without an increase in approximation error (and even if the error increases we can add more vectors to the RB). This make the RB solver adaptive i relation to the PC basis.

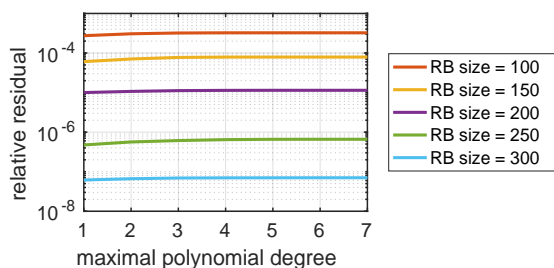


Fig. 3: The RB approximation error dependence on the size of the PC

## 5 Conclusion and future work

In this paper, we showed an efficient approach to the solution of very large systems out-coming from the SGM. The RB solver brings two important things: reduce of the computation complexity and adaptivity in the PC basis, which is the main advantage in comparison to the alternative in the form of e.g. conjugate gradients method. In the current state, our Matlab implementation can easily solve (within minutes) problems equivalent to the solution of systems of more than  $2 \cdot 10^9$  equations on one Solomon cluster node (24 cores, 128 GB of memory).

In the continuation of research of the SGM we want to: expand the solver for the mixed formulation of the Darcy flow equation, try different approaches to the construction of the RB, incorporate the RB solution of the SGM systems into Bayes inversion presented in [2], and implement a parallel version of the RB solver.

## Acknowledgement

This work was supported by The Ministry of Education, Youth and Sports from the National Programme of Sustainability (NPU II) project “IT4Innovations excellence in science – LQ1602”.

## References

1. Domesová, S.; Béréš, M. *Inverse Problem Solution using Bayesian Approach with Application to Darcy Flow Material Parameters Estimation*. Advances in Electrical and Electronic Engineering, 2017.
2. Béréš, M.; Domesová, S. *The Stochastic Galerkin Method for Darcy Flow Problem with Log-Normal Random Field Coefficients*. Advances in Electrical and Electronic Engineering, 2017.
3. Lord, G. J.; Powell, C. E.; Shardlow, T. *An introduction to computational stochastic PDEs*. Cambridge University Press, 2014.
4. Powell, C. E.; Silvester, D.; Simoncini, V. *An efficient reduced basis solver for stochastic Galerkin matrix equations*. SIAM Journal on Scientific Computing, 2017.
5. Haslinger, J.; Blaheta, R.; Hrtus, R. *Identification problems with given material interfaces*. Journal of Computational and Applied Mathematics, 2017.

# Fourier Representation of Paths in Path Integral Monte Carlo Simulations

Rajko Čosić

Department of Applied Mathematics, FEECS,  
VŠB – Technical University of Ostrava, 17. listopadu 15,  
708 33 Ostrava – Poruba, Czech Republic  
`rajko.cosic@vsb.cz`

**Abstract.** The main aim of this paper is to describe the algorithm that can deal with so-called critical slowdown. This is an effect which often occurs in path integral Monte Carlo simulations with large number of path variables (typically at low temperatures). The usual way to handle this problem is to utilize algorithm that enables so-called global moves instead of the single-slice moves. In this paper, the Fourier path representation is described. This algorithm successfully deals with the critical slowdown and can be easily implemented. Moreover, the connection with ergodicity enhancing methods, such as the parallel tempering algorithm, is very efficient.

**Keywords:** quantum systems, path-integral Monte Carlo, Fourier series

## 1 Introduction

One of the most frequently used approaches to simulate the quantum systems at nonzero temperatures is the path integral Monte Carlo (PIMC) method. There are two main problems which every PIMC algorithm has to deal with a) the ergodicity of the random walk which is often being overcome utilizing the *parallel tempering algorithm* [1] and b) the so-called *critical slowdown*. The critical slowdown of the PIMC simulation means that the diffusion through the configuration space decreases more and more no matter how efficient the single-slice move is. The key to overcome this behaviour is to do so-called *global moves* which involve moving more time slices at once. There are several different techniques to do so, e.g. multigrid based methods [2], bisection method [3], etc. We have chosen the *Fourier path representation* [4] because the implementation is very straightforward and also the connection to parallel tempering algorithm can be done in efficient way.

In Sec. 2, the path integral approach is recalled. Sec. 3 focuses on the Fourier path representation and discussion of the advantages. The last section, Sec. 4, summarizes the work and proposes the future possibilities.

## 2 Quantum to Classical system mapping

Now, let us briefly describe the path integral approach. Since this paper is focused on the Fourier path representation, only the core concept of Cartesian path representation is presented. Dear reader may find the detailed description elsewhere [3].

The PIMC approach is based on the famous quantum-classical system mapping (described in [3]). This mapping substitutes each of the quantum particles by the closed path.

Starting with the *Hamiltonian operator*

$$\hat{H}\psi(\mathbf{x}) = \underbrace{\frac{\hbar^2}{2m}\Delta\psi(\mathbf{x})}_{\hat{T}} + \underbrace{V(\mathbf{x})\psi(\mathbf{x})}_{\hat{V}}, \quad (1)$$

where  $m$  is the mass,  $\hat{T}$  is the *kinetic part* and  $\hat{V}$  is the *potential part* of the Hamiltonian operator.

The thermodynamics of the system is described by the *state sum*

$$Z = \text{Tr } e^{-\beta\hat{H}}, \quad (2)$$

where  $\beta = \frac{1}{k_B T}$ . In the position representation, the state sum takes following form:

$$Z = \int_{\mathbb{R}^{3N}} \rho(\mathbf{R}, \mathbf{R}, \beta) d\mathbf{R}, \quad (3)$$

where  $\mathbf{R}$  represents the spatial configuration of the system and  $\rho(\mathbf{R}, \mathbf{R}, \beta) = \langle \mathbf{R} | e^{-\beta\hat{H}} | \mathbf{R} \rangle$  is the *density matrix*.

Combining the *primitive approximation*

$$\lim_{\tau \rightarrow 0} e^{-\tau(\hat{T}+\hat{V})} = \lim_{\tau \rightarrow 0} e^{-\tau\hat{T}} e^{-\tau\hat{V}} \quad (4)$$

and the *Trotter formula* [5]

$$e^{-\beta(\hat{T}+\hat{V})} = \lim_{M \rightarrow \infty} \left( e^{-\tau\hat{T}} e^{-\tau\hat{V}} \right)^M, \quad (5)$$

we obtain the density matrix in a form of many-dimensional integral in which the kinetic and potential part can be solved independently (details can be found in [3], [6]). Solving those parts yields the density matrix in following form

$$\rho(\mathbf{R}_0, \mathbf{R}_M, \beta) = \int_{\mathbb{R}^{3N}} \cdots \int_{\mathbb{R}^{3N}} (4\pi\lambda\tau)^{\frac{3NM}{2}} e^{-\sum_{m=1}^M \left[ \frac{\mathbf{R}_{m-1} - \mathbf{R}_m}{4\lambda\tau} + \tau V(\mathbf{R}_m) \right]} d\mathbf{R}_1 \dots d\mathbf{R}_{M-1}, \quad (6)$$

where  $\lambda = -\frac{\hbar^2}{2m}$ .

The integral in Eq. (6) describes the classical system of  $N$  chains, each consisting of  $M$  *time slices*. Using (3), the integral over closed chains ( $\mathbf{R}_0 = \mathbf{R}_M$ ) of time slices is obtained, from which the thermodynamics can be calculated.

### 3 Fourier PIMC method

The Fourier PIMC (FPIMC) method [4] uses the sine basis to represent the path. The continuous closed curve is then represented by

$$\mathbf{x}(u) = \mathbf{R}_0 + \sum_{k=1}^{\infty} \mathbf{a}_k \sin\left(\frac{k\pi u}{\beta}\right), \quad (7)$$

where  $u \in [0, \beta]$ ,  $\mathbf{a}_k$  are the Fourier coefficients stored in  $3N$ -dimensional vectors and  $\mathbf{R}_0$  is the position of the first time slice.

The integral in Eq. (6) obtained using the cartesian path representation can be the rewritten to following form (for details see [7])

$$\rho(\mathbf{R}_0, \mathbf{R}_M, \beta) = (\text{const.}) \cdot \int_{\mathbb{R}^{3N}} \dots \int_{\mathbb{R}^{3N}} e^{-\sum_{k=1}^{\infty} \frac{\mathbf{a}_k^2}{2\sigma_k^2} - \int_0^{\beta} V(\mathbf{x}(u)) du} d\mathbf{a}_1, \dots, d\mathbf{a}_k, \quad (8)$$

where

$$\sigma_k^2 = \frac{2}{m\beta} \left(\frac{\beta\hbar}{k\pi}\right)^2 \quad (9)$$

and  $\mathbf{x}(u)$  is specified by Eq. (7).

The integral over the potential, however, is not known analytically. For its calculation, the cartesian path is reconstructed and the integral is calculated via the numerical quadrature. Since the Fourier representation is used in the Metropolis sampling [8], all the constants in Eq. (3), including the Jacobian of the transformation [9], can be neglected.

In numerical simulation, the basis is truncated and only first  $K$  frequencies are used. Let us note that, for given system, the number of frequencies needed for good description of the path is not known apriori and has to be estimated via tests.

Let us note that the number of time slices varies with the temperature level. The FPIMC approach enables us to use different numbers of time slices for different temperature levels in the parallel tempering PIMC simulation.

The FPIMC method can be parallelized the same way as the Cartesian PIMC method. Since the optimal number of processes is determined by the number of time slices, it is expected that the performance of the parallel tempering FPIMC method will be slightly better. The optimal workload in Cartesian PIMC simulations in dependency on the potential complexity is discussed in [11], similar tests for FPIMC method are in plan for the nearest future.



## 4 Summary

The FPIMC method is promising way to implement the global moves into the PIMC simulations. The method has been implemented within the library PIMC-Simul which is under development. The method can be used either standalone or with the parallel tempering algorithm. The connection with the parallel tempering algorithm exploits the natural synergy of these approaches in terms of variable number of time slices at different temperature levels.

The tests of the FPIMC method in terms of scalability, sufficient numbers of Fourier coefficients and accuracy will be performed on small clusters of charged helium and on small mercury clusters. The comparison of the Cartesian PIMC approach and the FPIMC approach has been discussed on some systems [10]. Our intention is to compare the efficiency in dependency on the computational complexity of the potential part which, according to our tests [11], plays significant role in scalability and performance of the simulation.

## References

1. Falcioni, M., Deem, M. W.: A biased Monte Carlo scheme for zeolite structure solution. *J. Chem. Phys.* 110, (1999).
2. Goodman, J., Sokal, A. D.: Multigrid Monte Carlo method. Conceptual foundations. *Phys. Rev. D* 40, (1989).
3. Ceperley, D. M.: Path integrals in the theory of condensed helium. *Rev. Mod. Phys.* 67, (1995)
4. Coalson, R. D.: On the connection between Fourier coefficient and Discretized Cartesian path integration. *J. Chem. Phys.* 85, (1986).
5. Trotter, H. F.: On the product of semi-groups of operators. *Proc. Am. Math. Soc.* 10, p. 545 (1959)
6. Ćosić, R.: Mapping of a quantum system of particles onto a classical system of cyclic polymers. WOFEX 2014, p. 436, ISBN 978-80-248-3458-0, (2014).
7. Doll, J. D.: Monte Carlo Fourier path integral methods in chemical dynamics. *J. Chem. Phys.* 81, (1984).
8. Metropolis N. et al.: Equation of state calculations by fast computing machines *J. Chem. Phys.* 21, (1953).
9. Miller, W., H.: Semiclassical Quantization of Non-Separable Systems. *J. Chem. Phys.* 63, (1975)
10. Chakravarty, C., Gordillo, M., C., Ceperley, D., M.: A comparison of the efficiency of Fourier- and discrete time-path integral Monte Carlo. *J. Chem. Phys.* 109, (1998)
11. Ćosić, R., Mrovec, M., Vitek, A., Kalus, R.: First Principles Modelling of Thermodynamical Properties. Civil-Comp Proceedings 2017.

# Sampling from Posterior Distribution of Material Parameters using an Approximation

Simona Domesová

Department of Applied Mathematics, FEECS,  
VŠB – Technical University of Ostrava, 17. listopadu 15,  
708 33 Ostrava – Poruba, Czech Republic  
`simona.domesova@vsb.cz`

**Abstract.** Inverse problems in partial differential equations involve the estimation of parameters using measured data (e.g. measured values of the state function or the flow function in some parts of the domain). This paper presents the Bayesian approach to the identification of material parameters of the Darcy flow problem on subdomains with given interfaces. In the case of the Bayesian approach, the unknown parameters of the material equation have the form of the random vector. The aim is to find the distribution of this random vector and to generate samples from it using the Metropolis-Hastings algorithm. Generating samples requires repeated solutions of the direct problem, which is generally a time consuming task. In this case, the solution of the direct problem is a solution of the differential equation using the finite element method. To reduce the computation complexity, the finite element solution can be replaced by a cheaper approximation. In this paper, the solution using the Stochastic Galerkin method is used as the approximation of the direct solution.

**Keywords:** Bayesian inversion, Darcy flow, Metropolis-Hastings, identification problem, posterior distribution, uncertainty quantification

## 1 Description of the problem

The need of solving inverse problems in partial differential equations arises in various engineering applications. This paper presents an application of the Bayesian approach to the solution of a groundwater flow inverse problem.

The model problem is a pumping test of hydraulic conductivity in an aquifer, which is solved on a square domain with given material interfaces. The material parameters are constant on each of the seven subdomains that are shown in Fig. 1, the subdomain  $\Omega_4$  consists of two separate parts. The task is to identify these seven material parameters based on results of the pumping test. This inverse problem was taken from [2], where it was solved using a deterministic iterative method.

The eight circles in Fig. 1 represent wells. The pumping test consists of 4 subtests. In each of them, one of the wells is chosen as an injection (the red circle

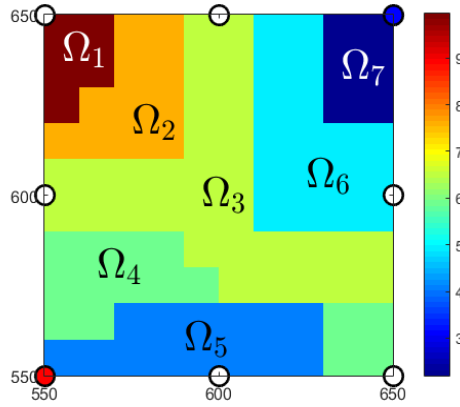


Fig. 1: Subdomains with given interfaces and the illustration of the wells

in Fig. 1), the opposite one is chosen as a drainage (the blue circle in Fig. 1), and the remaining six wells are points of measurements. The measured value is the pressure in the given point, which, in the case of real measurements, would correspond to the height of the water column in the specific well. From each of the four subtests, six measured values are obtained. Therefore, from the whole pumping test, we obtain twenty-four values, possibly corrupted by noise.

Solving the inverse problem requires the ability to solve the direct problem for various material samples. The square domain from Fig. 1 is surrounded by a bigger domain, see Fig. 2a. The four direct subproblems are for  $i \in \{1, 2, 3, 4\}$  given by the Darcy flow boundary value problem

$$\begin{aligned} -\operatorname{div}(\exp(k) \cdot \nabla p_i) &= f_i \text{ in } D = \langle 0, 1200 \rangle \times \langle 0, 1200 \rangle, \\ p_i &= 0 \text{ on } \partial D. \end{aligned}$$

The exponential of the material function  $k$  represents the hydraulic conductivity. For a given material, the results of the direct subproblem are obtained by solving this boundary value problem by the finite element method (FEM). Figure 2b shows an example of the solution for a specific material sample and one of the wells configurations. To obtain one solution of the whole direct problem, this boundary value problem is solved four times with different wells configurations and the required measurements are extracted from the solutions. This procedure defines the observation operator  $G : \mathbb{R}^7 \rightarrow \mathbb{R}^{24}$  that for the material parameters on the seven subdomains returns the 24 values of the pressure,

$$G(u_1, \dots, u_7) = (p_1, \dots, p_{24}).$$

## 2 Bayesian solution of the inverse problem

The objective of the solution using the Bayesian inversion differs significantly from the deterministic approach. While the deterministic approach searches for

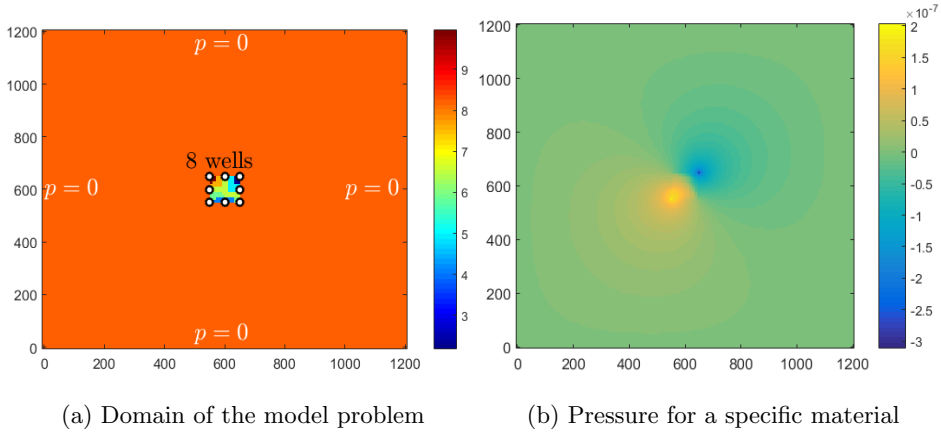


Fig. 2: Problem setting and solution on the whole domain

point estimates of the unknown parameters, the objective of the stochastic approach is to determine the probability distribution of the parameters (understood as random variables). This way it incorporates the uncertainty of the measurements to the solution and it can also take into account further information that is available about the parameters in the form of the prior distribution. The deterministic formulation of the inverse problem may not have a unique solution; however, the Bayesian formulation overcomes this problem.

We know the measurements  $\mathbf{y}$  that are corrupted by noise and we assume that the distribution of the noise is known. It is natural to assume the additive Gaussian noise with zero mean, i.e.

$$y = G(\mathbf{u}) + \boldsymbol{\eta},$$

where  $\mathbf{u} = (u_1, \dots, u_7)$  is a random vector and  $\boldsymbol{\eta} \sim N(\mathbf{0}, \gamma^2 I_{24})$  is the noise;  $I_m$  denotes an identity matrix of size  $m \times m$  and  $\gamma > 0$ . We also know the prior distribution of the random parameters, which expresses our prior belief about the material. Here we expect apriori that the distribution of the seven random parameters is normal with independent components and its mean is the vector  $\boldsymbol{\mu} = (9.7870, 7.4384, 6.6970, 6.2916, 4.2905, 4.7875, 1.7918)$  that was taken as the initial iteration in the paper [2], where the identification problem was solved deterministically. Therefore the prior information says that  $\mathbf{u} \sim N(\boldsymbol{\mu}, \sigma^2 I_7)$ , where  $\sigma > 0$ .

With this information, we can proceed to the Bayesian solution of the inverse problem. Based on the observed data and the prior information, the Bayesian theorem says that the posterior probability density function of the material parameters has the form

$$\pi(\mathbf{u}|\mathbf{y}) \propto f_{\boldsymbol{\eta}}(\mathbf{y} - G(\mathbf{u})) \pi_0(\mathbf{u}) \propto \exp\left(-\frac{\|\mathbf{y} - G(\mathbf{u})\|^2}{2\gamma^2} - \frac{\|\mathbf{u} - \boldsymbol{\mu}\|^2}{2\sigma^2}\right), \quad (1)$$

where  $f_{\boldsymbol{\eta}}$  denotes the joint probability density function of the noise and  $\pi_0$  denotes the prior density function.

Finding the posterior distribution of the material parameters was the objective; however, this is not the end of the work, because we would also like to describe this distribution, presumably by sampling from it.

### 3 Sampling from the posterior distribution

For the sampling from the posterior distribution (1), the Metropolis-Hastings (MH) algorithm can be used, see [3]. It is one of the MCMC methods that is intended for sampling from probability density functions that are known only up to a normalizing constant. The algorithm is based on proposing samples from an instrumental density that are accepted with some probability. This way a Markov chain with the limiting distribution  $\pi(\mathbf{u}|\mathbf{y})$  is constructed.

In the case of the standard MH algorithm, the observation operator  $G$  has to be evaluated for a new material sample in each step of the Markov chain. Even in the case of this simple model problem, it means four solutions by the FEM per one step of the MH algorithm, which is a time-consuming task. A possibly better approach would be to use a cheap approximation  $G_{\text{APP}}$  of the observation operator instead of some of the FEM solutions. A straightforward way would be to keep the MH algorithm unchanged and replace all the FEM solutions by the approximated solutions; however, this procedure would change the limiting distribution of the resulting Markov chain.

The paper [1] describes a modification of the MH algorithm that works with an approximation  $\pi_{\text{APP}}$  of the posterior distribution  $\pi$ . There is further shown that the limiting distribution of the resulting Markov chain is  $\pi(\mathbf{u}|\mathbf{y})$ . Here we define  $\pi_{\text{APP}}$  using the approximation of the observation operator, i.e.

$$\pi_{\text{APP}}(\mathbf{u}|\mathbf{y}) \propto \exp\left(-\frac{\|\mathbf{y} - G_{\text{APP}}(\mathbf{u})\|^2}{2\gamma^2} - \frac{\|\mathbf{u} - \boldsymbol{\mu}\|^2}{2\sigma^2}\right).$$

When assuming a symmetric instrumental density

$$q(\mathbf{u}, \mathbf{x}) = \frac{1}{\sqrt{(2\pi\sigma_{\text{MH}}^2)^n}} \exp\left(-\frac{(\mathbf{u} - \mathbf{x})^T (\mathbf{u} - \mathbf{x})}{2\sigma_{\text{MH}}^2}\right), \quad (2)$$

the algorithm of the modified MH method is the following:

- Choose  $\mathbf{u}_0$ .
- For  $t = 0, 1, \dots, T$ 
  - generate  $\mathbf{x}$  from  $q(\mathbf{u}_t, \mathbf{x})$  and calculate the “pre”-acceptance probability

$$\alpha_{\text{APP}}(\mathbf{u}_t, \mathbf{x}) = \min\left\{1, \frac{\pi_{\text{APP}}(\mathbf{x}|\mathbf{y})}{\pi_{\text{APP}}(\mathbf{u}_t|\mathbf{y})}\right\},$$

- if the sample  $\mathbf{x}$  is “pre”-accepted, calculate the acceptance probability

$$\alpha(\mathbf{u}_t, \mathbf{x}) = \min \left\{ 1, \frac{\pi(\mathbf{x}|\mathbf{y})}{\pi(\mathbf{u}_t|\mathbf{y})} \frac{\pi_{\text{APP}}(\mathbf{u}_t|\mathbf{y})}{\pi_{\text{APP}}(\mathbf{x}|\mathbf{y})} \right\},$$

- set  $\mathbf{u}_{t+1} = \mathbf{x}$  with probability  $\alpha(\mathbf{u}_t, \mathbf{x})$ , otherwise set  $\mathbf{u}_{t+1} = \mathbf{u}_t$ .

There are many possibilities of constructing  $G_{\text{APP}}$  including the FEM computation on a coarser grid, the stochastic collocation method and various methods for surrogate models construction. In this paper, the approximation of the FEM solution using the Stochastic Galerkin method (SGM) was used, see [4]. For the approximation in the random parameters, complete polynomials up to degree 3 were used. The four problems were solved separately with the same polynomial chaos basis and than the measurements were extracted. The SGM requires a precomputation, but subsequently the sampling is very cheap; for a specific material sample, the approximated results are obtained just by the evaluation of polynomial functions.

The rest of the process of generating almost uncorrelated samples is the same as in the case of the standard MH algorithm. When the Markov chain is created, its autocovariance is analyzed and based on this analysis, certain number of final samples is kept as almost uncorrelated.

The aim of this approach is to reduce the average number of the FEM calculations per one final sample. It can be influenced by changing the variance parameter  $\sigma_{\text{MH}}^2$  of the instrumental density (2), which leads to different acceptance rates. The acceptance rate is calculated as the ratio between the number of the accepted samples and the length of the Markov chain. Table 1 shows the numbers of solutions and the number of final samples for various acceptance rates. These results come from 24 independent Markov chains of length  $10^6$ .

Table 1: Efficiency of the MH algorithm depending on the acceptance rate

average acceptance rate	5.8e-5	3.8e-4	1.7e-3	1.0e-2	3.1e-2	1.0e-1
number of FEM calculations	1435	9300	40389	2.53e5	7.39e5	2.46e6
number of SGM calculations	24000000					
number of final samples	120	600	2400	7992	12000	24000
FEM calculations per one final sample	11.96	15.50	16.83	31.66	61.58	102.50
time per one final sample [s]	30.25	15.09	12.71	22.17	42.72	70.96

For a more comprehensive comparison of the results, the computation time of the evaluation of  $G$  using FEM (0.69 seconds on average) and the evaluation of  $G_{\text{APP}}$  using SGM ( $1.1 \cdot 10^{-4}$  seconds on average) should be also taken into consideration. Figure 3 shows, how the time spent by both types of solution per one final sample depends on the acceptance rate. We can notice that when the acceptance rate decreases, the number of FEM calculations is lower, so the time for one final sample is lower; but this only works to some point, from

which the Markov chains are too autocorrelated and the amount of final “almost uncorrelated” samples is too low.

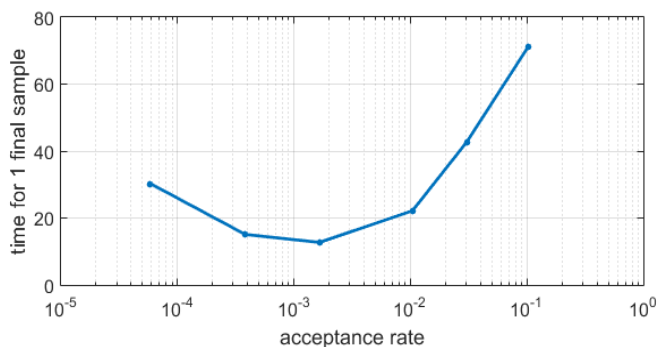


Fig. 3: Dependence of the time efficiency on the acceptance rate

For comparison, the sampling from the posterior distribution was also performed using the standard MH algorithm; 240 independent Markov chains of length  $4 \cdot 10^4$  were generated. Based on the autocovariance analysis, 9600 final samples were kept, i.e. the computation cost was 690 seconds per one final sample. Therefore, the use of the modified MH algorithm reduced the computation time approximately by the factor of 50.

## Acknowledgement

This work was supported by The Ministry of Education, Youth and Sports from the National Programme of Sustainability (NPU II) project "IT4Innovations excellence in science – LQ1602". Work is partially supported by Grant of SGS No. SP2017/56, VŠB – Technical University of Ostrava, Czech Republic.

## References

1. Christen, J. A.; Fox, C. *Markov chain Monte Carlo using an approximation*. Journal of Computational and Graphical statistics, 2005.
2. Haslinger, J.; Blaheta, R.; Hrtus, R. *Identification problems with given material interfaces*. Journal of Computational and Applied Mathematics. 2016.
3. Domesová, S.; Béréš, M. *Inverse Problem Solution using Bayesian Approach with Application to Darcy Flow Material Parameters Estimation*. Advances in Electrical and Electronic Engineering, 2017.
4. Béréš, M.; Domesová, S. *The Stochastic Galerkin Method for Darcy Flow Problem with Log-Normal Random Field Coefficients*. Advances in Electrical and Electronic Engineering, 2017.

# Parallel Space-time Finite Element Methods

Ladislav Foltyn

Department of Applied Mathematics, FEECS,  
VŠB – Technical University of Ostrava, 17. listopadu 15,  
708 33 Ostrava – Poruba, Czech Republic  
`ladislav.foltyn@vsb.cz`

**Abstract.** We present a finite element discretization method of the 2D heat equation over the time interval. The resulting system is solved iterative by Krylov-space methods. We propose a preconditioner based on a spatial domain decomposition and the Schur complement technique.

**Keywords:** preconditioning, space-time finite element method, Schur complement

## 1 Introduction

The traditional way to solve space-time problems is so-called time stepping method but this method has one big disadvantage. We are unable to realize its parallelization, so to use a full capacity of today's parallel computers, it is insufficient to solve problems only in a spatial domain. One possibility is to treat the time interval as a new spatial coordinate. If we have to solve a 2d (or 3d) problem over the time interval, we actually have to solve a 3d (or 4d) problem. Our attempt of added spatial coordinate acts as a fully implicit time stepping method and it brings some advantages like a big room for parallelization process or a global error control.

In the rest of the paper, a model problem and Schur complement technique will be introduced. Also some numerical experiments are shown in the end of the text.

This paper is based on [3], [4] and our latest work.

## 2 Space-time FEM

Consider a Dirichlet boundary value problem for the heat equation

$$\begin{aligned} c_H \frac{\partial u}{\partial t}(\mathbf{x}, t) - \Delta_{\mathbf{x}} u(\mathbf{x}, t) &= f(\mathbf{x}, t) \quad \forall (\mathbf{x}, t) \in \Omega \times (0; T) \\ u(\mathbf{x}, t) &= 0 \quad \forall (\mathbf{x}, t) \in \Gamma \times (0, T) \\ u(\mathbf{x}, 0) &= u_0(\mathbf{x}) \quad \forall \mathbf{x} \in \Omega \end{aligned} \tag{1}$$



where  $\Omega \subset \mathbb{R}^2$  is a bounded domain with Lipschitz boundary and  $\Gamma = \partial\Omega$ .  $c_H$  is a given heat capacity constant which is positive ( $c_H > 0$ ),  $f(x, t) \in L_2(0, T; H^{-1}(\Omega))$  is a given source term and we assume that  $u_0(\mathbf{x}) \in H_0^1(\Omega)$ .

After deriving variational formulation and following discretization process, we have to

$$\begin{cases} \text{Find } u^h \in \mathcal{U}^h, \text{ such that} \\ a(u^h, w^h) = b(w^h) - a(u_0^h, w^h) \quad \forall w^h \in \mathcal{W}^h, \end{cases} \quad (2)$$

where  $\mathcal{U}^h$  and  $\mathcal{W}^h$  are appropriate finite dimensional subspaces.

If we rewrite the discrete formulation into an algebraic form, we obtain

$$(\mathbf{M} + \mathbf{A}) \cdot \mathbf{u} = \mathbf{b} - (\hat{\mathbf{M}} + \hat{\mathbf{A}}) \cdot \mathbf{u}_0, \quad (3)$$

where  $(\mathbf{M} + \mathbf{A}) \cdot \mathbf{u}$  corresponds to  $a(u^h, w^h)$ ,  $\mathbf{b}$  to  $b(w^h)$  and  $(\hat{\mathbf{M}} + \hat{\mathbf{A}}) \cdot \mathbf{u}_0$  to  $a(u_0^h, w^h)$ .

### 3 Schur complement technique

For assembling the preconditioning method in the spatial domain, we are using a method described in [1], [2], so only the necessary steps in the algebraic form will be shown.

Before we begin, a discretization of the spatial domain into the finite elements is needed. In our example, we are using a mesh with equidistant step  $h$  and a coarse mesh with step  $H$  which is also equidistant, see a Figure 1. below. The time step will be discussed in following section.

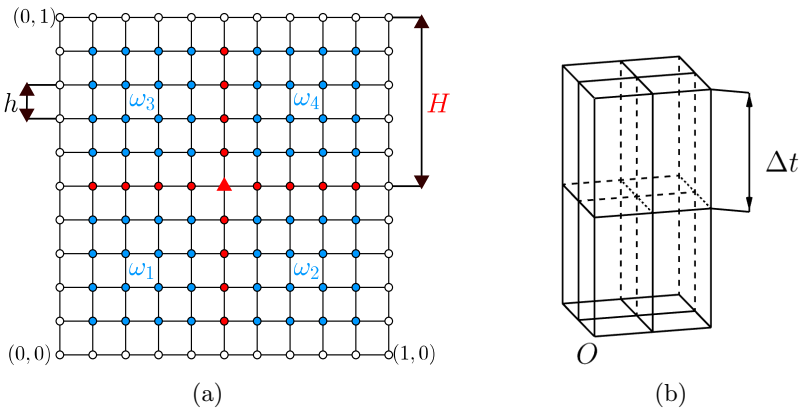


**Fig. 1.** (a) discretization of the spatial domain, (b) time step.

Next, we define a set of interior nodes  $\mathcal{I}$  which consists of nodes belonging to each individual subdomain (blue color in the Figure 1), and a set of nodes  $\mathcal{G}$

which correspond to a coarse mesh (red color in the Figure 1). Nodes equal to the initial condition and the Dirichlet boundary condition are not considered.

As described in [1], we reorder the resulting matrix into a form

$$A = \begin{pmatrix} A_{\mathcal{I}\mathcal{I}} & A_{\mathcal{I}\mathcal{G}} \\ A_{\mathcal{G}\mathcal{I}} & A_{\mathcal{G}\mathcal{G}} \end{pmatrix}, \quad (4)$$

where  $A_{\mathcal{I}\mathcal{I}}$  is a block diagonal matrix (one block equals to one subdomain) and other three matrices are consist of proper indices. This reordered matrix  $A$  is further decomposed into a lower, an upper and a diagonal matrices

$$A = \begin{pmatrix} I_{\mathcal{I}} & O \\ A_{\mathcal{G}\mathcal{I}} A_{\mathcal{I}\mathcal{I}}^{-1} & I_{\mathcal{G}} \end{pmatrix} \begin{pmatrix} A_{\mathcal{I}\mathcal{G}} & O \\ O & S \end{pmatrix} \begin{pmatrix} I_{\mathcal{I}} & A_{\mathcal{I}\mathcal{I}}^{-1} A_{\mathcal{I}\mathcal{G}} \\ O & I_{\mathcal{G}} \end{pmatrix}, \quad (5)$$

where  $O$  are adequate zero matrices and  $S$  is the Schur complement. One could see, that decomposition mentioned above is similar to  $LDL^T$  decomposition.

The key idea of the Schur complement preconditioning method is to replace the Schur complement  $S$  by its approximation  $\hat{S}$ .

In short, the Schur complement  $S$  consists of

$$S = \begin{pmatrix} S_{\mathcal{E}\mathcal{E}} & S_{\mathcal{E}\mathcal{V}} \\ S_{\mathcal{V}\mathcal{E}} & S_{\mathcal{V}\mathcal{V}} \end{pmatrix}, \quad (6)$$

where  $\mathcal{E}$  represents a set of nodes forming edges (red dots in the Figure 1) of the coarse mesh and  $\mathcal{V}$  is a set of vertexes (red triangle in the Figure 1) which join adjacent edges of the coarse mesh.

We also decompose the Schur complement by a decomposition similar to  $LDL^T$ . A decomposed Schur complement is in a form

$$S = \begin{pmatrix} I_{\mathcal{E}} & O \\ -R_{\mathcal{E}} & I_{\mathcal{V}} \end{pmatrix} \begin{pmatrix} S_{\mathcal{E}\mathcal{E}} & \tilde{S}_{\mathcal{E}\mathcal{V}} \\ \tilde{S}_{\mathcal{V}\mathcal{E}} & \tilde{S}_{\mathcal{V}\mathcal{V}} \end{pmatrix} \begin{pmatrix} I_{\mathcal{E}} & -R_{\mathcal{E}}^T \\ O & I_{\mathcal{V}} \end{pmatrix}, \quad (7)$$

where  $R_{\mathcal{E}}$  is an interpolation matrix of standard basis functions  $\varphi$  to basis functions over the coarse mesh  $\psi$ , see Figure 2. At this moment, the inverse of the Schur complement is still expensive, so to make it cheaper, we replace the Schur complement by the approximation

$$\hat{S} = \begin{pmatrix} I_{\mathcal{E}} & O \\ -R_{\mathcal{E}} & I_{\mathcal{V}} \end{pmatrix} \begin{pmatrix} \bar{S}_{\mathcal{E}\mathcal{E}} & O \\ O & A_{\mathcal{H}} \end{pmatrix} \begin{pmatrix} I_{\mathcal{E}} & -R_{\mathcal{E}}^T \\ O & I_{\mathcal{V}} \end{pmatrix}, \quad (8)$$

where  $\bar{S}_{\mathcal{E}\mathcal{E}}$  contains only blocks on its main diagonal and  $A_{\mathcal{H}}$  is a resulting matrix corresponding to the coarse mesh. In the end, we replace the Schur complement  $S$  by its approximation  $\hat{S}$  in (5) and use it as the preconditioner.

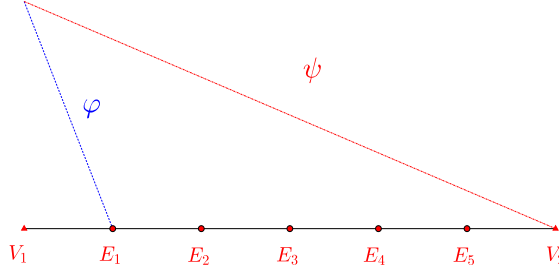


**Fig. 2.** Interpolation.

## 4 Numerical experiments

We solved following problem

$$\begin{aligned} 25 \frac{\partial u}{\partial t}(\mathbf{x}, t) - \Delta_{\mathbf{x}} u(\mathbf{x}, t) &= 1 & \forall (\mathbf{x}, t) \in (0; 1)^2 \times (0; 2) \\ u(\mathbf{x}, t) &= 0 & \forall (\mathbf{x}, t) \in \Gamma \times (0, 2) \\ u(\mathbf{x}, 0) &= \sin(\pi x) \sin(\pi y) & \forall \mathbf{x} \in (0; 1)^2. \end{aligned} \quad (9)$$

At first, we omitted the mass matrix  $M$ , i.e. we solved only symmetric part of the equation above, and the time step was equal to  $\Delta t = 2$ . The conjugate gradient method was used. Resulting numbers of iterations are shown in the Table 1.

**Table 1.** Numbers of iterations, time step  $\Delta t = 2$  (symmetric case, PCG method).

	$h = \frac{1}{4}$	$h = \frac{1}{8}$	$h = \frac{1}{16}$	$h = \frac{1}{32}$	$h = \frac{1}{64}$
$\mathbf{A}\mathbf{u} = \mathbf{b} - \hat{\mathbf{A}}\mathbf{u}_0$	3	8	17	34	69
Preconditioned system					
$H = \frac{1}{2}$	3	7	8	9	10
$H = \frac{1}{4}$		8	17	22	28
$H = \frac{1}{8}$			9	23	37
$H = \frac{1}{16}$				8	39

Next, we added the mass matrix  $M$  to the system, the time step had same length but GMRES method was used this time due to impaired symmetry of the system. We observed that there is no significant difference between numbers of iterations in this example (Table 2.) to the symmetry one (Table 1.) .

The last table, Table 3., contains numbers of iterations of the problem (9) which was discretized over the time interval by the time step  $\Delta t = 1$ . As it is

**Table 2.** Numbers of iterations, time step  $\Delta t = 2$  (GMRES method).

	$h = \frac{1}{4}$	$h = \frac{1}{8}$	$h = \frac{1}{16}$	$h = \frac{1}{32}$	$h = \frac{1}{64}$
$(M + A)\mathbf{u} = \mathbf{b} - (\hat{M} + \hat{A})\mathbf{u}_0$	3	8	18	35	68
Preconditioned system					
$H = \frac{1}{2}$	3	7	8	9	10
$H = \frac{1}{4}$		8	21	24	26
$H = \frac{1}{8}$			18	27	34
$H = \frac{1}{16}$				20	35

shown in Table 3., numbers of iterations were significantly increased. This is the expected result because the problem (1), in general, has different behaviour over the time interval than in the spatial domain.

**Table 3.** Numbers of iterations, time step  $\Delta t = 1$  (GMRES method).

	$h = \frac{1}{4}$	$h = \frac{1}{8}$	$h = \frac{1}{16}$	$h = \frac{1}{32}$	$h = \frac{1}{64}$
$(M + A)\mathbf{u} = \mathbf{b} - (\hat{M} + \hat{A})\mathbf{u}_0$	6	14	32	65	124
Preconditioned system					
$H = \frac{1}{2}$	8	11	13	14	15
$H = \frac{1}{4}$		39	42	48	52
$H = \frac{1}{8}$			68	91	100
$H = \frac{1}{16}$				153	308

Graphic output of the solution of the problem (9) is shown in Figure 3.

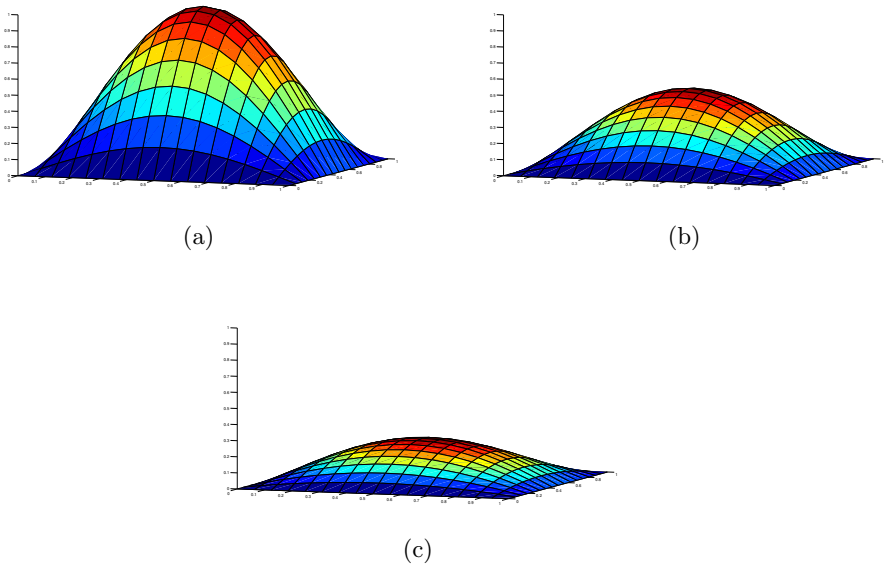


**Fig. 3.** Solution for (a)  $t = 0$ , (b)  $t = 1$ , (c)  $t = 2$ .

## 5 Outlooks

In the future work, we will discuss Parareal method and discontinuous Galerkin method.

## References

1. Bouchala, J., Lukáš, D., Malý, L., and Vodstrčil, P.: 2-Dimensional Primal Domain Decomposition Theory in Detail. *Application of Mathematics* (2015), vol. 60, nr. 3, pp. 265-283.
2. Bramble, J. H., Pasciak, J. E. and Schatz, A. H.: The construction of preconditioners for elliptic problems by substructuring. I. *Math. Comp.* **47** (1986), 103-134.
3. Neumüller, M.: *Space-time methods: Fast solvers and applications*. Graz: Verlag der Technischen Universität, 2013. 978-3-85125-291-0 (e-ISBN)
4. Steinbach, O.: *Space-time finite element methods for parabolic problems*. Institut für Numerische Mathematik, TU Graz, 2015.

# Equality Constrained Minimization Problem Solved by the Modified SMALE Algorithm

Pavla Jirůtková

Department of Applied Mathematics, FEECS,  
VŠB – Technical University of Ostrava, 17. listopadu 15,  
708 33 Ostrava – Poruba, Czech Republic  
pavla.jirutkova@vsb.cz

**Abstract.** We briefly describe the equality constrained minimization problem. A special attention is paid to the SMALE algorithm and to the description of its modification. The experiments and results are presented here.

## 1 Introduction

The SMALE (SemiMonotonic Augmented Lagrangian method for Equality constraints) algorithm is an efficient optimal method for the solution of large equality constrained quadratic programming (QP) problems proposed by Dostál [1] [2] and it is based on the augmented Lagrangian algorithm. The main advantage of the SMALE algorithm is a rather small threshold of the number of iterations which is independent of the constraint data. The modification of the algorithm brings an improvement of convergence. We expect that more advantages of the modification will show up at solving of the inequality constrained problems.

## 2 Equality constrained minimization

We assume the equality constrained minimization problem

$$\min_{\mathbf{x} \in \Omega_E} f(\mathbf{x}), \quad (1)$$

where  $f(\mathbf{x}) = \frac{1}{2} \mathbf{x}^\top \mathbf{K} \mathbf{x} - \mathbf{x}^\top \mathbf{f}$ ,  $\mathbf{K}$  is an  $n \times n$  symmetric positive definite matrix,  $\mathbf{f}$  is a given column  $n$ -vector,  $\Omega_E = \{\mathbf{x} \in \mathbb{R}^n : \mathbf{B} \mathbf{x} = \mathbf{c}\}$ ,  $\mathbf{B} \in \mathbb{R}^{m \times n}$ ,  $\text{Ker} \mathbf{B} \neq \{\mathbf{o}\}$ , and  $\mathbf{c} \in \text{Im} \mathbf{B}$ . We allow the constraint matrix  $\mathbf{B}$  with dependent rows. The problem (1) is equivalent to the solution of the saddle point system of linear equations

$$\begin{bmatrix} \mathbf{K} & \mathbf{B}^\top \\ \mathbf{B} & \mathbf{O} \end{bmatrix} \begin{bmatrix} \mathbf{x} \\ \boldsymbol{\lambda} \end{bmatrix} = \begin{bmatrix} \mathbf{f} \\ \mathbf{c} \end{bmatrix}, \quad (2)$$

where  $\boldsymbol{\lambda} \in \mathbb{R}^m$  is called a Lagrange multiplier. The system is also known as the Karush-Kuhn-Tucker system (KKT system) and it has a unique solution  $(\hat{\mathbf{x}}, \hat{\boldsymbol{\lambda}})$ . Since we defined the Lagrangian function  $L : \mathbb{R}^{n+m} \rightarrow \mathbb{R}$  by

$$L(\mathbf{x}, \boldsymbol{\lambda}) = f(\mathbf{x}) + \boldsymbol{\lambda}^\top (\mathbf{B} \mathbf{x} - \mathbf{c}), \quad (3)$$

the KKT system (2) can be expressed by

$$\nabla_{\lambda} L(\mathbf{x}, \lambda) = \mathbf{B}\mathbf{x} - \mathbf{c} = \mathbf{o}, \quad (4)$$

$$\nabla_{\mathbf{x}} L(\mathbf{x}, \lambda) = \nabla f(\mathbf{x}) + \mathbf{B}^{\top} \lambda = \mathbf{K}\mathbf{x} - \mathbf{f} + \mathbf{B}^{\top} \lambda = \mathbf{o}, \quad (5)$$

and the Hessian is

$$\nabla_{xx}^2 L(\mathbf{x}, \lambda) = \nabla^2 f(\mathbf{x}) = \mathbf{K}.$$

### 3 SMALE algorithm

In this paper we would like describe the algorithm used in our implementation based on the SMALE algorithm [3] for solution of the minimization problem

$$\min_{\mathbf{x} \in \mathbb{R}^n} f_{\rho}(\mathbf{x}),$$

where  $f_{\rho}(\mathbf{x}) = f(\mathbf{x}) + \frac{\rho}{2} \|\mathbf{B}\mathbf{x} - \mathbf{c}\|^2$ ,  $\rho \geq 0$  is the penalty parameter and  $\|\mathbf{B}\mathbf{x} - \mathbf{c}\|^2$  is the penalty function. The solution  $\hat{\mathbf{x}}_{\rho}$  is approximation of the solution  $\hat{\mathbf{x}}$  of (1). The augmented Lagrangian penalty function  $L : \mathbb{R}^{n+m+1} \rightarrow \mathbb{R}$  is defined by

$$L(\mathbf{x}, \lambda, \rho) = f(\mathbf{x}) + (\mathbf{B}\mathbf{x} - \mathbf{c})^{\top} \lambda + \frac{\rho}{2} \|\mathbf{B}\mathbf{x} - \mathbf{c}\|^2 = L(\mathbf{x}, \lambda) + \frac{\rho}{2} \|\mathbf{B}\mathbf{x} - \mathbf{c}\|^2,$$

where  $L(\mathbf{x}, \lambda)$  is the Lagrangian (3). The gradient of the augmented Lagrangian is given by

$$\begin{aligned} \nabla_{\mathbf{x}} L(\mathbf{x}, \lambda, \rho) &= \mathbf{K}\mathbf{x} - \mathbf{f} + \mathbf{B}^{\top} (\lambda + \rho(\mathbf{B}\mathbf{x} - \mathbf{c})) \\ &= (\mathbf{K} + \rho\mathbf{B}^{\top}\mathbf{B})\mathbf{x} - \mathbf{f} - \rho\mathbf{B}^{\top}\mathbf{c} + \mathbf{B}^{\top}\lambda \end{aligned} \quad (6)$$

and the gradient with respect to  $\lambda$  is the same as (4). The KKT system is now changed to

$$\begin{bmatrix} \mathbf{K}_{\rho} & \mathbf{B}^{\top} \\ \mathbf{B} & \mathbf{O} \end{bmatrix} \begin{bmatrix} \mathbf{x} \\ \lambda \end{bmatrix} = \begin{bmatrix} \mathbf{f} + \rho\mathbf{B}^{\top}\mathbf{c} \\ \mathbf{c} \end{bmatrix},$$

where  $\mathbf{K}_{\rho} = \mathbf{K} + \rho\mathbf{B}^{\top}\mathbf{B}$  is the Hessian. Let us denote by  $\hat{\mathbf{x}}_{\rho}$  the minimizer of  $L(\mathbf{x}, \lambda, \rho)$  and let us see the (6) and denote

$$\tilde{\lambda} = \lambda + \rho(\mathbf{B}\hat{\mathbf{x}}_{\rho} - \mathbf{c}).$$

Then the first KKT condition reads

$$\mathbf{K}\hat{\mathbf{x}}_{\rho} - \mathbf{f} + \mathbf{B}^{\top} \tilde{\lambda} = \nabla_{\mathbf{x}} L(\hat{\mathbf{x}}_{\rho}, \tilde{\lambda}) = \nabla_{\mathbf{x}} L(\hat{\mathbf{x}}_{\rho}, \lambda, \rho) = \mathbf{o},$$

and so the pair  $(\hat{\mathbf{x}}_{\rho}, \tilde{\lambda})$  satisfies that condition exactly.

In the original SMALE algorithm we find  $\mathbf{x}^k$  in each iteration of  $k$  such that

$$\left\| \nabla_{\mathbf{x}} L(\mathbf{x}^k, \lambda^k, \rho_k) \right\| \leq \min \left\{ M \left\| \mathbf{B}\mathbf{x}^k - \mathbf{c} \right\|, \eta \right\}, \quad (7)$$

where  $M > 0$ ,  $\eta > 0$ ,  $\rho_0 > 0$  and  $\lambda^0 \in \mathbb{R}^m$  is appropriately chosen (zero vector can be used), the parameter  $\rho_k$  and variable  $\lambda^k$  are recounted in each iteration.

The preconditioned conjugate gradient method (PCG) is used for finding of  $\mathbf{x}^k$  in (7), as well any other convergent algorithm for the minimization of the strictly convex quadratic function can be used.

### 3.1 Modification

In our modification of the SMALE algorithm we find  $\mathbf{x}^k$  in each iteration of  $k$  such that

$$\left\| \nabla_{\mathbf{x}} L(\mathbf{x}^k, \boldsymbol{\lambda}^k, \mathbf{C}_k, \rho_k) \right\| \leq \min \left\{ M_k \left\| \mathbf{B}\mathbf{x}^k - \mathbf{c} \right\|, \eta \right\}, \quad (8)$$

where the new matrix  $\mathbf{C} \in \mathbb{R}^{m \times m}$  is appeared and the parameter  $M_k$  is recounted in each iteration compared to the original SMALE, where is fixed. The gradient of the augmented Lagrangian used in (8) for  $k$ -th iteration means

$$\nabla_{\mathbf{x}} L(\mathbf{x}^k, \boldsymbol{\lambda}^k, \mathbf{C}_k, \rho_k) = (\mathbf{K} + \rho \mathbf{B}^\top \mathbf{C}_k \mathbf{B}) \mathbf{x}^k - \mathbf{f} - \rho_k \mathbf{B}^\top \mathbf{c} + \mathbf{B}^\top \boldsymbol{\lambda}^k.$$

Let us introduce denotations  $\mathbf{A}_k = \mathbf{K} + \rho \mathbf{B}^\top \mathbf{C}_k \mathbf{B}$  and  $\mathbf{b}^k = \mathbf{f} - \mathbf{B}^\top \boldsymbol{\lambda}^k + \rho_k \mathbf{B}^\top \mathbf{c}$ , then we can write

$$\nabla_{\mathbf{x}} L(\mathbf{x}^k, \boldsymbol{\lambda}^k, \mathbf{C}_k, \rho_k) = \mathbf{A}_k \mathbf{x}^k - \mathbf{b}^k.$$

Let us remind that we solve  $\mathbf{A}_k \mathbf{x}^k = \mathbf{b}^k$  by the PCG method.

### 3.2 Use of the matrix $\mathbf{C}$

The matrix  $\mathbf{C}_k \approx (\mathbf{B}\mathbf{B}^\top)^{-1}$  orthogonalize the matrix  $\mathbf{B}$ . We use the Lanczos method in a combination with the PCG method [4] for an assembly the matrix  $\mathbf{C}_k$  for  $k = 1, 2, \dots$  and we test three ways to use the matrix in the algorithm. Note that we take the matrix  $\mathbf{C}_0 = \mathbf{I}$  for an iteration  $k = 0$ .

The first way is the simplest one. We solve the matrix  $\mathbf{C}_k$  via PCG method as  $\mathbf{B}\mathbf{B}^\top \mathbf{y}_k = \mathbf{B}\mathbf{x}_{k-1}$ , where  $\mathbf{y}_k = \mathbf{C}_k \mathbf{B}\mathbf{x}_{k-1}$ , and we take  $\mathbf{C}_k = \mathbf{C}_1$  for each next iteration of  $k$ . It means we compute the matrix  $\mathbf{C}$  only once on the beginning and then we use it in other iterations.

In the second way we take the vector  $\mathbf{y}_{k-1}$  as an initial vector in PCG method for solution  $\mathbf{B}\mathbf{B}^\top \mathbf{y}_k = \mathbf{B}\mathbf{x}_{k-1}$ .

The third way is basically the same as the first one, but the matrix  $\mathbf{C}_k$  is computed in each iteration of  $k$ .

## 4 Numerical experiments and results

We test the implementation for four different benchmarks and moreover we apply six types of the matrix  $\mathbf{B}$  for each of them. How we mentioned in section 3.2 three ways of using the matrix  $\mathbf{C}$  are implemented and tested for each benchmark with each type of the matrix  $\mathbf{B}$ . We set  $\beta = 10, M_0 = 100, \rho_0 = \|\mathbf{K}\|$  and  $\eta = 10 \left\| \mathbf{f} - \mathbf{B}^\top \boldsymbol{\lambda} + \rho_k \mathbf{B}^\top \mathbf{c} \right\|$ .

### 4.1 Benchmarks

In this subsection we introduce all types of the matrix  $\mathbf{B}$  and two benchmarks with their graphical solutions which are used in the implementation.



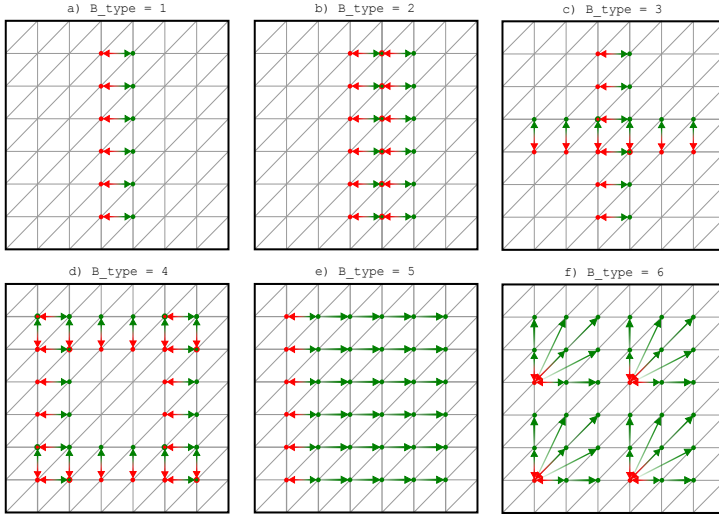


**Fig. 1.** Illustrated all types of the matrix  $\mathbf{B}$ .

We implemented six types of the matrix  $\mathbf{B}$ , see Figure 1. Let us note that nodes lying on the Dirichlet boundary are never glued to others, which means they are always included in the matrix  $\mathbf{B}$  as the zero values.

The first one glues two lines of nodes in a middle of the mesh, i.e.  $[-1, 1]$  is appeared in rows of the matrix  $\mathbf{B}$ , see Figure 1-a. This type is the only one with orthogonal rows. The  $\mathbf{B\_type} = 2$  glues three lines of nodes and so the matrix has not orthogonal rows, see Figure 1-b. The third type glues two lines of nodes in a middle of the mesh in both axis directions, see Figure 1-c. The fourths  $\mathbf{B\_type}$  glues second and third line of nodes in order from each side, see Figure 1-d. The  $\mathbf{B\_type} = 5$  is different from previous. There is the first node in each line glued to all others in the same line, see Figure 1-e. The last  $\mathbf{B\_type}$  is similar to fifth type. We decomposed the mesh to four subdomains and we glue the first node in each subdomain to all others in the same subdomain, see Figure 1-f.

Now we suppose a square domain of the size  $1 \times 1$  with the boundary  $\Gamma_i$  for  $i = 1, 2, 3, 4$  and the mesh is created by triangular elements with the discretization step  $h = \frac{1}{19}$ . Let us denote  $\Gamma_D$  as a set of boundaries with the Dirichlet condition and  $\Gamma_N$  as a set of boundaries with Neumann condition. The third  $\mathbf{B\_type}$  is chosen for following benchmarks.

### Benchmark 1

$$\begin{aligned} f(x, y) &= -2(x^2 + y^2), \forall x, y \in (-1, 1) \times (-1, 1), \\ g_D &= x^2 y^2, \forall x, y \in \Gamma_D, \\ g_N &= [2xy^2, 2yx^2], \forall x, y \in \Gamma_N, \end{aligned}$$

where  $\Gamma_D = \Gamma_1$  and  $\Gamma_N = \{\Gamma_2, \Gamma_3, \Gamma_4\}$ . The solution is shown in Figure 2.

## Benchmark 2

$$\begin{aligned} f(x, y) &= -4(\pi^2 \sin(2\pi x) \sin(2\pi y)), \forall x, y \in (0, 1) \times (0, 1), \\ gD &= 0, \forall x, y \in \Gamma_D, \\ gN &= [(2\pi \cos(2\pi x) \sin(2\pi y)), (2\pi \cos(2\pi y) \sin(2\pi x))], \forall x, y \in \Gamma_N, \end{aligned}$$

where  $\Gamma_D = \{\Gamma_1, \Gamma_2, \Gamma_3, \Gamma_4\}$  and  $\Gamma_N = \{\}$ . The solution is shown in Figure 2.

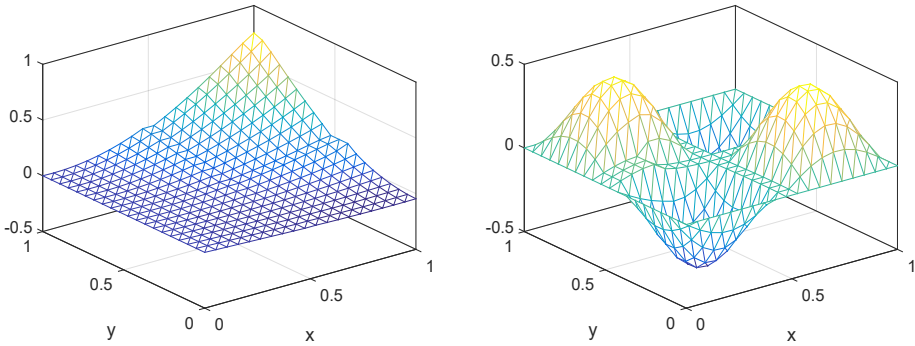


**Fig. 2.** Benchmark 1 (left) and benchmark 2 (right) with B\_type 3.

## 4.2 Results

In this section we show a number of iteration for an outer loop of the SMALE algorithm, for an inner loop of the PCG algorithm and for the PCG algorithm used to an assembly of the matrix  $\mathbf{C}$  (noted Lancz-PCG). See Table 1, 2. How we can see a number of the SMALE iterations is equal to 3 except one case (see Table 2, C\_type=1, B\_type=5).

## 5 Conclusion

We described the equality constrained minimization problem and the iterative solver named SMALE. Our new modification of the method was introduced and tested. In the last section we showed results of several experiments of this modified algorithm for two benchmarks.

**Table 1.** Iteration results for benchmark 1.

Benchmark 1: $f = -2*(x^2+y^2)$ , $gD = x^2*y^2$ , $gN = [(2*x*y^2), (2*y*x^2)]$ , $dir = [1\ 0\ 0\ 0]$						
C_type	1: $C_k = C_1$					
B_type	1	2	3	4	5	6
PCG iter.	1,138,187	1,187,250	1,142,195	1,190,250	1,90,145	1,37,142
Lancz-PCG iter.	1	2	3	5	2	2
SMALE iter.	3	3	3	3	3	3
C_type	2: $y_0 = C_k(Bx_k)$					
B_type	1	2	3	4	5	6
PCG iter.	1,138,187	1,187,254	1,142,195	1,190,257	1,90,145	1,37,231
Lancz-PCG iter.	1	2	3	5	2	2,2
SMALE iter.	3	3	3	3	3	3
C_type	3: $C_k(Bx_k) = Bx_k$					
B_type	1	2	3	4	5	6
PCG iter.	1,138,187	1,187,254	1,142,195	1,190,257	1,90,145	1,37,222
Lancz-PCG iter.	1	2	3	5	2	2,2
SMALE iter.	3	3	3	3	3	3

**Table 2.** Iteration results for benchmark 2.

Benchmark 2: $f = -4*(\pi^2*\sin(2*\pi*x)*\sin(2*\pi*y))$ , $gD = 0$ , $gN = [(2*\pi*\cos(2*\pi*x)*\sin(2*\pi*y)), (2*\pi*\cos(2*\pi*y)*\sin(2*\pi*x))]$ , $dir = [1\ 1\ 1\ 1]$						
C_type	1: $C_k = C_1$					
B_type	1	2	3	4	5	6
PCG iter.	1,5,50	1,19,79	1,19,96	1,25,99	1,1,29,34	1,8,65
Lancz-PCG iter.	1	2	4	5	2	2
SMALE iter.	3	3	3	3	4	3
C_type	2: $y_0 = C_k(Bx_k)$					
B_type	1	2	3	4	5	6
PCG iter.	1,5,71	1,19,129	1,19,140	1,25,152	1,1,29	1,8,104
Lancz-PCG iter.	1,2	2,2	4,4	5,5	2,2	2,2
SMALE iter.	3	3	3	3	3	3
C_type	3: $C_k(Bx_k) = Bx_k$					
B_type	1	2	3	4	5	6
PCG iter.	1,5,71	1,19,127	1,19,140	1,25,153	1,1,29	1,8,106
Lancz-PCG iter.	1,2	2,2	4,4	5,5	2,2	2,2
SMALE iter.	3	3	3	3	3	3

## References

1. Zdeněk Dostál, Semi-monotonic inexact augmented Lagrangians for quadratic programming with equality constraints, Optim. Methods Software 20, 6, 715-727, 2005.
2. Zdeněk Dostál, An optimal algorithm for a class of equality constrained quadratic programming problems with bounded spectrum, Comput. Optim. Appl. 38, 1, 47-59, 2007.
3. Zdeněk Dostál, Optimal Quadratic Programming Algorithms, with Applications to Variational Inequalities, SOIA, Springer, New York, US, vol. 23, 2009.
4. Petr Tichý, Incremental estimation of the largest and smallest Ritz values in the conjugate gradient method, SNA'17, Modelling and Simulation of Challenging Engineering Problems, 2017.

# On Modified Handicap Labelings

Petr Kovář<sup>1,2</sup> and Matěj Krbeček<sup>1</sup>

<sup>1</sup>Department of Applied Mathematics, FEECS,  
VŠB – Technical University of Ostrava, 17. listopadu 15,  
708 33 Ostrava – Poruba, Czech Republic

<sup>2</sup>IT4Innovation, VŠB – Technical University of Ostrava, 17. listopadu 15,  
708 33 Ostrava – Poruba, Czech Republic  
`petr.kovar@vsb.cz`

**Abstract.** Let  $G$  be a simple graph with  $n$  vertices.

Let  $A = \{1, 2, \dots, \frac{n}{2}\} \cup \{\frac{n+4}{2}, \dots, n+1\}$  and  $f : V \rightarrow A$  be a bijection where the weight of  $v$  is  $w(v) = \sum_{u \in N(v)} f(u) = \ell + f(v)$  for some positive integer  $\ell$ .  $f$  is called a generalized handicap labeling. This definition naturally weakens the requirement that the vertex labels are from  $A = \{1, 2, \dots, n\}$ . We show the existence of such labelings for many even-regular graphs.

**Key words:** handicap labeling, generalized handicap labeling, even regular graph.

## 1 Introduction

Miller, Rodger, and Simanjuntak [1] proved the existence of distance magic labeling for some basic classes of graphs. Path  $P_n$  is distance magic if and only if  $n = 1$  or  $n = 3$ . Cycle  $C_n$  is distance magic if and only if  $n = 4$ . Complete graph  $K_n$  is distance magic only for  $n = 1$ . Tree  $T$  is distance magic if  $T$  is either  $P_1$  or  $P_3$ . Arguman, Fronček, and Kamatchi [2] showed that  $r$ -regular distance magic graph with  $n$  vertices do not exist if  $r$  is odd. There are a lot of classes of distance magic graphs if  $r$  is even. In the paper [2] it was also proved that 2-regular distance magic graph can exist if and only if  $n$  is at least 4. And the construction of such graph is unique, it is  $t$  copies of cycle  $C_4$ .

Kovář, Kovářová, and Fronček [3] proved that a 4-regular distance magic graph exists if and only if  $n$  is at least 17. Existence of distance magic labelings of 6-, 8-, 10- and 12-regular graphs was proved by Kovář, Silber, Kabelíková, and Kravčenko [4]. 6-regular distance magic graph exists if  $n = 6$  or  $n$  is at least 17. Bottom boundary of 8-, 10- and 12-regular graphs is 15. Žáček [6] and Krbeček [5] showed that distance magic 14-regular graphs can exist if and only if  $n$  is bigger than 18. Kovář and Silber [7] proved that an  $(n - 3)$ -regular distance magic graph with  $n$  vertices exists if and only if  $n \equiv 3 \pmod{6}$  and that its structure is determined uniquely.  $G$  is isomorphic to  $K_{n/3}[\overline{K_3}]$ . As part of the text [8], Kovář and Žídek proved that  $(n - 5)$  and  $(n - 9)$ -regular distance magic graph exists if and only if  $n$  is at least 15. And  $(n - 7)$ -regular distance magic graph exists if  $n$  is at least 11. They also made a conjecture that for all even

$r \geq 16$  and all odd  $n \geq r + 5$  there exists  $r$ -regular distance magic graph with  $n$  vertices. First introduction of concept modified handicap labeling is in the thesis [9] by Krbeček, where the existence of 2-regular modified handicap graph is completely solved. Now we continue this work and we introduce constructions of  $r$ -regular modified handicap labeling where  $r$  is even and  $2 \leq r \leq n - 4$ .

## 2 Modified handicap labeling: $r$ -regular, $r$ is even and $2 \leq r \leq n - 4$

**Theorem 1.** *Let  $G$  be a 2-regular modified handicap graph, then holds:*

1.  $G$  has number of vertices  $n \equiv 0 \pmod{24}$  or  $n \equiv 6 \pmod{24}$ ,
2. each component of graph  $G$  is isomorphic to cycle  $C_6$ ,
3. sum of labels of any pair of opposite vertices is  $n + 2$ .

*Proof.* First and second point are proved in paper [9]. Now we prove point three.

Let  $i \in \{1, 2, \dots, 6\}$  be the number of vertex in each cycle,  $j \in \{1, 2, \dots, t\}$  is the number of cycle and  $v_{i,j}$  is  $i$ -th vertex of  $j$ -th cycle, we show that for any pair of vertices  $v_{i,j}, v_{i+3,j}$  of graph  $G$  holds  $f(v_{i,j}) + f(v_{i+3,j}) = n + 2$ , where  $f : V(G) \rightarrow M$  a  $M = \{1, 2, \dots, \frac{n}{2} - 1, \frac{n}{2} + 1, \frac{n}{2} + 2, \dots, n + 1\}$  is modified handicap labeling of graph  $G$  (variable  $i$  can be only from the set  $\{1, 2, \dots, 6\}$ , so the sum  $i + 3$  we count evaluate 6).

The proof of theorem 6.1 in [9] shows that for arbitrary  $a, b \in \{M\}$  such as that  $f(v_{1,j}) = a$  and  $f(v_{2,j}) = b$  labeling of each cycle  $j$  of graph  $G$  determines the remaining labels in each  $C_j$ .

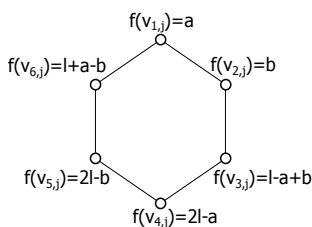


**Fig. 1.** Labeling  $j$ -th cycle of graph  $G$ .

That proof also shows that the constant of a modified handicap labeling  $\ell$  is equal  $\ell = \frac{(r-1)(n+2)}{2}$ . Thus,  $\ell = \frac{(n+2)}{2}$  for 2-regular graphs. Now we prove, that sum of labels of any pair of opposite vertices is  $n + 2$ .

–  $i = 1$  a  $i = 4$ :

$$f(v_{1,j}) + f(v_{1+3,j}) = f(v_{1,j}) + f(v_{4,j}) = a + 2\ell - a = 2\ell = 2 \cdot \frac{(n+2)}{2} = n + 2,$$

–  $i = 2$  a  $i = 5$ :

$$f(v_{2,j}) + f(v_{2+3,j}) = f(v_{2,j}) + f(v_{5,j}) = b + 2\ell - b = 2\ell = 2 \cdot \frac{(n+2)}{2} = n + 2,$$

–  $i = 3$  a  $i = 6$ :

$$f(v_{3,j}) + f(v_{3+3,j}) = f(v_{3,j}) + f(v_{6,j}) = (\ell - a + b) + (\ell + a - b) = 2\ell = 2 \cdot \frac{(n+2)}{2} = n + 2.$$

We showed that for any two vertices  $v_{i,j}, v_{i+3,j}$  is  $f(v_{i,j}) + f(v_{i+3,j}) = n + 2$ .

**Theorem 2.** *Let  $G$  be a 2-regular modified handicap graph with  $n$  vertices and  $G'$  is graph with  $\frac{n}{2}$  vertices which has each component of graph  $G'$  is isomorphic to cycle  $C_3$ , then there exists a homeomorphism  $h : G \rightarrow G'$ .*

*Proof.* Theorem says, that each component of a 2-regular modified handicap graph is isomorphic to cycle  $C_6$  and that the sum of labels of any pair of opposite vertices of each cycle is  $n + 2$ . This means that for each  $j \in \{1, 2, \dots, t\}$  holds:

$$f(v_{1,j}) + f(v_{4,j}) = f(v_{2,j}) + f(v_{5,j}) = f(v_{3,j}) + f(v_{6,j}) = n + 2.$$

Now we describe the construction of graph  $G'$ . We represent each pair of vertices of graph  $G$  which have the sum of their labels  $n + 2$  as a single vertex of graph  $G'$ . We define the following homeomorphism  $h : V(G) \rightarrow V(G')$ :

$$\forall \{v_{i,j}, v_{i+3,j} \in V(G)\} : h(v_{i,j}) = h(v_{i+3,j}) = v_{s,j}, \text{ where } v_{s,j} \in V(G')$$

Cycle  $C_6$  is a 2-regular graph, which has three pairs of opposed vertices. We assign one color to each pair as is shown in Figure 2. We see that each vertex of the cycle is connected with exactly one vertex of each remaining colors. This means that both red vertices (which they have not common neighbour) has exactly one blue vertex and one green vertex as a neighbour. Similarly both green vertices are adjacent to a mutually different red vertex and blue vertex. Also blue vertices must have the different red and blue neighbour.

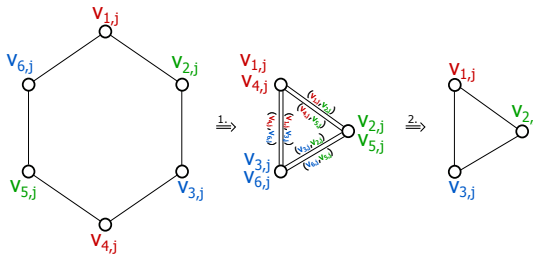


**Fig. 2.** Representation of  $j$ -th cycle  $C_6$  of graph  $G$  as  $k$ -th cycle  $C_3$  of graph  $G'$ .

Thus two edges, which connect vertices different color of the  $j$ -th cycle of graph  $G$ , will be represented in the graph  $G'$  only one edge (Figure.2). The



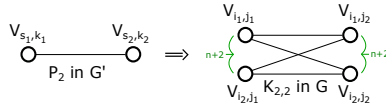


**Fig. 4.** Representation of add edge into graph  $G'$  as bipartite graph  $K_{2,2}$  added into graph  $G$ .

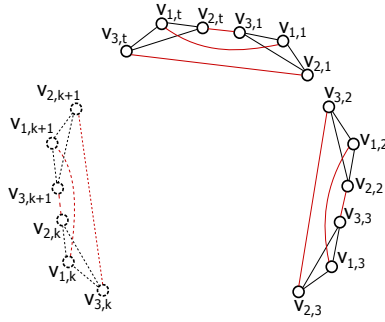


**Fig. 5.** Create a 3-regular graph  $G'$ , by adding 1-regular factor  $F$  (red edges).

$\{v_{i_1, j_1} v_{i_1, j_2}, v_{i_1, j_1} v_{i_2, j_2}, v_{i_2, j_1} v_{i_1, j_2}, v_{i_2, j_1} v_{i_2, j_2}\} \in P(G)$  where  $P(G)$  is set of edges added in graph  $G$ , and moreover holds, that  $h(v_{i_1, j_1}) = h(v_{i_2, j_1}) = v_{s_1, j_1}$  and  $h(v_{i_1, j_2}) = h(v_{i_2, j_2}) = v_{s_2, j_2}$ . We can see this in Figure 6. Because we adding into graph  $G$  the edges only for the edges from set  $P(G')$ , we guarantee that there will not arise any multi-edge.

If we add one edge to graph  $G'$ , then we must add four edges to graph  $G$ , this will increase the weight of these four vertices by value  $n + 2$ . This is due to the construction of graph  $G$ . Because we adding edges of  $G'$  form a  $\frac{r}{2}$ -regular factor in this graph, we know that we increase the weight of all vertices of graph  $G$  by multiple of  $n + 2$ . If we add maximal number of edges to graph  $G'$ , graph  $G'$  will be complete graph with  $\frac{n}{2}$  vertices. This means for graph  $G$ , that all your vertex will be connected. So each vertex of graph  $G$  will be connected to each other vertex of graph  $G$  with except three vertices. This three vertices are with him in the one cycle  $C_6$  of 2-regular graph  $G$  but they are not adjacent. We cannot add edges between this vertices, because they are together in one cycle  $C_3$  of graph  $G'$  and all of these edges are in the set of prohibited edges. So graph  $G$  can be at most  $n - 1 - 3 = (n - 4)$ -regular. If we increase regularity of graph  $G'$  by one then we increase regularity of graph  $G$  by two. At the same time, all labels of graph  $G$  will be raised by value  $n + 2$ . So if we want create  $r$ -regular graph  $G$ , where  $r \leq n - 4$ , we must add  $\frac{r-2}{2}$  edges to each vertex of graph  $G'$  ( $r - 2$ -regular because graph is 2-regular already at the beginning). At the end we must show, that if we add edges to graph  $G$ , the graph  $G$  will be still modified handicap graph. All vertices of 2-regular modified handicap graph



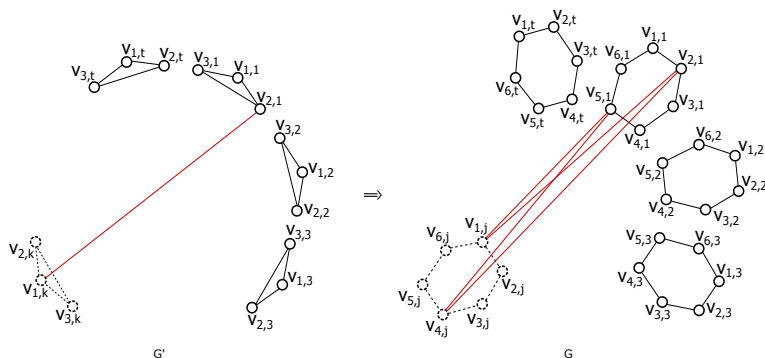


**Fig. 6.** Adding an edge to Chart  $G'$  and then adding the appropriate two edges to graph  $K_{2,2}$  to the  $G'$  chart.

$G$  have weight  $w_f(v_{i,j}) = \ell + f(v_{i,j})$ , if we add one edge to each vertex of  $G$  we will increase weight of these vertices value  $n + 2$ . So, in general we

$$w_f(v_{i,j}) = \frac{n+2}{2} + f(v_{i,j}) + \frac{r-2}{2}(n+2) = f(v_{i,j}) + \frac{(n+2)+(r-2)(n+2)}{2} = f(v_{i,j}) + \frac{(n+2)((r-2)+1)}{2} = f(v_{i,j}) + \frac{(r-1)(n+2)}{2} = f(v_{i,j}) + \ell$$

We showed that graph  $G$  will be again modified handicap graph.

### 3 References

1. M. MILLER, C. RODGER, and R. SIMANJUK, Distance magic labelings of graphs, AUSTRALASIAN JOURNAL OF COMBINATORICS Volume 28 (2003), Pages 305 – 315
2. S.ARUMUGAN, D. FRONČEK, and N. KAMATCHI. Distance Magic-Graphs A Survey, J. Indonesia. Math. 2011, s. 11 – 26.
3. P.KOVÁŘ, T. KOVÁŘOVÁ, and D. FRONČEK. A not on 4-regular distance magic graphs. 2012, roč. 54, s. 127 – 132.
4. P.KOVÁŘ, A.SILBER, P.KABELÍKOVÁ, and M.KRAVČENKO, On Regular distance magic graphs of odd order, ( Submitted).
5. M. KRBEČEK, Applications of 1-VMV labelings of graphs, Ostrava: VŠB-TU Ostrava, 2012.
6. J. ŽÁČEK, Utilization of 1-VMV labelings of graphs, Ostrava: VŠB-TU Ostrava, 2012. Bc.
7. P. KOVÁŘ and A. SILBER, Distance magic graphs of high regularity, Graphs Comb., 9, No. 2 (2012), pp. 213 – 219.
8. P. KOVÁŘ and Židek, project SOČ - český text, (Itemized).
9. M. KRBEČEK, Generalization of magic graph labelings and its application to tournament scheduling. Ostrava, 2014. Thesis. VŠB-TU Ostrava.

# Non-Affine Element Transformations in Linear Elasticity

Lukáš Malý

Department of Applied Mathematics, FEECS,  
VŠB – Technical University of Ostrava, 17. listopadu 15,  
708 33 Ostrava – Poruba, Czech Republic  
IT4Innovation, VŠB – Technical University of Ostrava, 17. listopadu 15,  
708 33 Ostrava – Poruba, Czech Republic  
lukas.maly@vsb.cz

**Abstract.** We solve the problem of linear elasticity using the TD-NNS mixed finite element method. An important part of the implementation of the finite element methods is a transformation from reference to physical elements. In the scope of the mixed formulation for linear elasticity, one has to involve conforming transformations of displacement vectors, stress and strain tensors. These transformations are determined based on the shape of the reference element and its barycentric coordinates. In this paper, we present the appropriate conforming transformations for three different shapes in three dimensions – hexahedron, prism, and tetrahedron.

## 1 Linear Elasticity

For the purpose of this paper consider a problem of linear elasticity in three dimensions. Let  $\Omega \subset \mathbb{R}^3$  be a Lipschitz domain, we are interested in finding the displacement vector  $\mathbf{u} : \mathbb{R}^3 \rightarrow \mathbb{R}^3$  and the stress tensor  $\underline{\sigma} : \mathbb{R}^3 \rightarrow \mathbb{R}^{3 \times 3}_{\text{SYM}}$  subjected to the assumptions of linear elasticity, volume forces  $\mathbf{f} : \mathbb{R}^3 \rightarrow \mathbb{R}^3$ , and the boundary conditions, that are either the Dirichlet or Neumann boundary conditions,  $\partial\Omega = \bar{\Gamma}_D \cup \bar{\Gamma}_N$ . Therefore, we solve the problem

$$\left\{ \begin{array}{ll} \underline{\mathbf{A}} \underline{\sigma} - \underline{\varepsilon}(\mathbf{u}) = 0 & \text{in } \Omega, \\ -\text{div} \underline{\sigma} = \mathbf{f} & \text{in } \Omega. \\ \mathbf{u} = \mathbf{u}_D & \text{on } \Gamma_D, \\ \underline{\sigma} \mathbf{n} = \mathbf{t}_N & \text{on } \Gamma_N, \end{array} \right. \quad (1)$$

where  $\mathbf{u}_D$  and  $\mathbf{t}_N$  are the prescribed boundary data,  $\mathbf{n}$  denotes the outer unit normal,  $\underline{\varepsilon}(\mathbf{u}) = \frac{1}{2} (\nabla \mathbf{u} + (\nabla \mathbf{u})^\top)$  is a symmetric strain tensor, and the  $\underline{\mathbf{A}}$  is the compliance tensor, which implements Hooke's linear material law, the Young modulus and the Poisson ratio.

To solve the problem (1) we apply the TD-NNS finite element method introduced by Schöberl et. al. in [3, 5]. It is a mixed formulation, where the displacements are sought in the vector-valued space  $\mathbf{H}(\text{curl})$  and the stresses lie in the

tensor-valued space  $\underline{\mathbf{H}}(\text{div div})$ . After a discretization of the domain  $\Omega$  into geometrical elements  $\mathcal{T}_h = \bigcup \{T\}$ , the authors approximate the displacements using Nédélec tangential continuous space  $\mathbf{V}_h$ , and the stresses using normal-normal continuous space  $\underline{\Sigma}_h$ , i.e.

$$\begin{aligned}\mathbf{V}_h &:= \left\{ \mathbf{v} \in [L^2(\Omega)]^3 : \mathbf{v} \in [P^1(\mathcal{T}_h)]^3, \mathbf{v}_t \text{ cont.}, \mathbf{v}_t = 0 \text{ on } \Gamma_D \right\}, \\ \underline{\Sigma}_h &:= \left\{ \underline{\sigma} \in [L^2(\Omega)]_{\text{SYM}}^{3 \times 3} : \underline{\sigma} \in [P^1(\mathcal{T}_h)]_{\text{SYM}}^{3 \times 3}, \sigma_{nn} \text{ cont.}, \sigma_{nn} = 0 \text{ on } \Gamma_N \right\}.\end{aligned}$$

Therefore, the mixed discrete TD-NNS finite element formulation reads as – find  $\underline{\sigma} \in \underline{\Sigma}_h$ ,  $\mathbf{u} \in \mathbf{V}_h$  such that

$$\begin{aligned}\int_{\Omega} (\underline{\mathbf{A}} \underline{\sigma}) : \underline{\tau} \, d\mathbf{x} + \langle \text{div} \underline{\tau}, \mathbf{u} \rangle_V &= \int_{\Gamma_D} u_{D,n} \tau_{nn} \, d\mathbf{s} \quad \forall \underline{\tau} \in \underline{\Sigma}_h, \\ \langle \text{div} \underline{\sigma}, \mathbf{v} \rangle_V &= - \int_{\Omega} \mathbf{f} \cdot \mathbf{v} \, d\mathbf{x} + \int_{\Gamma_N} \mathbf{t}_{N,\tau} \cdot \mathbf{v}_{\tau} \, d\mathbf{s} \quad \forall \mathbf{v} \in \mathbf{V}_h,\end{aligned}$$

with the duality product that can be evaluated due to smoothness of finite element functions using

$$\langle \text{div} \underline{\tau}, \mathbf{v} \rangle_V = \sum_{T \in \mathcal{T}_h} \left[ - \int_T \underline{\tau} : \underline{\varepsilon} \, d\mathbf{x} + \int_{\partial T} \tau_{nn} v_n \, d\mathbf{s} \right]. \quad (2)$$

## 2 Conforming Transformations

The essential aspect of the finite element methods is the *mapping trick*, where the physical finite elements are defined as a transformation of a reference element. This construction is very useful since it allows to perform many computations a priori on the reference element.

Let the transformation

$$\Phi : \hat{T} \rightarrow T$$

be a continuously differentiable, one-to-one and onto map. If  $\hat{\mathbf{x}}$  denotes a coordinate system on the reference element  $\hat{T}$ , then  $\mathbf{x} := \Phi(\hat{\mathbf{x}})$  is the corresponding coordinate system on the physical element  $T$ . The Jacobian and the Hessian of the  $i$ -th component of this transformation shall be denoted by  $F$  and  $H^i$

$$F_{ij}(\hat{\mathbf{x}}) = \frac{\partial \Phi_i}{\partial \hat{x}_j}(\hat{\mathbf{x}}), \quad H^i(\hat{\mathbf{x}}) = \frac{\partial^2 \Phi_i}{\partial \hat{x}_j \partial \hat{x}_k}(\hat{\mathbf{x}}), \quad 1 \leq i, j, k \leq 3.$$

The Jacobi determinant is given by  $J(\hat{\mathbf{x}}) := \det(F(\hat{\mathbf{x}}))$ . Similarly, for a facet  $F$  or an edge  $E$ , let  $J_F(\hat{\mathbf{x}})$ ,  $J_E(\hat{\mathbf{x}})$  be the transformation of measures of the facet transformation  $\hat{F} \rightarrow F$  or the edge transformation  $\hat{E} \rightarrow E$ , respectively. Due to the inverse theorem [4], the inverse of the Jacobian is the Jacobian of the inverse transformation  $\Phi^{-1} : T \rightarrow \hat{T}$ , i.e.

$$[F(\hat{\mathbf{x}})]^{-1} = F^{-1}(\Phi(\hat{\mathbf{x}})) = F^{-1}(\mathbf{x}), \quad F_{ij}^{-1}(\mathbf{x}) = \frac{\partial \Phi_i^{-1}}{\partial x_j}(\mathbf{x}).$$

An outer normal vector  $\hat{\mathbf{n}}(\hat{\mathbf{x}})$  on  $\hat{F}$  and a tangential vector  $\hat{\boldsymbol{\tau}}(\hat{\mathbf{x}})$  along  $\hat{E}$  are transformed to the physical element by

$$\mathbf{n}(\mathbf{x}) := \frac{J(\hat{\mathbf{x}})}{J_F(\hat{\mathbf{x}})} F(\hat{\mathbf{x}})^{-\top} \hat{\mathbf{n}}(\hat{\mathbf{x}}), \quad \boldsymbol{\tau}(\mathbf{x}) := \frac{1}{J_E(\hat{\mathbf{x}})} F(\hat{\mathbf{x}}) \hat{\boldsymbol{\tau}}(\hat{\mathbf{x}}).$$

Suitable transformation for the displacement vector and stress tensor have to preserve the degrees of freedom. Therefore, the following transformations are used,

$$\underline{\boldsymbol{\tau}}(\mathbf{x}) := \frac{1}{J(\hat{\mathbf{x}})^2} F(\hat{\mathbf{x}}) \underline{\hat{\boldsymbol{\tau}}}(\hat{\mathbf{x}}) F(\hat{\mathbf{x}})^\top \quad \text{for } \underline{\hat{\boldsymbol{\tau}}}(\hat{\mathbf{x}}) \in \underline{\hat{\boldsymbol{\Sigma}}}_h, \quad (3)$$

$$\mathbf{v}(\mathbf{x}) := F(\hat{\mathbf{x}})^{-\top} \hat{\mathbf{v}}(\hat{\mathbf{x}}) \quad \text{for } \hat{\mathbf{v}}(\hat{\mathbf{x}}) \in \hat{\mathbf{V}}_h. \quad (4)$$

We need to find the appropriate transformation also for the strain tensor  $\underline{\boldsymbol{\varepsilon}}(\mathbf{v})$ , it can be derived from (4) and its partial derivative

$$\begin{aligned} \frac{\partial v_i(\mathbf{x})}{\partial x_j} &= \frac{\partial}{\partial x_j} \left( \sum_k F_{ik}^{-\top}(\mathbf{x}) \hat{v}_k(\hat{\mathbf{x}}) \right) \\ &= \sum_k \left( \frac{\partial F_{ki}^{-1}}{\partial x_j}(\mathbf{x}) \hat{v}_k(\hat{\mathbf{x}}) + F_{ki}^{-1}(\mathbf{x}) \frac{\partial \hat{v}_k}{\partial x_j}(\hat{\mathbf{x}}) \right) \\ &= \sum_k \left( \frac{\partial^2 \Phi_k^{-1}}{\partial x_i \partial x_j}(\mathbf{x}) \hat{v}_k(\hat{\mathbf{x}}) + F_{ki}^{-1}(\mathbf{x}) \left( \sum_l \frac{\partial \hat{v}_k}{\partial \hat{x}_l}(\hat{\mathbf{x}}) \frac{\partial \hat{x}_l}{\partial x_j}(\mathbf{x}) \right) \right). \end{aligned}$$

After expressing this derivative for all  $i, j : 1 \leq i, j \leq 3$ , we end up with the form

$$\underline{\boldsymbol{\varepsilon}}(\mathbf{v}) = F(\hat{\mathbf{x}})^{-\top} \underline{\hat{\boldsymbol{\varepsilon}}}(\hat{\mathbf{v}}) F(\hat{\mathbf{x}})^{-1} + \sum_{i=1}^d \hat{v}_i(\hat{\mathbf{x}}) (H^{-1}(\mathbf{x}))^i, \quad (5)$$

where  $(H^{-1}(\mathbf{x}))^i$  denotes the Hessian of the  $i$ -th component of the inverse transformation. For affine transformations  $\Phi$ , the Jacobian  $F$  is constant, thus the inverse matrix is also constant and the Hessian vanishes. In what follows, we demonstrate two simple reference elements such that the appropriate transformations to general physical elements are not affine.

According to the presented TD-NNS finite element formulation and the duality form (2), we illustrate the conformity of integral values:

$$\begin{aligned} \int_F \sigma_{nn} q J_F \, d\mathbf{s} &= \int_{\hat{F}} \left( \frac{J_T}{J_F} F^{-\top} \hat{\mathbf{n}} \right)^\top \left( \frac{1}{J_T^2} F \underline{\boldsymbol{\sigma}} F^\top \right) \left( \frac{J_T}{J_F} F^{-\top} \hat{\mathbf{n}} \right) \hat{q} J_F^2 \, d\hat{\mathbf{s}} \\ &= \int_{\hat{F}} \hat{\sigma}_{nn} \hat{q} J_{\hat{F}} \, d\hat{\mathbf{s}}, \end{aligned}$$

where the  $q$  is a polynomial from the respective space.

### 3 Reference Elements

Between standard reference elements used in three dimensions belongs a hexahedron, prism, or tetrahedron, see Figure 1. While the tetrahedron is a simplex, the prism and hexahedron are tensor-product elements of simplices in two and one dimension – triangle and line. The transformation from these reference elements to the physical ones is given by a combination of the physical vertex coordinates and the barycentric coordinates [1],

$$\mathbf{x} := \Phi(\hat{\mathbf{x}}) = \sum_i V_i \hat{\varphi}_i(\hat{\mathbf{x}}), \quad \sum_i \hat{\varphi}_i(\hat{\mathbf{x}}) = 1, \forall \hat{\mathbf{x}} \in \hat{T}, \quad \hat{\varphi}_i(V_j) = \delta_{ij}.$$

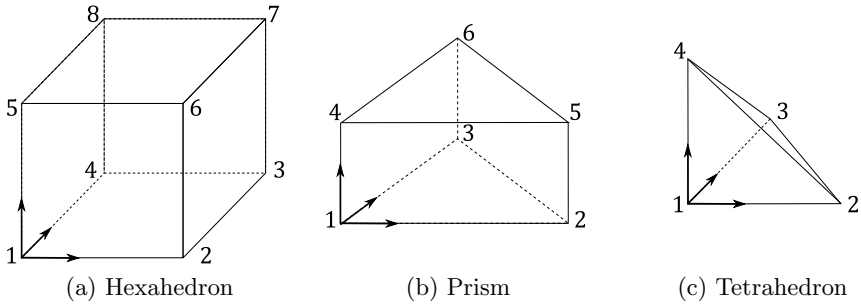


Fig. 1: Reference elements.

In the following part, we list the barycentric coordinates, the appropriate transformations, and Jacobians for individual elements.

#### *Hexahedron*

$$\begin{aligned} \hat{\varphi}_1 &= (1 - \hat{x}_1)(1 - \hat{x}_2)(1 - \hat{x}_3) & \hat{\varphi}_5 &= (1 - \hat{x}_1)(1 - \hat{x}_2)\hat{x}_3 \\ \hat{\varphi}_2 &= \hat{x}_1(1 - \hat{x}_2)(1 - \hat{x}_3) & \hat{\varphi}_6 &= \hat{x}_1(1 - \hat{x}_2)\hat{x}_3 \\ \hat{\varphi}_3 &= \hat{x}_1\hat{x}_2(1 - \hat{x}_3) & \hat{\varphi}_7 &= \hat{x}_1\hat{x}_2\hat{x}_3 \\ \hat{\varphi}_4 &= (1 - \hat{x}_1)\hat{x}_2(1 - \hat{x}_3) & \hat{\varphi}_8 &= (1 - \hat{x}_1)\hat{x}_2\hat{x}_3 \end{aligned}$$

The transformation from the reference hexahedron (Figure 1a) to a generic physical one is given by

$$\begin{aligned} \mathbf{x} := \Phi(\hat{\mathbf{x}}) &= \sum_{i=1}^8 V_i \hat{\varphi}_i(\hat{\mathbf{x}}) = \mathbf{a}_{000} + \mathbf{a}_{100}\hat{x}_1 + \mathbf{a}_{010}\hat{x}_2 + \mathbf{a}_{001}\hat{x}_3 + \mathbf{a}_{110}\hat{x}_1\hat{x}_2 + \\ &\quad \mathbf{a}_{101}\hat{x}_1\hat{x}_3 + \mathbf{a}_{011}\hat{x}_2\hat{x}_3 + \mathbf{a}_{111}\hat{x}_1\hat{x}_2\hat{x}_3. \end{aligned}$$

This transformation is a trilinear function, it is linear on individual edges and bilinear on faces. Moreover, the Jacobian remains the non-constant function,

$$F(\hat{\mathbf{x}}) = \begin{bmatrix} [\mathbf{a}_{100} + \mathbf{a}_{110}\hat{x}_2 + \mathbf{a}_{101}\hat{x}_3 + \mathbf{a}_{111}\hat{x}_2\hat{x}_3]^\top \\ [\mathbf{a}_{010} + \mathbf{a}_{110}\hat{x}_1 + \mathbf{a}_{011}\hat{x}_3 + \mathbf{a}_{111}\hat{x}_1\hat{x}_3]^\top \\ [\mathbf{a}_{001} + \mathbf{a}_{101}\hat{x}_1 + \mathbf{a}_{011}\hat{x}_2 + \mathbf{a}_{111}\hat{x}_1\hat{x}_2]^\top \end{bmatrix}^\top,$$

and thus the Hessian is non-zero. In this case one has to take into account the second term in the transformation of the strain tensor (5).

### *Prism*

$$\begin{aligned} \hat{\varphi}_1 &= (1 - \hat{x}_1 - \hat{x}_2)(1 - \hat{x}_3) & \hat{\varphi}_4 &= (1 - \hat{x}_1 - \hat{x}_2)\hat{x}_3 \\ \hat{\varphi}_2 &= \hat{x}_1(1 - \hat{x}_3) & \hat{\varphi}_5 &= \hat{x}_1\hat{x}_3 \\ \hat{\varphi}_3 &= \hat{x}_2(1 - \hat{x}_3) & \hat{\varphi}_6 &= \hat{x}_2\hat{x}_3 \end{aligned}$$

The transformation from the reference prism (Figure 1b) to a generic physical one is given by

$$\begin{aligned} \mathbf{x} := \Phi(\hat{\mathbf{x}}) &= \sum_{i=1}^6 V_i \hat{\varphi}_i(\hat{\mathbf{x}}) = \mathbf{a}_{000} + \mathbf{a}_{100}\hat{x}_1 + \mathbf{a}_{010}\hat{x}_2 + \mathbf{a}_{001}\hat{x}_3 + \mathbf{a}_{110}\hat{x}_1\hat{x}_2 + \\ &\quad \mathbf{a}_{101}\hat{x}_1\hat{x}_3 + \mathbf{a}_{011}\hat{x}_2\hat{x}_3. \end{aligned}$$

Similar to the case with hexahedron the transformation is a bilinear function and also here the Jacobian is not a constant matrix,

$$F(\hat{\mathbf{x}}) = [\mathbf{a}_{100} + \mathbf{a}_{101}\hat{x}_3, \mathbf{a}_{010} + \mathbf{a}_{011}\hat{x}_3, \mathbf{a}_{001} + \mathbf{a}_{101}\hat{x}_1 + \mathbf{a}_{011}\hat{x}_2],$$

and thus the Hessian has to be involved.

### *Tetrahedron*

$$\hat{\varphi}_1 = 1 - \hat{x}_1 - \hat{x}_2 - \hat{x}_3 \quad \hat{\varphi}_2 = \hat{x}_1 \quad \hat{\varphi}_3 = \hat{x}_2 \quad \hat{\varphi}_4 = \hat{x}_3$$

The transformation from the reference tetrahedron (Figure 1c) to a generic physical one is given by

$$\mathbf{x} := \Phi(\hat{\mathbf{x}}) = \sum_{i=1}^4 V_i \hat{\varphi}_i(\hat{\mathbf{x}}) = \mathbf{a}_{000} + \mathbf{a}_{100}\hat{x}_1 + \mathbf{a}_{010}\hat{x}_2 + \mathbf{a}_{001}\hat{x}_3.$$

In this case the transformation is linear and the Jacobian is a constant matrix,

$$F(\hat{\mathbf{x}}) = [\mathbf{a}_{100}, \mathbf{a}_{010}, \mathbf{a}_{001}].$$

## 4 Conclusion

We have introduced three basic types of the reference elements in three dimensions and their conforming transformations in a scope of the mixed finite element method for linear elasticity. We focus on general non-affine transformations since they are necessary for real problem computations. Presented transformations are linear, bilinear and trilinear functions for the tetrahedron, prism, and hexahedron, respectively. We point out that also for simple tensor-product elements, in contrast to simplices, the transformation has non-constant Jacobian and then the Jacobi determinant and Hessian have to be treated with care.

## Acknowledgements

This work was supported by TA ČR from the project TA03010140, by The Ministry of Education, Youth and Sports from the National Programme of Sustainability (NPU II) project ‘IT4Innovations excellence in science – LQ1602’, from the Large Infrastructures for Research, Experimental Development and Innovations project ‘IT4Innovations National Supercomputing Center LM2015070’, and by VŠB - Technical University of Ostrava under the grants SP2017/165 and SP2017/122.

## References

1. Liseikin, V.D.: Grid Generation Methods. Springer Publishing Company, Incorporated, 2nd edn. (2009)
2. Pechstein, A., Schöberl, J.: Anisotropic mixed finite elements for elasticity. *International Journal for Numerical Methods in Engineering* 90(2), 196–217 (2012), <http://dx.doi.org/10.1002/nme.3319>
3. Pechstein, A., Schöberl, J.: Tangential-displacement and normal-normal-stress continuous mixed finite elements for elasticity. *Mathematical Models and Methods in Applied Sciences* 21(08), 1761–1782 (2011), <http://www.worldscientific.com/doi/abs/10.1142/S0218202511005568>
4. Petersen, K.B., Pedersen, M.S.: The matrix cookbook (nov 2012), <http://www2.imm.dtu.dk/pubdb/p.php?3274>, version 20121115
5. Sinwel, A.: A New Family of Mixed Finite Elements for Elasticity. PhD thesis, Johannes Kepler University, Institute of Computational Mathematics (December 2008), <http://www.numa.uni-linz.ac.at/Teaching/PhD/Finished/sinwel>
6. Zaglmayr, S.: High Order Finite Elements for Electromagnetic Field Computation. PhD thesis, Johannes Kepler University, Institute of Computational Mathematics (August 2006), [www.numa.uni-linz.ac.at/Teaching/PhD/Finished/zaglmayr](http://www.numa.uni-linz.ac.at/Teaching/PhD/Finished/zaglmayr)

# Numerical Computation of Two Electron Integrals

Martin Mrovec

Department of Applied Mathematics, FEECS,  
VŠB – Technical University of Ostrava, 17. listopadu 15,  
708 33 Ostrava – Poruba, Czech Republic  
`martin.mrovec@vsb.cz`

**Abstract.** The paper deals with a numerical computation of Two Electron Integrals, which is the main ingredient of the precomputing phase of Hartree-Fock electronic structure calculations. The numerical computation requires an application of Tensor Numerical Methods to reduce the dimensionality of the problem. Furthermore, we focus on the parallelization of the problem and we present results of the scalability tests.

**Keywords:** Tensor Numerical Methods, Two Electron Integrals, Electronic structure calculations

## 1 Introduction

In electronic structure computations (Hartree-Fock or DFT [1]) we encounter calculation of so-called two electron integrals (TEI) [2]

$$b_{ijkl} = \int_{\mathbb{R}^3} \int_{\mathbb{R}^3} \frac{g_i(\mathbf{x}) g_j(\mathbf{x}) g_k(\mathbf{y}) g_l(\mathbf{y})}{\|\mathbf{x} - \mathbf{y}\|} d^3\mathbf{y} d^3\mathbf{x}, \quad (1)$$

where  $g_* : \mathbb{R}^3 \rightarrow \mathbb{R}$  are basis functions,  $i, j, k, l \in \{1, 2, \dots, N_B\}$  ( $N_B$  is a number of basis functions). The computation of TEI is the main ingredient of the so-called precomputing phase. In case of the electronic structure of molecules most of the standard software packages use the Gaussian-type basis (GTO) functions in the form

$$\phi_{nlm}^{GTO}(x_1, x_2, x_3) = N \cdot x_1^n \cdot x_2^l \cdot x_3^m \cdot e^{-\alpha(x_1^2 + x_2^2 + x_3^2)} \quad (2)$$

with integer exponents  $n, l, m$  and a normalization constant  $N$ . With these functions, the TEI are analytically integrable, which is their main advantage. Unfortunately, GTO basis functions poorly behave in the area of the atomic core, so for the required accuracy of the electronic structure calculation we have to enlarge the number of basis functions. Slater-type orbital (STO) basis functions can be written as

$$\phi_{nlm}^{STO}(x_1, x_2, x_3) = N \cdot (x_1^2 + x_2^2 + x_3^2)^{\frac{n-1}{2}} \cdot Y_{lm}(x_1, x_2, x_3) \cdot e^{-\alpha\sqrt{x_1^2 + x_2^2 + x_3^2}}, \quad (3)$$



where  $N$  is a normalization constant and  $Y_{lm}$  denotes a real spherical harmonics. Although the STO functions are physically more appropriate, they are not very popular due to the impossibility of the analytic integration. We work with the numerical representation of basis functions. The numerical approach comes with the possibility of using several types of basis functions in one computation (e.g. Gaussian and Slater-type orbitals) which may be advantageous for more accurate description of the many-electron wave function near the nuclei. Unfortunately, due to the numerical representation, the TEI computation becomes the dominant part of the whole electronic structure computation.

However, the computations of TEI can be effectively parallelized. The basis functions are discretized in compact subset of real 3D space (e.g. a cube). To reach a sufficient accuracy we have to use very fine discretization grids (in order of magnitude  $10^3 - 10^5$  in one dimension). We cannot store such data directly as three dimensional arrays due to the huge memory demands. To overcome this problem we use Tensor Numerical Methods [2]. They reduce the computational and storage costs from  $\mathcal{O}(n^d)$  to  $\mathcal{O}(dRn)$ , where  $d$  is the dimension of the problem and  $R$  is so-called rank parameter [3]. In addition to the reduction of the computational complexity, we can use the parallelism. E.g. for entry-wise product, we have to perform several linear algebra operations on one-dimensional vectors. The operations are fully independent and their number depends linearly on each of the rank parameters of given tensors. Therefore they can be performed parallelly.

Currently we are developing a Fortran 95 library for electronic structure calculations. In case of the precomputing phase the implementation uses a hybrid OpenMP/MPI approach which can be run on supercomputer infrastructure. In this paper we present results of the scalability tests.

## 2 Tensor representation of basis functions

Tensor structured representation of the multidimensional data is based on an idea of the singular value decomposition (SVD), which can be written (for a given matrix  $\mathbf{A} \in \mathbb{R}^{n \times n}$ ) as

$$\mathbf{A} = \mathbf{U}\mathbf{S}\mathbf{V}^T = \sum_{i=1}^R \sigma_i \mathbf{u}_i \mathbf{v}_i^T. \quad (4)$$

If matrix  $\mathbf{A}$  has a low rank  $R \ll n$ , it can be stored with only  $2Rn$  numbers (instead of  $n^2$ ) and, similarly, matrix-matrix and matrix-vector products have lower computational demands. For any tensor of order  $d$  ( $d$ -dimensional array) the corresponding representation is

$$\mathbf{A} = \sum_{k=1}^R c_k \mathbf{u}_k^{(1)} \otimes \dots \otimes \mathbf{u}_k^{(d)}, \quad (5)$$

where  $\otimes$  denotes the tensor product,  $c_k \in \mathbb{R}$  and  $\mathbf{u}_k^{(\ell)}$  are one-dimensional vectors of length  $n$ ,  $R$  is so-called Canonical rank. This representation is known as the Canonical representation [3].

Practically, a canonically represented tensor is stored in memory as a set of  $d$  matrices  $\mathbf{U}^{(\ell)} \in \mathbb{R}^{n \times R}$  which columns contain normalized side vectors  $\mathbf{u}_k^{(\ell)}$  and one-dimensional vector  $\mathbf{C} \in \mathbb{R}^R$  with coefficients  $c_k$  which correspond to singular values of the SVD.

In our implementation we use the tensor representation of discretized GTO and STO functions. The GTO functions are separable so their canonical representation is straightforward and has rank  $R = 1$ . On the other hand for finding a canonical representation of STOs we have to use special techniques such as Sinc-approximation [4]. The function is approximated with an error depending on the rank  $R > 1$ .

### 3 Parallelization

The parallelization of TEI computations is divided into two levels. The computation of a single TEI in a discretized form can be written as

$$b_{ijkl} \approx h^6 \langle \mathbf{G}_i \odot \mathbf{G}_j, \mathcal{P}_{\mathcal{N}} * (\mathbf{G}_k \odot \mathbf{G}_l) \rangle, \quad (6)$$

where  $\mathbf{G}_* \in \mathbb{R}^{n \times n \times n}$  are basis functions equidistantly discretized on a 3-dimensional interval  $[-A, A]^3$  with discretization step  $h$ ,  $\mathcal{P}_{\mathcal{N}}$  is a discretized Newton kernel  $\frac{1}{\|\mathbf{x}\|}$ ,  $*$  denotes a discrete convolution,  $\odot$  is a Hadamard (element-wise) product and  $\langle \cdot, \cdot \rangle$  is a dot product which corresponds to the Frobenius norm. First level of parallelization includes performing of mentioned operations. The second level consists in distribution of TEI computations among individual processes.

#### 3.1 Parallelization of a single TEI computation

Given two canonically represented tensors  $\mathbf{A}, \mathbf{B}$ ,

$$\mathbf{A} = \sum_{k=1}^{R_A} c_k \mathbf{u}_k^{(1)} \otimes \dots \otimes \mathbf{u}_k^{(d)}, \quad \mathbf{B} = \sum_{j=1}^{R_B} d_j \mathbf{v}_j^{(1)} \otimes \dots \otimes \mathbf{v}_j^{(d)}, \quad (7)$$

we can calculate their dot product as

$$\langle \mathbf{A}, \mathbf{B} \rangle = \sum_{k=1}^{R_A} \sum_{j=1}^{R_B} c_k d_j \prod_{\ell=1}^d \langle \mathbf{u}_k^{(\ell)}, \mathbf{v}_j^{(\ell)} \rangle. \quad (8)$$

This operation costs  $dR_A R_B n$  ( $\ll n^d$ ) scalar multiplications. To get a Hadamard product of tensors in the canonical format we use the following formula:

$$\mathbf{A} \odot \mathbf{B} = \sum_{k=1}^{R_A} \sum_{j=1}^{R_B} c_k d_j \bigotimes_{\ell=1}^d \left( \mathbf{u}_k^{(\ell)} \odot \mathbf{v}_j^{(\ell)} \right), \quad (9)$$

which costs  $dR_A R_B n$  ( $\ll n^d$ ) operations. Note that the resulting tensor has rank  $(\mathbf{A} \odot \mathbf{B}) = R_A R_B$ . In case of the discrete convolution we can write

$$\mathbf{A} * \mathbf{B} = \sum_{k=1}^{R_A} \sum_{j=1}^{R_B} c_k d_j \bigotimes_{\ell=1}^d \left( \mathbf{u}_k^{(\ell)} * \mathbf{v}_j^{(\ell)} \right). \quad (10)$$

We can notice that each multidimensional operation consists of a set of 1D operations. These operations are fully independent and in case of moderate-rank tensors ( $R \sim 10 - 100$ ) they can be effectively parallelized. In case of the Hadamard product and convolution we just store calculated vectors in new side matrices of sizes  $n \times R_A R_B$  and new coefficients in a vector of length  $R_A R_B$ . The sums in (8) and (10) are not computed. They only denote the canonical representation. Conversely, in case of the dot product we have to sum up products of results of one-dimensional operations. Since storage costs of tensor operations performed within single TEI computation are not high, they can be performed on many core device with shared memory, specifically computational nodes equipped with CUDA or MIC accelerators. In our implementation the OpenMP technology is used to parallelize the computation of each tensor operation.

### 3.2 Parallelization of TEI computations

The whole precomputing phase of an electronic structure calculation consists of calculation of  $N_B^4$  TEI. The number of computations can be reduced to approximately  $\frac{N_B^4}{8}$  thanks to the symmetry  $b_{ijkl} = b_{jikl} = b_{ijlk} = b_{klij}$ , which follows from the structure of the integral (1). However, looking at the equation (6) we can observe that distribution of the whole TEI computations can be ineffective. That's because some operations are redundant within the set of TEI. The number of the computations can be optimized by using the following scheme:

1. Parallel computation of  $N_B^2$  Hadamard products  $\mathbf{H}_{ij} = \mathbf{G}_i \odot \mathbf{G}_j$ . Thanks to the symmetry we can calculate only  $\frac{1}{2}N_B(N_B + 1)$  Hadamard products.
2. Parallel computation of  $N_B^2$  convolutions  $\mathbf{C}_{ij} = \mathcal{P}_{\mathcal{N}} * \mathbf{H}_{ij}$ . Thanks to the symmetry we can calculate only  $\frac{1}{2}N_B(N_B + 1)$  convolutions.
3. Parallel computation of approximately  $\frac{N_B^4}{8}$  dot products using formula  $b_{ijkl} \approx h^6 \langle \mathbf{H}_{ij}, \mathbf{C}_{kl} \rangle$ .

In our implementation the MPI protocol is used to distribute tensor operations. We use the Master-Slave approach to effectively distribute the data.

### 3.3 Scalability tests

Scalability tests have been performed on Salomon supercomputer using the standard computational nodes equipped with two Intel Xeon E5-2680v3, 2.5GHz processors with 12 cores and 128GB, DDR4@2133 MHz memory. Each MPI slave process uses one computational node. The master process sends individual tensor convolutions to slaves and receives processed data. At each node we can run

24 parallel threads at maximum. Scalability tests of GTO functions have been performed on a computational box discretized with 20000 points in each spatial dimension. Number of basis functions was equal to 9 so the whole computation consisted of 45 convolutions and Hadamard products and approximately 800 dot products. The rank parameter of the Newton kernel is equal to 30. Following graphs show the results of scalability tests. On Figure 1 we can see the strong scalability graphs (dependence of the computational time on the number of MPI processes and on the number of OpenMP threads). We can see that almost linear

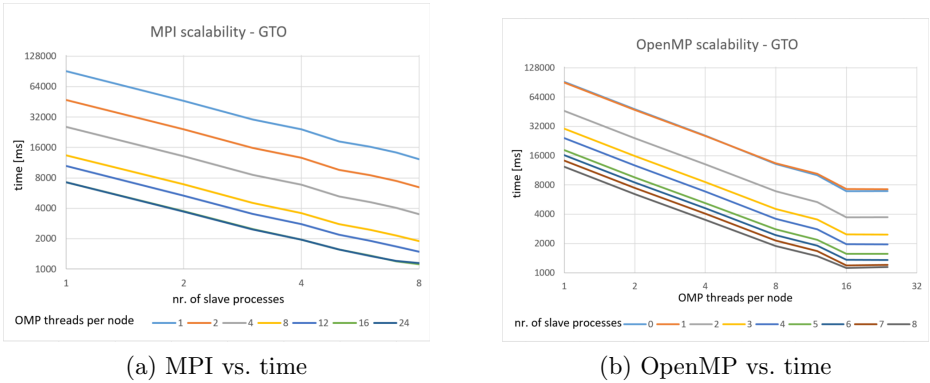


Fig. 1: Scalability of TEI computations using STO basis functions

scalability has been achieved. Further, the OpenMP scales well up to 16 threads per process. Due to the low rank parameter  $R$  of the Newton kernel further increasing of the threads has no effect to the computational time. Scalability tests of STO functions have been performed on a computational box discretized with 1000 points in each spatial dimension. The basis functions were approximated with rank  $R = 10$ . Number of basis functions was equal to 9. The rank parameter of the Newton kernel was equal to 30. Following graphs show the results of scalability tests. We can see that the algorithm scales almost linearly up to 8 slave processes while running 1-8 threads. In other cases the computational time starts to stagnate at some number of processes and the same behavior can be predicted in case of 1-8 threads reaching the sufficient number of slave processes. The stagnation is caused by the communication of the master process with slaves.

## 4 Conclusion

This paper has been focused on the numerical computation of TEI. Further the results of scalability tests of the numerical computation of TEI have been presented. These results are very important for further optimizations of our electronic structure calculation libraries. Some of the achieved results have been

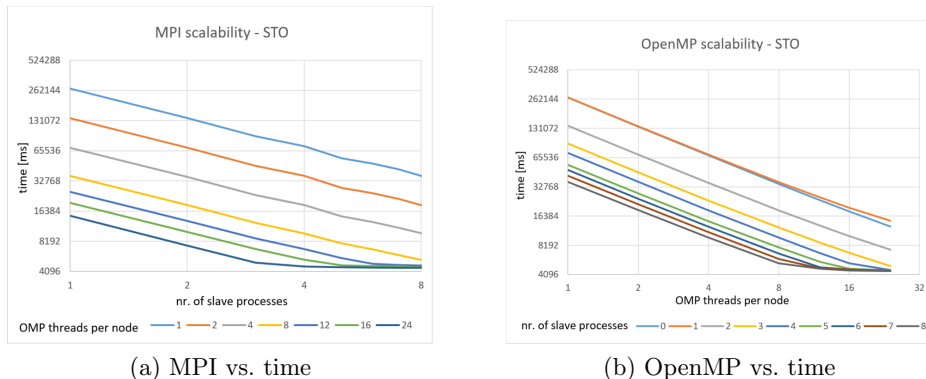


Fig. 2: Scalability of TEI computations using STO basis functions

already submitted and accepted or published (the approximation of STO functions in [5], the preliminary results of scalability tests at conference paper [6]).

## 5 Acknowledgements

This work was supported by The Ministry of Education, Youth and Sports from the National Programme of Sustainability (NPU II) project "IT4Innovations excellence in science - LQ1602", by Grant of SGS No. SP2017/122 and SP2017/168, VŠB - Technical University of Ostrava, Czech Republic.

## References

1. Saad, Y., Chelikowsky, J. R., Shontz, S. M.: Numerical Methods for Electronic Structure Calculations of Materials. *SIAM Review*. 2010, vol. 52, issue 1. DOI: 10.1137/060651653.
2. Khoromskaia, V., Khoromskij, B. N., Schneider, R.: Tensor-structured factorized calculation of two-electron integrals in a general basis. *SIAM Journal on Scientific Computing*, vol. 35(issue 2):A987–A1010, 2013.
3. Khoromskij, B. N.: Structured rank-( $r_1, \dots, r_d$ ) decomposition of function-related tensors in  $r_d$ . *Computational Methods in Applied Mathematics*, vol. 6(issue 2):–, 2006.
4. Hackbusch, W., Khoromskij, B. N., Pople, J. A.: Tensor-Product Approximation to Multidimensional Integral Operators and Green's Functions. *SIAM Journal on Matrix Analysis and Applications*. 2008, **30**(3), 1233–1253. DOI: 10.1137/060657017. ISSN 0895-4798.
5. Mrovec, M.: Tensor Approximation of Slater-Type Orbital Basis Functions: Advances in Electrical and Electronic Engineering, accepted submission
6. Ćosić, R., Mrovec, M., Vitek, A., Kalus, R.: First principles modeling of thermodynamical properties, in Proceedings of the Fifth International Conference on Parallel, Distributed, Grid and Cloud Computing for Engineering, P. Iványi, B.H.V. Topping, G.Várady (Editors), Civil-Comp Press, Stirlingshire, United Kingdom, paper 6, 2017.

# Molecular Dynamics

Stanislav Paláček

Department of Applied Mathematics, FEECS,  
VŠB – Technical University of Ostrava, 17. listopadu 15,  
708 33 Ostrava – Poruba, Czech Republic  
`stanislav.palacek.st@vsb.cz`

**Abstract.** Chemical reaction of  $CH_4 + O^+$  is significant in atmosphere of Saturn's moon Titan as shown recent Cassini-Huygens mission and this reaction is also in main interest of my research. For purpose of modelling dynamics of atoms and molecules I'm developing and testing program which was called MULTIDYN 3.0. This program will paralelly compute several thousands of semiclassical trajectories of given particles. Initial conditions are generated by using quantum mechanical distributions to get proper cross section and other parameters of mentioned reaction. MULTIDYN 3.0 is writing in FORTRAN 95 language.

## 1 Equations of motion

According to Hamiltonian formulation of Mechanics [4] we can describe motion of  $N$  particles by system of differential equations of first order:

$$\begin{aligned}\frac{d\mathbf{q}}{dt} &= \frac{\partial H}{\partial \mathbf{p}}, \\ \frac{d\mathbf{p}}{dt} &= -\frac{\partial H}{\partial \mathbf{q}}.\end{aligned}\tag{1}$$

Where  $\mathbf{q} = (q_1, \dots, q_{3N})$  are generalized coordinates and  $\mathbf{p} = (p_1, \dots, p_{3N})$  are conjugate momenta. Hamilton function of system could be in cartesian coordinates written as

$$H = \sum_{i=1}^N \frac{p_i^2}{2m_i} + V(q_1, \dots, q_{3N})\tag{2}$$

On condition that interaction potential  $V$  of the particles depend only on their coordinates, equations 1 after inserting 2 will be

$$\begin{aligned}\frac{dq_i}{dt} &= \frac{p_i}{m_i}, \\ \frac{dp_i}{dt} &= -\frac{\partial V}{\partial q_i}.\end{aligned}\tag{3}$$

Generally, equations 3 represent system of  $6N$  differential equations of first order  $\dot{\mathbf{x}} = \mathbf{f}(t, \mathbf{x})$  with initial condition in the form  $\mathbf{x}_0 = \boldsymbol{\eta}$ . Where for simplicity I defined vectors  $\mathbf{x} = [{}^1x, {}^2x, \dots, {}^{6N}x]^T$ ,  $\mathbf{f} = [{}^1f(t, \mathbf{x}), {}^2f(t, \mathbf{x}), \dots, {}^{6N}f(t, \mathbf{x})]^T$  and  $\boldsymbol{\eta} = [{}^1\eta, {}^2\eta, \dots, {}^{6N}\eta]^T$ .

For numerical integrations have been in MULTIDYN 3.0 implemented multi-step methods. As predictor I implemented Crane-Klopfenstein prediktor, equation (3.88) chap. IV in [1],

$$\begin{aligned} \mathbf{x}_{n+4} - 1.547652\mathbf{x}_{n+3} + 1.867503\mathbf{x}_{n+2} - 2.017204\mathbf{x}_{n+1} + 0.697353\mathbf{x}_n = \\ h(2.002247\mathbf{f}_{n+3} - 2.031690\mathbf{f}_{n+2} + 1.818609\mathbf{f}_{n+1} - 0.714320\mathbf{f}_n), \end{aligned} \quad (4)$$

and as a corector I implemented Adams-Moulton method, equation (3.86) chap. IV in [1],

$$\mathbf{x}_{n+4} - \mathbf{x}_{n+3} = \frac{1}{24}h(9\mathbf{f}_{n+4} + 19\mathbf{f}_{n+3} - 5\mathbf{f}_{n+2} + \mathbf{f}_{n+1}) \quad (5)$$

When are both fourth order methods used in PECE regime, there is very good interval of stability  $(-2.48;0)$ . As preprocessor to start multistep methods I implemented Runge-Kutta method of fourth order to gain continuity, equation (2.52) in [1], given by equations

$$\begin{aligned} \mathbf{x}_{n+1} &= \mathbf{x}_n + h(0.17476028\mathbf{k}_1 - 0.55148066\mathbf{k}_2 \\ &\quad + 1.20553560\mathbf{k}_3 + 0.17118478\mathbf{k}_4), \\ \mathbf{k}_1 &= \mathbf{f}(t_n, \mathbf{x}_n), \\ \mathbf{k}_2 &= \mathbf{f}(t_n + 0.4h, \mathbf{x}_n + 0.4h\mathbf{k}_1), \\ \mathbf{k}_3 &= \mathbf{f}(t_n + 0.45573725h, \mathbf{x}_n + 0.29697761h\mathbf{k}_1 \\ &\quad + 0.15875964h\mathbf{k}_2), \\ \mathbf{k}_4 &= \mathbf{f}(t_n + h, \mathbf{x}_n + 0.21810040h\mathbf{k}_1 - 3.05096516h\mathbf{k}_2 \\ &\quad + 3.83286476h\mathbf{k}_3), \end{aligned} \quad (6)$$

where  $h$  is integration step. Parameters of this method were choosen to minimize local discretization error. Parameters of mentioned methods are loaded from initialization file, so it is simple to use any other of fourth order methods. Multistep methods use functional values from preceding steps, so we need less evaluation of  $\mathbf{f}$ , than in case of Runge-Kutta method. This property is significant, when we calculate potential and its gradients by using ab initio quantum chemistry methods, which are computationally demanding on time.

At the beginning of development of MULTIDYN 3.0 I used Lennard-Jones potential for argon atoms and simulated impacts of argon atom with argon clusters. Later I implemented using of external program called MOLPRO for computation gradients of potential energy by ab initio quantum chemistry methods.

## 2 Initial conditions

At the beginning of integration we need to set suitable initial conditions. With two impacting atoms there is need only to set distances between impacting atoms and mutual velocity. With molecules, which are more complex particles, it becomes more complicated. There is need to set initial orientations, vibrations and rotations of participating molecules. To set orientation of molecules is also trivial.

## 2.1 Vibrations of molecule

Hamilton function of  $N$ -atomic molecule for nuclear motion can be in cartesian coordinates written as

$$H = \sum_{i=1}^{3N} \frac{p_i^2}{2m_i} + V(x_1, \dots, x_{3N}), \quad (7)$$

Potential energy in Hamiltonian may be expanded in Taylor series around equilibrium positions  $\mathbf{x}^0 = (x_1^0, \dots, x_{3N}^0)$ , in which on atoms acts zero forces. Terms of third and higher order can be truncated and Hamilton function in harmonic approximation can be written as

$$H = \sum_{i=1}^{3N} \frac{p_i^2}{2m_i} + \frac{1}{2} \sum_{i,j=1}^{3N} F_{i,j} (x_i - x_i^0)(x_j - x_j^0), \quad (8)$$

where  $F_{i,j} = \frac{\partial^2 V}{\partial x_i \partial x_j} |_{(\mathbf{x}=\mathbf{x}^0)}$  are elements of hessian matrix. For simplicity there is also possible to set constant term  $V(\mathbf{x}^0) = 0$ . By quantization we get Hamiltonian

$$\hat{H} = -\frac{\hbar^2}{2} \sum_{i=1}^{3N} \frac{\partial^2}{m_i \partial x_i^2} + \frac{1}{2} \sum_{i,j=1}^{3N} F_{i,j} (x_i - x_i^0)(x_j - x_j^0) \quad (9)$$

It is convinient to define mass weighted displacement coordinates  $\rho_i = \sqrt{m_i}(x_i - x_i^0)$  and hamiltonian is than

$$\hat{H} = -\frac{\hbar^2}{2} \sum_{i=1}^{3N} \frac{\partial^2}{\partial \rho_i^2} + \frac{1}{2} \sum_{i,j=1}^{3N} \tilde{F}_{i,j} \rho_i \rho_j, \quad (10)$$

where  $\tilde{F}_{i,j} = \frac{F_{i,j}}{m_i m_j}$  is mass weighted hessian. Hessian is symmetric and may be diagonalized with an orthogonal matrix  $\mathbf{Q}$ :

$$\mathbf{Q}^T \tilde{\mathbf{F}} \mathbf{Q} = \text{diag}(f_1, \dots, f_{3N-6}, 0, 0, 0, 0, 0, 0). \quad (11)$$

Zeros on diagonal of diagonalized hessian are related to move of centre of force and with rotation of molecule. By introducing normal coordinates  $\mathbf{q} = \mathbf{Q}^T \boldsymbol{\rho}$  Hamiltonian is simplified to

$$\hat{H} = \frac{1}{2} \sum_{i=1}^{3N-6} \left[ -\hbar^2 \frac{\partial^2}{\partial q_i^2} + f_i q_i^2 \right] \quad (12)$$

and we need to solve  $(3N - 6)$  independent Schrödinger equations for one dimensional harmonic oscillators:

$$\hat{H}_i |\psi_i\rangle = E_i |\psi_i\rangle, \quad (13)$$



where  $\hat{H}_i = \frac{1}{2} \left[ -\hbar^2 \frac{\partial^2}{\partial q_i^2} + f_i q_i^2 \right]$  is Hamiltonian,  $|\psi_i\rangle$  is wavefunction and  $E_i$  is vibration energy corresponding to  $i$ -th mode. Solutions for energies are

$$E_{i,n} = \hbar \sqrt{f_i} \left( n + \frac{1}{2} \right) \quad (14)$$

and for wavefunctions are

$$\psi_n(q_i) = \sqrt{\frac{f_i}{\pi^2 \hbar^2}} \frac{1}{n! 2^n} H_n \left( \sqrt{\frac{f_i}{\hbar^2}} q_i \right) \exp \left( -\sqrt{\frac{f_i}{\hbar^2}} \frac{q_i^2}{2} \right). \quad (15)$$

Square of  $\psi_n(q_i)$  correspond to probability of finding system in  $n$  state and in position  $q_i$  of  $i$ -th mode. Integral of this probability from minus infinity to  $q_i$  is called cumulative function

$$F_i(q_i) = \int_{-\infty}^{q_i} |\psi_n(q'_i)|^2 dq'_i. \quad (16)$$

to reach proper sampling, there is need to choose  $r_i$  from uniform distribution from interval  $(0, 1)$  and finding value of  $q_i$  for which  $F_i(q_i) = r_i$ . From equation 14 conjugate momenta of molecule in normal coordinates are calculated:

$$p_i^q = \pm \sqrt{2\sqrt{f_i}(n + 1/2) - f_i q_i^2}. \quad (17)$$

According to quantum physics there is possibility that system could be found in classically forbidden area where  $p_i^q$  would be imaginary. This behaviour is solved by adding condition and if is not fulfille,  $r_i$  is choosed again. In equation 17 we can see that momentum could have two signs. These are choosen randomly by equal probabbilities.

Normal coordinates  $\mathbf{q} = (q_1, \dots, q_{3N-6}, 0, \dots, 0)$  and conjugate momenta of system in normal coordinates  $\mathbf{p}^q = (p_1^q, \dots, p_{3N-6}^q, 0, \dots, 0)$  are then transformed to mass weighted displacement coordinates:

$$\boldsymbol{\rho} = \mathbf{Q}^T \mathbf{q}; \mathbf{p}^\rho = \mathbf{Q}^T \mathbf{p}^q. \quad (18)$$

Cartesian coordinates are found from equation

$$x_i = x_i^0 + \frac{\rho_i}{\sqrt{m_i}} \quad (19)$$

and corresponding momenta in cartesian coordinates are

$$p_i = \sqrt{m_i} p_i^\rho. \quad (20)$$

Because normal modes are approximate for finite displacements, a spurious angular momentum  $\vec{L}_s$  may arise from transformation to cartesian coordinates. This spurious angular momentum is calculated.

## 2.2 Rotations

The rotational angular momentum and its components now can be added. Methan is symmetric top molecule with rotational quantum number  $l$ . Size of rotational angular momentum is found from equation

$$L_0 = \sqrt{l(l+1)}\hbar. \quad (21)$$

Direction of this angular momentum is choosen randomly to get vector of rotational angular momentum  $\vec{L}_0$ . From this angular momentum is needed subtract spurious angular momentum:

$$\vec{L} = \vec{L}_0 - \vec{L}_s. \quad (22)$$

Resulting angular momentum is then added to molecule by adding rotational velocity  $\vec{v}_j = \vec{\omega} \times \vec{x}_j$  to each of the atoms, where

$$\vec{\omega} = \mathbb{I}^{-1} \vec{L} \quad (23)$$

and  $\mathbb{I}^{-1}$  is the inverse of the inertia tensor.

## 3 Tests

Calculations have not been done yet, only test calculations. In one of the tests I set the methane molecule to vibrate in only one vibration mode. It means that there where chosen only one  $q_i$  and calculated corresponding  $p_i$  and others  $q_j$  and  $p_j$  where set to be zero and transformed to cartesian coordinates. I did it for all modes and then with MULTIDYN 3.0 I calculated trajectories. By using Fast Fourier Transformation I analysed change of overall kinetic energy on time and received frequencies of vibrations as can be seen in figure 1. In the Table 1 we can compare eigenfrequencies calculated from eigenvalues of hessian and by Fourier analysis of kinetic energy of vibrating methane molecule. There is good agreement and smaller values in right column are also expected because they are not harmonics. Beside these tests were also tested conservation of integrals of motions (i.e. total energy, total momentum, total angular momentum) these were satisfactory.

## References

1. E. Vitásek, *Numerické metody*
2. J. Formánek, *Úvod do kvantové teorie*, Academia 2004
3. J. Chem. Phys. 43 (1965) 3259, Karpulus et al.
4. H. Goldstein, *Classical mechanics*

**Table 1.** Comparing of eigen frequencies of methane molecule calculated from eigen-  
vluves of hessian and by fourier analysis of total kinetic energy of vibrating methane  
molecule.

From eigenvalues	By fourier analysis
3245.9 cm <sup>-1</sup>	3213.0 cm <sup>-1</sup>
3245.9 cm <sup>-1</sup>	3213.0 cm <sup>-1</sup>
3245.9 cm <sup>-1</sup>	3229.8 cm <sup>-1</sup>
3147.7 cm <sup>-1</sup>	3137.3 cm <sup>-1</sup>
1666.3 cm <sup>-1</sup>	1665.4 cm <sup>-1</sup>
1666.3 cm <sup>-1</sup>	1665.4 cm <sup>-1</sup>
1453.8 cm <sup>-1</sup>	1446.7 cm <sup>-1</sup>
1453.8 cm <sup>-1</sup>	1446.7 cm <sup>-1</sup>
1453.7 cm <sup>-1</sup>	1446.7 cm <sup>-1</sup>

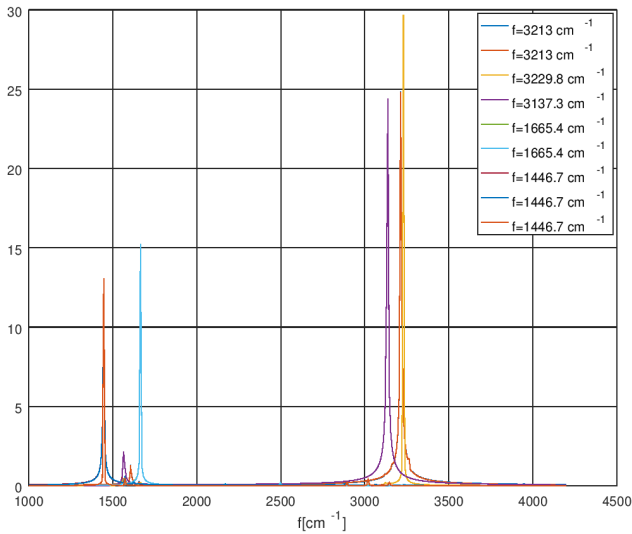


**Fig. 1.** Fourier analysis of vibrations of Methane molecules each prepared to vibrate  
in single mode.

# Preliminary Results of a SMALBE+MPGP Algorithms for Training a Linear SVM Classifier

Marek Pecha and David Horák

Department of Applied Mathematics, FEECS,  
VŠB – Technical University of Ostrava, 17. listopadu 15,  
708 33 Ostrava – Poruba, Czech Republic  
IT4Innovation, VŠB – Technical University of Ostrava, 17. listopadu 15,  
708 33 Ostrava – Poruba, Czech Republic  
[marek.pecha@vsb.cz](mailto:marek.pecha@vsb.cz)

**Abstract.** This paper deals with the preliminary results of a linear two-class Support Vector Machines (SVM) implemented in PERMON toolbox. We present the first insights into training PermonSVM classifier using quadratic programming (QP) algorithms from the PemonQP, i.e. Dostál's SMALBE, which is based on the augmented Lagrangian approach, and MPGP algorithms for box constrained QP. In presented benchmark on the URL dataset, we analyze the abilities of the QP solver with the respect to regularized parameter  $C$  and QP solver accuracy  $eps$ . In fact, we consider  $eps$  as the second parameter of the linear SVM and therefore we got better information about the tested algorithm behaviour.

## 1 SVM overview

In the last two decades, the Support Vector Machines (SVMs) have become a popular machine learning method for non-parametric modelling, classification, and regression analysis with applications ranging from genetics [1] to weather forecasting [2] due to its accuracy and obliviousness to dimensionality [3, p. 1]. The standard SVM, called the soft-margin SVM, was invented as a machine learning technique in 1995 by Corinna Cortes and Vladimir Vapnik [4]. In the fact, it is an extension of the hard-margin SVM [5] for non-perfectly linear classification problems.

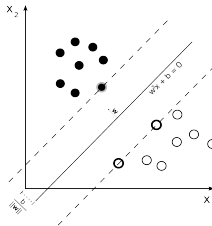


**Fig. 1.** An example of a binary classification problem solved by the linear SVM. The image is referenced from [6].

Basically, the SVM is a supervised binary classifier, i.e. a classifier that decides whether a sample falls into Class A (label 1) either Class B (label -1) by means of a model, which is determined from already categorized, so-called training, samples in a training phase of classifier. An essential idea of training the soft-margin SVM classifier is finding a *maximum-margin hyperplane* so that it divides as many samples belonging to Class A from the samples belonging to Class B as possible. The samples, which contribute to the definition of such hyperplane, are called the *support vectors* - the encircled samples in Fig. 1.

Let us denote training samples as a set of ordered pairs such that

$$T := \{(\mathbf{x}_1, y_1), (\mathbf{x}_2, y_2), \dots, (\mathbf{x}_m, y_m)\},$$

where  $m$  is a number of samples,  $\mathbf{x}_i \in \mathbb{R}^n$  ( $n \in \mathbb{N}$  represents a number of attributes) is sample  $i$  and  $y_i \in \{-1, 1\}$  denotes the label of sample  $i$ ,  $i \in \{1, 2, \dots, m\}$ . Let  $H$  be *maximal-margin hyperplane*  $\mathbf{w}^T \mathbf{x} + b = 0$ , where  $\mathbf{w}$  is a normal vector;  $\frac{b}{\|\mathbf{w}\|}$  determines the offset of the hyperplane  $H$  from the origin along its normal vector  $\mathbf{w}$ . The problem of finding the hyperplane  $H$  can be formulated as a constrained optimization problem in the following (primal) formulation

$$\min_{\mathbf{w}, \xi_i} \frac{1}{2} \mathbf{w}^T \mathbf{w} + C \sum_{i=1}^m \xi_i \quad \text{s.t.} \quad \begin{cases} y_i (\mathbf{w}^T \mathbf{x}_i + b) \geq 1 - \xi_i, \\ \xi_i \geq 0, \end{cases} \quad (1)$$

where  $C$  is a user-specified penalty<sup>3</sup> that controls the relative importance of minimizing  $\|\mathbf{w}\|$  (equivalent to maximizing the margin) and satisfies the constraint of the margin for each sample. Further,  $\xi_1, \xi_2, \dots, \xi_m$  are *slack variables* that handle the sensitivity of SVM to possible outliers. Rewriting the problem (1) by means of Lagrange multipliers, we obtain the simplified maximization problem as follows

$$\max_{\alpha_i} \sum_{i=1}^m \alpha_i - \frac{1}{2} \sum_{i=1}^m \sum_{j=1}^m \alpha_i y_i \mathbf{x}_i \mathbf{x}_j y_j \alpha_j \quad \text{s.t.} \quad \begin{cases} 0 \leq \alpha_i \leq C, \\ \sum_{i=1}^m \alpha_i y_i = 0, \end{cases} \quad (2)$$

where  $\alpha_1, \alpha_2, \dots, \alpha_m$  are the Lagrange multipliers. Formulation (2) is the dual formulation of the soft-margin SVM. For numerical computation convenience, we reformulate (2) as the QP problem by means of a matrix-vector representation so that

$$\min_{\alpha} \frac{1}{2} \alpha^T \mathbf{y}^T \mathbf{X}^T \mathbf{X} \mathbf{y} \alpha - \mathbf{e}^T \alpha \quad \text{s.t.} \quad \begin{cases} \mathbf{0} \leq \alpha \leq \mathbf{c}, \\ \mathbf{B}_E \alpha = \mathbf{0}, \end{cases} \quad (3)$$

where

$$\mathbf{X} := [\mathbf{x}_1, \dots, \mathbf{x}_m] \in \mathbb{R}^{n \times m}, \quad \mathbf{B}_E := [\mathbf{y}^T] \in \mathbb{R}^{1 \times m},$$

$$\alpha := [\alpha_1, \dots, \alpha_m]^T \in \mathbb{R}^m, \quad \mathbf{y} := [y_1, \dots, y_m]^T \in \mathbb{R}^m, \quad \mathbf{e} := [1, 1, \dots, 1]^T \in \mathbb{R}^m,$$

$$\mathbf{c} := [C, C, \dots, C]^T \in \mathbb{R}^m.$$

<sup>3</sup> The penalty  $C$  is often called a regularization parameter in SVM communities.

Further, we introduce dual to primal reconstruction formulas for the normal vector  $\mathbf{w}$  and the bias  $b$  such that

$$\mathbf{w} = \sum_{i=1}^m \alpha_i \mathbf{x}_i y_i, \quad (4)$$

$$b = \frac{1}{|I^{SV}|} \sum_{i \in I^{SV}} (y_i - \mathbf{x}_i^T \mathbf{w}), \quad (5)$$

where  $I^{SV}$  denotes a *support vector index set*, i.e.  $I^{SV} := \{i \mid \alpha_i > 0, i = 1, 2, \dots, m\}$ , and  $|I^{SV}|$  is cardinality of  $I^{SV}$ .

## 2 PermonSVM

PermonSVM is a machine learning tool developed at IT4Innovations National Supercomputing Center and Department of Applied Mathematics, VŠB – Technical University of Ostrava. It provides an implementation of the two-class classification via soft-margin SVM, designed to be used on clusters. PermonSVM<sup>4</sup> implements a scalable training procedure based on a linear kernel (so-called linear SVM), taking advantage of an implicit representation of the Gramm matrix, and scalable matrix vector product of PETSc matrices. The resulting QP problems with an implicit Hessian is solved by scalable QP solvers within the PermonQP<sup>5</sup> package, combining QP transforms, an augmented Lagrangian approach (SMALXE), and efficient solvers for box constrained QP. Our implementation of the SVM training procedure offers efficient utilization of parallel computers up to thousands of processor cores and allows the time of SVM training to be substantially shortened.

## 3 Numerical experiments

In the standard way of benchmarking algorithms used in linear SVM, it is supposed that the duration time of training procedure and quality of prediction highly depend on a regularization parameter  $C$  - grid-search is typically used for finding an optimal one. However, machine learning problems (unlike the computational mechanics problems) do not need to be solved with higher accuracy. Therefore, we assume that a optimal choice of an tolerance (*eps*) plays an insignificant role for achieved rate (percents of correctly classified samples) of classification and training procedure duration. Hence, we take an tolerance of the QP solver as the second parameter to be optimally determined and then, in following experiments, we analyze duration time of training procedure and prediction quality considering  $C$  and *eps*.

<sup>4</sup> Visit <http://permon.it4i.cz/permonsvm.htm> for further information about the PermonSVM package.

<sup>5</sup> Visit <http://permon.it4i.cz/permonqp.htm> for further information about the PermonQP package.

The experiments were run on the Salomon supercomputer [7] at IT4Innovations. Salomon consists of 1,008 compute nodes, totaling 24,192 compute cores with 129 TB RAM and giving over 2 Pflop/s theoretical peak performance. Each node is a powerful x86-64 computer equipped with 24 cores and at least 128 GB RAM. Nodes are interconnected by 7D Enhanced hypercube Infiniband network and equipped with two Intel Xeon E5-2680v3 processors.

We analyze the abilities of the QP algorithm in our experiments thus we try to eliminate an inalienable problems. Therefore, we run benchmark on one Salomon computational node on 24 cores in order to avoid the problems caused by overloading the network such as large scattering runtimes on experiments with same parameters. The overloading network problems are a common phenomenon on supercomputers and it is difficult to recognize them from algorithm scalability difficulties.

In the presented numerical experiments, we use Dostál's SMALBE + MPGP [8] in PermonQP as the QP algorithm for the SVM training procedure and benchmark it on the URL [9] dataset. The URL dataset contains 2.4 million samples with 3.23 million attributes. Further, the URL dataset is strongly sparse (it has 0.004% nonzero fill). The sparse classification datasets such ours are well-linearly separable thus making the URL dataset a good candidate for benchmarking PermonSVM. For the first insight of SMALBE + MPGP abilities, we discretize the parameter space so that the values of  $\epsilon$  are chosen from set  $\{0.01, 0.05, 0.1, 0.2, 0.3, 0.4, 0.5, 0.6, 0.7, 0.8, 0.9\}$  and values of  $C$  are chosen from set  $\{1e-10, 5e-5, 1e-5, 1, 5, 5e+1, 1e+2, 5e+2, 1e+3\}$ . Even if discretization of parameter space is quite coarse, the benchmark results give us good information about the abilities of SMALBE + MPGP for training the PermonSVM classifier. Further, URL does not contain the testing part so that we present the achieved rates on the whole dataset. The benchmark results are depicted in Fig. 2 and Fig. 3.

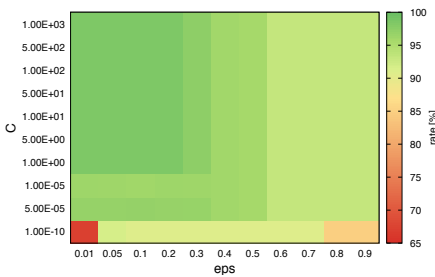


Fig. 2. Rate.

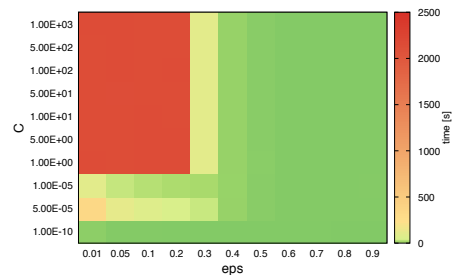


Fig. 3. Training time.

In Fig. 2 and Fig. 3, we can see that the rates and training times decrease when accuracy of the QP solver decreases for given  $C$  lying between  $1e-5$  and

$1e+3$ . It is the expected behaviour of the machine learning algorithm. Further, for given *eps* lying between 0.01 and 0.3, the rates and training times are increasing when regularization parameter *C* is increasing - it is expected algorithm behaviour, as well. Moreover, the rates have the values and training times ranging from 90.69% to 95.88% and 3.51s - 6.16s for *eps* from 0.4 to 0.9 and *C* from  $1e-5$  to 1000, respectively. Best interval rates, i.e. 97.28% - 98.35%, were achieved for *eps* and *C* lying from 0.01 to 0.3 and *C* from 5 to  $1e+3$ , respectively, - however, training times are 92.03s - 2135.01s.

## 4 Conclusions

In this paper, we present the preliminary results of a linear two-class SVM classifier called PermonSVM implemented in the PERMON toolbox. It provides a training procedure based on a linear kernel, taking advantage of an implicit representation of the Gramm matrix. We select the SMALBE + MGP algorithm for the SVM training procedure and benchmark it on the strongly sparse URL dataset containing 2.4 million samples. In the presented numerical experiments, we analyze the duration time of training procedure and prediction quality considering *C* and *eps* on the coarse discretized parameter space, i.e. 9 values of regularized parameter *C* and 11 values of *eps*. The rates have the values and training times ranging from 90.69% to 95.88% and 3.51s - 6.16s for *eps* from 0.4 to 0.9 and *C* from  $1e-5$  to  $1e+3$ , respectively. The best interval rates, i.e. 97.28% - 98.35%, were achieved for *eps* and *C* lying from 0.01 to 0.3 and from 5 to  $1e+3$ , respectively. However, training times are 92.03s - 2135.01s. To state general conclusions about suitability of our proposed approach for the SVM training procedure, we need to run significantly more benchmarks on various datasets, which is also a subject of our further research.

## References

1. Brown, M.P., Grundy, W.N., Lin, D., Cristianini, N., Sugnet, C.W., Furey, T.S., Ares, M. and Haussler, D.: Knowledge-based analysis of microarray gene expression data by using support vector machines. In Proceedings of the National Academy of Sciences, 97(1), pp.262-267. 2000.
2. Shi, J., Lee, W.J., Liu, Y., Yang, Y. and Wang, P.: Forecasting power output of photovoltaic systems based on weather classification and support vector machines. In: IEEE Transactions on Industry Applications, 48(3), pp.1064-1069. 2012.
3. Vishnu, A., Narasimhan, J., Holder, L., Kerbyson, D. and Hoisie, A.: Fast and accurate support vector machines on large scale systems. In: Cluster Computing (CLUSTER), 2015 IEEE International Conference on (pp. 110-119). IEEE. 2015.
4. Cortes, C. and Vapnik, V.: Support-vector networks. Machine learning, 20(3), pp.273-297. 1995. DOI: 10.1007/BF00994018.
5. Vapnik, V. and Chervonenkis, A.: On a class of perceptrons. In: Automation and Remote Control. 1964.
6. Wikimedia Commons, Graphic showing the maximum separating hyperplane and the margin, 2008. URL: [https://commons.wikimedia.org/wiki/File:Svm\\_max\\_sep\\_hyperplane\\_with\\_margin.png](https://commons.wikimedia.org/wiki/File:Svm_max_sep_hyperplane_with_margin.png).



7. SALOMON web page. Available at: <https://docs.it4i.cz/salomon/hardware-overview/>.
8. Dostál, Z.: Optimal Quadratic Programming Algorithms: With Applications to Variational Inequalities (Springer). 2009. ISBN 0387848053.
9. Ma, J., Saul, L., Savage, S. and Voelker, G. Identifying suspicious URLs: An application of large-scale online learning. In Proceedings of the Twenty Sixth International Conference on Machine Learning (ICML), pages 681-688, 2009.

## 5 Published results

### References

1. Marek Pecha and Pavel Skalný. Identifying the ductile fracture in steel materials via lloyd type algorithms. Proceedings of the Fifth International Conference on Parallel, Distributed, Grid and Cloud Computing for Engineering, 2017.
2. Jiří Tomčala, Marek Pecha, Jan Papuga. Parallelization of Fatigue Damage Calculation. Proceedings of the Fifth International Conference on Parallel, Distributed, Grid and Cloud Computing for Engineering 2017.
3. Marek Pecha, Václav Hapla, David Horák, Martin Čermák. Notes on the Preliminary Results of a red Linear Two-class Classifier in the PERMON toolbox. AIP Conference Proceedings, 2017 accepted.

# Using Bootstrap Methods with *R*-Project For Comparison Ways of Treatment of Critical Limb Ischemia

Lenka Příbylová

Department of Applied Mathematics, FEECS,  
VŠB – Technical University of Ostrava, 17. listopadu 15,  
708 33 Ostrava – Poruba, Czech Republic  
`lenka.pribylova@vsb.cz`

**Abstract.** In this paper we discuss a way, how to compare ways of treatment of critical limb ischemia. Our approach is based on an application of bootstrap methods using *R*-project. We compare empirical densities and empirical cumulative distribution functions of bootstrap means of cholesterol in treatment groups, further we compare 95% *t*-bootstrap confidence intervals, resp. 95% bootstrap medians confidence intervals, of cholesterol in treatment groups.

**Keywords:** bootstrap methods, critical limb ischemia, stem cells.

## 1 Bootstrap Methods

The bootstrap as synonymous of resampling was introduced by Efron in 1979. Efron main idea lays in using of the empirical distribution function in place of the unknown population distribution function in estimating a parameter of interest. Efron also invents the term *bootstrap*.

The main idea of bootstrap methods is focused on the replacing a small data set by bigger data set. New data set copies shape of the sample space distribution. The process is: from the small input data set is chosen a set of smaller range or same range with the repetition. The process is copied *B*-times. From new samples are enumerated sample averages. The set of the sample averages now represents bigger data set. The range of bigger data set is given by the number of bootstrap selections. Using the methods of the elementary probability theory can be proved, that the new data set keeps the same shape as the distribution of relevant parameter.

Bootstrap methods are convenient for the small data sets because these methods have faster convergence into the real distribution than using the central limit theorem. When using bootstrap methods it is not necessary to assume normality distribution of the sample space. Disadvantages of bootstrap methods are, that bootstrap selection can sometimes provide misleading image of the reality, especially for the data sets with outliers. Therefore it is necessary when applying of bootstrap method to find out, if bootstrap estimation is not distorted by the

outlier. For the identification of the outliers at the small data sets the method called *jackknife*.

Bootstrap methods could be applied only to estimate statistics for which it is known, that bootstrap approximation meet the theoretical properties: the consistence and the asymptotical accuracy. This assumptions are fulfil by most of the common statistics, as the sample average, the sample dispersion, the estimations in linear and general linear models. Most of the maximal likelihood estimations too.

### 1.1 Parametric Bootstrap

Let  $(X_1, X_2, \dots, X_N)$  be a sample with the cumulative distribution function  $F(X, \theta)$ . We are focused on the statistic  $\theta = \theta(X)$ . The knowledge of the shape of the distribution  $F$ , which is defined by the vector of the parameters  $\theta = (\theta_1, \theta_2, \dots, \theta_k)$ , is assumed. The estimates of the parameters are simulated by  $B$  bootstrap random samples, where  $N < B \ll N^N$ . For each random sample the sample estimate of the parameter  $\hat{\theta}_{N,i}^*$ ,  $i = 1, 2, \dots, B$  is enumerated. The enumerated sample estimates of the parameters are used to approximate the distribution of the estimation  $\hat{\theta}_N$ .

### 1.2 Non-parametric Bootstrap

Let  $(X_1, X_2, \dots, X_N)$  be a random selection from the distribution  $F(X, \theta)$ . The method is focused on the statistics  $\theta = \theta(X)$ , which we estimate from the data. In case of the non-parametric bootstrap an a-priori information about the shape of the distribution  $F$  is not assumed.

Unknown distribution function  $F$  is approximated by the empirical distribution function denote as  $\hat{F}_N$ .  $\hat{F}_N$  is used to simulate  $N$  observations. This means, that from the random selection  $(X_1, X_2, \dots, X_N)$  is chosen  $N$  elements with repetition. This way we obtain the first bootstrap sample. This procedure is repeated  $B$ -times. For each bootstrap sample obtained in this way estimation of the statistics  $\hat{\theta}_{N,i}^*$ ,  $i = 1, 2, \dots, B$  is enumerate. From these estimations the distribution of the estimation  $\hat{\theta}_N$  is approximated.

These definitions do apply to an independent data. In the case of the dependent data it is necessary to use paired bootstrap selections.

### 1.3 Confidence Intervals of Bootstrap Samples

Bootstrap methods use three types of confidence intervals:  $BC_\alpha$ ,  $ABC$ ,  $t$ -bootstrap intervals. For our purpose we focused on  $t$ -bootstrap intervals only.

Let bootstrap random selection be  $(X_1^*, X_2^*, \dots, X_N^*)$ . It is estimated  $\theta$  and the standard deviation  $\sigma_\theta$ . From the statistic

$$T = \frac{\hat{\theta} - \theta}{\hat{\sigma}_\theta} \quad (1)$$

are enumerated quantiles  $T^{(\alpha)}$  used to find the length of  $t$ -bootstrap confidence interval for the parameter  $\theta$ :

$$\left( \hat{\theta} - \hat{\sigma} T^{(\alpha)}, \hat{\theta} - \hat{\sigma} T^{(1-\alpha)} \right). \quad (2)$$

Bootstrap hypothesis testing has been developed as an extension of bootstrap confidence methods.

#### 1.4 Some of Computational Aspects of Bootstrap Methods.

From the theoretical view it would be convenient to do each of the  $\binom{2N-1}{N}$  different random selections, resp. each of the  $N^N$  possible random selections. Already for  $N = 30$  the number of the random selections is equal approximately  $2 \cdot 10^{44}$ , which is rather big number. Therefore often is on bootstrap sample applied the method Monte Carlo, where is  $B$ -times repeatedly simulated a sample. If should be an error by the application of the method Monte Carlo insignificant in relation to the error theoretical bootstrap estimation, it is recommend to choose  $B = N^2 \log(\log N)$  for the confidence intervals. For  $N = 30$  it is about 1 100 repetitions. Generally at minimum  $B = 1\,000$  bootstrap samples is recommended to estimate the quantiles and the distribution function.

In case of the similar statistic, which is sample mean, it is possible to obtain good results already by the  $B = 500$  repetitions. For the confidence intervals is recommended value  $B$  at the minimum 1 000, in the case of any other statistics it can be also 10 000 and more. Remark numbers of the bootstrap samples  $B$  must be more than is the range of the data set.

## 2 Using Bootstrap Methods For Comparison Ways of Treatment Of Critical Limb Ischemia

### 2.1 Description of the Medical Study

The main goal in the therapy of a critical limb ischemia (CLI) is an improvement of blood supply at affected limb. Traditional methods for the improvement of the blood rate are founded on the procedure within the blockade is removed by the surgery where it is by surgery remove of the blockade or on the procedure that allows blood rate around the blockade by the bypass with venous or the artificial grafts. The new approach of the treatment of critical limb ischemia is based on the application of the stem cells into the field of the damaged tissue.

The study dealing with the treatment of CLI is been verified on University Hospital of Ostrava. Into the study 53 patients is classified into the four groups. Data of each patient are recorded within seven medical controls. The application of stem cells can be realized by the intramuscular (group A), intravenous (group B) or intraarterial (group C) way. The group D is the control group of patients in which was not applied the preparation of the stem cells. The distribution of patients into the groups was done at random by the appropriate software.

## 2.2 Characterization of the Data

The range of input data set was small, so it was not possible to use elementary statistical methods where an assumption of normality is supposed. Sample space of the data had not normality distribution. At the first we tried to use Kruskal-Wallis test for comparison of medians of cholesterol in treatment groups. But Kruskal-Wallis test has a weak power of test, thus we could not prove an existence of statistically significant difference between medians of cholesterol level in treatment groups.

An approach which we demonstrated in this paper was based on bootstrap methods. We created bootstrap selections of the data in each of three treatment groups and then we analyzed these new data set.

## 2.3 Comparison of Treatment Groups of CLI using ECDF of Bootstrap Sample Means

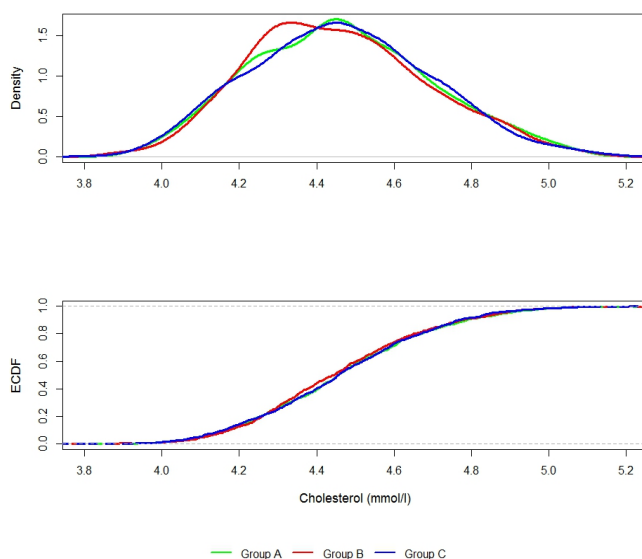


**Fig. 1.** Empirical densities and ECDF of bootstrap means of cholesterol in treatment groups

Using software *R* we created 1 000 bootstrap selections of cholesterol level at the final control in each of three treatment groups. We constructed empirical densities and empirical cumulative distribution functions of means of the bootstrap selections for the comparison treatment groups. We displayed shapes of empirical densities and empirical distribution functions of bootstrap means of

cholesterol in each of treatment group - see figure 1. We compared shapes of empirical densities and empirical cumulative distribution functions of cholesterol means at the visual view. There was not found significant difference between shapes of ECDF and densities of bootstrap means in treatment groups. Methods of the comparison shapes of the empirical distribution functions were done on the level of exploratory data analysis.

*Conclusion.* It does not exist significant difference between shapes of ECDF, resp. densities, of bootstrap means in treatment groups. This conclusion was based on exploratory data analysis.

**2.4 Comparison of Treatment Groups of CLI Using Bootstrap Confidence Intervals**

When we want to compare ways of treatment more exactly, we have to use a methods of statistical induction. In this section we used comparison of confidence intervals of means and medians for comparison cholesterol level in groups of treatment. If it would be exist statistically significant difference between groups, than relevant confidence intervals would have an empty intersection. 95% confidence interval reflects a significance level of 0.05 for hypothesis testing.

In the table 1 95% classical  $t$ -confidence intervals and 95%  $t$ -bootstrap confidence intervals of means of cholesterol at final control have been described. For construction of  $t$ -bootstrap intervals were used 10 000 repetitions for each group of treatment.

**Table 1.** 95% confidence intervals of means of cholesterol (mmol/l)

group of treatment	classical $t$ -confidence interval	$t$ -bootstrap confidence interval
A	(4.65,9.49)	(3.95,4.89)
B	(2.19,5.81)	(3.78,5.48)
C	(3.89,8.51)	(4.08,5.03)

In the table 2 95% classical confidence intervals for median and 95% bootstrap confidence intervals for medians of cholesterol at final control have been described. For construction of bootstrap intervals of medians were used 10 000 repetitions for each group of treatment.

**Table 2.** 95% confidence intervals of medians of cholesterol (mmol/l)

group of treatment	classical median conf. interval	bootstrap median conf. interval
A	(3.96,5.15)	(3.93,4.67)
B	(3.71,5.86)	(3.62,5.45)
C	(4.07,5.16)	(3.82,4.57)

Because input data set had small range,  $t$ -confidence intervals of means of original data were wide - see table 1. Nevertheless  $t$ -bootstrap confidence intervals of means are narrower than classical  $t$ -confidence intervals of means. For comparison of cholesterol in treatment groups was better to use  $t$ -bootstrap confidence intervals than classical  $t$ -confidence intervals. Medians confidence intervals of original data is possible to apply for comparison of cholesterol in treatment groups. Bootstrap medians confidence intervals are more narrow than classical medians confidence intervals.

The intersections of every pairs of bootstrap confidence intervals of means, resp. medians, of cholesterol in treatment groups were not empty. Therefore it does not exist statistically significant difference between 95%  $t$ -bootstrap confidence intervals of means, resp. 95% bootstrap confidence intervals of medians, of cholesterol in treatment groups.

*Comparison of the classical and bootstrap confidence intervals.* Bootstrap confidence intervals are narrower than classical confidence intervals. The reason is that it was used more observations for construction of bootstrap confidence intervals than for construction of classical confidence intervals.

*Conclusion.* It does not exist statistically significant difference between means, resp. medians, of cholesterol in treatment groups on 0.05 significant level. Means and medians of cholesterol level were not depend on treatment groups on 0.05 significant level.

### 3 Conclusion

In this paper we were discussed, how to compare ways of treatment of critical limb ischemia. We demonstrated an application of the bootstrap methods for comparison of treatment groups. We used empirical cumulative distribution functions and empirical densities for comparison cholesterol in treatment groups at the level exploratory data analysis. We compared means of cholesterol in treatment groups by comparison 95%  $t$ -bootstrap confidence intervals. Further we compared medians of cholesterol in treatment groups by comparison 95% bootstrap median confidence intervals. Using these methods we did not found statistically significant difference between cholesterol level in treatment groups on 0.05 significant level.

*Note.* In this article have been used software *R* (*R Core Team (2016). R: A language and environment for statistical computing. R Foundation for Statistical Computing, Vienna, Austria. URL <https://www.R-project.org/>*).

### Acknowledgement

This work has been supported by the FEECS VŠB – Technical University of Ostrava (Project No. SP 2017/56).

## References

1. Davison, A. C., Hinkley, D.V. : Bootstrap Methods and Their Applications, Cambridge, Cambridge University Press, 2003. ISBN 0-521-57471-4.
2. Efron, B., Tibshirani, R. J. : An Introduction to the Bootstrap, New York, Chapman & Hall, 1993. 436 s. ISBN 0-412-04231-2.
3. Nováček O. : Metody bootstrap, BP, supervizor M. Frobelská, UJEP Brno, 2013
4. Pavlíčková L. : Metoda bootstrap a její aplikace, DP, supervizor Z. Karpíšek, VUT Brno, 2009
5. Prášková Z.: Metoda bootstrap, Sborník prací 13. letní školy JČMF Robust 2004, s.299-314, ISBN 80-7015-972-3
6. Procházka V., Gumulec J., Jalůvka F., Šalounová D., Jonszta T., Czerný D., Krajča J., Urbanec R., Klement P., Martínek J., Klement G.: Cell Therapy, a New Standard in Management of Chronic Critical Limb Ischemia and Foot Ulcer, Cell Transplantation, Vol. 19, pp. 14131424, Cognizant Comm. Corp. USA, 2010, E-ISSN 1555-3892
7. Teraa M., Conte M.S., Moll F.L., Verhaar M.C. : Critical Limb Ischemia - Current Trends and Future Directions, Journal of the American Heart Association, 2016, Dallas, ISSN: 2047-9980



# Extremal Graphs from Geometric Designs

Tom Raiman

Department of Applied Mathematics, FEECS,  
VŠB – Technical University of Ostrava, 17. listopadu 15,  
708 33 Ostrava – Poruba, Czech Republic  
`tom.raiman.st@vsb.cz`

**Abstract.** In this paper we present properties of graphs that arise from geometric designs and consider their extremal properties. Inspiration for this paper was the work of Michael Hurley [2], which was further developed by Justína Karlovská [3]. We present some missing pieces of her work, namely we were able to prove under which conditions these graphs have girth 4 or 6.

**Keywords:** geometric design, girth of graph, cage

## 1 Introduction

The cage problem asks what is the smallest graph of given regularity and girth. Although it seems as an easy question after more than 50 years of study we can recognize few cages. It turns out that this topic is closely related to the study of Moore graphs. A  $(k, g)$ -graph is a graph with given regularity and girth. Girth is the length of a shortest cycle. Let  $n$  be the order of a  $(k, g)$ -graph, if  $n$  is the smallest possible then we call the graph  $(k, g)$ -cage. Natural question arises as to what is the smallest possible order of a  $(k, g)$ -graph. This is partially answered by so-called Moore bound denoted  $M(k, g)$ .

$$M(k, g) = \begin{cases} 1 + k + k(k-1) + \cdots + k(k-1)^{(g-3)/2}, & \text{if } g \text{ is odd,} \\ 2(1 + (k-1) + \cdots + (k-1)^{(g-2)/2}), & \text{if } g \text{ is even.} \end{cases} \quad (1)$$

A survey of known cages can be found in [1]. It is obvious that the order of a  $(k, g)$ -graph is equal or bigger than the Moore bound. If the order of a  $(k, g)$ -graph is equal to the Moore bound then such a graph is called a Moore graph. It is worth noting that Moore graphs are rare.

## 2 Basic properties of graphs of geometric designs

**Definition 1.** Let  $\mathbb{F}_q$  be a field, where  $q$  is a power of prime. Let  $U$  be an  $n$ -dimensional vector space over the field  $\mathbb{F}_q$ . Let  $T$  be the set of the  $t$ -dimensional vector subspaces of  $U$  and let  $K$  be the set of the  $k$ -dimensional vector subspaces

of  $U$ . Then we define graph  $G = (V, E)$  such that the vertex set corresponds to the union of the elements in  $T$  and  $K$ .  $E$  is the set of edges determined by the property, that two vertices are incident if and only if  $t$ -dimensional vector space is vector subspace of  $k$ -dimensional vector space.

For our purposes, it is meaningful to omit the following cases:

1.  $t = k$ , because such graph would have regularity one and there would no be cycles, which is one of the properties we are interested in. From that and Definition 1 follows that  $t < k$ .
2.  $t = 0$ , because there would be only one  $t$ -dimensional vector subspace (the trivial one).
3.  $k = n$ , because there would be only one  $k$ -dimensional vector subspace (the whole vector space).

Now let us introduce *Gaussian binomial coefficients*  $\begin{bmatrix} x \\ y \end{bmatrix}_q$ , which count the number of linearly independent  $y$ -dimensional vector subspaces in an  $x$ -dimensional vector space over field  $\mathbb{F}_q$ . [2]

Let  $x$  be any natural number and  $q$  any prime power, then we define

$$[x]_q = (1 + q + q^2 + \cdots + q^{x-1}), \quad (2)$$

and

$$[x]_q! = [1]_q [2]_q \cdots [x]_q. \quad (3)$$

Let  $[0]_q = [0]_q! = 1$  for all  $q$ . Then the Gaussian coefficient  $\begin{bmatrix} x \\ y \end{bmatrix}_q$  is defined as

$$\begin{bmatrix} x \\ y \end{bmatrix}_q = \frac{[x]_q!}{[y]_q! [x - y]_q!}. \quad (4)$$

The above formulas allow us to establish the number of vertices of the graphs from geometric designs.

**Lemma 1.** *Let  $G = (V, E)$  be the graph corresponding to the graph from Definition 1. Then for the set  $V(G)$  following holds:*

$$|V(G)| = \begin{bmatrix} n \\ t \end{bmatrix}_q + \begin{bmatrix} n \\ k \end{bmatrix}_q, \quad (5)$$

where  $\begin{bmatrix} n \\ t \end{bmatrix}_q$  is the number of elements in the set  $T$  and  $\begin{bmatrix} n \\ k \end{bmatrix}_q$  is the number of elements in the set  $K$ .

Equation (5) is natural, because the number of  $t$ - or more precisely  $k$ -dimensional subspaces in  $n$ -dimensional spaces is given by formula (4), where  $n$  stands for  $x$  and  $t$  or  $k$  stands for  $y$  and of course this two numbers must be added up.

Now we turn our attention to the degree of the vertices of a graph from Definition 1. First, we look at the degrees of vertices in  $k$ -subspaces. We observe that no  $k$ -dimensional space can contain another  $k$ -dimensional subspace. Then we observe that every subspace of  $K$  contains the same number of  $t$ -dimensional subspaces (this is how we defined incidence in our graph). From that we can use Formula 4, where  $k$  stands for  $x$  and  $t$  stands for  $y$ .

**Theorem 1.** *Let  $G = (V, E)$  be a graph from Definition 1 and let  $w$  be an arbitrary vertex from set  $K$ , then:*

$$\deg(w) = \begin{bmatrix} k \\ t \end{bmatrix}_q. \quad (6)$$

Now we determine the degrees of vertices corresponding to the  $t$ -subspaces. For any subspace in  $T$  holds the same argument that no  $t$ -dimensional space can contain another  $t$ -dimensional subspace. Also we can observe that every vertex in the set  $T$  has same degree. This due to that every  $k$ -space is produced from same number of different  $t$ -subspaces, but this number is  $\begin{bmatrix} k \\ t \end{bmatrix}_q$  and the number of  $k$ -spaces is  $\begin{bmatrix} n \\ k \end{bmatrix}_q$ . Since there is  $\begin{bmatrix} n \\ t \end{bmatrix}_q$   $t$ -subspace it follows that the product of the number of the  $t$ -subspaces and their respective degrees is equal to the product of the number of of the  $k$ -subspaces and their respective degrees. Based on this observation, we get the following formula.

**Theorem 2.** *Let  $G = (V, E)$  be a graph from Definition 1 and let  $z$  be an arbitrary vertex from set  $T$ , then it holds:*

$$\deg(z) = \frac{\begin{bmatrix} n \\ k \end{bmatrix}_q \begin{bmatrix} k \\ t \end{bmatrix}_q}{\begin{bmatrix} n \\ t \end{bmatrix}_q} \quad (7)$$

From the previous of paragraphs, we deduce the following corollary.

**Corollary 1.** *Every graph from Definition 1 is bipartite and no more than biregular.*

### 3 Extremal properties of graphs of geometric designs

Before we state any extremal properties let us consider the following example.

*Example 1.* Let  $n = 3, q = 2, k = 2, t = 1$ . We can calculate with the use of formulas (5), (6) and (7), that the graph with these parameters has  $|V(G)| = 14$  and degree of every vertex in this graph is  $\deg(z) = 3, z \in V(G)$ . This graph is the smallest possible example and can be found in [3], but we will recall it here for better understanding. We will denote the vertices in the set  $T$  with Arabic numbers and vertices in the set  $K$  with Roman numerals. Brackets in the  $t$ - and the  $k$ -spaces denote linear span.

One-dimensional vector spaces:

1.  $\langle(0, 0, 1)\rangle$
2.  $\langle(0, 1, 0)\rangle$
3.  $\langle(1, 0, 0)\rangle$
4.  $\langle(0, 1, 1)\rangle$
5.  $\langle(1, 0, 1)\rangle$
6.  $\langle(1, 1, 0)\rangle$
7.  $\langle(1, 1, 1)\rangle$

Two-dimensional vector spaces:

- I.  $\langle(0, 0, 1), (0, 1, 0)\rangle$
- II.  $\langle(0, 0, 1), (1, 0, 0)\rangle$
- III.  $\langle(0, 0, 1), (1, 1, 0)\rangle$
- IV.  $\langle(0, 1, 0), (1, 0, 0)\rangle$
- V.  $\langle(0, 1, 0), (1, 0, 1)\rangle$
- VI.  $\langle(1, 0, 0), (0, 1, 1)\rangle$
- VII.  $\langle(0, 1, 1), (1, 0, 1)\rangle$

Due to Definition 1 there is an edge if all vectors of a  $t$ -space are contained in

a  $k$ -space. For example we can see that 1-vector  $\langle(0, 0, 1)\rangle$  is contained in the 2-space  $\langle(0, 0, 1), (0, 1, 0)\rangle$ ,  $\langle(0, 0, 1), (1, 0, 0)\rangle$  and  $\langle(0, 0, 1), (1, 1, 0)\rangle$ .

The following is the picture of the graph under consideration.

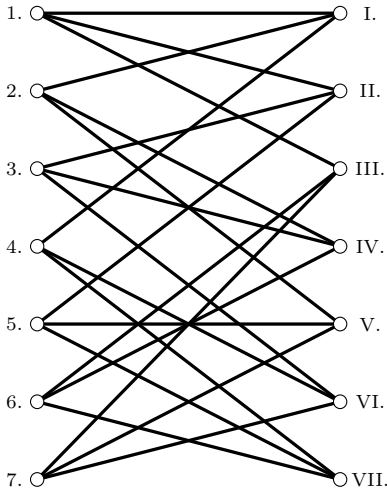


**Fig. 1.** Graph of geometric design with parametrs  $n = 3, q = 2, k = 2, t = 1$

We can see that the graph from Example 1 is regular. By investigating  $n, k, t$  we see that  $n = t + k$ , which is no coincidence. This observation suggests the following theorem.

**Theorem 3.** *Graphs from Definition 1 are regular if and only if  $n = k + t$ .*

*Proof.* The implication from the right to the left is straight forward, by simple comparison of Formulas (6), (7) and substitution for either  $n, k$  or  $t$ .

The implication from the left to the right is a little trickier and will be given in the extended version of this paper.

Since we do know when the graph of geometric design is regular we turn our attention to the question what can be its maximal girth. Let us remind ourselves that these graphs are bipartite, which means that the length of every cycle in the graph is even. From this follows following.

**Corollary 2.** *Every graph from Definition 1 has girth not less than 4.*

But if we take a good look at graph in Example 1 we would not be able to find cycle of length 4. Smallest cycle in this graph has length 6. This leads to the next question. What is the biggest girth in these graphs? Following theorem provides the answer.

**Theorem 4.** *Every graph from Definition 1 has girth no more than 6.*

*Proof.* Proof can be found here [3] and will be included in the extended version of this paper.

Now the natural question is when the graph from Definition 1 has girth 6. For this we can first look at the order of the graph and compare it to the Moore bound  $M(k, 6)$ . If  $G$  had the girth 6, it would have to satisfy the inequality  $|V(G)| \geq M(k, 6)$ , which we state by following inequality (where we assume that the graph is regular):

$$\begin{bmatrix} n \\ t \end{bmatrix}_q \geq 1 - \begin{bmatrix} n-t \\ t \end{bmatrix}_q + \left( \begin{bmatrix} n-t \\ t \end{bmatrix}_q \right)^2 \quad (8)$$

Inequality (8) gives us some basic necessary condition, whether graph from geometric design can have girth 6. In Table 1 we tested this inequality for different values of  $n, t$  ( $k$  can be obtained from Theorem 3). In Table 1 'Y' denotes that the inequality is satisfied and 'N' denotes that the inequality is not satisfied.

**Table 1.** Comparison table whether inequality (8) was satisfied over field  $\mathbb{F}_2$

		$n$																			
		3	4	5	6	7	8	9	10	11	12	13	14	15	16	17	18	19	20	21	
$t$	1	Y	N	N	N	N	N	N	N	N	N	N	N	N	N	N	N	N	N	N	
	2			Y	N	N	N	N	N	N	N	N	N	N	N	N	N	N	N	N	
	3					Y	Y	N	N	N	N	N	N	N	N	N	N	N	N	N	
	4							Y	Y	Y	N	N	N	N	N	N	N	N	N	N	
	5									Y	Y	Y	Y	N	N	N	N	N	N	N	
	6											Y	Y	Y	Y	Y	N	N	N	N	
	7													Y	Y	Y	Y	Y	N	N	
	8															Y	Y	Y	Y	Y	
	9																	Y	Y	Y	
	10																			Y	

If we look closely on Table 1, we observe that if  $k - t \geq 2$ , then from some  $n$  we are not able to satisfy Inequality (8). This is no coincidence as shown in the next theorem.

**Theorem 5.** *If  $k > t + 1$  then every graph from Definition 1 has girth equal to 4.*

*Proof.* Proof of this theorem will be given in the extended version of this paper.

It is also worth noting that for  $t = 1$  and  $t = 2$  the previous theorem can be proven directly from Inequality (8).

The only unsettled case is, when  $k - t = 1$ . After substituting suitable numbers in Inequality (8) we would see that this inequality would be always satisfied. Unfortunately this does not necessarily mean that there are no cycles of length 4.

**Theorem 6.** *If  $k - t = 1$ , then every graph from Definition 1 has girth equal to 6.*

*Proof.* Proof of this theorem will be given in the extended version of this paper.

## Acknowledgement

Work is partially supported by Grant of SGS No. SP2017/122, VB – Technical University of Ostrava, Czech Republic.

## References

1. Exoo, G., Jajcay, R.: Dynamic cage survey. *Electron. J. Combin.* 15(16), 4 (2008)
2. Hurley, M.: New geometric large sets. Ph.D. thesis, Florida Atlantic University (2016)
3. Karlovská, J.: Využitie metód lineárnej algebry na vyhľadávanie extrémálnych grafov. Bc. Thesis, Comenius University in Bratislava (2017)

# On Decomposition of Distance Magic Graphs of Odd Order

Adam Silber and Petr Kovář

Department of Applied Mathematics, FEECS,  
VŠB – Technical University of Ostrava, 17. listopadu 15,  
708 33 Ostrava – Poruba, Czech Republic  
adam.silber@vsb.cz

**Abstract.** There has been a number of articles of the scheduling of incomplete tournaments in the last years. A complete, fair incomplete, equalized incomplete, and handicap incomplete round robin tournaments have been introduced. The properties of the tournaments are slightly different depending on whether they mimic the difficulty of the round robin tournament or a certain advantage is given to weaker teams. But one property is common for all cases, namely every team meets the same number of opponents.

For scheduling an equalized incomplete tournament, the 1-distance magic graphs are used. By a 1-distance magic graph we denote such a graph  $G = (V, E)$  which allows distance magic labelling  $\lambda$ , a bijection from the set of vertices to  $\{1, 2, \dots, |V(G)|\}$  such that the sum of the labels of adjacent vertices is equal to the same number for each vertex. Many constructions of such graphs are known. We are interested in decomposition of these graphs to help us determine how many rounds of the tournament will be needed to finish the tournament as soon as possible.

## 1 Introduction

A round robin tournament of  $n$  teams is represented by a complete graph on  $n$  vertices in which each team plays against all the remaining  $n - 1$  teams. Such a tournament is usually considered fair. However, such tournaments are very time demanding due to numerous matches which have to be played. A *fair incomplete tournament* arises from a complete tournament by omitting certain matches so that every team plays the same number of matches and the total difficulty of opponents mimics the difficulty of the complete tournament for each team [3]. On the other hand, it is easy to observe that the omitted matches also form a kind of tournament, an *equalized incomplete tournament*, where every team plays the same number of matches and the total difficulty of opponents is the same for each team. Thus, an equalized incomplete tournament is the complement of a fair incomplete tournament and vice versa.

## 2 Distance magic graphs

An *equalized incomplete tournament* can be represented by a distance magic graph. The vertices of the graph represent teams while edges represent matches

played in the tournament. Label  $f(x)$  of the vertex  $x$  represents the rank of the team based on the last years performance. In this paper we identify vertex names with their labels, thus by  $x$  we understand the vertex labeled  $x$ .

**Definition 1.** A graph  $G$  of order  $n$  with vertex set  $V(G)$  and edge set  $E(G)$  is called distance magic [1] if there exists a bijection  $f : V(G) \rightarrow \{1, 2, \dots, n\}$  such that the weight of each vertex  $x$ , defined as

$$w(x) = \sum_{y \in N(x)} f(y),$$

where  $N(x)$  is the set of all vertices adjacent to  $x$ , is equal to the same magic constant  $k$ .

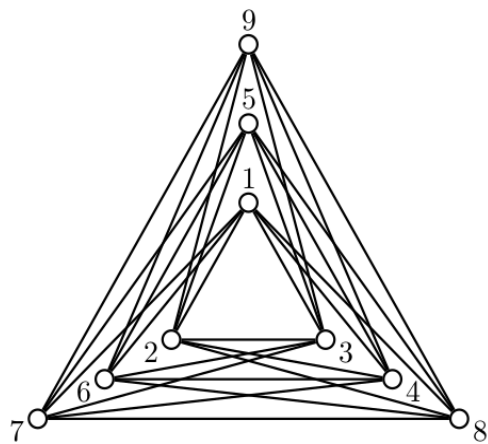


**Fig. 1.** An example of a distance magic graph.

There exists constructions of *distance magic graphs* for various numbers of teams [2], [4]. We would like to know how many rounds will be needed for the entire tournament to be played. We want to play all matches of the tournament as soon as possible, and as many matches in one round as possible.

### 3 Graph decomposition and colouring

In this section we want to describe what we understand by the decomposition of the graph representing the tournament and what is the connection between tournament decomposition and edge-colouring.

The edge-coloring problem asks whether it is possible to properly color the edges of a graph with at most  $k$  different colors. The coloring is proper when edges



incident with the same vertex have different colours. The minimum required number of colors for the edges of a given graph is called the chromatic index of the graph and is denoted as  $\chi'(G)$ .

We distinguish the edges of the graph by colouring. Matches played in the same round are coloured by the same colour. This surely gives us a proper edge colouring since the edges represent matches and no team can play more than one match in each round. Thus, the minimum number of rounds is equal to the chromatic index of the graph. By *Vizing's Theorem* we know, it will be  $\chi'(G) = \Delta(G) = r$ , or  $\chi'(G) = \Delta(G) + 1 = r + 1$  rounds respectively.

The decomposition of distance magic graph, respectively decomposition of matches on the rounds of the incomplete tournament, is given by the proper colouring of the graph. So, by decomposition of graph we understand decomposition by colouring. The *Vizing's Theorem* gives us a tight bound on the minimum number of required rounds.

#### 4 $\chi'(G) = \Delta(G) = r$ case

Since the  $\chi'(G) = \Delta(G) = r$  is a straightforward case in which the number of matches is the same for each round, because each team has to play exactly one match in each round. The proper colouring of the graph representing the tournament gives us the solution of which matches will be played in which round of the tournament.

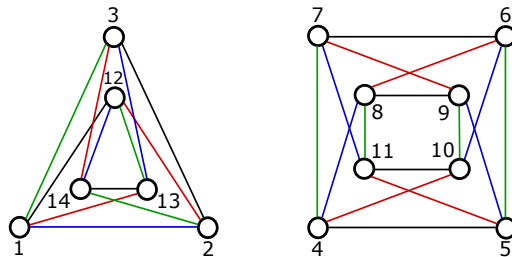


**Fig. 2.** An example of decomposition of distance magic graph of order 14.

#### 5 Distance magic graphs with odd number of vertices

In this section we deal with distance magic graphs with odd number of vertices. Since  $|V(G)|$  is odd,  $r$  must be even.

We would like to have the number of matches in the last round as low as possible. We show that for the last round there has to be at least  $\frac{r}{2}$  matches, at least  $\frac{r}{2}$  edges will be coloured by the colour of the last round.

**Theorem 1.** *Let  $G$  be an  $r$ -regular distance magic graph with odd number of vertices. Then  $\chi'(G) = \Delta(G) + 1 = r + 1$  and at least  $\frac{r}{2}$  edges will be coloured by the the colour of the last round.*

*Proof.* i)  $\chi'(G) = \Delta(G) + 1 = r + 1$  **by contradiction.**

Suppose  $\chi'(G) = \Delta(G) = r$ . Then every vertex is adjacent to  $r$  edges of  $r$  different colours. This implies that all teams participate in each rounds. Since the number of teams is odd and for each match a pair of teams is required this is not possible. Thus  $\chi'(G) = \Delta(G) + 1 = r + 1$  by *Vizing's Theorem*.

ii) **At least  $\frac{r}{2}$  edges will be colored by the the colour of the last round.** Each edge represents a match between two teams. Since in each round each team can play up to one match a maximum of matches in one round is half of the number of teams. The number of teams is odd so at least one team has to skip the round. In each round we choose a different team to skip the game. After  $r$  rounds there are  $r$  teams with one match to play. Since each edge represents a match between two teams there are at least  $\frac{r}{2}$  matches that left for the last round so at least  $\frac{r}{2}$  edges will be colored by the colour of the last round.

## 6 Conclusion

In this paper we present a connection between *distance magic labelings* of graphs and tournament scheduling. We show that the entire *incomplete tournament*, where every team plays exactly  $r$  matches, could be played out in  $r$  or  $r + 1$  rounds. Moreover, we show that there is a lower bound on the minimum of games played in the last round. In Figure 3 there is an example of a 4-regular *distance magic* graph of order 31 which represents an *equalized incomplete* tournament of 31 teams. The matches played in the same round of the tournament are of the same colour.

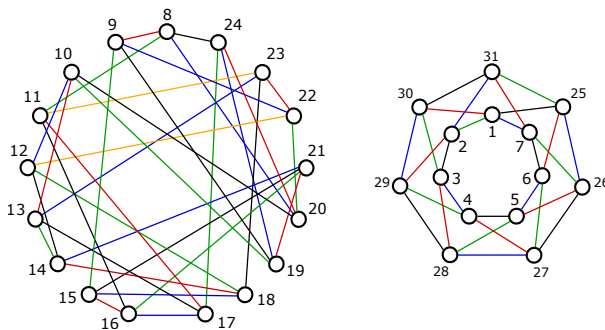


**Fig. 3.** An example of decomposition of distance magic graph of order 31.

## References

1. S. ARUMUGAM, D. FRONČEK, N. KAMATCHI, Distance Magic Graphs A Survey, *J. Indones. Math. Soc.*, Special Edition (2011), 11–26.
2. D. FRONČEK, Fair incomplete tournaments with odd number of teams and large number of games, *Congr. Numer.* 187 (2007), 83–89.
3. D. FRONČEK, P. KOVÁŘ, T. KOVÁŘOVÁ, Fair incomplete tournaments, *Bulletin of the ICA* 48 (2006), 31–33.
4. D. FRONČEK, P. KOVÁŘ, T. KOVÁŘOVÁ, Constructing distance magic graphs from regular graphs, *J. Combin. Math. Combin. Comput.*, 78 (2011), 349–354.
5. J. A. GALLIAN, A dynamic survey of graph labeling, *Electron. J. Combin.* 17, upated in December 7, 2015.
6. M. MILLER, C. RODGER, R. SIMANJUNTAK, Distance magic labelings of graphs, *Australas. J. Combin.* 28 (2003), 305–315.

# Local Eigenvalue Analysis using Contour Integral Method

Erika Straková<sup>1</sup> and Dalibor Lukáš<sup>1,2</sup>

<sup>1</sup>Department of Applied Mathematics, FEECS,  
VŠB – Technical University of Ostrava, 17. listopadu 15,  
708 33 Ostrava – Poruba, Czech Republic

<sup>1,2</sup>IT4Innovation, VŠB – Technical University of Ostrava, 17. listopadu 15,  
708 33 Ostrava – Poruba, Czech Republic  
{erika.strakova, dalibor.lukas}@vsb.cz

**Abstract.** The article presents a numerical method for computing eigenvalues of generalized eigenvalue problem. This is an essential problem in many areas of engineering such as analysis of mechanical vibrations, electrical networks, optical waveguides, or in quantum chemistry. The traditional algorithms often locate all eigenvalues and use costly diagonalization. The presented method computes eigenvalues of a matrix pencil only in a given domain of interest. The method relies on complex integrals of the resolvent operator.

**Keywords:** generalized eigenvalue problem, contour integral method

## 1 Introduction and Local Eigenvalue Analysis

We consider the generalized eigenvalue problem

$$Ax = \lambda Bx, \quad (1)$$

where  $A, B$  are  $n \times n$  complex or real matrices, which arises in many applications. The method presented in this article was proposed by Sakurai and Sugiura [1]. It reduces the original generalized eigenvalue problem to a linear eigenvalue problem of dimension  $k_\gamma$ , where  $k_\gamma$  is the number of eigenvalues inside the contour  $\gamma$ . Later the method was extended by Ikegami, Sakurai and Nagashima [2] using the resolvent theory and a more accurate algorithm (block SS method) was proposed.

At first we start with Weierstrass's canonical form.

### **Theorem 1. (*Weierstrass Canonical Form*)**

*Let  $(zB - A) \in \mathbb{C}^{n \times n}$  be a regular pencil. Then there exist nonsingular matrices*

$P, Q \in \mathbb{C}^{n \times n}$  such that

$$P(zB - A)Q = \begin{bmatrix} zI_{k_1} - J_1 & & & & \\ & \ddots & & & \\ & & zI_{k_d} - J_d & & \\ & & & zN_{d+1} - I_{k_{d+1}} & \\ & & & & \ddots \\ & & & & & zN_r - I_{k_r} \end{bmatrix}, \quad (2)$$

where  $J_i, N_i \in \mathbb{C}^{k_i \times k_i}$  are Jordan blocks,  $N_i$  is nilpotent and  $I_{k_i} \in \mathbb{C}^{k_i \times k_i}$  is the identity matrix.

According to the structure of the Jordan blocks we divide  $P$  and  $Q$  into block rows  $P_i \in \mathbb{C}^{k_i \times n}$  and block columns  $Q_i \in \mathbb{C}^{n \times k_i}$ , respectively, for  $i = 1, 2, \dots, r$ . By (2) we obtain

$$(zB - A)^{-1} = \sum_{i=1}^d Q_i (zI_{k_i} - J_i)^{-1} P_i + \sum_{i=d+1}^r Q_i (zN_i - I_{k_i})^{-1} P_i.$$

Let  $\alpha_i$  be an eigenvalue of matrix  $J_i$ . Then

$$(zI_{k_i} - J_i)^{-1} = \sum_{m=0}^{k_i-1} \frac{(J_i - \alpha_i I_{k_i})^m}{(z - \alpha_i)^{m+1}}$$

and

$$(zN_i - I_{k_i})^{-1} = - \sum_{m=0}^{k_i-1} z^m N_i^m.$$

The regular pencil  $(zB - A)^{-1}$  can be decomposed into

$$(zB - A)^{-1} = \sum_{i=1}^d Q_i \left( \sum_{m=0}^{k_i-1} \frac{(J_i - \alpha_i I_{k_i})^m}{(z - \alpha_i)^{m+1}} \right) P_i - \sum_{i=d+1}^r Q_i \left( \sum_{m=0}^{k_i-1} z^m N_i^m \right) P_i.$$

Let  $\gamma$  be a positively oriented closed Jordan curve and  $G$  interior of  $\gamma$ . For a non-negative integer  $n$ , the  $n$ -th order moment matrix of the pencil  $zB - A$  is defined by

$$M_n := \frac{1}{2\pi i} \int_{\gamma} z^n (zB - A)^{-1} dz. \quad (3)$$

We can extract Jordan blocks whose eigenvalues are contained in  $G$ . The following collective notations are constructed: The Jordan blocks  $J_i$ ;  $\alpha_i \in G$  are collected to form the  $k_{\gamma} \times k_{\gamma}$  Jordan matrix  $J_{\gamma}$ , where  $k_{\gamma} = \sum_{i; \alpha_i \in G} k_i$ . Similarly, the corresponding  $Q_i$  and  $P_i$  are collected to form  $Q_{\gamma} \in \mathbb{C}^{n \times k_{\gamma}}$  and  $P_{\gamma} \in \mathbb{C}^{k_{\gamma} \times n}$ , respectively.

By using the Residue theorem, the matrix in (3) can be written as:

$$M_n = Q_{\gamma} J_{\gamma}^n P_{\gamma}. \quad (4)$$

The following theorem can be derived due to expression in (4):

**Theorem 2.** *Let  $C, D$  be arbitrary  $n \times m$  matrices, where  $n > m \geq k_\gamma$ . We define the size-reduced moment matrices  $\mathbb{M}_0 = C^H M_0 D \in \mathbb{C}^{m \times m}$  and  $\mathbb{M}_1 = C^H M_1 V \in \mathbb{C}^{m \times m}$ . If ranks of  $C^H Q_\gamma$  and  $P_\gamma D$  are  $k_\gamma$ , the size-reduced matrix pencil  $z\mathbb{M}_0 - \mathbb{M}_1$  is equivalent to  $zI_{k_\gamma} - J_\gamma$ .*

## 2 Quadrature and numerical realization

The major step in the algorithm consists of evaluating the integrals in (3) for  $n = 0, 1$  by numerical quadrature and solving the linear systems involved in the evaluation of the integrand. We will consider the case in which  $\gamma$  is given by a circle with the center  $r$ , radius  $\rho$  and the integrals are evaluated via a trapezoidal rule. Thus, we obtain the following algorithm.

---

### Algorithm 1 Generalized eigenvalue algorithm

---

**Require:**  $r; \rho$ ; the number of integration points  $N$ ;  $m$  such that  $n > m \geq k_\gamma$ ,  $\text{tol}_{\text{rank}}$

**Ensure:**  $\lambda_1, \dots, \lambda_{k_\gamma}$

---

- 1: set  $\omega_j \leftarrow r + \rho e^{2\pi i(j+1/2)/N}$  for  $j = 0, 1, \dots, N-1$
  - 2: generate  $V \in \mathbb{C}^{n \times m}$  as random matrix
  - 3: compute  $p_j \leftarrow (\omega_j B - A)^{-1} V$  for  $j = 0, 1, \dots, N-1$
  - 4: set  $\mathbb{M}_0 = (1/N) \sum_{j=0}^{N-1} V^T p_j (\omega_j - r)$
  - 5: set  $\mathbb{M}_1 = (1/N) \sum_{j=0}^{N-1} V^T \omega_j p_j (\omega_j - r)$
  - 6: perform a singular value decomposition of  $\mathbb{M}_0$
  - 7: omit small singular value components i.e. find  $0 < k_\gamma \leq m$  such that  $\sigma_1 \geq \dots \geq \sigma_{k_\gamma} > \text{tol}_{\text{rank}} > \sigma_{k_\gamma+1} \approx \dots \approx \sigma_m \approx 0$
  - 8: set  $\bar{\mathbb{M}}_0 = \mathbb{M}_0(1 : k_\gamma, 1 : k_\gamma)$  and  $\bar{\mathbb{M}}_1 = \mathbb{M}_1(1 : k_\gamma, 1 : k_\gamma)$
  - 9: compute the eigenvalues of the matrix pencil  $z\bar{\mathbb{M}}_0 - \bar{\mathbb{M}}_1$
- 

To achieve better accuracy the Algorithm 1 was improved by Ikegami, Sakurai and Nagashima [2, 3]. Let  $v \in \mathbb{C}^n$  be an arbitrary vector and  $\mu_n = v^H M_n v$ . Define two  $m \times m$  Hankel matrices  $\mathbb{H}_m, \mathbb{H}_m^1$  as follows:

$$\mathbb{H}_m := \begin{bmatrix} \mu_0 & \mu_1 & \cdots & \mu_{m-1} \\ \mu_1 & \mu_2 & \cdots & \mu_m \\ \vdots & \vdots & & \vdots \\ \mu_{m-1} & \mu_m & \cdots & \mu_{2m-2} \end{bmatrix}, \quad \mathbb{H}_m^1 := \begin{bmatrix} \mu_1 & \mu_2 & \cdots & \mu_m \\ \mu_2 & \mu_3 & \cdots & \mu_{m+1} \\ \vdots & \vdots & & \vdots \\ \mu_m & \mu_{m+1} & \cdots & \mu_{2m-1} \end{bmatrix}. \quad (5)$$

If we choose row vectors of  $C^H$  in 2 as  $C_i^H = v^H M_i B$  and column vectors of  $D$  as  $D_i = B M_i v$ , the Hankel matrix  $\mathbb{H}_m$  is equal to  $\mathbb{M}_0$  and  $\mathbb{H}_m^1$  is equal to  $\mathbb{M}_1$ . Hence, the non-singular part of a matrix pencil  $z\mathbb{H}_m - \mathbb{H}_m^1$  is equivalent to  $zI_{k_\gamma} - J_\gamma$ , if  $v$  is random enough and there is no degeneracy in  $J_\gamma$ . The block Sakurai-Sugiura (SS) method is based on replacing  $\mu_n$  in (5) with matrix  $v^H M_n v$ .

**Algorithm 2** Block SS method

**Require:**  $r; \rho$ ; the number of integration points  $N$ ;  $m, L$  such that  $n > Lm \geq k_\gamma$ ,  
 $\text{tol}_{\text{rank}}$

**Ensure:**  $\lambda_1, \dots, \lambda_{k_\gamma}$

- 1: set  $\omega_j \leftarrow r + \rho e^{2\pi i(j+1/2)/N}$  for  $j = 0, 1, \dots, N-1$
- 2: generate  $V \in \mathbb{C}^{n \times m}$  as random matrix
- 3: compute  $p_j \leftarrow (\omega_j B - A)^{-1} V$  for  $j = 0, 1, \dots, N-1$
- 4: set  $\mathbb{M}_n = (1/N) \sum_{j=0}^{N-1} V^H(\omega_j)^n p_j(\omega_j - r)$  for  $n = 0, \dots, 2L-1$
- 5: construct the Hankel matrices  $\mathbb{H}_{Lm}, \mathbb{H}_{Lm}^1 \in \mathbb{C}^{Lm \times Lm}$  like in (5) with the entries  $\mu_n = \mathbb{M}_n$  for  $n = 0, \dots, 2L-1$
- 6: perform a singular value decomposition of  $\mathbb{H}_{Lm}$
- 7: omit small singular value components i.e. find  $0 < k_\gamma \leq Lm$  such that  $\sigma_1 \geq \dots \geq \sigma_{k_\gamma} > \text{tol}_{\text{rank}} > \sigma_{k_\gamma+1} \approx \dots \approx \sigma_{Lm} \approx 0$
- 8: set  $\overline{\mathbb{H}}_{Lm} = \mathbb{H}_{Lm}(1 : k_\gamma, 1 : k_\gamma)$  and  $\overline{\mathbb{H}}_{Lm}^1 = \mathbb{H}_{Lm}^1(1 : k_\gamma, 1 : k_\gamma)$
- 9: compute the eigenvalues of the matrix pencil  $z\overline{\mathbb{H}}_{Lm} - \overline{\mathbb{H}}_{Lm}^1$

### 3 Numerical results

We consider a matrix pencil  $(zB - A) \in \mathbb{R}^{3600 \times 3600}$ , where the matrices  $A, B$  are real valued and symmetric positive definite. The matrices arise from the coupled FEM-BEM discretization of the eddy current case of Maxwell's equations for simulations of electromagnetic forming of metallic sheets. For a more detailed description we refer to Fig.1.

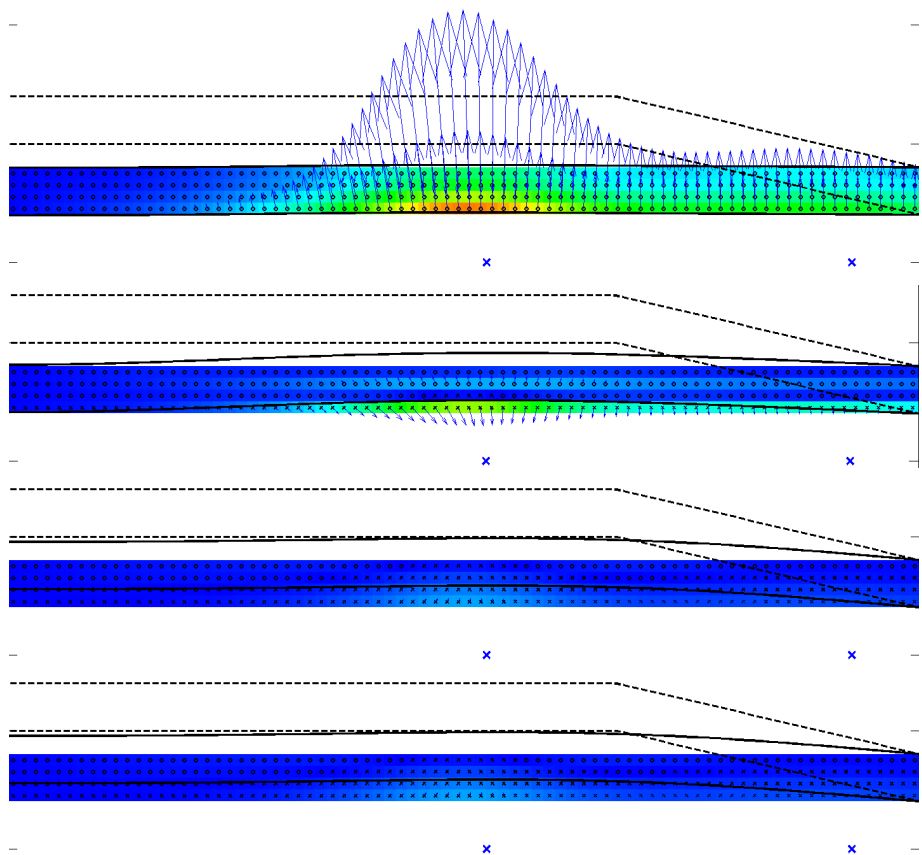
We search for eigenvalues of the matrix pencil  $zB - A$  inside the curve  $\gamma(t) := 1500 + 2000e^{2\pi it}$ ,  $t \in (0, 1)$ . The radius of the curve is chosen to locate exactly ten eigenvalues. As the input parameters for the Generalized eigenvalue algorithm 1 we used

$$N = 100, \quad m = 20, \quad \text{tol}_{\text{rank}} = 0.01$$

and for the Block SS algorithm 2 we used

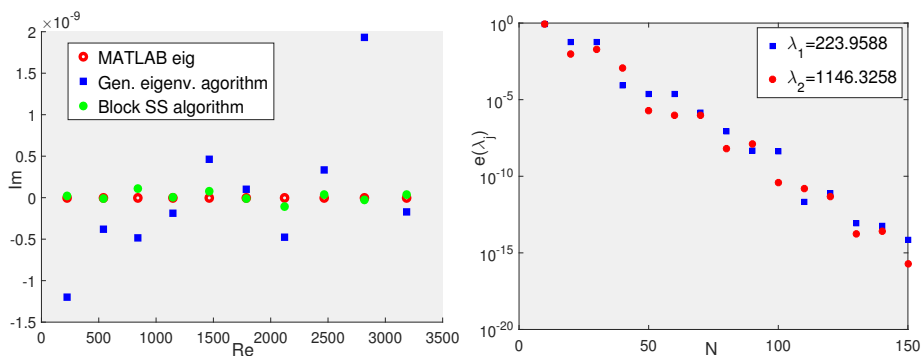
$$N = 100, \quad m = 10, \quad L = 2, \quad \text{tol}_{\text{rank}} = 0.01.$$

Fig. 2 (left) shows the results obtained by the both methods and MATLAB function `eig`. Difference of eigenvalues  $\lambda_1 = 223.9588$  (blue squares) and  $\lambda_2 = 1146.3258$  (red circles) between `eig` and Block SS method vs. number of integration points  $N$  are plotted in Fig. 2 (right).



**Fig. 1.** Snapshots of a simulation of electromagnetic forming of a cylindrical metallic sheet: The electromagnetic field and the mechanical displacements are sketched in the cylindrical coordinates (the axis is on the left hand side) at four times (top-down). We depict positions (blue crosses) of line circular turns of the excitation coil, eddy current distribution (colours and black circles/crosses), Lorentz forces (arrows), mechanical displacements (solid lines), and the form (dashed lines) against which the sheet is pressed. Note that after the Lorentz forces vanish the deformation of the sheet continues due to the inertial forces.





**Fig. 2.** Eigenvalues of the matrix pencil  $(zB - A)$  inside  $\gamma$  (left). The Block SS method vs. the number of integration points (right).

## References

1. Sakurai T. and Sugiura H., *A projection method for generalized eigenvalue problems using numerical integration*. J. Comp. Appl. Math. 159 (2003) 119–128.
2. Ikegami T., Sakurai T., and Nagashima U., *A filter diagonalization for generalized eigenvalue problems based on the Sakurai-Sugiura projection method*. J. Comp. Appl. Math. 233 (2010) 1927–1936.
3. Asakura J., Sakurai T., Tadano H., Ikegami T., and Kimura K., *A numerical method for nonlinear eigenvalue problems using contour integrals*. JSIAM Letters 1 (2009) 52–55.
4. Sakurai T., Futamura Y., and Tadano H., *Efficient parameter estimation and implementation of a contour integral-based eigensolver*. Journal of Algorithms and Computational Technology 7 (2013) 249–269.
5. Straková E., Lukáš D., and Vodstrčil P., *Finding Zeros of Analytic Functions and Local Eigenvalue Analysis Using Contour Integral Method in Examples*. Advances in Electrical and Electronic Engineering, VŠB-TUO (2017) 286–295.

# Using the Random Forests Algorithm for Medical Data Analysis

Adéla Vrtková

Department of Applied Mathematics, FEECS,  
VŠB – Technical University of Ostrava, 17. listopadu 15,  
708 33 Ostrava – Poruba, Czech Republic  
`adela.vrtkova@vsb.cz`

**Abstract.** Medical data usually contain various patients' information which naturally are represented as quantitative or qualitative variables. However, some difficulties can arise when more complex analysis of the so-called mixed data is of interest. Consequently, the analysis of medical data requires an application of more flexible methods. Firstly, the well-known random forests algorithm is described together with the alternative approach which eliminates possible bias in the algorithm. Then, a possible application to real medical data is suggested.

**Keywords:** classification tree, random forests algorithm, medical data

## 1 Motivation

Many multivariate methods (e.g. PCA) give satisfactory performance only when they are applied to certain type of variables (e.g. continuous variables, normally distributed etc.). In practice, these kinds of assumptions are often violated and the usage of these methods is not appropriate. When analysing data collected and provided by the University Hospital Ostrava, we had to face this situation quite often. Therefore, we started to focus on more flexible methods which are more suitable for the mixed data.

Moreover, especially prediction of patient's condition has been recently of interest, the condition is usually evaluated with an ordinal scale. According to our available literature, many authors used logistic regression or artificial neural networks for this purpose, e.g. see [3, 5]. The random forests algorithm has already been used for prediction purposes in ecology or the microarray data analysis, see [2, 6].

Considering our aim, which is working with mixed data with original variables of any kind for the purpose of prediction of patient's condition, we decided to use the random forests algorithm. The algorithm doesn't require any transformation of exploratory variables and it also provides useful estimates of variable importance. For avoiding bias in variable importance, it was decided to use the alternative approach, introduced in [8], which uses conditional inference trees.

## 2 The Random Forests Algorithm

### 2.1 Decision tree methods

Decision tree methods, described in [10], are non-parametric methods which are highly flexible and can be used either for regression or classification problems. Therefore, with the set of splitting rules, they can build a model which predicts the value of a target variable. They also have the ability to detect complex interactions among exploratory variables. The target variable determines whether the regression or classification tree model is used. In the case of prediction of patient's condition, which is usually described with an ordinal variable, the choice naturally falls on the classification tree.

The classification tree model, described in [4] uses so-called recursive binary splitting process which begins in the root node (the top of the tree) and continues in the sense of making the best split in each node until reaching the terminal node. The best split is made with consideration of all exploratory variables which could be both quantitative and qualitative. Of course, the choice of the split naturally should be done in the sense of minimizing some suitable criteria which in this case could be minimization of classification error rate

$$E = 1 - \max_k(\hat{p}_{mk}), \quad (1)$$

where  $\hat{p}_{mk}$  is the proportion of training observation in the  $m$ th terminal node region which are from the  $k$ th class. Other option is minimization of so-called Gini index which is defined as

$$G = \sum_{k=1}^K \hat{p}_{mk}(1 - \hat{p}_{mk}) \quad (2)$$

and can be described as a measure of total variance across all  $K$  classes. The necessary step from the classification tree model to the random forests is combining large amount of the classification trees.

### 2.2 Random forests

The first step in the algorithm, described in [1,2], is the selection of many bootstrap samples from the original dataset, where the number of bootstrap samples determines the number of trees. In the next step, the classification tree model is built for each bootstrap sample and at each node, certain number of exploratory variables is chosen randomly and they are used for making the best split in the sense of (1) or (2). This step is repeated until the terminal node is reached and the prediction from each tree is obtained. In the end, the predictions from all trees are aggregated within the meaning of the vote for the most popular category.

The setting of the number of trees and the number of randomly selected exploratory variables is mostly dependent on the data. However, there is recommendation for the choice of the number of randomly selected predictors. Usually,

the number should be approximately equal to the square root of the number of all exploratory variables.

In the first step of the algorithm, the trees don't use the whole dataset. Data, which are not used for building the tree, are called *out-of-bag* observations (OOB). From the OOB observations, OOB predictions can be obtained. With these predictions, we are able to compute the OOB error estimation which is an accurate estimation of the error rate. Moreover, thanks to the nature of the algorithm and the OOB error, performing cross-validation is not necessary.

Overall, the random forests algorithm can be used not only for classification problems but also for regression problems. It is able to model complex interactions among exploratory variables and it is robust to overfitting and outliers. Any transformation of exploratory variables is not necessary. The algorithm also provides information about the variable importance. Nevertheless, if different types of exploratory variables are present in the dataset, the bias of the variable importance towards continuous variables and categorical variables with many categories may occur. The alternative approach to the random forests algorithm was introduced in [7, 8].

### 2.3 The alternative approach

The main difference in the alternative approach is in using the conditional inference trees and the bootstrap sampling without replacement. During the selection of variables, the "standard" classification tree chooses the variables randomly, the conditional inference tree chooses from those predictors which have statistically significant relationship with the target variable. This should guarantee unbiased variable selection, otherwise continuous variables and categorical variables with many categories are artificially preferred.

The alternative approach also has promising features - already mentioned unbiased variable importance measures, ability to detect complicated interactions, flexibility and high classification accuracy. Also, it has already been implemented in the software R in the package `party`, for more details see [9].

## 3 Application

Both introduced versions of the random forests algorithm could be used for building the predictive model. Nevertheless, they can also be used only if the selection of several most important variables is of interest and those chosen variables are later used for further analysis.

Our dataset contains information about more than 600 patients who suffered from an ischemic stroke. Their condition after three months was evaluated with Modified Rankin Scale (our target variable) which is an ordinal variable which runs from 0 to 6, from no symptoms to death. The dataset also contains information about the age of the patient, gender, presence of arrhythmia or hypertension, patient's condition 24 hours after a stroke, BMI, etc. The primary

goal was building the predictive model which would use the information available within 24 hours after admission to the hospital for the long-term prediction.

Firstly, we faced the situation described earlier, that many multivariate methods couldn't be used due to the nature of the dataset. Then, we moved to the random forests algorithm which really gave us biased variable importance measures towards continuous variables (patient's age, BMI, length of medical procedure). Therefore, it was decided that the alternative approach would be suitable for our data.

We managed to build the model which predicted the patient's condition with 86% accuracy, see [11] for more details. However, we had to dichotomize the target variable, otherwise we weren't able to obtain satisfactory prediction accuracy. On the other hand, these results helped us to choose several most important variables which have an impact on the patient's condition and in the future, we want to add more variables from detailed analysis of patient's condition (e.g. blood coagulation, inflammatory response evaluation) and try to build a model which would be able to predict the original target variable.

## 4 Conclusion and future work

The random forests algorithm was described. We focused on the usage of the algorithm for classification problems, especially in the field of analysis of medical data. Also, we described the alternative approach which should prevent the possible bias in the algorithm. Then, we focused on the application of the algorithm for patient's condition prediction purposes.

For future work, the cooperation with the University Hospital Ostrava should continue for the purpose of building more precise predictive models of patient's condition. The predictive models should provide a useful tool which could be used by the hospital on a daily basis.

## Acknowledgement

The author acknowledges the support of VŠB-Technical University of Ostrava (Project No. SP2017/56). A paper [11] giving more detailed results from the application of the algorithm to the medical data about patients after an ischemic stroke was presented in the International Conference on Information and Digital Technologies in Žilina, Slovakia on 6/7/2017.

## References

1. Breiman, L.: Random forests. *Machine learning* 45(1), 5–32 (2001)
2. Cutler, D.R., Edwards, T.C., Beard, K.H., Cutler, A., Hess, K.T., Gibson, J., Lawler, J.J.: Random forests for classification in ecology. *Ecology* 88(11), 2783–2792 (2007)

3. Eftekhari, B., Mohammad, K., Ardebili, H.E., Ghodsi, M., Ketabchi, E.: Comparison of artificial neural network and logistic regression models for prediction of mortality in head trauma based on initial clinical data. *BMC Medical Informatics and Decision Making* 5(1), 3 (2005)
4. James, G., Witten, D., Hastie, T., Tibshirani, R.: An introduction to statistical learning, vol. 6. Springer (2013)
5. Ottenbacher, K.J., Smith, P.M., Illig, S.B., Linn, R.T., Fiedler, R.C., Granger, C.V.: Comparison of logistic regression and neural networks to predict rehospitalization in patients with stroke. *Journal of clinical epidemiology* 54(11), 1159–1165 (2001)
6. Statnikov, A., Wang, L., Aliferis, C.F.: A comprehensive comparison of random forests and support vector machines for microarray-based cancer classification. *BMC bioinformatics* 9(1), 319 (2008)
7. Strobl, C., Boulesteix, A.L., Kneib, T., Augustin, T., Zeileis, A.: Conditional variable importance for random forests. *BMC bioinformatics* 9(1), 307 (2008)
8. Strobl, C., Boulesteix, A.L., Zeileis, A., Hothorn, T.: Bias in random forest variable importance measures: Illustrations, sources and a solution. *BMC bioinformatics* 8(1), 25 (2007)
9. Strobl, C., Hothorn, T., Zeileis, A.: *Party on!* (2009)
10. Tutz, G.: *Regression for categorical data*, vol. 34. Cambridge University Press (2011)
11. Vrtková, A.: Predicting clinical status of patients after an acute ischemic stroke using random forests. In: *Information and Digital Technologies (IDT), 2017 International Conference on*. IEEE (2017), (Conference proceedings in preparation)

# Mixture Failure Rate: A Study based on Product of Spacings

Tien T. Thach and Radim Briš

Department of Applied Mathematics, FEECS,  
VŠB – Technical University of Ostrava, 17. listopadu 15,  
708 33 Ostrava – Poruba, Czech Republic  
`tien.thanh.thach.st@vsb.cz`

**Abstract.** In this study, we are dealing with our new concept of failure rate, called mixture failure rate, from our previous study using the product of spacings as an alternative to the traditional likelihood for both classical and Bayesian estimation to estimate the parameters and reliability characteristics. We also use a well-known tool for optimization, the cross-entropy (CE) method, to maximize the product of spacings function. Alternatively, Markov chain Monte Carlo (MCMC) method is also used for Bayesian inference. A simulation study is provided to compare CE with MCMC, and differences between the estimates obtained by the two approaches are evaluated.

## 1 Introduction

Engineering systems, while in operation, are always subject to environmental stresses and shocks which may or may not alter the failure rate function of the system. In such situations, a failure distribution is generally used to describe mathematically the failure rate on the system. Many authors have tried to solve this problem through the mixture of distributions (Mann et al. [2], Sinha [3], Lawless [1]), but they were faced with many problems. In 1997, Sharma and others proposed to solve this problem through a mixture of failure rates, but their work at that time still have many limited. According to Sharma and others [4], the failure rate function of the system be in either of the following two states:

$$h(t) = p\lambda + (1 - p)\lambda t, \quad \lambda, t > 0, 0 < p < 1.$$

State 1: Initially it experiences a constant failure rate model and this model may (or may not) change with probability  $q$  ( $p = 1 - q$ ).

State 2: If the stresses and shocks alter the failure rate model of the system with probability  $q$ , then it experiences a wear-out failure model. In our previous studies [6],

$$h(t) = p\lambda_1 + (1 - p)\lambda_2 t^k, \quad \lambda_1, \lambda_2, k, t > 0, 0 < p < 1 \quad (1)$$

we implemented a new parameter  $k$  to make the failure function more flexible and we also differentiated between the two parameter  $\lambda_1$  and  $\lambda_2$  to make it more reasonable in applications.

## 2 Characteristics of the life-time distribution

Using the well-known relationship between p.d.f. and failure rate function and in view of (1), the p.d.f. of the life-time  $T$  is

$$f(t) = \begin{cases} (p\lambda_1 + (1-p)\lambda_2 t^k) \exp \left\{ - \left( p\lambda_1 t + (1-p)\frac{\lambda_2}{k+1} t^{k+1} \right) \right\}, & t > 0 \\ 0, & \text{otherwise.} \end{cases} \quad (2)$$

The reliability function is

$$R(t) = \exp \left\{ - \left( p\lambda_1 t + (1-p)\frac{\lambda_2}{k+1} t^{k+1} \right) \right\}, \quad t > 0. \quad (3)$$

The MTTF is given by

$$MTTF = \mathbb{E}(T) = \int_0^\infty R(t) dt = \int_0^\infty \exp \left\{ - \left( p\lambda_1 t + (1-p)\frac{\lambda_2}{k+1} t^{k+1} \right) \right\} dt.$$

This integral can be obtained by using some suitable numerical methods.

## 3 Estimation of parameters and reliability characteristics

### 3.1 Maximum product of spacings estimation

Let  $\mathcal{D} : t_1, \dots, t_n$  be the random failure times of  $n$  items under test whose failure time distribution is as given in (2) and  $\boldsymbol{\theta} = (p, \lambda_1, \lambda_2)$ , and let  $t_{i:n}$  denote the  $i^{th}$  order statistics. The spacings  $D_i$ 's are defined as follows:

$$D_1 = F(t_{1:n}) = 1 - R(t_{1:n}), \quad D_{n+1} = 1 - F(t_{n:n}) = R(t_{n:n}) \\ D_i = F(t_{i:n}) - F(t_{i-1:n}) = R(t_{i-1:n}) - R(t_{i:n}), \quad i = 2, 3, \dots, n$$

where  $R(t)$  is given in (3). Maximum product of spacings (MPS) estimator choose  $\boldsymbol{\theta}$  which maximizes the product of spacings:

$$S(\mathcal{D}|\boldsymbol{\theta}) = \prod_{i=1}^{n+1} D_i \quad (4)$$

In our study, we maximize the product of spacings function (4) using CE algorithm (the CE method was explained thoroughly in [7]) and obtain the maximizer  $\hat{\boldsymbol{\theta}} = (\hat{p}, \hat{\lambda}_1, \hat{\lambda}_2)$ , and then using the invariance property of MSP estimators, we can find the MPS estimators for  $R(t)$ ,  $h(t)$  and  $MTTF$ .

### 3.2 Bayesian estimation

For our mixture model, the Bayesian model is constructed by specifying a prior distribution,  $\pi(\boldsymbol{\theta})$ , for  $\boldsymbol{\theta} = (p, \lambda_1, \lambda_2)$ , and then multiplying with the product of spacing function (4) to obtain the posterior distribution.

$$\pi(\boldsymbol{\theta}|\mathcal{D}) = \frac{S(\mathcal{D}|\boldsymbol{\theta})\pi(\boldsymbol{\theta})}{\int S(\mathcal{D}|\boldsymbol{\theta})\pi(\boldsymbol{\theta})d\boldsymbol{\theta}} \quad (5)$$



The proposed priors for parameters  $p, \lambda_1$ , and  $\lambda_2$  may be taken as

$$\begin{aligned}\pi(p) &= \frac{1}{B(a, b)} p^{a-1} (1-p)^{b-1}, \quad a, b > 0. \\ \pi(\lambda_1) &= \frac{\alpha_1^{\beta_1}}{\Gamma(\beta_1)} \lambda_1^{\beta_1-1} e^{-\alpha_1 \lambda_1} \quad \alpha_1 > 0, \beta_1 > 0. \\ \pi(\lambda_2) &= \frac{\alpha_2^{\beta_2}}{\Gamma(\beta_2)} \lambda_2^{\beta_2-1} e^{-\alpha_2 \lambda_2} \quad \alpha_2 > 0, \beta_2 > 0.\end{aligned}$$

For all parameter, we assume independent priors. Then the joint prior distribution for  $\theta = (p, \lambda_1, \lambda_2)$  is

$$\pi(\theta) \propto p^{a-1} (1-p)^{b-1} \lambda_1^{\beta_1-1} \lambda_2^{\beta_2-1} e^{-(\alpha_1 \lambda_1 + \alpha_2 \lambda_2)}.$$

In our study, we use adaptive Metropolis-Hastings sampling [5] to generate sample  $\theta^{(i)} = (p^{(i)}, \lambda_1^{(i)}, \lambda_2^{(i)})$ ,  $i = 1, \dots, n$  from the posterior distribution (5). Then, Monte Carlo integration estimates  $p^*$ ,  $\lambda_1^*$ ,  $\lambda_2^*$ ,  $h^*(t)$  and  $R^*(t)$  by calculating the means:

$$\begin{aligned}p^* &= \mathbb{E}(p|\mathcal{D}) \approx \frac{1}{n} \sum_{i=1}^n p^{(i)}, \quad \lambda_1^* = \mathbb{E}(\lambda_1|\mathcal{D}) \approx \frac{1}{n} \sum_{i=1}^n \lambda_1^{(i)}, \quad \lambda_2^* = \mathbb{E}(\lambda_2|\mathcal{D}) \approx \frac{1}{n} \sum_{i=1}^n \lambda_2^{(i)} \\ h^*(t) &= \mathbb{E}(h(t)|\mathcal{D}) \approx \frac{1}{n} \sum_{i=1}^n h(t; \theta^{(i)}), \quad R^*(t) = \mathbb{E}(R(t)|\mathcal{D}) \approx \frac{1}{n} \sum_{i=1}^n R(t; \theta^{(i)})\end{aligned}$$

## 4 Illustrative example

In this section, we present an example to illustrate the estimation procedures discussed in this paper. We consider data given in Table 1, which were generated in case  $p = 0.3, \lambda_1 = 0.1, \lambda_2 = 0.2$  and  $n = 30$  and the shape parameter  $k$  is considered to be fixed to two. In this study, we use both CE and MCMC method to estimate the parameters and reliability characteristics. In order to obtain MCMC estimators, prior parameters are arbitrarily taken as  $a = b = 2$  and  $\alpha_1 = \alpha_2 = 0.1, \beta_1 = \beta_2 = 1$  and we ran the Metropolis-Hastings algorithm to construct Markov chain of length 50000 with burn-in of 1000 and reduced the autocorrelation by retaining only every 5 iterations of the chain and obtain 9801 samples. Table 4 shows our CE and MCMC point estimates for  $p, \lambda_1, \lambda_2$  and  $MTTF$ . Fig. 1 shows posterior distributions and traces of each parameter of the Bayesian model obtained by Metropolis-Hastings algorithm, and Fig. 2 shows time courses of reliability and failure rate function obtained by both CE and MCMC method. On the basis of these results, we see that MCMC and CE gave comparable results relatively to small sample size.

## 5 Simulation study

A Monte Carlo simulation study is conducted to compare the performance of CE and MCMC estimators for the parameters of mixture failure rate. For each of the

**Table 1.** Data simulation in case  $p = 0.3, \lambda_1 = 0.1, \lambda_2 = 0.2, k = 2$  and  $n = 30$

3.697	1.001	4.112	4.322	2.192	0.844	3.314	2.085	0.259	3.746
2.361	2.183	2.910	2.382	2.790	2.599	2.899	2.353	2.824	2.774
2.371	2.239	1.012	1.570	3.795	4.352	2.722	1.625	3.277	1.770

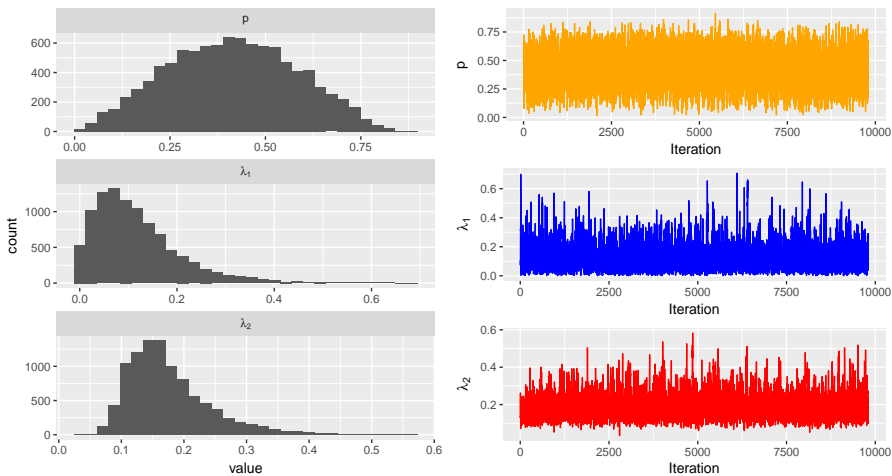


**Fig. 1.** Histograms and traces of each parameter of the Bayesian model

**Table 2.** Point estimates for  $p, \lambda_1, \lambda_2$  and  $MTTF$

	True value	CE	MCMC
$p$	0.3	0.395	0.428
$\lambda_1$	0.1	0.158	0.128
$\lambda_2$	0.2	0.163	0.185
$MTTF$	2.379	2.532	2.605

following choice of parameters, we simulate 1000 sets of data with sample size  $n = 25, 50, 100$  and  $200$ , respectively, and based on each set of data we computed the CE and MCMC estimator for the model parameters,  $\theta = (p, \lambda_1, \lambda_2)$ . In order to obtain MCMC estimators, prior parameters are taken as in section 4, and we ran the Metropolis-Hastings algorithm to construct Markov chain of length 20000 with burn-in of 1000 and reduced autocorrelation by retaining only every 5 iterations of the chain and obtain 3801 samples.

- $p = 0.1, \lambda_1 = 0.1, \lambda_2 = 0.2, k = 1, 2, 3$
- $p = 0.5, \lambda_1 = 0.1, \lambda_2 = 0.2, k = 1, 2, 3$
- $p = 0.9, \lambda_1 = 0.1, \lambda_2 = 0.2, k = 1, 2, 3$

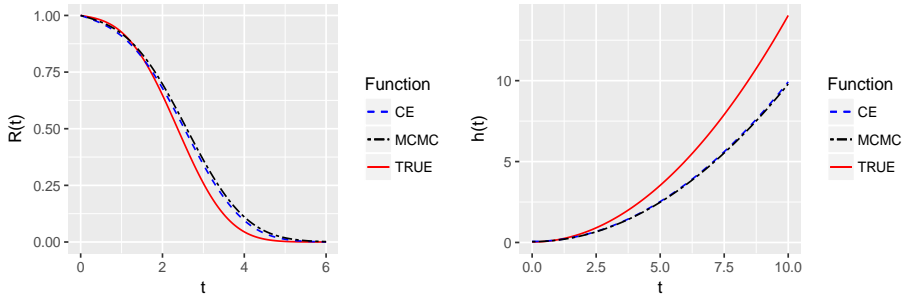


**Fig. 2.** The time courses of reliability and failure rate functions

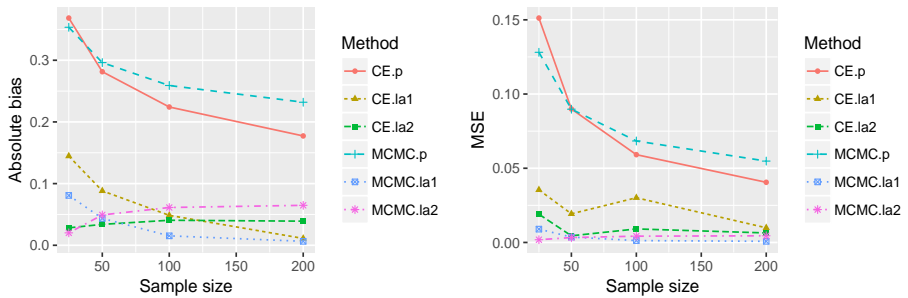


**Fig. 3.** Comparison of bias and MSE of  $\hat{\theta}$  and  $\theta^*$  for  $\theta = (0.1, 0.1, 0.2)$ ,  $k = 1$

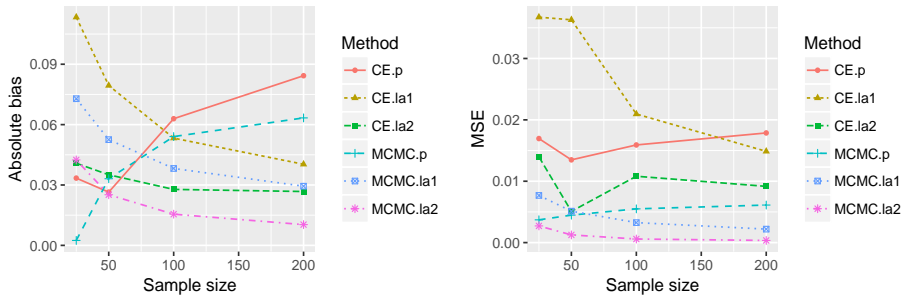


**Fig. 4.** Comparison of bias and MSE of  $\hat{\theta}$  and  $\theta^*$  for  $\theta = (0.5, 0.1, 0.2)$ ,  $k = 1$

Due to page restrictions, Figs. 3-5 are a part of our simulation results. They show the bias and MSE obtained from the simulation study. From the comparison of estimates, we observe the following:

- When  $p$  is close to 0 and sample size is small, say less than 50, MCMC performs a bit better than CE with respect to bias and MSE. But when sample is larger than or equal to 50, CE performs better than MCMC. In this case, the bias for  $p$  is quite high for both methods.

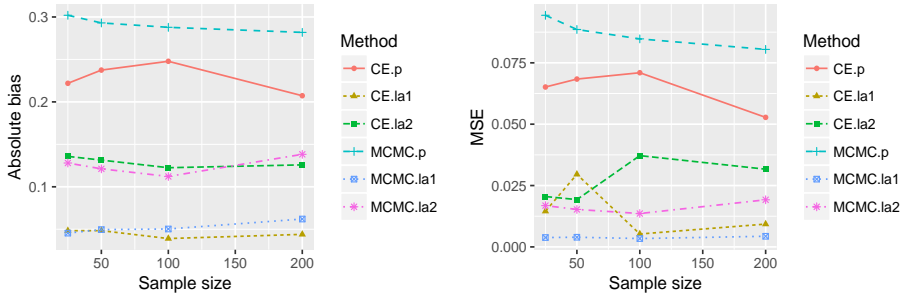


**Fig. 5.** Comparison of bias and MSE of  $\hat{\theta}$  and  $\theta^*$  for  $\theta = (0.9, 0.1, 0.2)$ ,  $k = 1$

- When  $p$  equals to 0.5, both CE and MCMC method gave small bias and MSE. In this case, MCMC performs better than CE.
- When  $p$  is close to 1, MCMC shows higher bias and higher MSE for  $p$  than CE. In this case, the bias for  $p$  is quite high for both methods.
- The bias becomes less with increasing  $k$ .

## 6 Conclusion

Compared to our previous study, this study shows that the estimators based on product of spacings function are more stable and less bias as well as MSE than the estimators based on likelihood function. Nevertheless, when  $p$  is close to 0 or 1, the bias and MSE for  $p$  given by both method are still high to ignore.

## References

1. Lawless, J. F.: *Statistical Models and Methods for Life-time Data*, 2nd ed. Wiley-Interscience, 2002.
2. Mann, N., Schaffer, E., Singpurwalla, N.: *Methods for Statistical Analysis of Reliability and Life Data*, New York: Wiley, 1974.
3. Sinha, S. K.: *Reliability and Life Testing*, USA: Wiley Eastern Ltd, 1986.
4. Sharma, K. K., Krishna, H., Singh, B.: *Bayes estimation of the mixture of hazard rate model*, Reliability Engineering and System Safety, vol. 55, pp. 9–13, 1997.
5. Chivers, C.: *MHadaptive: General Markov Chain Monte Carlo for Bayesian Inference using adaptive Metropolis-Hastings sampling*, R package version 1.1-8. [Online]. Available: <https://CRAN.R-project.org/package=MHadaptive>
6. Thach, T. T., Bris, R., Coolen, P. A. F.: *Mixture Failure Rate: A study based on cross-entropy and MCMC method*. Proceedings of the International Conference on Information and Digital Technologies. IEEE Inc, 2017.
7. Rubinstein, R. Y., Kroese, D. P.: *The Cross-Entropy method: a unified approach to combinatorial optimization, Monte-Carlo simulation and machine learning*, Springer Science & Business Media, Inc, 2004.

# Influence of Load by High Power on the Optical Coupler

Lukáš Bednárek

Department of Telecommunications, FEECS,  
VŠB – Technical University of Ostrava, 17. listopadu 15,  
708 33 Ostrava – Poruba, Czech Republic  
lukas.bednarek@vsb.cz

**Abstract.** This paper deals by findings of the influence of the load by laser with high optical power on the transmission parameters of the optical coupler. The investigated coupler has one input and eight outputs (1x8). Load by laser with high optical power is realized using a fiber laser with a cascade configuration EDFA amplifiers. The output power of the amplifier is approximately 250 mW. Duration of the load is moving from 104 hours to 139 hours. After each load, input power and output powers of all branches are measured. Following parameters of the optical coupler are calculated using formulas: the insertion losses of the individual branches, split ratio, total losses, homogeneity of the losses and cross-talk between different branches. All measurements are performed at wavelengths 1310 nm and 1550 nm. Individual optical powers are measured 20 times, due to the exclusion of statistical error of the measurement. After measuring, the coupler is connected to the amplifier for next cycle of the load. The paper contains an evaluation of the results of the coupler before and after four cycles of the burden.

**Keywords:** optical coupler, aging, stress by high optical power, insertion losses

## 1 Introduction

Passive optical elements, which are used in PON networks, are exposed to ever increasing loads. These elements were not originally designed for such loads. Therefore faster aging of such elements occurs than initially expected. Aging of parameters of passive optical components is not only limiting for communication purposes. This aging decreases even the sensitivity of optical sensors. Since, aging of parameters cause worse passage of light through the optical components, thereby reducing the sensitivity of the optical sensor and the consequent bad evaluation of the scanned value. The paper deals with the optical coupler which is widely used both in PON networks and in optical fiber interferometers (most Mach-Zehnder type).

Loading coupler has a configuration with one input and eight outputs (1x8). Specifically, we deal with five basic transmission parameters. The investigated parameters are insertion loss of individual branches, split ratio, total losses, homogeneity of

losses and directionality between the output branches. The paper shows the first research of a load of the coupler by high optical power. Loads were carried out in 4 cycles with a total time of 466 hours.

## 2 Load of optical coupler and measurement method

A load of the optical coupler was carried using a cascade involvement of EDFA amplifiers. A more detailed description of this arrangement is given below.

Fiber amplifier with erbium doped fiber (FiberCore IsoGain I-6) was manufactured as the first stage. Erbium doped fiber produces light with a wavelength of 1550 nm. A laser diode with a wavelength of 978 nm provides energy to this fiber. Appended light power is 600 mW. Pumping light with a wavelength of 980 nm is supplied through the 1550/980 nm WDM coupler. The erbium doped fiber with a length of 6 meters is followed. Behind him, coupler with a split ratio of 90/10 is connected. Output with 10 % of the power creates an output part of the entire first stage. Output with 90 % of the power is attached to the isolator which is connected to the input of 1550/980 nm WDM coupler. The loop is created because of this. Therefore, it is a laser with a circular resonator. The output power of the first stage is 75.85 mW.

Standard EDFA amplifier creates the second stage. The used laser diode has an output power of 500 mW at a wavelength of 980 nm. A 1550/980 nm WDM coupler with an integrated isolator brings pumping light to the erbium doped fiber. The used fiber was Liekki ER110-4/125 with a length of 40 cm. This short length was used because of the high absorption of the fiber of about 110 dB per meter. The resulting output power is 250 mW, which is also taken as the load power.

A device EXFO AXS-200/350 provided the measurement. This device was used as a source of optical power and as the detector at the same time. The measurement was carried out in two phases. In the first step, an input optical power was measured. The input power was measured by a 1C method according to the standard (ISO/IEC 14763-3 (Implementation and Operation of Customer Premises Cabling, Testing of Optical Fiber Cabling)), thus using the three optical fibers. A short optical patchcord connected optical fibers from and to the device. This adjustment was necessary to remove the influence of the auxiliary optical fibers (from the laser and to the detector). The transmission power from the laser was set to 2 mW for the wavelengths 1310 nm and 1550 nm. Measured optical power was lower, but losses were minimal. This power was considered as input power  $P_0$ . In the second phase, the middle fiber was removed and replaced by measured coupler. Input branch of the coupler was connected to the fiber from laser and output branches were gradually connected to the optical fiber leading to the detector. All the branches of the coupler were measured at the wavelengths 1310 nm and 1550 nm. The measured powers were designated as  $P_1$  up to  $P_8$ . All measured powers were measured 20 times. Measurement error is thus eliminated. The average of these values was taken as the resulting value to calculate the parameters of the optical coupler.

### 3 Results

Meanwhile, we have made four load cycles. The lengths of the individual cycles were 139 hours, 113 hours, 110 hours and 104 hours. The total load time was 466 hours. Load cycles are carried out in succession. Among loads, the delay which was caused by measurement was approximately 4 hours.

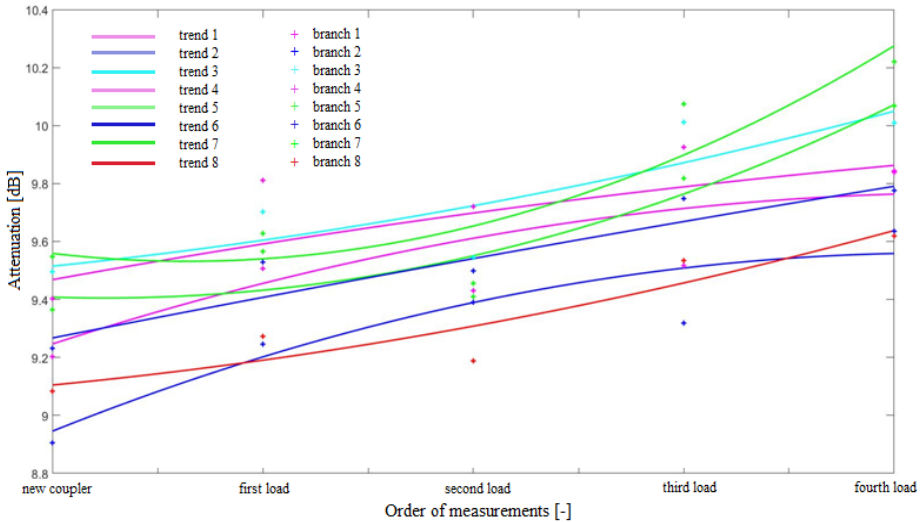


**Fig. 1.** The insertion loss for wavelength of 1310 nm

Figure 1 shows a graph of insertion loss for a wavelength of 1310 nm. Approximated curves show the trend of insertion loss for individual branches. All branches have an increasing trend. Only, branch 6 has a constant course. However, a difference of insertion losses is minimal for the new coupler and coupler after four cycles of a load.

The measurement showed the following values after 4th load: maximum insertion loss was 9.79 dB for branch 4 and minimum insertion loss was 9.25 dB for branch 3.

In Figure 2, a graph shows insertion loss for a wavelength of 1550 nm. All branches have a strong upward trend. The difference of insertion losses is approximately 1 dB for all branches before load and after four cycles of loading. Dispersion of measured values is less than at the previous wavelength. Measured values are very similar in 3rd and 4th of the loading. The maximum insertion loss was 10.69 dB for branch 4; conversely, the minimum insertion loss was 10.01 dB for branch 8.

Figure 3 displays the approximated curves of the split ratio for the wavelength of 1310 nm. Branches 1, 4 and 6 have a rising trend. Conversely, the branches 5 and 7 have a strong downward trend, whereby is offset a rising trend in other branches. Branches 2, 3 and 8 have a constant or slightly rising trend. From the graph, we can see that the dispersion of value is large for the 3rd load and 4th load. However, the maximum change of split ratio is approximately 2.5 % for branch 1. After cycles of load, the maximum split ratio was 14.2 % for the branch 8, and the minimum split ratio was 10.3 % for branch 1.

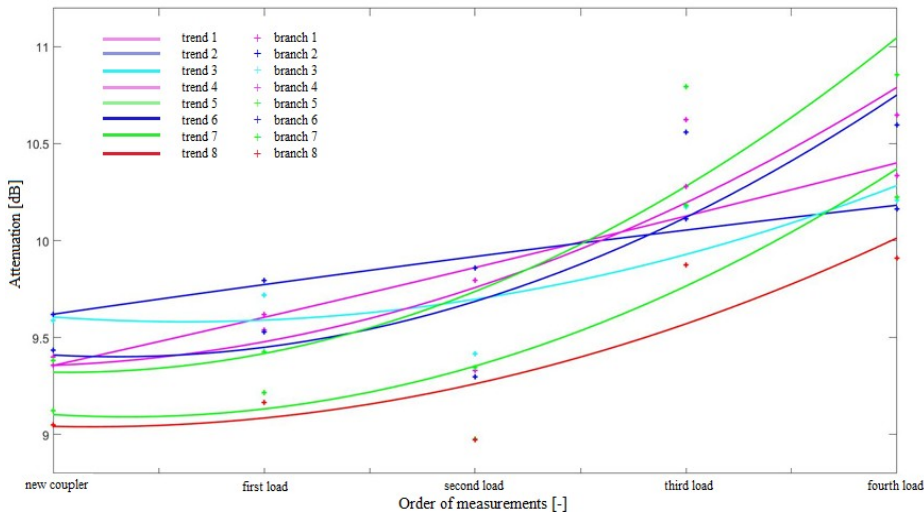


Fig. 2. The insertion loss for wavelength of 1550 nm

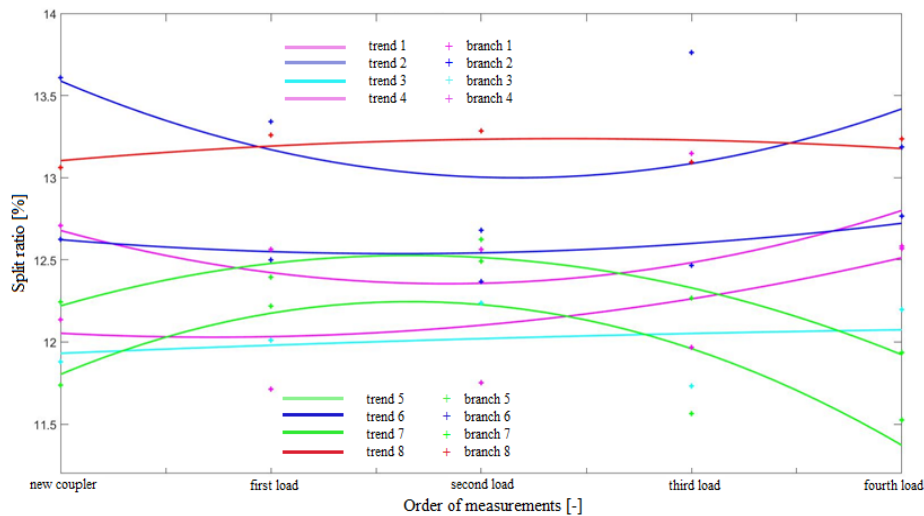
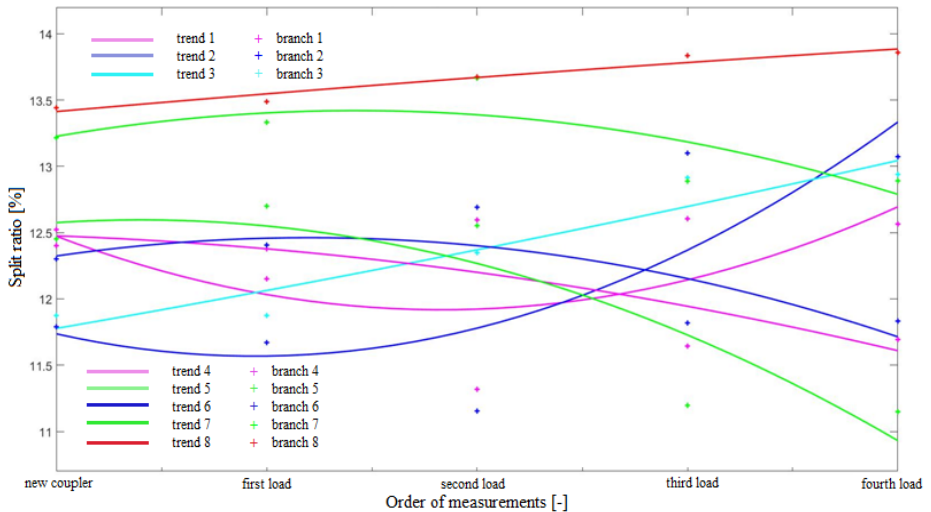


Fig. 3. The split ratio for wavelength of 1310 nm

Curves of the split ratio, for a wavelength of 1550 nm, are displayed in Figure 4. Already at first glance, the curves of individual branches are different than at the previous wavelength. Branches 1 and 6 have a strong upward trend. Branches 3 and 8 have a rising trend. Branches 2, 4, 5 and 7 have a decreasing trend. The dispersion of values is smaller than at previous wavelength; the biggest variance is in 3rd load. After the 4th load, a maximum split ratio was 13.45 % for the branch 8, and a minimum split ratio was 11.54 % for the branch 6.





**Fig. 4.** The split ratio for wavelength of 1550 nm

The next paragraph describes the total loss parameter. The wavelength of 1310 nm has a slightly downward trend. On the other hand, the wavelength of 1550 nm has a strong upward trend. Scattering of the measured values is large for a wavelength of 1550 nm. For the wavelength of 1310 nm, the total losses have a maximum value of 0.46 dB at the first load. Conversely, the minimum value is 0.15 dB at the second load. For the wavelength of 1550 nm, the total losses have a maximum value of 1.13 dB at the third load. The minimum value of total losses is 0.33 dB at the second load.

The waveforms and the measured data of the homogeneity of losses are as following. The trend is rising for a wavelength of 1550 nm. On the other hand, the wavelength of 1310 nm has a constant or slightly rising trend. Homogeneity of losses is approximately 0.6 dB for a new coupler, the first and the last loads. At the second and third loads, the value of homogeneity of losses increased on approximately 0.9 dB. Maximum homogeneity of losses was 1.13 dB for a wavelength of 1310 nm at the second load. The highest homogeneity of losses was 0.92 dB for the second wavelength at third load. Minimum values of homogeneity losses were 0.54 dB for a wavelength of 1310 nm at last load and 0.57 dB for a wavelength of 1550 nm at the new coupler.

The last investigated parameter is directionality. I measured a substantial amount of data, so these data are not listed here, but I only described these data. For the new coupler, the directionality was higher than 73 dB for all combinations of output branches. The only exception was a combination of 3-4, where the directionality had the value of 66 dB for both wavelengths. The first loading caused reduction of directionality on the 69 dB for the wavelength of 1310 nm and 70 dB for the wavelength of 1550 nm for all combinations. Conversely, the combination of 3-4 is improved on values of 67 dB and 68 dB at the first load. The second load caused a significant deterioration of directionalities. For all combinations, values decreased to 56 dB for a

wavelength of 1310 nm and 58 dB for the second wavelength. The third loading brought again improve directionalities for all combinations of output branches. Values were approximately 71 dB for the wavelength of 1310, and 72 dB for the wavelength of 1550 nm. The last load did not cause the change of directionalities. The values were almost the same as in the previous load.

## 4 Conclusion

The individual branches of the coupler have the little variance of values of insertion losses for each load and each wavelength. This variance results from the fact that it is not possible to produce a coupler so that all branches have the same insertion losses. Displayed graphs of split ratios show that distribution of power between the different branches slightly varies after the load. This variance is most likely caused by a small change in the coupling region. The split ratio is dependent on this coupling region. The sum of the values must be 100 %, which is met in each load. The parameter of total losses showed a big difference between wavelengths. While load caused an increase of values for the wavelength of 1550 nm, values were similar for the wavelength of 1310 nm in all loads. Homogeneity of losses showed an increasing trend for both wavelengths. Measured values match the theory. The higher values are only for second and third loads. It is due to large differences in insertion losses. The parameter of directionality reached values which are sufficient for trouble-free operation of the coupler in all measurements. Only the second load caused a significant deterioration of directionality, but values were still above the threshold for operation without any problems.

## 5 References

1. Vasinek V., Hajek L., Bednarek L., Vanderka A., Hlavinka T., Marcinka O., *Influence of gamma radiation on optical fibers and devices* In: International Conference on Photonics Solutions 2015, 2015, DOI: 10.1117/12.2196372
2. Bednarek L., Marcinka O., Perecar F., Papes M., Hajek L., Nedoma J., Vasinek V., *The aging process of optical couplers by gamma irradiation* In: Photonic Fiber and Crystal Devices: Advances in Materials and Innovations in Device Applications IX, 2015, DOI: 10.1117/12.2187044
3. Perecar F., Marcinka O., Bednarek L., Lucki M., Liner A., Hajek L., Papes M., Jaros J., Vasinek V., *The impacts of ageing effects due to radiation burden on optical fiber couplers* In: Photonic Fiber and Crystal Devices: Advances in Materials and Innovations in Device Applications IX, 2015, DOI: 10.1117/12.2187517
4. Vasinek V., Siska P., Bednarek L., Latal J., Koudelka P., Marcinka O., *Ageing of fiber optical devices* In: Next-Generation Optical Communication: Components, Sub-Systems, and Systems IV, 2015, DOI: 10.1117/12.2087165
5. Bednarek L., Hajek L., Vanderka A., Nedoma J., Fajkus M., Zboril O., Vasinek V., *The influence of thermal aging on the optical coupler*, In: Photonic Fiber and Crystal Devices: Advances in Materials and Innovations in Device Applications X, 2016, DOI: 10.1117/12.2236294

# VoIP Honeypot Development used in the CESNET Network

Ladislav Behán

Department of Telecommunications, FEECS,  
VŠB – Technical University of Ostrava, 17. listopadu 15,  
708 33 Ostrava – Poruba, Czech Republic  
ladislav.behan@vsb.cz

**Abstract.** VoIP is the telecommunication technology, which continually develops and provides telecommunications services to a wide range of customers. VoIP providers are investing considerable funds into the development of its own network infrastructure, as well as to its safety. Ensure security of the VoIP services is not entirely trivial matter and attacks on telecommunication solutions, built on VoIP technology, will grow with a larger number of customers. For this reason, it is necessary to detect these attacks, catch the progress of such an attack and then prepare an effective defense against these attacks. The best way to detect attacks on VoIP infrastructure is VoIP Honeypot. The main motivation for the development of own honeypot for VoIP service is nonexistent actively developing project with a similar task, which is adapting the new security, threats and it is developed according to the needs of the telecommunications market. Honeypot for VoIP services is purely software matter and the development of these solutions will be based on the virtualization, especially with a focus on VMware. The solution will be based on a Linux distribution and will be prepared in a virtual environment for the simplest deployment and clustering.

**Keywords:** honeypot, VoIP attacks, VoIP honeypot, Register flood, Invite flood, Options flood, Spit attack.

## 1 INTRODUCTION

This paper describes the use of honeypots in a VoIP infrastructure. These systems become increasingly necessary as the number of IP-based telephony solutions rises. Nearly all large companies today rely on some kind of IP telephony in their internal communication. This situation only induces greater hacker interest in these services. Nowadays, many companies have experienced abuse such as social engineering or spit calls.

Threat analysis and detection is recently a highly discussed topic. However, there is no solution suitable for VoIP telephony. There are projects aimed at detecting attacks and preparing so-called fake attack targets. Most of these projects ended their development. A typical example of a VoIP honeypot is the Artemisa project. Development of Artemisa project ended in 2011 and there is no REGISTER flood detection integrated.

Another project that is focused on VoIP technology is Dionaea project. This project does not fully focus on VoIP technology. It also focuses on another network services and the VoIP support is not very sophisticated.

A very important feature of all honeypots is the export of captured attacks and possibly the subsequent analysis of these attacks by standard tools. We will integrate the export into standard format and also into the CESNET MENTAT system.

VoIP telephony was previously used by a small number of users. At present, more and more participants are connected via VoIP without having clue about it. Typical examples are the 4<sup>th</sup> generation mobile networks and VoWiFi technology. Based on the needs of security experts and VoIP companies, VoIP honeypot will be developed to simplify the detection of attacks on VoIP infrastructure.

The main goal of this project will be to design and develop custom VoIP honeypot solution. This honeypot will be developed as an open source project with relevant documentation, so it can be developed and modified by various organizations.

This project will focus mainly on SIP (Session Initiation Protocol), which is nowadays very often used as a signaling protocol in VoIP telephony. The main features of VoIP honeypot will include both threat detection and proactive responses on attacks on VoIP infrastructure.

VoIP honeypot will include following features:

- INVITE flood attack detection,
- OPTIONS flood attack detection,
- REGISTER flood attack detection,
- Integration of SPIT detection mechanism,
- audio and video message recording,
- Automatic search for sources of attacks by using WhoIS service.

There will be an information and communication solution integrated into our honeypot:

- Collaboration and information exchange between VoIP honeypots – information of source and type of attacks will be passed between honeypots,
- VoIP Honeypots will create fake VoIP traffic among themselves, which increases the possibility of attack,
- Logged data will be stored in a structured format,
- MENTAT data export support will be added
- Honeypot VoIP management will be done through VoIP Honeypot admin.

A test platform will be created and deployed by at least three members of the CESNET association and one foreign organization within the NREN group, which is also a member of the TERENA group.

The rest of this paper is organized as follows: In Section 2, the implementation of CESNET honeypot is described in details. The Section 3 shows the interim results. Section 4 concludes the paper.

## 2 DESIGN AND IMPLEMENTATION OF THE CESNET HONEYPOT

Our VoIP honeypot solution is implemented in C programming language. The program consists of three parallel running threads.

The first thread captures and filters all packets on a defined interface by using libpcap. In honeypot configuration file, you can also set the pcap filter to capture specific packet types. In our honeypot, we focus on the UDP protocol filtration through which SIP communication takes place. If one of the INVITE, REGISTER or OPTIONS messages appears at the interface, then these messages are further processed. If a certain number of identical packets are received during the preset time interval then one of the flood attacks is detected. Honeypot will then find out the attackers IP address and by using the WhoIS function it determines the origin of the attacker. Honeypot will finally generate message which will be exported to the CESNET MENTAT system and it will send information about the attack to other honeypots.

*INVITE FLOOD;188.138.41.235;195.113.113.152;5086;5060;PlusServer GmbH;Welserstr. 14;51149 Koeln*

The second thread focuses on detecting SPIT attacks and also creating false VoIP traffic. For its functionality, it uses features from the pjsua library. Based on the set values in the configuration file, honeypot registers to the Asterisk PBX as a SIP phone. In the event of successful registration, it subsequently receives the calls or creates a telephone connection at random intervals to randomly selected numbers generated from a preset number range. Another feature of this thread is SPIT attack detection. In the case of an incoming call, honeypot will answer the call. If the total call duration was less than for example 10 seconds, the call is considered as a potential SPIT attack, the caller ID is stored in the database. However, if the inbound call is repeatedly marked as a suspicious and the threshold rating factor value is exceeded it will be considered as a SPIT attack, the WhoIS mechanism will determine its origin, MENTAT message is generated and other honeypots are informed about this attack.

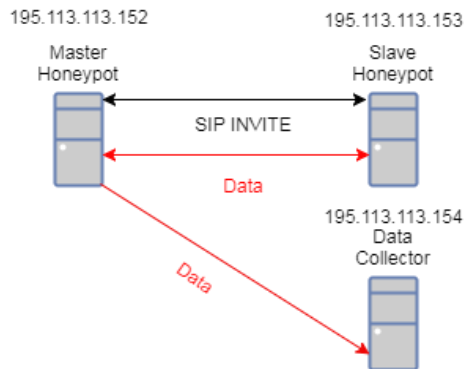


**Fig. 1.** Honeypot architecture

The last thread is intended for server-client communication. In our proposed architecture, there is one master server honeypot and all others are slave honeypots. This communication thread retrieves information from the other threads about the attack via shared memory. If the honeypot master server was attacked, he sends the information about the attack to all other honeypots. If one of the slave devices was attacked, slave honeypot informs server about the attack, which then sends this information further to all other honeypots in our network.

3      **INTERIM RESULTS**

In Table 1 you can see an overview of the countries from where the attacks were made and the total number of attacks on our honeypot. According to the data processed, the most active attackers are from France.

**Table 1.** All attacks

COUNTRY	COUNT
France	754
Germany	142
Czechia	38
Ireland	36
Untraceable IP	1167

Table 2 shows the total count of INVITE flood attacks. We register most of the attacks again from France.

**Table 2.** Invite Flood

COUNTRY	COUNT
France	47
Czechia	10
Untraceable IP	107

Table 3 shows us the number of REGISTER flood attacks.

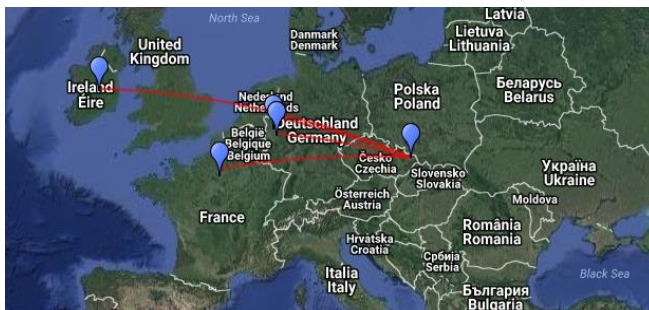
**Table 3.** Register Flood

COUNTRY	COUNT
France	707
Germany	35
Czechia	18
Ireland	36

The number of OPTIONS flood attacks is shown in Table 4. We register this type of attack only from Czechia.

**Table 4.** Options Flood

COUNTRY	COUNT
Czechia	10

**Fig. 2.** Map of attacks

## 4 CONCLUSION

In this article, we demonstrated the implementation of a VoIP honeypot which will be used in the CESNET network. First of all, we have integrated INVITE, OPTIONS and REGISTER flood detection. SPIT attack detection is also integrated in our system. We integrated the WhoIS mechanism into honeypot which can determine the country of the attacker. All VoIP honeypots are creating fake VoIP traffic among themselves, they also exchange information of source and type of attacks and they support MENTAT data exportation.

As it was mentioned before, honeypot is currently in the testing phase. At the time of writing this article, there is only one honeypot running in our school network. In the near future, the honeypot network will be expanded by two other locations in Czechia

and one honeypot will be located in Colombia University. However, as you can see within a month of our test operation, we recorded over 2000 attacks.

## 5 REFERENCES

- [1] Voznak, M., Kapicak, L., Mikulec, M., Nevlud, P., Zdralek, J.: The Interactions of SOAP-based Web Services for Recording and Replaying Video Files, Computer Networks 2012, In SPRINGER Communications in Computer and Information Science, CCIS Volume 291/2012, Szczyrk, June 2012, pp. 1-13, DOI 10.1007/978-3-642-31217-5\_1
- [2] Kapicak, L., Nevlud, P., Mikulec, M., Zdralek, J.: Objective Assessment of IP Video Calls with Asterisk, In Journal Advances in Electrical and Electronic Engineering, Vol. 10, Issue 4, 2012, ISSN 1336-1376
- [3] Uhrin, D., Partila, P., Voznak, M., Chmelikova, Z., Hlozak, H., Orcik, L.: Design and Implementation of Czech Database of Speech Emotions, 22nd Telecommunications Forum Telfor, TELFOR 2014, November 2014, pp. 529-532.
- [4] Reghuvaran, C., Bestak, R., Patra, S. K.: An Interference Cancellation Scheme for D2D Multi-Link Communication Underlying Cellular Network. Annals of Telecommunications. 2015, vol. 71, no. 1, p. 47-60. ISSN 0003-4347.
- [5] Mach, P., Bestak, R., Becvar Z.: Optimization of association procedure in WiMAX networks with relay stations. Telecommunication Systems. 2013, vol. 52, no. 3, p. 1697-1704. ISSN 1018-4864.
- [6] F. Rezac, M. Voznak, J. Ruzicka, "Security Risks in IP Telephony", CESNET CONFERENCE 2008-SECURITY, pp.31-38, 2008
- [7] F. Rezac, M. Voznak, K. Tomala, J. Rozhon, J. Vychodil, "Security Analysis System to Detect Threats on a SIP VoIP Infrastructure Elements" in Advances in Electrical and Electronic Engineering, Vol. 9, No. 5, pp. 225-232, 2011.
- [8] M. Voznak, F. Rezac, K. Tomala, "SIP Penetration Test System", TSP 2010: 33RD INTERNATIONAL CONFERENCE ON TELECOMMUNICATIONS AND SIGNAL PROCESSING, pp. 504-508, 2010.
- [9] M. Voznak, F. Rezac, "SPAM over Internet telephony", in Proceedings of 11th International Conference on Research in Telecommunication Technology (RTT 2009), Srby, pp. 119-121, 2009.



# Analysis of Bitrate and Chroma Subsampling on Video Quality Assessment

Jaroslav Frnda

Department of Telecommunications, FEECS,  
VŠB – Technical University of Ostrava, 17. listopadu 15,  
708 33 Ostrava – Poruba, Czech Republic  
jaroslav.frnda@vsb.cz

**Abstract.** This paper deals with the analysis of offered video quality for two well-known codecs dedicated for digital TV broadcasting, namely H.264 and H.265 (HEVC). Chroma subsampling and bitrate have a significant influence on their quality and operators have to find a compromise how to set these parameters. H.265 is successor of H.264 and offers better compression ratio but on the other hand, needs higher computational power. Objective metrics are based on mathematical models and calculate a score that represents visual quality of codecs. Several test scenarios were performed and obtained results allowed us to compare the level of quality for both video codecs.

**Keywords:** Bitrate, H.264/AVC, H.265/HEVC, SSIM, Subsampling

## 1 Introduction

In the last decade video service has begun a majority part of all data transmitted via IP based networks. The video quality is affected by several parameters, especially resolution, bitrate, compression technique and finally transmission link imperfection. New video codecs allow to bring still higher resolutions and visual quality accompanied by increased efficiency of network capacity consumption. By 2016, 4K television market (that adopted UHD resolution 3840x2160 as 4K standard, but it is not a “true” 4K resolution) share had increased greatly as prices fell dramatically during last two years. Many sports performances and new TV series are now available for end-users who have 4K TV with HEVC decoder. Today some institutes and research teams deal with video quality evaluation but most of them focus on the FullHD resolutions [1], [4], [10]. Because of this, paper describes impact of H.264/AVC and H.265/HEVC compression standards on the video quality also for UHD resolution. In papers [11-12] the objective quality assessment of the newest compression standards as H.265/HEVC and VP9 has been examined but the reference and still the most used compression standard H.264 was not considered. In all mentioned papers, the influence of chroma subsampling on the video quality has not been analysed. Therefore, the aim of this paper is to parse how the chroma subsampling effects the video quality measured by selected objective metrics.

## 1.1 Chroma Subsampling

Chroma subsampling is the practice of encoding images by implementing less resolution for chroma information than for luma information. This is due to our human visual system which is less sensitive to colour than to luminance. So, the video system can be optimized by devoting more bandwidth to the luma component (usually denoted Y or Y' after gamma correction), than to the colour difference components Cb and Cr. The subsampling scheme is commonly expressed as a three part ratio A:B:C (e.g. 4:2:2). The parts are (in their respective order):

- A: horizontal sampling reference (width of the conceptual region). Usually 4.
- B: number of chrominance samples (Cr, Cb) in the first row of A pixels.
- C: number of changes of chrominance samples (Cr, Cb) between first and second row of A pixels.

The scheme with no subsampling is 4:4:4, the most used subsampling scheme for digital broadcasting is 4:2:0 (bandwidth is halved compared to no chroma subsampling) [6], [10].

## 1.2 H.264/AVC and H.265/HEVC Compression Standards

Although H.264/AVC codec was developed in 2003 is still one of the most used compression standards. It has been designed for a wide range of applications, ranging from video for mobile phones through web applications to TV broadcasting (HDTV). H.264/AVC also defines profiles and levels. There are several profiles currently defined: Baseline, Main, Extended and High which is adopted by Blu-ray Discs and digital TV broadcasting. Level is a specified set of constraints that indicate a degree of required decoder performance for a profile. For example, a level of support within a profile specifies the maximum picture resolution, frame rate, and bit rate that a decoder may use [1], [5].

The High Efficiency Video Coding (HEVC) standard is the most recent joint video project of the ITU-T Video Coding Experts Group (VCEG) and the ISO/IEC Moving Picture Experts Group (MPEG) standardization organizations, working together in a partnership known as the Joint Collaborative Team on Video Coding (JCT-VC). H.265/HEVC has the same basic structure as previous standards such as MPEG-2 and H.264/AVC. The result is a video coding standard that can enable better compression, at the cost of potentially increased processing power. With H.265/HEVC, it should be possible to store or transmit video more efficiently than with earlier technologies such as H.264/AVC. This means that at the same picture size and quality HEVC video sequence should occupy less storage or transmission capacity than the equivalent H.264 video sequence. Secondly, at the same storage or transmission bandwidth, the quality and/or resolution of an HEVC video sequence should be higher than the corresponding H.264 video sequence [2], [7].

### 1.3 Objective assessment methods

The video quality evaluation can be divided into objective and subjective assessment. The subjective assessment consists of the use of human observers (people) who score the video quality. It is the most reliable way how to determine the video quality. The disadvantage of these methods is that they are time consuming and human resources are needed. Because of this fact, the objective methods are mostly used. They consist of the mathematical computational methods called “metrics” that produce values that score the video quality. The well-known and mostly used objective metrics are peak signal-to-noise ratio (PSNR), video quality metric (VQM) and structural similarity index (SSIM). First metric is the oldest one with worse adaption of human perception than metrics SSIM and VQM [2], [3], [4].

The SSIM metric measures three components, the luminance similarity, the contrast similarity and the structural similarity and combines them into one final value, which determines the quality of the test sequence. It is due to the human vision system that is highly specialized in extracting structural information from the viewing field and it is not specialized in extracting the errors. Owing to this factor, SSIM metric achieves good correlation with subjective impression. As an output is defined a score from 0 to 1 where 1 represents two identical pictures [1], [2].

## 2 Measurements

Nowadays some free databases (research teams offer theirs testing databases for free of use) containing testing video sequences used for video quality evaluation. We used a database contains uncompressed video sequences in YUV format with UHD resolution [8]. In our experiments three types of test sequences were used:

- “Construction Field” – shot on the construction site, where the static background is represented by buildings under construction, dynamic objects are represented by construction vehicles (excavator) and walking workers. The slow-motion scene captured statically.
- “Runners” – the running challenge. The camera is static, located in the front of the runners slightly angled to the side (higher spatial information). Scene is relatively dynamic
- “Wood” – the forest scenery. The shot on the trees in the forest (captured objects are static), the motion of the camera is from the left to the right side and the motion is accelerating in the sequence. Relatively high value of the spatial and temporal information.



**Fig.1.** Video sequence Construction Field (left) and Runners (right)

All sequences were in the UHD resolution (3840x2160) and 16:9 aspect ratio with 30 fps (frames per second). The length of these sequences was 300 frames, i.e. 10 seconds. The measurement procedure consists of following steps:

First, all sequences were downloaded from [8] in the uncompressed format (\*.yuv) and used as the reference sequences. Afterwards, they were encoded to both MPEG compression standards, H.264/AVC and H.265/HEVC, using the x264 and x265 tool respectively (FFmpeg software). The target bitrates were 1 up to 15 Mbps and the GoP size was set to the half of the framerate, i.e. M=3, N=15. Finally, the quality between these sequences (encoded back to YUV format) and the reference (uncompressed) sequence was compared and evaluated. This was done using the MSU Measuring Tool Pro version 3.0. SSIM objective metric for the measurements was used [9].

**3 Results**

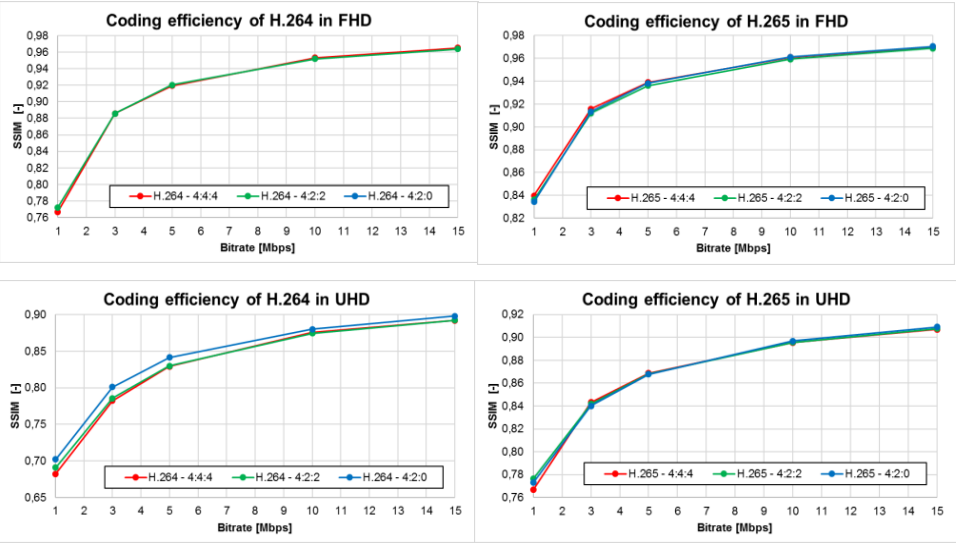


**Fig.2.** The impact of the chroma subsampling on the video quality of both compression standards of all test sequences for both resolutions.

Figures above show the impact of the chroma subsampling on the video quality measured by SSIM metric of both compression standards for all test sequences for FHD and UHD resolution. Calculated results depending on the codec, resolution and bitrate.

According to the experimental results several conclusions can be pronounced:

- The impact of chroma subsampling on the video quality is negligible – there is no difference between unsampled (4:4:4) and subsampled (4:2:2; 4:2:0). It follows that it is more useful and reasonable to use chroma subsampled – you can save up to 50% of the bandwidth by the same quality.
- As we assumed the H.265/HEVC compression standard yields better compression efficiency than H.264/AVC compression standard - at the same resolution and bitrate the compression quality of H.265/HEVC standard is better than H.264/AVC. The quality of both compression standards rises logarithmically with increasing bitrate – in low bitrates the quality grows faster than in high bitrates.
- The coding efficiency of H.265/HEVC standard is more visible in UHD resolution.

## 4 Conclusion

This paper deals with the influence of chroma subsampling on video quality measured by objective metric for H.264/AVC and H.265/HEVC compression standards. The evaluation was done for several types of sequences with Full HD and Ultra HD. The experimental results showed that there is no impact of chroma subsampling on the video quality – there is no difference between unsampled (4:4:4) and subsampled (4:2:2; 4:2:0). According to the results it can be also said that H.265/HEVC codec yields better compression efficiency than H.264/AVC and the difference is more visible in UHD resolution. The bigger difference in quality is in lower bitrates - with increasing bitrate the quality of H.264/AVC codec approach the H.265/HEVC codec.

## Acknowledgements

This work was supported by the internal grant of Faculty of Electrical Engineering and Computer Science SGS No. SP2017/174.

## Recent publications

1. J. Frnda, M. Voznak, L. Sevcik, *Impact of packet loss and delay variation on the quality of real-time video streaming*, In SPRINGER Telecommunication Systems, Volume 62, Issue 2, 2016, pp. 265-275. DOI: 10.1007/s11235-015-0037-2.
2. J. Frnda, M. Voznak, L. Sevcik, P. Fazio, *Prediction Model of Triple play services for QoS Assessment in IP Based Networks*, In Journal of Networks, Vol. 10, No. 4, pp. 232-239, April 2015, DOI: 10.4304/jnw.10.4.232-239.
3. J. Frnda, M. Voznak, M. Hlozak, J. Slachta, J. Lin, *Application Tool for Prediction and Implementation of QoS in IP Based Network*, In SPRINGER Advances in Intelligent Systems and Computing AISC, Volume 370, 2015, pp. 143-154.

4. J. Frnda, M. Voznak, L. Sevcik, *Network Performance QoS Prediction*, In SPRINGER Advances in Intelligent Systems and Computing AISC, Volume 297, 2014, pp. 165-174, DOI: 10.1007/978-3-319-07776-5\_18.
5. J. Frnda, J. Rozhon, M. Voznak, J.C.-W. Lin, T.-Y. Wu, *A New Tool for Quality of Multimedia Estimation Based on Network Behaviour*, In ELSEVIER: Perspectives in Science , Vol. 7, March 2016, pp. 87-94. DOI: 10.1504/IJICT.2016.073636.
6. M. Uhrina, J. Frnda, L. Sevcik and M. Vaculik, "Impact of H.264/AVC and H.265/HEVC compression standards on the video quality for 4K resolution," in Advances in Electrical and Electronic Engineering, vol. 12, iss. 4, pp. 368-376, 2014. ISSN 1336-1376.
7. J. Frnda, L. Sevcik, M. Uhrina, M. Voznak, *Network Degradation Effects on Different Codec Types and Characteristics of Video Streaming*, In Journal Advances in Electrical and Electronic Engineering, Vol. 12, Issue 4, 2014, pp. 377-383, ISSN 1336-1376.

## Other references

8. Test Sequence [online]. Available at: <http://medialab.sjtu.edu.cn/web4k/index.html>.
9. MSU Measurement Tool Pro version [online]. Available at: [http://compression.ru/video/quality\\_measure/vqmt\\_pro\\_en.html#start](http://compression.ru/video/quality_measure/vqmt_pro_en.html#start).
10. D. Grois, D. Marpe, A. Mulayoff. and O. Hadar, *Performance Comparison of H.265/MPEG-HEVC, VP9, and H.264/MPEG-AVC Encoders*, Picture Coding Symposium (PCS), 8.-11.12.2013, San Jose, USA, pp. 394-397. ISBN: 978-1-4799-0292-7.
11. N. Ramzan, Z. Pervez and A. Amira, *Quality of Experience Evaluation of H.265/MPEG-HEVC and VP9 Comparison Efficiency*, 26th International Conference on Microelectronics (ICM), 14.-17.12.2014 Doha, Qatar. pp. 220-223. INSPEC Accession Number: 15026442.
12. M. Rerabek, P. Hanhart, P. Korshunov and T. Ebrahimi, *Quality Evaluation of HEVC and VP9 Video Compression in Real-Time Applications*, 7th International Workshop on Quality of Multimedia Experience (QoMEX), 26.-29.5.2015, Costa Navarino, Messina, Greece. EPFL-CONF-207496.

# Optical Vehicle-to-Vehicle (V2V) Communication: Analyze of Photometric Quantities STOP Škoda Octavia III

Peter Hajduk and Vladimír Vašínek

Department of Telecommunications, FEECS,  
VŠB – Technical University of Ostrava, 17. listopadu 15,  
708 33 Ostrava – Poruba, Czech Republic  
`peter.hajduk.st2@vsb.cz`

**Abstract.** The article focuses on the implementation of vehicle to vehicle (V2V) communication technology in the field of road traffic safety, by way of light-emitting diodes (LED), which serve for the transmission of an optical signal within the range of the visible optical radiation (VLC). LED technology is nowadays used standardly in higher versions of car headlights and tail-lights, where it fulfills signaling functions as well as headlight functions. The future of V2V technology lies in the hybrid application of optical wireless communication which utilises LED sources on the side of the optical transmitter and a camera system (OCI, optical communication imaging sensor) on the side of the receiver, along with mobile technologies transmitting information about the state and character of the roadway. The authors of the work carried out research in the area of verifying the possibility of implementing the function of a STOP rear lamp in a Škoda Octavia III. in V2V communication, with the legislative demands for the specific function of the signal light in mind.

**Keywords:** Photometric quantity; VLC; Bias-Tee; V2V communication.

## 1 Introduction

Optical wireless data transfer between vehicles (V2V) is a new field of research, based on VLC technology. This technology is undergoing dynamic growth, as a result of the European Union's effort to react to the rapid increase in the frequency of road traffic accidents. The emphasis is put on raising active and passive safety, and therefore on the two basics of external automobile lighting – to see and be seen. The concept of road traffic safety is supported by research conducted by premier automotive manufacturers (BMW, Audi), where the applying of hybrid V2V communication is assumed. In this concept, mobile technologies transmit information about the roadway at greater distances (fog, rain), with OWC used for data transfer at shorter distances, about sudden changes in the roadway, when a quick response of the system >190ms (braking, change of direction) is important. Naturally, the utilisation of an optical V2V communication system opens up a series of problems. These include the necessity of integrating the modulator into the electronic control units of a headlight, as well as its placement in built-up and housing development areas. Another issue is the ful-

filling of legal regulations concerning the individual functions of a rearlight, along with the homogeneity of a specific function determined by the car manufacturer.

## 2 Optical V2V communication system

Research in the field of optical communication between vehicles (V2V) is seeing expansion mainly in conjunction with the light-emitting LED diode for optical wireless communication (OWC). The optical source utilising the LED diode represents an appropriate OWC device for transmitting an optical signal within the visible spectrum of the VLC, with the possibility of modulating LED at high transmission speeds, with a long operational lifespan, effectiveness, and allowing automobile designers to create concepts typical for individual marques. This technology is commonly utilised in tail-lights, brake lights, headlights or in traffic signaling [1].

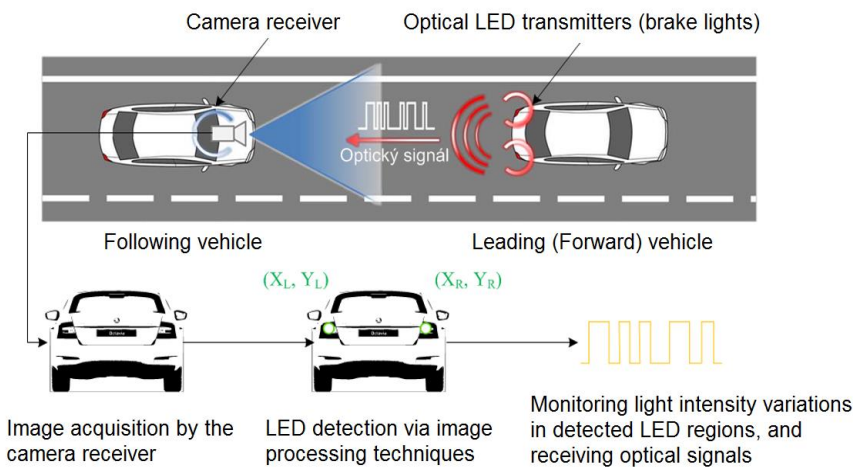


**Fig. 1.** Illustration of the optical V2V communication system.

The optical signal receiver in OWC automobile systems is comprised of a camera device utilising a special CMOS image sensor, referred to as a communication image sensor (OCI, optical communication image) [2]. The OCI uses so-called communication pixels (CPx), specialised for high-speed receiving of an optical signal. In addition to that, it contains an input circuit that reacts to intense light sources, e.g. LED, thus facilitating their detection. This means that the OWC technology uses a camera (an image sensor) providing non-crosstalk communication with multiple-access LED without a complex protocol and processing, preventing the mixing of an optical signal with noise, such as directly falling rays of sunlight. The applying of a camera system as a part of V2V communication also counts with the utilisation of camera systems, which are currently being used in the automotive industry for safety and comfort applications.



### 3 Optical V2V transmitter

The proposed concept of an optical transmitter within the context of the transfer concept is influenced by regulation ECE R 07, which is intended for the automotive industry and concerns the function of the STOP signal lighting of a vehicle. Therefore, the optical transmitter factors in the decrease of optical radiation intensity in cases of applying advanced modulation formats, which could have transmission rate a negative influence on the function of the rear lamp from a perspective of the lamp's legality in road traffic.

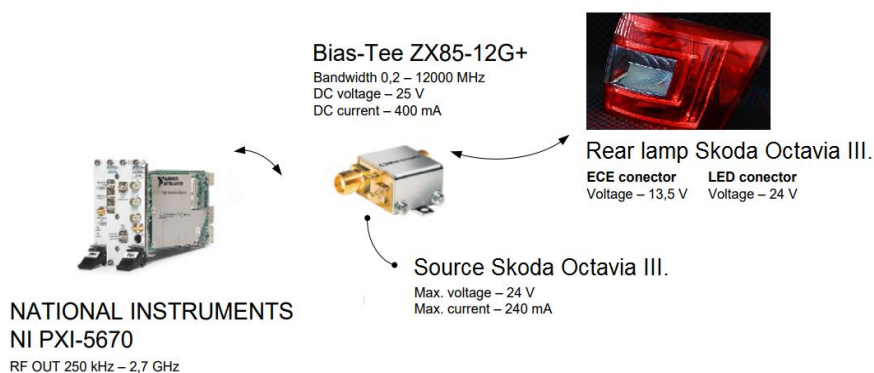


**Fig. 2.** Design concept of optical transmitter system STOP Škoda Octavia III.

The Bias-Tee ZX85-12G+ device in the proposed transmission system concept serves for the merging of an unidirectional signal on the DC port with the radio frequency signal on the RF port [3]. The combined RF+DC signal is used for setting the work point of the modulation of the individual LED segments of a STOP function. The DC port feed is implemented via the control electronics of the rearlight.

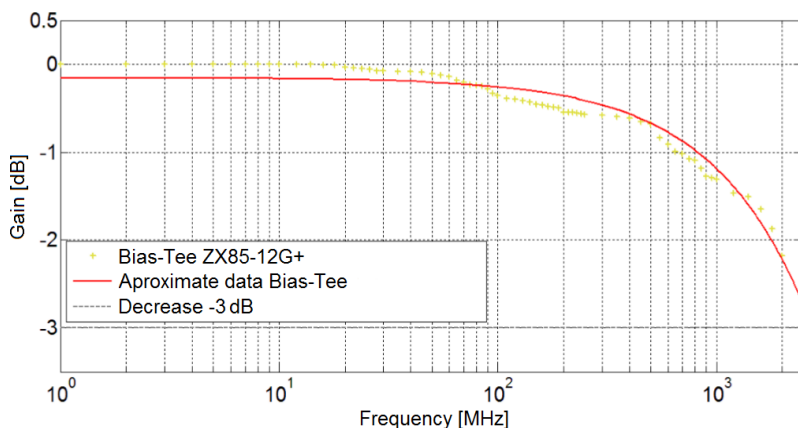


**Fig. 3.** Results of measurements output Bias-Tee ZX85-12G+.

## 4 Measurement

The analysis of the photometric quantities of a STOP rear light's radiated optical radiation was carried out in an experimental testing room with the use of a goniophotometer device. The device is defined in the ECE 37 (Economic Commission for Europe) as a source with nominal geometric and photometric properties.

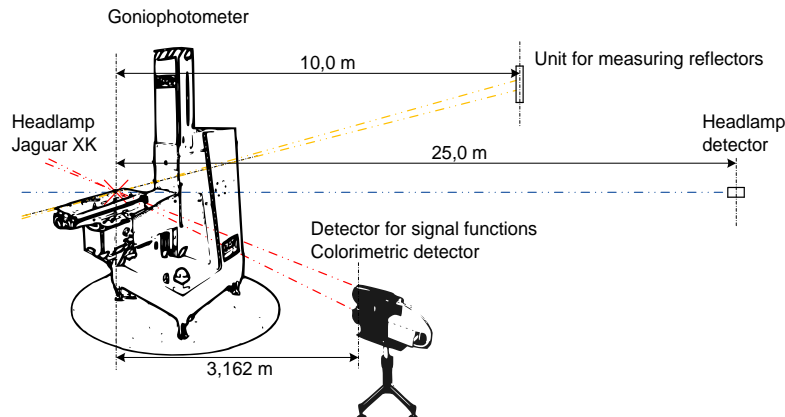


Fig. 4. Experimental lab for measurements of photometric values automotive rear lamps.

The rearlight of the Škoda Octavia III. was positioned on a shifting arm of a goniophotometer device during photometric quantities analysis. Testing of the STOP lighting proceeded at a maximum voltage of  $U_F = 13,5$  V and environmental temperature of  $T_a = 25$  °C. The detector for signal functions and the colorimetric detector were positioned at a referential distance of 3,162 m from the source of optical radiation. The optical centre of the rearlight was determined before initiating the measurement process itself [4].

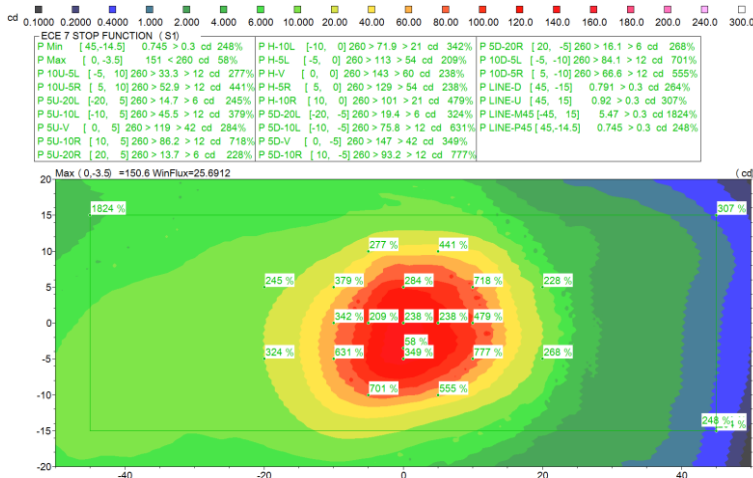


Fig. 5. Results of isocandel map and the protocol of intensities in the measurement points of the STOP function.

Based on the resulting isocandel map and the protocol of intensities in the measurement points of the STOP rearlight function, it is clear that the integrating of V2V optical communication by way of the advanced modulation format does not have a statistically significant impact on the photometric prediction, and therefore on the fulfilling of the ECE R 07 legal requirements. The evaluation of the STOP function fluctuates within the bounds of an acceptable variation, as defined by both the homologation institution and the rearlight manufacturer, who adds a certain margin in the test points influenced production technology.

## 5 Conclusion

The goal of this article was to carry out an analysis on the feasibility of implementing a homologated rearlight, intended for road traffic, in V2V communication as an optical transmitter in the transfer concept, with the use of advanced modulation formats. In our case, the rearlight was that of an Škoda Octavia III., where the STOP function was used, with the original control electronics. The resultant analysis of the isocandel map and the protocol of intensities in the measurement points proves, that a rearlight supplemented an active modulation system complies with the legislative regulation ECE R 07 pertaining to the function of STOP, and so the modified version of the rearlight is eligible for implementation in road traffic.

## 6 References

1. TAKAI, Isamu, Tomohisa HARADA, Michinori ANDOH, Keita YASUTOMI, Keiichiro KAGAWA a Shoji KAWAHITO. Optical Vehicle-to-Vehicle Communication System Using LED Transmitter and Camera Receiver. IEEE Photonics Journal. 2014, vol. 6, issue 5, s. 1-14. DOI: 10.1109/jphot.2014.2352620.
2. M. S. Z. Sarker et al., "Design and implementation of a CMOS light pulse receiver cell array for spatial optical communications," Sensors, vol. 11, no. 2, pp. 2056–2076, Feb. 2011.
3. MINI-CIRCUITS. Coaxial Bias-Tee: ZX85-12G+. Brooklyn, NY. Dostupné z: <http://194.75.38.69/pdfs/ZX85-12G+.pdf>.
4. HAJDUK, Peter. *Study effect of LED modulation on photometric quantities and beam homogeneity from automotive lighting*. Ostrava, 2015. Master thesis. Vysoká škola báňská - Technická univerzita Ostrava - VŠB-TUO.

# Radiation Influence on the Attenuation of the Cabled and Uncabled Optical Fibers

Lukáš Hájek and Vladimír Vašínek

Department of Telecommunications, FEECS,  
VŠB – Technical University of Ostrava, 17. listopadu 15,  
708 33 Ostrava – Poruba, Czech Republic  
lukas.hajek@vsb.cz

**Abstract.** Optical networks are definitely will be the most used type of media for high-speed information transport. The problem that could appear in the future years and that will undoubtedly limit another increasing of transmission capacity is aging of the optical fibers and components. These research relates to cabled and uncabled multimode fibers with geometrical size 62.5/125  $\mu\text{m}$ . The impact of radiation to optical fiber/cable was tested. During this test, samples were exposed to the total dose of radiation with the total value of 1.5 kGy and 60 kGy. The measurement of loss was made with the help of OTDR method with the five breaks during measuring. Simultaneously, the method of direct measurement of loss 1C was used. This approach was used for online measuring when every 15 minutes the values of insertion loss were recorded during the whole testing.

**Keywords:** 1C, ageing, attenuation, dose, gamma irradiation, OTDR.

## 1 Introduction

Optical networks have already built up their strong position in telecommunication and communication technologies. Due to its advantages, such as high transmission speed, insensitivity to electromagnetic field interference, large bandwidth and availability of material for the production of transmission media, they have become an inherent and difficult to overcome technology of today's and future times. The high lifetime of  $\text{SiO}_2$  material has not yet led the manufacturer, internet providers and users to ask simple question. Do optical fibers get older? And if so, how quickly and what impact this aging process will have on the parameters of optical transmission or backbone networks?

The process of accelerated aging is achieved by two phenomena, thermal and radiation loading. By cyclic alternation of thermal and radiation loading we can accelerate this effect. The influence of radiation and temperature on optical fibers has already been investigated. Dominant influence on the attenuation parameters of the optical fiber has the effect of radiation. The RIA effect (radiation induced attenuation) manifests in the fiber which is exposed to radiation aging) [1]. This effect causes an increase of optical fiber attenuation of 10 to 100 percent, depending on the power of the

emitter and the total radiation dose. Early studies clearly show that dopand plays a significant role, which is used to increase the refractive index of the core and cladding of the optical fiber [2]. The most commonly used dopand for the production of optical fibers are rare rocks such as Germanium (Ge). Due to improving the extraction process, this element can now be obtained easily in pure form. This makes it one of the most economical options while choosing element for production of optical fibers. Unfortunately, as the research shows, fibers that are doped with Germanium or their oxidants are noticeably sensitivity to radiation. On the contrary, fibers made by different technology with using fluorine oxide show little change in comparison with Germanium [3] and [4]. Unfortunately, these fibers are so expensive that they are only used for special applications. These applications may include sensor networks in nuclear power station, for pressure, temperature and radiation leakage control, etc. [5].

## 2 Measurement and Testing Setup

### 2.1 Measured Samples

Samples of multimode fibers were chosen for testing purposes. The sample MM\_1 (Fig. 1. a) and sample MM\_2 and MM\_3 (Fig. 1. b). The sample MM\_1 represents a separate fiber in tight secondary protection of 900  $\mu\text{m}$  in 3 mm protection with Kevlar fibers filling. The sample MM\_2 and MM\_3 is optical cable composed of 24 fibers of the same type as the fiber MM\_1 with a central support element.

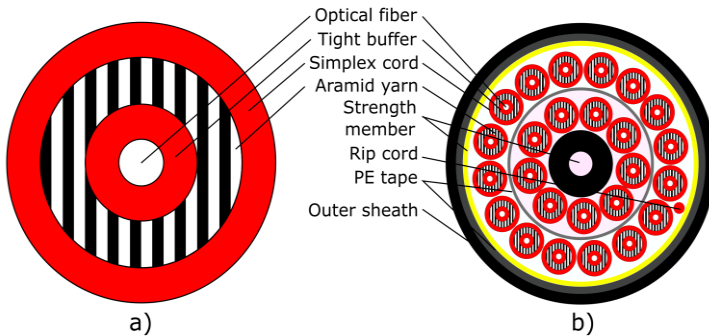


**Fig. 1.** Drawings of used multimode optical fiber/cable samples.

For sample MM\_2 and MM\_3, the filament was welded together on the both sides to extend the testing length. Five random fibers were selected from the inner ring and five fibers from the outer ring. These fibers were welded together and placed in protective boxes at the end of the fiber optic cable.

# 2.2 Measurement Devices

Optical fiber attenuation measurements were performed according to EN 60793-1-40 with the use of EXFO instruments. The AXS-200/352-12D was used to measure IL (Insertion Loss). Parameters of this device are shown in the Tab. 1. This device has also been used for continuous measurement of optical fiber attenuation at radiation.

**Table 1.** Parameters of the EXFO AXS-200/352-12D.

Parameters of the AXS-200/352-12D	
<sup>d</sup> Detector	Ge
<sup>d</sup> Wavelength range (nm)	800 - 1650
<sup>d</sup> Power range (dBm)	10 to -70
<sup>d</sup> Power uncertainty	$\pm 5\%, \pm 0.1 \text{ nW}$
<sup>d</sup> Resolution (dB)	$\pm 0.01$ (10 to -60 dBm)
<sup>s</sup> Spectral width (nm)	50
<sup>s</sup> Output power (dBm)	$\geq -20$
<sup>s</sup> Nominal wavelength (nm)	850, 1300

*d* - detector property, *s* - source property.

The measurement by OTDR method according to EN 60793-1-40 C was performed with the EXFO OTDR-FTB-7200D. The measurement procedure complies with the description in section 2.4. with the exception that together with launch fiber the same fiber was used as ranked fiber.

**Table 2.** Parameters of the EXFO FTB-7200D.

Parameters of the OTDR-FTB-7200D	
Wavelength (nm)	$850 \pm 20, 1300 \pm 20$
Event dead zone (m)	1
Distance range (MM)	0.1 - 40
Pulse width (ns)	5, 10, 30, 100, 275, 1000
Loss resolution (dB)	0.001
Sapling resolution (m)	0.04 - 5

# 2.3 Insertion Loss Measurement (1C)

At the measurement by the B (1C) method, mandrel wrappers were used. These serve to stabilize the energy distribution of the modes and reduce the impact of parasitic and tunneling modes. As a mode filter (Mandrel Wrap), a plastic roller was used on both the Launch Reference fiber side and the Receiver Reference fiber side. This roller has a diameter of 23 mm which fits with MM fiber of 125/62.5  $\mu\text{m}$  in an outer protection of 2 mm (specified by TIA 568). Around the roller, the fiber was turned six times.

## 2.4 Attenuation Measurement (OTDR)

The OTDR method is based on the detection of backscattered light waves. The optical fiber contains a large number of non-homogeneities and nonlinearities that produce a backward spreading Rayleigh dispersion. This dispersion is amplified by the APD photodiode on the detector side. Thanks to this, it is possible to measure optical fiber attenuation using only one end of the optical path. The Fresnel's reflection is another phenomena that occurs on optical paths and occurs wherever light passes to the core/air-gap/core interface. This method is widely used in optical communication networks for its main advantage. The advantage is ability to locate fault type and location with very high spatial accuracy.

For classical measurements, Death Zone Compensation Fiber must be use to compensate the dead zone beyond the first connector of the analyzed route. This fiber is usually 200 m – 500 m long. The lengths of this fiber depends on the used measuring pulse width.

## 3 Results

In Fig. 3 a) – d) the measurement results for RA (Radiation Ageing) and AD (Accident Dose) tests with different radiation doses (1.5 and 60 kGy) are displayed. Fiber/cable samples MM\_1 and MM\_2 are compared at wavelengths 850 nm and 1300 nm. Graphs show results from 1C and OTDR measurements for both samples at given time intervals, and an intermittent black line highlight the average value for these measurements. From the measured results it is evident that the radiation disturbs the atomic structure of the SiO<sub>2</sub> optical fiber and exhibits by increasing attenuation that is significantly higher at a lower wavelength of 850 nm.

For individual measurements, a mathematical fit function can be deduced to describe most accurately the increase in attenuation relative to the radiation dose size influencing the optical fiber/cable:

$$Att_{850\text{ nm}} = -3E - 5 \cdot Dose^2 + 0.180 \cdot Dose + 2.616 ; R^2 = 0.999, \quad (1)$$

$$Att_{1300\text{ nm}} = 0.006 \cdot Dose + 0.325 ; R^2 = 0.996, \quad (2)$$

$$Att_{850\text{ nm}} = -1E - 8 \cdot Dose^2 + 0.001 \cdot Dose + 1.391 ; R^2 = 0.955, \quad (3)$$

$$Att_{1300\text{ nm}} = -3E - 7 \cdot Dose^2 + 0.024 \cdot Dose + 37.46 ; R^2 = 0.908, \quad (4)$$

where Eq. (1) and Eq. (2) express polynomial and linear regression for wavelengths 850 nm and 1300 nm relative to the RA test, Eq. (3) and Eq. (4) express second order polynomial regression for AD test at wavelengths 850 nm and 1300 nm.

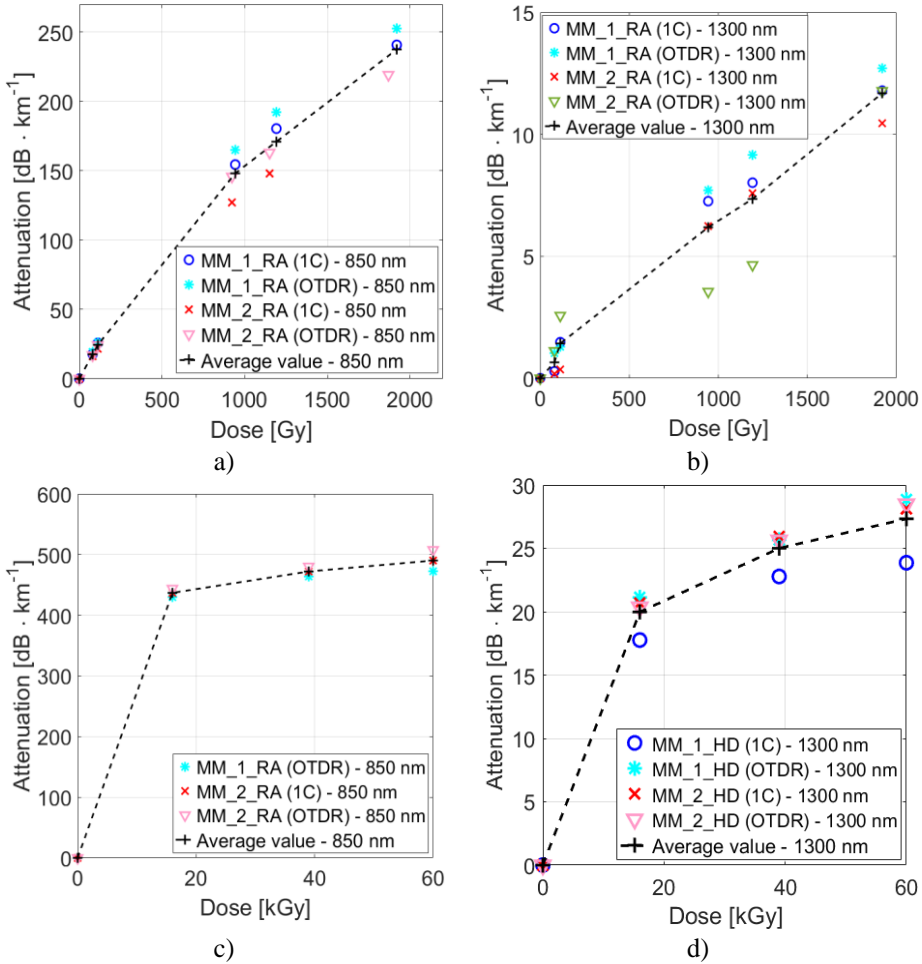


**Fig. 2.** The comparison of measurement results for RA and AD: a) the comparison of measurements by methods 1C and OTDR for samples MM\_1 and MM\_2 for wavelength 850 nm in the RA test, b) the comparison of measurements by methods 1C and OTDR for samples MM\_1 and MM\_2 for wavelength 1300 nm during the test RA, c) the comparison of measurements by methods 1C and OTDR for samples MM\_1 and MM\_2 for wavelength 850 nm during the test AD, d) the comparison of measurements by methods 1C and OTDR for samples MM\_1 and MM\_2 for wavelength 1300 nm during the test AD.

## 4 Conclusion

The article summarizes part of the research, which is focused in the field of optical fiber and fiber components ageing. The results show that the radiation has an effect on material attenuation curve of the optical fiber. It is not known exactly what and how it goes inside an optical fiber that is directly exposed to radiation. But it is clear, that this effect is much stronger at lower wavelengths of 850 nm than at 1300 nm. From



the measured results, it is possible to compile mathematical models for calculating the dependence between the amount of absorbed radiation by the fiber material and the insertion loss of the optical fiber.

## 5 Acknowledgements

The research described in this article could be carried out thanks to the active support of the projects no. SP2017/79, SP2017/97, VI20172019071, VI20152020008, TA04021263. This article was prepared within the frame of sustainability of the project No. CZ.1.07/2.3.00/20.0217 "The Development of Excellence of the Telecommunication Research Team in Relation to International Cooperation" within the frame of the operation programme "Education for competitiveness" that was financed by the Structural Funds and from the state budget of the Czech Republic.

## 6 References

1. GIRARD, S., J. KUHNHENN, A. GUSAROV, B. BRICHARD, M. VAN UFFELEN, Y. OUERDANE, A. BOUKENTER and C. MARCANDELLA. Radiation effects on silica-based optical fibers: recent advances and future challenges. *IEEE Transaction on Nuclear Science*. 2013, vol. 60, no. 3, pp. 2015 - 2036. ISSN 0018-9499.
2. GHERARDI, L., P. MARELLI, A. SERRA and G. VIZZOLI. Radiation Effects on Doped Silica-core Optical Fibers. *Nuclear Physics B*. 1993. vol. 32, pp. 436 - 440. ISSN 0550-3213.
3. FOLEY, S. *Fluorine-Doped Core Boosts Radiation Resistance of Single-Mode Fiber*. Laser Focus World. 2009. Available at: <http://www.aflglobal.com/productionFiles/resources/White-Papers/90390-623e-LFW.aspx>.
4. STAJANCA, P., L. MIHAI, D. SPOREA, D. NEGUST, H. STURM, M. SCHUKAR and K. KREBBER. Effect of Gamma Radiation on Prefluorinated Polymer Optical Fibers. *Optical Materials*. 2016, vol. 58, pp. 226 - 233. ISSN 0925-3467.
5. GUSAROV, A. I., F. BERGHMANS, O. DEPARIS, A. FERNANDEZ, Y. DEFOSSE, P. MEGRET, M. DECRETON and M. BLONDEL. High Total Dose Radiation Effects on Temperature Sensing Fiber Bragg Gratings. *Photonics Technology Letters*. 1999, vol. 11, no. 9, pp. 1159 - 1161. ISSN 1041-1135.

# Comparison of Selected Optical Properties of Thin Layers of PDMS with Luminophores

Jan Jargus

Department of Telecommunications, FEECS,  
VŠB – Technical University of Ostrava, 17. listopadu 15,  
708 33 Ostrava – Poruba, Czech Republic  
[jan.jargus@vsb.cz](mailto:jan.jargus@vsb.cz)

**Abstract.** Nowadays, the use of silicone materials has been expanded because they have many excellent physical and chemical properties due to which find application in many industries. Polydimethylsiloxane is frequently used material, which can be mixed with some other substances during preparation. For example, when we mix polydimethylsiloxane (PDMS) with luminophore, we get new material with some interesting properties. This article is focused on the comparison of selected optical properties of thin layers of PDMS with luminophores.

## 1 Introduction

The silicone materials have use for various industrial applications. The main applications include production of solar panels, the production of LEDs, electronics, heat dissipation, automotive, aviation, cosmonautics, etc [1]. But our attention is focused on exploring the selected optical properties of mixture of PDMS and luminophore. There are many kinds of luminophores and polydimethylsiloxanes, and we have begun to investigate the properties of a mixture of PDMS Sylgard 184 and some types of luminophores. We used four luminophores from company Phosphor Technology and one luminofor from company Crytur for our experiments. At first we monitored the color temperature of our samples and then we measured the attenuation. The first part of the article is focused on familiarization with the theme of colour correlated temperature (CCT) and attenuation. The equipment for measuring is shown in the next chapter and then experimental measurements are presented. Finally, the results of our measurements are summarized.

## 2 Colour correlated temperature and attenuation

Light colour is a property of light evoking a visual perception, which is given spectral composition of light [2]. Colour correlated temperature (CCT) determines the colour of the light corresponding to the colour of a black body for a given temperature. In

Figure 1 we can see the colour chart, wherein the black line in the middle diagram determines the colour of a black body, depending on its temperature. In this diagram,  $T_c$  denotes CCT. White light is considered in a range of colour temperatures from about 2700K to 6500K.

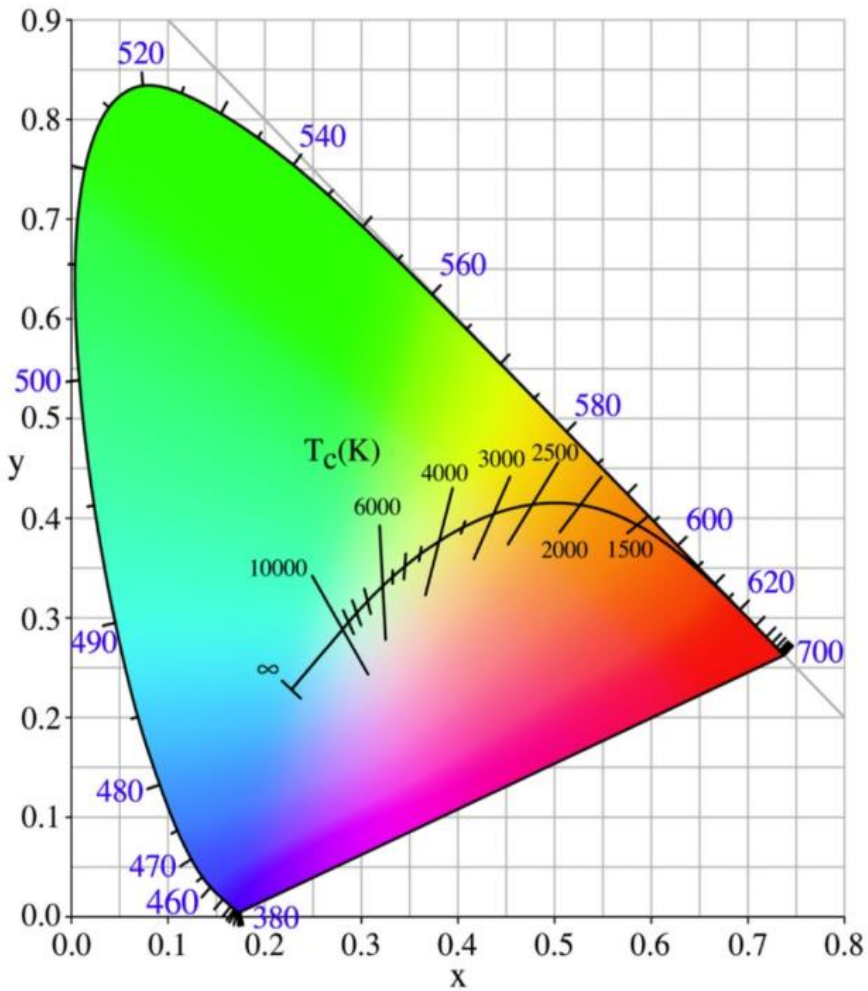


**Figure 1.** Colour chart of the colour correlated temperature

The attenuation is defined by the equation 1,

$$u = 10 \log \frac{P_1}{P_2} \quad (1)$$

where  $P_1$  denotes input power and  $P_2$  output power.

3 The equipment for measuring

Sylgard 184 was used, which was blended in a ratio of 1:10 with reagent. The mixture was stirred manually about 30 seconds and then 5 minutes on a shaker Vortex Genius 3 on speed 1. Then the mixture was placed in a refrigerator at 120min with temperature 280.5K to remove bubbles. Then selected type of luminophore was added to the mixture and five samples with fixed ratios were created, as we can see in table 1.

**Table 1.** The values of the samples and the concentration of the luminophore

Sample	Diameter of sample [mm]	Layer thickness of sample [mm]	Tradename of luminophore	Weight ratio luminophore: PDMS
1	16	1.5	CRYTUR	1:35
2	16	1.5	QMK58/N-U6	1:35
3	16	1.5	QMK58/F-D1	1:35
4	16	1.5	QMK58/F-U1	1:35
5	16	1.5	QMK58/F-U2	1:35

The mixture was subsequently 4h stirring and shaking on a rotary shaker and with a speed of 1 revolution for 3 min and with a longitudinal shaking of 5 cycles per second. At first the colour correlated temperature and the spectral characteristics were measured for each sample and then we determined the attenuation. Measurement schema for CCT is shown in figure 2 and for attenuation is shown in figure 3.

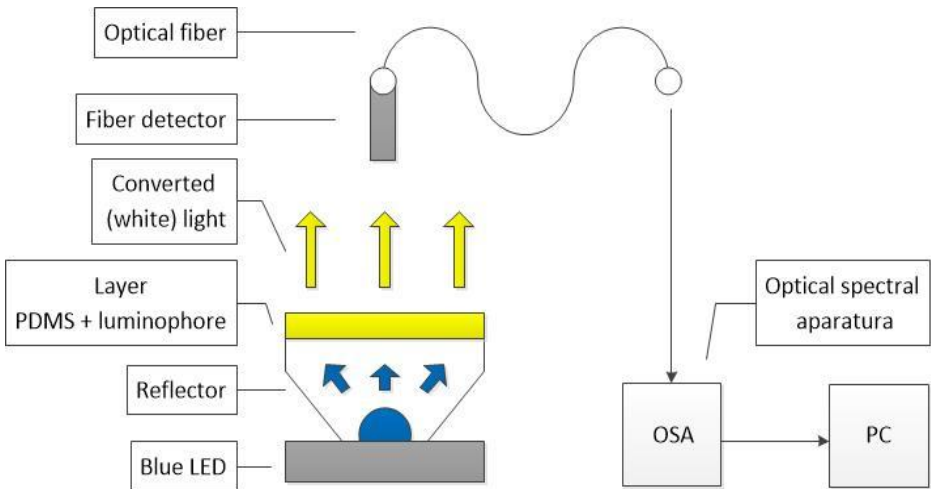


**Figure 2.** The measurement scheme for CCT

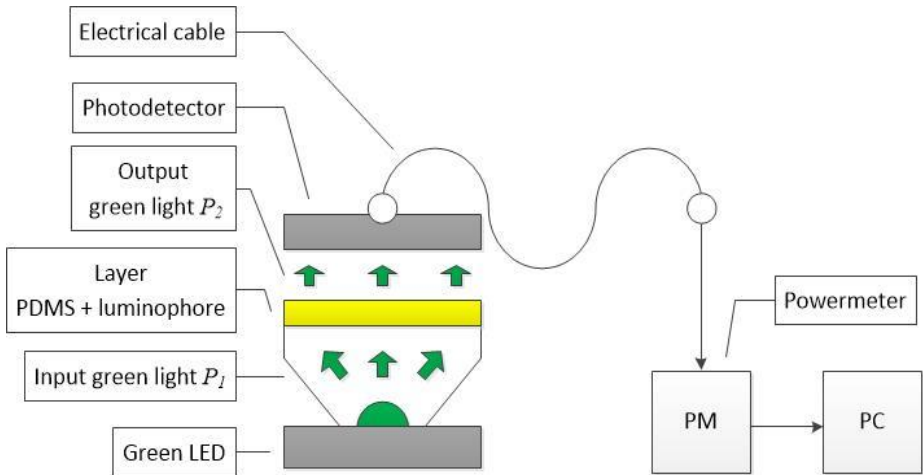


**Figure 3.** The measurement scheme for attenuation

Blue LED with a maximum emission at a wavelength of 467nm was used in the measuring assembly for CCT and then we used green LED with central emission wavelength 532nm for attenuation measurement. These LEDs were powered by a regulated voltage source HM8143 with power voltage 2,5V. The spectrum and the colour correlated temperature of the samples were measured using a spectrometer Ocean Optics USB 4000. Attenuation measurements were realized by power and energy meter Thorlabs PM100USB and photodetector Thorlabs S120VC. At the following figures, we can see some details of the measuring assembly.

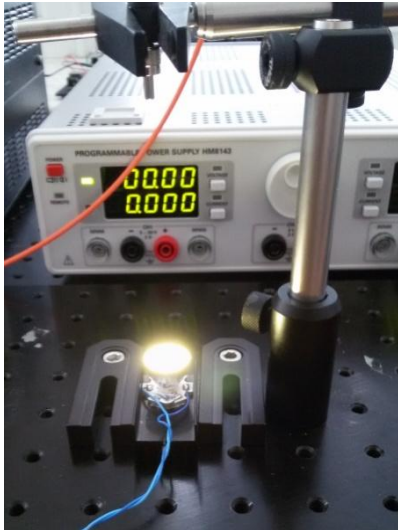


**Figure 4.** The measuring assembly for CCT (detail)

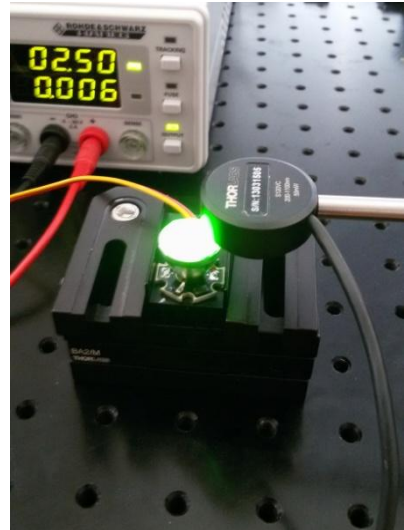


**Figure 5.** The measuring assembly for attenuation (detail)

#### 4 The experimental measuring

At first the measurements of CCT were carried out. Samples 1 and 2 had undefined CCT and the converted light was still blue. When we used the other samples we obtained white light with defined CCT. Measurement results are in the following table.

**Table 2.** The colour correlated temperature of the samples.

Sample	Tradename of luminophore	Weight ratio luminophore: PDMS	CCT [K]
1	CRYTUR	1:35	undefined
2	QMK58/N-U6	1:35	undefined
3	QMK58/F-D1	1:35	5237
4	QMK58/F-U1	1:35	5907
5	QMK58/F-U2	1:35	5191

We can see spectral characteristics of the samples at the figure 6. It is obvious, that samples 1 and 2 (blue and red line in figure 6) have only a small portion of converted light and that's way they have blue colour of transmitted light. The other samples emit white light, because considerable part of input blue light is converted into wide range of wavelengths.

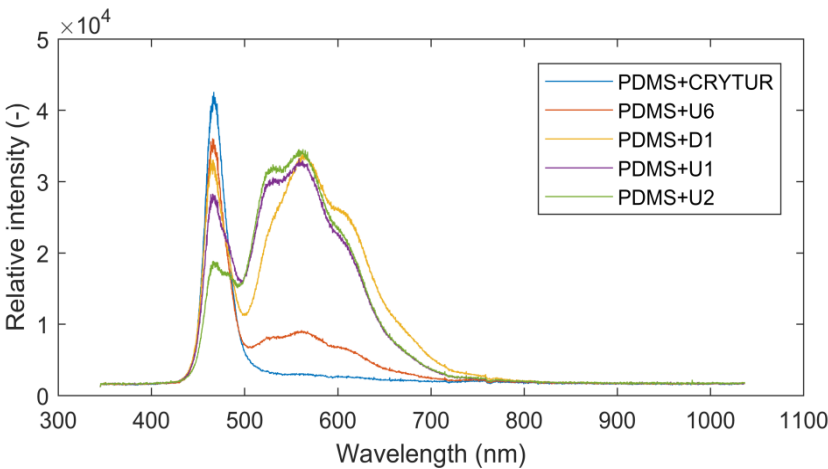


**Figure 6.** The spectral characteristics of the samples

Further, we found out input power  $P_1$  emitted by green LED because it was important value for the attenuation measurements. Taking into account that  $P_1=1.1985\text{mW}$  and values of output power  $P_2$  we have measured, so we can see results of attenuation measurements in table 3.

**Table 3.** The attenuation of the samples

Sample	Mix PDMS with luminophore	Output power $P_2$ [mW]	Attenuation of 1.5mm thin layer [dB]
1	CRYTUR	0.9025	1.23
2	U6	0.6888	2.41
3	D1	0.5798	3.15
4	U1	0.5027	3.77
5	U2	0.4943	3.85

## 5 Conclusion

This article was focused on the comparison of selected optical properties of thin layers of PDMS with luminophores. Importance using of silicone materials was mentioned in the beginning. Then themes of the colour correlated temperature and attenuation were outlined. The description of the equipment for measuring and the preparing of the samples followed further. The results of measurements are content of the next chapter.

From the results obtained in tables 2-3 and figure 6 we can draw some conclusions. At first, to produce white light from a blue light source, samples 3 through 5 are suitable, but this is true for the luminophore weight ratio in PDMS 1:35. As can be seen from table 3, samples 3-5 have considerable attenuation since we lose more than half of the input power for these samples with layer thickness 1.5mm at a wavelength of 532 nm. However, research in this area will continue, because we want to measure thin layers also for other concentrations luminophore in PDMS.

## References

1. NORRIS, A., J. DEGROOT, F. NISHIDA, U. PERNISZ, N. KUSHIBIKI a T. OGAWA. Silicone Materials for Optical Applications. *DOW Corning* [online]. 2003 [cit. 2015-08-07]. Dostupné z: [http://www.dowcorning.com.cn/zh\\_CN/content/publishedlit/75-1007-01\\_single.pdf](http://www.dowcorning.com.cn/zh_CN/content/publishedlit/75-1007-01_single.pdf)
2. VRBOVÁ, M. a kol.: *Lasery a moderní optika*. Prometheus, 1. vydání, 1994, ISBN 80-85849-56-9

# Fiber-optic Technology in Sensory Applications

Jan Nedoma

Department of Telecommunications, FEECS,  
VŠB – Technical University of Ostrava, 17. listopadu 15,  
708 33 Ostrava – Poruba, Czech Republic  
[jan.nedoma@vsb.cz](mailto:jan.nedoma@vsb.cz)

**Abstract.** The article summarizes author's activities during three years of his study, his research and development activities related to the studies and research projects. The topic of dissertation thesis is the Nondestructive fiber-optic system for measurement of speed in road traffic.

**Keywords:** interferometer, optical fiber, speed, thesis

## 1 Introduction

Allow me to introduce myself. My name is Mr. Jan Nedoma. I am a full-time doctoral student and employee at the Faculty of Electrical Engineering and Computer Science at the Technical University of Ostrava. My education program is called Computer Science, Communication Technology and Applied Mathematics and field of study called Communication Technology. Head of my dissertation thesis is professor Vladimír Vasínek. The theme of my thesis is entitled "*Nondestructive fiber-optic system for measurement of speed in road traffic*". State doctoral exam I was passed at the end of the second year of my study on May 27, 2016. Since March 2016, I became a full-time employee at the Department of Telecommunications. My job position is called "Science and Research Assistant". I preparing and writing the projects for various grant competitions, also I work on these projects and further I preparing and writing different publications from the field of fiber-optics. Based on results in the second years of my studies, I received an incentive grant of doctoral programs of the Technical University of Ostrava awarded for outstanding achievements in science and research. To the date 7/2017, I have a total of 67 accepted or published publications (20 as the main author) and 11 applied outcomes (of which two valid Czech patents). Among my best outputs during my studies, I can include three publications (Q1 with IF. 2677) devoted to the use of optical fibers in biomedicine applications. During three years of my studies I gained total of 1156 credits.

## 2 Activities related to the dissertation thesis

As an interesting alternative to existing conventional sensors and detectors, there is a possibility of using fiber-optic sensors. The subject of my dissertation thesis is the verification of this fact using fiber-optic interferometry for measuring speed in road



and rail traffic. These compiled sensors can both replace the current detectors and also open up a new application potential. In many cases, due to their properties sensors can find applications in areas where their use is still not possible or expensive (a passive mode from the viewpoint of power supply towards conventional electrical sensors). A substantial advantage of optical fibers is the insensitivity to electromagnetic interference, the material does not rust, and it can operate over a wide temperature range. The flexibility and size of optical fibers allow their simplified installation. The massive expansion of fiber-optic cables offers the possibility of connecting the existing telecommunications fiber-optic networks along roads. This fact confirms that the direction of the development field was correctly chosen, and it also underlines the considerable list of positive characteristics of fiber-optic sensors.

The measuring arrangement for analyzing the speed of vehicles or trains is based on two identical units placed in strictly defined distance  $L$  apart, see Fig.1. Based on the measured time span between the measuring unit  $\Delta T$  and the known distance  $L$ , we can evaluate the speed of passing vehicles, see Eq. 1.

$$v_{car} = \frac{L}{\Delta T} \quad (1)$$

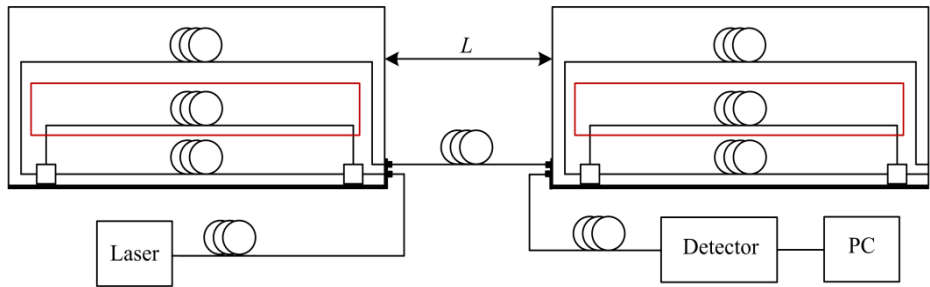


**Fig. 1.** Scheme for measurement of the speed of vehicles.

The written application (on PC) makes the reference measurement of the background noise. It is necessary to set the parameter  $L$  (in the range of 1-50 m) which determines the distance spacing between interferometric units. For detecting the vehicle or train, the trigger value must be determined five times greater than the noise value. The timer switches on if the first unit detects the pass-by of the vehicle or train (if the signal has a sufficient level of the SNR (Signal to Noise Ratio) - trigger level). The timer switches off if the second unit detects the pass-by of the vehicle (if the signal has a sufficient level of SNR - trigger level). The application calculates speed from a fixed defined distance  $L$  of interferometers and from the time interval  $\Delta T$  of the pass-by of the vehicle between interferometers, see Fig. 2.

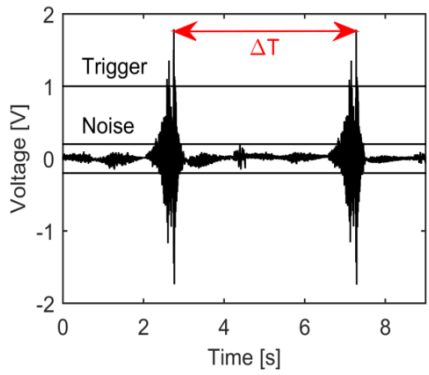


**Fig. 2.** Detection of maximum amplitude (the evaluation of time interval).

Table 1 shows the some experimental measurement of speed of the vehicles up to 55 kph. The measured data are compared with the GPS data which have an accuracy of 1.08 kph. Ten measurements were accomplished for each speed value. The table gives the average speed values. The maximum absolute deviation was 1.53 kph with  $\pm 1$  kph the tolerance of GPS. We can say that the system demonstrates reliable values (including tolerance GPS) considering the tolerance of  $\pm 3$  kph indicated for segmental measuring systems in the CZE for measurement of speed to 100 kph.

**Tab.1:** Experimental measurement of speed.

Reference speed [kph] (GPS)	Measurement speed [kph]	Relative difference [%]	Absolute difference [kph]
10	10.77	7.7	0.77
15	15.43	2.86	0.43
21	21.87	4.14	1.87
26	26.74	2.84	0.74
31	31.82	2.64	0.82
35	35.81	2.31	0.81
41	42.53	3.73	1.53
45	46.12	2.48	1.12
50	51.28	2.56	1.28
55	55.75	1.36	0.75

### 3 Projects

As part of my studies, I was actively involved in solving eleven projects, namely:

1. TA ČR Intelligent modules for lighting and communication
2. TA ČR Safety of optical transport networks and the development of opt. parts for electric power and electrical appliances
3. TA ČR GAMA PP1 PRE SEED fund VŠB Technical University of Ostrava

4. MV GUARDSENSE I The modern structure of photonic sensors and new innovative principles for intrusion detection systems, integrity and protection of critical infrastructures
5. MV Project GUARDSENSE II Comprehensive security and critical infrastructure facilities addressed fiber optic sensors using modern information systems
6. SGS SP2016/149 New types of photonic systems
7. SGS SP2015/130 Research on aging elements of optical networks
8. SGS SP2017/79 New types of photonic systems for IoT
9. MV Smart technical textiles for increasing the security of critical infrastructures
10. MPO (SIDAS) System for smart detection and collision conditions signalling for improving of railway security
11. MPO Device for measurement and processing of biosignals with the use of fiber optic sensors

As an co-author, I participated in the drafting and submission of 7 projects for the organization with named Technology Agency of the Czech Republic (TA CR) and for the Ministry of Industry and Trade of the Czech Republic (MPO), as the main author with my colleagues and under supervisor prof. Vasinek, we gained the project for Ministry of Industry and Trade with entitled "*Device for measurement and processing of biosignals with the use of fiber optic sensors*" in the total budget of 15 442 800 CZK. For the current TRIO 3 challenge, in cooperation with prof. Vasinek we have prepared a project called "*Photonic system for detection and monitoring of railway vehicles*" in the total budget of 14 910 300 CZK.

## 4 Publications activities

From the date 9/2014 since to the date 7/2017, I have a total of 68 accepted or published publications (20 as the main author) and 11 applied outcomes (of which two valid Czech patents from the biomedical and security applications). Among my best outputs during my studies, I can include 3 publications (Q1 with IF. 2677) devoted to the use of optical fibers in biomedical applications.

In the first impact article, we briefly describe the design, construction, and functional verification of a hybrid multichannel fiber-optic sensor system for basic vital sign monitoring. This sensor uses a novel non-invasive measurement probe based on the fiber Bragg grating (FBG). The probe is composed of two FBGs encapsulated inside a polydimethylsiloxane polymer (PDMS). The PDMS is non-reactive to human skin and resistant to electromagnetic waves, UV absorption, and radiation. We emphasize the construction of the probe to be specifically used for basic vital sign monitoring such as body temperature, respiratory rate and heart rate. The proposed sensor system can continuously process incoming signals from up to 128 individuals.

In the second impact article, we focused on the design, realization, and verification of a novel phonocardiographic based fiber-optic sensor and adaptive signal processing system for noninvasive continuous fetal heart rate (fHR) monitoring. Our proposed system utilizes two Mach-Zehnder interferometric sensors. Based on the analysis of real measurement data, we developed a simplified dynamic model for the generation and distribution of heart sounds throughout the human body. Building on this signal model, we then designed, implemented, and verified our adaptive signal processing system by implementing two stochastic gradient-based algorithms: the Least Mean Square Algorithm (LMS), and the Normalized Least Mean Square (NLMS) Algorithm. With this system we were able to extract the fHR information from high quality fetal phonocardiograms (fPCGs), filtered from abdominal maternal phonocardiograms (mPCGs) by performing fPCG signal peak detection.

In the third impact article, we focused on the design, implementation, and verification of a novel method for optimization of the control parameters (such as step size  $m$  and filter order  $N$ ) of LMS and RLS adaptive filters used for noninvasive fetal monitoring. The optimization algorithm is driven by considering the ECG electrode positions on the maternal body surface in improving the performance of these adaptive filters. The main criterion for optimal parameter selection was the Signal-to-Noise Ratio (SNR). We conducted experiments using signals supplied by the latest version of our LabVIEW-Based Multi-Channel Non-Invasive Abdominal Maternal-Fetal Electrocardiogram Signal Generator, which provides the flexibility and capability of modeling the principal distribution of maternal/fetal ECGs in the human body. Our novel algorithm enabled us to find the optimal settings of the adaptive filters based upon maternal surface ECG electrode placements. The experimental results further confirmed the theoretical assumption that the optimal settings of these adaptive filters are dependent on the ECG electrode positions on the maternal body and therefore, compared to other existing methods and recommendations, we were able to achieve far better results. These improvements in turn could lead to a more accurate detection of fetal hypoxia. Consequently, our approach could offer the potential to be used in clinical practice to establish recommendations for standard electrode placement and find the optimal adaptive filter settings for extracting high quality fetal ECG signals for further processing.

## **5 Pedagogic part and other activities at the Department of Telecommunications**

In all winter semesters, I was actively involved in ensuring the teaching in the subject ZEL (Groundwork Electronics) and I also worked as supervision during exam tests. In all summer semesters, I taught courses ÚDKT (Introduction to Communication Technologies) and OK II (Optical Communications II). I was a member of two cathedral commissions. As an opponent, I've evaluated an eleven bachelor thesis. As a leading bachelor thesis, I led three students. I worked full-year presentation of the

Department of Telecommunications. The proportion of work consisted mainly in the preparation and presentation of the presented subjects of the Department of Telecommunications Engineering at secondary schools, the building of FEI or open days.

# Measurement of CCT Planar Structures Made of Polydimethylsiloxane Doped with Yellow Luminophore

Martin Novák

Department of Telecommunications, FEECS,  
VŠB – Technical University of Ostrava, 17. listopadu 15,  
708 33 Ostrava – Poruba, Czech Republic  
`martin.novak.st@vsb.cz`

**Abstract.** The paper describes the measurement of correlated color temperature (CCT) of white light generated by YAG luminophore, which was distributed homogeneously in the polymer material using a rotary shaker. The output is to evaluate the quality of white light when warming planar structures with a laser for different weight ratios of the luminophore. The paper also describes the publishing and teaching activities for the academic year 2016/2017.

**Keywords:** Polydimethylsiloxane, PDMS, luminophore, chromaticity temperature, CCT

## 1 Introduction

Polymer material called polydimethylsiloxane (PDMS) was used to make planar structures. PDMS is an optically transparent substance having a similar refractive index (Figure 1) as a standard optical fiber used for telecommunication applications. Polydimethylsiloxane has a high attenuation (0.5 dB/cm), so it cannot be used for long distance data transmission as standard optical fibers, but it is used in lighting technology for the LED application. This high attenuation is mainly due to absorption and scattering losses in the material. PDMS is a liquid with a viscosity of between 500-150.000 mPa·s, which passes into a solid state by vulcanization. If a suitable catalyst (curing agent) is not added to the PDMS, vulcanization cannot occur. The essential features of PDMS include excellent thermal stability, easy preparation, chemical resistance and UV light resistance.

Wavelength [nm]	Refractive index [-]	
	PDMS	SiO <sub>2</sub>
<b>900</b>	1.411	1.458
<b>1310</b>	1.402	1.446
<b>1550</b>	1.399	1.444

**Fig. 1:** Refractive index PDMS/SiO<sub>2</sub>

Luminophores are solids of several  $\mu\text{m}$  in size, which absorb a portion of light energy at a defined wavelength (445 – 470 nm) and emit this absorbed energy in the form of white light. Some types of luminophores, such as Ytrito-Aluminum Grenade  $\text{Y}_3\text{Al}_5\text{O}_{12}:\text{Ce}^{3+}$  (YAG: Ce) after excitation with a blue light source, make up the missing colors in the visible spectrum (red and green) to produce white light. White light can be categorized into three categories: neutral white, warm white and cold white. Each of these shades has its particular chromaticity temperature. Below is the spectral response (Figure 2) and the color diagram (Figure 3) of the QMK58/F-U2 luminophore, which was excited by the FF-01 power LED.

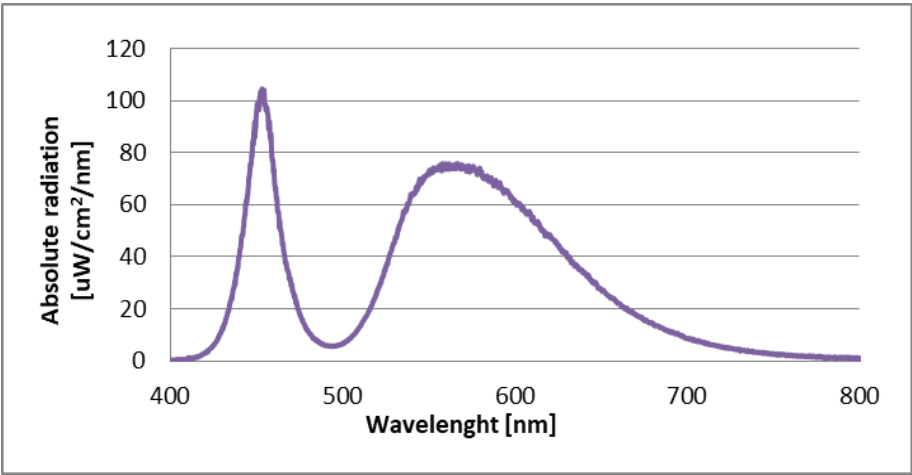


Fig. 2: Spectral characteristic of QMK58/F-U2

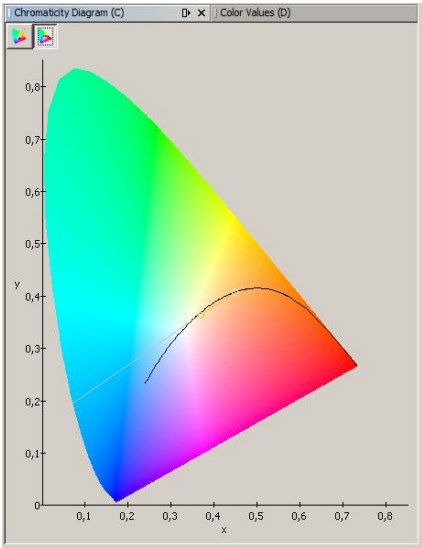


Fig. 3: Chromaticity diagram of QMK58/F-U2

## 2 Sample preparation and methodic of measurement

The realized planar structures are made of Sylgard 184 two-component silicone rubber. The components were mixed at a defined ratio of 10:1 (PDMS, curing agent), as recommended by the manufacturer. Mixing was carried out in two phases, in the first step we are talking about manual mixing, and in the second phase, the homogenizing preparation was used in the form of an ultrasonic bath. The luminophores QMK58/F-U2 in three different weight ratios were weighed and added into the homogeneous mixture of PDMS and a curing agent. The formed mixture of PDMS and luminophores was placed on a rotary shaker, where it was homogenized for one hour. From the prepared homogeneous mixture of PDMS and luminophore, a total of 90 planar structures were created on which were realized the further measurements. Planar structures were vulcanized in a temperature box at  $100 \pm 3$  °C. The measuring workplace (Figure 4) contains the following components: electrical source, laser, light aperture, PDMS cylindrical waveguide, the planar structure made of PDMS doped with luminophore, thermometer, spectrometer, temperature and CCT sensor. The used laser has a wavelength of 455 nm and an optical power of 5 W. Measurements were carried out continuously for 3 hours, with results being recorded every 10 minutes.

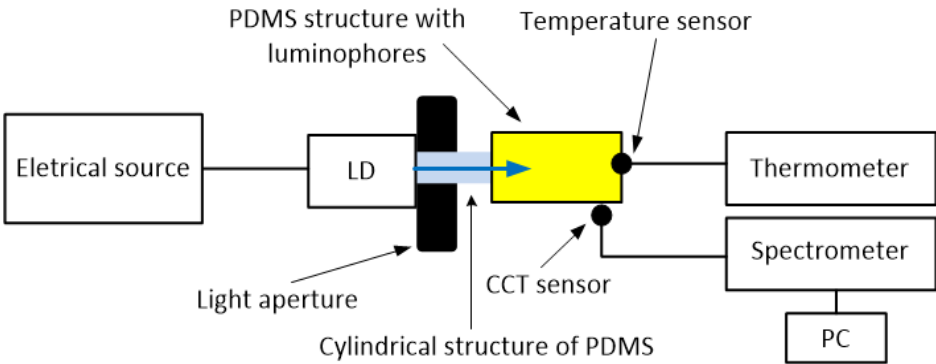
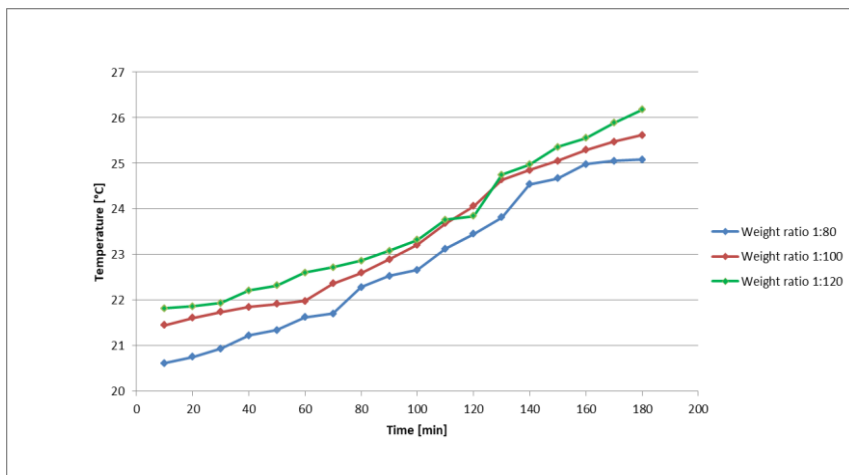


Fig. 4: Complete scheme of measuring workplace

## 3 Results

The first graph (Figure 5) shows how the temperature of the realized planar structures changes over time, even for three different luminophore ratio. The plotted characteristics have an increasing tendency, which is due to the absorption of the PDMS itself and the luminophores. Both components convert optical energy into thermal energy and heat up structures over time. The value of CCT varies over time with all the weight ratios is shown in Figure 6.





**Fig. 5:** Temperature dependence of planar structures made of PDMS with luminophore admixture

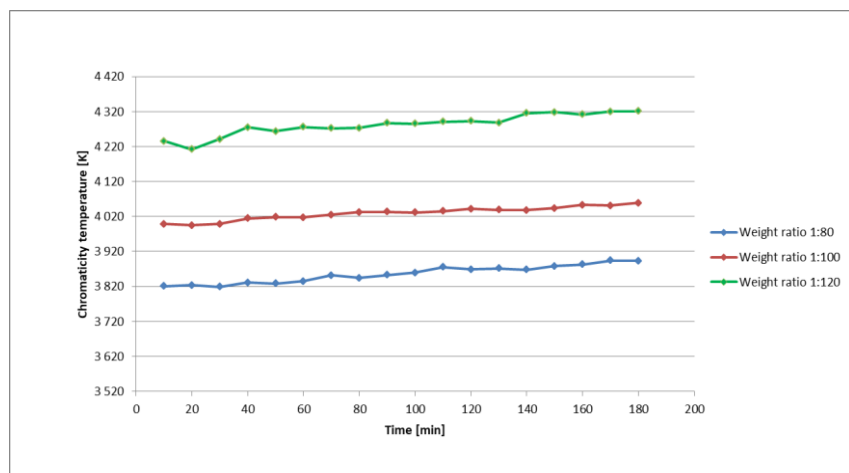


**Fig. 6:** CCT dependence of planar structures made of PDMS with luminophore admixture

## 4 Conclusion

From the measured results, it is clear that the temperature response of the prepared structures over time increases with the increasing weight ratio. The more luminescent particles the structure contains, the more light energy is converted into thermal energy. Thermal effects negatively affect the life of the element, and there is a slight variation in CCT over time as is shown in Fig. 6. The small fluctuations of the CCT almost do not recognize the human eye, but due to the heating of the light source (laser), the luminance of planar structures decreased. Stability of the radiation source and weight ratio of the luminophore can affect the resulting white light output quality.

## 5 Projects

In the second year of doctoral studies, I was actively involved in the solution of five projects:

1. Project GUARDSENSE II - Comprehensive security and critical infrastructure facilities addressed fiber optic sensors using modern information systems.
2. Project SIDAS - Intelligent collision detection and signaling system for increased line safety.
3. Project TAČR II - Intelligent communication and lighting modules.
4. Project MPO - Biosignal measuring and processing equipment using fiber optic sensors.
5. Project SGS - New types of photonic systems for IoT.

About my work on projects:

As part of the GUARDSENSE II project, I have participated in several experimental measurements with fiber-optic FBG sensors that were primarily designed to monitor critical infrastructures (detection and weighing of vehicles, detection of intrusion into buildings). In the SIDAS project, I worked on how to install the FBG sensors on the rolling track and how to encapsulate these sensors. It was also the goal of timely detection of vehicles in front of the railroad crossing to reduce the risk of collision with the train set. As part of the MPO project, I have been working on developing a sensor for vital sign monitoring (breath, pulse, temperature). The object of the research was to determine the appropriate encapsulation of the sensor, to determine its temperature sensitivity and the sensitivity to very small response (deformation) of the human body. In the TAČR II and SGS projects I have been developing new photonic systems focused on new types of polymeric materials (optimization of homogeneous mixture preparation, optical measurement, and mechanical properties testing). In non-project activities, I participated in the installation and monitoring of deformation forces in the Žilina tunnel and weighing of municipal waste using FBG sensors (Figure 7).



**Fig. 7:** Implementation of optical fiber for deformation monitoring in the tunnel (left) and application of FBG sensor on mechanical construction of the garbage truck for dynamically weighing of municipal waste (right).

## 6 Publications activities

I am an author of two accepted utility patterns (Lighting fixture with a source of excitation radiation and a luminescent layer, A luminescent light of a bulb type). Next, I am the lead author of the publication "Analysis of optical properties of polydimethylsiloxane (PDMS)", which I presented at the conference SPIE Optics + Optoelectronics held in Prague on April 26, 2017. I also co-authored six other publications, which were presented at SPIE conferences in America and the Czech Republic.

## 7 Pedagogic part

During the second year of doctoral studies, I actively participated in the teaching of subjects Optical Communications I and Optical Communications II. For students, I have been preparing laboratory assignments, numerical examples and tests.

## 8 References

1. Güner T., Köseoğlu D., Demir M.M., Multilayer design of hybrid phosphor film for application in LEDs. *Optical Materials*. 2016. DOI: 10.1016/j.optmat.2016.08.023. ISSN: 09253467
2. Chen L.-C., Lin W.-W., Chen, J.-W., Fabrication of GaN-Based White Light-Emitting Diodes on Yttrium Aluminum Garnet-Polydimethylsiloxane Flexible Substrates. *Advances in Materials Science and Engineering*. 2015. DOI: 10.1155/2015/537163. ISSN: 16878434
3. Holgersson P., Sutherland D.S., Kasemo B., Chakarov., Patterning and modification of PDMS surface through laser micromachining of silicon masters and molding. *Applied Physics A: Materials Science and Processing*. 2005. DOI: 10.1007/s00339-004-3082-3. ISSN: 09478396
4. Lin H.-Y., Tu Z.-Y., Ku P.-C., Lin C.-C., Kuo H.-C., Large area lighting applications with organic dye embedded flexible film. *Proceedings of SPIE - The International Society for Optical Engineering*. 2015. DOI: 10.1117/12.2077462. ISSN: 0277786X
5. Ioppolo T., Manzo M., Dome shaped micro-laser encapsulated in a flexible film. *Laser Physics*. 2014. DOI: 10.1088/1054-660X/24/11/115803. ISSN: 1054660X

# Docker is a Useful Tool to Design Information Systems

Lukáš Orčík and Miroslav Vozňák

Department of Telecommunications, FEECS,  
VŠB – Technical University of Ostrava, 17. listopadu 15,  
708 33 Ostrava – Poruba, Czech Republic  
{lukas.orcik, miroslav.voznak}@vsb.cz

**Abstract.** Nowadays, only one database technology will be not enough to design and implement complex information systems. Infrastructure of the information system contains tens or hundreds of working nodes that are running on different services such as firewall, VPN, DHCP server, mail server, authentication and authorization server, load balancers, various types of databases, application servers and many other services. There is a need for a large number of hardware to operate that many services. This problem was partially solved by virtualization, but virtualization also has its limitations and boundaries. These limits are mainly visible if you build a infrastructure on a micro-service-oriented architecture. The problem is in the large number of virtualized nodes that have to be managed. To solve this problem there is a technology called Docker. This technology is very often compared with virtualization, although this comparison is not a completely correct. The Docker is not a new technology, but it just makes another effort of how to solve the same node problem. The main difference is that the docker does not virtualize the hardware but does the so-called operating system virtualization. As a developer of information systems, this gives me new opportunities for more efficient operation of the development environment.

**Keywords.** Docker, Containers, Virtualization, Microservices

## 1 Containers

The demands required on modern information systems are very high. Today's information systems have many functions, they are not just computers used to run corporate information pages or mailboxes. In technological advanced companies they create new business opportunities, manage business and people, collect data not only from customers, but from many data sources and give new opportunities in many areas. Create a comprehensive service which should provide a lot of functions is inefficient from many points of view. Therefore, it is preferable to create easy services and operate them in a separate environment. In simple service we can do a better control about their functionality, do a quick upgrade or change environment. These easy services are called micro-service, it is a variant of service-oriented architecture. Microservices have one major feature, they need a large number of work nodes. For example, if we need 20 databases running on the same technology, for virtualization we need 20 operating systems for each database. In the case of the dock it is different, for overdosing 20 databases only

one operating system is needed. In the case of the dock, it is important, for overdosing of 20 databases only one operating system is needed. The Docker shares the core of the operating system in isolation between individual databases. So we will save the computing resources we would need for operating systems [1]. The figure 1 illustrates the illustrated example in a simplified form. On the left side is a model of virtualization and the right model used by the docker. In virtualization, the basic object is called an image, and it is a container for the docker. The container can be understood as an isolated process that uses the shared core of the operating system. The Docker shares separately the operating system core between individual databases. So we will save the computing resources that we would need to run operating systems. Figure 1 illustrates the described example in a simplified form. We can use the Docker on the Linux, Windows, and Mac operating systems. On the left side there is a model of virtualization and on the right there is model used by the docker. The basic object in virtualization is called an image and in docker the object is called container. The container can be understood as an isolated process that uses the shared core of the operating system. We can use the Docker on the Linux, Windows, and Mac operating systems.

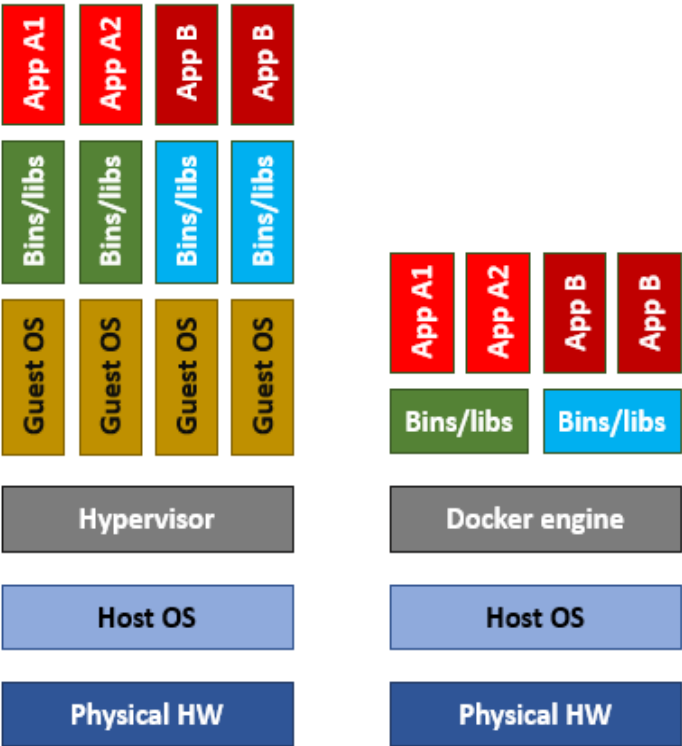


Fig. 1. Model used by virtualization and by docker

Therefore applications are loaded into containers with their settings and other data needed to run the application. The start of the container is immediate and does not take part of the operating system memory for running the operating system. The Docker architecture consists of 3 base elements, a docker client, a docker engine and a docker machine. The docker client is a REST client that communicates with the Docker engine and it allows users to work with containers. This client includes a docker cli console that allows us to operate the docker engine. There are also graphical clients available that we can install in the plugin form. Docker engine is a part of the technology on which the containers are running separately, this part also contains a REST interface that allows clients to connect to this engine. The docker machine administers the docker applications. Because the docker is an open source technology, we are getting more new tools that are moving this technology to get simpler for ordinary users. Docker compose, Docker Networking, Docker DNS, Docker Load Balancing and Docker Swarm are very useful tools. I really like Docker Compose tool because it really facilitates and automates work with a large number of containers. By using a configuration written in a single file called `docker-compose.yml`, we can create and configure multi-container environments. Docker Networking helps us to link multicontainer applications and it also offers us separate virtual networks. By using virtual networks, we can specifically define the rules of communication between these individual containers. Own DNS mechanism is provide by Docker DNS. We do not have to assign any IP addresses to our containers but they are available under the domain names that are defined in the `docker-compose.yml` file. In case you want to offer high availability of services it is appropriate to use load balancer. Docker load balancer provides own mechanism based on DNS principle and it allows easier scaling. The last tools which is very useful is Docker Swarm. Docker Swarm is needed in case you want to run docker in a production deployment where is the performance of several physical servers needed. This simplifies the deployment, management and operation of the container cluster.


## 2 Install and compose up

You can install Docker on several versions of MS Windows, Linux and Mac [2]. The application can be downloaded from the official docker website. There are two versions available: Docker CE and Docker EE [3]. The CE version is free version for user community. The EE version is paid and is designed for commercial purposes where customer needs service support and requires several tools needed to run docker. After docker installation, the application is ready to use. We can access it by using Docker cli console where we insert necessary commands. For illustration, I will show you the application source code with two containers, which we can create by using Docker compose tool.

We create a folder and then we create a file named `docker-compose.yml` in it. We insert a configuration to this file which we can see in Figure 2. Then we save this file with "docker compose up" command. In the docker console cli we write a command to

run both of these containers. In case it is a first launch, then the docker creates the application containers according to the specification and fills them with data. After the containers creation, the application will run them and you are able to use applications stored in these containers.

```
version: "2"
services:
  web:
    build: web
    command: python app.py
    ports:
      - "5000:5000"
    volumes:
      - ./web:/code # modified here to take into account the new app path
    links:
      - redis
    environment:
      - DATADOG_HOST=datadog # used by the web app to initialize the Datadog library
  redis:
    image: redis
# agent section
```



**Fig. 2.** docker-compose.yml file with commented source code

### 3. Conclusion

To me as a cloud solutions developer, the docker gives me new opportunities to develop modern applications. I use the docker technology in two TACR projects that are focused on Bigdata area. Displaying large amount of data is one of the most difficult problem. End-user graphical user interface must be designed in a very sophisticated way to provide high Quality of experience of the final application. Application has to be fast and responsive so that user can work with it in real-time conditions. Therefore, the microservice architecture appears to be one of the best options how to solve problems by working with Bigdata. Contrary to virtualization, it can save the server computation capacity and it provides me space for new services deployment. Another advantage is that I can work with various technologies that I do not have to install but I deploy them as containers, so I can test if certain technology is suitable for solving specific problem. I plan to deploy Docker in projects that are designed for national transporters, mobile network providers or public administration. In the future, it will allow us better integration with services provided by it4innovations.

Finally, there is a question if to use virtualization or mentioned docker. My answer to this question it is best to use both technologies. They complement each other well. Where you need more sophisticated solution there you can use docker and where the computational power is needed, there is better to use virtualization. To me as a developer, my docker gives me new possibilities to design modern applications and it also allows me to compatibly maintain the development environment which I need for my work. Application conversion from development to production environment is just a matter of few minutes.

## References

1. What is Docker and why is it so darn popular? [online]. 2017 [cit. 2017-07-30]. Available from: <http://www.zdnet.com/article/what-is-docker-and-why-is-it-so-darn-popular/>
2. About Docker in Windows [online]. 2017 [cit. 2017-07-30]. Available from: <http://www.in-foworld.com/article/3163257/application-development/what-you-need-to-know-about-docker-in-windows.html>
3. Docs docker [online]. 2017 [cit. 2017-07-30]. Available from: <https://docs.docker.com>



# Design of an All-Fiber EDFA Laser System for Simulation Power Load of Backbone Network

Radek Pobořil

Department of Telecommunications, FEECS,  
VŠB – Technical University of Ostrava, 17. listopadu 15,  
708 33 Ostrava – Poruba, Czech Republic  
radek.poboril@gmail.com

**Abstract.** This article is focused on the design of an all-fiber laser that was supposed to be used for simulating power load similar to the power load in backbone networks. The first part of the article is a brief introduction to the topic of lasers and erbium doped fiber amplifiers. The following parts present design of a fiber laser with ring cavity, and measuring the ideal length of a doped fiber and the split ratio of the output coupler. After proposing the first stage –a laser– we focused on the construction of the two following stages –EDFA pre-amplifier and EDFA amplifier. There were used fibers with various levels of erbium ion density, namely ISO-GAIN I6, and Liekki ER110-4/125. The resulting output power of the whole system was 320 mW. This value is sufficient when we take into account that we used only single-mode fibers with energy pumped directly to the fiber core. The output wavelength of the whole laser system was 1559 nm.

**Keywords:** Doped fibers, Erbium, Fiber laser, High power

## 1 Introduction

In this technologically advanced time it is necessary to maintain existing optical networks in perfect condition [1]. To keep their top quality, numerous protections against mechanical as well as thermal damage have been developed in the course of time. There are various types of rubber and plastic, also Kevlar, metal, water-repellent gels, etc. Naturally, also the optical fibers themselves have evolved – their structure and purity of production is being improved. Despite all this, however, ravages of time affect optical fibers. We can even say the fibers age. When aging, each material loses its properties, whether it is mechanical strength or ability to conduct light. Optical fibers that are currently in use have not originally been designed for wavelength division multiplex, and therefore they were not supposed to manage such enormous power density. The intensity of a WDM light beam exceeds the intensity of time-division multiplexing. But it is not only the light power that act on the fiber. There is also the influence of environment, namely moisture, temperature and pressure fluctuation etc.

All these factors contribute to the adverse impact on the optical fiber. This experiment is focused on the effect of high output of light applied to the optical fiber [2], [3].

First, it was necessary to obtain a radiation source that would be suitable for the whole experiment and its associated experiments. Considering an extremely high cost of acquisition of such apparatus, the only way was to design and construct it on our own. Requirements for such laser were simple: stable output power, stable wavelength and the widest spectrum possible with a peak near 1550nm. Given the required wavelength of the laser, we used an erbium-doped fiber. Erbium has a sufficiently wide emission spectrum around 1550nm and is comparatively affordable. When constructing the whole laser, we counted with a multiple stage system. The first stage was created as a radiation source around 1550, and subsequently this radiation was amplified using erbium-doped fiber amplifiers connected in cascade.

## 2 First stage

The first stage of the laser system serves as the source of signal for the rest of the laser system. It is the so called “seed” which will be amplified in the subsequent stages. In our case it is a laser with ring resonator. The pumping source supplies the power the system with energy in the form of radiation at the wavelength of 980nm and the output of 600mW[4]. Using a WDM coupler 980/1550nm, this radiation comes to the input of the erbium-doped fiber. The other end of the fiber is connected to the output coupler in the ratio of 90:10%, where the 10% is used as the output of the entire first stage. The signal then passes through the isolator and goes back to the first WDM coupler, which makes it a complete loop [5]. The length of the doped fiber was simulated in the software Gain master by the manufacturer of the FiberCore fiber. The type of fiber was IsoGain I-6 (with absorption 8 dB/m) and its length was 6m. Considering the cost of the doped fiber we used simulation because of its non-destructive advantages [6]. Another important element was the output coupler. Step by step we tested couplers with division ratios 1/99, 2/98, 5/95 and 10/90. Given that the output power always increased, we used a coupler with the highest division ratio. Other couplers could not be used for financial reasons. Financial demands played a big role in the experiment because all the components connected in the loop had to endure high performance. If we count all the losses in the laser loop, the power was greater than 1W [7]. Standard components in optical networks have usually power handling of 300–400mW. When testing, at first we used a standard isolator for telecommunication networks with power handling of the already mentioned 300mW. This isolator was destroyed after 3 hours of operation. The doped fiber radiated in both directions, therefore it was necessary to use the optical isolator. Without it we would get only half of the performance because the radiations would interfere with each other.

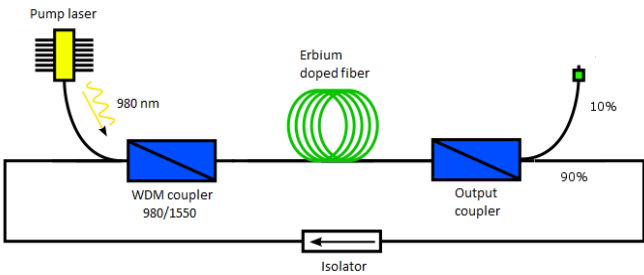


Fig. 1: First laser stage

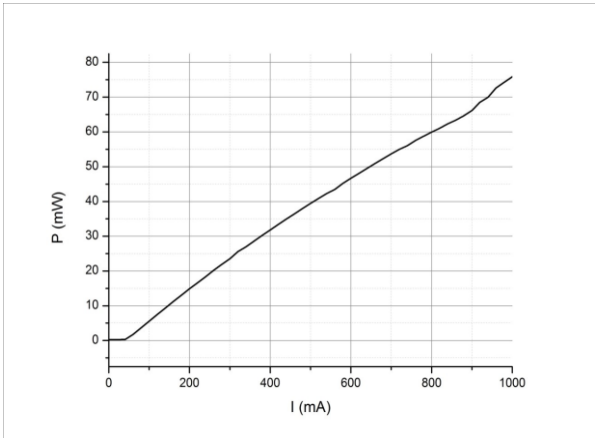


Fig. 2: a) Output power 1<sup>st</sup> stage

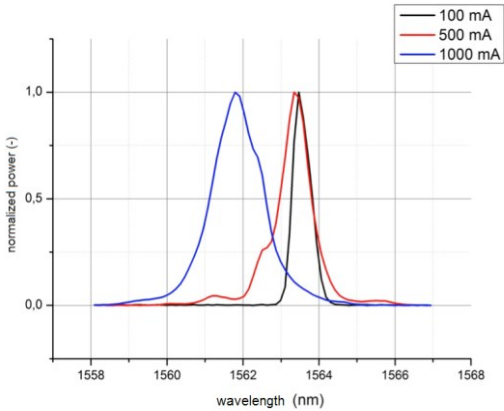


Fig. 2: b) Spectrum 1<sup>st</sup> stage

The optical performance supplied by the pump laser was 600mW. With such pumping power (typically with this type of fiber there is only 100–150mW) there was a considerable loss of energy in reabsorption of the electron to a higher level. This

phenomenon could be seen with the eye because the whole fiber was glowing green. Unfortunately, for achieving the maximum performance it was necessary for the whole laser to work in the saturation mode. The efficiency of the laser was very low, only about 12%. The output power of the laser was influenced by each attenuation found in the laser loop. Therefore, it was necessary not to use connectors, but to weld all parts together [8].

Output parameters of the first stage were 75.85mW at the pumping power of 600mW. It can be assumed that by increasing the pumping power the performance would grow. However, the laser used in this experiment got to its maximum values allowed by the manufacturer. The output power was greatly dependent on the power of the pumping laser. This phenomenon is logical because the wavelength changed depending on the pumping level of the doped fiber. If the fiber is not sufficiently pumped, the output wavelength will be higher.

In our measurements we got to 3 levels of power for the pumping laser. For the first value of 100 mA the output wavelength was 1563.5mW, 200mA corresponded with 1563.3mW. At maximum pumping power the fiber got finally sufficiently energized and the output wavelength approached the value of 1561.8mW. Values in the graph of spectra are normalized to 1. What we intend to show here is not the power but spectral shifts.

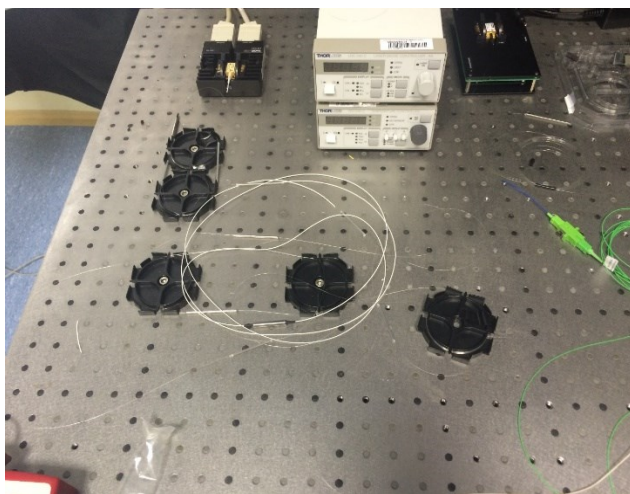


Fig. 3: 1<sup>st</sup> stage of the laser system

### 3 Second stage and third stage

For the second stage of the laser system we used a standard EDFA amplifier with the fiber Liekki ER110-4/125. Again, due to its cost, the length of the fiber was simulat-

ed. Fibers have high absorption of radiation at the wavelength of 980nm. This absorption is 110 dB/m. Thanks to such high absorption a very short fiber was used – only 40cm. The pumping radiation is supplied by a pump and it is 500mW. The radiation goes through a WDM coupler that is connected to the doped core. The coupler that has already been used has an integrated isolator, which reduces the number of connections between individual components. The output power of the second stage is shown in the fig. 5a. The output power is plotted in dependence of the pumping power on the power of pump of the seed laser. The graph shows that the power increases with the increase of the pumping power. However, it is also clear that it is approaching its saturation. Figure 5b describes the output spectrum for the power of the seed level 100, 500, 1000mA, and 900mA at the pumping source of the amplifier [9], [10].

The third stage of the laser system is very similar to the second one. Again, there is an EDFA amplifier in the same connection. The only difference is the use of the fiber IsoGain I-6 that is 13m long with absorption 8 dB/m. Figure 6a shows the output power of the amplifier at the setting of 100, 500, 1000mA at the first stage, 900mA at the second stage, and 100, 500 and 900mA at the third stage. The resulting output spectrum has its peak of 1562.5 and the output power of 321mW.

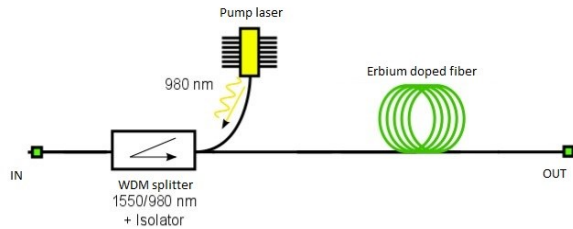


Fig. 4: Design of EDFA used for 2<sup>nd</sup> + 3<sup>rd</sup> stage

## 4 discussion and conclusion

In this article we've focused on a proposal of a fiber laser that would be used as a source of high optical performance for loading optical fibers and fiber-optic components. The entire source should simulate power load similar to that in an optical network. In the first part we focused on the construction of a fiber laser that was supposed to serve as a seed for the whole connection. The maximum output power was approximately 75mW. The signal was then amplified in two consecutive EDFA amplifiers. There were two types of erbium-doped fibers used in the whole construction. For larger lengths we used the fiber IsoGain I-6. The second one was the highly doped Liekki ER110-4/125 that had high absorption of 110 dB/m. When using a fiber of great length and low absorption, or conversely short length and high absorption, the wavelength was shifted to higher values. Given that the whole system was continuous, there was no need to deal with dispersion of doped fibers.

The overall system performance achieved was 321mW. Considering the construction used by a standard doped fiber with pumping into the core, we consider it a success. However, we have the ambition to build a system with higher performance, but with the need of pumping through the cladding of the optical fiber.

In the last part of the article we showed a test connection for loading the optical fiber. The results show that it is necessary to stabilize the whole system. This will be performed by covering the entire system, and also by active cooling by ventilation and Peltier effect. After this modification the system should be stable and resistant to temperatures of the surrounding environment. Right after its finalization, the system was used for power loading of the optical fibers and also fiber-optic components.

## 5 References

1. Ramaswami, R., Sivarajan, K. N., Sasaki, K. H. [Optical Networks: A Practical Perspective.], Morgan Kaufmann Burlington, 157-196 (2009)
2. Hewak, D. [Properties, Processing and Applications of Glass and Rare Earth-Doped Glasses for Optical Fibres.] INSPEC, London, 1-440 (1998)
3. RP Photonics Encyclopedia, "Rare-Earth-Doped Gain Media" [https://www.rp-photonics.com/rare\\_earth\\_doped\\_gain\\_media.html](https://www.rp-photonics.com/rare_earth_doped_gain_media.html) (2016)
4. Berkdemir, C., Ozsoy, S., "On the Temperature-Dependent Gain and Noise Figure Analysis of C-Band High-Concentration EDFAs with the Effect of Cooperative Upconversion," *Journal of Lightwave Technology*, 1122-1127 (2009)
5. Hajireza, P., Emami, S. D., Abbasizargaleh, S., Harum, S. W., Kumar, D., Abdul-Rashid, H. A. , "Temperature Insensitive, Broad and Flat Gain C-Band EDFA Based on Macro-Bending," *Progress in Electromagnetics Research*, 37-48 (2010)
6. Becker, P. C., Olsson, N. A., Simpson, J. R., "Erbium-Doped Fiber Amplifiers: Fundamentals and Technology," San Diego: Academic Press, (1999)
7. Kozak, M., Jaumard B., Bohac, L., "On Regenerator Placement in Loss-less Optical Burst Switching Networks," *Proc. 36th International Conference on Telecommunications and Signal Processing*. Piscataway: IEEE, 311-315 (2013)
8. Pobořil, R., Siska, P., Latal, J., Smrz, M., Cubik, J., Kepak, S., & Vasinek, V., "Measuring Optimal Length of the Amplifying Fiber in Different Working Conditions of the Amplifier." *Advances In Electrical And Electronic Engineering*, 557 - 566 (2014).
9. Dhar, A., Pal, A., Das, S., & Sen, R., "Tm-Yb Doped Optical Fiber Performance with Variation of Host-Glass Composition," *Advances in Electrical and Electronic Engineering*, 582 - 589 (2014).
10. Dhar, A., Kasik, I., Podrazky, O., and Matejec, V., "Fabrication and Properties of Er-Doped Nanocrystalline Phase-Separated Optical Fibers," *Advances in Electrical and Electronic Engineering*, 29 - 35 (2013).

# Active Pre-equalizer for Broadband Over Visible Light

Tomáš Stratil and Vladimír Vašínek

Department of Telecommunications, FEECS,  
VŠB – Technical University of Ostrava, 17. listopadu 15,  
708 33 Ostrava – Poruba, Czech Republic  
tomas.stratil@vsb.cz

**Abstract.** This paper introduces a new technology called Broadband over Visible Light (BVL) which combines two technology solutions like Visible Light Communication (VLC) and Broadband over Power Line (BPL). This new technology is suitable for converting modern LED lighting systems into communication systems. However, there are some deficiencies in BVL technology such as the low bandwidth of LED optical transmitters. Pre-equalization may be solution for this problem. This paper proposes higher bandwidth using pre-equalization circuit. Also, it shows real experimental results demonstrating an improvement of bandwidth and transmission rate.

**Keywords:** Equalization, Labview, pre-equalization, Software-defined radio, Visible Light Communication, VLC.

## 1 Introduction

White light LEDs as a transmitter for communication link have big disadvantage as low bandwidth. Low bandwidth is caused by optoelectronic response of the LED and due to physical principles of fluorescence in a thin layer of phosphor which is responsible for creating white light from blue light. Fluorescence inserts some delay to the optical signal and thus influences the maximum bit rate. White power LEDs achieve several MHz of bandwidth [3]. Some researchers achieve 10 MHz of bandwidth due to optical band pass filter on detection side, where only blue part of wavelength processes pass on photodetector without delayed yellow part from fluorescence. Equalization techniques are used for elimination of LEDs optoelectronic response to achieve higher bandwidth [1], [2]. This article deals with this actual issue and brings new unpublished results, which can help to develop BVL technology.

## 2 Bandwidth of LEDs

Broadband Power Line technology operates in the frequency range from 2 MHz to 32 MHz bandwidth at HomePlug AV specification and provides a 200 Mbps PHY channel rate and 150 Mbps information rate. Suitable bandwidth of optical

transmitter has to be reached for cooperating HomePlug AV specification with VLC. The frequency response of high power light LED Philips Fortimo LED DLM 3000 44 W/830 was measured. Network analyzer Rhode-Schwarz ZVB 4 (3 kHz to 4 GHz), [4] was used with our own designed circuit Bias-T [5] and [6]. PIN photodetector Thorlabs PDA10A-EC was applied on detection side. Philips Fortimo LED DLM 3000 44 W/830 has system efficiency 62 lm/W. This LED light source offers an advantage for VLC measuring and testing, because of its concept of construction. There were used blue LED chips, which are directly placed on the aluminum block for effective cooling. External diffuser in front of blue LED chips converts part of blue (lower) wavelengths range into higher wavelengths due to phosphor layer. This white light LED has patented remote phosphor technology. This LED light source meets requirements for future duplex communication. Photodetector operating in the infrared wavelength range could be used behind diffuser with the phosphor layer. Measured values of frequency response were fitted by cubic function to eliminate roughness caused by noise and other signal distortion. The smoother curve of frequency response provides ideal conditions to design the pre-equalization circuit. A bandwidth of  $-3$  dBm at 2 MHz was achieved with a high power white light LED as shown in Fig. 5. While  $-3$  dBm bandwidth was achieved at 7 MHz with blue part of radiation without phosphor effect.

## 2.1 Design of Pre-equalizer

The purpose of equalization is to compensate signal distortion in a communication channel. The main distortion of the signal was produced by the optical transmitter at VLC channel due to an optoelectronic response of LED and delay of the phosphor. [1]. We used well-known equalization techniques and techniques for designing filters to reach suitable bandwidth. Appropriate bandwidth was reached with really simple electronic circuit, because simplicity of designed circuit was important requirement.

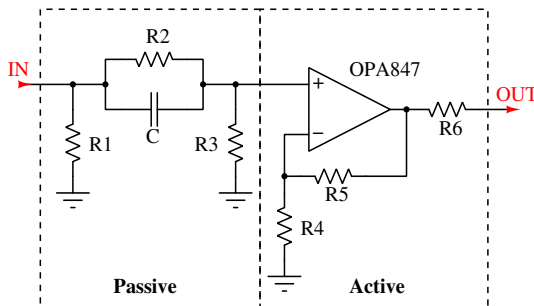


Fig. 1: Circuit diagram of active pre-equalizer with OPA847



Pre-equalization circuit was designed according to reversal of measured frequency response, which can be seen in Fig. 5. The circuit is composed of active and mainly passive part, which determines shape of frequency response. The passive part of circuit is high pass filter, which causes 35 dBm attenuation, as it can be seen in Fig. 2. The active part of circuit contains operational amplifier OPA847 eliminating attenuation of the passive part. The complete circuit provides frequency response closed to the reversal of measured frequency response. Circuit diagram of pre-equalizer can be seen in Fig. 1. The transfer function of the pre-equalization circuit was expressed as:

$$H(j\omega) = \left(1 + \frac{R5}{R4}\right) \cdot \frac{R3}{\frac{R2}{j\omega R2C + 1} + R3}, \quad (1)$$

where  $\omega$  is defined as  $2\pi f$ .

## 2.2 Simulations

Passive part of circuit shapes the curve of frequency response and contains parallel connection of resistor R2 and capacitor C and resistor R3, which is parallelly connected to them. Fig. 2 shows the curves from simulations, where the effect of components values on the shape of frequency response can be noticed. The best result of reversal frequency response was reached by the components  $R2 = 2 \text{ k}\Omega$ ,  $C = 22 \text{ pF}$  and  $R3 = 200 \text{ }\Omega$ .

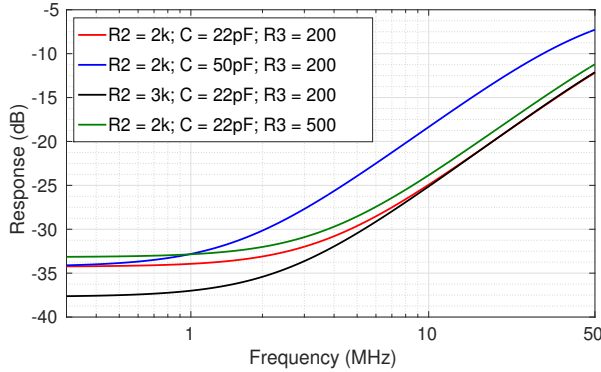


Fig. 2: Simulation results of passive part of pre-equalizer and effect components values on frequency response.

Operational amplifier OPA847 was used in active part of pre-equalization circuit. The OPA847 provides an unique combination of a very low input voltage noise, along with a very low distortion output stage to give one of the highest dynamic range of op amps available. Voltage-feedback of op amps, unlike current-feedback designs, can use a wide range of resistors values to set up their gain.

R4 was set to  $39.2\ \Omega$  and R5 was optimized according to desired gain. Using this guideline ensures that the noise added at the output due to the Johnson noise of the resistors does not significantly increase the total noise over the  $0.85\ \text{V}/\sqrt{\text{Hz}}$  input voltage noise for the op amp itself. This R4 value is suggested as a good starting point for design of the circuit.

Curves gained by simulations of different adjusted values of feedback resistor R5 are shown in Fig. 3, where open-source simulation software Qucs was used. R4 value was  $39.2\ \Omega$  whereas we were trying to achieve ideal amplification for pre-equalization circuit by adjusting value R5.  $R5 = 750\ \Omega$  provided the best result of reversal frequency response and achieved gain  $+20\ \text{V/V}$  of operation amplifier. Values of R4 and R5 affected complete amplification of active part of the circuit. On the other hand they also affected shape of the frequency response of overall pre-equalization circuit as shown in Fig. 3.

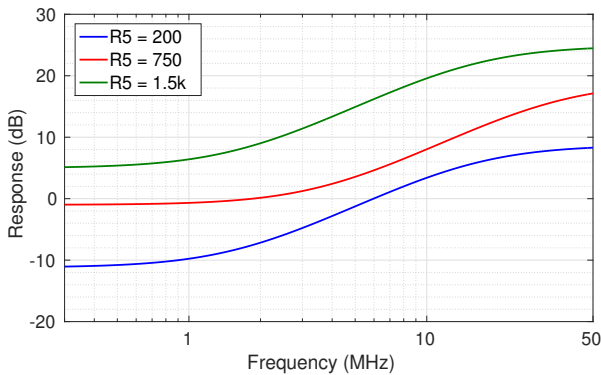


Fig. 3: Simulation results of active part of pre-equaliser and different feedback resistor values effect on frequency response.

## 2.3 Measurement

The frequency response of constructed pre-equalizer was measured and the results were compared with simulations. Network analyzer Rhode-Schwarz ZVB 4 (3 kHz to 4 GHz) was used. Results from simulations, measurements and reverse are shown in the Fig. 4. Frequency response from simulations and measurements of pre-equalization circuit are almost same to the reverse frequency response, which is desirable. Operational amplifier OPA847 operates up to 40 MHz as seen in Fig. 4. This is due to high amplification of OPA847, however 40 MHz is sufficient for BVL technology solution. The designed pre-equalizer circuit attenuates the input signal by about 1dBm in the frequency range 0.2 to 2 MHz. Designed and constructed circuit achieves power level 15 dBm at 40 MHz. Bandwidth from 2 MHz to 40 MHz of designed circuit is compliant according to HomePlug AV technology solution of Broadband Power Line communication.

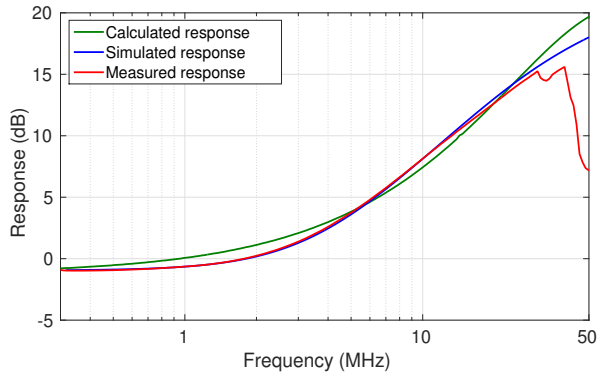


Fig. 4: Frequency response of designed circuit given by reverse, simulation and measurement.

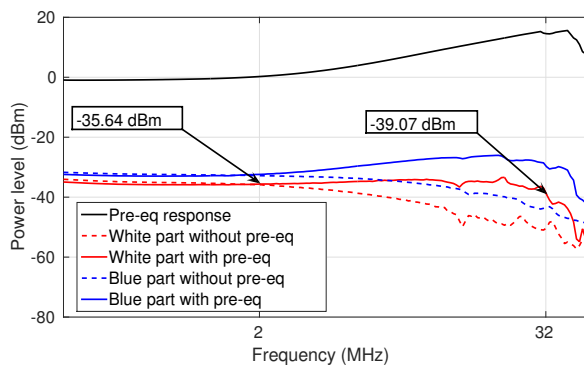


Fig. 5: Effect of pre-equalizer on frequency response of white light LED and blue light LED.

### 3 Conclusion

In this paper pre-equalization of VLC transmitter has been presented. In order to get suitable frequency response of VLC transmitter based on phosphor white LED light source, we have been proposed equalization circuit used in our VLC system. The aforementioned HomePlug AV technology bandwidth from 2 MHz to 32 MHz was achieved with 3.43 dBm attenuation by commercial phosphorescent white light LED and proposed equalizer circuit. The objectives of this paper were to achieve suitable frequency response for the mentioned BVL technology solution. The proposed system demonstrably improves operational bandwidth in VLC system and could be regarded as suitable system improvement for future Broadband over Visible Light (BVL) technology deploy.

### References

1. HUANG, X., Z. WANG, J. SHI, Y. WANG and N. CHI. 1.6 Gbit/s phosphorescent white LED based VLC transmission using a cascaded pre-equalization circuit and a differential outputs PIN receiver. *Optics Express*. 2015, vol. 23, no. 17, pp. 22034–22042. ISSN 1094-4087. DOI: 10.1364/OE.23.022034.
2. H.L. MINH, D. OBRIEN, G. FAULKNER, L. ZENG, K. LEE, D. JUNG, Y. J. Oh a E. T. WON, 100-Mb/s NRZ Visible Light Communications Using a Postequalized White LED *IEEE Photonics Technology Letters*, Vol. 21, No.15, August 2009. DOI: 10.1109/LPT.2009.2022413
3. D. C. O'BRIEN, H. LE MINH, G. FAULKNER, M. WOLF, L. GROBE, J. LI, and O. BOUCHET, Indoor Gigabit optical wireless communications: Challenges and possibilities in *Free-Space Laser Communications X*, San Diego, California, USA, 2010, pp. 781408-7. DOI: 10.1109/ICTON.2010.5549136
4. KIM, N.-T. Ultra-wideband bias-tee design using distributed network synthesis. *IEICE Electronics Express*. 2013, vol. 10, no. 15, pp. 1–8. ISSN 1349-2543. DOI: 10.1587/elex.10.20130472.
5. T. STRATIL, P. KOUDELKA, J. JANKOVYCH, V. VASINEK, R. MARTINEK and T. PAVELEK, Broadband over Visible Light: High power wideband bias-T solution, *2016 10th International Symposium on Communication Systems, Networks and Digital Signal Processing (CSNDSP)*, Prague, 2016, pp. 1-5. DOI: 10.1109/CSNDSP.2016.7574002
6. STRATIL T, KOUDELKA P, LATAL J, VASINEK V, MARTINEK R, NAZERAN H. Design and testing of high power wideband Bias-T for broadband over visible light using software-defined radio. In: *2016 IEEE 17th Annual Wireless and Microwave Technology Conference, WAMICON 2016*; 20162016 Available from: [www.scopus.com](http://www.scopus.com) DOI: 10.1109/WAMICON.2016.7483841

# Measurement Numeric Aperture of The Optical Fiber Exposed to Thermal and Radiation Aging

Aleš Vanderka

Department of Telecommunications, FEECS,  
VŠB – Technical University of Ostrava, 17. listopadu 15,  
708 33 Ostrava – Poruba, Czech Republic  
ales.vanderka@vsb.cz

**Abstract.** This paper deals with the aging of optical fibers influenced by temperature and radiation. There are analyzed changes in the structure of the optical fiber, related to the propagation of light in the fiber structure. In this case for numerical aperture. For experimental measurement was used MM fiber OM1 with core diameter 62.5  $\mu\text{m}$ , cladding diameter 125  $\mu\text{m}$  in 2.8 mm secondary coating. Aging of the optical fiber was achieved with dry heat and radiation. For this purpose, we were using a temperature chamber with a stable temperature of 105 °C where the cables after two months. Cables were then irradiated with gamma radiation  $^{60}\text{Co}$  in doses of 1.5 kGy and then 60 kGy. These conditions simulated 50 years aging process of optical cables. According to European Standard EN 60793-1-43:2015 was created the automatic device for angular scan working with LabVIEW software interface. Numerical aperture was tested at a wavelength of 850 nm, with an output power 1 mW. Scanning angle was set to 50° with step 0.25°. Numerical aperture was calculated from the position where power has fallen from maximal power at  $e^2$  power. The measurement of each sample was performed 10 hours after thermal and radiation aging. The samples were subsequently tested after six months from the last irradiation. In conclusion, the results of the experiment were analyzed and compared.

**Keywords:** MM optical fiber, thermal and radiation aging, numerical aperture.

## 1 Introduction

Nowadays, aging of optical fiber is a current issue. In optical networks, traffic raised several times recently. It has the effect more rapid degradation of materials of optical fibers and hence degradation of optical parameters. Therefore, researches are focused on this area. Attenuation of the optical fiber is one of the most important parameters of the optical fiber. However, this area is already examined by other research groups. In this article, the presented research is focused on changes in the numerical aperture. This parameter relates the refractive index of core and cladding and also depends on the optical fiber materials. In operating conditions, research of aging is very lengthy because the optical fibers do not age so fast as would be needed for research. Therefore, the optical fibers were aging by the methods of high temperature and gamma

radiation. The presented results show the influence of temperature and gamma irradiation on the parameter of numerical aperture. Four samples of multimode fibers were analyzed. The first sample was the reference (new optical fiber). The second sample underwent by thermal aging (100 °C during 90 days). The third sample underwent by thermal aging and radiation aging (at the dose 1.5 kGy). The fourth sample underwent by thermal aging, radiation aging (1.5 kGy) and radiation aging (at the dose 60 kGy).

## 1.1 Numerical Aperture

The Numerical Aperture (NA) is ability of an optical fiber to receive a light. Numerical aperture can be calculate using the refractive index of the core and cladding or measured using far-field measurement. Far-field measurement is defined in IEC 60793-1-43: 2015. The angular scan method was chosen for the test. Measuring assembly was composed of the radiation source with a wavelength of 850 nm with optical power of 1 mW, mode-filter and dark plastic box. In the box, the rotation stage (CR1\_Z6) and intensity sensor (S120-C) were placed.

The optical fiber was placed in the SC/PC fast connector. The front of fiber was placed above the center of the rotation axis of the detector, whereby circular shift is ensured. Minimal distance of the detector  $R$  and end face of optical fiber was calculated by Eq. (1). The used distance was 5 cm.

$$R \geq \frac{d^2}{\lambda} , \quad (1)$$

where  $d$  - the fiber core diameter (62.5  $\mu\text{m}$ ),  $\lambda$  - the wavelength (850 nm). Maximal diameter of detector was calculated by Eq. (2)

$$D = 4R \sin(\delta) , \quad (2)$$

where  $D$  is the detector aperture diameter (mm),  $\delta$ - angular resolution (°) and  $R$  - distance between the detector and end face fibers.

The application was created for purposes of measurement in LabVIEW. Application controlled rotation stage (CR1\_Z6) and collected data from the intensity sensor (S120-C). The angle of 80° with a resolution of 0.25° was set for measurement of the spot. Period of one step took 2 seconds. During this time, we wrote data which were averaged (2000 measured data). Figure 2 shows setting in LabVIEW. Scheme of an arrangement of measuring workplace can be seen in the Fig.1.

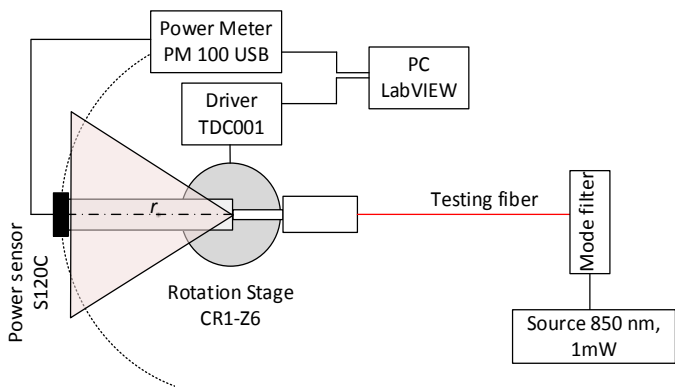


Fig. 1. Scheme of an arrangement of NA measurements.

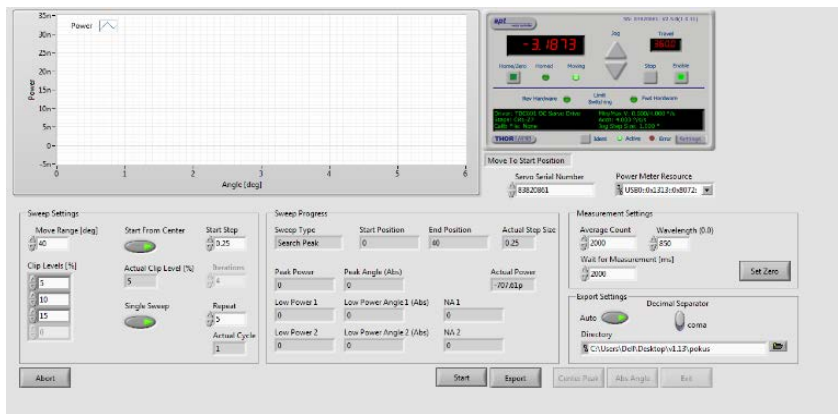


Fig. 2. Front panel in LabVIEW program.

2 Results

The light spot was measured five times for each sample in two perpendicular axes. These resulting measurements were averaged subsequently. After, only one-half of the curve was created by averaging. The resulting curves are plotted in Fig. 3. There was observed a small decrease in peak power for thermal aging sample compared to the reference sample. Angle increased about 0.25° at dropped from a peak value of 5 %. More influenced sample was at 1.5 kGy where the angle increased about 0.35°. The last sample, which was still irradiated 60 kGy, was the most affected. At the last sample, the angle increased about 1.77°.

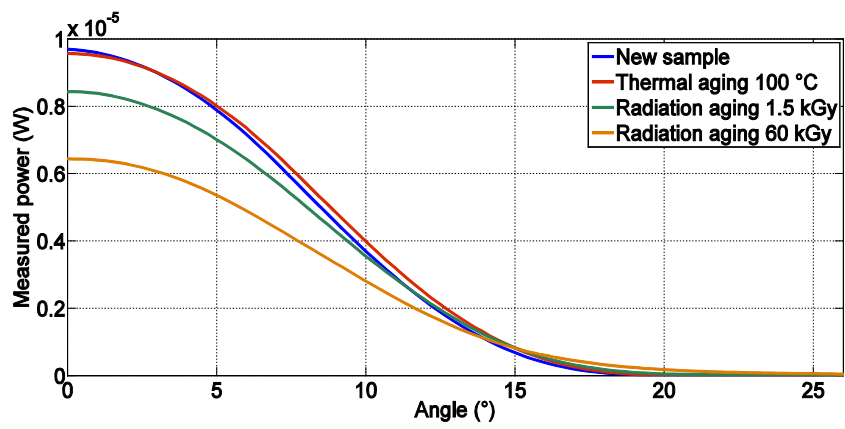


Fig. 3. Measured radiation angle for test samples.

According to the following formula, the numerical aperture was calculated for the angle at 5% of the measured maximum power:

$$NA = \sin \theta \tag{3}$$

The numerical aperture increased about 0.0042 compared to the reference for the temperature aging sample. At the irradiated sample of 1.5 kGy, the numerical aperture increased about 0.0059. We recorded an increase in the numerical aperture about 0.0296 for a sample of 60 kGy.

Table 1. Calculated numerical aperture for test samples.

	New sample	100 °C (90 days)	Gamma irradiation 1.5 kGy	Gamma irradiation 60 kGy
NA	0.27311	0.27733	0.27900	0.30275

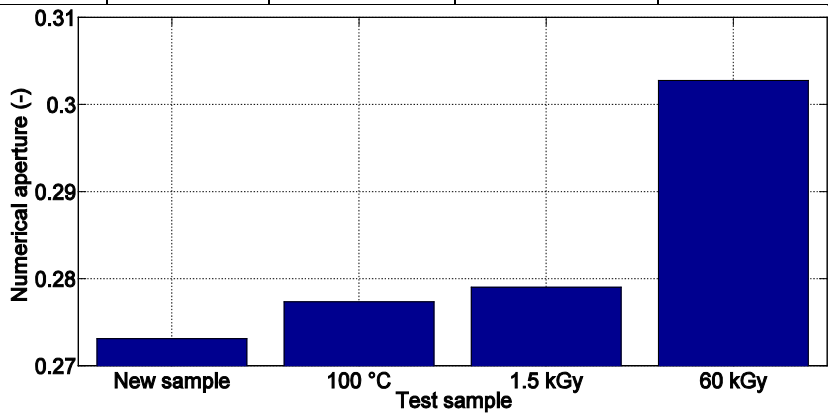


Fig. 4. Change of the numerical aperture for test samples.



### 3 Conclusion

The results show that the thermal aging, which accelerates the aging of the optical fiber, has little influence on the change of numerical aperture. A  $^{60}\text{Co}$  irradiation which simulates the radiation aging has a very significant influence. The ratio of refractive indexes of the core and cladding is changed probably. This is caused by changes in the structure of crystalline lattice of the enamel of optical fiber. It is seen that the change of the numerical aperture is not directly proportional to the dose of gamma radiation. The graph shows the increase in the value of numerical aperture at a dose of 60 kGy, but this increase is not great in comparison with a smaller test dose of gamma radiation. However, the question is whether a larger numerical aperture of fiber is harmful or not. The theory suggests that the numerical aperture gives the ability of fiber to tie up light into its core and cladding. Thus, this ability is higher at a larger numerical aperture, and thus we better tie up light. However, irradiation has a huge effect on the attenuation of the optical fiber (see. References). From a communication point of view, irradiation by gamma radiation is destructive for optical fibers, since the attenuations reach values which are not suitable for operation of optical networks. Therefore, it is necessary to carry out further research in the field of radiation aging and the aging of the optical fiber and optical components. The team of authors is already engaged in this research, and the results will be presented in subsequent articles.

### 4 References

1. HAWN, D. P., C. M. PETRIE, T. E. BLUE and W. WINDL. In-situ gamma radiation induced attenuation in silica optical fibers heated up to 600°C. *Journal of Non-Crystalline Solids*. 2013, vol. 12, iss. 3, pp. 192-200. ISSN 0022-3093. DOI: 10.1016/j.jnoncrysol.2013.08.013.
2. JIN, J., R.-M. XU, J.-X. LIU and N.-F. SONG. Effect of Radiation Dose on Radiation-induced Attenuation and Temperature Dependence in Optical Fiber. *ACTAPHOTONICASINICA*. 2013, vol. 42, iss. 11, pp. 1272-1276. ISSN 1272-1276. DOI: 10.3788/gzxb20134211.1272
3. J, SONG, J. GUO, X. WANG and J. JIN. Temperature dependence of radiation-induced attenuation of optical fibers. *Chinese Optics Letters*. 2012, vol. 10, iss. 11, pp. 110604-110606. Available at: <http://col.osa.org/abstract.cfm?URI=col-10-11-110604>.
4. SEKULIC, R., N. SLAVKOVIC, M. SRECKOVIC, M. KOVACEVIC and M. STAMENOVIC. The influence of gamma radiation on polarization mode dispersion of fibers applied in communications. *Nuclear Technology and Radiation Protection*. 2012 vol. 27, iss. 2, pp. 171-177. ISSN 1212-5075. DOI: 10.2298/NTRP1202171S.
5. BEDNAREK, L., O. MARCINKA, F. PERECAR, M. PAPES, L. HAJEK, J. NEDOMA, and V. VASINEK. The aging process of optical couplers by gamma irradiation. In: *Photonic Fiber and Crystal Devices: Advances in Materials and Innovations in Device Applications IX*. San Diego. 2015 pp. 1-13. ISBN 978-1-62841-752-4. DOI: 10.1117/12.2187044.

# Measurement of Chromaticity Temperature and Polydimethylsiloxane Attenuation Constants

Jan Zavadil

Department of Telecommunications, FEECS,  
VŠB – Technical University of Ostrava, 17. listopadu 15,  
708 33 Ostrava – Poruba, Czech Republic  
jan.zavadil@vsb.cz

**Abstract.** The paper describes the production of cylindrical waveguides from pure polymer polydimethylsiloxane (PDMS) doped by luminophore. Furthermore, in the paper is a determination of attenuation constants for pure samples and a determination of chromaticity temperature for doped samples. For the production of these samples was used a silicone gel and Sylgard 184 phosphor Yttrium Aluminum Oxide doped by the Ceria. Part of this work is the current description of publishing and pedagogical activities for the academic year 2016/2017.

**Keywords:** polydimethylsiloxane, PDMS, luminophore, chromaticity temperature, attenuation constant

## 1 Introduction

Polydimethylsiloxane is an inorganic viscous liquid. One of its main features is the temperature stability which is determined by its molecular bonds of Si-O and a high binding energy. It is also one of the cleanest silicone polymers. Thanks to its high resistivity, it is among the excellent electrical insulators. For this reason, it is commonly used to encapsulate printed circuit boards. PDMS has high resistance to radiation, UV radiation, and chemicals. Thanks to its optical properties, it is a very interesting optic material. The refractive index for wavelength 1550 nm is reported to be 1.399, and its visible spectral transmittance is 96 %.

## 2 Sample preparation and methodics of measurement

Two-component Sylgard 184 elastomer was used to produce PDMS samples. This two-component is made by the Sylgard 184 elastomer and by a curing agent (Figure 1). Both components must be mixed according to the ratio (1:10). This ratio may be expressed in milliliters or grams using laboratory scales (weighing method is better). Curing is done using heat. It is possible to use a hot-air oven or place samples in the boiling water. Recommended temperature range of curing is from 50 to 150 °C, at 100 °C, the cure is around 60–90 minutes. This Sylgard 184 elastomer also cures itself spontaneously at room temperature, this process lasts 48–72 hours. Luminophore Yttrium Aluminum Oxide supplemented with Cerium (Figure 2) was added to this sample in various ratios with respect to the weighed mixture

Samples were made in sterile tubes. The diameter of the tubes was 5 mm, and the length was 50 mm. The use of the tubes allows the formation of a cylindrical sample structure. A mechanical method was used to mix the PDMS and the curing agent. This process produces unwanted bubbles in the samples. Two methods were used to remove bubbles. The first method used was the spontaneous removal of bubbles. This method is lengthy. Samples must be placed in the refrigerator for at least 24 hours. The second method is to use an ultrasonic bath, this method is more effective than spontaneous removal and the bubble removal time is about 2 hours. After removing the bubbles in an ultrasonic bath, the samples were placed in a hot air oven at 120 °C or boiling water at 100 °C. The cure time was 60 minutes. After curing, the samples were divided into smaller samples of 5 mm length. An attenuation constant was determined for these use samples.

The process of production of the doped samples is the same as for unsampled specimens. To ensure the best mixing and distribution of the phosphor was used the rotary press shaker made of the Merkur kit and the stepper motors (Fig. 3). The duration of one turn of the stepper motor was set to 4 minutes. Mixing the luminophores in the PDMS sample took approximately 6 hours. The samples were again cured and divided into smaller samples of 5 mm length. The temperature of chromaticity was measured in samples doped by luminophore.

The measuring station consists of a light source LED with wavelength 470 nm, a photodetector ThorLabs S121C, power meter ThorLabs PM100D and an aperture made of impermeable material and spectrometer USB-650 by OceanOptics.

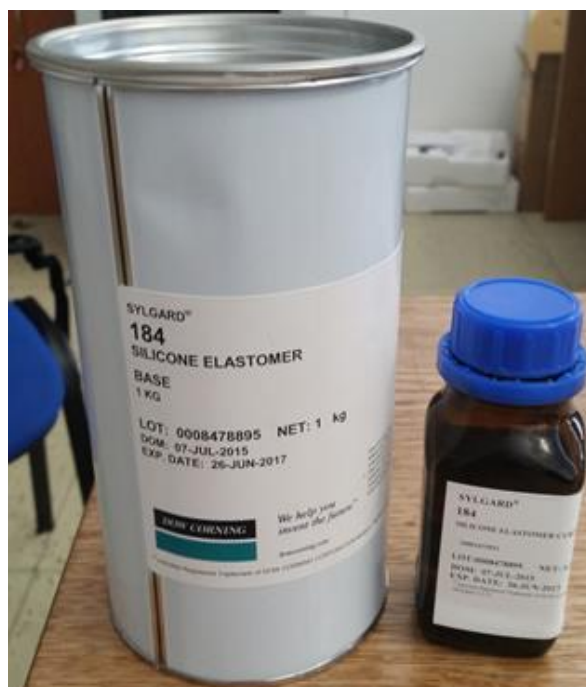


**Fig. 1:** Sylgard 184 and curing agent



**Fig. 2:** Luminophore Yttrium Aluminium Oxide supplemented with Cerium

### 3 Results

The results represent the value of the attenuation constants in the 5 mm length samples. Two ways of processing were used. With the use of ultrasonic baths to remove bubbles, better homogeneity of the entire clean sample was ensured, on the other hand, these samples reached a greater attenuation constant. The reason is the following. When using ultrasound, the molecular bonds of PDMS break down, and therefore the attenuation constant is increased. Manually processed samples placed in the refrigerator show a smaller attenuation constant. The disadvantage is a greater dispersion of the attenuation constant in the individual samples.

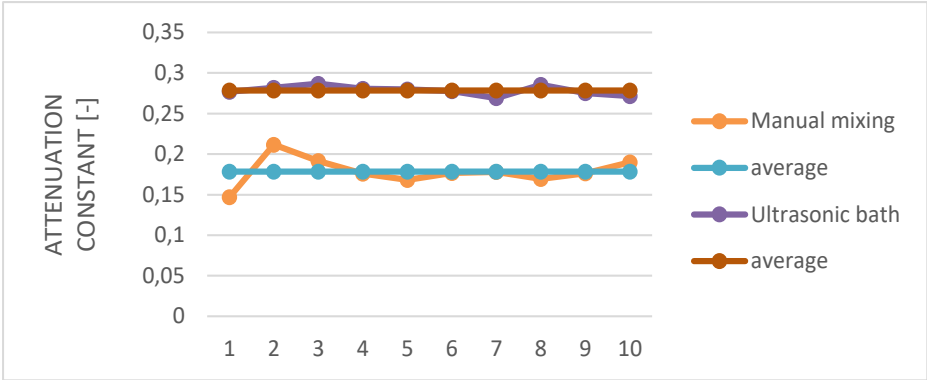


Fig. 3: Attenuation constant of the PDMS

The method for producing the sample with the luminophore is the same as for the sample preparation without the luminophore. Spectral characteristics and temperature of chromaticity were measured for samples. The chromaticity temperature measured was around 6100 K.

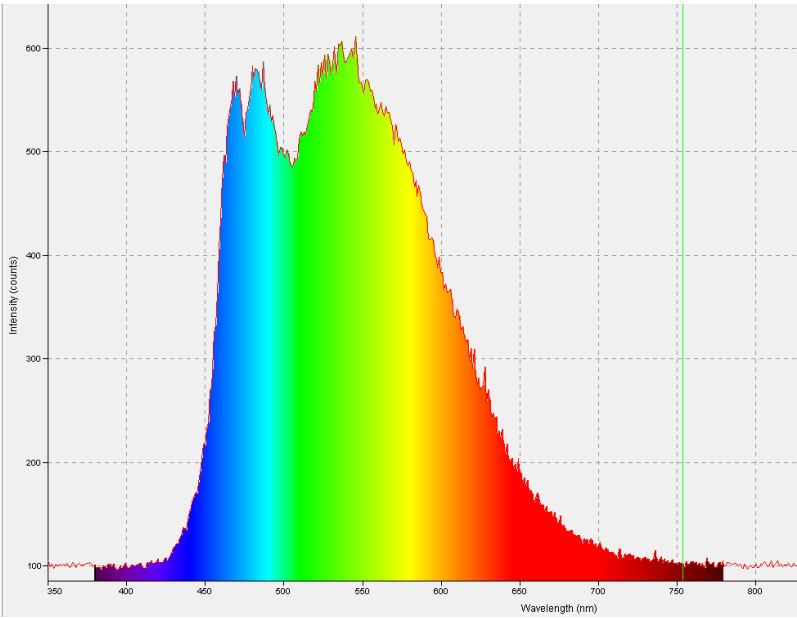
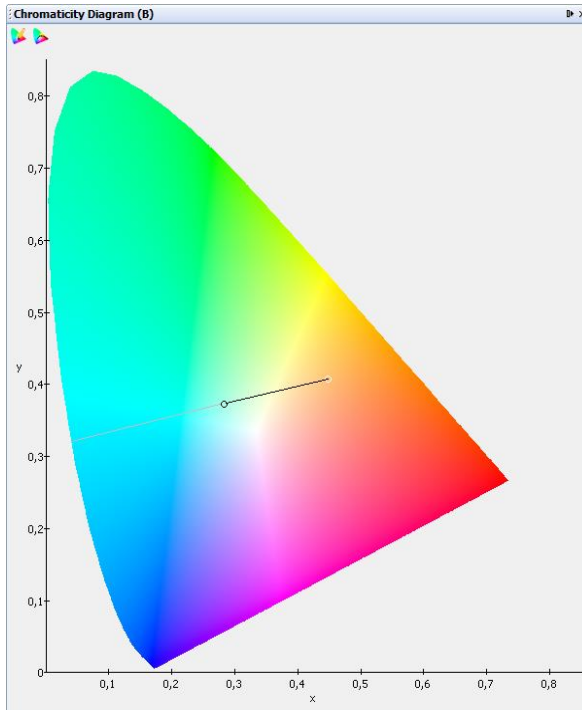


Fig. 4: Spectral characteristics



**Fig. 5:** Color Temperature

## 4 Conclusion

The magnitude of the attenuation constant is as important as the waveguide homogeneity. It is therefore important to find a compromise between these values. The preparation method plays a big role. When producing waveguides, it is important to keep the environment clean. Adding a luminophore allows you to achieve good results in a white light generation by exposing a blue color LED. The chromaticity temperature is in ranged between 5500–7500 K.

## 5 Projects

In the first year of doctoral studies, I was involved in two projects:

1. Project GUARDSENCE II
2. SGS SP2017/79

Within these projects, I participated in the development of experimental methods with PDMS doped luminophores and the technological process of production and measurement. I have made some experiments in the production of luminescence waveguides

to obtain the best possible white light. I have also been involved in collaborating in developing a new type of sensor for vital sign monitoring. This sensor uses a Bragg grating that is encapsulated into PDMS to provide better measurement and protection of Bragg grating.

## 6 Publications activities

I participated as a co-author on two articles. The articles are focused on measurements using Bragg gratings. One was published at a conference in Barcelona. The second article was published in the journal AEEE. I am also a co-author of the patent application and utility model, which is focused on PDMS.

## 7 Pedagogic part and Other activities

In the winter semester, I was involved in teaching the subject ZEL (Fundamentals of Electronics). I actively participated in the promotion of the Department of Telecommunications Technology in the form of a presentation at the Secondary Industrial School in Jedovnice. I also actively helped colleagues with preparations for measuring several projects. I have been involved in providing teaching in classrooms managed by CIT as an administrator.

## 8 References

1. ZAVADIL, Jan. *Studium optických vlastností PDMS s příměsemi* [online]. 2016 [cit. 2017-08-17]. Dostupné z: <http://hdl.handle.net/10084/115969>. Diplomová práce. Vysoká škola báňská - Technická univerzita Ostrava.
2. Güner T., Köseoğlu D., Demir M.M., Multilayer design of hybrid phosphor film for application in LEDs. *Optical Materials*. 2016. DOI: 10.1016/j.optmat.2016.08.023. ISSN: 09253467
3. Holgerson P., Sutherland D.S., Kasemo B., Chakarov., Patterning and modification of PDMS surface through laser micromachining of silicon masters and molding. *Applied Physics A: Materials Science and Processing*. 2005. DOI: 10.1007/s00339-004-3082-3. ISSN: 09478396
4. DAUM, V., J. KRAUSER a O. ZIEMANN. *POF Handbook : optical short range transmission systems*. Springer, 2001. ISBN 978-3-540-76628-5.

# Fiber Optical Sensor of Electric Current with Bragg Grating

Stanislav Žabka

Department of Telecommunications, FEECS,  
VŠB – Technical University of Ostrava, 17. listopadu 15,  
708 33 Ostrava – Poruba, Czech Republic  
`stanislav.zabka.st@vsb.cz`

**Abstract.** This article deals with the measurement of electric current in the energy via optical fiber Bragg grating sensors. Nowadays, the measurement of the electrical current by using optical fiber most commonly based on the principle of Faraday effects, thus the magneto-optic effect. FOCS (Fiber-Optic Current Sensor) is very accurate, modular and easy to install. Another advantage is the isolation of the measuring part from the primary technology, which is sensed. Optical fibers can also be used to measure the inside of the transformer. It also offers the possibility of measuring the temperature of winding. Also, this article summarizes author's activities during one year of his study, his research and development activities related to the studies and research projects.

**Keywords:** optical fiber, web presentation, sensors

## 1 Introduction

Allow me to introduce myself. My name is Mr. Stanislav Žabka. I am a doctoral student at the Faculty of Electrical Engineering and Computer Science at the Technical University of Ostrava. My education program is called Computer Science, Communication Technology and Applied Mathematics and field of study called Communication Technology. I am also working as Java developer in big software corporation and I am using these skills to achieve the best results when it comes to create software which handles and computes big data from sensors. In my first year of study I am extending my knowledge in communication technologies, especially optical sensors. I am part of several projects from the field of fiber-optics. In past I was working as web page creator using CMS Joomla and now I am creating new web page for department of Telecommunication Technologies. To the date 7/2017, I have a total of 3 accepted or published publications.

## 2 About my dissertation work

The fiber-optic sensor is based on the use of Faraday's magneto-optical effect (year of discovery is 1845), in which there is a magnetic rotation of plane of the polarized light. However, the use of this phenomenon for the measurement of electrical quanti-



ties has only occurred thanks to the development of fiber optic technology. The rate of twisting of the polarization plane is directly proportional to the path  $d$ , after which the light in the given environment spreads and size of the components of the vector of magnetic induction  $B$  in the direction of light propagation [1]. The orientation of the vector determines the meaning of the polarization plane. The size of the angle of rotation  $\beta$ , by which the polarization plane is rotated can easily be calculated by a simple relationship:

$$\beta = V \times B \times d,$$

where:  $V$  – Verdet constant,  $B$  – density of magnetic induction,  $d$  – length of path. The Verdet constant depends on the wavelength of the light and it is an optical "constant" that describes the strength of the Faraday-effect for a particular material. Figure 1 shows the proposed basic principle of the fiber-optic current sensor FOCS. The basis of my work is to create the special FBG sensors with a special material called polydimethylsiloxane (PDMS) [2]. This material is inner to electromagnetic interferences (EMI). The Sensing fiber will contain individual gratings and allow us to monitoring the temperature in addition to monitoring the current [3].

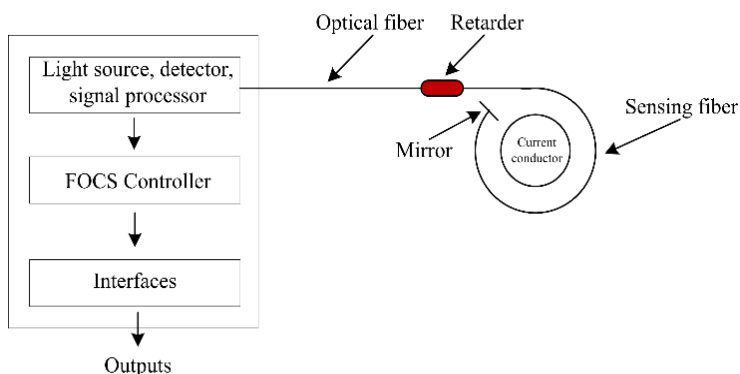


**Fig. 1.** The proposed basic principle of the fiber-optic current sensor FOCS.

During the first year of my study, I was to design a measurement scheme and forms for the creation of FBG sensors. Now I prepare a simulation of parameters of individual FBG sensors. Also, I created a new internet presentation for my team optice.

The purpose of this internet presentation can be divided to three main part:

- Public presentation of department
- Information for students
- Private part for employees

To make page interesting for potential partners or customers, we have splitted all content to 4 main categories. So it is easy to find all information using no more than 3 clicks. It should be also responsive and work on mobile devices. There is big focus on

companies in telecommunication industry so main page contains newest information like ongoing projects, technical articles, partners and contacts, please see Fig. 2.

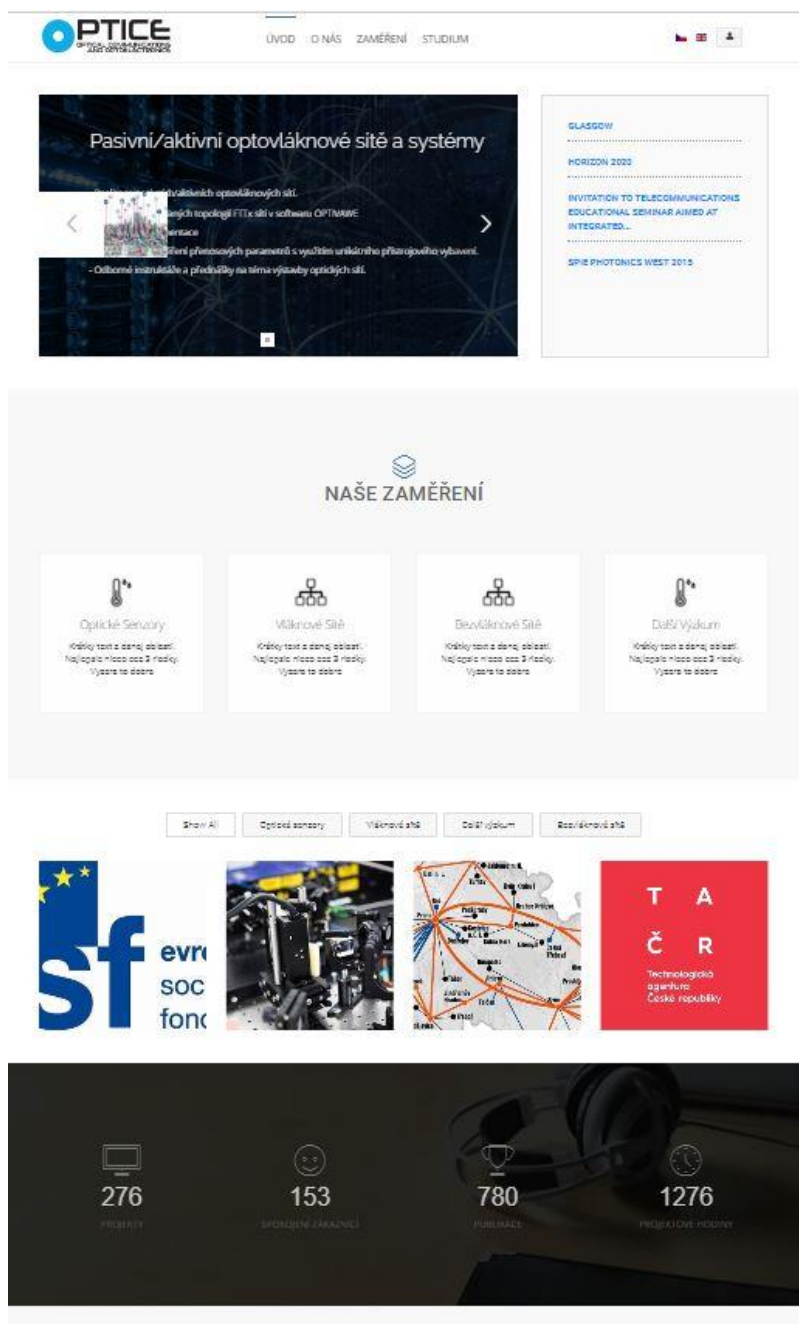


Fig. 2. Main page.

There is also general part with description of department and gallery containing pictures and photos from projects and events where students and employees were involved.

### 3 Projects

As part of my studies, I was actively involved in solving 2 projects, namely:

1. Measuring the weight of trash bins, while being lifted by truck: We were using optical fibers and sensor to detect deformation of fiber attached to lifting arm. We did many measurements to get reference values. Then I prepared software that calculates other missing values such as the weight of trash.
2. SGS SP2017/79 New types of photonic systems for IoT.

### 4 Publications activities

From the date 9/2016 since to the date 7/2017, I have a total of 3 accepted or published publications.

In the first article, we briefly describe the design of innovative fiber optic sensors system. The described methodology presents the use of a Mach-Zehnder interferometer and Bragg gratings together as a sensor system for detecting and monitoring movement within the defined perimeter of  $2.5 \times 1$  m. Perimeter disruptions can be detected by Bragg gratings due to its large deformation sensitivity in transversal or perpendicular directions.

In the second conference paper we focused on the fundamental problem of fiber optic interferometry which is a proposal storing and fixing of the measuring arm and its influence on the frequency range and sensitivity of the interferometer. We focused on this issue and analyzed different types of fixing materials. The results clearly showed that it is necessary to pay attention to fixation materials in the design of the measuring arm of the interferometer for use in practical applications.

The aim of third conference paper was evaluation and comparison of three different signals from three different sensors in application of monitoring the Heart Rate of the human body. We assembled two different types of fiber optic sensors. The first type of sensor uses Fiber Bragg Grating and monitoring of heart rate is based on Ballistocardiography principle. The second type of sensor utilizes fiber interferometer and monitoring of heart rate is based on Phonocardiography (PCG). In case of third type (reference signal), heart rate signal was acquired with the use of standard gel electrodes and modules fixed to the monitored person's chest using a real-time monitoring system for an Electrocardiography (ECG) with virtual instrumentation.

## **5      Pedagogic part and other activities at the Department of Telecommunications**

In summer semesters, I was part of courses ÚDKT (Introduction to Communication Technologies). It should be for me a preparation for next semester, where I need to handle lessons by myself. I helped with preparation of class and leading students during their practical activities. I had to handle several devices that are part of laboratories for this subject.

## **6      Future work**

In the second year of my study, I will create optical waveguides from PDMS. These individual waveguides will be formed by individual FBGs. In addition, practical measurements of the current and temperatures in the measuring chambers will be made. I will also work on projects and prepare 3 publications on my dissertation topic.

## **7      References**

1. P. Siddons, N. C. Bell, Y. Cai, C. S. Adams, and I. G. Hughes, "A gigahertz-bandwidth atomic probe based on the slow-light Faraday effect," *Nat. Photonics*, vol. 3, no. 4, 2009.
2. Fendinger, N. J., "Polydimethylsiloxane (PDMS): Environmental Fate and Effects," *Organosilicon Chemistry Set*, Weinheim, Germany: Wiley-VCH Verlag GmbH s. 626 (2005).
3. L. Weller, K. S. Kleinbach, M. A. Zentile, S. Knappe, I. G. Hughes, and C. S. Adams, "Optical isolator using an atomic vapor in the hyperfine paschen-back regime," *Opt. Lett.*, vol. 37, no. 16, 2012.

# Algorithms Comparison for Electrical Insulator Key Features Detection

Jakub Osuchowski

Opole University of Technology, Faculty of Electrical Engineering, Automatic Control and Informatics, Institute of Computer Science, Prószkowska 76, 45-758 Opole, Poland

[jakub.osuchowski@gmail.com](mailto:jakub.osuchowski@gmail.com)

**Abstract.** This article contains a preliminary study into the detection of electrical insulators in digital images acquired during a power line inspection. The article presents also three different methods for insulator key features detection. The inspection of high voltage power lines is an important task in order to prevent failure of the overhead transmission line. Due to the enormous amount of digital data generated during a high voltage lines inspection, there is a need to automate the detection process of power insulators in digital images. The purpose of this work is to outline the problems with insulators detection with computer vision and image processing methods and show the differences between the three key features detection algorithms, i.e. SURF, BRISK and FAST algorithms.

**Keywords:** SURF algorithm, BRISK algorithm, FAST algorithm, object detection, electrical insulator

## 1 INTRODUCTION

Overhead power lines play a crucial role in the delivery of electric power to the end consumer. The transmission of electricity can be carried out using overhead lines or underground cables. Overhead line consists of three main components: conducting wires, transmission tower and insulators. Overhead lines insulators serve two main functions. They isolate the wires from the ground and tower structure, as well as provide mechanical support for the conductive wires. To successfully fulfill their functions insulators must be designed not only to withstand any electrical stresses that may occur throughout their long lifespans but also to tolerate the mechanical forces applied by elements such as wind and the weight of the conductor. Overhead line insulators diagnosis during power line operation is a very important process. Today's demand for electricity causes enormous pressure on distributors of electric power, to minimize the working downtime of overhead line. Achieving this goal requires conducting maintenance and monitoring of labor power line. It is estimated that 50% of the cost of maintaining overhead lines are costs associated with replacement, reparation and diagnostics of insulators. Failures of insulators account for approximately 70% of power line downtime [1]. Diagnostics of insulators serve three major tasks:

identification of damaged insulators, evaluation of the insulator degradation degree and detection of badly made or improperly selected insulators. One of the basic methods of overhead line monitoring is a visual inspection. This method allows to easily detect obvious failures and defects. The problems here are detailed observation and poor visual accessibility of insulator. The solution is to use a helicopter or unmanned aerial vehicle (UAV) and high-resolution cameras. Such images or videos can be analyzed online during the flight or after completion of the flight. Use of UAV vehicles makes inspection of overhead lines more efficient and precise, but unfortunately this method generated a considerable amount of data that must be analyzed [2].

## 2 Electrical insulators

Insulators used in overhead lines are currently manufactured from porcelain, glass and polymeric composite materials. Porcelain insulators have been in use for over a century and are still valued by the companies specialized in distribution of the electricity. These insulators are made from clay, quartz and feldspar and then glazed in order to shed water in a more effective manner. Porcelain insulators are available in several forms, depending on their function. Another kind of overhead line insulators are polymer insulators, sometimes called composite. They make up a significant part of the market in the field. These insulators have many advantages: lower weight, greater mechanical strength and they are more resistant to vandalism than glass and porcelain insulators. About 60% to 70% of the newly installed insulators are the composite ones. Overhead line insulators are shaped in a way, which maximizes the length of leakage paths along the surface from one end of the insulator to the other. For this purpose, surface is formed in a wave or a series of concentric downwardly cups. The cups act like umbrellas, ensuring that part of the surface of the insulator remains dry even in wet meteorological conditions [1], [3].

Insulators used in overhead lines, particularly in high-voltage lines require regular inspection. It is necessary due to their degradation by atmospheric factors, the effects of temperature, as well as high voltage and mechanical stress. The failure of the insulator occurs, when one of the two of its main functions (insulation and mechanical support) is not fulfilled. [4] Different types of insulators are subject to various types of failure. There is a number of factors that might lead to the insulator failure, such as: manufacturing defects, incorrectly selected insulators, vandalism, extremely difficult working conditions, pollution and meteorological conditions. The most common failure of overhead line insulators is plates cracking due to the expansion of the cement which was used to connect the plate with the cap. Another type of failure is corrosion of the hooks. It occurs in areas exposed to moisture and accumulation of the pollution. The result of corrosion is weakening of the insulator and in the worst case, disconnection of the wire. Another type of insulator damage is crumbling core, which occurs only in polymer insulators, however. These insulators are also affected by other failures. The most serious are: the erosion of the plates due to the accumulation of dirt and salt, the tearing of the plates by strong winds and destruction of the plates by the action of the birds. Glass and porcelain insulators are cracking frequently due to van-

dalism. In porcelain insulators vandalism results in breaking off of a piece of the plate. With respect to the glass insulators, even a minor damage causes the fracture of the whole plate, due to the hardening. These insulators have also tend to break spontaneously, due to release of tension accumulated during the toughening process. The most common detection method of insulators damages is visual inspection. This method provides a simple and cost-effective means of detecting specific obvious defects such as heavy corrosion of the metal hardware, broken shells, and large cracks. The success of this technique is largely dependent on the level of detail that can be perceived from the observation point. This method is therefore employed only as part of a routine line patrol [1], [2].

### 3 Key features detection and description

The task of detecting matches between two images or objects is part of a number of applications concerned with the methods of processing digital images, i.e. 3D reconstruction, image recording or object recognition. Identifying matches between images may be divided into three main stages. Firstly, algorithms based on the detection of local features detect interest points in given images, such as corners. Next, the neighbors of the keypoints are recorded in the form of vectors which are then matched between different images. Based on their location, vectors of displacement are computed. The quality of the algorithm largely depends on the quality of the determined interest points and their description. Algorithms should detect those points in suitable locations independently of changes to the exposure, location and orientation of the image, and to a certain extent independently of changes to the viewpoint or scale [5].

One of the most commonly used algorithms for the detection and description of local features is SIFT (Scale Invariant Feature Transform). This algorithm transforms an image into a large collection of local feature vectors, generating image pyramids with smaller and smaller resolutions. The images that constitute a pyramid are differentiated, as they are obtained by subtracting two images created as a result of filtering the initial image using the Gaussian filters of different parameters. Such local features are mostly insensitive to changes in lighting, rotation and scale thanks to the application of the DoG (Difference of Gaussians) pyramid. Another algorithm characterized by high operation speed and stability of detected keypoints is FAST (Features from Accelerated Segment Test). This algorithm contains a segment test criterion, based on a circle made up of 16 pixels surrounding a candidate point  $p$ . The keypoint detector classifies  $p$  as a keypoint if the circle contains  $n$  contiguous pixels, all of which are brighter than the intensity of the candidate point plus a threshold value  $t$ , or darker than  $I_p - t$ . Due to the fact that the data returned by FAST algorithm cannot be used as a basis for generating a descriptor, SIFT descriptor is often used to describe the features. Another algorithm for the detection and description of features is BRISK (Binary Robust Invariant Scalable Keypoints), which is based on the FAST spatial-octave algorithm for detection purposes, and on testing binary patterns to describe the detected points. The descriptors for BRISK contain 512 bits. They compute the

weighted Gaussian mean on a set derived from a point pattern located in the proximity of a characteristic point [6], [7].

Another algorithm for detecting and describing local features is SURF (Speeded-Up Robust Features) algorithm, which is partly based on SIFT, but it is characterized by substantially accelerated speed with only slightly deteriorated accuracy of local feature matching. SURF detection uses the determinant of the Hessian matrix, but it only applies basic approximation methods. The determinant of the Hessian matrix is applied as a measure of local variation around a point, and the point is selected when the determinant is the highest. In order to accelerate computation, the algorithm uses indirect image representation, i.e. the so-called integral image. It is computed based on the input image by summing pixel values. Thanks to the application of this method, the size of the image does not influence the operation of the algorithm. This allows processing of high-resolution images. SURF descriptor uses Haar wavelet distribution in the region of interest. First, orientation is ascribed to the keypoint. Then, a square region is built around it. This resulting region is divided into smaller 4x4 regions. Thanks to that, the spatial information is retained. For each of the subregions, features for exemplary points, distributed regularly in the vertices of a 5x5 grid, are computed. The computed values create a four-dimension descriptor [5], [8].

## 4 The study

The main objectives of the measures taken was to analyze the possibility of enhancing selected elements that match a given pattern (insulator) in an image. For this purpose, efficiency of three key features detection algorithms has been tested. The number of features the algorithm detects in the image, the percentage of features detected on the insulator, and the time of feature detection were investigated. The set of data on which the study was based was comprised of images obtained with the use of different tools and acquisition methods. The images depicted scenes recorded from a UAV (Unmanned Aerial Vehicle), a helicopter, and as a result of personal inspection by foot. The devices used were Canon 5D Mark II and GoPro Hero 4. The set of data includes scenes with real and working insulators (Fig. 1.)



Scene 1



Scene 2





Scene 3



Scene 4

**Fig. 1.** Selected digital images depicting insulators on existing power lines.

Scenes have been selected to represent different types of insulators in different working conditions.

Table 1 shows the results of the analysis performed for four different scenes and three key features detection algorithms.

**Table 1.** The results of the analysis

Number of scene	Name of algorithm	Number of features	Percent on insulator [%]	Detection time [s]
Scene 1	SURF	17456	7.6822	1.7969
Scene 1	BRISK	12490	10.2562	0.1406
Scene 1	FAST	29018	10.173	0.0625
Scene 2	SURF	8990	11.7686	1.0156
Scene 2	BRISK	7994	10.608	0.0781
Scene 2	FAST	20051	11.9096	0.0312
Scene 3	SURF	3008	7.2473	1.25
Scene 3	BRISK	1557	7.3218	0.0781
Scene 3	FAST	2308	6.8024	0.0156
Scene 4	SURF	11555	8.0831	2.2031
Scene 4	BRISK	8809	4.2343	0.1562
Scene 4	FAST	20225	2.6304	0.0625

As can be seen in table 1 the operation of algorithms varies considerably between scenes. The first study indicator was the number of features found in the entire image. As can be seen, least features was detected by the BRISK algorithm for all the scenes. However, the ratio of the number of features varies significantly between scenes. For most cases, most features were detected by the FAST algorithm. The second determinant of the algorithm's operation was percent of features found on the insulator. In this case much depends on the type of scene, but the most stable was SURF algorithm (always above 7%). In the last step, the speed of the key feature detection was investigated. The FAST algorithm proved to be the fastest algorithm. The surf algorithm

turned out to be considerably slower than the rest of the algorithms. This is very important if the algorithm would work in online condition.

## 5 CONCLUSION

Early detection of overhead line insulators failures is critical to avoid costly downtimes of whole high voltage power line. By using computer vision and imaging processing methods it is possible to designate frames in video sequences and predefine regions of interest which contain insulators. Thanks to these actions the cost and time of line inspections can be significantly reduced. The use of UAV vehicles and imaging methods may also allow in the future to create a complete and autonomous transmission line inspection system. Choosing the right key features detection algorithm is very important because it has a big influence on the accuracy and speed of the insulator identification.

## 6 References

1. Anjum, S.: A Study of the Detection of Defects in Ceramic Insulators Based on Radio Frequency Signatures. University of Waterloo, (2014)
2. Wang, X., Zhang, Y.: Insulator Identification from Aerial Images Using Support Vector Machine with Background Suppression. In: ICUAS, (2016)
3. Holtzhausen, J.: High voltage insulators. *Electrical Engineering*, vol. 53, no. 11.(1994)
4. Bretuj, W., Fleszy, J., Wieczorek, K.: Diagnostyka izolatorów kompozytowych eksploatowanych w liniach elektroenergetycznych, *Przegląd Elektrotechniczny (Electrical Review)*, vol 5a, no. 5; (2012)
5. Bay, H., Tuytelaars T., Van Gool L.: SURF: Speeded Up Robust Features. In: ECCV, vol 3951, (2006)
6. Mikolajczyk, K., Schmid C.: Indexing based on scale invariant interest points, In: ICCV, vol.1, pp. 525-531 (2001)
7. Lowe, D. G.: Object recognition from local scale-invariant features. In: ICCV, vol.2. (1999)
8. Zhao, Z., Liu, N.: The recognition and localization of insulators adopting SURF and IFS based on correlation coefficient. *Optik*, vol. 125, pp. 6049-6052, (2014)

# UAV as a System which Enables Localization of Pollutants on the Industrial Area

Sławomir Szymocha

Opole University of Technology, Faculty of Electrical Engineering, Automatic Control and Informatics, Institute of Computer Science, Prószkowska 76, 45-758 Opole, Poland

slawomir.szymocha@doktorant.po.edu.pl

**Abstract.** The author presents a structure of unmanned aerial vehicles. The system enables the real-time spatial detection of the pollutants distribution in the industrial area. There is a possibility of very fast measurement of certain factors found in the air due to advantages of the aerial vehicle. The examination is correlated with GPS coordinates. Vehicle sends the real-time data, the analysis of which is possible by means of a web application. UAV transfers the measurement data through a GPRS modem. The information is saved locally on a platform as well as remotely on a server. In addition, ground measurement is conducted with ground measuring vehicles in order to verify changes occurring within the time period.

**Keywords:** air pollution, measurement of the air quality, UAV, unmanned aerial vehicle

## 1 INTRODUCTION

Article focuses on the role of unmanned aerial vehicles in the process of measuring environmental conditions. Significant advantage of air quality measurement carried out by aerial unit might be observed over ground-based unit.[1] The main limitation of a ground-based unit is its position invariability and difficulty in its relocation. In Poland, the measurement is carried out in most cases by stationary units of measurement. Each unit must be properly prepared and located. The stationary measurement unit has a container construction. The outer casing is made of layered slabs i.e. metal and an isolating layer that protects device against sudden changes in temperature. The device must be connected to a direct power source, which is electric network. This is related to the energy consumption of the measuring equipment. On hot days, air conditioning consumes most of energy in order to provide stable temperature conditions inside the measuring station. Maintenance of specific temperature ranges ensures repeatability of measuring values and eliminates temperature tolerance errors of the measurement sensors. Installment of the measuring unit requires land development permit and supply of media i.e. electricity. The unit itself must be insured and secured with an alarm to reduce the risk of vandalism. The specificity of a stationary measuring unit construction significantly impairs its relocation. Aerial unit enables to measure air compounds on a very wide area. Spatial

measurement might be a subject to significant quality errors, but its advantages are in favor of its use. Article overviews the use of UAV units to measure quality of air. Thanks to the use of the aerial platform, it is possible to perform the measurement directly over the place where air pollutants are emitted and observe spatial distribution of the pollution. This is important in determining the occurrence of a particular type of pollution.

## **2 AIR POLLUTION**

According to the World Health Organization, more than 80% of people is breathing poor quality air, because large countries do not comply with air quality standards, especially India, where industrialization greatly deteriorated air quality.[2] The quality of the air can be described as poor or very poor. Factories do not use emission reduction filters, many of them uses low-quality fuel. Combination of low quality fuel with too low combustion temperature and lack of any filtration systems causes significant environmental pollution. With rise of pollution levels, life quality decreases and morbidity due to respiratory diseases increases. Increase of pollution causes increase in blood pressure among obese people and people with cardiovascular problems. [4] Breaching the air quality threshold poses a threat to the life of a group of society with health problems. As early as the nineteenth century, the negative impact of air on human life was observed, especially in very industrialized areas. Usually deaths were not associated with a specific illness, but with time, the impact of air on human health was noticed. Air samples were taken into the glass vessels and the quantities of substance deposited on the bottom were examined. Current air quality studies must be low-cost and offer satisfactory results and extensive measurement.[3] This can be achieved by use of aerial unit operating in autonomous or semi-autonomous system.[8] The type of pollutant to be examined depends on the user's preferences of the measurement system. The system proposed by the author enables measurement of seven different compounds in the air. The quality of the measurement depends on the temperature, pressure and humidity. The unit proposed by the author takes into account each of these factors. Strong rainfall may distort the measurement due to the influence of humidity on the sensors. Breach of dew point by any of the sensor disqualifies proper measurement. The condensation of water on the inner parts of the sensor prevents proper measurement and interpretation of its results.

## **3 MEASURING UNIT**

The author of the article selected WaspMote as a measuring unit, which is evaluating board equipped in a number of cable joints. The device is controlled by the processor from AVR family and it is equipped in outer GPS antenna and GPRS modem (fig. 1).[7]

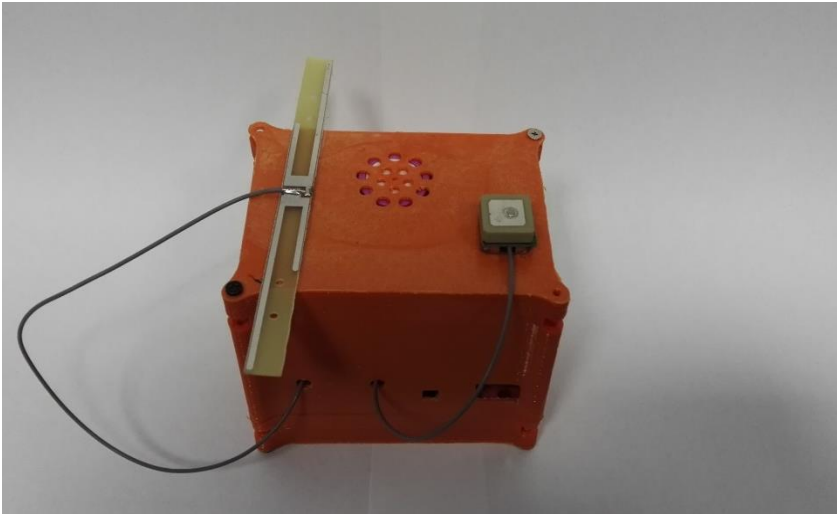


Fig.1 Measuring unit

On the left side, there is a GPS receiver and on the right side, there is the GPRS communication antenna. The unit is equipped with its own lithium-ion battery module. The battery capacity enables several hours of measuring. When designing the casing, lightness and durability were important factors for the designer. The casing was made in 3D printing technology.[5] The orifices allow to take samples and to evaluate the air. Comparison of UAV measurement results to specific standards is performed by the software developed by the author. The results are presented on the website and are saved locally on SD card. This is especially important in case of loss of registered data. Thanks to the multi-stage data saving and diversity of data backup location, the security was significantly increased. The device is equipped with several measuring slots. During measurement it is possible to use up to seven measurement sensors, adapted to dedicated development board. (Figure 2). 'GAS poro' adapter board enables the use of calibrated sensors. Confirmation of calibration is confirmed by the statement.

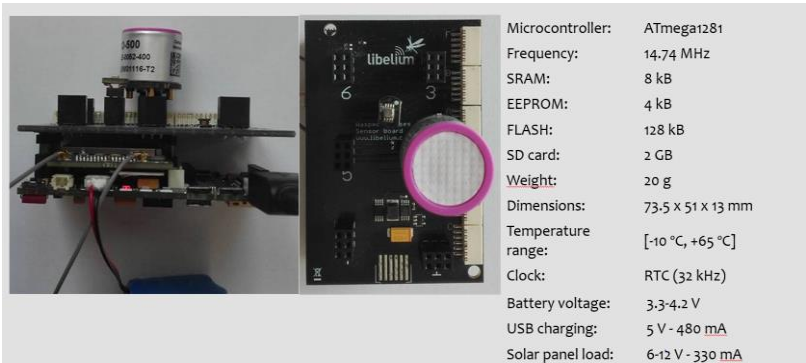


FIG.2 Measuring unit with CO sensor.

Test measurement was conducted on the premises of the production plant in the middle-sized agglomeration. The site of the measurement was a cement plant. The CO measurement was performed by calibrated sensor placed under the drone. Measurement points were linked to the position by GPS trajectory. The resulting image shows CO distribution over a large area and takes into account areas characterized by higher CO concentration. (Fig. 2). The distribution of the agent was affected by both, the height and wind direction. No irregularities were detected during the flight over the combustion chimney.

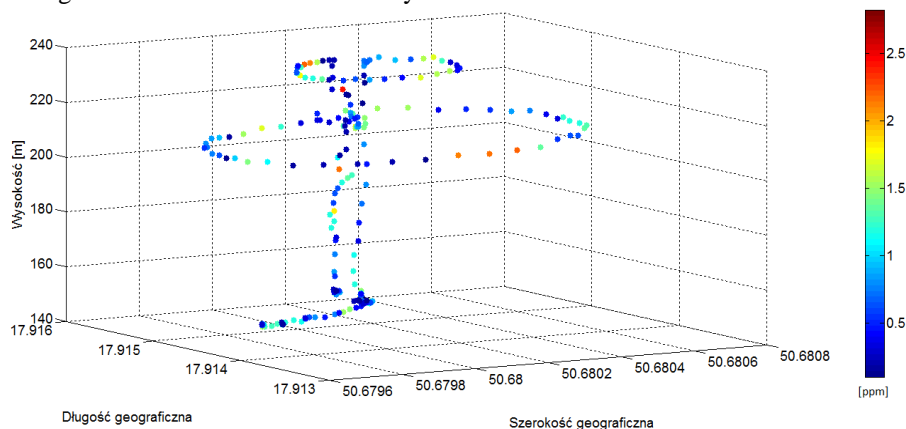


Fig.2 Results of test measurement

## 4 Conclusions

Thanks to the use of flying measurement units it is possible to measure wide area with a single measuring device. Spatial measurement using GPS trajectories allows to correlate measurement results with their actual location. The mobile measuring unit offers great opportunities in terms of locating the sources of pollutants and their types and it is an alternative to the stationary measuring points, that are difficult to relocate. [6] Spatial measurement enables to determine the concentration of a given agent at the height and position specified by the user. Spatial imaging of measurement helps to determine the location of a leak of given substance. With the development of autonomous systems, it would be possible to perform a fully autonomous measurement of air quality in a given area. According to the author, the best way to spatially measure obstacle-free and densely built up areas is to use UAV fully programmable with virtual mapping based on spatial documentation. This

documentation can be prepared by using the LIDAR system. For built-up areas, it is required to register the pilot's flight path during manual control or use manual control only. The author conducted test measurement at the cement manufacturing plant. The plant is fueled with solid fuel and the stove is connected to a large chimney. No abnormalities were found during the measurement. Results of the measurements fell within public air quality standards.

## 5 References

1. Haas P., Balistreri C., Pontelandolfo P., Triscone G., Development of an unmanned aerial vehicle UAV for air quality measurements in urban areas, 32nd AIAA Applied Aerodynamics Conference, 2014
2. Osseiran N., Chriscaden K., Air pollution levels rising in many of the world's poorest cities, World Health Organization, <http://www.who.int/mediacentre/news/releases/2016/air-pollution-rising/en/>
3. Lonel I., Popescu F., *Methods for Online Monitoring of Air Pollution Concentration*, INTECH Air Quality, 2010
4. Sroczyński J., Wpływ zanieczyszczeń powietrza atmosferycznego na zdrowie ludzi. Wrocław 1988
5. SZYMOCHA S.: Możliwości zastosowania bezzałogowych pojazdów latających do analizy jakości powietrza; Przegląd Naukowo-Metodyczny Rok X Nr 1/2017 (34), ISSN: 1899-3524, pp. 958
6. SZYMOCHA S.: UAV as an Alternative Platform Used in Stationary Air Condiciosn Measurements; Zeszyty Naukowe Politechniki Opolskiej Elektryka z. 75 Nr/2017, pp. 103 ISSN 1429-1533
7. Waspote Technical Guide, [http://www.libelium.com/downloads/documentation/waspote\\_technical\\_guide.pdf](http://www.libelium.com/downloads/documentation/waspote_technical_guide.pdf)
8. Gugliermetti L., Sabatini M., Palmerini G.B., Carpentiero M., Air quality monitoring by means of a miniaturized sensor onboard an autonomous wheeled rover, IEEE 2nd International Smart Cities Conference: Improving the Citizens Quality of Life (2016), ISC2 2016 -Proceedings. pp. 1-4





# Author Index

- Andrešič, David, 178
- Bailová, Michaela, 273
- Baleja, Richard, 65
- Bednárek, Lukáš, 377
- Behán, Ladislav, 383
- Běloch, Michal, 279
- Béřeš, Michal, 284
- Blažek, Vojtěch, 1
- Bos, Petr, 7
- Briš, Radim, 19, 371
- Cigánek, Jiří, 13
- Ćosić, Rajko, 290
- Cuong Dinh Tran, 71, 90, 96
- Dedek, Jan, 120
- Dočekal, Tomáš, 126
- Domesová, Simona, 294
- Dung Vo Tien, 19
- Fait, Michal, 183
- Foltyn, Jan, 132
- Foltyn, Ladislav, 300
- Frnda, Jaroslav, 389
- Fulneček, Jan, 25
- Gasz, Rafał, 189
- Gecová, Kateřina, 138
- Golembiovský, Matěj, 102
- Goňo, Radomír, 19, 31, 37
- Hajduk, Peter, 395
- Hájek, Lukáš, 400
- Halfar, Radek, 144
- Hanzelka, Jiří, 195
- Hau Huu Vo, 71, 90
- Hawliczek, Petr, 31
- Hendrych, Jakub, 201
- Horák, Bohumil, 156
- Horák, David, 336
- Chamrád, Petr, 77
- Chau Si Thien Dong, 71, 90
- Janečko, Tomáš, 207
- Jargus, Jan, 406
- Jirůtková, Pavla, 306
- Kahánková, Radana, 150
- Kašpar, Adam, 213
- Kocman, Stanislav, 83
- Kojecký, Lumír, 219
- Kolařík, Jakub, 108
- Kotík, Vojtěch, 213
- Kovář, Petr, 312, 355
- Koziorek, Jiří, 120
- Král, Martin, 37
- Krbeček, Matěj, 312
- Kunčický, Radim, 225
- Lazecký, David, 43
- Leonowicz, Zbigniew, 19
- Lukáš, Dalibor, 360
- Malý, Lukáš, 318
- Martinek, Radek, 150
- Mikolajek, Martin, 156
- Mišák, Stanislav, 25
- Mozdřeň, Tomáš, 49
- Mrovec, Martin, 324
- Nedoma, Jan, 412
- Novák, Martin, 418
- Novák, Tomáš, 65
- Novosád, Ladislav, 55
- Ondraczka, Tomáš, 162
- Orčík, Lukáš, 424
- Osuchowski, Jakub, 457
- Paláček, Stanislav, 330
- Pavelková, Radka, 168
- Pečínka, Pavel, 83
- Pecha, Marek, 336
- Petružela, Michal, 61
- Platoš, Jan, 213
- Pobořil, Radek, 429
- Przeczek, Samuel, 114
- Příbylová, Lenka, 342
- Raiman, Tom, 349
- Sang Dang Ho, 71, 90, 96
- Silber, Adam, 355
- Simkanič, Radek, 231
- Sokanský, Karel, 7, 65

Straková, Erika, 360  
Stratil, Tomáš, 435  
Szymocha, Sławomir, 463

Šaloun, Petr, 178  
Štáková, Markéta, 237  
Šuránek, Pavel, 168

Thach, Tien T., 371  
Thinh Cong Tran, 71, 90, 96  
Tomaszek, Lukáš, 244

Urbanczyk, Tomáš, 173

Vala, David, 138, 156, 168  
Vanderka, Aleš, 441  
Vantuch, Tomáš, 250  
Vašínek, Michal, 256  
Vašínek, Vladimír, 395, 400, 435  
Vozňák, Miroslav, 424  
Vrtková, Adéla, 366

Zatloukal, Filip, 261  
Zavadil, Jan, 446  
Znoj, Jiří, 267

Žabka, Stanislav, 452  
Žídek, Jan, 120, 150

Editors: Michal Krátký, Jiří Dvorský, Pavel Moravec  
Dept. of Computer Science  
VŠB – Technical University of Ostrava

Title: WOFEX 2017

Place, year, edition: Ostrava, 2017, 1<sup>st</sup>

Page count: 485

Edit: VŠB – Technical University of Ostrava,  
17. listopadu 15, 708 33 Ostrava-Poruba  
Czech Republic

Impression: 200

Not for sale.

ISBN 978-80-248-4056-7